

This is a non peer reviewed preprint submitted to EarthArxiv

It has been accepted pending minor revisions in the Treatise of Geochemistry. Expected publication date 2024. Please feel free to contact us with any suggestions!

Determining the Pressure – Temperature – Composition (P-T-X) conditions of magma storage

Penny E. Wieser¹, Matthew L.M. Gleeson¹, Simon Matthews^{2, 3}, Charlotte DeVitre¹, Esteban Gazel⁴

1. Earth and Planetary Sciences, UC Berkeley. penny_wieser@berkeley.edu, gleesonm@berkeley.edu, cdevitre@berkeley.edu

2. Earth Science Department, University of Cambridge, sm905@cam.ac.uk

3. Institute of Earth Sciences, University of Iceland, Iceland.

4. Department of Earth and Atmospheric Sciences, Cornell University, Ithaca, NY 14850, USA, egazel@cornell.edu

Determining the Pressure – Temperature – Composition (P-T-X) conditions of magma storage

Penny E. Wieser¹, Matthew L.M. Gleeson¹, Simon Matthews^{2,3}, Charlotte DeVitre¹, Esteban Gazel⁴

1. Earth and Planetary Sciences, UC Berkeley. penny_wieser@berkeley.edu, gleesonm@berkeley.edu, cdevitre@berkeley.edu

2. Earth Science Department, University of Cambridge, sm905@cam.ac.uk

3. Institute of Earth Sciences, University of Iceland, Iceland.

4. Department of Earth and Atmospheric Sciences, Cornell University, Ithaca, NY 14850, USA, egazel@cornell.edu

Key Points

- Many mineral-melt barometers have standard errors of $\pm 2\text{--}3$ kbar ($\pm 7\text{--}11$ km), which limits their ability to provide detailed constraints on magma storage in relatively thin-crust settings (MORB and OIB).
- Different models/equations can yield very different PT conditions; model choice must be considered as one of the largest sources of systematic error in a given study.
- The paucity of independent test datasets for many methods makes it difficult to truly assess their performance; statistics calculated using the calibration dataset where many variables are known are overly optimistic of performance in natural systems.
- It has become increasingly clear that melt inclusion studies which did not account for the vapour bubble may have underestimated storage depths by more than a factor of 2, requiring re-evaluation of melt inclusion volatile contents and storage depths globally.

Key words

1. Mineral Thermobarometry
2. Thermodynamics
3. Melt Inclusions
4. Fluid inclusions
5. Raman Spectroscopy
6. Hygrometry
7. Chemometry
8. Experimental Petrology
9. FAIR Research Framework
10. MELTS modelling
11. Pyroxene
12. Amphibole
13. Plagioclase

Abstract (100 words)

Determining the pressures and temperatures at which melts are stored in the crust and upper mantle, and the major element composition, redox state and volatile contents of these melts, is vital to constrain the structure and dynamics of magmatic plumbing systems. In turn, constraining these parameters helps understand the geochemical and structural evolution of the Earth's lithosphere, and periods of unrest at active volcanoes. We review common thermobarometers, hygrometers and chemometers based on mineral and/or liquid compositions, before discussing recent advances in melt and fluid inclusion barometry, Raman-based elastic thermobarometry, and thermodynamic modelling methods. Where possible, we investigate the accuracy and precision of each technique, and the implications for the application of each method to different research questions.

1. Introduction.

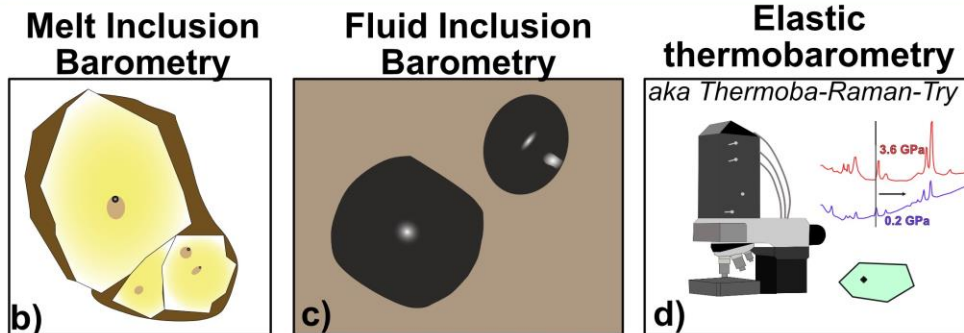
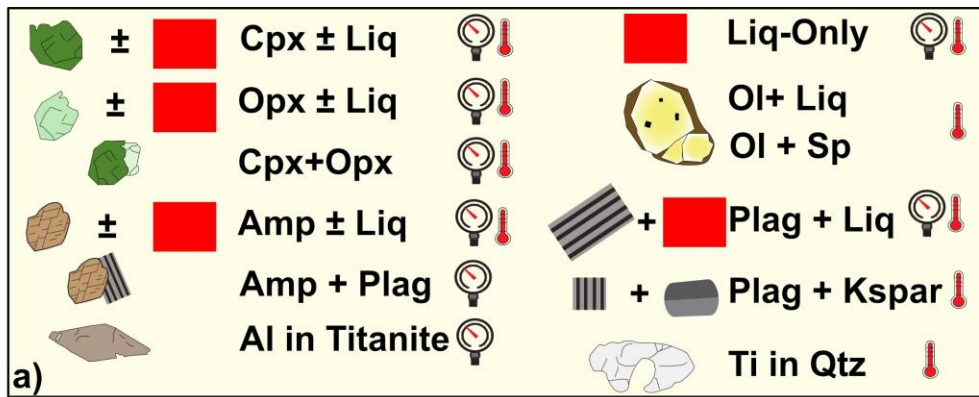
Determining the pressures, and therefore depths, at which magmas are stored and evolve in the crust and upper mantle is vital to understand the chemical and structural evolution of volcanic plumbing systems, with implications for our understanding of the formation of mineral deposits, and the evolution of the Earth's lithosphere (Lee and Anderson, 2015). Precisely constraining magma storage depths at a specific volcano using

50 past eruptive deposits can also provide vital context to help inform the interpretation of monitoring signals
51 during periods of volcanic unrest (e.g., distinguishing magmatic and hydrothermal signals, Pritchard et al., 2019).

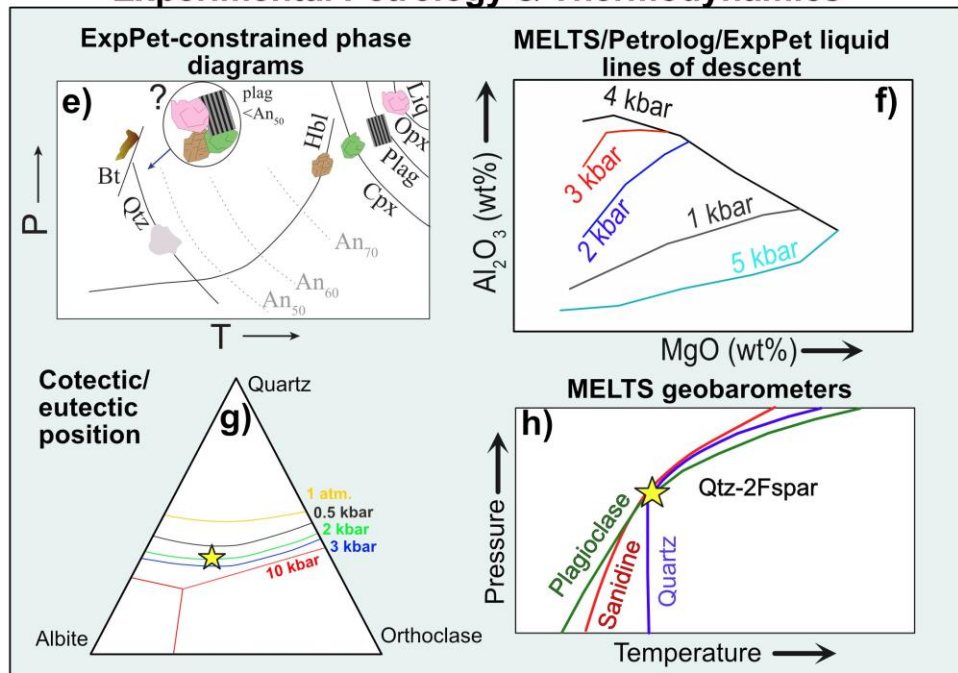
52 Constraining the temperatures of different magmatic processes can reveal the thermal evolution of
53 magmatic systems and are vital inputs for many other common workflows in igneous petrology, such as
54 calculations of timescales from elemental diffusion in erupted crystals (termed “diffusion chronometry” or
55 “geospeedometry”). In fact, because diffusion rates are strongly sensitive to temperature (following an
56 Arrhenius relationship), uncertainty in temperature is one of the largest sources of error when obtaining
57 timescales using these chronometers (Chakraborty and Dohmen, 2022; Costa et al., 2020). For example, Mutch
58 et al. (2019a) show that timescales calculated from Cr diffusion in spinel change from ~4000 years at 1190°C to
59 ~1000 yrs at 1230°C. Thus, uncertainty in temperatures affects interpretations of timescales of crustal residence
60 (Mutch et al., 2019a), re-awakening from quiescence to eruption (Shamloo and Till, 2019), and calculations of
61 magma ascent rates (Mutch et al., 2019b). Of course, accurately constraining magma storage depths is also vital
62 for magma ascent rate calculations, where the speed is calculated by dividing the depth to the inferred magma
63 body by the time calculated from diffusion chronometry (Barth et al., 2019; Klügel, 1998).

64 Here, we describe a multitude of approaches to determine the pressures (P) and temperatures (T) at
65 which magmas were stored in the lithosphere, as well as ways to determine the chemistry of stored melts (Fig.
66 1). We pay particular attention to differences between models (Section 1.1) and the precision and accuracy of
67 calculations (Section 1.2). For barometers, we first evaluate variations in crustal thickness in a wide variety of
68 tectonic settings to compare with estimates of the precision of different barometry methods (Section 1.3). Then,
69 we review the methods used to convert measured mineral compositions (with or without an equilibrium melt)
70 into magma storage pressures and temperatures (mineral barometry and thermometry), and to calculate the
71 chemistry and H₂O contents of the melts from which a specific mineral composition grew (chemometry and
72 hygrometry respectively, Section 2).

Mineral Thermobarometry



Experimental Petrology & Thermodynamics



73

74 *Figure 1: Summary of some of the methods used to determine pressures and temperatures of magma storage.*
 75 *Part e) adapted from Rutherford (2003), f) from Cashman and Edmonds (2019), g) and h) adapted from Gualda*
 76 *et al. (2012) and Gualda and Ghiorso (2014), respectively.*

77

78

79 We also evaluate the methods and uncertainties involved in melt inclusion barometry, with a specific
 80 focus on the influence of CO₂ stored within melt inclusion vapour bubbles on calculated pressures (Section 3).

81 The general proliferation of Raman spectroscopy in the Earth Sciences (Dubessy et al., 2012) has not only been
 82 important for performing direct measurements of melt inclusion vapour bubbles; it has also pushed forwards
 83 two other barometric methods. First, Raman spectroscopic measurements of fluid inclusions can provide a
 84 substantially faster method of calculating storage depths than traditional microthermometric techniques
 85 (Section 4). Second, Raman measurements of mineral inclusions in-situ can also be used to calculate pressures
 86 and temperatures (thermobarometry, Section 6). Experimental petrology is not only vital for the formulation
 87 and calibration of mineral-melt thermobarometers and volatile solubility models, it can also be used to provide
 88 direct constraints on magma storage in a specific volcanic system (Section 7). Finally, we discuss approaches
 89 using thermodynamic constraints on phase stability in igneous systems (Section 8), methods not covered in
 90 detail in this review (Section 9) and summarize the general proliferation of community data repositories and
 91 open-source tools to help inform model calibration, and aid calculations of magma storage conditions (Section
 92 10).

93 1.1 Assessing and comparing models

94 When calculating pressure, temperature, and/or melt chemistry from the composition of erupted
 95 melts, crystals and their inclusions, the result can be highly sensitive to the choice of
 96 model/equation/parameterization, relating the measured quantity (e.g., Cpx, Amp, melt inclusion composition)
 97 to the intensive variable (e.g., P, T). Below, we discuss the origin of all these different models, and best practices
 98 for model intercomparison.

99 Mineral thermobarometry (Section 2) utilizes chemical reactions involving the crystallization or re-
 100 equilibration of minerals which are accompanied by a change in volume (sensitive to P) and/or a change in
 101 entropy (sensitive to T, e.g., Putirka, 2008). Chemometry (and hygrometry) relies on the fact that the
 102 composition of crystallizing/re-equilibrating phases is sensitive to the composition of the melt phase. Some
 103 thermobarometry and chemometry expressions are firmly rooted in thermodynamics, with compositional terms
 104 and the functional form of the equation determined from a specific reaction. Typically, these expressions have
 105 coefficients attached to thermodynamic terms which are calibrated empirically using the measured
 106 compositions of minerals in experiments conducted at well-constrained P-T-fO₂-H₂O conditions (e.g., the
 107 Plagioclase-Liquid hygrometer of Waters and Lange, 2015).

108 More commonly, available equations have a general form based on thermodynamics, with the addition
 109 of more empirically derived terms to improve the fit to the calibration dataset (e.g., Neave and Putirka, 2017).
 110 For example, many of the Cpx-Liq barometers of Putirka (2008) have a functional form based on Jadeite
 111 exchange between the liquid and Cpx, which is associated with a change in volume, so is P sensitive (Putirka et
 112 al., 1996):

$$113 \quad P = a + \frac{bT}{10^4} + \frac{cT}{10^4} \ln(\text{Jd}^{\text{Cpx-Liq}}) + \dots [\text{Equation 1}]$$

114 Additional terms help to improve the fit between the calculated parameter and the known experimental
 115 conditions. The inclusion of these terms may be informed at least in part by thermodynamic reasoning (e.g.,
 116 Masotta et al., 2013; Neave and Putirka, 2017; Putirka, 2008). For example, Putirka (1996) EqP1 has a term for
 117 the cation fractions of Na and Al:

$$118 \quad \text{EqP1} = \text{Equation 1 terms} \dots + 367 (X_{\text{Na}}^{\text{Liq}} * X_{\text{Al}}^{\text{Liq}}) [\text{Equation 2}]$$

119 The fact that the best fit involved the multiplication of Na and Al cation fractions implies that these two
 120 components have identical activity coefficients (Putirka et al., 1996). However, the thermodynamic
 121 interpretation is often obscured by decisions to reduce the complexity of equations, such as wanting to avoid
 122 introducing multiple temperature-dependent terms (see Equation 12 of Putirka et al., 1996). In general as
 123 calibration datasets have grown larger, more empirical terms have been added that have a less clear
 124 thermodynamic basis. For example, Putirka (2008, Eq31) has many additional terms relative to EqP1, including
 125 terms for the Ca, Na, K, Si, Mg and Fe_t liquid cation fractions, H₂O in the liquid, and for EnFs, DiHd, and Al cation
 126 fractions in the Cpx:

$$127 \quad \text{Eq31} = \text{Equation 1 terms} \dots + 106 X_{\text{Ca}}^{\text{Liq}} - 166 (X_{\text{Na}}^{\text{Liq}} + X_{\text{K}}^{\text{Liq}})^2 - 50.2 X_{\text{Si}}^{\text{Liq}} * (X_{\text{Mg}}^{\text{Liq}} + X_{\text{Fe}}^{\text{Liq}}) - 3.2 \log(\text{DiHd}) -$$

$$128 \quad 2.2 \log(\text{EnFs}) + 0.86 \log(X_{\text{Al,6 cat}}^{\text{Cpx}}) + 0.4 * \text{H}_2\text{O} [\text{Equation 3}]$$

129 New models not only arise through the addition of new empirical terms, but also through the recalibration of
 130 the coefficients of older equations. For example, Masotta et al. (2013) recalibrate the coefficients of Putirka

131 (2008) for a new dataset of alkaline magmas. Other thermobarometers are purely empirical, including terms and
132 mathematic expressions like logs, exponentials, and different powers which improve the fit to the calibration
133 dataset without a firm tie to the thermodynamics of a specific chemical reaction. For example, the liquid-only
134 thermometer of Helz and Thornber (1987) was calibrated based on the linear relationship between MgO and T
135 in experiments on the Kilauea Iki lava lake. The amphibole-only barometer of Ridolfi and Renzulli (2012) uses
136 multivariate least squares regression to determine the relationship between P and amphibole composition
137 across a number of different P ranges, with highly variable functional forms (Eq1a, Eq1b and Eq1e take the
138 exponential of amphibole cation fractions, Eq1c and Eq1d do not). The results from these equations are selected
139 or combined using an algorithm to give a single P, this algorithm was then tweaked by Ridolfi, (2021), generating
140 yet another model.

141 Most recently, machine learning approaches using regression trees have been used to parameterize the
142 relationship between mineral and melt composition and experimental conditions (e.g., Higgins et al., 2022;
143 Jorgenson et al., 2022; Petrelli et al., 2020). Unlike purely thermodynamic, or mixed thermodynamic-empirical
144 expressions, these approaches do not use any underlying thermodynamic knowledge. They are trained using
145 measured oxide contents, rather than thermodynamically informed mineral components such as Jadeite,
146 Diopside etc. The lack of thermodynamic basis may affect their ability to extrapolate beyond the compositions
147 and P-T conditions for which they are calibrated, but one advantage is that these models can be easily updated
148 as new experimental data becomes available if the code for model training is released.

149 The diversity of empirical, thermodynamic, and machine-learning models for mineral-based
150 thermobarometry/hygrometry/chemometry has resulted in a somewhat overwhelming choice of models to
151 calculate magma storage conditions. Concerningly, these different models can return vastly different results.
152 Wieser et al. (2023a) show that different Cpx-Liq and Cpx-only thermobarometers applied to the same Cpx-Liq
153 pair passing equilibrium tests yield pressures spanning >10 kbar and temperatures spanning >100°C. Clearly,
154 model choice is one of the largest sources of uncertainty when performing such calculations.

155 Melt inclusion barometry uses a volatile solubility model to calculate the pressure at which a specified
156 melt composition (major+volatile elements) is volatile saturated (for a specific temperature). These solubility
157 models range from being purely empirical (Liu et al., 2005; Shishkina et al., 2014) to models formulated in a
158 purely thermodynamic framework (Ghiorso and Gualda, 2015; Papale et al., 2006). Some models lie between
159 these end members, having a general form indicated by thermodynamics and some empirical coefficients
160 accounting for silicate melt composition (semi-empirical, e.g., Dixon, 1997; Iacono-Marziano et al., 2012). Even
161 for fully thermodynamical models, the sign and magnitude of many coefficients attached to thermodynamic
162 terms have been criticized as being physically implausible (see Ghiorso and Gualda, 2015 and Wieser et al. 2022a
163 for discussion of the Papale et al. 2006 model). In addition to their different functional forms, the calibration
164 datasets of solubility models are also highly variable with respect to the range of melt compositions, fluid
165 compositions, and P and T. For example, the model of Shishkina et al. (2014) was calibrated on variably alkaline,
166 relatively mafic melts, and expresses volatile solubility empirically using the cation fractions of Ca, K, Na, Mg, Fe,
167 Si and Al for CO₂, and K and Na for H₂O. In contrast, the solubility model of Dixon (1997) was calibrated on a
168 more restricted range of relatively mafic tholeiitic to alkaline melt compositions. This model has a
169 thermodynamic form, with an empirical correction for the effect of melt composition that is only dependent on
170 the concentration of SiO₂ in the melt. The model MagmaSat (Ghiorso and Gualda, 2015) was calibrated on a very
171 wide range of melt compositions (tholeiite and alkaline, from basalts to rhyolites), and is a fully thermodynamic
172 solubility model sensitive to all the commonly measured major oxide species. Unsurprisingly, given these
173 differences in model formulation and calibration datasets, calculated saturation pressures can vary greatly
174 between models, with systematic offsets of at least a factor of two not being uncommon (Wieser et al., 2022a).

175 In stark contrast to uncertainties associated with model choice when performing mineral
176 thermobarometry or melt inclusion barometry, fluid inclusion barometry (Section 4) relies on the CO₂ equation
177 of state to convert the measured density of a CO₂-rich fluid into a P for a specified entrapment temperature.
178 Other than an ideal gas law (which does a poor job at high P), different published CO₂ equation of states predict
179 very similar P for a given CO₂ density and T (~ 1–5% difference, Böttcher et al., 2012; Lamadrid et al., 2017; Span
180 and Wagner, 1996; Sterner and Pitzer, 1994; Wieser and DeVitre, 2023). For example, at 1150°C for $\rho_{CO_2} = 0.8$
181 g/cm³, the relatively simple empirical expression of Sterner and Pitzer (1994) gives 5.008 kbar, while the more
182 complex thermodynamic model of Span and Wanger (1996) gives 4.956 kbar (~3% difference). However, the
183 conversion between measured CO₂ density to depth is substantially less simple when trapped fluids contain
184 other species, such as H₂O or SO₂ (Hansteen and Klugel, 2008; Hurai, 2010). It is difficult to estimate the initial
185 molar ratios of each species, and EOS for these mixed fluids are poorly constrained (if parameterized at all). Fluid

186 inclusion barometry is also not immune to systematic error; re-equilibrium of the host crystal during magma
187 ascent can increase the inclusion volume, and thus reduce the CO₂ density (and thus the calculated
188 pressure/depth, Hansteen and Klugel, 2008; Wanamaker and Evans, 1989).

189 Thermodynamic approaches to determining the conditions of magma storage and evolution are also
190 sensitive to the choice of model (Section 8). Thermodynamic models are typically constructed from two key
191 components: (i) a dataset of standard state properties (e.g., enthalpy of formation, heat capacity, etc.) for all
192 minerals of interest, and (ii) solution models for phases with variable compositions (describing how composition
193 influences the thermodynamic properties of the phase). Within igneous petrology and volcanology the MELTS
194 ‘family’ of thermodynamic models are the most widely used (Ghiorso et al., 2002; Ghiorso and Sack, 1995;
195 Gualda et al., 2012). The original MELTS model was developed by Ghiorso and Sack (1995), building on the
196 thermodynamic database of Berman (1988) to include thermodynamic models of relevant igneous solid
197 solutions (e.g., Ghiorso, 1990; Ghiorso and Sack, 1991; Sack and Ghiorso, 1994, 1991, 1989). Since the release
198 of this original MELTS model, various updates have been published. pMELTS includes a revised liquid
199 thermodynamic model optimised for mantle-like bulk compositions (Ghiorso et al., 2002). Rhyolite-MELTS
200 v.1.0.2 incorporates changes to the thermodynamic properties of quartz and the orthoclase endmember of the
201 alkali feldspars that enable the eutectic behaviour of high-silica rhyolitic magmas to be recreated (i.e.
202 crystallization over a narrow T range, Gualda et al., 2012). Rhyolite-MELTS v1.2.0 incorporates the mixed H₂O-
203 CO₂ fluid model MagmaSat, and is recommended for use away from the granitic ternary minimum. Rhyolite-
204 MELTSv1.1.0 incorporates the updated CO₂ solubility model, but retains the old H₂O solubility model of rhyolite-
205 MELTSv1.0.2 for calculations at the ternary minimum (Ghiorso and Gualda, 2015).

206 An alternative group of thermodynamic models developed by Tim Holland, Roger Powell and co-
207 workers (Holland and Powell, 2004, 1998, 1990) have traditionally been utilized in metamorphic studies
208 (Tamblyn et al., 2020), but have recently been updated for applications to mantle melting and igneous systems.
209 For example, Jennings and Holland (2015) expand the model system, optimizing its performance for calculations
210 of peridotite melting behaviour and the phase relationships of basaltic liquids at crustal to mantle conditions.
211 Most recently, Holland et al. (2018) presented an updated thermodynamic database that is calibrated on a range
212 of compositions, from peridotites through to granites. The Holland dataset is mostly accessed through a variety
213 of software tools. THERMOCALC calculates the location of known phase boundaries and mineral reactions
214 (Powell et al., 1998). Alternatively, Perple_X (Connolly, 2009, 2005) and Theriak-Domino (de Capitani and
215 Petrakakis, 2010) use a Gibbs Free Energy minimization approach to calculate the phase assemblage and
216 compositions specified P-T conditions.

217 Comparisons between the MELTS and Holland-Powell families of models are relatively uncommon;
218 Jennings and Holland (2015) compare the results of mantle melting calculations, and Hernández-Urbe et al.
219 (2022) compare the equilibrium crystallization behaviour of an N-MORB magma. Importantly, Hernández-Urbe
220 et al. (2022) do not compare fractional crystallization pathways, noting that these would be “relatively laborious”
221 with current software tools. The recent release of MAGEMin, a Gibbs Free Energy minimisation package utilizing
222 the Holland et al. (2018) thermodynamic models written in the programming language C (Riel et al., 2022) allows
223 MELTS-like workflows to be performed including fractional crystallization. MAGEMin has a Julia interface and
224 can be run in Python3 using pyMELTScalc (Gleeson et al. 2023), greatly aiding model intercomparison between
225 the Holland and MELTS databases (see Section 8). There are also several more empirical models which have
226 been used as alternatives to MELTS to model fractional crystallization in magmas, and therefore could place
227 constraints on P and T (see Section 8). These include COMAGMAT (Ariskin et al., 1993) and Petrolog3
228 (Danyushevsky and Plechov, 2011). In Section 8, we show that the choice of thermodynamic model to use (and
229 even the version of MELTS used) has a large influence on calculations of magma storage conditions (see also
230 Hernández-Urbe et al., 2022).

231

232 1.2. Statistics to compare models

233 When trying to decide which model/equation to use to calculate magma storage conditions, and to
234 assess whether the chosen method has sufficient resolution to address the science question of interest, it is
235 important to assess both accuracy and precision. Accuracy describes how close the measurement or model
236 prediction is to the true value, while precision describes how close repeated measurements are to one another.
237 For example, if you measure a small, very homogenous region of a Cpx crystal five times using an electron probe
238 microanalyser (EPMA), and calculate Cpx-only pressures from these measurements, you may obtain 5, 5.5, 6,
239 4.9, and 6.2 kbar. The precision could be quantified using 1 standard deviation of these measurements (e.g.,

240 ±0.47 kbar). However, the Cpx may have formed at 8 kbar, in which case these calculations are relatively precise,
 241 but inaccurate (mean offset of 2.5 kbar). It is also worth distinguishing between random and systematic errors.
 242 Random error describes scatter about the true value (affecting precision, not accuracy), while systematic error
 243 describes a constant offset from the true value (affecting accuracy not precision).

244 Most publications calibrating a new mineral-melt thermobarometer or chemometer describe the fit
 245 between calculated and experimental values for a given parameter using RMSE and R^2 values (see Table 1,
 246 RMSE=SEE for linear regressions). When equations are applied to natural systems, these RMSE errors are often
 247 quoted as the error on the calculation. This is problematic for several reasons. The RMSE and R^2 alone do not
 248 properly distinguish between random and systematic error, so fails to capture the complexity of the error on
 249 the calculation. 6 different metrics (Table 1) can be useful to assess model performance. In this review, we put
 250 particular emphasis on the Mean Bias Error (MBE), the gradient and intercept in addition to R^2 and RMSE help
 251 to identify systematic error.

252

Metric	Good at	Bad at
R^2 value: Correlation coefficient of the linear regression between the measured (x) and predicted (y) value.	Assessing precision and random uncertainty. Low precision (lots of random uncertainty) = low R^2 value.	Assessing accuracy and systematic uncertainty.
Gradient and Intercept of the linear regression	Assessing systematic uncertainty, which will generate a gradient different from 1, and an intercept different from zero.	Assessing precision/random uncertainty (as averages all measurements).
Root mean square error (RMSE) aka. SEE $RMSE = \sqrt{\frac{1}{N} \sum_{i=1}^N (x_i - y_i)^2}$	Describes how concentrated the data is around the linear regression.	Struggles to distinguish between low precision and accurate vs. high precision with a systematic offset. Sensitive to outliers.
Mean Absolute Error (MAE) $MAE = \frac{1}{N} \sum_{i=1}^N x_i - y_i $	Similar to the RMSE but no squared term. Gives less weight to larger errors than the RMSE	Struggles to distinguish between low precision and accurate vs. high precision with a systematic offset
Mean Bias Error (MBE) $MBE = \frac{1}{N} \sum_{i=1}^N (x_i - y_i)$	Identifies average model bias, as no absolute or squared term.	Doesn't identify random error, as + and - errors cancel out.

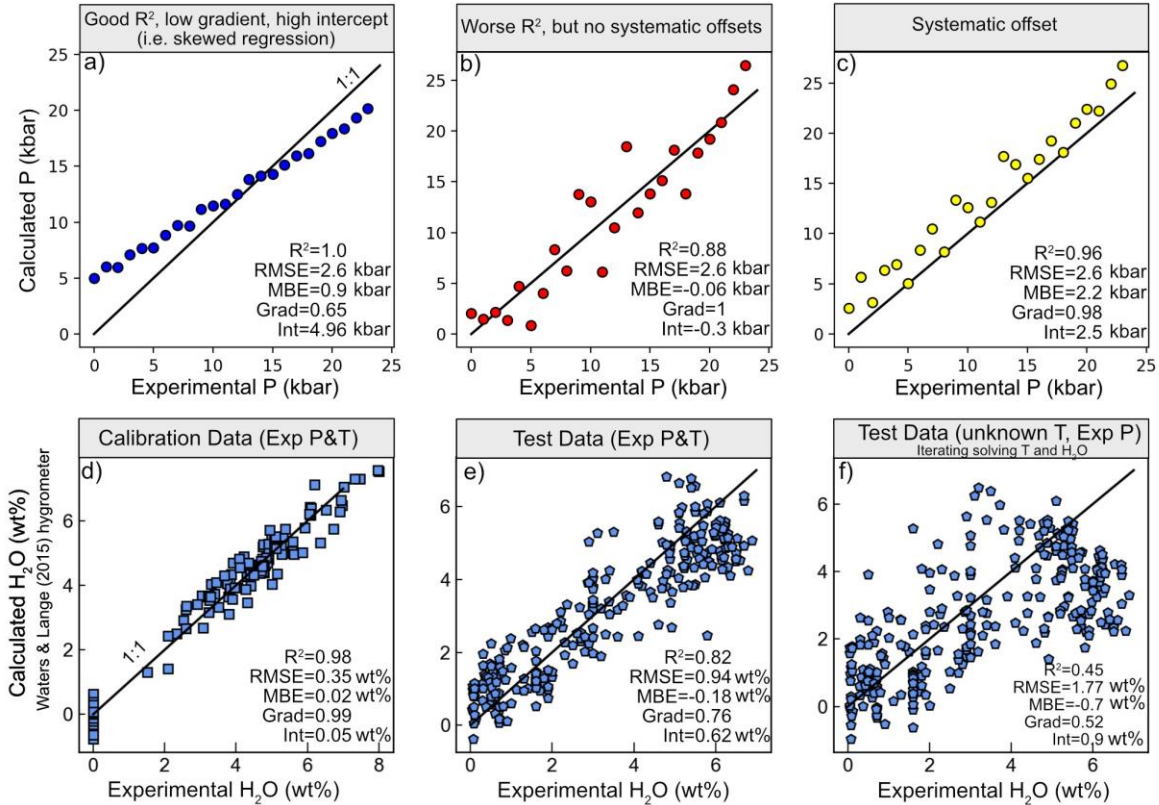
253

254 *Table 1: Metrics used to assess models, where x is the measured parameter (e.g., P, T) and y is the model-*
 255 *predicted parameter. RMSE and SEE are identical for a linear regression, for higher order regressions, they differ*
 256 *as only the SEE accounts for the degrees of freedom.*

257

258 In Fig. 2, we demonstrate the issues associated with using *only* the root mean square error (RMSE)
 259 and R^2 to assess model performance. Instead, we suggest that the RMSE, R^2 , gradient, intercept and MBE should
 260 all be presented on figures to allow assessment of both random and systematic uncertainty (e.g. Putirka et al.
 261 2003). To demonstrate this, we compare the relative performance of three hypothetical barometers, plotting
 262 the experimental P on the x axis, and the calculated P on the y axis (Fig. 2). All barometers have the same RMSE
 263 error. However, it is visually apparent that their performance varies greatly. While Fig. 2a has a very high R^2
 264 value, its low gradient and high intercept reveals that it substantially overpredicts P at $P < 12$ kbar, and
 265 underpredicts P at $P > 12$ kbar. While Fig. 2b has a lower R^2 value, it has no substantial systematic offsets, meaning
 266 it is a far more accurate barometer across a wide range of pressures than that shown in Fig. 2a (indicated by the
 267 gradient close to one, an intercept close to zero, and the low MBE). The barometer in Fig. 2c also has a gradient

268 close to 1, but the higher intercept and MBE indicate that it systematically overpredicts at all pressures. Clearly,
 269 if you wish to distinguish the absolute depth of magma storage, perhaps to compare to geophysical inversions
 270 of magma storage depths, or signals of unrest, the barometer in Fig. 2b is the best, despite its lower R^2 . However,
 271 if you only wish to distinguish differences in storage pressures between different crystal populations (without
 272 caring about the actual depth), the barometer in Fig. 2a is the best, as it is the most precise. Use of all 5 metrics
 273 in tandem is essential for identifying systematic and random uncertainty.



274
 275 *Figure 2: Schematic figure showing the limitations of using just R^2 and RMSE to assess thermobarometers. a-c)*
 276 *Three hypothetic barometers with the same RMSE, but vastly different performance. d-f) Comparing*
 277 *experimental and calculated H_2O using the Waters and Lange (2015) hygrometer for: d) the calibration dataset*
 278 *using experimental T and P, e) the ArcPL dataset using experimental T and P, and f) the ArcPL dataset iteratively*
 279 *solving H_2O and T (using Eq24a of P2008, see Section 2.8 for more detail).*

280
 281 It is also challenging to directly compare the quoted RMSE and R^2 values from different models,
 282 because these statistics are not equivalent. Many of the statistics reported in the abstracts of papers proposing
 283 new equations describe how well the model fits the calibration dataset (e.g., the commonly quoted ± 1.7 kbar
 284 value for the Cpx-Liq barometer of Putirka et al. 2003; the ± 0.35 wt% H_2O value for the Waters and Lange, 2015,
 285 Plag-Liq hygrometer). In other papers, the number reported in the abstract is the fit to a test dataset (e.g.,
 286 Jorgenson et al., 2022; Petrelli et al., 2020), which inevitably makes the equation look “worse” than one assessed
 287 using calibration data. Indeed, it is apparent in the main text of many thermobarometry papers that the RMSE
 288 is much larger when applied to test data not used in the calibration dataset, or when applied to a global dataset
 289 containing a mix of new and calibration data (e.g., RMSE=4.2 kbar for the Cpx-Liq Putirka et al. 2003 barometer
 290 vs. the commonly quoted RMSE=1.7 kbar, Fig. 3a). The size of the test dataset can also vary greatly, influencing
 291 the statistics. For example, the test dataset of Petrelli et al. (2021) only contains 59 experiments conducted at
 292 <15 kbar, which come from only 4 studies. Some reported statistics are calculated using only experiments for a
 293 select subregion of compositional space (e.g., Neave and Putirka, 2017 for Cpx-Liq equilibria in tholeiites), while
 294 others report the fit for a global dataset with a much larger compositional range, again leading to larger apparent
 295 errors (e.g., Putirka 2008). For many equations, there is so little spare data for each composition, all data was
 296 used for calibration, so the authors do not use a test dataset (e.g., Waters and Lange, 2015 for Plag-Liq
 297 hygrometry, Giorso and Gualda, 2015 for volatile solubility). Additionally, some proportion of the error in any
 298 quoted statistic (e.g. RMSE) will represent uncertainty in the experimental data used for testing (both analytical

299 and experimental sources of scatter), making it difficult to differentiate failures of the calibration equation vs.
300 the data used to assess it. This is a particular problem for models where higher quality data was saved for
301 calibration, with less strict filters applied to test data (Putirka et al. 2003, 2008, K. Putirka, written comms).

302
303 Ideally when calibrating any new equation/model (for thermobarometry, chemometry, volatile solubility
304 modelling etc.), data should be subdivided into a test dataset and a calibration dataset. It is then standard
305 practice for many machine learning workflows to further subdivide the calibration dataset into train and
306 validation datasets (this split may be made repeatedly during model training, e.g., Petrelli et al. 2020). The train-
307 validation split allows investigation of the effect of adding/removing terms, changing the regression algorithm,
308 and tweaking the regression tuning parameters. Only once the model is fully tweaked should it be applied to the
309 test dataset to assess its performance on unseen data. While it is then tempting to continue to change
310 parameters to improve the fit to the test dataset, this strategy is generally criticized in the world of machine
311 learning, as it means the testing dataset has “leaked” into the training of the model, so no longer provides an
312 independent assessment of the model validity. The complete isolation of a testing dataset prior to model tuning
313 and choice of parameters is important for machine learning and other regression workflows, because otherwise
314 it is difficult to assess model performance on samples which are distinct in P-T-X space from those used in model
315 calibration (Lones, 2021). To address this, in some biomedical studies, a test dataset is kept completely separate,
316 and held under “lock and key” by a honest broker to avoid such leakage (Dobbin and Simon, 2011; Shedden,
317 2008). In igneous petrology, the difficult balance to strike is between having a large test dataset to robustly
318 assess model performance, versus having too small a calibration dataset to adequately capture variation in melt
319 or mineral composition.

320
321 It is also worth noting that the RMSE value is an average for the fit across the entire P or T range, while the actual
322 error when applied to natural samples will vary as a function of P and T. RMSE and R^2 values are also not always
323 calculated across the same P and T range (e.g., 0–40 kbar for Putirka, 2008, 0–20 kbar for Petrelli et al. 2020).
324 These pressure ranges are also often far larger than the pressure ranges of interest in volcanic systems, and
325 models tend to perform worse at lower pressures (Putirka, 2008).

326
327 Finally, mineral-melt thermobarometers and chemometers are often assessed using experimental data, where
328 T, P (and often H_2O and fO_2) are constrained. In natural systems, it is common that several intensive parameters
329 are poorly constrained. For example, a T and H_2O -sensitive barometer is normally assessed using the test
330 dataset, inputting the experimental temperature and the measured H_2O content in the experimental charge.
331 Similarly, thermometers with P-sensitive terms are normally assessed using the experimental P, and
332 hygrometers are assessed using experimental T and P. In natural systems, the most common scenario is that
333 *both* P and T are unknown, so must be iteratively solved using a thermometer and a barometer. Thus, to estimate
334 a realistic error when applied to natural systems, statistics should be calculated by iteratively solving the same
335 variables that would be unknown in natural samples. Of course, this adds additional uncertainty; when applying
336 a T-sensitive barometer, any deviation from the true T will affect the calculated P. Additional uncertainties
337 related to parameters which cannot be iteratively solved (e.g., uncertainty in H_2O in Cpx-Liq thermobarometers)
338 should be propagated with Monte-Carlo techniques using a realistic uncertainty for H_2O in a specific system of
339 interest (e.g. Wieser et al. 2022b).

340
341 Using the T-sensitive Plag-Liq hygrometer of Waters and Lange (2015) as an example, we
342 demonstrate how the apparent performance of an equation can vary based on the number of constrained
343 intensive parameters, and the dataset used to test it. First, we show H_2O contents for the model calibration
344 dataset using experimental temperatures (Fig. 2d). This comparison yields the RMSE quoted in the abstract of
345 the Waters and Lange (2015) paper that is commonly quoted in the literature as the error on the method (± 0.35
346 wt%). Next, we evaluate this hygrometer using a newly compiled test dataset of variably hydrous experiments
347 at 0–17 kbar spanning from basalts to dacites (ArcPL, Wieser et al., 2023a-b). We only include experiments where
348 H_2O was measured using quantitative methods (Fourier Transform infrared spectroscopy - FTIR, secondary ion
349 mass spectrometry - SIMS, Raman, calibrated volatiles-by-difference, solubility laws, see Section 2.8), and
350 discard experiments which were present in the Waters and Lange (2015) calibration dataset. Using experimental
351 T to calculate H_2O for this new test dataset yields statistics that are noticeably worse than those calculated from
352 the calibration dataset (e.g., ± 0.94 wt% vs. ± 0.35 wt%, Fig. 2e). In a scenario where T is not known (i.e., when
353 this method is applied to natural systems), the statistics decline further: iterating the hygrometer with the Plag-
354 Liq thermometer of Putirka (2008, Eq24a) results in a RMSE of ± 1.77 wt% (Fig. 2f, see Section 2.8 for detailed

355 discussion). Thus, simply quoting the uncertainty from the original publication may underestimate the error by
356 a factor of ~5 when applied to natural systems. We observe similarly large declines in model performance
357 moving from calibration to test data to iterative solving for many mineral-melt equilibria (see Section 2, and
358 Wieser et al. 2023a).

359

360 Thus, at present, it is not possible to select the best thermobarometer for a given application simply
361 based on quoted statistics alone. Instead, to pick the most suitable model, it is worthwhile to check the natural
362 compositions of interest vs. the calibration range of the model of interest (calibration datasets for many models
363 are available in Thermobar, Wieser et al. 2022b). After identifying models calibrated on suitable compositions,
364 we encourage authors to compile a test dataset of experimental compositions most similar to their system.
365 Ideally these experiments would not have used during calibration of the equation. If the planned workflow in
366 the natural system will involve iterative calculations, these same iterative workflows should be applied to the
367 test dataset. These tests will provide a more realistic estimate of the uncertainty associated with the calculation
368 than simply quoting RMSE values. If there is very little data to help pick, it may be best to perform calculations
369 using several different equations calibrated on relevant compositional and P-T ranges. An average for all these
370 models could be calculated, with the difference between models giving insight into the error in the calculation.
371 At the moment, only a very small proportion of studies compare the results from multiple equations (e.g.,
372 Erdmann et al., 2016; Geiger et al., 2018; Sas et al., 2017; Sheehan and Barclay, 2016 for Cpx-Liq equilibrium,
373 Rasmussen et al., 2022; Wieser et al., 2021 for volatile solubility).

374

375 **1.3. What accuracy and precision are required?**

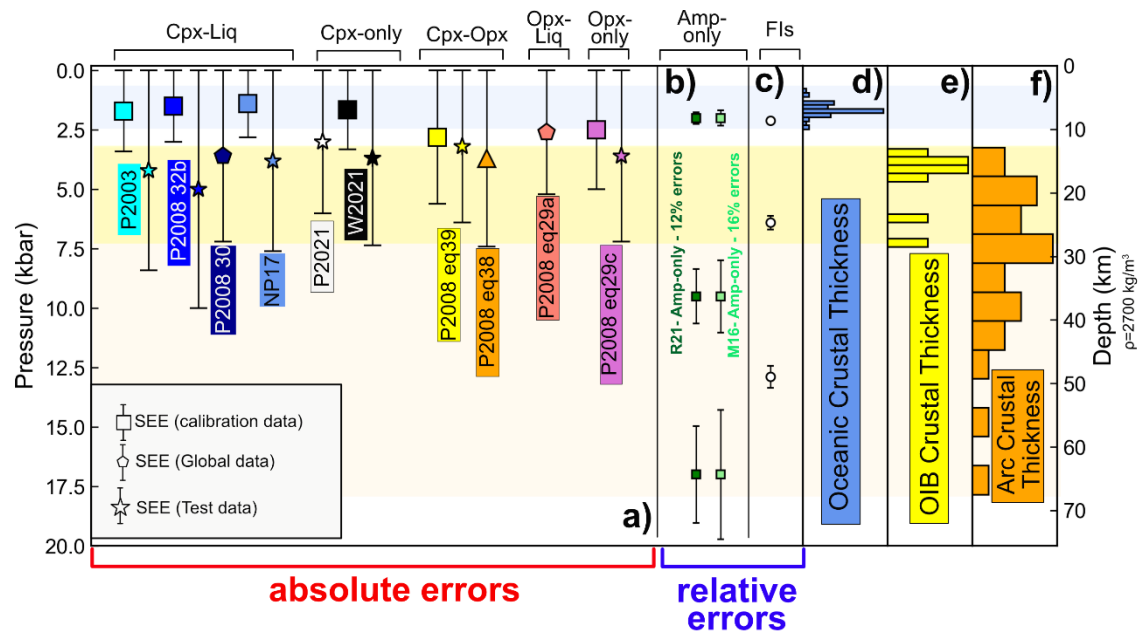
376 In the 2008 RiMG short course, K. Putirka described his Cpx barometer as: '*a chisel, not a pen knife*' (K.
377 Putirka, written comms). Once realistic estimates are made of the precision and accuracy of different
378 thermobarometers using relevant test datasets, it is worth thinking about what scientific questions can be
379 addressed with confidence within the associated uncertainties of each methods. Petrological barometers
380 calculate pressure, which can be converted into depth by making assumptions about crustal and upper mantle
381 densities. Converting pressures to depths allows comparisons to geophysical inversions of magma storage
382 locations within the crust (e.g., Rasmussen et al., 2022), and to field observations in exposed crustal and upper
383 mantle sections. Thus, it is useful to think of errors in the context of crustal and lithospheric thicknesses
384 worldwide.

385 Oceanic crust formed away from the influence of mantle plumes ranges in thickness from ~5–8.5 km,
386 with an average thickness of $\sim 7 \pm 0.8$ km (White et al., 1992). Assuming an average density of 2900–3000 kg/m³
387 (Afonso et al., 2007), this corresponds to an average Moho pressure of ~2 kbar. To be able to conclusively pull
388 apart different crustal storage geometries (e.g., upper vs. lower crust) and distinguish between storage regions
389 at different levels in the crust, a RMSE error of ± 0.25 –0.5 kbar would be needed. No mineral-based barometers
390 applicable to MORB lavas achieve anything like this precision (Fig. 3a vs. d). In fact, even if magma is stored
391 below the Moho (e.g., in slow spreading ridges, Bennett et al., 2019; Drignon et al., 2019), available mineral-
392 melt models can't confidently differentiate upper mantle vs. crustal storage.

393 Crust in OIBs is thicker than in MORB settings because the newer volcanic pile rests on top of older
394 oceanic crust (total crustal thickness of 14–24 km in Hawai'i, Leahy et al., 2010; 14–15 km in La Palma, Ranero
395 et al., 1995), and/or because the plume increases melting extents at the mid-oceanic ridge (e.g., ~11–39 km in
396 Iceland). The elevated crustal thickness in OIBs, corresponding to pressures of 3–4 kbar or greater, means that
397 mineral-based barometers with uncertainties of 2–3 kbar can begin to distinguish storage at the Moho vs. the
398 shallow (e.g., Gleeson et al., 2021). Mineral-based barometers are also aided by the fact that OIB lithosphere
399 can be extremely thick relative to MORB as a result of conductive cooling as the oceanic crust moves away from
400 the ridge (e.g., 45–60 km thick in the Galápagos, Gibson and Geist, 2010; 50–110 km thick in the Hawaiian
401 Islands, Li et al., 2004), and many OIB magmas are stored at sub Moho depths (e.g., Barker et al., 2021; DeVitre
402 et al., 2023; Gleeson et al., 2021). Again, this makes uncertainties of 2-3 kbar less problematic. It is only in
403 volcanic arcs, and particularly continental arcs with thicker crust (Profeta et al., 2016) that mineral-melt
404 barometers can reliably distinguish between storage in the upper, middle and lower crust.

405 While mineral-melt thermobarometers often show a reasonably constant error regardless of the
406 pressure, solubility models show a clear increase in uncertainty at higher volatile contents, so errors are

407 commonly described using percentage errors (e.g., $H_2O = \pm 10\%$ and $CO_2 = \pm 20\%$ for Shishkina et al., 2014,
 408 $H_2O = \pm 10\%$ and $CO_2 = \pm 17\%$ for Iacono-Marziano et al., 2012). Systematic offsets between solubility models also
 409 tend to increase reasonably proportionally with increasing P (Wieser et al., 2022a). Even the large errors
 410 resulting from volume estimates during vapour bubble reconstructions when performing melt inclusion
 411 barometry (more detail in section 3) are percentage, not absolute errors. Many uncertainties associated with
 412 fluid inclusion barometry scale with pressure (Fig. 3, see Section 4). In general, methods with percentage errors
 413 that scale with the value of the quantity, rather than absolute errors, are better suited to distinguishing subtle
 414 variations in magma storage in relatively thin-crustal tectonic settings (Fig 3b-c). Interesting, Ridolfi (2021) and
 415 Mutch et al. (2016) express the errors on their amphibole barometers as percent errors (e.g. 12- 16%, see Fig.
 416 3b), although, these errors only describe the fit to the calibration data, and their magnitude is highly debated
 417 (see Erdman et al. 2016, and section 2.6).



418

419 *Figure 3: Comparison of quoted errors on barometers to estimates of crustal thickness (assuming $\rho=2700 \text{ kg/m}^3$).*
 420 *a) We anchor each method with an absolute uncertainty such that the upper part of the 1σ error bar sits at 0*
 421 *kbar. This visualization shows the range of pressures/depths which cannot be statistically distinguished from*
 422 *storage at the surface. The symbol shape represents whether the quoted SEE/RMSE was for the calibration*
 423 *dataset, a test dataset, or global data. b-c). Relative (%) uncertainties are shown for different pressures. for e),*
 424 *we calculate FI errors assuming an uncertainty in CO_2 density of $\pm 0.01 \text{ g/cm}^3$ and $\pm 50 \text{ K}$ for entrapment T).*
 425 *Oceanic crustal thickness compilation from Chen (1992), OIB thicknesses compiled for this study (see supporting*
 426 *information), Continental arcs from Profeta et al. (2016). Errors for melt inclusions are highly sensitive to bubble*
 427 *volumes, so a generic example cannot be given (see Fig. 24b). Abbreviations: **P2003**: Putirka et al. (2003), **P2008**:*
 428 *Putirka (2008), **NP17**: Neave and Putirka (2017), **W2021**: Wang et al. (2021), **R21**: Ridolfi (2021), **M16**: Mutch et*
 429 *al. (2016).*

430 1.4. Influence of analytical error on precision and accuracy

431 Measurement of any quantity in igneous systems is subject to analytical error. Mineral and melt
 432 compositions are typically measured using an electron microprobe (EPMA), which is associated with random
 433 and systematic uncertainties (see Wieser et al. 2023b for a more detailed discussion). Pressure estimates from
 434 melt inclusions rely on volatile measurements by FTIR or SIMS, EPMA measurements of the host and melt phase,
 435 Raman spectroscopy measurements of the vapour bubble, and estimates of the relative volume of the vapour
 436 bubble (see Section 3 for a detailed discussion). Pressure estimates from fluid inclusions rely on measurements
 437 of the fluid using Raman Spectroscopy/Microthermometry, and an independent estimate of T using mineral or
 438 mineral-melt thermometry (e.g. using EPMA analyses). Thermodynamic methods of inverting liquid

439 compositions or liquid lines of descent rely on EPMA or energy-dispersive spectroscopy (EDS) measurements of
440 glasses, or whole-rock X-ray fluorescence (XRF) measurements.

441 As many of the methods discussed in this review rely on EPMA analysis, we briefly discuss the
442 uncertainties relating to this method. The fundamentally random process of x-ray generation, and subsequent
443 detection by spectrometers is a significant source of uncertainty, termed 'counting statistics'. The magnitude of
444 this uncertainty depends on the concentration in the sample and the beam current and voltage (affecting x-ray
445 production), and the analysis time and spectrometer efficiency (affecting x-ray detection). Most simply, unless
446 long count times and higher beam currents are used, low concentration elements (<1 wt%) tend to be associated
447 with relatively large percentage errors. When analytical errors on all measured oxides are propagated through
448 barometry equations using Monte-Carlo methods, they can generate a large range in calculated P and T.

449 For example, Wieser et al. (2023b) show that measurement of Na₂O in crustal Cpx using popular
450 analytical conditions (e.g. 10 s, 10 nA) is associated with $1\sigma=10-40\%$. Most importantly, the magnitude of this
451 error is often underestimated by factors of 2–4X because secondary standards with higher Na₂O concentrations
452 than the sample are routinely used to assess precision. The large imprecision is problematic because Na₂O in
453 Cpx is often used to calculate the P-sensitive Jadeite component. Propagating typical analytical errors through
454 popular expressions for Cpx-Liq thermobarometry can generate highly correlated PT arrays spanning 3–5 kbar,
455 which could be incorrectly interpreted as transcrustal storage (Wieser et al., 2023b-c). Analytical errors also
456 affect the experimental data used to calibrate thermobarometers. As many experimental studies perform <5
457 measurements on each phase, random analytical error does not get sufficiently averaged out, so the reported
458 phase composition may not be the true phase composition (affecting model calibration, and calculated statistics
459 on test data, see Wieser et al. 2023b, see also Section 2.3).

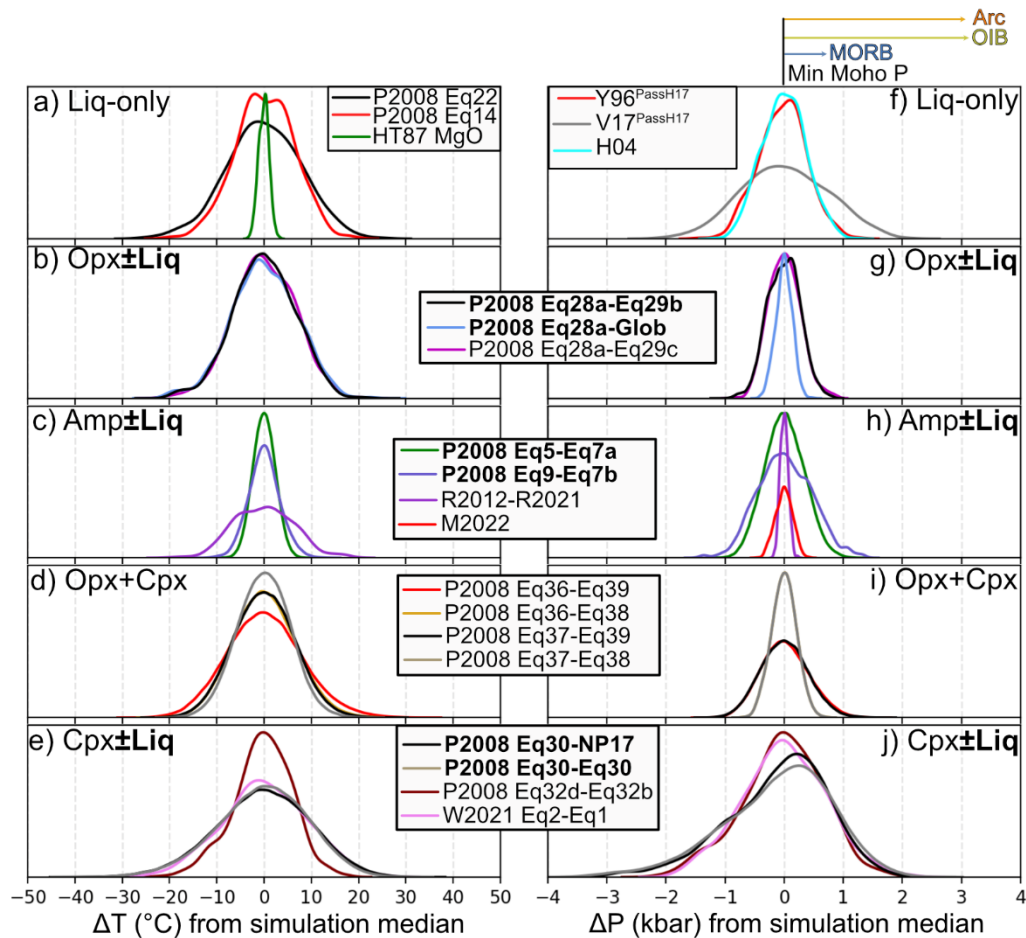
460 To visually demonstrate the effect of analytical error on different mineral-melt thermobarometers, we
461 perform Monte-Carlo simulations using Thermobar (Wieser et al., 2022b, Fig. 4). We use analytical errors
462 estimated by the EPMA based on counting statistics for experimental phase compositions reported by
463 Krawczynski et al. (2012). For each phase, we produce 500 synthetic compositions with each element normally
464 distributed about a measured value in the experiment, with the standard deviation equal to that estimated by
465 the EPMA. We also include $\pm 5\%$ relative error for H₂O in the liquid, which is a very conservative estimate of the
466 error associated with FTIR and SIMS measurements. For two-phase equilibrium (e.g., Cpx-Liq), we consider all
467 possible matches between the 500 synthetic compositions for each phase (250,000 pairs total). We then perform
468 thermobarometry calculations on all synthetic compositions, showing the spread of calculated P and T relative
469 to the median of the distribution (Fig. 4).

470 In general, the influence of analytical error on calculated T is relatively minor ($1\sigma < 20^\circ\text{C}$). The broadest
471 distribution of calculated temperatures comes from equations that are very sensitive to melt H₂O content, such
472 as Liq-only T from P2008 Eq14 and Eq22 (Fig. 4a), Opx-Liq T from P2008 Eq28a (Fig. 4b), and Cpx-Liq T from
473 P2008 Eq30 (Fig. 4e). For calculated P, the spread of simulations is highly variable, with barometry methods
474 sensitive to a component with a relatively low concentration showing a very wide spread of pressure (e.g., Na in
475 Cpx, Fig. 4j). In contrast, barometers sensitive to high concentration elements show very narrow distributions
476 (e.g., Al in Amphibole, Ridolfi, 2021, Medard and Pennec, 2022, Fig. 4h).

477 We also test the OPAM liquid barometer, where pressures are calculated from the composition of melts
478 co-saturated in olivine, plagioclase, and augite (see Section 2.2). As the experiments of Krawczynski et al. (2012)
479 are too H₂O-rich for OPAM, we use estimates of analytical precision for measurements of submarine basaltic
480 glasses from the Galápagos Spreading Centre (Gleeson and Gibson, 2021). Notably, the analytical errors have a
481 very similar magnitude to those from Krawczynski et al. (2012). This method is very sensitive to analytical
482 uncertainty, returning a similar range of calculated pressures to Cpx-based mineral-based barometers. The
483 model of Voigt et al. (2017) is particularly sensitive, because of the inclusion of a term for the Cr content of the
484 liquid, which has a low concentration, so is associated with poor analytical precision.

485 Overall, the effect of propagated analytical error on P and T depends greatly on the selected equation
486 (e.g., Fig. 4f and i), as well as the analytical conditions used. Thus, studies should propagate EPMA-estimates of
487 counting statistic errors from each analysis using their chosen equation. Secondary standards should only be
488 used to assess accuracy, not precision, as precision of an EPMA analysis is very closely related to the concentration

489 of the element of interest, so varies greatly depending on the individual mineral composition. Analytical errors
 490 should be propagated for all thermobarometric techniques, including melt inclusion and fluid inclusion
 491 barometry (see Section 5 for an example). If propagated analytical errors are of similar magnitude to the
 492 resolution required to investigate the geological process of interest, time must be spent optimizing analysis (See
 493 section 2.3). It should of course be noted that analytical variability is only one possible source of error.
 494 Simulations may indicate a precision of 0.1 kbar (random error), but the method may be inaccurate by 3 kbar at
 495 the conditions of interest (systematic error).



496
 497 *Figure 4: Monte Carlo simulations of the influence of analytical precision on thermometry (a-e) and barometry*
 498 *(f-j) calculations. All panels except f show analytical uncertainties from EPMA counting statistics from*
 499 *Krawczynski et al. (2012) with H₂O of ±5%. As OPAM (panel f) is not applied to arc magmas, we propagate EPMA*
 500 *errors from natural Galápagos glasses from Gleeson and Gibson (2021). The bars at the top show approximate*
 501 *minimum and maximum Moho pressures from each tectonic setting (see Fig. 3).*

502
 503 **2. Mineral Thermobarometry and Chemometry**

504 The seminal review of Putirka (2008, hereafter P2008) summarizes several decades of
 505 thermobarometric work, and proposes a large number of new empirical expressions linking the compositions of
 506 Cpx±Liq, Opx±Liq, Cpx+Opx, Plag±Liq, and Plag+Kspar to P and T. These new equations have similar forms to
 507 those published in older papers, but have recalibrated coefficients, and additional terms to improve
 508 performance when applied to the large compilation of experiments published in 2008 (LEPR; Library of
 509 Experimental Phase Relationships, Hirschmann et al., 2008). In the same issue, Anderson et al. (2008)
 510 summarized available P-T constraints on granitic rocks. To avoid repetition, we largely focus on new methods
 511 developed since 2008, as well as assessing the performance of these 2008 models using new experiments
 512 published in the last 15 years. Specifically, we assess models using a new test dataset of experiments conducted
 513 on arc magma compositions (ArcPL – Arc post LEPR, Wieser et al. 2023a-b) at variably hydrous (H₂O= 0–16.6
 514 wt%, median=4.7 wt%) crustal conditions (0–17 kbar). Importantly, the experiments in this new dataset were

515 not used during the calibration of most models, and any overlaps were removed when testing a specific model.
516 Our focus on arcs is partially a result of the experimental data available not used in model calibration, but also
517 reflects the fact there has been very little focus on this tectonic setting, despite the fact it is one of the few places
518 where the crust is thick enough that mineral-based barometers may be able to resolve different crustal storage
519 regions within uncertainty (Fig. 3). Additionally, there has been very little evaluation of these methods in this
520 tectonic setting. For methods not applicable to arc magmas (e.g. OPAM, section 2.2), we compile other available
521 experiments. For other methods, we do not believe sufficient ‘test’ experiments are available for MORB, OIB
522 and alkali lavas to build on the comparisons presented by Masotta et al. (2013), Masotta and Mollo (2019),
523 Neave et al. (2019) and Neave and Putirka (2017).

524

525 **2.1. Liquid-only thermometry**

526 A huge variety of liquid-only thermometers exist, with varying complexity and calibration ranges. For
527 example, the thermometer of Helz and Thornber (1987) uses just the MgO content of the liquid, calibrated on
528 compositions from the Kīlauea Iki lava lake. In contrast, P2008 eq14 has terms for the MgO, FeO_t, Na₂O, K₂O,
529 H₂O and Mg# in the liquid, and was calibrated/tested on 1536 olivine-saturated liquids. There are also a number
530 of olivine-liquid thermometers with a term for the partitioning of Mg between olivine and liquid (D_{Mg}^{Ol-Liq}). In
531 their supporting spreadsheet, Putirka (2008) replace this term with the theoretical value of D_{Mg} predicted by
532 Beattie (1993) to produce a liquid-only thermometer. Here, we discuss the best-performing thermometers for
533 our new test dataset.

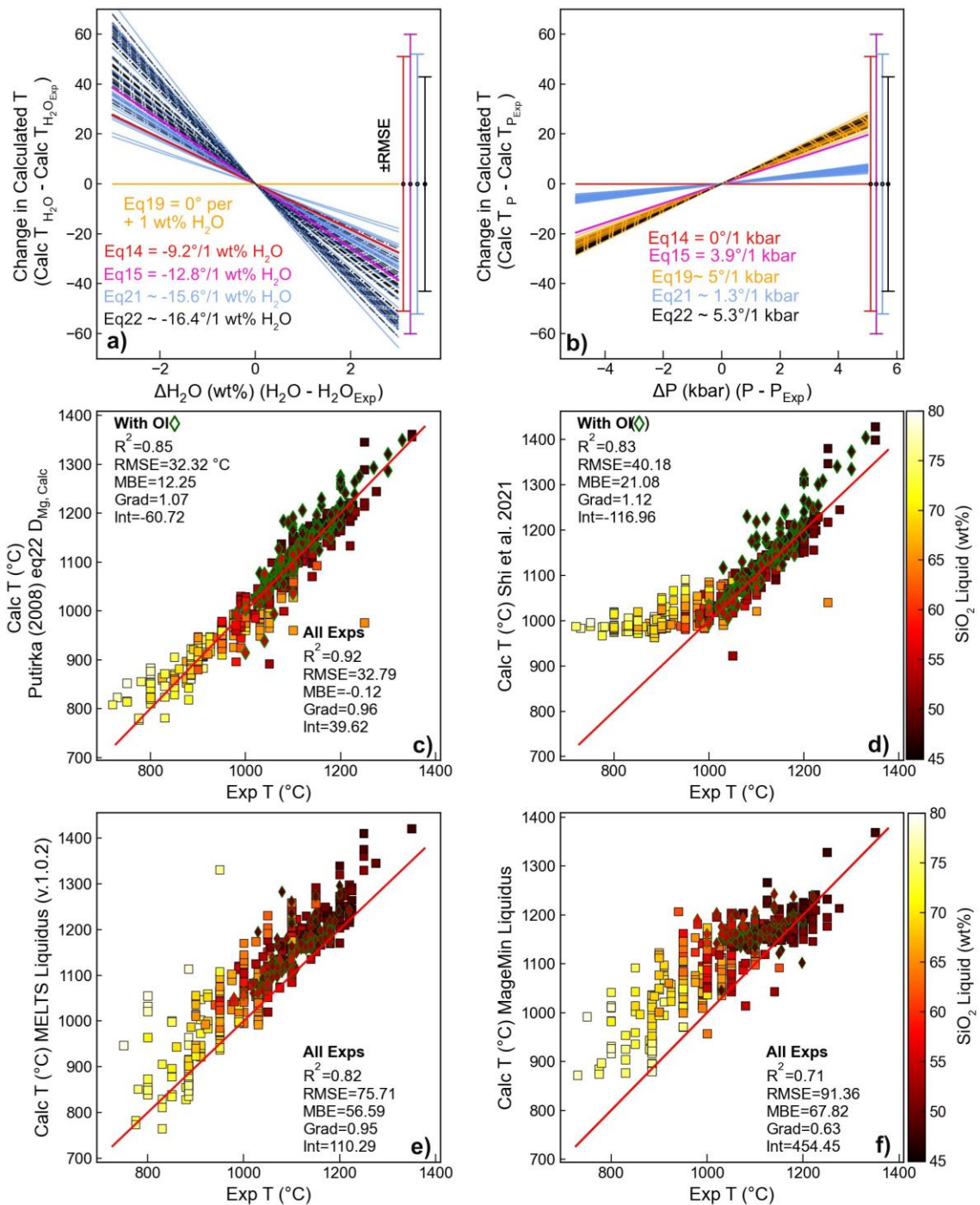
534 As P and H₂O may be poorly constrained in many systems, we first assess the sensitivity of various
535 thermometers to these parameters. We randomly select 40 experiments - for each liquid composition, we make
536 100 duplicates with the experimental H₂O content perturbed by ±3 wt% (Fig. 5a), and separately perturb the
537 experimental P by ±5 kbar (Fig. 5b). We take the calculated T at these perturbed values and subtract the
538 calculated T at the measured P and H₂O (ΔT , ΔP). Thermometers with a H₂O term show variable, but relatively
539 high sensitivity to H₂O, with the average calculated T dropping by ~9 to 16°C per wt% H₂O added (Fig. 5a). For
540 comparison, we show the quoted RMSE of each thermometer. Uncertainty in H₂O of 3 wt% introduces a
541 systematic error comparable in size to the stated RMSE (Fig. 5a). Thermometers are substantially less sensitive
542 to P; uncertainty in P of 5 kbar results in <30°C of variation. Even a full 10 kbar of uncertainty in P doesn’t exceed
543 the quoted RMSE (Fig. 5b).

544 Given the sensitivity of calculated temperatures to H₂O, we only use experiments where H₂O was
545 determined using quantitative methods (calibrated volatile-by-difference, FTIR, SIMS, Raman spectroscopy). We
546 perform calculations using experimental P and measured H₂O, because there are no suitable liquid barometers
547 or hygrometers to iterate for all these unknowns. For the ArcPL dataset, the best liquid-only thermometer is an
548 adapted version of the Ol-Liq thermometer of P2008 Eq22, where the olivine D_{Mg} term is replaced with the
549 calculated D_{Mg} value from Beattie (1993), converting it into a Liq-only thermometer (Fig. 5c). Surprisingly, this
550 adapted Ol-Liq thermometer does a very good job of predicting T in experiments without olivine, including melts
551 with high SiO₂ contents (square symbols). We also use the new liquid-only thermometer calibrated on
552 experiments containing olivine from Shi et al. (2021). This thermometer performs very well for experiments
553 containing olivine, with slightly better statistics than Eq22 D_{Mg} (Fig. 5d). Unsurprisingly, given it was calibrated
554 with Ol-bearing liquids in mind, it drastically overpredicts T at MgO<~ 2–3 wt% for experiments without olivine
555 (Supporting Fig. 1) – although this still presents an interesting contrast with Eq22 D_{Mg} .

556 We also calculate the liquidus T using rhyolite-MELTS v1.2.0, v.1.0.2 and pMELTS (Gualda et al. 2012;
557 Gualda and Ghiorso, 2015, Ghiorso et al., 2002, Fig. 5e, Supporting Fig. 2). All three versions of MELTS give similar
558 statistics; pMELTS has the higher R² and lowest MBE and RMSE (R²=0.89, MBE=44°C, RMSE=58°C), but shows
559 significantly worse performance than v1.0.2 for the lowest T liquids. It is notable that the MBE for all 3 versions
560 is relatively high A (44–56°C vs. -0.12°C for eq22 D_{Mg}), which demonstrates that MELTS consistently
561 overestimates liquidus temperatures (Fig. 5e). The other disadvantage of MELTS calculations vs. empirical
562 approaches is that the calculations are very computationally expensive; 2000 liquidus calculations take 47
563 minutes using pyMELTScalc (through alphaMELTS for Python) compared with 0.015 seconds using eq22 D_{Mg} in
564 Thermobar on a desktop computer with 128 Gb RAM and a 10-core 10th generation Intel i-9 processor. Liquidus

565 temperatures can also be calculated using the Holland et al. (2018) thermodynamic model, implemented
 566 through the Julia-based Gibbs Free Energy minimization software MAGEMin (Reil et al. 2022). The fit between
 567 the experimental and calculated T is considerably worse than that achieved by rhyolite-MELTS v1.2.0, with
 568 temperatures often overestimated by 100–200°C, particularly for experiments performed at <1100°C (Fig. 5f).
 569 These calculations take similar times to MELTS calculations. In summary, if melt H₂O contents are well
 570 constrained, empirical liquid-only thermometers such as eq22DMg of Putirka (2008) perform surprisingly well
 571 across a surprisingly wide range of melt compositions.

572



573

574 *Figure 5: Assessing Liquid-only thermometers. a-b) Sensitivity of calculated T to H₂O (a) and pressure (b). For 40*
 575 *randomly selected experiments (each represented by a line), we perturbate the experimental H₂O content by ±3*

576 wt% (a), and pressure by ± 5 kbar (b). These plots show that increasing H_2O causes a drop in calculated T , and an
577 increase in P causes an increase in T . c-f) Experimental T vs. calculated T for experiments where H_2O was
578 measured by quantitative methods (FTIR, SIMS, Raman, calibrated volatiles by difference). Experiments
579 containing olivine are shown as green-outlined diamonds, and experiments without olivine as black-outlined
580 squares. All symbols are colored by the SiO_2 content of the melt. MELTS (part e) and MAGEMin (part f) liquidus T
581 calculated using $Fe^{3+}/Fe_T=0.15$ (calculated T are not very sensitive to Fe^{3+} but having $Fe^{3+}>0$ is necessary for the
582 algorithm to converge).

583

584 2.2. Liquid-only barometry

585 Barometric methods based on the composition of silicate melts rely on the fact that the thermodynamic
586 variance of the system (i.e., the degrees of freedom) is lower in multi-phase saturated systems, so the melt
587 composition contains information about the conditions of magma storage. This is typically discussed with
588 regards to magma evolution along mineral cotectics, or at invariant points such as eutectics, where the degrees
589 of freedom is close to zero (i.e., high-silica rhyolites, Ludden, 1978; Vogt, 1931). The positions of these cotectics
590 and eutectics are sensitive to pressure because of differences in the volume of common igneous minerals. Thus,
591 if the influence of P and melt composition on the location of cotectics/eutectics can be determined by
592 thermodynamic or empirical parameterisations, measured compositions of lavas saturated in the required
593 phases can be used to calculate P (e.g., Grove et al., 1992; Gualda et al., 2012; Wilke et al., 2017; Yang et al.,
594 1996, Fig. 1g).

595 Thermodynamic approaches to liquid-only barometry have become increasingly common in the last
596 decade, with the rhyolite-MELTS thermodynamic models used to assess the storage pressure of evolved,
597 rhyolitic magmas from several locations worldwide (Gualda and Ghiorso, 2014; Harmon et al., 2018; Pamukcu
598 et al., 2015). The application of thermodynamic methods to liquid-only barometry is addressed in detail in
599 Section 8. Here, we instead focus on empirical methods calibrated using experimental data.

600 2.2.1. OPAM Barometry

601 Experimental work on the location of the olivine-plagioclase-augite-melt (OPAM) cotectic has been
602 ongoing for at least 3 decades. Early work constrained the position of the OPAM cotectic at 0.001 kbar in the
603 simplified $CaO-MgO-Al_2O_3-SiO_2$ (CMAS)+ FeO (Shi, 1992) and $CMAS+FeO+Na_2O$ systems (Shi, 1993). Further
604 experiments on natural MORB compositions demonstrated that minor components in the liquid phase (e.g., Ti,
605 Na, and K) and the expansion of the clinopyroxene stability field at higher pressures strongly influences the
606 cotectic position (Grove et al., 1992; Yang et al., 1996). Using these observations, Grove et al. (1992) provided a
607 set of empirical equations to locate the position of the olivine+plagioclase+melt and OPAM cotectics as a
608 function of melt chemistry and pressure. Yang et al. (1996, hereafter Y96) built on this work with an updated
609 parameterisation for the location of the OPAM cotectic, expressing the Mg, Ca, and Al molar fractions (X_{Mg} , X_{Ca} ,
610 and X_{Al}) of an OPAM-saturated melt as a function of P and the remaining molar fractions (e.g., X_{Si} , X_{Ti}). For
611 example, their expression for the molar fraction of Ca has the following form:

$$612 X_{Ca} = 1.133 - 0.00339 * P(kbar) - 0.569 * X_{Na} - 0.776 * X_K - 0.672 * X_{Ti} - 0.214 * X_{Fe} - 3.355 * X_{Si} +$$
$$613 2.830 * X_{Si}^2 \text{ [Equation 4]}$$

614 In 2017, these equations were updated by Voigt et al. (2017, hereafter V17), who used new experimental data
615 to show that Cr_2O_3 has a strong influence on clinopyroxene phase stability. Their equations have the same
616 functional form, with an addition of a term for the molar fraction of Cr, separate terms for ferrous and ferric Fe
617 molar fractions, and updated coefficients for the other parameters:

$$618 X_{Ca} = 1.07 - 0.02707 * P(GPa) - 0.634 * X_{Na} - 0.618 * X_K - 0.515 * X_{Ti} - 0.188 * X_{Fe^{2+}} - 0.597 *$$
$$619 X_{Fe^{3+}} - 3.044 * X_{Si} + 2.477 * X_{Si}^2 - 9.367 * X_{Cr} \text{ [Equation 5]}$$

620 Herzberg (2004) (hereafter H04), developed an alternative approach, relating P to liquid components projected
621 onto an Anorthite, Diopside, Enstatite ternary diagram from Olivine:

$$622 P(GPa) = -9.1168 + 0.2446 * (0.4645 * En + An)$$

623 $-0.001368 * (0.4645 * En + An)^2$ [Equation 6]

624 Despite the greater simplicity of pressure calculations using the H04 OPAM parameterisation, the Y96
625 and V17 equations for calculated molar fractions have formed the basis of most OPAM barometry over the last
626 decade (V17: Bell et al., 2021; Stock et al., 2018, Y96: (Baxter et al., 2023; Caracciolo et al., 2022, 2020;
627 Halldórsson et al., 2022). The methods used to extract pressure information from these expressions vary. Early
628 studies used the equations of Y96 to calculate the position of the OPAM cotectic at multiple pressures and
629 plotted these positions on an olivine-clinopyroxene-quartz pseudoternary diagram (projected from plagioclase).
630 Visual comparison of the position of the calculated OPAM cotectic to natural melt compositions projected onto
631 the same pseudoternary diagram were used to estimate the pressure of magma storage (Geist et al., 1998;
632 Maclennan et al., 2001). Kelley and Barton (2008) use a complex approach calculating theoretical and measured
633 normative mineral components at different pressures, regressing these components against pressure to
634 determine the best fit for each measured sample. More recent studies have determined the pressure of the
635 minimum misfit between calculated X_{Mg} , X_{Ca} , and X_{Al} using the equations of Y96 or V17, and measured X_{Mg} , X_{Ca} ,
636 and X_{Al} in their samples without requiring the conversion to normative mineral components (Hartley et al. 2018).

637 Regardless of the calculation method used to obtain P, OPAM barometry requires input melt
638 compositions to be saturated in all 3 solid phases (olivine, clinopyroxene, and plagioclase). Solving for pressure
639 using the equations of Y96 or V17 for samples that are not saturated in all 3-phases could lead to erroneous
640 results and may explain the wide range in calculated P estimated for some systems (e.g., 1.4– 7.7 kbar at Laki in
641 Iceland; Kelley and Barton, 2008). Therefore, it is important to determine which samples are co-saturated before
642 interpreting OPAM calculations. One way to ensure 3-phase saturation in the target melts is via textural
643 observations, such as petrographic observations of euhedral crystals with no disequilibrium textures.
644 Alternatively, in systems with abundant whole-rock or matrix glass data spanning a range of MgO contents,
645 comparing liquid lines of descent with mass balance approaches or fractional crystallization models (e.g.,
646 MELTS, Petrolog3, Danyushevsky and Plechov, 2011; Gualda et al., 2012) can be used to confirm 3-phase
647 saturation.

648 An approach that can be applied to individual liquid compositions without textural or LLD context to
649 calculate P and check for cosaturation was developed by Hartley et al. (2018). They determine the probability of
650 three-phase saturation using a Chi-squared distribution to calculate the misfit between the predicted (X_i^{Pred})
651 and measured (X_i^{Meas}) molar fractions for Mg, Ca and Al:

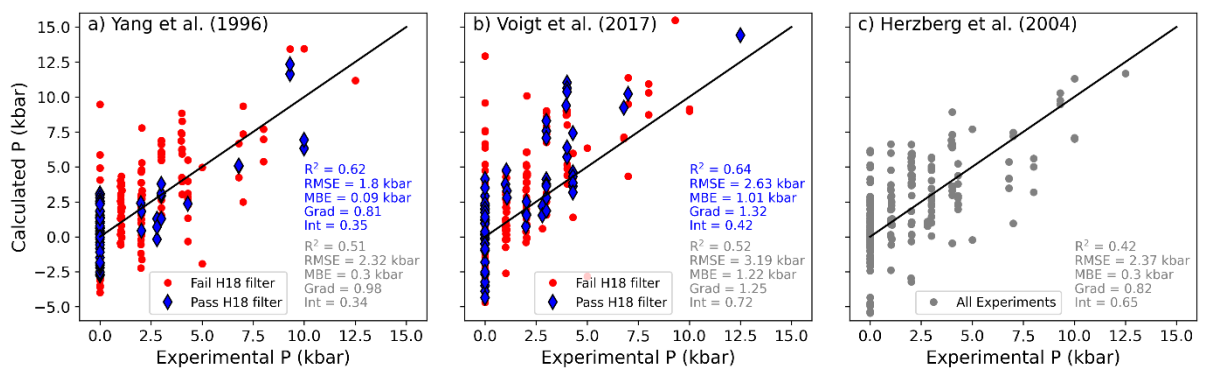
$$652 \chi^2 = \sum_{i=1}^3 \left[\frac{X_i^{Meas} - X_i^{Pred}}{\frac{\sigma_{X_i} X_i^{Meas}}{100}} \right]^2 \text{ [Equation 7]}$$

653 Here, σ_{X_i} is an estimate of the relative analytical uncertainty for each cation under consideration
654 (expressed as a percentage). As X_i^{Pred} is a function of the system pressure, users can determine the best-fit
655 model pressure by locating the position of the minimum possible χ^2 value (χ^2_{Min}). To assess whether the melt
656 is truly three-phase saturated, Hartley et al. (2018) compare χ^2_{Min} to the cumulative distribution function of
657 the Chi-squared distribution with 2 degrees of freedom. A probability is selected as a cut off value (e.g., p=0.05,
658 p=0.2) - Hartley use a probability of fit, P_f , which can be thought of as 1 minus the p value. If χ^2_{Min} is less than
659 the critical value of the chi squared cumulative distribution function for this chosen cut off (i.e., chosen p-value
660 and n=2 degrees of freedom), the liquid is assumed to be three-phase saturated. By considering the results of
661 OPAM calculations on experimental melt compositions (including the Yang et al. 1996 calibration data), Hartley
662 et al. (2018) determine that a 'probability of fit' filter of p~0.2 ($P_f=0.8$) results in a good fit between the
663 experimental and calculated pressures, while minimising the number of 'false negatives' (i.e., melt compositions
664 which are OPAM saturated, but would fail this test). The minimisation method and co-saturation check of Hartley
665 et al. (2018) (hereafter H18) has been utilised by several studies investigating the storage conditions of MORBs
666 and OIBs (Bell et al., 2021; Stock et al., 2018, Baxter et al., 2023; Caracciolo et al., 2022, 2020; Halldórsson et al.,
667 2022).

668 Baxter et al. (2023) evaluated the performance of the Y96 equations using 315 OPAM saturated
669 experimental melt compositions, ranging from 1 atm to 12.5 kbar pressure. They filter these experiments using

670 the H18 filter and exclude those with MgO<4 wt%, leaving 95 experiments. Comparing calculated and
 671 experimental pressures for these filtered experiments yields a RMSE of ± 1.51 kbar, which is similar to the
 672 'random error' of ± 1.32 kbar estimated by Hartley et al. (2018, definition uncertain). However, both studies
 673 evaluated the performance of the Y96 equations using a dataset including some experiments used in the Y96
 674 calibration. For example, 57% of the 95 experiments assessed by Baxter et al. (2023) are part of the Y96
 675 calibration dataset. If we rerun the comparison using only experimental data that was not used in the Y96
 676 calibration the RMSE increases from ± 1.51 kbar to ± 1.89 kbar. A particular issue is that only 7/41 of the remaining
 677 experiments were conducted at >0.001 kbar, making it very hard to assess the performance of the Y96
 678 barometer without new test data at higher pressures.

679 To test the performance of all three OPAM barometers listed here (Y96, V17, and H04), and the success
 680 of the H18 filter, we compile an experimental dataset of OPAM saturated experiments not used to calibrate
 681 either Y96 or V17. N=188 overlap with the dataset of Baxter et al. (2023), with N=38 experiments not in that
 682 compilation. Fig. 6 demonstrates that there are strong correlations between the calculated and experimental
 683 pressures for all OPAM methods when the H18 saturation check is not applied (R^2 of 0.51, 0.52, and 0.42 for
 684 Y96, V17, and H04 respectively, all symbols, grey statistics on Fig. 6). Despite having the highest R^2 value of the
 685 three methods tested here, calculated pressures determined using the V17 expressions display the largest
 686 uncertainties (RMSE=3.19 kbar) and a systematic offset to high pressures (MBE = 1.22 kbar, Fig. 6b). The Y96
 687 expression has a smaller systematic offset (gradient=0.98, MBE=0.3 kbar), as well as a lower RMSE (2.32 kbar,
 688 Fig. 6a). The parameterisation of H04 also returns a relatively low RMSE (2.37 kbar) and similar MBE to the Y96
 689 method (0.3 kbar), but has a lower gradient of the correlation (0.82; Fig. 6c).



690

691 *Figure 6: Experimental vs. calculated P using the OPAM expressions of Yang et al. (1996), Voigt et al. (2017) and*
 692 *Herzberg (2004) for OPAM-saturated experiments on MORB-like compositions. The calculated pressure was*
 693 *determined using the Chi-squared method of Hartley et al. (2018, H18) for the Yang et al. (1996) and Voigt et al.*
 694 *(2017) equations (a,b). Samples passing the co-saturation filter of Hartley et al. (2018) are shown as blue*
 695 *diamonds, while those that fail are shown as red circles. The filter is not applicable to the method of Herzberg et*
 696 *al. (2004, part c).*

697 The larger uncertainty and systematic offset in pressures estimated using V17 likely originates from the
 698 sensitivity of these expressions to the Cr_2O_3 content of the melt phase. Only 53 of the 225 experiments used in
 699 this analysis (~24%) report melt Cr_2O_3 contents, despite most experiments using natural basalt compositions
 700 that likely contain at least trace amounts of Cr_2O_3 . Adding Cr_2O_3 into the melt phase changes the stability of
 701 pyroxene (see Fig. 3, Onuma and Tohara, 1983), and thus the pressure estimated by OPAM barometry (Voigt et
 702 al., 2017). Consequently, the systematic offset to higher pressures obtained by applying the V17 expressions to
 703 our compiled experimental database might result from the absence of reported Cr_2O_3 in most experiments, and
 704 uncertainty as to whether Cr was even present in starting materials (Wieser et al. 2023b). Additionally, it is
 705 unclear how precise the analyses of Cr_2O_3 in these experiments are; typical analytical conditions can result in
 706 large errors for this low concentration oxide (propagating into a much wider spread of pressures than using Y96
 707 or H04, Fig. 4f). Despite its poor performance on our test dataset, we cannot rule out the possibility that V17
 708 may be the best parameterization in natural Cr containing systems, even if it behaves poorly on Cr-free
 709 experiments. Further experimental work on Cr-bearing experiments where the Cr content of the melt was

710 characterized with high precision at a range of pressures are required to assess the performance of the V17
711 expressions as an OPAM barometer in natural systems.

712 Interestingly, although all N=225 experiments were OPAM saturated, only 27% (N=61) pass the H18
713 cosaturation filter when the equations of Y96 are used (blue diamonds, Fig. 6a). While the statistics for calculated
714 vs. experimental pressures are greatly improved using only experiments which pass the filter, it is concerning
715 how many false negatives this filter produces, particularly as only 18 of the experiments which passed the filter
716 were performed at pressures above 0.001 kbar. To further assess the performance of the H18 saturation filter,
717 we isolated experiments on MORB-like compositions that are saturated in only one or two (N = 172) of the three
718 key mineral phases in OPAM barometry. Using the Y96 expression, 19% of these non-OPAM saturated
719 experiments pass the H18 co-saturation filter (false positives). These results demonstrate that the H18 co-
720 saturation filter should not be used in isolation to identify which samples are suitable for OPAM barometry.
721 Therefore, petrological observations of three-phase saturation remain critical for determining pressures via
722 OPAM barometry.

723 To date, OPAM barometry has mostly been used to evaluate the storage pressure of MORBs, or
724 tholeiitic to transitional OIBs (as these compositions broadly overlap with the calibration dataset of Yang et al.
725 1996). Unfortunately, the uncertainty associated with OPAM barometry assessed using our independent test
726 dataset (RMSE = 1.8 – 2.32 kbar, Fig. 6) indicates that this method does not have the resolution to distinguish
727 between upper vs lower crustal storage at most mid-ocean ridges. However, at hotspot influenced ridges (e.g.,
728 Iceland) and regions of plume derived volcanism (e.g., ocean islands), the thickened crust (Fig. 3e) means that
729 OPAM can provide insights into the characteristics of magma storage in these locations if independent checks
730 for 3-phase saturation are performed prior to pressure calculation (via petrographic observations or liquid line
731 of descent analysis). For example, melt inclusion and matrix glass data from Barðarbunga, Iceland, indicates that
732 there is a slight difference in the entrapment pressure of melt inclusions and the final equilibration pressure of
733 the matrix glasses (Hartley et al. 2018; Caraccioli et al. 2022).

734 **2.2.2. Other liquid-based barometers**

735 The effect of H₂O on phase boundaries in the OPAM system has not been investigated in detail, meaning
736 this method cannot be applied to arc magmas with confidence. To provide a liquid-based thermobarometer with
737 application to more hydrous systems like volcanic arcs, Blundy (2022) create parametrizations for the stability
738 of clinopyroxene-hornblende-orthopyroxene-plagioclase-ilmenite (CHOMPI) as a function of P, T, and the ratio
739 of H₂O and CO₂ in the fluid, including a cosaturation check to establish whether CHOMPI phases were present
740 based on just a liquid composition. However, Wieser et al. (2023d) show this cosaturation test classifies ~44%
741 of ArcPL experiments lacking the CHOMPI assemblage as CHOMPI-saturated (false positives), and unsurprisingly
742 these experiments show a poor correspondence between calculated and experimental pressure (as the system
743 is not low variance). The logic behind the CHOMPI approach has been generalized to liquids saturated in a wider
744 variety of phases by Weber and Blundy (2023), who apply a regression tree machine learning algorithm to a
745 training dataset of liquids ranging from basalt to rhyolite. As this model is still being tweaked and is currently a
746 preprint (Weber, written comms), we do not comment on it further.

747 **2.3. Clinopyroxene±Liquid**

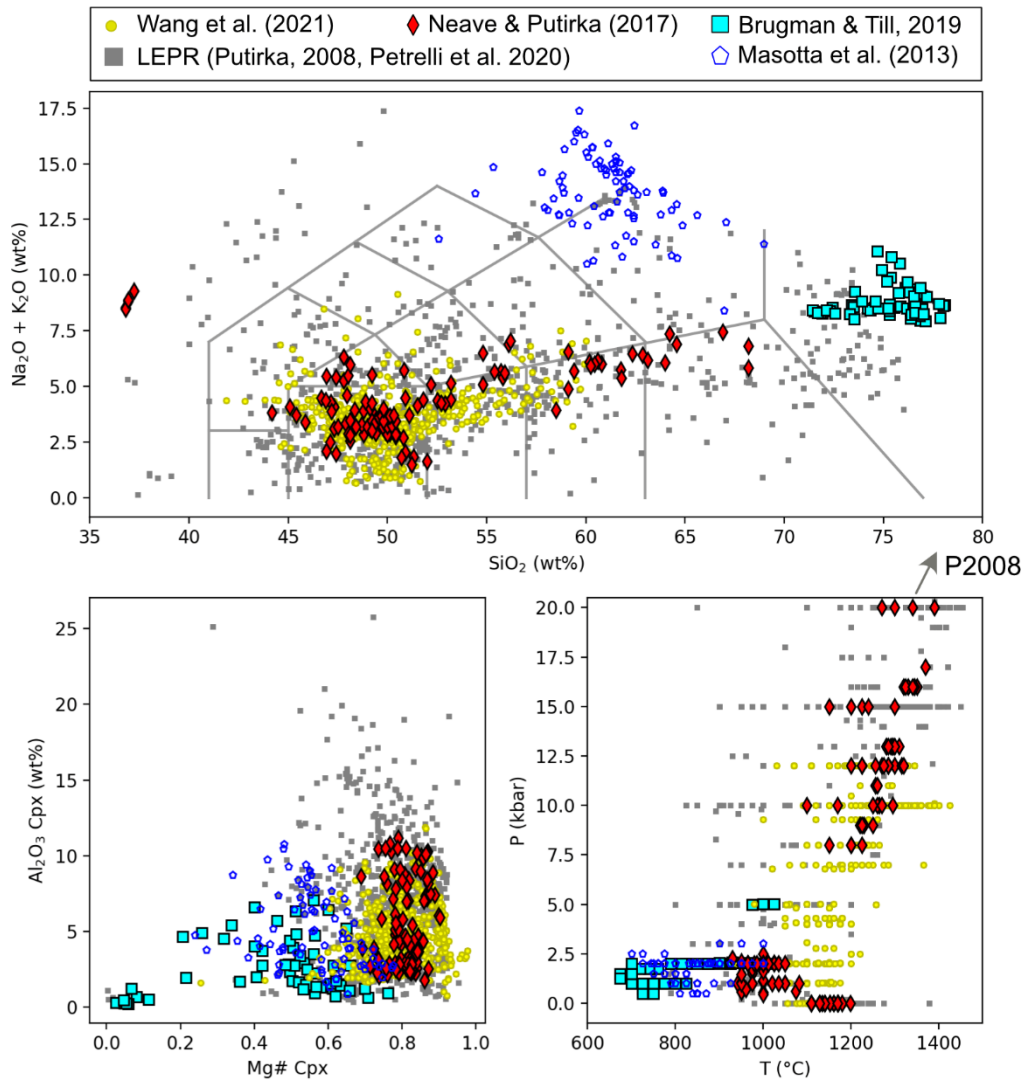
748 The majority of Cpx-Liq thermobarometers rely on the exchange of diopside hedenbergite (DiHd,
749 CaFeSi₂O₆) and Jadeite (Jd, NaAlSi₂O₆) between Cpx and liquid. Here, we briefly summarize the most recent
750 parameterizations of Cpx equilibrium, and workflows that have been developed for calculating P and T in natural
751 systems. A detailed discussion of pre-2008 models can be found in Putirka (2008, and refs within), and a
752 description of the best Cpx-Liq models for our test dataset and sensitivity to P and T as well as the best
753 equilibrium tests to use can be found in Wieser et al. (2023a-b).

754 Putirka (2008) propose a number of equations based on Cpx-Liq equilibria (Eq30, Eq31, Eq32c for P,
755 Eq33 for T), expanding and recalibrating the models of Nimis (1995) and Putirka et al. (1996, 2003) to account
756 for an increase in experimental data (particularly hydrous experiments). More recently, several new equations
757 have been calibrated which focus on a more limited subset of compositional space than these global regressions
758 (Fig. 7). Neave and Putirka (2017) calibrate a Cpx-Liq barometer for application to tholeiitic basalts from ocean
759 island settings (specifically Iceland) using 6 experimental studies (N=113 experiments) from LEPR with mafic-
760 intermediate compositions, and pressures ranging from atmospheric to 20 kbar (Neave and Putirka, 2017, Fig.

761 7, red diamonds). Masotta et al. (2013) conduct experiments and compile available literature data on melts with
762 trachytic to phonolitic compositions (Fig. 7, blue pentagons), calibrating a Cpx-Liq barometer applicable to more
763 alkaline compositions (which are poorly represented in the calibration dataset of P2008). Their expressions have
764 a very similar/identical form to those of Putirka (2008), with recalibrated coefficients. Brugman and Till (2019)
765 note that in high-silica melts, there is very little Al_2O_3 in Cpx (<2 wt%), and the calculated Jd component is very
766 low or even zero. Along with the fact that high Si compositions are very poorly represented in P2008, they
767 showed that existing Cpx-Liq thermometers overestimated temperatures in evolved melts by up to 170°C. Thus,
768 Brugman and Till (2019) compiled recent studies from the literature on rhyolitic compositions (e.g., Almeev et
769 al., 2012; Bolte et al., 2015; Gardner et al., 2014) supplemented with their own experiments on the Scaup Lake
770 Rhyolite (Fig. 7, cyan squares), to calibrate a new thermometer for highly evolved melts which is independent
771 of Jadeite, P, and H_2O content.

772 Another key shift in the use of Cpx-based barometry since 2008 has accompanied the rapid rise in
773 programming literacy amongst petrologists, allowing the development of new workflows based on existing
774 thermobarometry equations. For example, while experimental studies have clearly paired Cpx and liquid
775 compositions, it is significantly more challenging in natural systems to identify such pairs. Typically, a given
776 volcanic eruption will erupt a narrow range of liquid compositions along with a much more chemically diverse
777 crystal cargo, incorporating Cpx crystals grown from a wide variety of melt compositions. Additionally, many
778 whole rock compositions are a mix of crystals and melts, and not representative of true liquids (Reubi and
779 Blundy, 2009; Ubide et al., 2022). A variety of algorithms have been developed to try to identify matched pairs,
780 by combining erupted Cpx compositions with liquids erupted over a longer time period at a given edifice, or even
781 compilations of whole-rock data from an entire volcanic region.

782 For example, Maclennan et al. (2001) assessed magma storage pressures of basalts from the Icelandic
783 Northern Volcanic Zone by filtering possible Cpx-Liq matches using the K_D equilibrium test of Putirka (1999).
784 Winpenny and Maclennan (2011) devised a more complex test for Cpx-Liq equilibrium, using equation 35 of
785 Wood and Blundy (1997) for K_D , and trace element equilibrium tests. Specifically, they use trace elements
786 measured in Cpx, and then use the partition coefficients from Wood and Blundy (1997) to calculate the expected
787 trace element contents of equilibrium liquid compositions. By comparing these predicted liquid compositions to
788 available trace element data for compiled liquids (for Ce or La, Nd or Sm, and Yb, Dy and Y depending on data
789 availability), they assess all possible matches between Cpx erupted at Borgarhraun, and ~1000 whole-rock and
790 glass analyses from Icelandic Basalts for equilibrium. However, this method requires trace element data in both
791 Cpx and liquids/whole-rock, which isn't widely available in the literature for different volcanic systems (and is
792 rarely collected as part of thermobarometric studies). Furthermore, the trace element partition coefficients used
793 in these calculations are highly sensitive to the temperature of the system, complicating calculations (Sun and
794 Liang, 2012; Wood and Blundy, 1997).



795

796 *Figure 7: Calibration range of Cpx-Liq and Cpx-only thermobarometers. Since the compilation of the LEPR*
 797 *database in 2008 (Hirschmann et al., 2008) used to calibrate Putirka (2008) and Petrelli et al. (2020, grey*
 798 *squares), many new thermobarometers have focused on specific regions of compositional space: Brugman and*
 799 *Till (2019, cyan squares), Masotta et al. (2013, blue pentagons), Neave and Putirka (2017, red diamonds). TAS*
 800 *lines drawn using Stevenson (2015).*

801

802 Neave and Putirka (2017) and Neave et al. (2019) develop an R code (also used by Gleeson et al., 2021
 803 and Stock et al., 2018) to assess equilibrium in Cpx-Liq pairs using components which can be calculated from
 804 elements measured routinely by electron microprobe (Diopside-Hedenbergite, DiHd; Enstatite-Ferrosilite, EnFs;
 805 Calcium Tschermak, CaTs). Specifically, they assess the difference in the measured components in the Cpx and
 806 the equilibrium components calculated from the liquid composition using Eq35 of P2008 for K_D , from Mollo et
 807 al. (2013) for DiHd and EnFs, and Putirka (1999) for CaTs. As the selected K_D equilibrium equation is sensitive to
 808 T, and DiHd, EnFs and CaTs to P and T, equilibrium tests must be calculated alongside P and T estimates. A
 809 computationally optimized algorithm loosely based on the Neave R algorithm (which was never publicly
 810 released) was published as part of the Open-Source Python3 tool Thermobar (Wieser et al. in 2022b). This tool
 811 allows comparison of 100s of Cpx and Liq within seconds, with highly customizable equilibrium filters. Even with
 812 fast matching codes, identifying Cpx-Liq pairs is associated with substantial uncertainty regarding choice of
 813 equilibrium tests, and the chosen cut-off parameter (see Wieser et al. 2023a for arc magmas). In many systems,
 814 very few to no matches are found with erupted liquids, requiring generation of synthetic liquids to match to
 815 measured Cpx (e.g., Scruggs and Putirka, 2018). Another approach is to pair Cpx rims with matrix glass or
 816 groundmass separates (Klügel et al., 2020), although because this method focuses on rims, it may only reveal

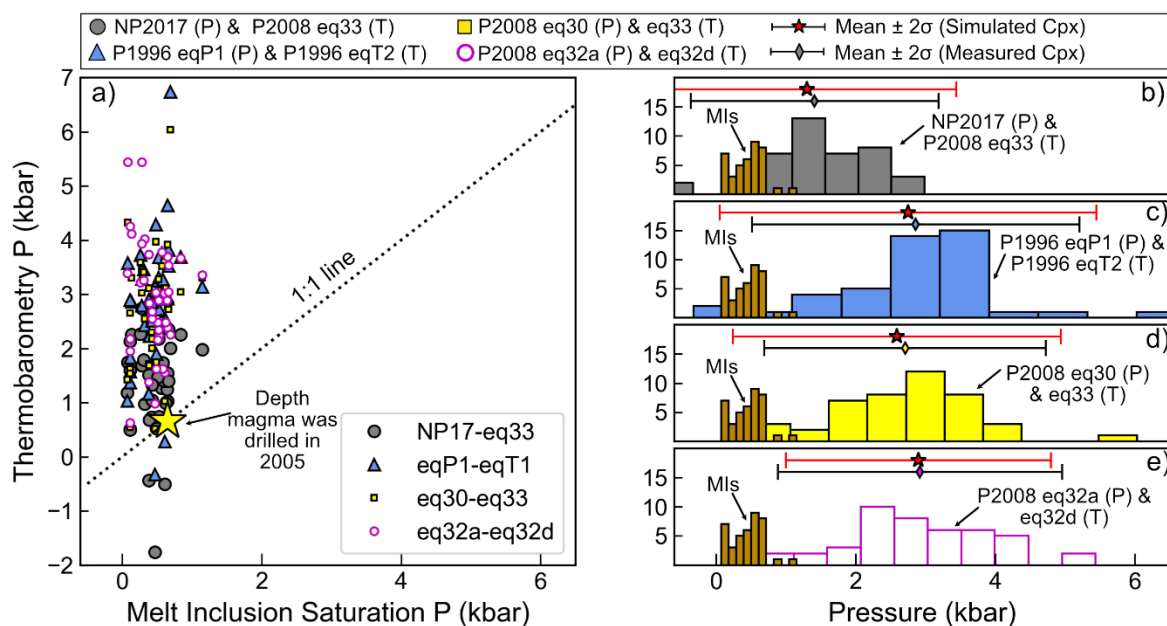
817 the depth of the uppermost storage chambers (neglecting deeper pressure information preserved in core
818 compositions).

819 Issues associated with identifying equilibrium liquids can be circumvented using Cpx-only barometers.
820 Putirka (2008) present two Cpx-only barometers (eq32a-b) and a Cpx-only thermometer (eq32d). Wang et al.
821 (2021) show that these (and other existing) Cpx-only thermobarometers perform poorly in mafic and
822 intermediate melt compositions. To address this, Wang et al. (2021) select 559 experiments conducted at 0–12
823 kbar with liquid SiO₂ contents between 42–60 wt% to calibrate a new barometer which is independent of T and
824 H₂O (Fig. 7, yellow circles). They use the PyTorch python library (Paszke et al., 2019) to implement a gradient
825 descent algorithm to select Cpx cation components to include in a non-linear term for a Cpx-only barometer,
826 rather than selecting components based on thermodynamic reasoning. They also present a thermometer, which
827 is independent of P but requires knowledge of the H₂O content of the liquid.

828 Most recently, supervised machine learning methods have been applied to Cpx-based equilibrium to
829 develop thermobarometry expressions (e.g., random forests, Higgins et al., 2022, extra trees, Jorgenson et al.,
830 2022; Petrelli et al., 2020). Unlike more traditional empirical thermobarometers which are underlain by
831 thermodynamic principles, measured oxide data are fed into these algorithm, rather than calculated
832 components such as Jadeite. Wieser et al. (2023a) show that the Cpx-only barometers of Wang et al. (2021) and
833 Jorgenson et al. (2022) show similar performance to popular Cpx-Liq barometers for the ArcPL dataset, justifying
834 the use of Cpx-only barometers as an alternative to trying to identify equilibrium liquids. That said, just because
835 Cpx-Liq and Cpx-only barometry show similar performance, it is worth nothing that neither approach performs
836 particularly well, with neither method yielding R²>0.74, or RMSE <2.1 kbar. Additionally, all expressions have
837 low gradients, overpredicting at lower pressures, and underpredicting at higher pressures.

838 The relatively poor performance of Cpx-based barometry on independent test datasets (e.g., high
839 RMSE, low gradients, inability to distinguish magma storage within ~10–15 km) is at least partially the result of
840 low analytical precision when measuring Na₂O in experiments used to calibrate and test barometers (see Wieser
841 et al. 2023b, and Section 1.4). Analytical precision also affects measurements of natural samples and can result
842 in an anomalously large spread of calculated P and T, which can be incorrectly attributed to transcrustal storage
843 because of spurious trends in P-T space. For example, Wieser et al. (2023c) show that a the entire P-T range of
844 the lunar Cpx analysed by Luo et al. (2023) can be explained by the propagation of analytical uncertainty. To
845 further demonstrate the importance of such error propagation, we calculate pressures using Cpx and melt
846 inclusion compositions from the first two weeks of the 2018 eruption of Kīlauea Volcano (Wieser et al., 2022c).
847 Cpx-hosted melt inclusions yield relatively shallow saturation pressures, which overlap very well with the
848 pressure at which a highly evolved magma was drilled in this region in 2005 (Teplow et al., 2009, yellow star, Fig.
849 8a). We use the PEC-corrected melt inclusion compositions and analyses of the Cpx composition close to the
850 melt inclusion to calculate Cpx-Liq and Cpx-only pressures. These barometers return a much greater spread of
851 pressures than melt inclusion saturation pressures, with a notable offset to significantly higher values (Fig. 8). In
852 fact, these calculated depths are similar to the 3–4 kbar estimated by Putirka (2008) for Cpx erupted during the
853 Pu’u O’o eruption of Kīlauea. However, there are no other geological or geophysical indications that Cpx-
854 saturated magmas are stored this deep.

855 To interpret the large spread of calculated pressures, we simulate 5000 Cpx compositions, with the
856 variability of each oxide following a normal distribution centred on the mean measured Cpx composition, with
857 a standard deviation equal to the average counting statistic precision estimated from the EPMA output. We
858 calculate pressures using these 5000 synthetic Cpx paired with the average liquid composition, and show ±2σ of
859 these simulations as a red error bar (Fig 8b-e). The simulated spread in calculated pressures resulting from
860 analysis of an entirely homogenous Cpx using typical EPMA operating conditions almost exactly matches the
861 observed spread in calculated pressures (2σ error bars for each overlain on each histogram). This illustrates how,
862 without sufficient averaging of individual analyses, it would be easy to incorrectly invoke storage at a range of
863 pressures spread throughout the crust. While iteration of Putirka (2008, eq30) for T and Neave and Putirka
864 (2017) for P produces calculated pressures that align within error of the melt inclusion saturation pressures, the
865 other Cpx-based barometers estimate far too high pressures compared to melt inclusions and drilling depths.
866 This demonstrates both the lack of precision and accuracy of Cpx-based methods. Even without analytical
867 uncertainty, the RMSE on these barometers mean there is no way to reliably distinguish storage at ~0.5 kbar
868 from storage at 4 kbar; limiting the applicability of these methods in systems where magma is stored in the
869 upper part of a relatively thin crust.



870
 871 *Figure 8: Comparison of melt inclusion saturation pressures (Wieser et al. 2022c), and Cpx-Liq and Cpx-only*
 872 *barometry for samples erupted during the first two weeks of the 2018 Kīlauea eruption. a) Melt inclusion*
 873 *saturation pressures calculated in MagmaSat (Ghiorso and Gualda, 2015) using VESlcal (Iacovino et al., 2021)*
 874 *cluster tightly at shallow pressures. These pressures are very similar to the pressure at which an evolved magma*
 875 *body was drilled in 2005 in the same area (yellow star, Teplow et al. 2009). Cpx-Liq and Cpx-only pressures*
 876 *calculating using PEC-corrected melt inclusion-host pairs show substantial scatter, extending to substantially*
 877 *deeper pressures. B-e) Histograms showing calculated pressures for each iterative mineral barometry calculation.*
 878 *Error bars with black lines show $\pm 2\sigma$ for these calculations. Red error bars show $\pm 2\sigma$ for Monte-Carlo simulations*
 879 *for the mean composition of each Cpx and Liq, with 5000 Cpx compositions simulated using estimates of*
 880 *analytical precision for these Cpx measurements.*

881
 882 The relatively poor performance of many Cpx-based barometers can also be attributed to the fact that
 883 many expressions are parameterized in terms of Cpx components (e.g. Jd, DiHd) calculated from EPMA oxide
 884 data (e.g., Neave and Putirka, 2017, Putirka, 2008). An alternative technique calculates site occupancy and cell
 885 volumes using a combination of single-crystal X-ray diffraction and measured oxide data (Dal-Negro et al., 1989).
 886 This technique was used extensively in the 80s-90s, and was recently applied by Tommasini et al. (2022) to
 887 natural Cpx crystals from Popocatepetl Volcano. They show that XRD-informed site assignments and the
 888 resulting calculated mineral components differ greatly from the routines used by Neave and Putirka (2017) and
 889 Putirka (2008) using EPMA data alone. This discrepancy between components calculated using EPMA data and
 890 the true crystal structure may reflect an additional source of uncertainty plaguing Cpx-based barometers. Single
 891 crystal XRD may also be vital to help us determine where Na is going (pairing with Al, Fe³⁺ or Cr³⁺), which will
 892 further enhance our understanding of how Cpx composition relates to pressure. However, while single-crystal
 893 X-ray diffraction has been applied to natural crystals, the small size of experimental Cpx means that it is very
 894 difficult to obtain these parameters for experiments in order to calibrate expressions using these parameters
 895 (Dal-Negro et al., 1989, Tommasini et al. 2022). Additionally, a workflow involving XRD would be far more time
 896 consuming from a sample preparation perspective than existing EPMA-based techniques, which may severely
 897 restrict its uptake by the community, even if it results in improved barometer performance.

898 A number of papers have also shown the importance of considering the petrogenetic history of a Cpx
 899 population when interpreting thermobarometry calculations. For example, Hammer et al. (2016) assessed the
 900 influence of disequilibrium crystal growth on Cpx barometry using X-ray mapping and quantitative spot analyses
 901 of clinopyroxene crystals from a post-shield ankaramite erupted from Haleakalā volcano, Hawai'i. Their work
 902 demonstrates the complexity of interpreting Cpx compositions in regions where disequilibrium growth
 903 processes occur. Specifically, texturally and compositionally distinct domains within individual crystals thought
 904 to have formed by high degrees of undercooling during crystallisation have distinct distributions of Cpx Jd
 905 contents, so return very different P estimates. They find offsets within individual crystals up to ~3.5 kbar. In

906 contrast, Ubide et al. (2019a, 2019b) calculate P-T-H₂O for different domains in sector zoned Cpx from Stromboli,
907 and show remarkably constant results regardless of the textural context (although without individual calculated
908 PTs, it is not possible to directly compare the statistical differences between these different studies). Clearly,
909 further work is required to understand how the formation of different chemical domains in magmatic systems
910 affect the distribution of P- and T-sensitive Cpx components, and thus the results from thermobarometric
911 calculations.

912 The relatively recent appreciation that most magmas are stored in predominantly crystal-rich “mushy”
913 environments also adds additional complexity to the interpretation of clinopyroxene-based barometric
914 estimates, because clinopyroxene chemistry can be influenced by chemical processing in these crystal-rich
915 regions. For example, residual melt compositions can be modified by reactive porous flow, driven by
916 disequilibrium between a percolating melt phase and the surrounding crystal framework (Boulanger et al., 2020;
917 Gleeson et al., 2021; Lissenberg and MacLeod, 2016; Sanfilippo et al., 2020). Critically, the melts formed from
918 this process are rarely observed at the surface, which makes it difficult to quantify their chemistry to pair with
919 erupted Cpx compositions. Cpx-Liq and Cpx-only barometry is also affected by the fact that reactive porous flow
920 might drive interstitial melt compositions (and thus the Cpx compositions) outside the compositional range used
921 to calibrate existing expressions (Fig. 7). Gleeson et al. (2021) demonstrate the importance of accounting for
922 mush processes in their study of Cpx from wehrlite xenoliths found on Isla Floreana in the southern Galápagos.
923 These crystals have Na₂O contents up to ~1.3 wt% and returned apparent crystallisation pressures up to ~18
924 kbar using the clinopyroxene-only thermobarometers of Putirka (2008; eq. 32b-32d). In contrast, Cpx-Opx
925 barometry (using the same crystals), melt inclusion and clinopyroxene-liquid thermobarometry from
926 neighbouring scoria cones on the same island indicate that magma storage was dominantly located at around
927 ~7 kbar (Gleeson et al., 2022, 2021). Based on rare earth element signatures in these pyroxenes (elevated LREE
928 contents relative to MREE and HREE contents) the authors concluded that the anomalously high pressure
929 estimates of the wehrlitic clinopyroxene crystals result from chemical modification of Na₂O (and REE) by reactive
930 porous flow in olivine ±clinopyroxene mush zones. Comparison with other thermobarometric techniques (E.g.,
931 Opx-Cpx, melt inclusions, Gao et al., 2022, Gleeson et al. 2021), as well as identifying trace element patterns
932 indicative of reactive flow, provide one method to interpret the spuriously high pressure estimates returned
933 from these cumulate Cpx.

934 In summary, to push Cpx-based thermobarometry forward, we need to improve the experimental
935 datasets available to calibrate and test barometers (see Wieser et al. 2023a-b), develop new methods to relate
936 chemical components to parameters we can easily measure in natural samples and experimental charges (e.g.,
937 Tommasini et al. 2022), and increase our understanding of natural processes causing variation in Cpx
938 compositions (e.g., Gleeson et al., 2021; Hammer et al. 2017, Neave et al., 2019; Ubide et al., 2019b, 2019a),

939 **2.4. Orthopyroxene±Liq**

940 Beattie (1993) presented the first Opx-Liq thermometer based on the use of non-regular solution
941 models to calculate saturation temperatures. Putirka (2008) then calibrated two different equations (Eq28a,
942 28b) using the LEPR dataset, both of which are sensitive to P and H₂O. Eq28a uses the composition of the Opx
943 and Liq, while Eq28b only uses the composition of the liquid to calculate the temperature of Opx saturation.
944 Wood (1974) published the first Opx barometer, which used the Al content of Opx in equilibrium with Garnet.
945 Putirka (2008) calibrated a more widely applicable Opx-only barometer (Eq29c) and two Opx-Liq barometers
946 (Eq29a, Eq29b) using the LEPR database. The main pressure-sensitive component in Eq29a is a Jadeite-like
947 component in the Opx, while Eq29b uses the (Fe, Mg)₂Al₂SiO₆ Opx component. Both equations also contain terms
948 for other liquid cation fractions, and opx cation fractions on the basis of 6 oxygens. Eq29c (Opx-only) uses the
949 cation fractions of Al, Ca, Cr and Al in the Opx, as well as terms for T. It is worth noting that several of the Putirka
950 (2008) Opx thermobarometers are prone to numerical issues resulting from the presence of logarithmic terms.
951 For example, Eq29c (Opx-only) has a term for the logarithm of the cation fraction of Cr in Opx. If Cr was not
952 measured or reported in Opx, this term cannot be evaluated (the case for 63% of the experiments in our test
953 dataset). Similarly, Eq28b has a term calculated from the log of the (Fe, Mg)₂Al₂SiO₆ component in the Opx
954 divided by terms involving the cation fractions of Si, Al, Fe, Mn, and Mg in the liquid. In ~9% of experiments
955 (mostly at <3 kbar, but a few at 5 and 8 kbar), the (Fe, Mg)₂Al₂SiO₆ component in the Opx is 0, the log of which
956 yields infinity. A value of zero for the (Fe, Mg)₂Al₂SiO₆ component can also occur in Opx where the calculated
957 Al_{Vl} component is zero, which is particularly common in low pressure Opx (Al_{Vl}=0 in 7% of the Opx considered
958 here, all at <2.5 kbar). To address the numerical issue associated with the (Fe, Mg)₂Al₂SiO₆ component, in later
959 versions of the spreadsheets from Putirka (2008), two additional Opx-Liq barometers were included (“Global”

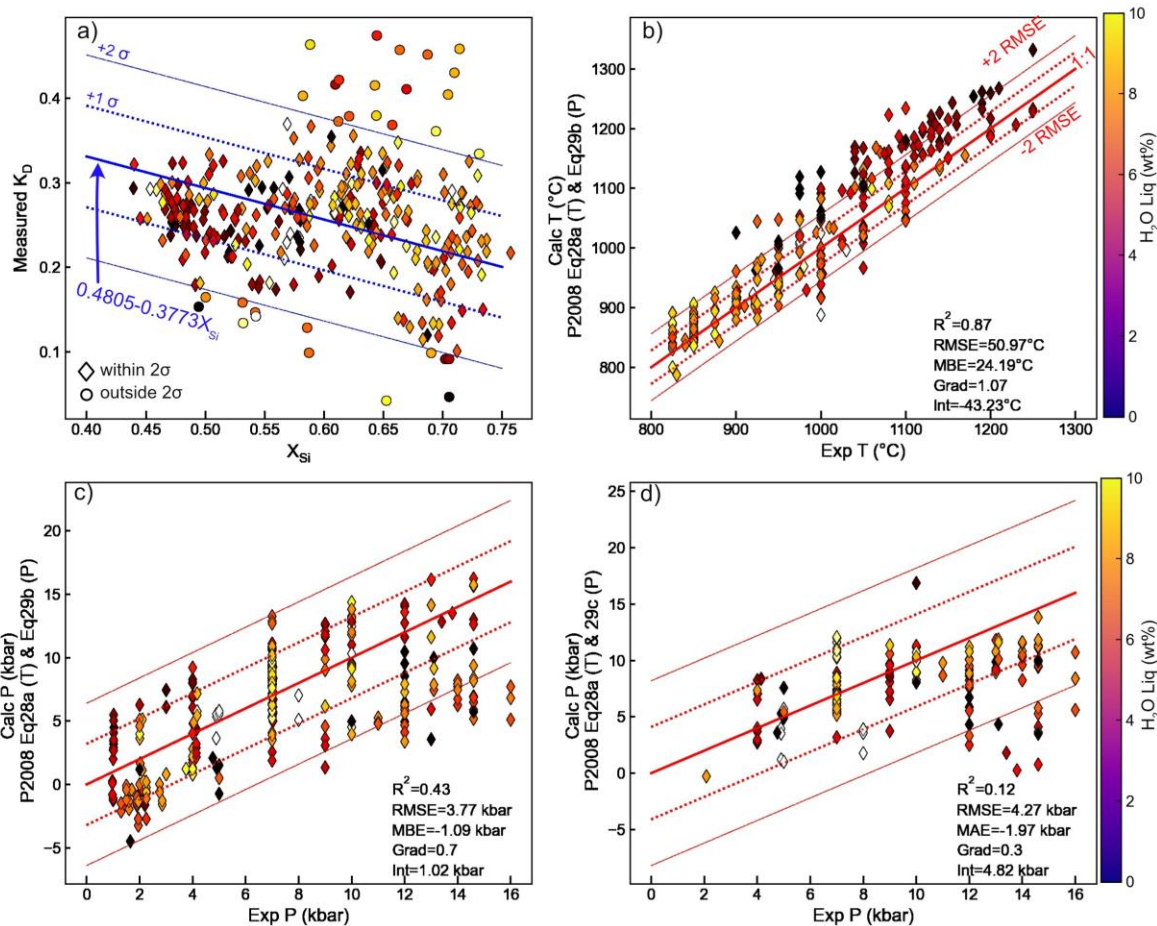
960 and “Felsic”). These equations simply use the ratio of the measured Al₂O₃ content in Opx and Liq. The global
961 model was calibrated on 795 Opx-Liq pairs, and the felsic model on 40 pairs.

962 In natural systems, it is even more difficult to assess the equilibrium relationships between erupted Opx
963 and Liquid compositions than for Cpx-Liq, because only $K_{D,Fe-Mg}^{Opx-Liq}$ has been widely explored as an equilibrium
964 test. Putirka (2008) find that K_D in experimental charges roughly correlates with the cation fraction of Si in the
965 liquid (X_{Si}) ($1\sigma=0.06$). In the ArcPL dataset, there is no significant correlation between K_D and X_{Si} ($R^2=0.01$, Fig.
966 9a), although ~67% lie within the given error bound of the predicted value. In natural systems is it very plausible
967 that liquids and orthopyroxenes that are not chemically related could yield K_D values passing these relatively
968 broad equilibrium tests (particularly if 2σ is used as the cut off). One way to avoid this problem is to use an Opx-
969 only barometer (e.g., Eq29c of P2008), However, this equation contains a temperature-sensitive term, and given
970 no Opx-only thermometer exists to our knowledge, a liquid composition may still need to be used to estimate
971 (or iteratively calculate) the temperature.

972 Using experimental P and H₂O (that was measured by quantitative methods), Eq28a (Opx and Liq
973 comps) and Eq28b (only Liq comps) are remarkably good thermometers. Eq28a has a slightly higher R^2 (0.90 vs
974 0.85), and lower RMSE (39 vs. 48°C, Supporting Fig. 3). Using experimental T and H₂O measured by quantitative
975 methods, Eq29b is the best Opx-Liq barometer ($R^2=0.58$, RMSE=3.01 kbar, Supporting Fig. 4), and has a decent
976 gradient and intercept relative to other mineral-melt barometers we evaluate in this review (grad=0.67, int=1.2).
977 Eq29a performs slightly worse in terms of R^2 and RMSE but has a slightly better gradient and intercept ($R^2=0.50$,
978 RMSE=3.65 Gradient=0.74, Int=0.3 kbar). The global barometer is noticeably worse ($R^2=0.47$, RMSE=3.47 kbar,
979 grad=0.59, int=1.4). The Opx-only barometer (Eq29c) is difficult to compare because of the presence of many
980 experiments without reported Cr measurements in Opx that return numerical errors; for available data, $R^2=0.04$,
981 RMSE=4.63 (Supporting Fig. 4d).

982 As discussed, it is probable in natural systems that neither T nor P is known, and melt H₂O is relatively
983 uncertain. We investigate the sensitivity of calculated P to T, and calculated T to P (Fig. 10) by perturbing the
984 experimental T by $\pm 100^\circ\text{C}$ and P by ± 5 kbar. The Putirka (2008) Global and Felsic barometers have no T term, so
985 show no changes in P with T. Eq29a (dark blue lines, Fig. 10a) shows a relatively small increase in calculated P
986 with increasing T, while Eq29b shows a larger increase (light blue lines, Fig. 10a). Eq29c, the Opx-only barometer,
987 shows variable sensitivity to T, with P increasing in some samples, and decreasing in others as T is increased
988 (grey lines, Fig. 10a). The strong change in calculated P as a function of T for Eq29c, a drop of up to 10 kbar for
989 $+100^\circ\text{C}$ for some samples, is problematic, as there is no way to determine temperature simply from Opx
990 compositions at present. The three Opx-Liq thermometers also show variable changes with P (some increasing,
991 some decreasing, Fig. 10b). However, the uncertainty in calculated T for changes in P of 10 kbar (equivalent to
992 the crustal thickness in most arcs) is comparable to the stated RMSE on these thermometers.

993 Overall, the relatively large change in calculated P (and to a lesser extent T) with relatively small changes in the
994 other parameter means that we can expect Opx-based thermobarometers to show far worse statistics when
995 solved iteratively than when tested with only a single unknown.



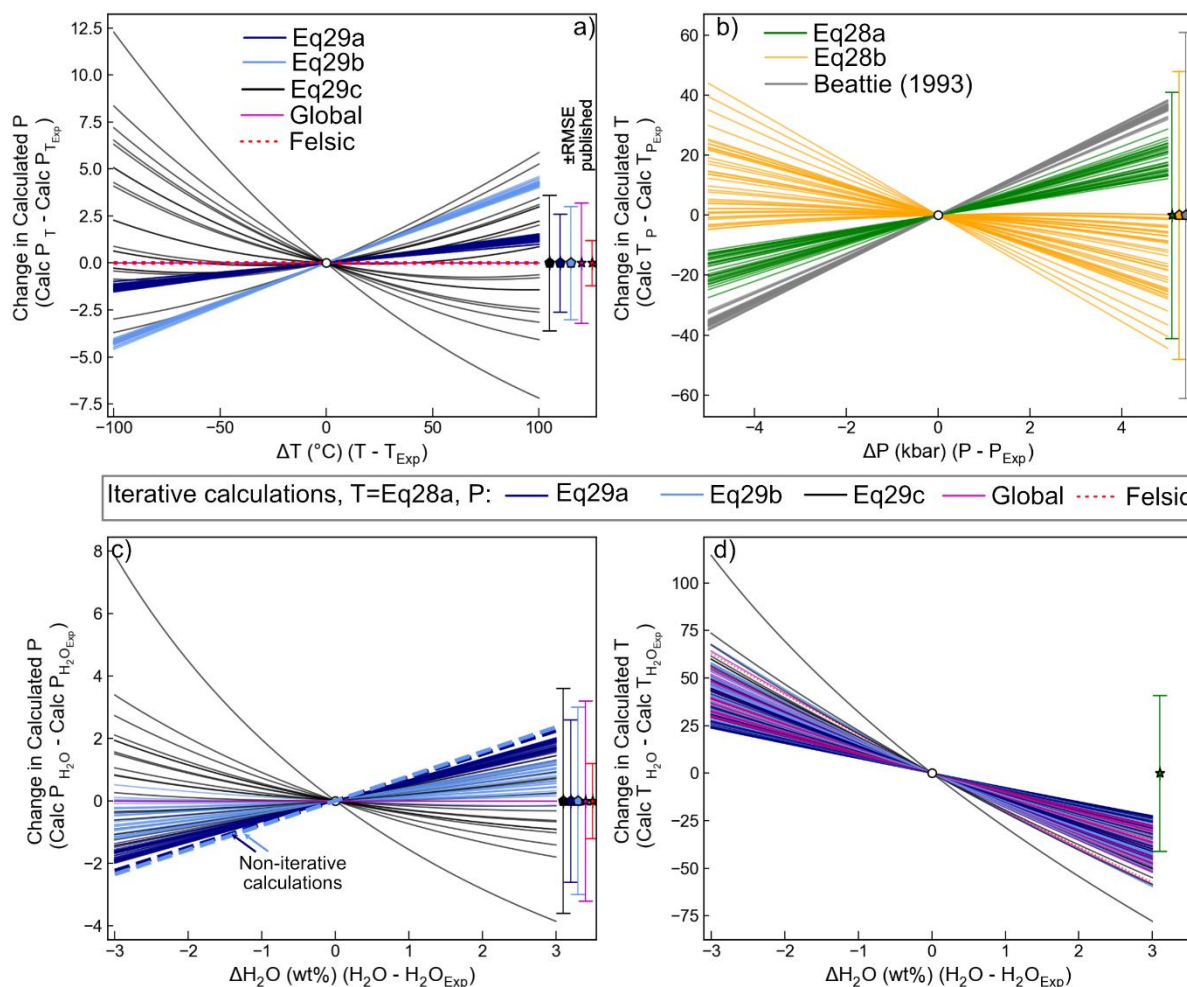
996

997 *Figure 9: Opx-Liq and Opx-only Thermobarometry. a) Comparison of measured K_D with that predicted from the*
 998 *X_{Si} content of the liquid using Putirka (2008). b-c) Comparison of calculated and experimental T and P by iterating*
 999 *Eq28a(T) and Eq29b(P). d) Iteration of Eq28a (for T, Opx-Liq) with Eq29c (Opx-only, P) of Putirka (2008). Dotted*
 1000 *lines around the 1:1 line show \pm the quoted σ , with dashed lines showing $\pm 2\sigma$. All symbols colored by H_2O content,*
 1001 *with $H_2O > 10$ wt% white, to emphasize the scale at lower H_2O contents.*

1002 We also investigate the change in P when using iterative calculations when we perturb the experimental
 1003 H_2O content by ± 3 wt%. When T from Eq28a is iterated with all barometers, calculated T decreases with
 1004 increasing H_2O (Fig. 10d). Iteration of Eq28a (T)-Eq29a (P) (dark blue line) and Eq28a (T)-Eq29b (P) (light blue
 1005 line) show a small increase in calculated P with increasing H_2O content (Fig 10c). Both these barometers have
 1006 terms multiplying H_2O by a constant, resulting in a consistent change in P for varying H_2O contents in non-
 1007 iterative calculations ($+0.748$ kbar/1 wt% H_2O for Eq29a, and $+0.784$ for Eq29b, dashed blue lines, Fig. 10c).
 1008 However, because increased H_2O contents cause T to drop using Eq28a (Fig. 10b), which causes a decrease in
 1009 the calculated P (Fig. 10a), the influence of H_2O on calculated P in iterative calculations is slightly less than that
 1010 obtained in calculations using the experimental T. This complex feedback between equations during iterative
 1011 calculations results in a greater variability in the influence of H_2O on calculated P for different samples. Eq29c
 1012 has no H_2O term but shows the strongest sensitivity to T (Fig. 10a), resulting in a large drop in P with increasing
 1013 H_2O when iterated with Eq28a (Fig. 10c). The high sensitivity of Eq29c to H_2O is concerning because an Opx-only
 1014 barometer is most likely to be applied in systems where liquid compositions (and thus, H_2O contents) are poorly
 1015 constrained. As the Global and Felsic barometers have no T or H_2O term, they show no sensitivity to H_2O .

1016

1017



1018

1019 *Figure 10: Assessing the sensitivity of Opx thermobarometry to variation in P, T and H₂O for N=40 randomly*
 1020 *selected experiments. a) Change in calculated P for perturbing the experimental T by ± 100 °C. b) Change in*
 1021 *calculated T by perturbing P by ± 5 kbar. c-d) Change in calculated P and T for iterative calculations perturbing*
 1022 *experimental H₂O content by ± 3 wt%. For all plots, the calculated P or T at experimental conditions is subtracted*
 1023 *from the calculation at experimental conditions (plotting at 0, 0). Calculations performed in Thermobar (Wieser*
 1024 *et al., 2022b).*

1025 Ideally, given the effects of H₂O on calculated P and T (Fig. 10c-d), we would only assess experiments
 1026 where H₂O is known by quantitative methods (as for Liq-only). However, only 147/324 experiments from 10/23
 1027 studies have reported Opx-Liq compositions where H₂O was measured quantitatively. Thus, all experiments are
 1028 shown in Fig. 9, with the same calculations using only experiments with quantitative H₂O measurements shown
 1029 in Supporting Fig. 5 (which shows worse statistics).

1030 Iterating the best thermometer (Eq28a) and barometer (Eq29b) yields a very good match to
 1031 experimental T in ArcPL using experimental H₂O contents (Fig. 9b). The thermometer performs worse for
 1032 experiments with low H₂O contents (darker symbols, < 2–3 wt%). Based on a similar observation for the LEPR
 1033 dataset, Putirka (2008) suggest that Opx may re-equilibrate faster in more hydrous liquids. Calculated P from
 1034 iteration of Eq28a-Eq29b is reasonably accurate (Fig. 9c, grad=0.7, MBE=-1.09 kbar, int=-1 kbar), but very
 1035 imprecise (RMSE=3.77 kbar), so this barometer will be of limited utility in relatively thin-crustal settings such as
 1036 OIBs and MORBs (Fig. 3). Unlike for thermometers, there is no clear relationship between barometer
 1037 performance and H₂O content. Although we cannot perform very many calculations for Eq29c because of the
 1038 absence of Cr data, calculated Opx-only pressures (Eq29c) iterated with Eq28a shows a reasonable
 1039 correspondence to the 1:1 line (Fig. 9d) at <12 kbar, although substantially more experiments with reported Cr
 1040 contents are required to robustly assess this barometer.

1041 Overall, Opx-Liq thermobarometry has been relatively neglected given its performance; no new
 1042 calibrations have been proposed since 2008. In particular, the relative absence of systematic uncertainty when
 1043 Opx-based barometers are tested on ArcPL contrast strongly with other mineral barometers discussed here. We
 1044 suggest that future experimental and theoretical work to further develop Opx-based thermobarometry is
 1045 warranted, with a particular focus on the development of more robust equilibrium tests. Ensuring starting
 1046 materials contain Cr contents comparable to natural systems, and ensuring all elements are measured at high
 1047 precision within experimental Opx (particularly Cr) may lead to improved thermobarometry calibrations. This
 1048 may provide a particularly promising barometer in arc magmas, where Opx is relatively common, and magmas
 1049 are relatively H₂O-rich.

1050 2.5. Two Pyroxene (Cpx-Opx) Thermobarometry

1051 Two pyroxene (Cpx-Opx) thermobarometry is widely used in the literature, likely reflecting the fact that
 1052 these phases crystallize together across a wide range of P, T, and H₂O contents in a variety of tectonic settings.
 1053 For example, Cpx-Opx thermobarometry has been applied to OIB basalts from the Galápagos by Gleeson et al.
 1054 (2021), to mafic arc basalts from SW Japan by Zellmer et al. (2014), and to arc dacites from the Aucanquilcha
 1055 Volcanic Cluster by Walker et al. (2013). Additionally, it is common that Cpx and Opx form crystal clusters, and
 1056 calculations from these touching pairs are easier to justify than trying to select equilibrium liquids for each crystal
 1057 (c.f. Opx-Liq and Cpx-Liq thermobarometry). Opx-Cpx thermobarometry can also be applied in systems where it
 1058 is difficult to analyse the composition of the liquid (e.g., highly crystalline lavas or xenoliths, Gao et al., 2022;
 1059 Gleeson et al., 2021).

1060 As discussed above for Opx-Liq equilibrium, one of the main limitations of Cpx-Opx thermobarometry
 1061 is the paucity of equilibrium tests to help filter out pairs which are not in equilibrium (in experiments and natural
 1062 samples). The only established equilibrium test compares the exchange of Fe-Mg in Cpx and Opx ($K_{D,Fe-Mg}^{Cpx-Opx}$).
 1063 Putirka (2008) suggest that $K_D=1.09\pm 0.14$ in high temperature systems, while $K_D=0.7\pm 0.2$ in subsolidus systems.
 1064 However, it is difficult to know where to draw the line between these different filters; what value would be
 1065 correct to use in a supra-solidus dacitic-rhyolitic melt that is a similar temperature to a subsolidus mafic
 1066 cumulate? K_D values for our compiled experiments lie mostly within the high T bracket ($\pm 1\sigma$ shown in pink),
 1067 although a number extend to higher values (Fig. 11a). There is no strong relationship between T and measured
 1068 K_D . Another way to assess the equilibrium value would assume that the Cpx and Opx are each in equilibrium
 1069 with the liquid, so the Opx-Cpx K_D value can be obtained from the Cpx-Liq and Opx-Liq K_D values from Putirka
 1070 (2008):

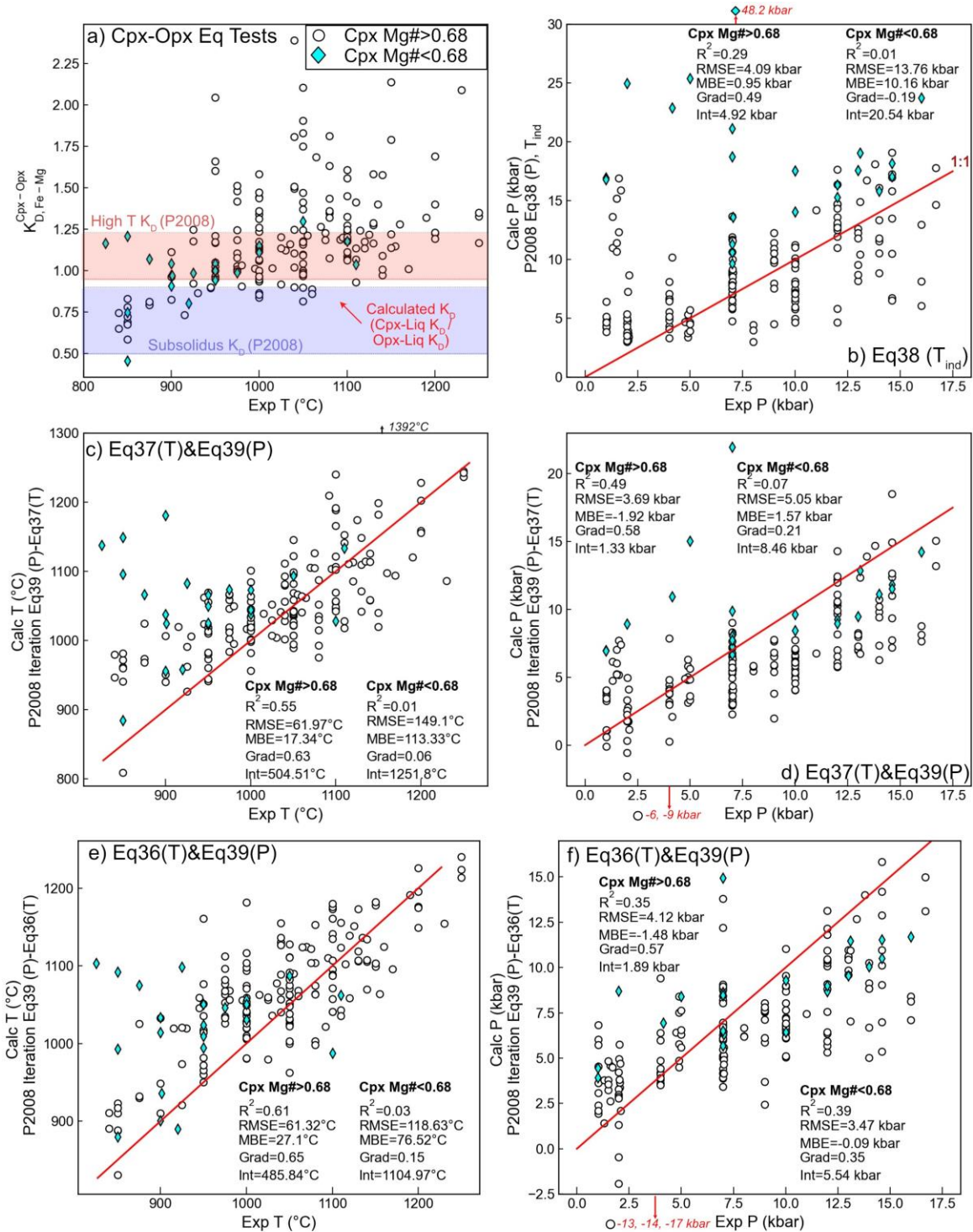
$$1071 K_{D,Fe-Mg}^{Cpx-Opx} = \frac{K_{D,Fe-Mg}^{Cpx-Liq}}{K_{D,Fe-Mg}^{Opx-Liq}} = \frac{e^{-0.107 - \frac{1719}{T(K)}}}{0.4805 - 0.3733 * X_{Si,Liq}} \text{ [Equation 8]}$$

1072 This approach could be advantageous, because there are far more Cpx-Liq and Opx-Liq experiments
 1073 than Cpx-Opx experiments, so the individual Px-Liq equilibrium values are better constrained. Values calculated
 1074 using this expression lay between the subsolidus and high T value (red dots, Fig. 11a), with very little variation
 1075 with temperature. This is because higher T drives up the Cpx-Liq K_D , but higher T liquids tend to have lower Si
 1076 contents, which drives up Opx-Liq K_D . Unfortunately, Equation 8 appears to underestimate the K_D value for many
 1077 of the experimental samples given here, which is perhaps unsurprising as we find the Cpx-Liq K_D expression
 1078 underestimates many of the Cpx-Liq K_D values (by up to ~0.5), while the Opx-Liq expression tends to
 1079 overestimate many of the Opx-Liq K_D values. Dividing these two relatively uncertain quantities compounds
 1080 errors. The fact so many of our experimental Cpx-Opx pairs sit outside any estimate of equilibrium could suggest
 1081 that several are not in equilibrium, so should not be used to assess thermobarometers. However, we find no
 1082 discrepancy between K_D and the offset between calculated and predicted P and T. This suggests instead, that
 1083 more experimental and theoretical work is needed to robustly assess K_D . Thus, we proceed to assess
 1084 thermobarometers using all Cpx and Opx pairs in the ArcPL compilation.

1085 The T-independent barometer of P2008 (Eq38) performs very poorly for high Mg# Cpx ($R^2=0.29$,
 1086 RMSE=4.09) and even worse for low Mg# Cpx (<0.68, cyan diamonds, Fig. 11b, $R^2=0.01$, RMSE=13.72). Iteration
 1087 of P2008 Eq37–39 and Eq36–Eq39 show very similar statistics to one another for calculated P and T, with Eq36–
 1088 Eq39 showing slightly better behaviour. Neither thermometer is very promising (Fig. 11c, e) producing more of

1089 a data cloud than a meaningful correlation. Iterated barometers are similarly disappointing; even for Cpx with
 1090 Mg#>0.68, the RMSE is 3.69 kbar (Eq3 7–Eq39, Fig. 11d) and 4.12 kbar (Eq3 6–Eq39, Fig. 11c).

1091 Overall, we suggest that substantially more experiments where Opx and Cpx are stabilized at a variety
 1092 of pressures and melt compositions are required to improve Cpx-Opx barometers, particularly in more evolved
 1093 systems with lower Cpx Mg#. Additional experiments would also help to better constrain controls over the
 1094 equilibrium value at a variety of temperatures and melt compositions.



1095

1096 *Figure 11: Assessing two-pyroxene thermobarometers. a) Measured $K_{D,Fe-Mg}^{Cpx-Opx}$*
 1097 *against experimental T. The range of equilibrium values from Putirka (2008) for “HighT” and “Subsolidus”*

1098 systems are shown as colored bars. K_D values calculated from the Cpx-Liq (T-dependent) and Opx-Liq (Si-
1099 dependent) K_D values (Equation 12) are shown as small red dots. b-f) Comparison of predicted and experimental
1100 P and T for different combinations of equations from P2008. 1:1 line shown in red. In all plots, Cpx-Opx pairs with
1101 Cpx Mg#<0.68 are colored cyan, and Mg#>0.68 colored white. To maintain scale, a few experiments returning
1102 extreme values are excluded from plots. Their y coordinate is labelled with a red arrow.

1103 2.6. Amphibole thermobarometry and Chemometry

1104 Amphibole (Amp)-only and Amp-Liq thermobarometry have been used extensively to calculate P and T
1105 in volcanic and plutonic igneous systems (e.g., Higgins et al., 2022; Scruggs and Putirka, 2018). Amphibole
1106 chemometers are also becoming widely used to probe the compositions of melts present at depth within
1107 plumbing systems which are not always well represented at the surface (e.g., Humphreys et al., 2019; Zhang et
1108 al., 2017).

1109 2.6.1 Amphibole thermobarometry

1110 Amphibole barometry stems from the seminal work of Hammestrom and Zen (1986), who showed that
1111 the Al^{VI} and Al^{Tot} contents of hornblendes from calc-alkaline plutons emplaced at different depths correlate with
1112 estimates of pressure, and that the same compositional-pressure relationships were seen in experimental
1113 products. Hollister et al. (1987) analysed rim compositions from plutons where the pressure of emplacement
1114 could be estimated from phase assemblages in the surrounding country rock. They confirmed the Al-pressure
1115 relationship of Hammestrom and Zen (1986) and proposed an updated calibration. Additional calibrations have
1116 also been developed for Amp-Plag, Amp-Garnet, and Amp-Plag-Qtz (see Molina et al., 2021 and refs. within).

1117 More recently, Mutch et al. (2016) present an Amp-only barometer parameterized in terms of Al^{Tot}
1118 calibrated using a dataset comprising: i) their new experiments on 3 different bulk compositions, ii) the
1119 experiments of Johnson and Rutherford (1989), Schmidt (1992), Thomas and Ernst', 1990), iii) published analyses
1120 from plutons with independent depth constraints (Ague, 1997; Hammestrom and Zen, 1986), and iv) their new
1121 analyses on amphiboles from the Yerrington Batholith in Nevada. Mutch et al. (2016) exclude experiments where
1122 garnet or phengite was stabilized, as this alters the Al^T -pressure relationship. Importantly, their compiled dataset
1123 shows a curvature in Al^T vs. pressure space relationship at 0.5–3 kbar not seen by previous workers. They
1124 parameterize this empirically relating pressure to a second order polynomial of Al^T .

1125 While Al^T in amphibole is controlled by both T and P, so can only be used as a barometer on an isotherm
1126 or near a solidus (Médard and Le Pennec, 2022), correlations between P and Al^{VI} have been noted by Krawczynski
1127 et al. (2012), Helz (1982), Larocque and Canil (2010) and Schmidt (1992) in a wide variety of systems. Médard
1128 and Le Pennec (2022) present a T-independent barometer using a simple linear regression of P and Al^{VI} ,
1129 calibrated on 47 published experimental compositions with Si-rich silicate melts in equilibrium with Biotite,
1130 Plagioclase, and Magnetite. They state that this barometer has a RMSE of 0.86 kbar (or 0.72 kbar for <4 kbar).
1131 They also test their expression on 22 biotite-bearing experiments not used in calibration, which lie within the
1132 stated RMSE window. However, all their tests are at <4 kbar, which makes it difficult to evaluate the precision
1133 of the barometer at higher pressures.

1134 Importantly, all the Al-based amphibole-only barometers discussed so far are only applicable in the
1135 presence of certain phases. For example, Hammestrom and Zen (1986) warned about the applicability of their
1136 regressions in rocks without quartz, where Al^T can be significantly higher at a given P. Mutch et al. (2016)
1137 emphasize that their barometer should only be applied to amphibole rims in equilibrium with melts saturated
1138 in plagioclase (An_{15-80}), biotite, quartz, alkali feldspar, Fe-Ti oxides, and apatite (e.g., near solidus, low variance
1139 volcanic systems). In higher T melts with fewer co-crystallizing phases and higher thermodynamic variance, the
1140 equilibria controlling amphibole composition are still poorly understood (Putirka, 2016). Médard and Le Pennec
1141 (2022) test their barometer using 7 Bt-free experiments, resulting in a RMSE of 1.4 kbar, which is a large % error
1142 given these experiments were conducted at ~ 1–2 kbar. Thus, they suggest that this barometer should not be
1143 used in biotite-free rocks. While limited in their applicability to silicic systems saturated in a large number of
1144 phases, the amphibole-only barometers discussed thus far are extremely useful for determining pluton
1145 emplacement depths and crustal exhumation rates in orogenic belts, or when investigating the formation and
1146 evolution of Porphyry copper deposits (Anderson, 1996; Hollister et al., 1987; Mutch et al., 2016).
1147

1148 In contrast to these studies focused on low variance silicic systems, Ridolfi et al. (2010) compile calcic
1149 amphibole analyses from experiments conducted on a wide range of melt compositions and phase assemblages

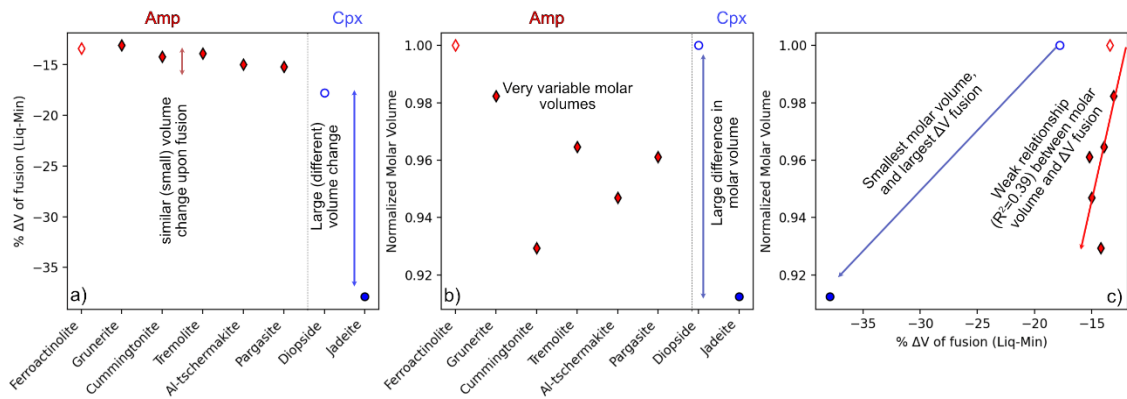
1150 to generate an empirical amphibole-only thermometer (Eq1), oxybarometer (Eq2) and hygrometer (Eq3). Ridolfi
1151 et al. (2010) justify the application of Amp-based methods in less evolved systems with fewer phases (and
1152 therefore higher variance) by pointing out that most volcanic amphiboles exist close to their stability limits
1153 (shown by abundant breakdown textures). They suggest that close to the amphibole stability curve, the variance
1154 of the system is lower so amphibole composition is more closely related to P, T and fO_2 . Ridolfi et al. (2010) also
1155 present an Al^T barometer calibrated on 9 amphiboles (Eq4) but find that attempts to perform a similar calibration
1156 on their larger experimental dataset performs poorly, particularly for magnesiohastingsite amphiboles which
1157 are common in nature, but sparse in available experiments.

1158 Ridolfi and Renzulli (2012) compile additional experiments and apply more stringent filters to produce
1159 an amphibole-only barometer (e.g., removing amphiboles with 1σ for $SiO_2 > 0.9$ wt%, Piston cylinder experiments
1160 conducted at < 6 kbar etc.). Of the 61 experimental amphiboles remaining, 19 (31%) are magnesiohastingsite,
1161 which is close to the proportion of magnesiohastingsites (42%) in their natural compilation. This is in stark
1162 contrast to the dataset of Ridolfi et al. (2010), which contained no magnesiohastingsites (or pargasites or
1163 kaersutites). Ridolfi and Renzulli (2012) create several different regressions to calculate P using amphibole cation
1164 fractions calculated on the basis of 13 oxygens. For example, Eq. 1a was calibrated on $N=61$ experiments, and
1165 expresses P in terms of the exponential of compositional terms (Si, Ti, Al, Fe, Mg, Ca, Na, K). However, using
1166 comparisons to seismic depths from Ridolfi et al. (2010) for a variety of natural systems, they show that this
1167 equation overestimates at low P, and underestimates at high P. They calibrate 4 additional expressions using a
1168 smaller subset of analyses ($N=20-41$) in different pressure ranges (Eq1b and 1e use exponentials, 1c and 1d use
1169 multilinear regressions). They present an algorithm where the user calculates P for each equation, and these
1170 different values are averaged/combined in a variety of different ways to construct a final P.

1171 To test the expressions of Ridolfi and Renzulli (2012), Erdmann et al. (2014) compile a series of
1172 experiments not used in their calibration dataset. While T, melt SiO_2 content and fO_2 are reasonably well
1173 predicted in their new dataset, they demonstrate a very poor correspondence between calculated and
1174 experimental P, and calculated and experimental H_2O contents. Erdmann et al. (2014) suggest the P discrepancy
1175 results from the fact that the Si-Al content of an amphibole is more strongly related to the liquid composition
1176 and T than P. In particular, they note that the calibration dataset of Ridolfi and Renzulli (2012) is skewed, with
1177 amphiboles from felsic and intermediate melts clustered at lower P, and mafic to intermediate melts at higher
1178 Molina et al. (2021a) also publish a short note stating that they test Ridolfi and Renzulli (2012) using a dataset
1179 of experiments compiled by Molina et al. (2021b), and obtain “*unsustainable pressure estimates*”.

1180 Putirka (2016) further examine Amp-only and Amp-Liq equilibrium, presenting two P-independent
1181 Amp-only thermometers (Eq5 and SiHbl), two P-dependent Amp-only thermometers (Eq6 and Eq8), two P-
1182 independent Amp-Liq thermometer (Eq4b and Eq9), and a P-independent Liq-only amphibole saturation
1183 thermometer (Eq4a). He also presents three T-independent Amp-Liq barometers (Eq7a, b, c). Using an extensive
1184 test dataset, Putirka (2016) show that Amp-only and Amp-Liq equilibrium do a reasonably good job of predicting
1185 pressure when averaged, but conclude that P estimates from individual amphibole grains are ‘*nearly useless for*
1186 *understanding crustal processes*’. They hypothesize that the main limitation of Amp-based barometry is the fact
1187 that none of the common amphibole components have particularly large changes in volume when they
1188 precipitate from the liquid (ΔV fusion), or large molar volume contrasts between different components in the
1189 amphibole itself. For example, even though Jadeite in pyroxene is not a particularly sensitive barometer at
1190 crustal conditions, relative to Diopside it has a significantly more negative ΔV fusion (Fig. 12a), and a smaller
1191 molar volume (8% smaller, Fig. 12b, Putirka, 2016). As Jadeite has both a smaller molar volume and a more
1192 negative ΔV fusion (Fig. 12c), the amount of Jadeite vs. Diopside in Cpx are sensitive to P. In contrast, there is a
1193 pretty weak relationship between the ΔV fusion and the molar volume for different amphibole components (Fig.
1194 12b-c, Putirka, 2016). While the exchange of different amphibole components is not particularly P-sensitive,
1195 Putirka (2016) do show that the partition coefficient of Al between amphibole and liquid is correlated to P,
1196 explaining why amphibole barometers are normally parameterized in terms of Al and other oxides, rather than
1197 explicitly calculated mineral components (e.g. Jadeite in Cpx).

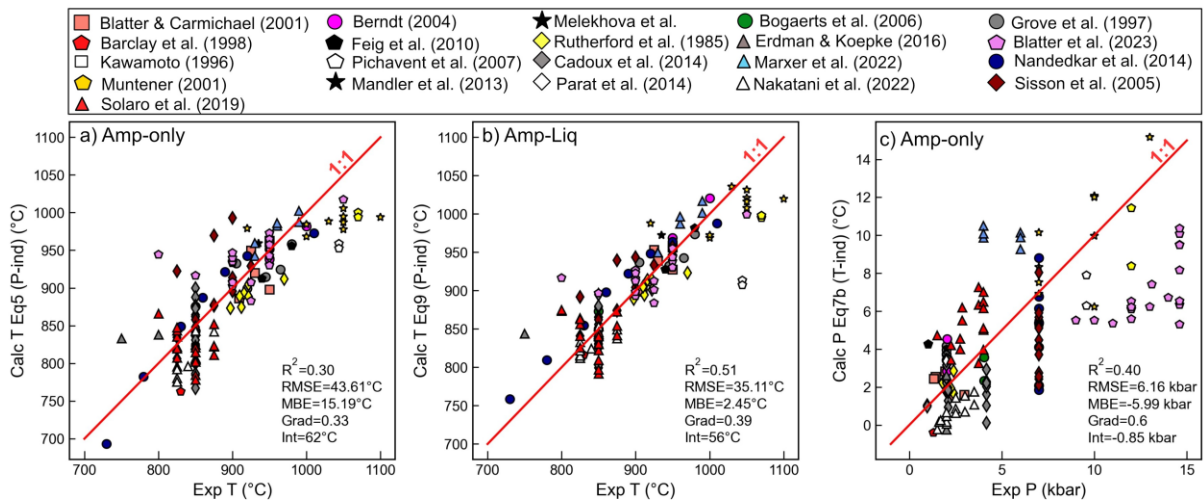
1198



1199

1200 *Figure 12. Comparison of molar volumes and volumes of fusion for Amp vs. Cpx components. a) Changes in*
 1201 *volume following precipitation of different mineral components from the liquid (ΔV fusion). Amphibole*
 1202 *components show significantly smaller changes than jadeite, and the different Amp components show very*
 1203 *similar ΔV fusion. b) Molar volume normalized to the component of each phase with the highest molar volume*
 1204 *(ferroactinolite for Amp, Diopside for Cpx). c) Correlation between normalized molar volume and ΔV fusion.*
 1205 *Thermodynamic data from table 1 of Putirka (2016).*

1206 We use data not included in the calibration of the Putirka (2016) equations to test their performance (see
 1207 Supporting Figs. 6–8), and sensitivity to other terms present in the regression. The best performing Amp-only
 1208 thermometer for this dataset is Eq5 ($R^2=0.7$, $RMSE=41.5^\circ C$, Fig. 13a, Supporting Fig. 6), which has the advantage
 1209 of being independent of P and H_2O in the liquid. The best Amp-Liq thermometer is Eq9 ($R^2=0.76$, $RMSE=34^\circ C$,
 1210 Fig. 13b, Supporting Fig. 8), which is P independent and not very sensitive to H_2O in the liquid (Supporting Fig. 7,
 1211 $\sim 1^\circ C$ change in T per 1 wt% H_2O). Like Putirka (2016), we find that all three Amp-Liq barometers show
 1212 disappointing statistics ($RMSE= 3\text{--}4$ kbar, $Grad=0. 3\text{--}0.5$, Supporting Fig. 8, e.g., Fig. 13c). In particular, the
 1213 pressures for the higher P experiments of Blatter et al. (2023), and Muntener et al. (2001) are greatly
 1214 underestimated, although the barometer does a reasonable job of the lower P data, which clusters around the
 1215 1:1 line at $\sim 2\text{--}5$ kbar. The skew at high P means that even after the averaging suggested by Putirka (2016), Amp-
 1216 Liq barometry can give misleading results.



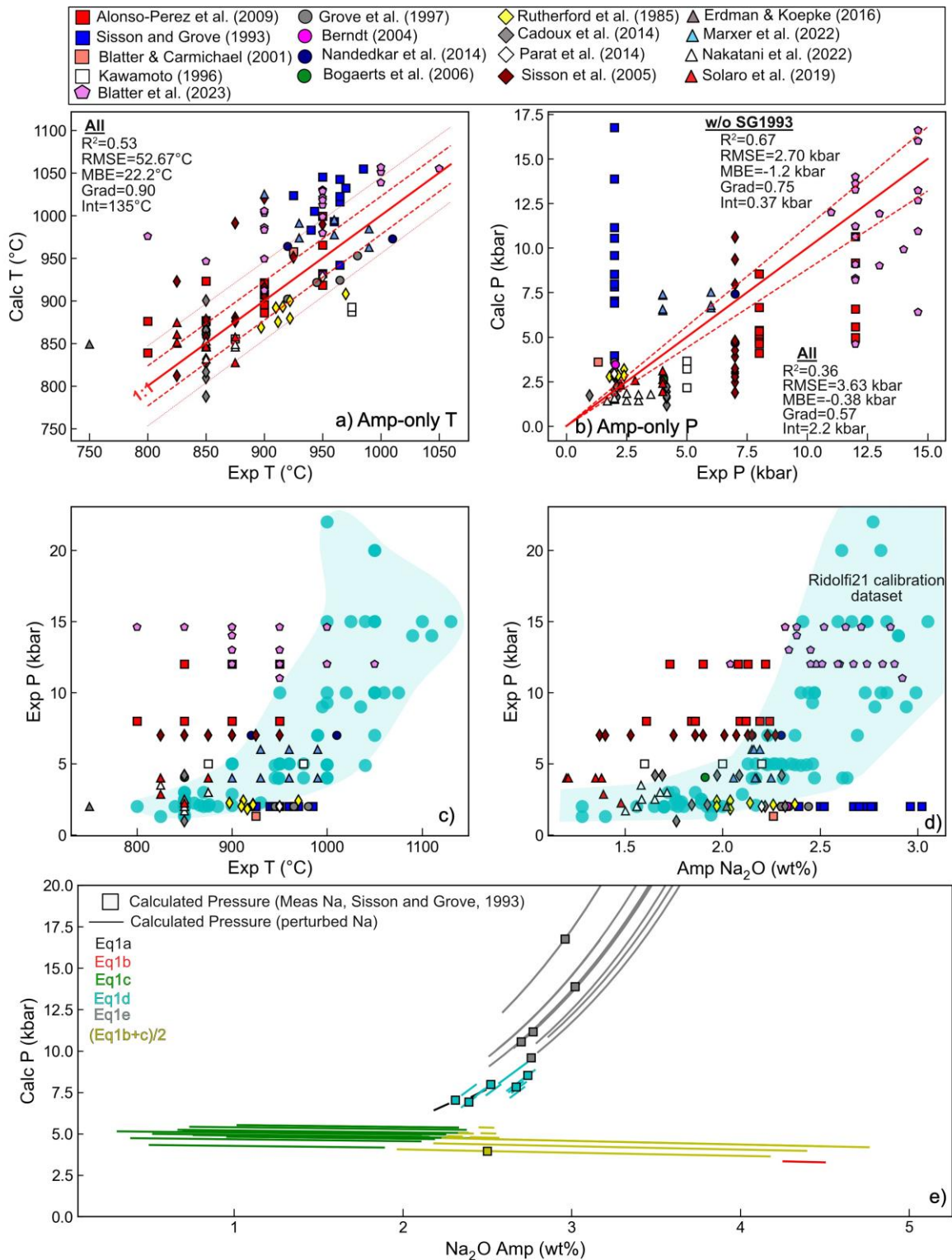
1217

1218 *Figure 13 – Assessing Amp-Liq and Amp-only thermobarometers from Putirka (2016) using experiments not used*
 1219 *during model calibration. Only experiments passing the K_D filter of Putirka (2016) are shown.*

1220 Ridolfi (2021) recently updated the Ridolfi and Renzulli (2012) amphibole-only barometer, perhaps
 1221 partially in response to the criticism of Erdmann et al. (2014), Molina et al. (2021) and Putirka (2016), and
 1222 partially because of an increase in the number of amphibole-bearing experiments. Using an expanded
 1223 experimental dataset, they tweak the algorithms used to select between different P equations and add more

1224 stringent filters to give users warning of when the equations are being applied to amphiboles failing quality tests
1225 or outside the model calibration range (based on totals, unbalanced charge, low B cations, etc, low and high Ca
1226 cations, low Mg cations). We tested this new algorithm and filter criteria on a dataset of experiments not used
1227 during calibration (Alonso-Perez et al., 2009; Berndt, 2004; Blatter and Carmichael, 2001; Bogaerts et al., 2006;
1228 Cadoux et al., 2014; Erdmann and Koepke, 2016; Grove et al., 1997; Kawamoto, 1996; Marxer et al., 2022;
1229 Nakatani et al., 2022; Parat et al., 2014; Rutherford et al., 1985; Sisson et al., 2005; Sisson and Grove, 1993;
1230 Solaro et al., 2019, Blatter et al. 2023). Of our compiled experiments (N=193), 112 pass the quality check filters
1231 of Ridolfi (2021, Fig. 14a). Calculated P show a moderate correspondence to experimental P, although
1232 calculations clearly lie well outside the stated $\pm 12\%$ error in the abstract of Ridolfi (2021, red dashed lines, Fig.
1233 14b). The overall fit to all experiments yields $R^2=0.36$ and $RMSE=3.6$ kbar. The experiments conducted at 2 kbar
1234 by Sisson and Grove (1993) show particularly poor results, returning pressures which are up to 15 kbar too high.
1235 Excluding these experiments yields $R^2=0.67$ and $RMSE=2.7$ kbar. Compared to the Putirka (2016) Amp-Liq
1236 barometers, this Amp-only barometer does a much better job of recreating the high pressures of Blatter et al.
1237 (2023), although it does still underestimate to a degree. Despite the criticism of this method in the literature, it
1238 is noteworthy that Amp-only barometry doesn't perform any worse than Opx-Liq and Opx-Cpx based on our
1239 dataset - none of these methods are precise enough to be useful to many volcanological questions. It just seems
1240 that Amp-based methods have received the bulk of the critique until recently. As amphibole-only T from Ridolfi
1241 and Renzulli (2012) require a P to be entered, we also test how effective this thermometer is using pressures
1242 obtained from the 2021 barometer. For these 112, the correlation between calculated and experimental T is
1243 reasonably good (Fig. 14a, $R^2=0.53$, $RMSE=53^\circ\text{C}$), although the RMSE is twice that stated in the abstract of Ridolfi
1244 (2021, 22°C , shown with dashed red lines, Fig. 14a).

1245 We examined the Sisson and Grove (1993) experiments in the context of the calibration dataset of
1246 Ridolfi (2021) to try to understand the poor performance of the barometer. These experiments plot to
1247 substantially higher amphibole Na_2O contents at lower pressures than any of the calibration experiments (Fig.
1248 14d). To investigate whether this offset to lower Na_2O contents could explain the anomalously high calculated
1249 P, for each Sisson and Grove (1993) amphibole, we perturb the Na_2O content by ± 2 wt%. Pressures for measured
1250 amphibole compositions are shown as squares (Fig. 14e), with a line stretching from each square showing the
1251 change in pressure as Na_2O is changed. The colors indicate the root equation from Ridolfi (2021) algorithm used
1252 to determine P, with the rapid jumps in pressure reflect a flip to a different equation selected by the algorithm.
1253 For the samples with high calculated P (>7.5 kbar), it is very clear that Eq1e (and to a lesser extent 1d and 1a) is
1254 highly sensitive to the Na_2O content, rapidly shooting up to extremely high pressures for very small changes in
1255 Na contents. It may well be that these natural samples lie outside the Na_2O range used to calibrate Eq1e (the
1256 calibration data for each specific equation is not available). The Alonso-Perez et al. (2009) experiments (red
1257 squares) where pressure is underestimated are also clearly offset from the calibration dataset in T – Na_2O space
1258 (Fig. 14c). This comparison emphasises the importance of ensuring that sample compositions are well
1259 represented in the calibration dataset of the chosen model, not just in terms of P-T space, but also compositional
1260 space. It also shows that having the correct functional form for a barometer rooted in thermodynamics is
1261 essential to minimize extrapolation issues commonly seen with empirical fits.



1262

1263 *Figure 14: Assessing Amp-only thermometers and barometers. a) Comparing experimental and calculated T using*
 1264 *the thermometer of Ridolfi and Renzulli (2012) iterated with Ridolfi (2021). b) Comparing experimental and*
 1265 *calculated P using the new barometer of Ridolfi (2021, T-independent). c-d) Visualizing experimental*
 1266 *compositions relative to the calibration dataset (cyan dots and field) of Ridolfi (2021). Many of the experiments*
 1267 *showing the largest discrepancies in calculated pressure (e.g., red and blue squares, magenta diamonds) lie*
 1268 *outside the calibration range of Ridolfi (2021) in Pressure-Na₂O space. e) To visualize the effect of Na₂O on*
 1269 *calculated pressure, we perturb the Na₂O content of the experiments of Sisson and Grove (1993) by ± 2 wt%. The*
 1270 *lines are not continuous, with jumps to a different pressure as the algorithm flips between different 'root'*

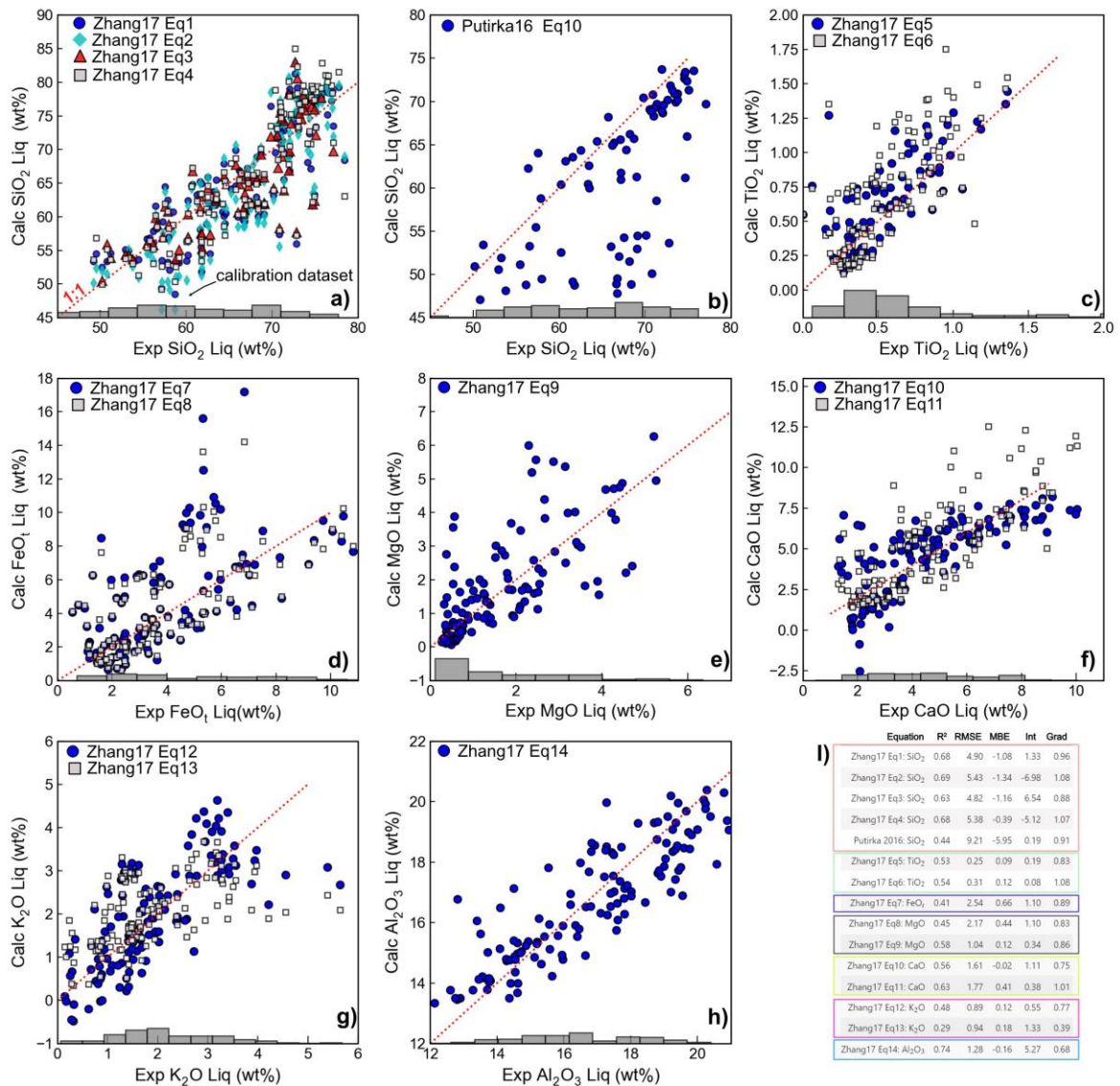
1271 equations (indicated by the color of the line). Experimental Na_2O (and calculated pressures) are indicated with
1272 squares, with the calculations following the perturbation shown as lines.

1273

1274 2.6.2 Amphibole Chemometry

1275 Ridolfi and Renzulli (2012) also present equations to calculate the contents of SiO_2 , TiO_2 , Al_2O_3 , FeO_t ,
1276 MgO , CaO , and K_2O in the melt from which amphiboles crystallized. These equations are parameterized in terms
1277 of amphibole composition and pressure. However, given the uncertainties discussed above calculating pressures
1278 from amphibole compositions, these P-sensitive parameterizations can be problematic to implement in natural
1279 systems. Erdmann et al. (2014) show that the predicted SiO_2 content is a reasonable match above 65 wt% SiO_2 ,
1280 but tends to overpredict SiO_2 for more mafic melts. Putirka (2016) use their newly compiled dataset to produce
1281 an updated expression (Eq10) for melt SiO_2 from the amphibole using the temperature of the melt and the cation
1282 fraction of Al in the amphibole.

1283 Zhang et al. (2017) compile a reasonably similar calibration dataset to Putirka (2016), and produce
1284 multiple regressions to calculate melt oxide components from a variety of amphibole site positions (e.g., Si-Ti-
1285 Mg-Fe-Ca in amphibole for predicting SiO_2 in the melt). These expressions are P-independent, and only Eq3 (for
1286 SiO_2) and Eq5 (for TiO_2) are T-sensitive. Zhang et al. (2017) calibrate multiple equations for some melt oxide
1287 contents (e.g., 4 equations for SiO_2 , 2 equations for FeO_t). We test the 133 ArcLEPR amphiboles which pass the
1288 Zhang et al. (2017) equilibrium filter ($K_{\text{D, Fe-Mg}}=0.28\pm0.11$, and do not appear in their calibration dataset. The
1289 calculated statistics are similar if a K_{D} filter isn't used. Overall, unlike many of the barometers discussed in this
1290 review, these chemometers perform very well for experiments they were not calibrated on (Fig. 15). Eq2 of
1291 Zhang et al. (2017) does a good job of predicting melt SiO_2 content across a wide range, showing much better
1292 performance than Eq10 of Putirka, 2016 (Fig. 15a vs. b). The statistics of the fit are similarly good for melt Al_2O_3
1293 (Eq14). There is more scatter for other oxides, and reasonably large differences between the different provided
1294 equations, but it is not always clear which equation is better (e.g., Fig. 15c). It is notable that the worst
1295 performance is seen for experiments with oxide contents towards the tail end of the calibration dataset (grey
1296 histograms, Fig. 15). For example, Eq12 and Eq13 do a good job of predicting K_2O until ~3.5 wt% K_2O ; very few
1297 experiments in the calibration dataset had such high K_2O contents (Fig. 15g). Similarly, the fit is better at lower
1298 MgO contents, where the calibration dataset is concentrated (Fig. 15e). In general, our tests demonstrate that
1299 amphibole compositions can be used to estimate the melt compositions from which they grew, as long as the
1300 results are carefully evaluated relative to the calibration range of the model.



1301

1302 *Figure 15 – Assessment of amphibole chemometers of Zhang et al. (2017, panel a, c-h) and Putirka (2016, panel*
 1303 *b). For equation 3 and 5 of Zhang et al. (2017) and Putirka (2016) eq10, we use temperatures calculated from co-*
 1304 *solving T from Ridolfi and Renzulli (2012) and P from Ridolfi (2021). Putirka (2016) eq10 also requires P from*
 1305 *Ridolfi (2021) to be input. These equations have fewer datapoints on the plot, as we exclude P and Ts where*
 1306 *Ridolfi (2021) returns an input warning. i) shows the statistics for each equation. The filtered test dataset*
 1307 *comprises 133 experimental charges not used by Zhang et al. (2017) during calibration, and 10 experimental*
 1308 *charges from Barclay (2004), Blatter and Carmichael (2001), and Grove et al. (1997), which were used by Zhang*
 1309 *et al. (2017) in their test, but not calibration dataset.*

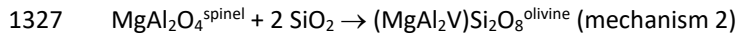
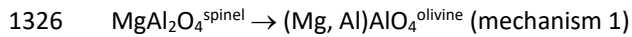
1310 We do not test predictions of H₂O and fO₂ using amphibole-only chemometers, as there are limited
 1311 reliable experimental data with well constrained values for these parameters that were not used during model
 1312 calibration.

1313 2.7. Olivine-Spinel Aluminium-exchange thermometry

1314 The aluminium content of olivine has been used as a thermometer in the mantle (De Hoog et al., 2010),
 1315 and Al partitioning between olivine and spinel has been used in igneous rocks (Wan et al., 2008; Coogan et al.,
 1316 2014). Here we focus on the olivine-spinel Al-exchange thermometer, which offers an advantage over Mg-Fe
 1317 olivine-liquid thermometry because Al in spinel and olivine and Cr in spinel are more resistant to diffusional
 1318 modification during crystal storage and transport than Fe-Mg in olivine (Spandler & O'Neill, 2009). Additionally,
 1319 while olivine crystals are frequently out of equilibrium with erupted liquids (Sides et al., 2014b; Wieser et al.,

1320 2019), the fact spinels are trapped inside olivine crystals makes it more straightforward to identify mineral-
1321 mineral pairs that grew together.

1322 The mechanism by which aluminium substitutes into olivine remains somewhat uncertain, despite the
1323 fact that constraining this reaction is vital to identify which chemical parameters should appear in a
1324 thermodynamically-constrained thermometry model. Of the possible substitutions, two mechanisms have been
1325 the focus of the most attention:



1328 In the first mechanism there is a coupled substitution of Al into both the octahedral and tetrahedral
1329 sites in olivine, while the second has substitution only onto the octahedral site, with charge balance maintained
1330 by vacancies (V). It is also possible coupled substitutions could take place with Cr and Na in the octahedral site
1331 (and Al in the tetrahedral site), or Al in the octahedral site with Fe^{+3} in the tetrahedral site (Taura et al., 1998).
1332 Critically, if the mechanism 1 is dominant, the thermometer should depend only on the Al contents of the co-
1333 existing olivine and spinel (in addition to any chemical parameters controlling the activity coefficient for Al in
1334 either phase), but if mechanism 2 dominates, the thermometer will depend also on the activity of SiO_2 (a_{SiO_2}).

1335 A thermometer based on Al-exchange was first calibrated by Wan et al. (2008) using a series of
1336 experiments at 1 bar with the bulk composition varied such that olivine and spinel co-crystallised at a range of
1337 temperatures and Cr contents. They found that the experimental data could be adequately modelled with a
1338 formula depending on the ratio of Al in olivine to Al in spinel, as well as the spinel Cr# ($\text{Cr}/[\text{Cr} + \text{Al}]$, molar). The
1339 dependency on Cr# comes from its effect on the activity coefficient of Al in spinel. Wan et al. (2008) justified the
1340 extrapolation of the thermometer to higher P and T than the calibration dataset by comparing temperatures
1341 derived from the Al-exchange thermometer with temperatures calculated from the two-pyroxene thermometer
1342 for a suite of olivine and spinel bearing mantle xenoliths. Although there was considerable scatter around the
1343 1:1 line ($1\sigma = 64^\circ\text{C}$) they found no systematic offset between the two thermometers. The behaviour of the
1344 thermometer at 1 bar was tested with an additional set of experiments, for which experimental temperatures
1345 were reproduced with $1\sigma=22^\circ\text{C}$.

1346 The thermometer was further tested and recalibrated with new experimental data by Coogan et al.
1347 (2014), extending the calibration range to higher $f\text{O}_2$ values ($\Delta\text{QFM}=-0.5$ to $\Delta\text{QFM} = +1.3$). They also tested the
1348 thermometer's dependence on a_{SiO_2} . They found $f\text{O}_2$ had no systematic effect on the performance of the
1349 thermometer and the effect of a_{SiO_2} was within the uncertainty of the thermometer, indicating that Al
1350 incorporation into olivine by vacancy formation (mechanism 2) is unlikely to be important in most systems. This
1351 was corroborated by an experimental diffusion study by Zhukova et al. (2017) which found that Al incorporation
1352 by vacancy formation was favoured only at higher a_{SiO_2} values than is found in most igneous systems where the
1353 thermometer is applied. Further improvements have been made to both the calibration and the mathematical
1354 formulation of the thermometer by Zhang and Namur (2022).

1355 Despite the increased calibration range of the Coogan et al. (2014) model, many natural samples
1356 possess olivine and spinel pairs with compositions which still lie outside the calibration range. This includes the
1357 study reporting the highest equilibration temperatures from this method ($\sim 1570^\circ\text{C}$, Trela et al., 2017), which
1358 have spinels with Cr_2O_3 contents higher than any of the spinel crystals used to calibrate the thermometer. Trela
1359 et al. justified such an extrapolation based on the global correlation between the Al_2O_3 K_D and spinel Cr#, and
1360 the fact that these melts also recorded extreme mantle potential temperatures and olivine liquidus T_s . However,
1361 it has also been suggested in other locations that application of this method to spinel crystals with much higher
1362 TiO_2 contents than the calibration dataset may be invalid, because these higher TiO_2 may affect the activity
1363 coefficient of Al in spinel (e.g., Jennings et al., 2019; Wong et al., 2022). Jennings et al. (2019) suggest that in the
1364 absence of a wider calibration range, it is best to apply the thermometer only to spinel crystals that are close to
1365 the calibration range.

1366 To robustly assess how effectively the olivine-spinel method can be extrapolated, we need a suite of
1367 experiments with compositions lying outside the current calibration range. However, because application of the

1368 thermometer relies on precise measurements of the low concentrations of Al_2O_3 in olivine, generally only
1369 experiments performed for the purpose of calibrating this thermometer can be used, and all such experiments
1370 have been used during model regression (by Wan et al. 2009, or Coogan et al. 2014). Experiments conducted for
1371 other purposes cannot be used to formulate a test dataset, because Al_2O_3 concentrations in olivine were
1372 generally not measured at all, or were measured with low precision.

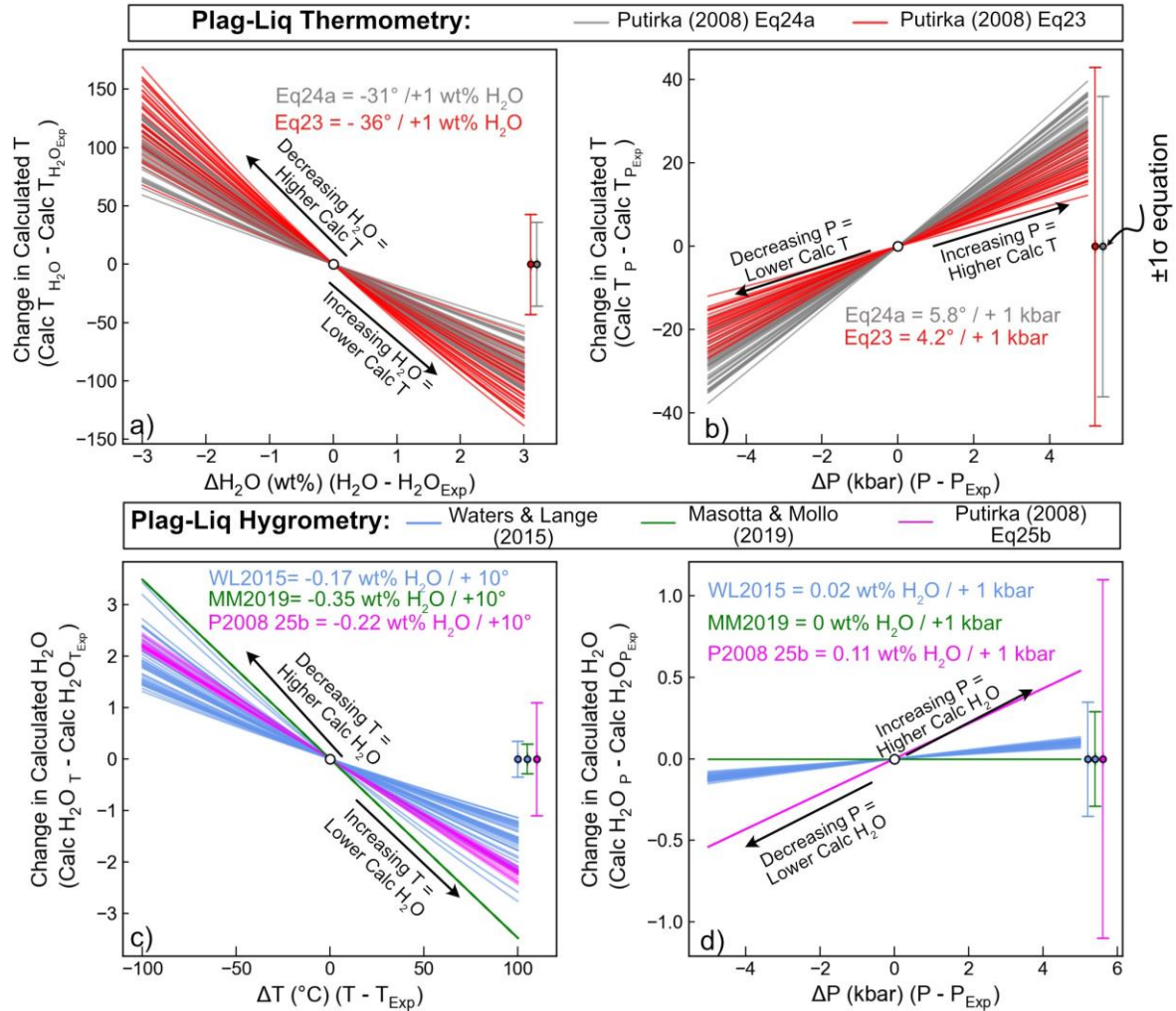
1373 The lack of an independent test dataset also makes it difficult to robustly constrain the uncertainty of
1374 this method even when applied within the calibration range. Most studies cite the quoted standard error on the
1375 fit for the calibration data as being a minimum estimate of the uncertainty (Matthews et al., 2021, 2016; Wong
1376 et al., 2022), but as discussed above, statistics calculated on calibration datasets tend not to reflect the true
1377 error when applied to data not used for calibration. A final problem with this method is that there is no
1378 independent equilibrium test to assess whether the spinel and olivine are in equilibrium. The ubiquity of Mg-Fe
1379 diffusive resetting means these elements are an unreliable test of equilibrium (c.f. Prissel et al., 2016). The slow
1380 diffusion of Al in olivine (Spandler & O'Neill, 2009) means that parts of a host olivine crystal could be out of
1381 equilibrium with their spinel inclusions if olivine crystallisation occurred over a protracted time with changing
1382 temperature (or melt composition). Maps of the aluminium content of olivine crystals have revealed near-
1383 ubiquitous zoning in crystals from Iceland (Matthews et al., 2021), adding complexity to identifying equilibrium
1384 pairs. Matthews et al. (2021) and Trela et al. (2017) therefore recommended the aluminium content of olivine
1385 crystals should be mapped with a high current electron beam before identifying locations for quantitative
1386 analysis.

1387 **2.8. Plagioclase-Liquid thermometry and hygrometry**

1388 Plagioclase (Plag) is a very common mineral in a wide variety of tectonic settings (e.g., MORBs, OIBs,
1389 Arcs), motivating the development of a number of thermometers, barometers and hygrometers parameterizing
1390 the exchange of components between plagioclase and liquid (Putirka, 2008, 2005; Sugawara, 2001; Waters and
1391 Lange, 2015). However, the exchange of the anorthite (An)-albite (Ab) component between liquid and Plag is
1392 sensitive to T, P, and H_2O . If none of these variables are constrained by independent methods, there is a
1393 substantial solution space to explore. There also isn't much consensus as to what equilibrium tests should be
1394 used to filter Plag-Liq pairs. Putirka (2008) note that Ab-An exchange values for experiments ($K_D^{\text{An-Ab}}$) are
1395 normally distributed, with experiments with $T < 1050^\circ\text{C}$ having values of 0.1 ± 0.05 , and experiments with
1396 $T > 1050^\circ\text{C}$ having values of 0.27 ± 0.1 . However, plotting our experimental data (along with the calibration dataset
1397 of Waters and Lange, 2015) shows a more continuous variation of K_D with temperature (Supporting Fig. 9)
1398 although there is a relatively abrupt step up to higher values between $1000\text{--}1100^\circ\text{C}$. We tentatively suggest this
1399 step up may result from the C1–I1 structural phase transition which occurs near this temperature, which has
1400 been shown to affect plagioclase Mg partitioning behaviour (Mutch et al., 2022). Using the criteria of Putirka
1401 (2008) would exclude a number of experiments close to the cut off (Supporting Fig. 9)– We instead apply an
1402 exponential fit through the experimental data (excluding experiments outside ± 0.11 , Supporting Fig. 9a-b). Not
1403 applying this filter affects calculated statistics very little for the following discussion.

1404 First, we assess sensitivity of thermometers to H_2O (Fig. 16a), thermometers to P (Fig. 16b),
1405 hygrometers to T (Fig. 16c), and hygrometers to P (Fig. 16d), by independently perturbing experimental P, T and
1406 H_2O . It is apparent from Fig. 16a that Plag-Liq temperatures are strongly sensitive to H_2O ; an increase of just 1
1407 wt% H_2O causes an average drop in T of $\sim 31^\circ\text{C}$ for eq24a and 36°C for eq23. This change in calculated T is
1408 comparable to the RMSE of these thermometers. Thermometers are less sensitive to P; with the calculated
1409 change in T only reaching the same magnitude as the RMSE for a change of ~ 10 kbar (Fig. 16b). Notably, the
1410 Plag-Liq hygrometers of Masotta and Mollo (2019), Putirka (2008) and Waters and Lange (2015) are extremely
1411 sensitive to T; calculated H_2O contents drop by the standard error estimate of the hygrometer for a change in T
1412 of just $10\text{--}20^\circ\text{C}$ (Fig. 16c). These hygrometers are less sensitive to P, with P changes of 10 kbar causing variations
1413 well within the quoted RMSE (Fig. 16d).

1414



1415

1416 *Figure 16: Testing the sensitivity of Plag-Liq thermometers to H₂O (a) and pressure (b), and Plag-Liq hygrometers*
 1417 *to T (c) and P (d). 40 experiments from our new compilation were randomly selected (each represented by a*
 1418 *colored line). We perform calculations at the experimental P, T and H₂O content (0,0) on all plots, and then vary*
 1419 *H₂O by ± 3 wt% (a), P by ± 5kbar (b, d), and T by ± 100 °C (c). We subtract the quantity calculated at experimental*
 1420 *conditions from the quantity at these new conditions. Error bars show the quoted RMSE on each expression. We*
 1421 *label the average perturbation for these 40 samples on the figure.*

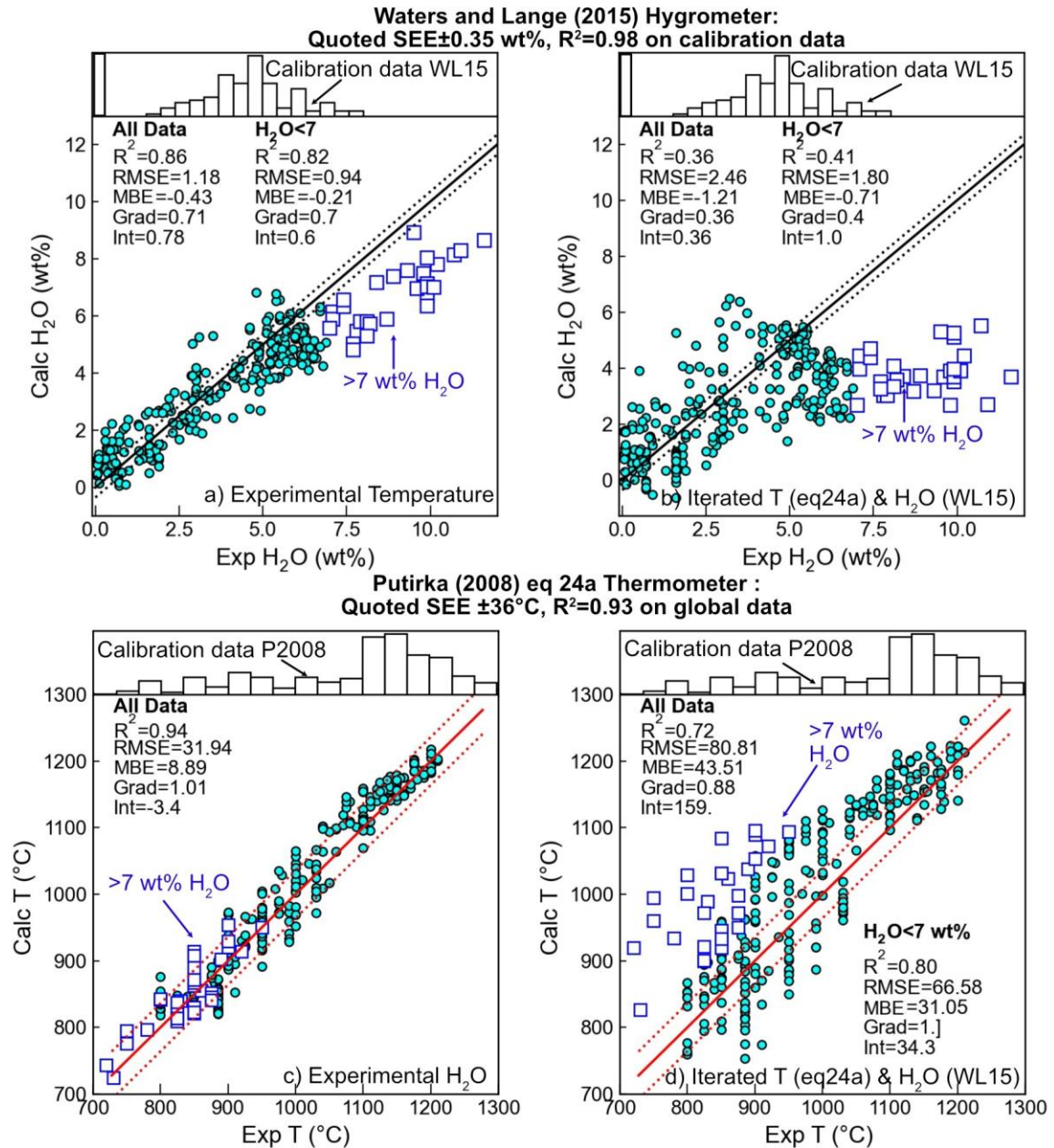
1422

1423 Before assessing hygrometers using our new dataset, it is worth considering how well we really know the “true”
 1424 value of H₂O in each experiment. In the compiled Plag-Liq dataset, only 33% measure water by FTIR, 5% by SIMS
 1425 and 4.8% by Raman spectroscopy. A further 16% report water using the electron microprobe water-by-
 1426 difference method, with some mention of a calibration method. 17% have calculated H₂O using a solubility
 1427 model, assuming pure H₂O saturation, or using a measured X_{H₂O} value in the fluid (Andújar et al., 2015; Costa,
 1428 2004; Mandler et al., 2014), or enough information for us to perform these calculations using MagmaSat in
 1429 VESlcal (Ghiorso and Gualda, 2015, Iacovino et al. 2019). Interestingly, Waters and Lange (2015) calibrate their
 1430 hygrometer by calculating H₂O in each experiment in their calibration dataset using the solubility model of Zhang
 1431 et al. (2007), rather than using measured H₂O contents. If they had they used MagmaSat instead, calculated H₂O
 1432 contents for these experiments would differ by an average of 0.3 wt% (the max discrepancy is 0.78 wt%), which
 1433 would likely result in slightly different model parameters. Additionally, if the starting materials contained even
 1434 small amounts of CO₂ (e.g., from contamination, Blatter et al., 2013), the amount of H₂O in the melt would not
 1435 equal that calculated using a pure H₂O solubility model.

1436 Ideally, we would restrict our comparison to experiments which performed FTIR, SIMS or Raman
1437 measurements of H₂O. However, this results in a much smaller dataset, with N=163 vs. N=358 if calibrated VBD
1438 and solubility water contents are included. This smaller dataset also has a very restricted T range (Supporting
1439 Fig. 10). It also seems unjustified to exclude experiments using solubility models, given that is how the H₂O
1440 contents were determined to calibrate the Waters and Lange (2015) model. Thus, we choose to proceed with
1441 the larger experimental dataset.

1442 Using experimental T and P, the Waters and Lange hygrometer performs reasonably well on the ArcPL
1443 dataset, with a RMSE of ± 1.21 wt% (Fig. 16a). There is a marked deviation to anomalously low calculated H₂O
1444 contents for experiments with H₂O > 7 wt% (cyan squares); if these are excluded, the RMSE is 0.94 wt%, although
1445 this is still far higher than the quoted RMSE of 0.35 wt%. The poor performance at high H₂O may reflect the fact
1446 that these super-hydrous compositions are poorly represented in the calibration dataset of this hygrometer
1447 (white histogram, Fig. 16a-b). When using experimental H₂O contents and pressures, the statistics reported for
1448 the thermometer of P2008 Eq24a on a global dataset are very similar to those estimated from our new dataset
1449 (we calculate RMSE=33°C vs. the stated RMSE=36°C shown as red dotted lines, Fig. 16c).

1450 As discussed in section 1.2, the extreme sensitivity of Plag-Liq thermometers to H₂O content, and
1451 hygrometers to T, means that the comparisons shown in Fig. 16a and c do not accurately represent the true
1452 error when these equations are applied to natural systems, where in the vast majority of instances, neither H₂O
1453 nor T is known. To address this issue with many under constrained intensive variables, we investigate whether
1454 H₂O and T can be solved iteratively using a plagioclase hygrometer and thermometer, as an adaptation of the
1455 popular workflow of iterating barometers and thermometers. Arguably, as we perform these calculations using
1456 experimental P, we are still overestimating their performance on natural systems where H₂O, T and P are all
1457 unknown. The absence of a reliable plagioclase-liquid barometer (see Section 2.9) means that three-way
1458 iteration will not work. However, given these equations are far less sensitive to pressure (Fig. 16), uncertainty in
1459 pressure shouldn't hinder the model performance substantially.



1460

1461 *Figure 16. Evaluating Plag-Liquid hygrometers (a-b) and thermometers (c-d). Only experiments with H₂O*
 1462 *measured by quantitative methods are shown. a) Calculations of H₂O using Waters and Lange (2015) with*
 1463 *calculations performed using experimental T. The hygrometers performance drops substantially for H₂O>7; the*
 1464 *white histogram on top indicates that relatively few experiments used to calibrate this model had such high H₂O*
 1465 *contents. b) Iterative calculations using Waters and Lange (2015) and Putirka (2008) eq24a. c) Calculations using*
 1466 *Putirka (2008) eq24a and experimental H₂O contents, and d) Iterative calculations using Putirka (2008) eq24a*
 1467 *and Waters and Lange (2015). 1:1 line shown with ±stated RMSE for each expression*

1468 Unsurprisingly, iteration of Plag-Liq hygrometers and thermometers yields worse statistics than
 1469 hygrometry calculations performed using experimental T. For example, excluding experiments with H₂O>7 wt%,
 1470 the iterated RMSE is 1.77 wt% (vs. 0.94 wt% using experimental; Fig 16a vs. b). Calculated T using the iterative
 1471 method are also substantially worse than those obtained using known H₂O contents (RMSE=66 vs. 33°C for all
 1472 data, RMSE=58°C for H₂O<7 wt%, Fig. 17c-d). The statistics for these iterative calculations are more indicative of
 1473 the sort of precision these methods can achieve in natural system. We also suggest that such an iterative
 1474 approach may be more accurate than calculating H₂O using temperatures derived from other phases which may

1475 not have formed at the same temperature as Plag (e.g., Fe-Ti thermometry, Black and Andrews, 2020; Crabtree
1476 and Lange, 2011; Pineda et al., 2021).

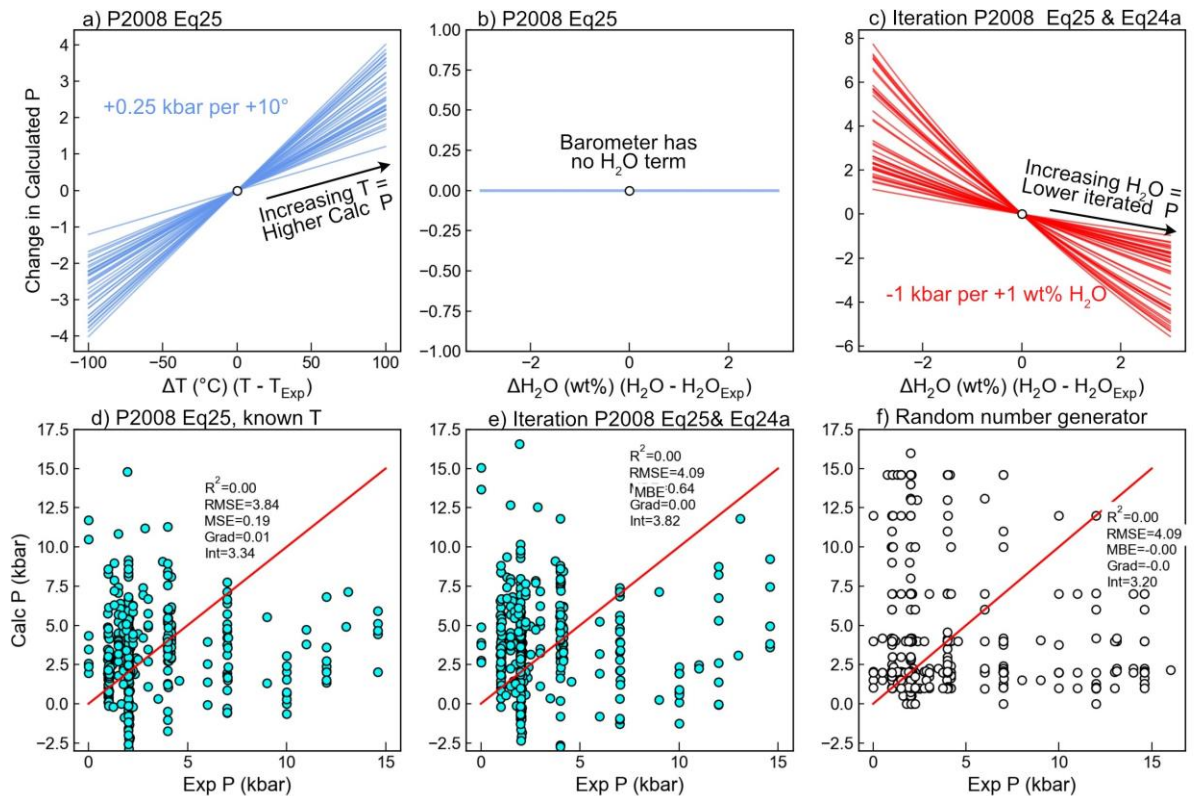
1477 The iterated thermometer has reasonable performance compared to other mineral-melt
1478 thermometers discussed, and the hygrometer has sufficient precision to distinguish dry (0–2 wt%), moderately
1479 wet (2–4 wt%) and wet (>4 wt%) lavas. However, when applied outside of the experimental products used for
1480 calibration, Plag-Liq hygrometry cannot achieve anything like the $\ll 0.5$ wt% error often quoted for this method.
1481 Future improvements would be possible with a larger dataset of experiments where H₂O contents are known,
1482 as combining different methods for estimating H₂O contents in experiments undoubtedly adds uncertainty,
1483 particularly when using volatile contents calculated using volatile solubility models (see Wieser et al., 2022a).
1484 Additionally, given the relative success of iterating two different expressions with different underlying datasets,
1485 we suggest that recalibrating Plag-Liq hygrometers without a T term, but with compositional terms like those in
1486 Plag-Liq thermometers to incorporate the effect of temperature, may be more successful than having to iterate
1487 two independently calibrated expressions.

1488 **2.9. Plagioclase-Liquid barometry**

1489 Putirka (2005) proposed a Plag-Liq barometer calibrated on 187 Plag-Liq pairs, which yields a RMSE of
1490 ± 1.8 kbar for the calibration dataset and $\text{RMSE}=\pm 2.2$ kbar on $N=292$ test data. However, Putirka (2008) re-
1491 evaluated this barometer using new experimental data, and found that it performed very badly, with a
1492 $\text{RMSE}=\pm 3.8$ kbar excluding 1 atm data, and even worse statistics when this 1atm data was included. They tried
1493 to find a global model to adequately predict pressures in their new dataset and found that while some regression
1494 worked on some subsets of the database, no regression could fit all data. They suggested that new experiments
1495 with the specific purpose of developing a Plag-Liq barometer are required to move forward. Despite their
1496 warning that “*the status of plagioclase-liquid as a barometer is firmly in doubt*”, a concerningly large number of
1497 studies have performed Plag-Liq barometry after 2008 (e.g., Budd et al., 2016; Cheng et al., 2014; Dahren et al.,
1498 2012; Geiger et al., 2018, 2016a, 2016b; Guo et al., 2018; Jamshidi et al., 2015; Siegburg et al., 2018). The
1499 majority of these studies quote a ± 2.47 kbar RMSE to justify this approach. However, this value from Putirka
1500 (2008) was only the fit to under half the data; the full dataset gave $\text{RMSE}=\pm 3.6\text{--}3.8$ kbar.

1501 As Plag-Liq barometers are still being widely used in the community, we briefly assess their sensitivity
1502 to T and H₂O, and then evaluate their performance on our new dataset. The T term in P2008 Eq25b means that
1503 the barometer is reasonably sensitive to T, with an average increase in +0.25 kbar per +10°C increase in T (Fig.
1504 18a). The barometer alone isn’t sensitive to H₂O. However, this barometer is normally used in natural systems
1505 through iteration with the Eq24a thermometer, which is H₂O-sensitive (Fig. 18b). When iterated, the barometer
1506 is very H₂O-sensitive; an increase in H₂O by 1 wt% causes the P to drop by an average of ~ 1 kbar (Fig. 18c).

1507 We assess barometry performance on our test dataset, filtering out pairs which fail the anorthite-albite
1508 (An-Ab) equilibrium test provided in the supporting spreadsheet of Putirka (2008). Using experimental T, the
1509 barometer performs extremely poorly ($\text{RMSE}=3.8$ kbar, R^2 of 0, Fig. 18d). When P and T are iterated, the
1510 performance is even worse ($\text{RMSE}=4.0$ kbar, Fig. 18e). It is notable that in Fig. 18d-e that experiments performed
1511 at 2 kbar yield $P>10$ kbar, while experiments performed at 10 kbar yield $P<0$ kbar. To put the performance of
1512 these barometers into perspective, we compare each experimental P to a random experimental pressure drawn
1513 without replacement from the experimental dataset (Fig. 18f). The RMSE for this randomly selected number is
1514 almost identical to that of the iterated barometer. Thus, until new experiments are done to specifically
1515 investigate the Plag-Liq barometer, this method is only as reliable as researchers using a random number
1516 generator spanning the crustal thickness in their location of interest than Plag-Liq barometry to estimate magma
1517 storage pressures!

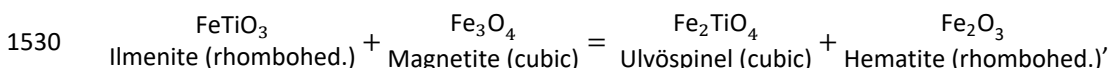


1518

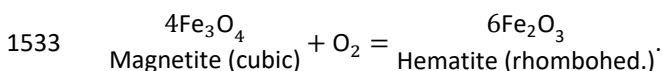
1519 *Figure 18. Assessment of the Plag-Liq barometer of Putirka (2008) Eq25. a-b) Assessing sensitivity of the*
 1520 *barometer to T and H₂O for a subset of experiments. c) Testing the sensitivity of the iterative combination of Eq25*
 1521 *(P) and Eq24a (T) to melt H₂O content. d) Testing the barometer using experimental T and H₂O contents, after*
 1522 *applying the An-Ab equilibrium test of Putirka (2008). e) As for panel d, but solving P and T iteratively (still using*
 1523 *experimental H₂O). f) Assessing the performance of a randomly selecting a P value from the experimental*
 1524 *dataset.*

1525 2.10. Fe-Ti oxides

1526 The partitioning of Fe and Ti between cubic and rhombohedral oxides has been employed in estimating
 1527 magmatic T and f_{O_2} . The Fe-Ti geothermobarometer is advantageous owing to the rapid cation exchange
 1528 between the oxides, allowing equilibrium to be restored quickly following a change in magmatic conditions (days
 1529 to weeks; Venezky and Rutherford, 1999). The exchange is described by the following reaction:



1531 where there is solid solution between ilmenite and hematite (the rhombohedral oxides), and magnetite and
 1532 ulvöspinel (spinel series, or cubic oxides). The dependence on oxygen fugacity is described by the redox reaction:



1534 The main challenge in calibrating a Fe-Ti geothermobarometer comes from the extremely complex solid
 1535 solution of the rhombohedral oxides. Naturally occurring rhombohedral oxides incorporate significant quantities
 1536 of MgO, MnO, and Al₂O₃ in addition to FeO, Fe₂O₃, and TiO₂, and have complex cation ordering transitions at
 1537 lower temperatures, in addition to magnetic ordering. This means that complex expressions are required to
 1538 accurately represent endmember activities, and multiple miscibility gaps exist. This complexity prevents simple
 1539 empirical calibration of a geothermobarometer expression, and instead requires numerical solutions of
 1540 expressions derived from a complex thermodynamic formulation.

1541 The first implementation of the Fe-Ti geothermobarometer was made by Buddington and Lindsley
 1542 (1964), and improved by a number of subsequent studies as further experimental data became available (e.g.,
 1543 Andersen and Lindsley, 1988; Spencer and Lindsley, 1981). The most recent update of the geothermobarometer

1544 was provided by Ghiorso and Evans (2008), building on the older thermodynamic model of Ghiorso and Sack
1545 (1991) using a calibration dataset with 5X more experiments (N=267 vs. N=57) and much better experimental
1546 constraints on cation ordering. In particular, the calibration range was extended to significantly higher T and fO_2 ,
1547 where previous versions of the model extrapolated poorly. Each update to the thermometer represents
1548 increasing sophistication of the underlying thermodynamic model, and therefore more complex numerical
1549 techniques to apply them as a geothermobarometer. An open-source implementation of the
1550 geothermobarometer was provided by Ghiorso and Prissel (2020) through the ENKI portal.

1551 Blundy and Cashman (2008) use an independent set of experiments to estimate the uncertainty on
1552 several versions of the Fe-Ti geothermobarometer, finding one sigma uncertainties of 44°C and 0.2–0.34 log
1553 units fO_2 for the Ghiorso and Evans (2008) model, but no systematic deviation at high or low temperatures.
1554 However, it is likely that the uncertainty will vary across composition space, as the sensitivity of the thermometer
1555 depends on the composition of the Fe-Ti oxides, with the best sensitivity below the NNO buffer and away from
1556 the miscibility gap (Ghiorso and Evans, 2008).

1557 **2.11. Ti in Quartz (TitaniQ) thermometer**

1558 In silicic rocks where quartz is a dominant phenocryst (e.g., granites and rhyolites), there are far fewer
1559 available thermometers relative to more mafic systems. To address this, Wark and Watson (2006) perform
1560 experiments containing quartz and rutile at 600–1000°C at 10 kbar to produce an empirical relationship relating
1561 the Ti content of quartz to the temperature. They state that this thermometer has an uncertainty of $\pm 2^\circ\text{C}$ at
1562 $>500^\circ\text{C}$ using SIMS measurements of Ti, and that this thermometer can also be applied to systems without rutile
1563 if an independent estimate of Ti activity is obtained (e.g., from Fe-Ti equilibrium). This thermometer was
1564 recalibrated by Kawasaki and Osanai (2008) using natural metamorphic rocks in ultrahigh temperature granulites
1565 and Thomas et al. (2010), who perform additional experiments between 5–20 kbar, generating an expression
1566 incorporating a term for pressure.

1567 Importantly, Thomas et al. (2010) implied that if temperature was known independently, the equation
1568 could be inverted to solve for pressure. Wilson et al. (2012) test this inversion method on samples from the
1569 Oruanui eruption, which has been well studied, so has independent estimates of pressure from melt inclusions,
1570 and temperature and Ti activity from Fe-Ti oxides. They show that using Fe-Ti oxides to constrain temperature
1571 and Ti activity, calculated pressures from Ti in quartz are 3–10X higher than those inferred from melt inclusion
1572 saturation pressures. Similarly, if melt inclusion and Fe-Ti oxide temperatures and pressures are used, inferred
1573 Ti activity is far too low. If pressures are used from melt inclusions and Ti activity from Fe-Ti oxide, temperatures
1574 are well below the H_2O -saturated solidus for granite. Similar discrepancies with previously published pressures,
1575 temperatures and Ti activities are present for calculations on the Bishop tuff. Wilson et al. (2012) suggest that
1576 Ti activities may be highly variable in igneous systems, so activities from Fe-Ti oxides cannot be reliably used
1577 with TitaniQ. Additionally, they suggest Ti in Qtz records complex histories that cannot be simply related to
1578 changes in pressure and temperature over other variables, such as quartz growth conditions or melt
1579 composition. For example, Huang and Audétat (2012) show that Ti concentrations in Qtz depend on the crystal
1580 growth rate, so this thermobarometer should not be applied to hydrothermal fluids where growth rates are fast
1581 and highly variable.

1582 Thomas and Watson (2012) partially rebut Wilson et al. (2012), in particular critiquing the validity of
1583 their calculations of Ti activity (e.g., Ghiorso and Gualda, 2013) and temperature estimates from Fe-Ti oxides
1584 (Ghiorso and Evans, 2008) in the Oruanui rhyolites that underly a lot of the arguments of Wilson et al. (2012).
1585 Instead, Thomas and Watson (2012) use MELTS to estimate temperature and Ti activity based on the affinity for
1586 rutile saturation from inputted melt compositions, yielding pressures similar to melt inclusions. They admit that
1587 the approach of Wark and Watson (2006) was oversimplified in its suggestion of using a fixed value of Ti activity.
1588 An excellent discussion of this Bishop Tuff controversy can be found in Putirka (2017), along with adjustment of
1589 published coefficients for different equations.

1590 Acosta et al. (2020) identified that Ti in Qtz temperatures are offset ~ 100 – 150°C to lower temperatures
1591 than other thermometers in silicic systems, particularly at <4 kbar. To address the source of these offsets, they
1592 perform hydrothermal quartz growth experiments at 800°C and 1 kbar with different fluid compositions. They

1593 find that Ti in Qtz is sensitive to the Ti/Si ratio of the fluid, rather than the concentration or activity of Ti. Clearly,
1594 significantly more experimental work is needed to determine magma storage conditions precisely and accurately
1595 in silicic systems from Ti in Qtz.

1596 **3. Melt inclusion barometry**

1597 Melt inclusions (MIs) are small pockets of melt trapped during crystal growth, which become isolated
1598 from the external melt as the surrounding crystalline host fully encloses them. MI which were trapped from a
1599 volatile-saturated magma can be used to deduce magma storage depths because the solubility of CO₂ and H₂O
1600 in silicate melts is a strong function of pressure (Dixon, 1997; Goranson, 1931). If MI were trapped from a
1601 volatile-undersaturated magma, calculated pressures are minimum estimates (Hauri et al., 2018; Matthews et
1602 al., 2016).

1603 Numerous recent reviews have detailed the theory, methods and advances relating to melt inclusion
1604 analysis and interpretation, as well as several specific problems associated with determination of magma storage
1605 depths from these archives. For example, Wallace et al. (2021) present a comprehensive review of olivine-hosted
1606 melt inclusions, describing melt inclusion formation, post-entrapment crystallization, and the wealth of
1607 information recorded by melt inclusions (e.g., trace element contents for tracking magma batches, processes
1608 controlling magmatic H₂O contents, calculating ascent rates, and storage pressures). Rose-Koga et al. (2021)
1609 provide a number of guidelines involving sample preparation, analysis and data reporting associated with melt
1610 inclusion analysis and interpretation. Barth and Plank (2021) discuss the processes which can alter H₂O contents
1611 in melt inclusions after their entrapment, producing regime diagrams describing how melt inclusions can act as
1612 hygrometers and barometers (revealing pre-eruptive H₂O contents), or speedometers (revealing ascent rates
1613 using H⁺ diffusion). Wieser et al. (2022a) provide a detailed history of different solubility models used to calculate
1614 melt inclusion saturation pressures and highlight the large discrepancies between different models. In particular,
1615 they emphasize the importance of carefully examining the calibration range of each solubility model compared
1616 to the P-T-X range of melt inclusions from a given volcano. To avoid repetition, we refer readers to these papers,
1617 and focus our discussion on issues involving magma storage depth determinations from melt inclusions which
1618 have not yet been reviewed in detail. We specifically focus on the growing realization that the CO₂ contents of
1619 melt inclusions have been significantly underestimated, because of the presence of a substantial CO₂ within
1620 vapour bubbles that were not measured in most published studies.

1621 **3.1 Vapour bubble growth systematics**

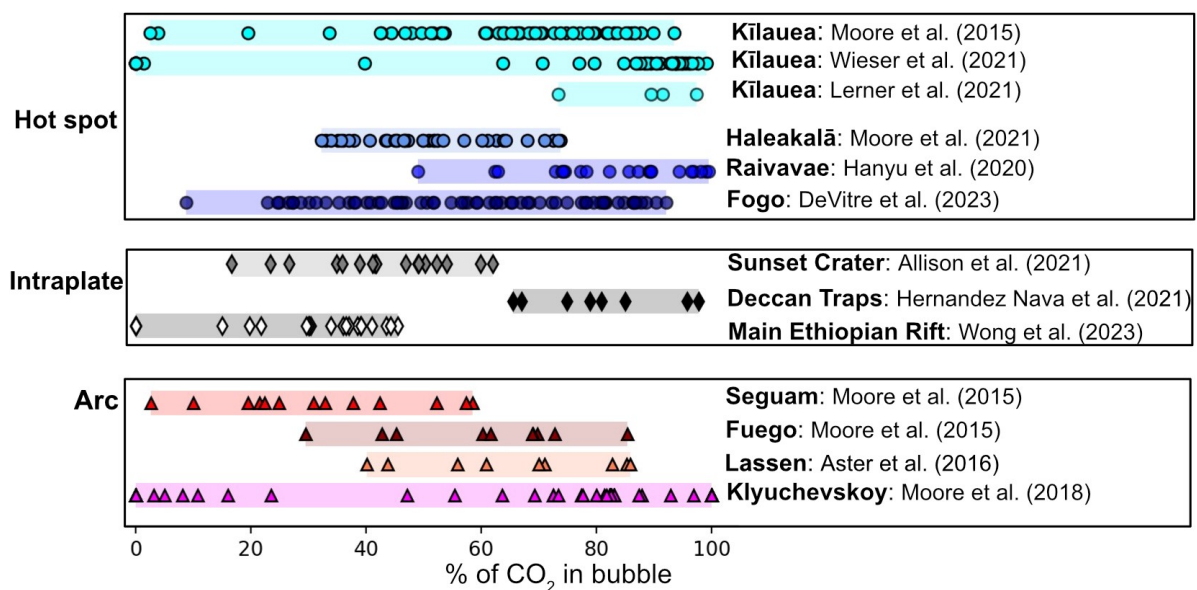
1622 The vast majority of studies have used olivine-hosted melt inclusions to determine magma storage
1623 depths (e.g., Aster et al., 2016; Moore et al., 2015; Ruscitto et al., 2010; Sides et al., 2014; Wallace et al., 2021).
1624 This focus on olivine may reflect the fact that it is one of the first crystallizing phases (important for studies
1625 focusing on the most primitive melt compositions), it is relatively abundant, and tends to have melt inclusions
1626 which are larger than those in other phases from the same sample suite (Bennett et al., 2019, Wieser et al.
1627 2022c). It has also been suggested that the absence of cleavage in olivine makes leakage less likely than in say
1628 pyroxene, which has a strong cleavage (Kress and Ghiorso, 2004). Finally, the simple chemistry of olivine, well-
1629 constrained $K_{D,Fe-Mg}$, and low partition coefficients for REE and other trace elements of geological interest means
1630 that correcting melt inclusions for post-entrapment crystallization (PEC) is more straightforward than in
1631 plagioclase and pyroxene (Danyushevsky and Plechov, 2011; Kress and Ghiorso, 2004; Neave et al., 2017; Wieser
1632 et al., 2022c).

1633 However, as a consequence of the fact that olivine is often the first phase to crystallize in a magma,
1634 there is significant potential for melt inclusions to experience substantial amounts of cooling prior to eruption
1635 (e.g., ~150–170°C in high forsterite olivines from the 2018 eruption of Kīlauea, Lerner et al., 2021; Wieser et al.,
1636 2021). This results in a large amount of PEC. Crystallization of denser olivine from less dense silicate melt,
1637 combined with differential contraction of the melt and host during cooling, causes the pressure in the inclusion
1638 to drop, driving the growth of a vapour bubble (often termed a shrinkage bubble, Kress and Ghiorso, 2004;
1639 Steele-Macinnis et al., 2011; Wallace et al., 2015). Because the solubility of CO₂ is strongly dependent on
1640 pressure, if there is sufficient time between bubble growth and syn-eruptive quenching, a significant proportion
1641 of the total CO₂ content of the melt inclusion will diffuse into the vapour bubble (Fig. 19, MacLennan, 2017,
1642 Wieser et al. 2021). Rapid diffusive re-equilibration of H₂O between the melt inclusion and a more H₂O-poor

1643 carrier melt as a result of fast H⁺ diffusion rates in olivine can also drive the growth of a vapour bubble (Aster et
 1644 al., 2016; Gaetani et al., 2012).

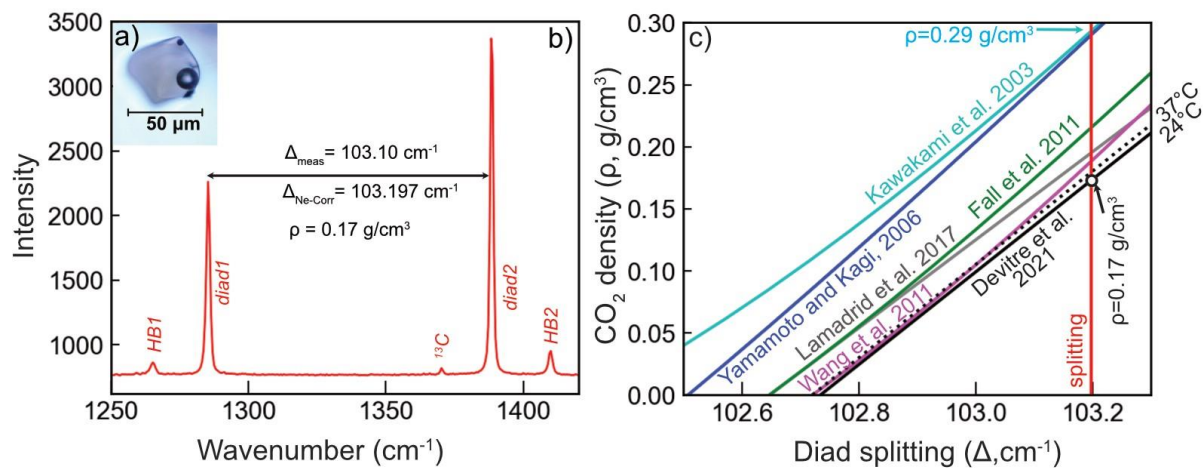
1645 3.2 Raman measurements of vapour bubbles

1646 In situ Raman spectroscopic measurements of vapour bubbles over the last decade have demonstrated
 1647 that a large and often dominant proportion of the total CO₂ content of melt inclusions is held within the bubble
 1648 (Fig. 19, Allison et al., 2021; Aster et al., 2016; DeVitre et al., 2023a; Hanyu et al., 2020; Hernandez et al., 2018;
 1649 Lerner et al., 2021; Moore et al., 2015, 2018, 2021; Wieser et al., 2021). To our knowledge, the first Raman
 1650 analyses of a melt inclusion vapour bubble were made by Steele-Macinnis et al. (2011) in samples from Solchiaro
 1651 Volcano, Italy. They found a distinctive signal consisting of two strong peaks which is indicative of the presence
 1652 of a CO₂ fluid (Fig. 20b). This contradicted the dominant hypothesis at the time that these bubbles were vacuums
 1653 or voids. In two almost concurrent papers, Hartley et al. (2014) and Moore et al. (2015) present Raman
 1654 measurements in melt inclusion vapour bubbles from Laki, Kīlauea, Fuego and Seguam, demonstrating that 40
 1655 to >90% of the total CO₂ is held within the bubble. More recent work has found similar proportions in a wide
 1656 range of volcanoes spanning a range of tectonic settings (Fig. 19).



1657
 1658 *Figure 19 – Percent of the total melt inclusion CO₂ content held in the vapour bubbles from studies which have*
 1659 *used an instrument-specific Raman calibration. Refs: Allison et al., 2021; Aster et al., 2016; DeVitre et al., 2023a;*
 1660 *Hanyu et al., 2020; Hernandez Nava et al., 2021; A. H. Lerner et al., 2021; Moore et al., 2021, 2018, 2015; Wong*
 1661 *et al., 2023.*

1662 Raman spectroscopic analyses of CO₂ in vapour bubbles rely on the strong correlation between the
 1663 density of CO₂ and the distance between the two strong CO₂ spectral peaks collectively termed the Fermi diad.
 1664 This distance is commonly called the splitting, diad splitting, or diad separation (Δ , Fig. 20b). However, the
 1665 relationship between density and diad splitting has been shown to vary as a function of instrument hardware
 1666 and acquisition parameters (Lamadrid et al., 2017, Fig. 20c). This means that the relationship between the diad
 1667 splitting and CO₂ density must be determined for the acquisition parameters and specific data processing
 1668 strategy used by each Raman laboratory. The absolute differences in CO₂ densities for a measured diad splitting
 1669 on different Raman instruments are very large (Fig. 20c). For example, the vapour bubble shown in Fig. 20a yields
 1670 a splitting of 103.10 cm⁻¹ on the Cornell WITEC Alpha300R (Fig. 20b). Following the protocol of Lamadrid et al.
 1671 (2017), this splitting is corrected based on the measured distance between two peaks from the atomic spectra
 1672 of Ne to give a splitting of 103.197 cm⁻¹. Using the densimeter calibrated for this exact instrument, acquisition
 1673 parameters and Ne correction regime (DeVitre et al. 2021), the density of this bubble is $\rho=0.17$ g/cm³ (Fig. 20c).
 1674 However, if the densimeter of Kawakami et al. (2003) was instead used, the calculated density would be nearly
 1675 twice as high ($\rho=0.29$ g/cm³, Fig. 20c).



1676
 1677 *Figure 20 – Determining CO₂ density using Raman Spectroscopy. a) Image of an olivine-hosted melt inclusion*
 1678 *from the Twin Lakes Crater, OR. b) Raman spectra showing the strong Fermi diad (peaks at ~1285 and 1388 cm⁻¹)*
 1679 *with hot bands on either side. The distance between the peaks is the diad splitting ($\Delta=103.10$ cm⁻¹). After*
 1680 *correction for the measured splitting of the Ne emission spectra (Lamadrid et al. 2017), this corresponds to a CO₂*
 1681 *density of 0.17 g/cm³ using the splitting-density relationship developed on this specific instrument (DeVitre et al.*
 1682 *2021). c) The relationship between density and splitting is different on each Raman instrument (e.g., DeVitre et*
 1683 *al., 2021; Fall et al., 2011; Kawakami et al., 2003; Lamadrid et al., 2017; Rosso and Bodnar, 1995; Wang et al.,*
 1684 *2019; Yamamoto and Kagi, 2006). If the Kawakami et al. (2003) densimeter was used for this vapour bubble, it*
 1685 *would give a density of 0.29 g/cm³.*

1686
 1687 The most robust way to calibrate a specific Raman spectrometer for a given analytical protocol is to measure
 1688 the diad splitting for ultra-pure CO₂ gas held at a variety of pressures (and thus densities). This is often achieved
 1689 using a high-pressure optical cell (HPOC) or a fluid density calibration apparatus (FDCA). These apparatus feed
 1690 pure CO₂ gas into a chamber where the pressure is tightly controlled (and ideally the temperature too). The
 1691 measured P and T in the cell can be converted into a CO₂ density using the CO₂ equation of state (EOS, e.g., Span
 1692 and Wagner, 1996). Raman measurements are made on this trapped fluid with known density, and the splitting
 1693 is determined for each Raman acquisition. The relationship between the measured diad splitting and CO₂ density
 1694 is often parameterized over a number of discrete density windows, as the shape of the curves vary (DeVitre et
 1695 al., 2021).

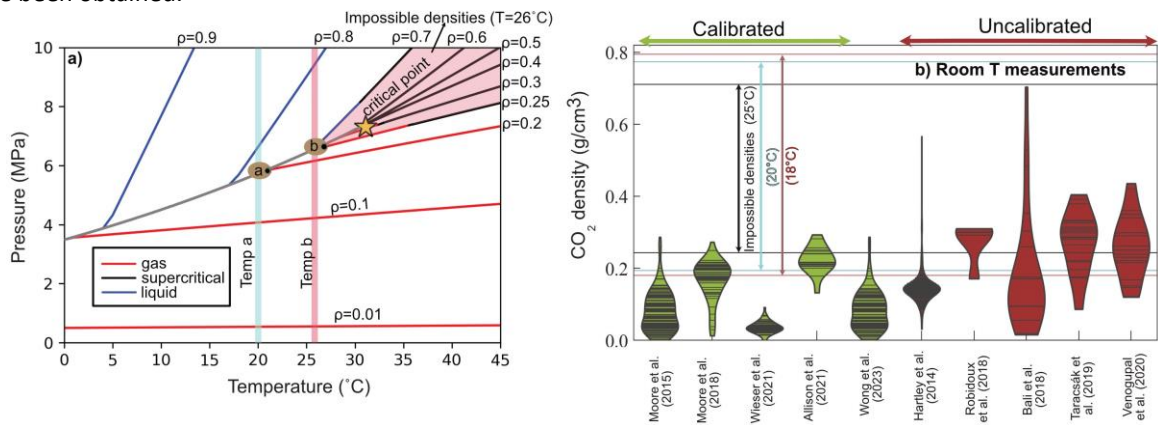
1696 Despite the importance of measuring CO₂ in melt inclusion vapour bubbles being recognised in ~2014–2015
 1697 (Hartley et al., 2014; Moore et al., 2015) and the calibration issue being highlighted in 2017 (Lamadrid et al.,
 1698 2017), only published melt inclusion vapour bubble measurements made at Virginia Tech and Cornell have
 1699 calibrated their Raman using a gas cell apparatus.

1700 Only the Cornell calibration closely controls and measures the T of the CO₂ gas, which is required to convert
 1701 pressure into density with high accuracy and precision (DeVitre et al., 2021). A few more laboratories have used
 1702 lower cost methods, where samples with known CO₂ densities are measured in a manner analogous to primary
 1703 standards for EPMA calibration. For example, Allison et al. (2021) developed a calibration line by measuring the
 1704 splitting-density relationships for fused silica capillary capsules (FSCC). The CO₂ density in these capsules was
 1705 calculated from the mass of loaded CO₂ and the volume of the capillary, which allowed the calibration line to be
 1706 determined at low densities (FSCCs ranged from 0.008–0.133 g/cm³). Wieser et al. (2021) calibrated their Raman
 1707 at low densities using 19 synthetic fluid inclusions (SFI) in quartz standards (0.04–0.14 g/cm³) which were
 1708 measured on the calibrated Virginia Tech Raman, with the same calibration being used by Wong et al. (2023).
 1709 Mironov et al. (2020) use a similar approach, developing a calibration line using 8 melt inclusion vapour bubbles
 1710 measured at Virginia Tech with densities between 0.013–0.22 g/cm³.

1711 Other studies measuring vapour bubbles have converted measured diad splitting into densities using a
 1712 published calibration line developed in a different laboratory (e.g., Bali et al., 2018; Hartley et al., 2014; Taracsák
 1713 et al., 2019; Venugopal et al., 2020). The choice of densimeter in these studies varies widely, and the choice of
 1714 one densimeter instead of another is not justified. For example, Hartley et al. (2014) using Kawakami et al. (2003,

1715 cyan line on Fig. 19c), Taracsák et al. (2019) and Venugopal et al. (2020) using Wang et al. (2011, salmon line),
 1716 and Bali et al. (2018) and Robidoux et al. (2018) using Fall et al. (2011, green line). The offset of their densities
 1717 from the true value is not known, although a correction could be applied retrospectively if samples with known
 1718 CO₂ densities were analysed on the same instrument with the same analytical conditions.

1719 Thermodynamic limits on the density of CO₂ at ambient conditions reveal the issue with the selection
 1720 of a densimeter from the literature developed for a different instrument. The CO₂ phase diagram shows that at
 1721 room T (20–26°C), the maximum possible density of CO₂ gas is ~0.2–0.26 g/cm³ (Fig. 21a). A vapour bubble with
 1722 a higher bulk density will consist of an inner sphere of CO₂ gas of ρ=0.2–0.26 g/cm³, and a coexisting outer shell
 1723 of CO₂ liquid with ρ>0.7 g/cm³ (see inclusion at Temp b on Fig. 21a). It is not thermodynamically possible for
 1724 densities between these values to be measured by Raman spectroscopy unless the sample is heated above the
 1725 critical point of CO₂ at 31°C (supercritical CO₂ can have any density, Span and Wagner et al. 1996). While a small
 1726 amount of laser heating may occur during Raman analysis, which can account for the small number of
 1727 measurements above 0.26 g/cm³ on calibrated instruments (Fig. 21b, DeVitre et al., 2023b; Dubessy et al., 2012;
 1728 Hagiwara et al., 2021), the presence of a significantly larger number of measurements with ρ>0.26 g/cm³ in
 1729 studies which did not perform an instrument specific calibration indicates that these densities have been
 1730 overestimated through selection of an inappropriate literature calibration. For example, had the Kawakami et
 1731 al. (2003) densimeter been used for the melt Inclusion in Fig. 20a, an impossible density of 0.29 g/cm³ would
 1732 have been obtained.



1733 **Figure 21 – a) Phase diagram of CO₂, drawn using the NIST webbook with the Span and Wagner (1996) EOS. At**
 1734 **Temp a (20°C), a CO₂ fluid with ρ>0.2 g/cm³ will comprise of a vapour with ρ=0.194 g/cm³, and a liquid with**
 1735 **ρ=0.773 g/cm³. At Temp B (26°C), the liquid will have a density of ~ρ=0.7 g/cm³ and the vapour will have a density**
 1736 **of ~ρ=0.25 g/cm³. Impossible densities at 26°C are shown in pink. b) Compilation of the densities of room T melt**
 1737 **inclusion vapour bubble measurements by Raman spectroscopy, shown as a Violin plot where each horizontal**
 1738 **line represents 1 measurement. Studies which used an instrument-specific calibration are colored green, those**
 1739 **which did not are colored dark red. The maximum density of a vapour and minimum density of a liquid phase at**
 1740 **three temperatures are shown with horizontal lines. Even with a room T of 25°C, many of the densities reported**
 1741 **by uncalibrated studies are thermodynamically impossible. Refs: (Allison et al., 2021; Bali et al., 2018; Hartley et**
 1742 **al., 2014; Moore et al., 2018, 2015; Robidoux et al., 2018; Taracsák et al., 2019; Venugopal et al., 2020; Wieser**
 1743 **et al., 2021; Wong et al., 2023)**

1745 Once the relationship between measured splitting and CO₂ density for a specific Raman instrument and data
 1746 reduction strategy is determined, the amount of the CO₂ held in the vapour bubble (in ppm equivalent in the
 1747 glass) is calculated using mass balance:

$$1749 \quad CO_2(\text{ppm equivalent}) = 10^4 \frac{Vol\%_{VB} \times \rho_{CO_2}}{\rho_{melt}} \text{ [Equation 8]}$$

1750
 1751 Where $Vol\%_{VB}$ is the vol% of the vapour bubble, ρ_{CO_2} is the density of the CO₂ fluid (determined by
 1752 Raman spectroscopy), and ρ_{melt} is the density of the silicate melt (e.g., using DensityX, Iacovino and Till, 2019).
 1753 Equation 8 can be used to demonstrate the large effect of the choice of densimeter on calculated CO₂ contents.
 1754 For example, using a typical melt density (e.g., 2.7 g/cm³) and a bubble volume percent of ~3.9% (as in the melt

1755 inclusion shown in Fig. 20a), the true vapour bubble CO₂ density of 0.17 g/cm³ means the bubble contributes
1756 2455 ppm CO₂ to the melt inclusion. However, if a literature densimeter was randomly chosen from those in Fig.
1757 20b, the amount of CO₂ contributed by the bubble could be as high as 4188 ppm. These discrepancies in Raman
1758 calibration propagate to large uncertainties in magma storage depths. Wieser et al. (2021) show that for a typical
1759 Kīlauea melt inclusion with a vapour bubble occupying 5% of the inclusion volume, different densimeters could
1760 yield storage depths ranging from 4 to 18 km. Thus, constraining the splitting to CO₂ density relationship for
1761 each individual instrument is vital to avoid the introduction of very large systematic errors on calculated storage
1762 pressures (and therefore depths). Arbitrary choice of a Raman calibration is likely the largest source of
1763 systematic error in many published melt inclusion studies, only overshadowed by studies which didn't measure
1764 the bubble at all. Raman analyses without an instrument-specific calibration must be considered as qualitative.
1765 They are useful to determine whether CO₂ is present in vapour bubbles in any given system, but systematic
1766 errors spanning a factor of 3 are unacceptable when it comes to determining magma storage depths.

1767

1768 **3.3 Other uncertainties reconstructing vapour bubbles**

1769 Once a Raman instrument is calibrated, there are four additional major sources of uncertainty affecting
1770 estimates of the amount of CO₂ held in vapour bubbles, discussed below.

1771 **3.3.1. Volume proportions of vapour bubbles**

1772 The first source of uncertainty is associated with determining the relative volume of the vapour bubble
1773 and melt inclusion (i.e. the $Vol\%_{VB}$ term in Equation 8). The vast majority of melt inclusion studies estimate
1774 volumes using transmitted light images, where a best fit ellipse is fitted to the 2D outline of the melt inclusion
1775 and vapour bubble, and the third (z) dimension is estimated either as an average of the two visible axes, or the
1776 minimum of the two measured axes. Tucker et al. (2019) simulate the uncertainty associated with 2D sectioning
1777 of 3D ellipsoids, concluding that the best estimate is obtained when the third (z) dimension is calculated from
1778 the average of the 2 visible dimensions. They quantify the 1 σ uncertainty of this method (-48% to +37%), which
1779 translates into a significant error in calculated storage depths where vapour bubbles contain a large proportion
1780 of the total inclusion CO₂.

1781 However, in many cases, melt inclusions have faceted faces (e.g., Fig. 20a) or more complex shapes that
1782 can deviate significantly from a perfect ellipsoid. For example, a best fit ellipse fitted to a more cubic shape may
1783 result in the melt volume being overestimated, and by extension, the bubble volume and CO₂ content
1784 underestimated (Hanyu et al., 2020). Mironov et al. (2020) compared methods of calculating the z dimension
1785 using the measured x-y dimensions to direct measurements of the 3rd dimension using a vertically calibrated
1786 microscope, or by polishing two orthogonal faces so the x-y and z direction can be measured. They find that
1787 volume measurements using z from a vertically calibrated microscope or by polishing an orthogonal plane were
1788 in good agreement ($\pm 10\%$) with each other, but differed from the z-axis assumption methods by up to 45%.
1789 Thus, they suggest that researchers should measure the 3rd axis using these relatively low-cost methods, rather
1790 than inferring it from 2D measurements.

1791 The most accurate and precise approach is to determine the volume of each phase using x-ray
1792 tomography (i.e. nanoCT, μ CT; Richard et al., 2019; Hanyu et al., 2020; Jorgenson et al., 2021). Hanyu et al.
1793 (2020) showed that optical methods fitting ellipses tend to overestimate MI volumes by $\sim 20\%$, even in fairly
1794 ellipsoidal shaped MI (they did not assess the effect of strong asymmetry or faceting). Attempts have been made
1795 to constrain volumes using 3D confocal Raman imaging (Aradi et al., 2021; Schiavi et al., 2020). There are
1796 additional complications associated with the fact that the different refractive indices of the host crystal, melt and
1797 vapour can cause vertical distortion (Everall, 2010). This can make vapour bubbles appear oblate (Schiavi et al.,
1798 2020). Raman mapping is also significantly slower than μ CT, and data segmentation is even more time
1799 consuming.

1800 Most recently, DeVitre et al. (2023a) perform nano-CT scans for MI of various shapes and sizes,
1801 including those with extreme asymmetry or faceting. They compare these CT volumes to those calculated using
1802 2D methods (measuring x-y, calculating z), and 3D methods where z is measured using a vertically calibrated
1803 microscope, or by polishing an orthogonal surface. For relatively ellipsoidal shapes, the median offset between
1804 2D and CT methods is $\sim \pm 15\text{--}20\%$ (similar to Hanyu et al. 2020), although for certain melt inclusion morphologies,
1805 the offsets can be $\sim \pm 50\%$, similar to the uncertainty estimated from slicing simulations of Tucker et al. (2019) of

1806 1σ = -48% to +37%. For the most faceted or complex shaped MI, the systematic mis-prediction of volume inflicted
1807 using averaging or minimum axis 2D methods results in an uncertainty of up to ~3 kbar in the saturation
1808 pressures (i.e. meaning MI could have been trapped at crustal levels at 7–8 km, or in the mantle, 17–18km). For
1809 regular, relatively ellipsoidal-shaped melt inclusions, DeVitre et al. (2023a) find that measuring the 3rd dimension
1810 (via microscope, motorized-z stage Raman, or on an orthogonal plane) returns values within $\pm 10\%$ of CT
1811 measurements, although the offsets are larger for more irregularly shaped inclusions. Overall, DeVitre et al.
1812 (2023a) suggest that the orthogonal plane method is the most time- and cost-effective way to reduce uncertainty
1813 associated with bubble volumes. While CT is clearly superior, these measurements cost ~100\$/hr, with high
1814 quality scans needing several hours. Data reduction is also time consuming and computationally expensive. At
1815 the moment, the CT method has not been scaled up to datasets typical of melt inclusion studies (e.g., $N > 100$) in
1816 a time or cost-effective manner. We suggest that it makes more sense to constrain the volumes of all melt
1817 inclusion to within $\pm 20\%$ of the true value for all melt inclusions (and published studies), compared with a smaller
1818 number of super precise CT scans, and a larger number of imprecise 2D optical methods. Developing fast,
1819 inexpensive, and precise ways to estimate vapour bubble volumes is an important frontier to address to optimize
1820 melt inclusion barometry.

1821

1822 **3.3.2. Secondary phases in vapour bubbles**

1823 Another major source of uncertainty when reconstructing bubble CO_2 comes from the presence of
1824 carbon-bearing phases on the wall of the bubble, which may sequester 100s-1000s of ppm of CO_2 (Aster et al.,
1825 2016; Moore et al., 2015; Schiavi et al., 2020; Tucker et al., 2019; Venugopal et al., 2020). These phases can be
1826 identified optically in larger bubbles (Tucker et al., 2019), and produce distinctive peaks in Raman spectra,
1827 particularly if the laser is focused near the bubble wall or line scans and 3D maps are used (Fig. 22d, Moore et
1828 al., 2015; Robidoux et al., 2018; Schiavi et al., 2020). Secondary phases can also be identified using BSE, SE and/or
1829 EDS imaging on an SEM of an exposed bubble walls (Robidoux et al., 2018; Schiavi et al., 2020; Tucker et al.,
1830 2019; Wieser et al., 2020).

1831 The occurrence of secondary phases on bubble walls is highly variable, and their genesis is poorly
1832 understood. It appears that carbonate species (e.g., Mg, Fe, Na, and Ca carbonates) are more common in more
1833 H_2O -rich melt inclusions (e.g., arcs and wet OIBs vs. dry OIBs such as Kīlauea). Even at a given volcano, some
1834 eruptions may have a reasonable proportion of melt inclusions containing carbonate (e.g., 1960 Kīlauea, Moore
1835 et al., 2015; Tucker et al., 2019), while other eruptions have no carbonate (e.g., 2018 Kīlauea, Lerner et al., 2021;
1836 Wieser et al., 2021). Most intriguingly, even within a single crystal, some melt inclusions contain carbonate while
1837 others do not, and within a single melt inclusion with multiple bubbles, some have all their CO_2 as carbonate,
1838 some have a mix of carbonate and CO_2 fluid, and some consist only of CO_2 fluid (Fig. 23). It has been suggested
1839 that solid phases form on bubble walls as a paragenetic sequence during cooling of the vapour bubble, with
1840 sulfide precipitation at 500–700°C, magnesite (MgCO_3) precipitation at < 350 °C, and carbonate and sulfide
1841 precipitation from liquid H_2O at < 150 °C (Robidoux et al., 2018).

1842

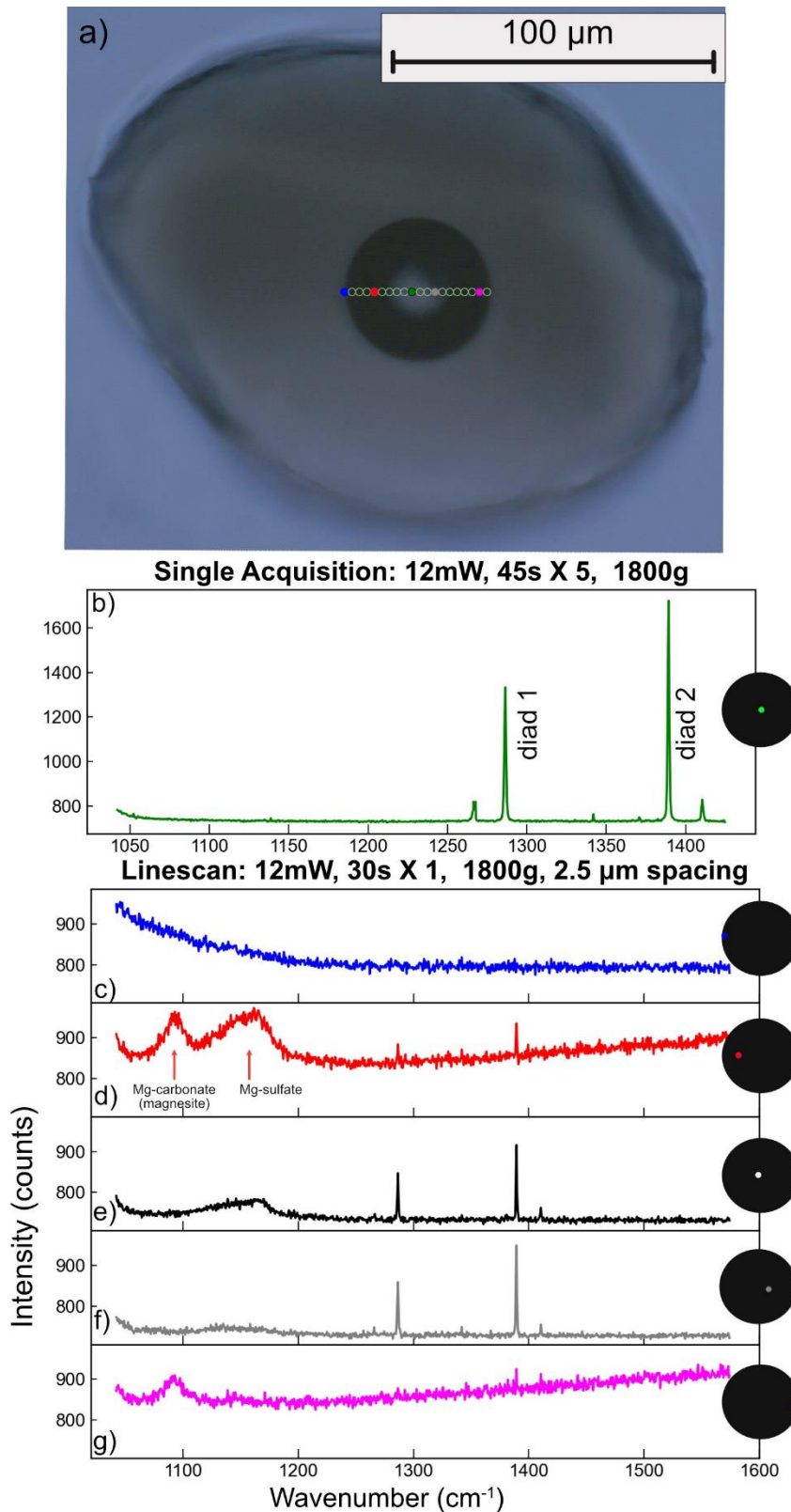


Figure 22 – Comparing a Raman acquisition in the centre of a melt inclusion vapour bubble (scan b) with individual acquisitions taken as part of a line scan across the bubble (c-g). A carbonate and sulfate peak is only apparent at specific locations near the bubble edge, and does not appear in the central acquisition.

Clearly, the carbonate forming reactions are subject to very local variations in condition (on the scale of the diameter of a single melt inclusion), and significant further work is required to understand them further. Quantifying the amount of CO₂ present within carbonate is non-trivial. Tucker et al. (2019) do preliminary mass balance calculations based on optical observations, considering different thicknesses of carbon on the wall of bubbles. Schiavi et al. (2020) determine the volume of carbonate and S-bearing species using 3D Raman mapping, showing that solid phases can account for 21–50% and 16–60% of the C and S budget respectively. Several experimental approaches have been developed for bubble-bearing melt inclusions as an alternative to mass balance reconstructions using Raman Spectroscopy (see below), some of which can help to resolve the carbonate problem.

3.3.2.1 Experimental homogenization approaches

1889 Two broad homogenization strategies have been used to account for Carbonate in vapour bubbles. The ‘in situ’
 1890 strategy involves reheating of individual crystals in a Linkam or Vernadsky heating stage in an fO_2 controlled Ar
 1891 or He atmosphere, making observations of the melt inclusion of interest under an optical microscope. The crystal
 1892 is heated until the vapour bubble and other secondary phases redissolve, and then the sample is rapidly
 1893 quenched to obtain a single-phase melt inclusion. This method allows the operator to view the melt inclusion
 1894 and quench the crystal just after the inclusion homogenizes, meaning a different reheating path can be used for

1895 each crystal. The 'bulk' strategy heats crystals in batches in various experimental apparatus. This had the
1896 advantage of being far less time consuming and allowing reheating at different pressures (see below), but has
1897 the disadvantage of meaning crystals trapped at a range of temperatures may be overheated or underheated
1898 (e.g., Esposito et al., 2012).

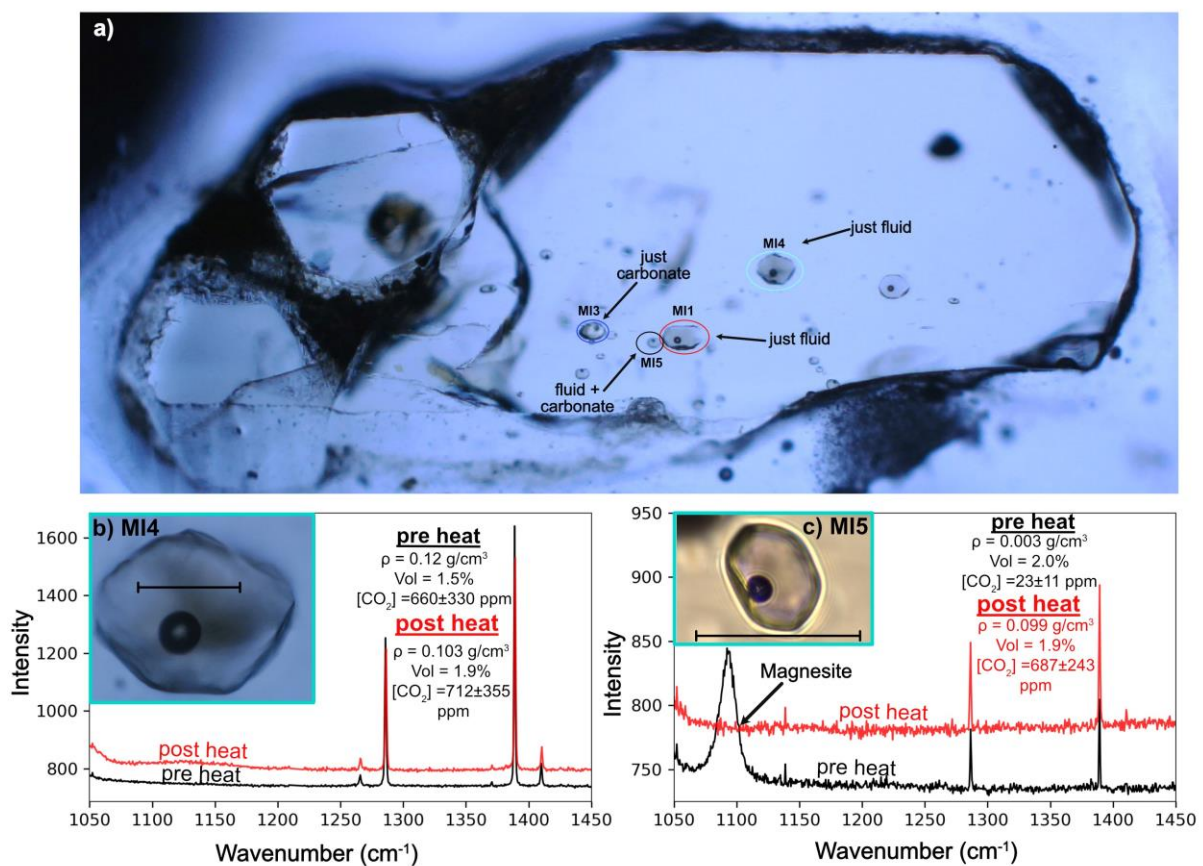
1899 Regardless of whether a single crystal or a batch of crystals is heated, performing reheating experiments
1900 at atmospheric pressure often results in vapour bubbles not fully redissolving, or dissolving at spuriously high
1901 temperatures. For example, Le Voyer et al. (2017) individually heat melt inclusions from Mt. Shasta in the
1902 Cascade Arc using a Vernadsky-type heating stage, noting that many inclusions retain their vapour bubble, even
1903 if they are heated up to 1500°C. The failure to homogenize the bubble has been attributed to the fact that at
1904 atmospheric pressure, the host exerts less pressure on the melt inclusion than was present during natural
1905 cooling at depth in the magmatic system (Danyushevsky et al., 2002; Esposito et al., 2012). Additionally, if
1906 sufficient time passes between post-entrapment crystallization and syn-eruptive quenching, chemical changes
1907 such as FeO or H⁺-loss through the host crystal may occur, which cannot be reversed by reheating (Aster et al.,
1908 2016; Bucholz et al., 2013). To account for the excess bubble growth resulting from these irreversible changes,
1909 the inclusion must be overheated, often by many hundreds of degrees to get the bubble to disappear. This is
1910 concerning because overheating results in extensive re-equilibration between the melt inclusion and host,
1911 erasing important chemical information (e.g., major element zoning preserving quench rate, Newcombe et al.,
1912 2014; information on the amount of PEC; Wieser et al., 2021). An additional problem with heating at 1
1913 atmosphere is that melt inclusions may rupture/decrepitate (Tuohy et al., 2016). This is a particular problem for
1914 melt inclusions closer to the polished surface or the crystal, inclusions trapped at high pressures in the plumbing
1915 system, and more H₂O-rich inclusions.

1916 Crystals can also be heated at elevated pressures (e.g., Piston cylinder apparatus, Rasmussen et al.,
1917 2020, internally heated gas pressure vessel, Skirius, 1990). The confining pressure exerted around the crystal
1918 can help prevent decrepitation, and aid bubble dissolution. To get around the issue that reheating can cause H⁺
1919 loss, and to try to resorb bubbles which have experienced extensive H⁺ loss, Mironov et al. (2015) homogenize
1920 melt inclusions in an internally heated pressure vessel (IHPV) under high H₂O pressure achieved through a
1921 hydrated silicate melt matrix. Specifically, they heat melt inclusions from lavas which are thought to have
1922 diffusively lost 3 wt% H₂O (such extensive H₂O-loss favours near-ubiquitous bubble growth). They find that
1923 bubbles remain after heating under dry and damp conditions, but a large proportion disappear at higher H₂O
1924 pressures where the melt inclusion is rehydrated. This indicates that, at least in wet arc magmas, diffusive H₂O
1925 loss can account for the observation that bubbles often persists after heating (rather than resulting from a lack
1926 of confining pressure during heating in 1 atm apparatus). This reheating method was adapted by Rasmussen et
1927 al. (2020), who use a piston cylinder apparatus with KBr and Mg(OH)₂ as the hydrated matrix to achieve a higher
1928 experimental success rate.

1929 One limitation of these hydrated experimental reheating methods is that the initial H₂O content of the
1930 system must be estimated when preparing the hydrated matrix, and melt inclusion water contents will be reset
1931 to this value (Buso et al., 2022). While Rasmussen et al. (2020) use unheated melt inclusion volatile contents as
1932 a guide, there is still the risk of adding too much or too little H₂O to any specific inclusion. Additionally, while an
1933 approximate estimate of initial H₂O contents can be placed based on the point of homogenization, there is a
1934 non-unique play off between the confining P, T and H₂O content required to obtain complete homogenization
1935 of the bubble (e.g. Mironov et al., 2015 show that instead of increasing H₂O by 1 wt%, P could be increased by
1936 6.5 kbar, or T increased by 100°C). Thus, as with the techniques mentioned above, a limitation of these bulk
1937 homogenization experiments is that the same experimental conditions must be applied to all melt inclusions in
1938 a given capsule, even if they formed on different P-T-H₂O paths in nature (Rasmussen et al., 2020).

1939 All the methods discussed so far attempt to redissolve the bubble entirely, so measurements only need
1940 to be performed on a single homogenous glass phase. In contrast, DeVitre et al. (2023a) developed a reheating
1941 method where the aim is to redissolve the carbonate phase back into the vapour bubble where it can be
1942 measured using Raman spectroscopy, rather than redissolve the bubble into the melt. They heat individual
1943 crystals using a Linkam TS1400XY stage which can heat from room T to 1400°C at up to 200 °C/min, and can
1944 quench using Ar or He flow combined with a water-cooled plate at 240 °C/min. Heating is conducted in an *f*O₂
1945 controlled Ar atmosphere to prevent oxidation of the melt and olivine. As the melt inclusion is progressively
1946 heated under a microscope, it passes through the glass transition temperature, and goes dark. The liquidus

1947 temperature is estimated from the major element composition of the system and a reasonable range of volatile
 1948 contents (using MELTS, or a liq thermometer). As the liquidus temperature is reached, the melt inclusion clears
 1949 to a brown glass, and the inclusion is held at this temperature for ~8–10 minutes to redissolve any carbonate on
 1950 the walls of the bubble back into the fluid phase, before being rapidly quenched on a water-cooled plate. The
 1951 advantage of this method is that it only heats the inclusion to the liquidus, rather than to higher temperatures
 1952 needed to resorb the bubble. Heating to the lowest possible T is advantageous, because it limits olivine
 1953 dissolution, and preserves the major element information held in the melt and olivine. Raman acquisitions
 1954 collected before and after heating indicate that the carbonate is effectively redissolved back into the bubble
 1955 (Fig. 23e), and that inclusions experience minimal H₂O-loss. After heating, bubbles without carbonate return CO₂
 1956 contents within uncertainty of pre-heating estimates (CO₂ contents change by ~±10% accounting for slight
 1957 changes in bubble volume, or errors associated with measuring the same bubble proportion using 2D images).
 1958 The main disadvantage of this method over complete homogenization methods is the fact that Raman is used
 1959 to measure the bubble after heating, which requires accurate estimates of the relative volume of the vapour
 1960 and melt phase.



1961
 1962 *Figure 23: Olivine crystal with numerous melt inclusions with variable carbon partitioning between fluid and solid*
 1963 *phases. A) Two melt inclusions (MI1, MI4) have a strong fermi diad but no carbonate phases (see spectra b),*
 1964 *while MI5 has a fermi diad and a carbonate peak (see spectra c), and MI3 has just a carbonate peak b) pre and*
 1965 *post-heating, MI4 has very similar densities and volumes, with CO₂ contents within error. c) pre-heating, MI5 has*
 1966 *a prominent magnesite peak, and weak Fermi diads. After reheating using the method of DeVitre et al., 2023a,*
 1967 *the amount of CO₂ increases substantially, and the magnesite peak completely disappears. Scalebar on b-c shows*
 1968 *50 μm*

1969
 1970 **3.3.3. Theoretical vapour bubble reconstruction methods**

1971 A variety of methods have also been developed to reconstruct the CO₂ content of a vapour bubble
 1972 theoretically, although there have been relatively few comparisons with Raman approaches on a single inclusion
 1973 basis (e.g. Aster et al., 2016, Wieser et al. 2021). Anderson and Brown (1993) investigated bubble CO₂ in a suite

1974 of melt inclusions from Kīlauea Iki, calculating an internal pressure for each melt inclusion using the measured
1975 CO₂ content in the melt phase of the inclusion. This internal pressure was then used to calculate the density of
1976 CO₂ in the coexisting vapour phase using an equation of state. To convert these densities into CO₂ amounts, they
1977 assumed all bubbles occupied 0.5 vol% prior to syn-eruptive quenching, which is the point at which CO₂ diffusion
1978 and bubble growth become decoupled. Riker (2005) adapt this method for Mauna Loa, calculating the pre-
1979 quench bubble volume as a factor of the T drop experienced by each melt inclusion, accounting for the fact
1980 different melt inclusions experience different amounts of cooling, and therefore PEC. Aster et al. (2016) further
1981 adapt this method for melt inclusions from Lassen Volcanic Centre, Cascades, tracking the volume of a growing
1982 vapour bubble using phase volume and density information from Rhyolite-MELTS, and vapour compositions to
1983 partition elements into the bubble using the volatile solubility model of Iacono-Marziano et al. (2012). This
1984 method was also used in the Cascades by Johnson and Cashman (2020) and Walowski et al. (2016).

1985 In contrast to these methods reconstructing the vapour bubble volume *prior* to bubble expansion
1986 accompanying syn-eruptive quenching, Tucker et al. (2019) use the equation of state method outlined by
1987 Anderson and Brown (1993) to calculate CO₂ density in the bubble, and then calculate the amount of CO₂ in the
1988 bubble using the measured bubble volume. This measured-volume method generates extremely high CO₂
1989 estimates (and therefore storage pressures) for Hawaiian melt inclusions (4000–10,000 ppm). Using the
1990 measured bubble volume assumes that the vapour bubble and melt continue to exchange CO₂ until the glass
1991 transition T (~725°C), such that the bubble is always in equilibrium with the measured melt composition.
1992 However, vapour bubbles experience two distinct phases of growth. The first phase of bubble growth at high T
1993 accompanies PEC or diffusive H₂O loss. High temperatures mean that CO₂ can easily diffuse from the melt into
1994 the growing vapour bubble. The second phase of bubble growth occurs during syn-eruptive quenching, where
1995 CO₂ becomes diffusion-limited as the temperature drops, but the bubble volume continues to grow until the
1996 temperature cools below the glass transition temperature (Maclennan, 2017). Wieser et al. (2021) compare the
1997 Tucker EOS method to direct Raman measurements at Kīlauea and show that the Tucker method overestimates
1998 the amount of CO₂ in the bubble by a factor of 10–20X compared to the Raman method for melt inclusions which
1999 grew most their bubble during syn-eruptive quenching (where CO₂ migration was diffusion limited). The
2000 measured-volume EOS method results in calculated magma storage depth of 5–20 km for melt inclusions where
2001 the Raman method (and geophysics) indicate were actually trapped at 1–5 km. For melt inclusions contained in
2002 high-Fo olivines, where most of the bubble grew during PEC at high temperatures, EOS methods are still 1.5–2X
2003 too high, as the method still neglects a non-negligible increase in bubble volume upon quench which is not
2004 accompanied by CO₂ diffusion.

2005 To unravel the relative importance of these two stages of vapour bubble growth, good estimates are
2006 required of the amount of PEC, the amount of H₂O-loss, the quench rate, and the glass transition T (Maclennan,
2007 2017; Rasmussen et al., 2020). Rasmussen et al. (2020) produce a Python3 tool, MIMiC (Melt Inclusion
2008 Modification Corrections), which calculates bubble CO₂ using empirical parametrizations of volume and density
2009 changes, with uncertainties quantified by Monte-Carlo techniques. However, while constraining the amount of
2010 PEC is relatively straightforward in systems with a well-defined liquid line of descent where the initial FeO
2011 content can be easily estimated (e.g., Kīlauea Volcano, Wieser et al., 2021), it can be very challenging in systems
2012 with a large amount of scatter in FeO at a given MgO number (e.g., Rasmussen et al., 2017; Walowski et al.,
2013 2019), perhaps because of variability in primary FeO contents and/or mixing of diverse melt compositions (e.g.,
2014 Maclennan, 2008). Reconstructing initial H₂O contents can also be very challenging, and the arc magmas from
2015 which melt inclusions were trapped may be substantially more hydrous than the amount of H₂O left in the melt
2016 inclusion (Gavrilenko et al., 2019; Goltz et al., 2020).

2017

2018 3.3.4. Co-entrapped vapour bubbles

2019 All the methods discussed thus far rely on the assumption that vapour bubbles formed after melt
2020 inclusion entrapment, through some combination of PEC, cooling, and H⁺ loss. However, it has been long
2021 recognised that bubbles may also become trapped at the point of melt inclusion formation. These are termed
2022 co-entrapped bubbles. In fact, determining magma storage depths from melt inclusion saturation pressures
2023 *requires* that the melt was volatile saturated at the point of melt inclusion formation. This assumption

2024 necessitates that there is an excess volatile phase available to co-entrap. If co-entrapped bubbles are added
2025 back in by mass balance techniques, the amount of CO₂ could be drastically overestimated.

2026 Many studies simply select a threshold volume above which bubbles are assumed to be co-entrapped
2027 (e.g., 5%, Lowenstern, 2003; Robidoux et al., 2018, or 10%, Buso et al., 2022; Moore et al., 2015). However, the
2028 maximum vapour bubble volume that can form without requiring co-entrapment is a function of the amount of
2029 cooling, and the amount of diffusion H⁺ loss, and varies greatly between different eruptions (Tucker et al., 2019).
2030 Tucker et al. (2019) examine distributions of bubble volumes from Hawai'i, discarding outliers which clearly lie
2031 outside the main distribution of bubble volumes (8 vol%+). In suites where there are abundant fluid inclusions
2032 in crystals addition to bubble-bearing melt inclusions, co-entrapped bubbles can often be identified based on
2033 the fact that they have larger relative volumes than other vapour bubbles, and CO₂ densities more similar to
2034 fluid inclusions (Lerner et al., 2021, Hanyu et al., 2020).

2035 Alternatively, co-entrapped bubbles can be identified by comparing bubble volumes to variables such
2036 as H₂O content, CO₂ density, and PEC amount. For example, Wieser et al. (2021) show that there is a correlation
2037 between the amount of PEC (0–33%) and the volume of the vapour bubble (1–6 vol%) at Kīlauea. The 5% cut off
2038 from Lowenstern (2003) would clearly be inappropriate in this instance. Instead, samples lying significantly off
2039 the observed PEC-volume trend were classified as co-entrapped. While bubble growth in H₂O-poor, CO₂-rich
2040 systems can be relatively well predicted based on the amount of PEC and the cooling path alone (Maclennan,
2041 2017; Riker, 2005; Wieser et al., 2021), it is more complicated in H₂O-rich magmas which have the potential to
2042 experience large amounts of bubble growth following H₂O loss. In these situations it is more robust to use bubble
2043 growth models, and any bubbles which exceed even the most extreme model scenarios were likely co-entrapped
2044 (e.g., Allison et al. 2021, DeVitre et al. 2023a). For example, Ruscitto et al. (2011) report the presence of bubbles
2045 with volumes spanning 6–16 vol % in high Mg olivines from Mt. Shasta, and conclude that these bubble volumes
2046 can grow through a combination of PEC and H₂O loss, so were not necessarily co-entrapped. In contrast, Allison
2047 et al. (2021) found that melt inclusions at Sunset Crater, Arizona, with bubbles >3.5 vol% were likely to be co-
2048 entrapped. These two contrasting scenarios highlight the issue with selecting a single universal volume % as a
2049 cut off.

2050 Even using bubble growth models, the details of specific inclusion must be considered, else co-
2051 entrapped bubbles with volumes within the range predicted by the growth model could be overlooked, even if
2052 they were co-entrapped. Allison et al. (2021) subdivide bubble-bearing melt inclusions from Sunset Crater, AZ,
2053 into 2 groups based on bubble volumes, densities, offset trends in Olivine forsterite-total CO₂ space, and bubble
2054 growth models. They conclude that group 2 inclusions (>3.5 vol%) co-entrapped a bubble. To more robustly
2055 identify co-entrapped vapour bubbles, we are in desperate need of a forward-model of bubble growth,
2056 accounting for both H₂O and CO₂. The model of Maclennan (2017) only considered CO₂ (not H₂O) and is not
2057 publicly available. While the Monte-Carlo methods incorporated in the model of Rasmussen et al. (2020) have
2058 huge potential for this problem, currently this code only works to correct melt inclusions, and cannot be run
2059 forward for a hypothetical P-T-X path post-entrapment. In summary, it is becoming very clear that the CO₂
2060 contents of bubbles must be accounted for to obtain reliable storage depths, and that as a community,
2061 substantially more work is required to a) develop reliable bubble growth models to ensure co-entrapped bubbles
2062 don't result in spurious CO₂ contents b) calibrate individual Raman instruments and perform measurements at
2063 >33°C and appropriate laser powers c) improve methods to determine relative volumes d) further investigate
2064 experimental homogenization methods.

2065 **3.4. Decrepitation**

2066 Another issue affecting melt inclusion saturation pressures is the process of decrepitation, where the
2067 internal pressure of the inclusion exceeds the strength of the host mineral, and cracks open. Decrepitation
2068 commonly occurs during magma ascent, as the confining pressure exerted by the surrounding liquid drops.
2069 Maclennan (2017) compile a global dataset of melt inclusions from MORBs, OIBS, and continental settings,
2070 noting that 95% yield saturation pressures <2 kbar, which is close to the experimental decrepitation threshold
2071 of Wanamaker et al. (1990). Using their model of P-T-V-X evolution of melt inclusions, they conclude that
2072 pressure difference between olivine and melt causes decrepitation in most tectonic settings, so preserved CO₂
2073 contents are minimum estimates. They note that decrepitation can be partially mitigated if the melt inclusion is

2074 trapped from a significantly undersaturated melt, so the melt inclusion experiences significant cooling and PEC
2075 at depth before it ascends, because this reduces the internal pressure of their inclusion. Similarly, sequestration
2076 of CO₂ in a vapour bubble can also help to reduce the pressure of the liquid below the decrepitation threshold.
2077 The modelling of Maclennan (2017) suggested that entrapment pressures up to twice the decrepitation
2078 threshold (i.e., ~4 kbar) could be preserved if ascent conditions allow for bubble formation while remaining
2079 below the decrepitation threshold.

2080 However, a number of studies have been published since 2017 yielding significantly higher saturation
2081 pressures than the compilation of Maclennan (2017). In the glass phase alone, DeVitre et al. (2023a) measure
2082 CO₂ contents of up to 1.3 wt% resulting in glass-only saturation pressures of ~1-7 kbar. Once CO₂ in the vapour
2083 bubble is included, pressures rise to ~2-11 kbar. Similarly high glass CO₂ contents (1.2 wt%) are reported by Buso
2084 et al. (2022) in melt inclusions from the French Massive Central, corresponding to entrapment depths of >10
2085 kbar. Once bubbles are dissolved using homogenization methods, saturation pressures extend to 15–25 kbar.
2086 Glass-only measurements from Haleakala, HI, cluster at 1–3 kbar, and extend to 2–6 kbar after accounting for
2087 the bubble (Moore et al., 2021). Melt inclusions from Isla Floreana in the Galápagos record glass-only saturation
2088 pressures of 1.1–7.2 kbar (median=5 kbar, bubbles not measured). Critically, one bubble-free inclusion records
2089 a glass-only saturation pressure of ~7 kbar. This high pressure overlaps with the pressure calculated from Cpx-
2090 based barometry, indicating it is not an outlier (Gleeson et al., 2022, 2021), and the lack of decrepitation cannot
2091 be attributed to the presence of a bubble keeping the inclusion below the decrepitation threshold. There are
2092 numerous other examples of saturation pressures calculated from the glass phase only yield saturation
2093 pressures >2 kbar from many alkali ocean island settings (e.g., French Polynesia, Hanyu et al., 2020; El Hierro,
2094 Taracsák et al., 2019), and studies accounting for the glass and bubble exceeding 2-4 kbar (e.g., Sunset Crater,
2095 AZ, at 3-5 kbar, Allison et al., 2021, Deccan Traps between ~ 2–7 kbar, Hernandez Nava et al., 2021).

2096 The existence of melt inclusions with glass-only saturation pressures of >>2-4 kbar and glass + bubble
2097 saturation pressures of >4 kbar suggests decrepitation may not be as important a process as Maclennan (2017)
2098 suggests. While Maclennan (2017) conclude that “*decrepitation of melt inclusions, where the inclusion ruptures
2099 and loses CO₂ to the external melt, is the dominant process that controls the observed distribution of CO₂ in the
2100 compiled data set*”. We suggest that the paucity of alkaline, CO₂-rich settings in the compilation of Maclennan
2101 (2017), combined with the fact most studies did not measure the vapour bubble, led to a dataset that was
2102 skewed to anomalously low pressures.

2103 **3.5. Melt inclusions hosted in other mineral species**

2104 While storage depths calculated from olivine-hosted melt inclusions have dominated the literature in
2105 the past few decades, there are a growing number of studies measuring melt inclusions in plagioclase (Bennett
2106 et al., 2019; Blundy et al., 2010; Drignon et al., 2019; Koleszar et al., 2012; Neave et al., 2017; Wieser et al.,
2107 2022c), ortho- and clinopyroxene (Araya et al., 2019; Koleszar et al., 2012; Wieser et al., 2022c), and amphibole
2108 (Koleszar et al., 2012). In more silicic systems, quartz-hosted inclusions are also commonly examined (Bégué et
2109 al., 2015; Quinn, 2014; Wallace et al., 1999), along with plagioclase (Bacon et al., 1992, Wright et al., 2012) and
2110 ortho- and clinopyroxene (Wright et al., 2012).

2111 Saturation pressures from inclusions in other phases often overlap with those determined from olivine
2112 (Wieser et al., 2022c), and may even yield deeper saturation pressures (Bennett et al. 2019) indicating that the
2113 “rupture resistance” of these other mineral phases may have been underestimated. Also, to gain an unbiased
2114 understanding of storage condition in a wide range of melt compositions, it is certainly advantageous to consider
2115 more than one mineral phase, particularly as in many systems olivine is restricted to a relatively narrow range
2116 of melt compositions (if present at all). However, significantly more work is needed to understand bubble growth
2117 and post-entrapment processes in these other phases, as well as rates of diffusive H₂O-loss.

2118

2119 **4. Fluid inclusion Barometry**

2120 Crystals growing in a fluid-saturated magma trap pockets of melt and exsolved fluid in varying
2121 proportions, varying from pure melt (melt inclusions), melt and varying proportions of fluids (melt inclusions
2122 with co-entrapped vapour bubbles), and pockets of pure fluid with little or no attached melts (fluid inclusions –
2123 FI, Steele-Macinnis et al., 2011). In CO₂-rich, H₂O-poor volcanic systems such as mid-oceanic ridge basalts and
2124 ocean island basalts (OIBs), the exsolved vapour phase (and thus the fluid being trapped) is almost pure CO₂ at

2125 pressures >200 bars (Gerlach and Graeber, 1985). In these relatively anhydrous systems, the density of FI can
2126 act as an excellent barometer, because the density of a CO₂-rich fluid, along with an estimate of its entrapment
2127 temperature, can be converted into a pressure using the pure CO₂ equation of state (e.g., Span and Wagner,
2128 1996).

2129 Despite clear potential, a Web of Science search demonstrates that FI barometry has been
2130 underutilized by igneous petrologists in the last 10 years relative to other petrological barometers (Fig. 24c-d).
2131 Conventionally, the densities of FIs have been determined by observing phase changes during heating and
2132 cooling in a temperature-controlled microscope stage (microthermometry, Sorby, 1858). The relatively small
2133 number of existing studies in volcanic settings that use microthermometric techniques to obtain FI densities
2134 show the enormous potential of this method (Fig. 24c, see Hansteen and Klügel, 2008 and refs within). For
2135 example, FI in quartz-rich xenoliths from volcanoes in the Aeolian arc yield densities corresponding to both deep
2136 (~16–20 km) and shallow (4–6 km) pressures within the crust (Frezzotti et al., 2003). The deeper regions likely
2137 represent the primary magma storage zones, with shallower depths recording re-equilibration of FI during
2138 temporary residence at shallower levels during ascent towards the surface. The ability of FI to identify multi-
2139 stage ascent has also been demonstrated at Mt Etna (Frezzotti et al., 1991) at Mt. Etna, Cabo Verde (Klügel et
2140 al., 2020), Azores (Zanon and Frezzotti, 2013) and the Canary Islands (Hansteen et al., 1998).

2141 It has long been established that Raman spectroscopy can be used as an alternative to
2142 Microthermometry to determine the density of CO₂-rich fluid inclusions (e.g., Rosso and Bodnar, 1995). More
2143 recently, improvements in the spatial and spectral resolution of confocal Raman spectroscopy, along with the
2144 development of precise ways to calibrate the relationship between peak parameters and CO₂ density for
2145 different Raman instruments (e.g., DeVitre et al., 2021; Kawakami et al., 2003; Lamadrid et al., 2017, see section
2146 3.2) has made it possible to determine fluid inclusion densities using Raman spectroscopy (Dayton et al., 2023;
2147 Kobayashi et al., 2012; Rosso and Bodnar, 1995). Raman analyses have many advantages over
2148 Microthermometry:

2149 1. Confocal Raman spectrometers are becoming increasingly common in universities, where they are
2150 widely used in other subdisciplines within the Earth Sciences (e.g., paleontology, mineral physics). In contrast,
2151 the use of heating-cooling stages and the associated expertise to conduct microthermometry is more restricted.

2152 2. Raman analyses are faster (2–4 mins) compared with the 10s of minutes required to conduct a single
2153 heating and cooling experiment. This is particularly true if there is only one fluid inclusion within the field of view
2154 at high magnification. Microthermometry can be faster on fluid inclusion trails as phase changes in multiple
2155 inclusions can be observed in one experiment.

2156 3. Raman analyses only require only one surface to be ground down to within ~50–100 µm of the fluid
2157 inclusion, with a good enough polish to be able to visualize the FI on the Raman microscope. Normally, all that
2158 is required to achieve this is relatively fine wet-and-dry paper (2000–7000 grade) and a quick 30 s polish on 1
2159 µm Aluminium polishing paper, while microthermometry requires a crystal to be prepared into a double polished
2160 wafer, with a good enough polish to see phase changes in detail.

2161 4. Raman spectroscopy can be used on CO₂ fluid inclusions with a very wide range of densities (e.g.
2162 0.01–1.24 g/cm³) densities. In contrast, it is very hard to observe the homogenization temperature of a fluid
2163 inclusion with a density less than the critical density of CO₂ (<~0.47 g/cm³) or a density higher than the triple
2164 point (>1.18 g/cm³) using microthermometry (Kobayashi et al., 2012).

2165 5. Raman spectroscopy can be applied on FIs with diameters down to ~1 µm (Frezzotti et al., 2012,
2166 Dayton et al., 2023), while it is very difficult to observe phase changes during microthermometry for inclusions
2167 < 3–10 µm (Kobayashi et al., 2012). This is of particular importance in volcanic systems, where many fluid
2168 inclusions are very small (and smaller inclusions are more resistant to decrepitation during ascent, Bodnar et al.,
2169 1989; Campione et al., 2015; Wanamaker et al., 1990).

2170 Relative to melt inclusion analyses and mineral barometry, estimates of magma storage depths from
2171 FIs are significantly more precise than both melt inclusions and mineral barometry, and have fewer sources of
2172 systematic uncertainty relating to the conversion of the measured quantity (density) to pressure. Unlike the
2173 complex relationships relating pressure to mineral components (e.g., Jd in Cpx) or dissolved H₂O and CO₂
2174 concentrations in silicate melts, the CO₂ equation of state is extremely well constrained, with very little offset
2175 between different parameterizations (~3% at 7 kbar, Span and Wagner, 1996; Sterner and Pitzer, 1994; Wieser
2176 and DeVitre, 2023). Additionally, unlike many mineral-melt barometers which are very temperature sensitive,
2177 the P calculated from the EOS is not all that sensitive to T (Fig. 24a). To demonstrate the high precision of this
2178 method, we propagate a ±30 K uncertainty in trapping temperature and a Raman analytical error of ±0.02 g/cm³
2179 using Monte-Carlo methods (Wieser and DeVitre, 2023), which yields a 12% 1σ error at 0.6 kbar, a 7% error at
2180 2.2 kbar, and a 5% error at 5.2 kbar. These errors are significantly smaller than other petrological barometers
2181 (Fig. 24b). A final advantage over melt inclusion barometry is that far fewer analytical steps are required to

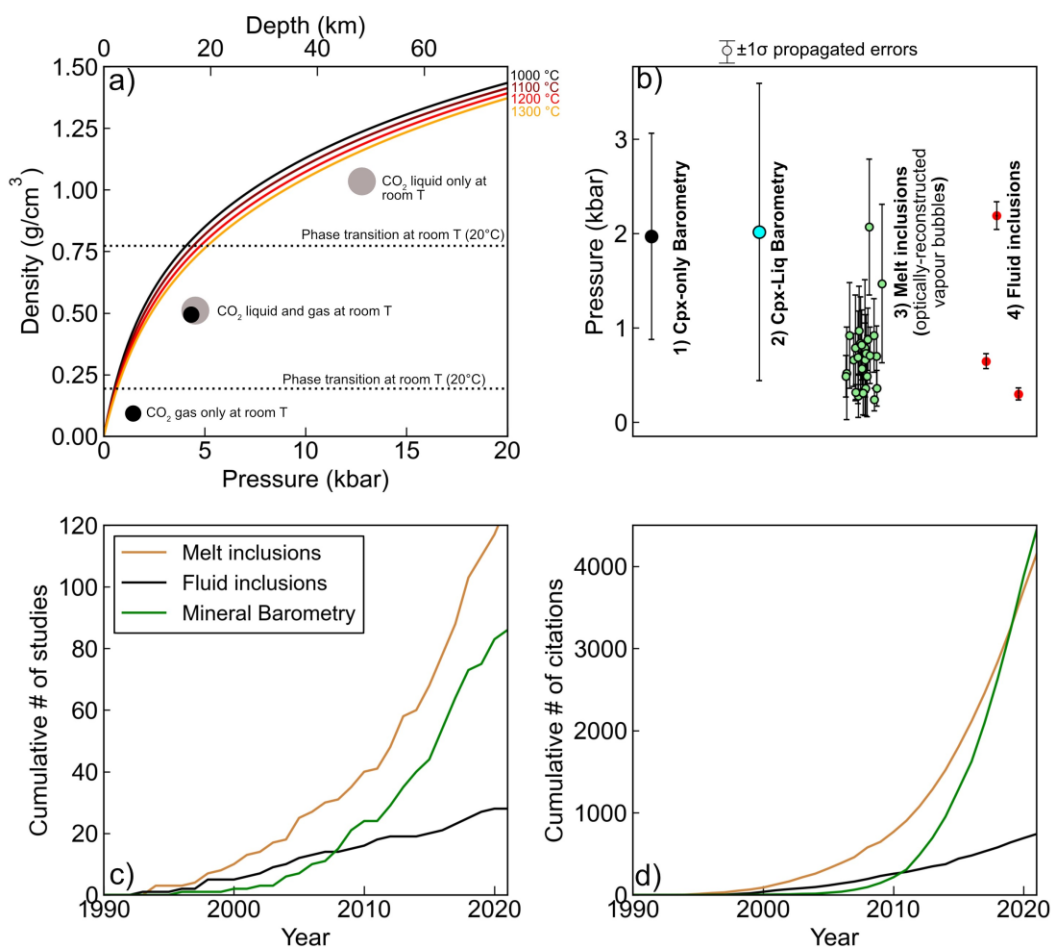
2182 obtain FI pressures (no μ CT, FTIR/SIMS, EPMA measurements of glass), increasing the speed at which depths can
2183 be determined, at a far lower cost (Dayton et al., 2023). This speed is aided by open-source Python3 packages
2184 which help to automate data processing and CO₂ equation of state calculations, which were previously some of
2185 the slower parts of the Raman fluid inclusion method (Wieser and DeVitre, 2023).

2186 Several sources of systematic error must still be considered when interpreting fluid inclusion pressures.
2187 First, like melt inclusions, fluid inclusions may experience decrepitation and rehealing upon ascent. These fluid
2188 inclusions can yield anomalously shallow densities. Second, the pressure the inclusion exerts on the host can
2189 also cause plastic deformation of the host, increasing the inclusion volume. These two processes are captured
2190 by two of the three 'Roedders' rules of fluid inclusions: '2) *the inclusion represents a constant volume*, 3) *nothing*
2191 *has been added or lost from the inclusion*' (Bodnar, 2017; Roedder, 1984). Namely, fluid inclusion barometry
2192 assumes that a fixed mass of CO₂ was trapped in the crystal, with a fixed volume, meaning the inclusion has a
2193 fixed density, so the density measured in the laboratory is the same as the density at which the inclusion was
2194 trapped. Decrepitation violates rule 3 (and possibly 2 as well), while re-equilibration violates rule 2. While
2195 numerous work has been conducted to determine re-equilibration processes for quartz-hosted fluid inclusions
2196 (Bakker, 2017; Boullier et al., 1989; Pecher, 1981; Qin et al., 1992), to our knowledge, the only experimental
2197 constraint on olivine re-equilibration was performed by Wanamaker and Evans (1989). They re-equilibrate fluid
2198 inclusions within San Carlos olivine by holding crystals at 1400°C and atmospheric pressure for several days. We
2199 suggest that further experimental work is required to confidently predict how fluid inclusions in common mafic
2200 phases (olivine, pyroxenes etc) re-equilibrate when subject to a specific P-T-t path, with the aim of having models
2201 which can be run for a given set of samples similar to those used to model H⁺ loss from melt inclusions (E.g.,
2202 Barth and Plank, 2021). However, it is clear from analyses of fluid inclusions in mantle xenoliths that return
2203 crustal pressures that re-equilibration should be taken as the norm rather than the exception, and fluid
2204 inclusions will normally be reset to the pressures corresponding to the final region of prolonged magma stalling
2205 prior to eruption (Hansteen and Klugel, 2008).

2206 The presence of fluid species other than CO₂ can also influence the accuracy of calculated pressures by
2207 both Raman spectroscopy and microthermometry. In igneous systems, the most common species present in the
2208 exsolved fluid phase are H₂O, SO₂, Cl, F, H₂S, N₂, CH₄, CO, and He. While some species are strongly Raman active
2209 with peaks that are close enough to the CO₂ diad to be visible in most high resolution acquisitions (e.g. SO₂
2210 produces a sharp peak at 1151 cm⁻¹, Frezzotti et al., 2012), others will require a separate acquisition centered at
2211 higher wavenumbers (e.g. the N₂ peak is at 2331 cm⁻¹, CH₄ at 2917, Frezzotti et al., 2012), and monoatomic
2212 gases (e.g. He) are Raman inactive, meaning they don't produce any peaks. Molar proportions can be estimated
2213 from peak area ratios and knowledge of scattering cross sections for different Raman-active gases (Burke, 2001).
2214 Some fluid species can also be identified (and sometimes quantified) from changes in the freezing and melting
2215 temperatures by microthermometry (Hansteen and Klugel, 2008; Van Den Kerkhof, 1990), although in many
2216 cases, the relevant phase diagram has not been constrained (e.g. C-He).

2217 Mixed H₂O-CO₂ fluids present a particularly challenging problem to fluid inclusion barometry, because
2218 H₂O is so ubiquitous in the exsolved vapour phase in igneous systems. In arc magmas H₂O will be present in non
2219 negligible molar proportions at all crustal levels (>>10 mol%, Wieser et al. 2023d). Even in CO₂ dominated
2220 systems (e.g. Hawai'i), exsolved fluids will have substantial proportions of H₂O in the vapour phase as magmas
2221 ascend towards the surface. H₂O can be identified by microthermometry through the appearance of clathrate
2222 phases, and by Raman spectroscopy through identification of the O-H stretching band at ~3600 cm⁻¹ (Azbej et
2223 al., 2007). However, at room temperatures, H₂O will be present as a thin film of liquid along the edge of the
2224 inclusion. This can make it very hard to identify by Raman spectroscopy, unless the inclusion is heated to the
2225 point at which H₂O dissolves into CO₂ (e.g., to ~150°C, Esposito et al., 2016). It has also been demonstrated that
2226 this H₂O film can react with the host crystal or a thin film of melt around the fluid inclusion (Andersen et al.,
2227 1984; Esposito et al., 2016; Frezzotti et al., 2002), and/or be lost through diffusive re-equilibration with a
2228 degassed carrier melt (Mackwell and Kohlstedt, 1990). This means it can be hard to identify which FIs had non
2229 negligible quantities of H₂O at the time of entrapment.

2230 The presence of other fluid species complicates calculations of pressure in two ways. First, CO₂ densities
2231 obtained by Raman spectroscopy or microthermometry are normally converted into an entrapment pressure
2232 using a pure CO₂ EOS, which will deviate from the true relationship defined by a mix of the species of interest.
2233 Secondly, the reaction of secondary phases to form precipitates on walls, solid crystals, or liquid films means
2234 that the measured density represents only that of the residual CO₂ fluid phase, not the initial trapped fluid.
2235 Hansteen and Klugel (2008) discuss possible corrections for mixed fluids in their review (e.g. estimating H₂O/CO₂
2236 ratios, then using a mixed H₂O-CO₂ EOS). Looking forward, we suggest that further work into mixed fluid
2237 equation of states and phase diagrams, as well as experiments of fluid inclusion re-equilibration, is required to



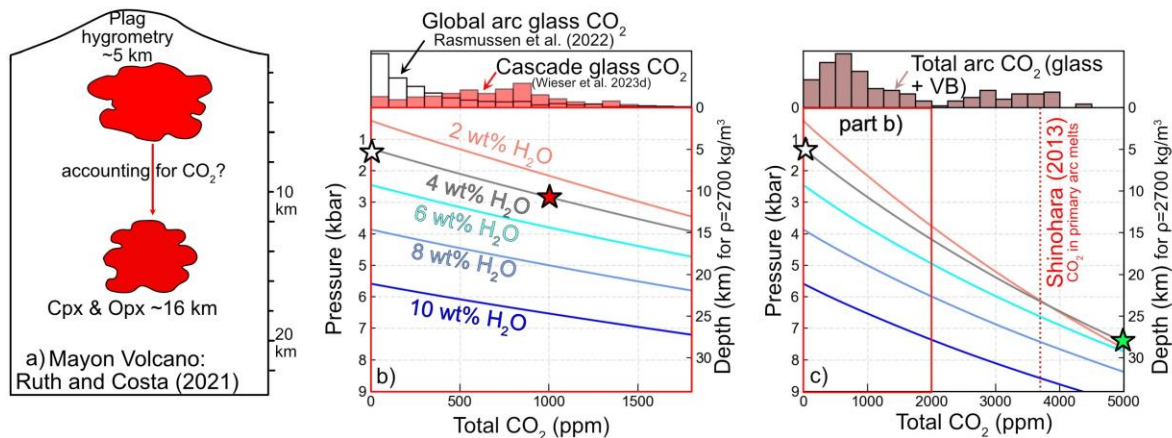
2239 *Figure 24: a) Relationship between pressure and the density of a pure CO₂ fluid (calculated using the Span and*
 2240 *Wagner, 1996 EOS implemented in CoolProp, Bell et al., 2014). Storage depths shown for crustal densities of*
 2241 *$\rho=2700 \text{ kg/m}^3$. b) Monte Carlo simulations of 1σ errors for different barometry methods resulting from analytical*
 2242 *uncertainty. Uncertainties calculated using Putirka (2008) eq32d-32b for Cpx-only and eq3 3–30 for Cpx-Liq*
 2243 *arising from the EPMA analytical uncertainties of Neave et al. (2019, see Wieser et al. 2023b). Melt inclusion*
 2244 *uncertainties show propagated errors in melt inclusions with vapour bubbles from the 2018 eruption of Kilauea*
 2245 *(Wieser et al. 2021). The large relative errors ($\pm 50\%$, $\sim 1\text{--}1.5 \text{ kbar}$) arise from reconstructions of the volume of*
 2246 *the vapour bubble using optical microscopy (with $z=(x+y)/2$, after Tucker et al. 2019). 1σ errors on calculated*
 2247 *pressures for 3 FIs trapped at different crustal pressures, assuming an analytical error of 0.02 g/cm^3 from Raman*
 2248 *spectroscopy, and uncertainty in T of $1\sigma=30 \text{ K}$. c) Web of Science search for number of articles using each method*
 2249 *for barometry (full search criteria given in supporting information), and d) number of citations to these articles.*

2251 **5. Can hygrometers be used as barometers?**

2252 At the opposite end of the spectra to determining pressures from fluid inclusions in CO₂-rich systems
 2253 assuming the exsolved fluid is pure CO₂, many studies have used H₂O contents to estimate pressures using a
 2254 pure H₂O solubility model, either through direct measurements in melt inclusions (e.g., Blundy and Cashman,
 2255 2005, Rutherford et al., 1985) or calculated H₂O contents from mineral and mineral-melt hygrometers (e.g.,
 2256 Amphibole Mg#s – Goltz et al., 2020, Krawczynski et al., 2012, Plag-Liq hygrometry – Ruth and Costa, 2021). For
 2257 example, Ruth and Costa (2021) conduct thermobarometry on a variety of phases from Mayon Volcano (Fig.
 2258 25a). Cpx-Liq, Opx-Liq and Cpx-Opx pressures show a prominent peak at $\sim 4 \text{ kbar}$ (16 km). In contrast, they invoke
 2259 a shallower magma reservoir at $\sim 5 \text{ km}$ based on H₂O-only saturation pressures calculated from plagioclase-
 2260 liquid hygrometry (and H⁺ in pyroxene). However, it is well established that primary arc magmas have non-
 2261 negligible quantities of CO₂ (Shinohara, 2013; Wallace, 2005). While such H₂O-only calculations are often quoted

2262 as minimum estimates, it is worth questioning whether such minimum estimates are even useful, given that
 2263 uncertainty in the amount of CO₂ can change the calculated pressure by up to an order of magnitude (Black and
 2264 Andrews, 2020; Wieser et al., 2022a).

2265 Using a global compilation of CO₂ in the glass phase of melt inclusions (Rasmussen et al., 2020, white
 2266 histogram, Fig. 25b) and a compilation from the Cascade arc (red histogram, Fig. 25b, Wieser et al., 2023d), it is
 2267 apparent that arc magmas have, at the very minimum, several hundred to a thousand ppm of CO₂. These
 2268 quantities of CO₂ have a very significant effect on the calculated saturation pressures. For example, the H₂O-only
 2269 saturation pressure of a typical arc basalt with 4 wt% H₂O (Plank et al., 2013) is ~ 1.3 kbar (white star on grey line)
 2270 (line), while the saturation pressure accounting for 1000 ppm CO₂ is 2.8 kbar (red star on grey line, Fig. 25b). In
 2271 reality, it is becoming apparent that glass-only melt inclusion measurements have substantially underestimated
 2272 the CO₂ content of arc magmas. A compilation of CO₂ contents in arc magmas for studies accounting the vapour
 2273 bubble extends up to ~5000 ppm (Fig. 25c). For a magma with 4 wt% H₂O, a H₂O-only saturation pressure
 2274 underestimates the true storage depth of a magma with 5000 ppm CO₂ by a factor of 5.7X (Fig. 25c, white star
 2275 vs. green star). While H₂O depths are indeed minimum estimates, this example shows just how misleading they
 2276 can be. Even for a magma with 10 wt% H₂O, H₂O-only pressures underestimate by ~1.8X if there is 5000 ppm
 2277 CO₂. Thus, we speculate in many cases that accounting for CO₂ will push hygrometry estimated magma storage
 2278 pressure substantially deeper, perhaps more in line with other barometry estimates (Fig. 25a).



2279
 2280 *Figure 25: Sensitivity of saturation pressures to CO₂ contents. a) Schematic model of plumbing system at Mahon*
 2281 *Volcano, adapted from Ruth and Costa (2021), where the depth of the shallower reservoir was calculated using*
 2282 *a H₂O-only solubility model. b-c) Increase in saturation pressure with CO₂ for 5 different H₂O contents (for a*
 2283 *typical mafic Cascade melt composition, SiO₂=54.3 wt%), calculated using the solubility MagmaSat (Ghiorso and*
 2284 *Gualda, 2015) in VESlcal (Iacovino et al., 2021). The histograms in b) show a global compilation of arc CO₂*
 2285 *contents just measuring the glass phase (Rasmussen et al., 2022), and a compilation from the Cascade Arc. c)*
 2286 *Expanded x scale (region shown in b indicated in the red box) up to 5000 ppm CO₂. Histogram shows a compilation*
 2287 *of total arc CO₂ accounting for the vapour bubble through Raman spectroscopy or homogenization (from Mironov*
 2288 *et al., 2015; Moore et al., 2018, Rasmussen et al., 2020). We overlay the estimate of primitive arc magma CO₂*
 2289 *contents from Shinohara (2013)*

2290
 2291 Therefore, we suggest that H₂O-only saturation pressures should only be used in systems where it has been
 2292 demonstrated that very little CO₂ is present, in the same way that fluid inclusion barometry using the pure CO₂
 2293 EOS can only be used in systems where there is very little H₂O in the fluid phase. In more CO₂-rich systems,
 2294 calculations should be performed for a wide range of possible CO₂ contents to determine the uncertainty
 2295 associated with H₂O-only saturation pressures.

2296 6. Elastic Thermobarometry/Thermoba-Raman-try

2297 Elastic thermobarometry exploits information held within the crystal structure of mineral inclusions
 2298 and hosts to determine formation and re-equilibration conditions (Cisneros and Befus, 2020). As these
 2299 measurements are typically made by Raman spectroscopy because the band/peak positions of many minerals

2300 are P-sensitive, this technique was termed *Thermoba-Raman-try* by Kohn (2014). One form of elastic
2301 thermobarometry uses host-inclusion pairs. At the time of mineral growth and entrapment, the host and
2302 inclusion have the same pressure. However, after entrapment, the different thermal expansivity (change in
2303 volume with T) and compressibility (change in volume with P) of the two mineral species means that a residual
2304 pressure develops as the pair cool and/or ascend to the surface. The magnitude of the residual pressure depends
2305 on the P-T path taken (see Fig. 1 from Kohn, 2014). The final stress measured in the inclusion is a function of the
2306 initial P-T conditions of trapping, and the influence of differential contraction of the host-mineral pair (which
2307 can be modelled using knowledge of expansivity and incompressibility of different mineral species; Kohn, 2014).
2308 The most effective barometers are those where there is a large difference between the isothermal
2309 compressibility of the inclusion and host (i.e., changes in volume during pressure changes), while the most
2310 effective thermometers are those with the largest variations in isobaric expansivity (i.e., changes in volume
2311 during temperature changes).

2312 Traditionally, elastic thermobarometry techniques have been applied to inclusion-host pairs in
2313 metamorphic systems or xenoliths. Diamond, garnet and zircon are commonly examined hosts, and host-
2314 inclusion pairs include olivine-in-diamond, coesite-in-diamond, and coesite-in-zircon (Kohn, 2014, Cisneros and
2315 Befus, 2020). *Thermoba-Raman-try* techniques can be remarkably precise; the estimated error in calculated
2316 pressure for Qtz-in-Gt inclusions is 0.3–0.5 kbar, resulting from uncertainty in the Raman band position of 0.5
2317 cm^{-1} (Kohn, 2014).

2318 Befus et al. (2018) provide the first assessment of elastic thermobarometry in igneous systems by
2319 pressurizing feldspar in a diamond anvil cell and measuring the Raman bands in situ. They find a clear shift of
2320 peak positions to higher pressure from 0 to ~30 kbar, with Raman shifts of the band at $\sim 485 \text{ cm}^{-1}$ of $\sim 0.42 \text{ cm}^{-1}$
2321 per kbar for Albite, 0.45 cm^{-1} per kbar for andesine, and 0.31 cm^{-1} per kbar for anorthite. Their calibrations
2322 relating peak position with pressure could be applied to natural feldspars inclusions with known compositions,
2323 using models of host-inclusion relaxation along a PT path. They suggest that the main limitation of applying this
2324 technique to shallower crustal storage where peak shifts are rather small results from the limited spectral
2325 resolution of many Raman spectrometers ($\sim 1 \text{ cm}^{-1}$). However, the most recent generation of Raman
2326 spectrometers have improved spectral resolution ($0.1\text{--}0.4 \text{ cm}^{-1}$). Additionally, Befus et al. (2018) fit a cubic spline
2327 to the Raman data. If the peak shape can be determined (i.e. a Lorentzian or Gaussian), peak fitting can achieve
2328 significantly higher precision than the spectra resolution (Yuan and Mayanovic, 2017). This increase in spectral
2329 resolution accompanying peak fitting is vital for precise quantification of CO_2 densities using Raman
2330 spectroscopy. For example, a WITEC alpha300R Raman has a spectra resolution of 0.57 cm^{-1} using the 1800
2331 grating. However, the peak fitting error on the CO_2 peaks using a pseudovoigt ranges from 0.002–0.05 cm^{-1}
2332 (error quantified in *lmfit* implemented in *DiadFit*, Newville et al., 2016; Wieser and DeVitre, 2023).

2333 Befus et al. (2018) also note that feldspar inclusions within olivine and clinopyroxene could act as an
2334 effective thermometer (with a predicted resolution of $\sim 100^\circ\text{C}$). This seminal paper was followed by an
2335 assessment of a wider set of inclusion-host pairs by Cisneros and Befus (2020). They identify the need for
2336 significant further work for elastic thermobarometry to become useful in igneous systems (e.g., understanding
2337 anisotropy on residual P, viscoelastic effects, nonideal geometries). Despite the potential of this method, in the
2338 5 years that have passed since Befus et al. (2018) and 3 years since Cisneros and Befus (2020), none of the citing
2339 studies have applied *Thermoba-Raman-try* methods to volcanic rocks. Significantly more work is needed, along
2340 with comparison to other methods, to gain community acceptance of these techniques. However, the recent
2341 proliferation of interest and expertise in Raman spectroscopy by igneous petrologists measuring vapour bubbles
2342 should aid such efforts.

2343

2344 **7. Experimental Petrology**

2345 Experimental petrology fundamentally underpins the melt inclusion, mineral-melt thermobarometry,
2346 and *Thermoba-Raman-try* methods discussed so far, because the composition of experimental products are used
2347 to calibrate models. However, experimental petrology can also be used directly to investigate magma storage
2348 conditions in a specific system. Generally, such experiments use a starting composition characteristic of a specific
2349 volcanic system or eruption, and perform experiments at a range of P, T, H_2O and $f\text{O}_2$ conditions. Then,
2350 experimental phase compositions are compared to natural samples to determine the most probable storage
2351 conditions (e.g., comparing glass compositions, mineral core and rim conditions, occurrence of breakdown
2352 reactions; First et al., 2021; Rutherford et al., 1985; Weber and Castro, 2017).

2353 For example, Voigt et al. (2022) perform experiments at 0.25–5 kbar and 850–1100°C on natural starting
2354 materials from the 1257 Samalas eruption. They observe plagioclase and amphibole in their samples, so the PT

2355 space between amphibole breakdown and plagioclase instability places constraints on pre-eruptive PT
2356 conditions. Generally, once a stability region is identified, additional constraints are required to narrow down
2357 the magma storage conditions (Bohrson and Clague, 1988). For example, Cadoux et al. (2014) overlay Fe-Ti oxide
2358 temperatures on their phase diagrams, concluding that the observed phase assemblage at Santorini is recreated
2359 experimentally at 2 and 4 kbar.

2360 When performing experiments to deduce magma storage conditions at a given volcano, there can be a
2361 very large solution space to explore, in terms of pressure, temperature, and f_{O_2} . If a natural Cpx has
2362 compositional similarities to one grown experimentally at a specific set of conditions, it is difficult to quantify
2363 the true uncertainty on storage conditions without exploring a very large number of experimental conditions to
2364 determine whether a very similar composition may appear at a different set of P-T- f_{O_2} conditions, particularly
2365 from a slightly different bulk composition). It is also vital to consider the composition of the fluid phase, which
2366 is often described in terms of the partial pressure of H₂O, P_{H_2O} , or the mole fraction of H₂O in the starting
2367 composition or fluid phase, X_{H_2O} . In order to reduce the size of one variable of the solution space, many
2368 experiments are performed at water-saturated conditions (i.e., $X_{H_2O} = 1$, Blatter and Carmichael, 2001; First et
2369 al., 2021; Grove et al., 1997; Nakatani et al., 2022; Sisson and Grove, 1993; Voigt et al., 2022). However, many
2370 natural systems may not contain enough H₂O to be volatile saturated at high pressures, or may contain relatively
2371 large amounts of CO₂, meaning the system is volatile saturated in a fluid with $X_{H_2O} < 1$. Experiments with H₂O
2372 below the quantity required for H₂O saturation have been performed (e.g., Kawamoto, 1996), as have
2373 experiments in equilibrium with mixed CO₂-H₂O fluids (e.g., Alonso-Perez et al., 2009; Cadoux et al., 2014),
2374 although these are far less common than pure H₂O-saturated experiments.

2375 Interestingly, there are many reports in the literature of phase stability being affected by X_{H_2O} . For
2376 example, Keppler (1989) investigate solidus temperatures in the haplogranite system, and find that the solidus
2377 position varies as a function of the fluid phase composition for a mix of H₂O and CO₂. However, if X_{H_2O} is reduced
2378 by the addition of N₂ instead, this relationship is not seen. These experiments indicate that at X_{H_2O} close to 1,
2379 CO₂ is not just acting as an inert component to reduce the activity of H₂O, but is modifying the structure of the
2380 melt. Rutherford et al. (1985) also note that experiments where X_{H_2O} is reduced by the presence of H₂ are not
2381 directly comparable to those where it is reduced by CO₂ (e.g., the addition of CO₂ is not simple Henry's law
2382 behaviour).

2383 It has been shown numerous times that CO₂ affects the stability of amphibole. Given the increasing
2384 amounts of CO₂ being measured in melt inclusions in mafic arc magmas (Fig. 19), it is highly likely that the
2385 majority of high Mg# amphiboles examined at the surface formed in a system with $X_{H_2O} \ll 1$. For example, Ridolfi
2386 et al. (2010) suggested that large amounts of CO₂ in a relatively high T igneous system with relatively low
2387 amounts of H₂O stabilizes OH⁻ bearing phases such as amphibole. They suggest this may occur because of
2388 increasing solubility of OH⁻ in the melt with increasing CO₂ dissolution. For example, King and Holloway (2002)
2389 suggest a reaction where molecular CO₂ and H₂O react to form carbonate and OH⁻. Ridolfi et al. (2010) note that
2390 the paucity of magnesiohastingsite amphiboles in predominantly H₂O-saturated experiments may indicate that
2391 these compositions only form at high T and high CO₂ contents. Krawczynski et al. (2012) also find amphibole is
2392 stabilized at a higher temperature, with a lower Mg#. in experiments with more CO₂.

2393 In their experiments on the Mt. St. Helens dacite, Rutherford et al. (1985) find radical changes in the
2394 crystallization temperature of different phases as CO₂ is added, reducing P_{H_2O} at a constant P_{total} ; Plag, Px and
2395 Fe-Ti oxides crystallization temperatures increase, while the amphibole liquidus temperatures decrease.
2396 Additional experiments by Rutherford and Devine (1988) confirm that the observed phase stability is produced
2397 experimentally at 920°C, P=220Mpa, and $X_{H_2O}=0.67$. Rader and Larsen (2013) perform experiments on low MgO
2398 basaltic-andesites to constrain the impact of small amounts of CO₂, running experiments at a range of T (90–
2399 1200°C) and P (0.001–1.8 kbar) at both $X_{H_2O}=1$ and $X_{H_2O} \sim 0.7$. They found that the plagioclase stability curve was
2400 the most sensitive to X_{H_2O} , shifting 25°C for $X_{H_2O} \sim 0.7$. They also observe shifts in amphibole stability. Finally,
2401 Cadoux et al. (2014) found that at 850°C and 4 kbar, there was more amphibole present when X_{H_2O} was 0.9 than
2402 1. They also find changes in the stability of both pyroxenes, ilmenite and plagioclase, as well as the liquidus phase
2403 with changes in X_{H_2O} . In particular, they find that orthopyroxene is generally not stable where $X_{H_2O}=1$ at 2–4 kbar.

2404 In summary, these experiments show that X_{H_2O} is clearly a very important variable to investigate in
2405 further experiments, and comparison of natural samples to experimental products should factor in possible
2406 differences in X_{H_2O} . We believe this avenue of investigation is particularly important given the last decade of
2407 Raman work has clearly demonstrated that mafic arc magmas have substantially more CO_2 (and thus a lower
2408 X_{H_2O} ratio) than previously thought.

2409

2410 **8. Thermobarometers based on thermodynamic modelling**

2411 Thermodynamic modelling is a powerful tool in igneous systems for exploring various hypotheses, such as
2412 whether the chemical variations in a suite of lavas can be produced by equilibrium or fractional crystallization
2413 alone, or whether processes such as crustal melting/assimilation are required (Heywood et al., 2020). However,
2414 in addition to general hypothesis testing, thermodynamical models have also been used to place quantitative
2415 constraints on magma storage conditions. Two main methods are discussed below, matching liquid lines of
2416 descent to erupted lava compositions, and multiphase saturation methods.

2417 **8.1 Liquid lines of descent**

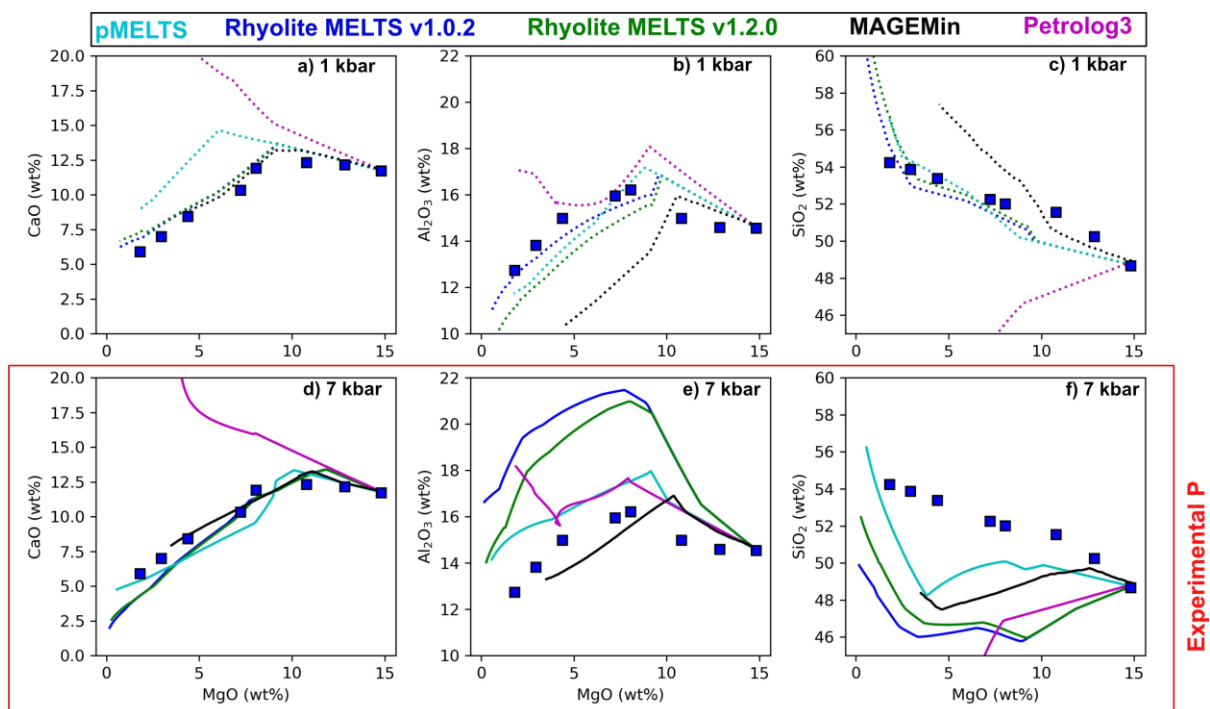
2418 One method to determine magma storage conditions compares fractional crystallization models
2419 conducted at different conditions (e.g., P , fO_2 , melt H_2O content) to observed liquid lines of descent (LLD, e.g.,
2420 whole-rock XRF, glass EPMA data). The conditions producing the best fit model are taken as indicative of the
2421 magma storage conditions in the system of interest. Comparison of observed and modelled LLDs have been used
2422 to deduce storage conditions in explosive silicic eruptions (e.g., the Campanian Ignimbrite, Campi Flegrei, Fowler
2423 et al., 2007, and the Bishop Tuff, Long Valley, Fowler and Spera, 2010), in trachytes and pantellerites of the East
2424 African Rift (Gleeson et al., 2017; Hutchison et al., 2018; Peccerillo, 2003; Ronga et al., 2010), in peralkaline
2425 rhyolites from Atlantic Ocean hotspots (Jeffery et al., 2017, 2016), and in basalts from Mauna Loa (Gaffney,
2426 2002).

2427 LLD methods are typically performed in MELTS, but other tools for modelling fractional crystallization
2428 such as COMAGMAT or Petrolog3 could also be used (Ariskin et al., 1993; Danyushevsky and Plechov, 2011). In
2429 general, studies perform calculations to identify whether the observed variations in measured oxide
2430 concentrations can be produced by protracted fractional crystallisation within the crust. If so, the best fit model
2431 is often determined by visual comparison between model outputs and natural samples (e.g., Fowler et al. 2007)
2432 or statistical methods. For example, Gleeson et al. (2017) develop an algorithm to calculate the smallest misfit
2433 between each datapoint and the modelled LLD path for each MELTS model. They combine the residuals of all
2434 individual samples into a weighted RMSE offset for each model.

2435 In certain situations, storage conditions determined by LLD methods are supported by independent
2436 lines of evidence. For example, there is a close agreement between the depths of magma storage estimated by
2437 MELTS modelling and geophysical estimates of magma storage depths in the East African Rift (Hutchison et al.
2438 2016; Gleeson et al. 2017), and between MELTS-estimated fO_2 and experiment constraints (Scaillet and
2439 Macdonald, 2001). However, as pointed out by Gleeson et al. (2017), even the best-fit models display systematic
2440 offsets between the MELTS predictions and the natural data for certain oxides (e.g., CaO, P_2O_5). These offsets
2441 indicate that there are several inaccuracies or omissions in the MELTS thermodynamic models (e.g. absence of
2442 amphibole or biotite in calc-alkaline magmas) that present severe limitations for the use of MELTS-based
2443 crystallisation models as a thermobarometric technique.

2444 In most cases, MELTS correctly identifies the directionality caused by changing P , H_2O , or fO_2 on the LLD
2445 (e.g. enhancing or suppressing the stability of a given mineral). However, it is unclear whether the predicted
2446 mineral stability for a given value of P , H_2O , or fO_2 is correct, or whether it is just relative differences that are
2447 trustworthy. While MELTS modelling may be able to distinguish a dry vs. wet LLD, it may not be able to determine
2448 whether a magma has 0.1 or 0.6 wt% H_2O . It has been shown that MELTS models at Kīlauea Volcano must be
2449 run with melt H_2O contents far below those measured in melt inclusions to recreate the MgO content at which
2450 plagioclase and Fe-Ti oxide crystallize (Garcia, 2003; Wieser et al., 2022c). If H_2O contents were not
2451 independently constrained, such models could lead to incorrect inferences about the hydration state of magmas
2452 at this volcano.

2453 To assess LLD methods further, we compare the measured composition of experimental liquids
 2454 produced during fractional crystallisation experiments on a H₂O-poor tholeiitic basalts to MELTS crystallisation
 2455 models (Villiger et al., 2007). We run a fractional crystallization model at the specified experimental pressure (7
 2456 kbar), *f*O₂ and H₂O content. We also run models at pressures of 1, 4 and 10 kbar (Fig. 26a, Supporting Figs. 11–
 2457 13). We use three different MELTS versions (pMELTS, rhyolite-MELTS v1.0.2 and v1.2.0), Petrolog3
 2458 (Danyushevsky and Plechov, 2011), and MAGEMin (Riel et al., 2022) using the Holland et al. (2018)
 2459 thermodynamic database. Both versions of rhyolite-MELTS show a very poor fit at the experimental pressure,
 2460 predicting extensive Al₂O₃ enrichment and SiO₂ depletion relative to the experimental products (dark blue and
 2461 green lines, Fig. 26e-f). The fit is far better at 1 kbar, which could lead to anomalous inferences of magma storage
 2462 depth if only LLD methods were used. pMELTS doesn't show such extreme Al₂O₃ enrichment at the experimental
 2463 pressure, but the fit for Al₂O₃ is still better at 4 kbar than 7 kbar, and the fit for SiO₂ is best at 1–4 kbar (cyan
 2464 lines). It is worth noting that pMELTS has a different liquid model than rhyolite-MELTS. Petrolog3 shows
 2465 anomalous SiO₂ depletion at all pressures (magenta lines, Fig. 26), and none of the 4 pressures used here provide
 2466 a satisfactory fit to most elements (Supporting Fig. 11). The Holland et al. (2018) database, implemented through
 2467 MAGEMin, certainly does the best job of recreating Al₂O₃ systematics, although the fit to SiO₂ is far better at 4
 2468 kbar than 7 kbar (black lines, Fig. 26, Supporting Fig. 11).

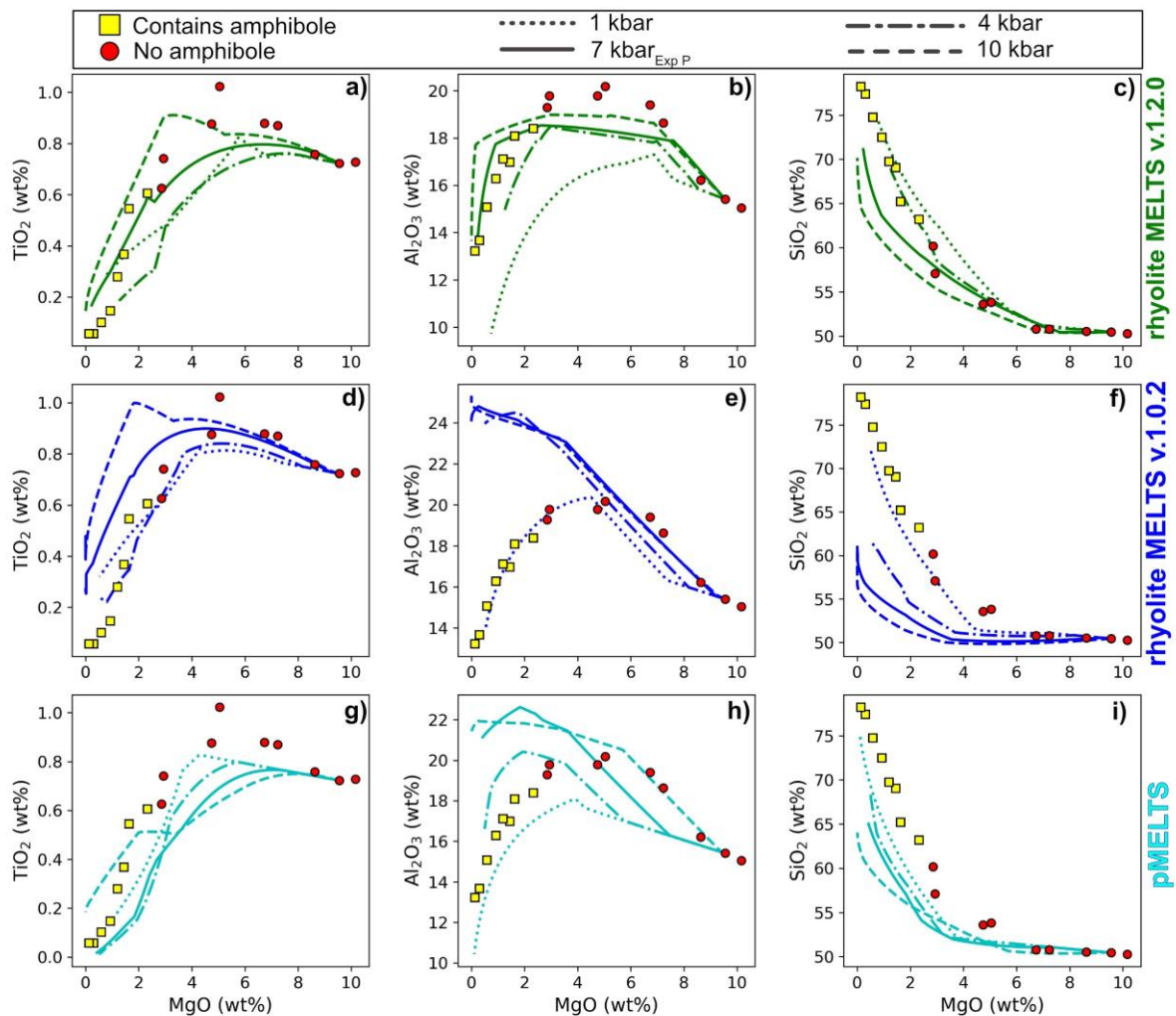


2469
 2470 *Figure 26 – Comparison of fractional crystallisation models run in rhyolite-MELTS, pMELTS, Petrolog3 and*
 2471 *MageMin (using the Holland et al. 2018 database) to fractional crystallization experiments from a nominally*
 2472 *anhydrous, tholeiitic basalt from Villiger et al. (2007). MELTS calculations are performed at the experiment *f*O₂*
 2473 *(NNO), with H₂O=0.2 wt% (i.e. nominally anhydrous). While experiments were conducted at 7 kbar (solid lines),*
 2474 *models run at 1–4 kbar provide a much better fit (particularly regarding the onset of plagioclase). Other pressures*
 2475 *shown in Supporting Fig. 11.*

2476 To further assess LLD methods, we use all three MELTS versions to model the fractional crystallization
 2477 experiments of Nandedkar et al. (2014) conducted on a hydrous arc basalt (Fig. 27). The hydrous nature of these
 2478 experiments means that the differences between rhyolite-MELTS v1.2.0 and v1.0.2 are far more noticeable
 2479 compared to the H₂O-poor experiments of Villiger et al. (2007). Using v1.2.0, models run at 4 to 10 kbar provide
 2480 a reasonable match to observed oxide contents. In contrast, using v1.0.2, models run at 1 kbar provide the best
 2481 fit to both SiO₂ and Al₂O₃. It is concerning that these models give such different results, given they are used
 2482 somewhat interchangeably in the literature, and obviously, any studies conducted prior to the release of v1.2.0

2483 in 2015 must have used v1.0.2. pMELTS shows behaviour between the two rhyolite-MELTS models, with trends
 2484 best recreated at 1–4 kbar.

2485 These comparisons to two experimental studies demonstrate that the pressure you would deduce from LLD
 2486 methods is very sensitive to both the choice of model and the oxides used for assessment of the ‘best model’.
 2487 In neither comparison does the experimental pressure stand out as the best model fit. It is also worth noting
 2488 that for both these examples, we are using known fO_2 and H_2O contents. In reality, it is likely that P , fO_2 , and
 2489 H_2O are all uncertain, which leaves a very large solution space to explore (and can result in even greater
 2490 ambiguity regarding the best fit model). Overall, we conclude that in their current state, LLD methods are not a
 2491 reliable way to deduce storage pressure, particularly given the result can differ so much simply based on the
 2492 choice of fractional crystallization model. It may be that an update of the MELTS liquid model, and/or tweaks to
 2493 the thermodynamic data controlling the mineral stability fields (as performed for the qtz-2 fspar ternary) can
 2494 revive this method. These comparisons also demonstrate that it is absolutely vital for papers to state the version
 2495 of MELTS that they used.



2496

2497 *Figure 27 – Comparison of fractional crystallization experiments from Nandedkar et al. (2014) at 7 kbar to MELTS*
 2498 *fractional crystallization models run using three different versions. Experiments containing amphibole are shown*
 2499 *in yellow, those without amphibole in red. Models were run at the experimental fO_2 and H_2O contents, at 1, 4, 7*
 2500 *(Exp P) and 10 kbar. MELTS models run in pyMELTScalc using alphaMELTS for Python (Gleeson et al., 2023,*
 2501 *Antoshechkina and Ghiorso, 2018).*

2502 **8.2 Multi-phase saturation**

2503 As discussed in Section 2.2, pressure influences the location of mineral cotectics and eutectics. Under
 2504 the assumption that the measured composition of a multi-phase saturated melt might contain information

2505 about the pressure of the system, rhyolite-MELTS has been used to address the crystallisation pressure of silicic
2506 and intermediate magmas that are co-saturated in quartz+feldspar (Bégué et al., 2014; Gualda et al., 2019;
2507 Gualda and Ghiorso, 2014; Pamukcu et al., 2015), feldspar+orthopyroxene±quartz (Pamukçu et al., 2021) or
2508 plagioclase+clinopyroxene+orthopyroxene (Harmon et al., 2018).

2509 Specifically, these methods work by performing crystallisation calculations at several discrete pressures
2510 (and a specified H_2O and fO_2 value). T is progressively dropped from the liquidus, and the appearance of different
2511 phases is tracked. Mineral saturation curves (see Fig. 28a-b) are determined from these individual isobaric
2512 crystallization calculations. A residual is calculated as the maximum temperature difference between the
2513 saturation curves of the phases of interest (ΔT , Fig. 28c). In many cases, the mineral saturation curves never
2514 intersect exactly at a single point, so the best fit pressure is calculated from the minimum point on the residual
2515 curve. A solution is only considered valid if the residual T gets within a pre-specified threshold value of a perfect
2516 intersection (e.g., 5°C for quartz – plagioclase – alkali-feldspar equilibrium; Gualda and Ghiorso, 2014). This
2517 threshold varies - in their application of this method to Plag-Opx-Cpx equilibrium, Harmon et al. (2018) compare
2518 experimental pressures to calculated pressures with minimum residuals from 16–121°C.

2519 One complication of these methods is that the position of saturation curves is not just influenced by
2520 pressure, but also fO_2 and melt H_2O content. This means for natural samples; calculations must be repeated at
2521 different melt fO_2 and H_2O contents to identify the location of the minimum T offset in multivariate P - fO_2 - H_2O
2522 space. In an ideal world, this would mean that MELTS could be used simultaneously as a barometer,
2523 oxybarometer, and hygrometer. However, in reality, this very large solution space can result in substantial errors
2524 which do not reproduce the true conditions for P , fO_2 , or H_2O .

2525 **8.2.1 Quartz – 2 Feldspar MELTS barometry**

2526 Interest in using the co-saturation of quartz, plagioclase and alkali feldspar to help constrain pressure
2527 (Gualda and Ghiorso, 2014) led to a substantial update to the MELTS algorithm in 2012. To recreate the near
2528 invariant behaviour of pumice and melt inclusion compositions from the early erupted Bishop Tuff which have
2529 major and trace element systematics indicating a low degree of freedom, Gualda et al. (2012) tweaked the
2530 enthalpy of formation of quartz and the potassic endmember in the alkali-feldspar solid-solution (Gualda et al.
2531 2012, rhyolite-MELTS v1.0.2). Using this new model, and the residual T method described above, Gualda and
2532 Ghiorso (2014) estimated storage pressures for a variety of quartz-saturated rhyolites. They compared these
2533 MELTS pressures to H_2O - CO_2 saturation pressures from the Bishop Tuff (Anderson et al., 2000), the Younger
2534 Toba Tuff (Chesner and Luhr, 2010) and the Mamaku Ignimbrite (Bégué et al., 2014), and found a close
2535 agreement. Based on the results in Fig. 10 of Gualda and Ghiorso (2014), we calculate an R^2 of 0.75 and RMSE
2536 of 0.38 kbar for $N=30$ melt inclusions when performing a linear regression between the two pressure methods.
2537 However, it is worth noting $N=17$ of these inclusions are from the Bishop Tuff, which was used as a reference
2538 point for the tweaking of the rhyolite-MELTS model calibration (Gualda et al. 2012).

2539 The rhyolite-MELTS quartz-feldspar barometers have since been applied to several other systems
2540 worldwide. This includes the application of quartz-plagioclase barometry to rhyolitic eruptions of the Taupo
2541 Volcano Zone, New Zealand (Bégué et al., 2014), and quartz – 2-feldspar barometry on the matrix glass of the
2542 Peach Spring Tuff, USA (Pamukcu et al., 2015). Results indicate spatial and/or temporal variations in the magma
2543 storage conditions beneath the Taupo Volcanic Zone, as well as correlations between rhyolite SiO_2 contents and
2544 pressure (Bégué et al., 2014; Pamukçu et al., 2020). However, these papers have been the subject to a number
2545 of comment-reply articles (e.g., Wilson et al., 2021, Pamukçu et al., 2021). Most notably, Wilke et al. (2017)
2546 question the accuracy of the rhyolite-MELTS barometer following comparison of the results of the rhyolite-
2547 MELTS geobarometer with their new empirical expression for the pressure of quartz+feldspar saturated liquids.
2548 The Wilke et al. (2017) method, termed DERP (Determining Rhyolitic Pressures), is based on experiments on
2549 haplogranitic compositions which examine the influence of melt H_2O content (or activity) and the normative
2550 melt An content (largely determined by the CaO content of the liquid) on the quartz+feldspar saturation surface.
2551 Comparison of rhyolite-MELTS and DERP barometric results for melt-inclusions and matrix glasses from the
2552 Taupo Volcanic Zone and Peach Spring Tuff revealed a large offset between the two methods, with DERP typically
2553 returning pressures around twice as large as those from rhyolite-MELTS. The pressure discrepancy between the
2554 two methods correlates with the normative melt An content (a key part of the new DERP parameterisation).

2555 Thus, Wilke et al. (2017) suggest that rhyolite-MELTS may underestimate magma storage pressures in Ca-bearing
2556 rhyolites.

2557 The relative performance of DERP and rhyolite-MELTS was revisited by Gualda et al. (2019b), who
2558 argued that the use of multi-linear fits in DERP to determine the influence of P, An content and H₂O on the quartz
2559 – 2 feldspar thermal minimum results in a functional form that is thermodynamically impossible. As a result,
2560 extrapolation of the DERP barometer outside the range of the calibration data could lead to systematic errors.
2561 Gualda et al. (2019b) also question the use of TitaniQ as an independent barometer to compare to the results
2562 from DERP in Wilke et al. (2017), as the Ti content in quartz is influenced by a wide number of parameters,
2563 including the mineral growth rate and melt Ti activity, which may limit its use as a geobarometer (see section
2564 2.11). To assess the performance of the 2 barometers in natural systems, Gualda et al. (2019b) compare the
2565 results derived from the DERP and rhyolite-MELTS barometers to independent pressure estimates from H₂O-
2566 CO₂ saturation in melt inclusions and amphibole thermobarometry. In general, the barometric estimates
2567 provided by rhyolite-MELTS are in good agreement with the independent pressure estimates. DERP-derived
2568 pressures are typically more scattered and often higher than those derived from melt inclusion or amphibole
2569 thermobarometry. However, given the issues with amphibole barometry discussed in section 2.6, such
2570 comparisons should perhaps be interpreted with caution.

2571 Wilke et al. (2019) responded by stating that the large range of pressured estimated by the DERP
2572 barometer in Gualda et al. (2019b) result from its sensitivity to glass Na₂O and K₂O contents, which are used to
2573 calculate the normative Qz, Or, and Ab values. Wilke et al. (2019) suggest that in hydrous rhyolitic glasses where
2574 alkali migration during analysis is a serious issue, DERP should only be used to estimate storage pressures when
2575 data quality is assured. Furthermore, Wilke et al. (2019) note that the experimental compositions used to
2576 calibrate the DERP barometer all contain normative corundum, meaning that all CaO in the glass is used to
2577 calculate the normative An content. In many natural samples, such as the Peach Spring Tuff used by Pamukcu et
2578 al. (2015), lower Al₂O₃ contents lead to the presence of Wollastonite in the normative mineral assemblage,
2579 complicating the determination of the normative melt An content. As normative Wollastonite is not accounted
2580 for in the DERP calibration, this could explain the offset between the two barometers and indicates that DERP
2581 should only be used in systems where Corundum appears in the normative mineral assemblage.

2582 Therefore, for most natural samples where Wollastonite is present in the normative mineral
2583 assemblage, the rhyolite-MELTS geobarometer might be more reliable than empirically calibrated alternatives
2584 like DERP. Nevertheless, questions regarding the application of the rhyolite-MELTS barometer to natural systems
2585 still remain, especially as the test datasets used to evaluate this barometer have largely relied on data from the
2586 Bishop Tuff (part of the 2012 recalibration). In addition, inclusion of the updated H₂O-CO₂ model of Ghiorso and
2587 Gualda (2015) in the rhyolite-MELTS calculations (i.e., rhyolite-MELTS v1.2.0) shifts the quartz and sanidine
2588 stability field to such an extent that 3–phase saturation cannot be simulated at any pressure for the compositions
2589 of Gualda and Ghiorso (2014) and Pamukcu et al. (2015). This indicates a further update to the quartz + sanidine
2590 ± plagioclase thermodynamic properties is necessary to align with the most recent volatile solubility model, so
2591 that users do not need to perform calculations for magmas that are typically saturated in a mixed H₂O-CO₂ fluid
2592 phase using an outdated H₂O solubility model (Ghiorso et al. 1995). We are not of aware of any new experiments
2593 that can be used as an independent test dataset for resolving the rhyolite-MELTS vs. DERP debate, and to gain a
2594 better understanding of the errors involved. Further experiments in this compositional range will be vital to
2595 move this approach forward in a rigorous manner.

2596 **8.2.2 Plagioclase – 2 pyroxene MELTS barometry**

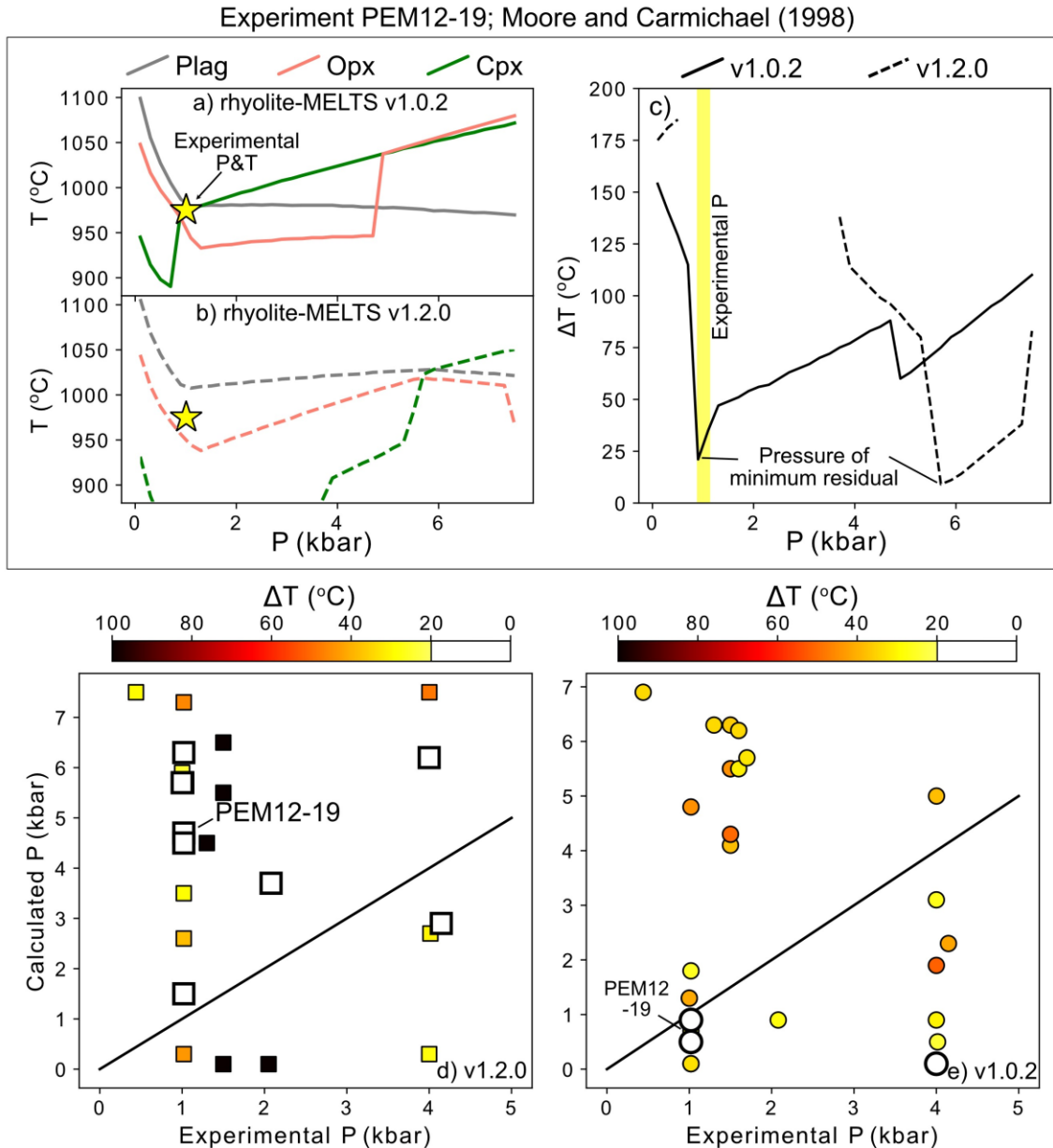
2597 Since the inception of the rhyolite-MELTS geobarometer in 2014, the general method developed by
2598 Gualda and Ghiorso (2014) has been expanded to examine the cosaturation of other phases. Harmon et al.
2599 (2018) suggest that the rhyolite-MELTS thermodynamic models could be used to provide pressure estimates for
2600 intermediate magmas saturated in plagioclase, clinopyroxene and orthopyroxene.

2601 To test the plagioclase – 2–pyroxene geobarometer, Harmon et al. (2018) apply their method to N = 8
2602 experiments from the LEPR database that are saturated in 2 or more of the phases of interest. As the plagioclase
2603 - 2 pyroxene geobarometer is significantly more sensitive to *f*O₂ and H₂O content than the quartz 2–feldspar

2604 barometer, they use experimental fO_2 and melt H_2O contents for these comparisons to eliminate the multi-
2605 dimensional aspects of mineral stability, allowing the best fit pressure to be found. Of the 8 experiments they
2606 use, only one returned a ΔT between the 3 mineral saturation curves of $<20^\circ C$, with the minimum T offset for
2607 other experiments stretching up to $121^\circ C$ (i.e., the saturation curves never intercept close to one another).

2608 The single experiment with a minimum T offset $<20^\circ C$ (1140mf #27 from Grove et al. 1997) returns a
2609 predicted P only 0.2 kbar offset from the true experimental P. If the threshold for the minimum T offset is
2610 relaxed, experiments with minimum T offsets between 20 and $40^\circ C$ also return P estimates within ~ 0.25 kbar of
2611 their experimental P. However, convergence of only 4 experiments conducted at 0.00 1–1 kbar where fO_2 and
2612 melt H_2O contents are known makes it difficult to robustly assess the accuracy of the geobarometer in natural
2613 systems when applied up to the 5 kbar limit suggested by Harmon et al. (2018).

2614 We investigate this method further using experiments from variably hydrous magmas cosaturated in
2615 plagioclase, orthopyroxene and clinopyroxene present in the ArcPL dataset conducted within the pressure range
2616 suggested by Harmon et al. (2018, 0–5 kbar, N=39). As for LLD methods, we find that the version of MELTS used
2617 for these calculations drastically affects calculations of storage conditions. Based on the flowchart provided on
2618 the MELTS-OFM website (<https://melts.ofm-research.org/MELTS-decision-tree.html>), rhyolite-MELTS v1.2.0
2619 should be used for these calculations, as these experiments contain dissolved H_2O ($\pm CO_2$). However, Harmon et
2620 al. (2018) use rhyolite-MELTS v.1.0.2. For experiment PEM12–19 from Moore and Carmichael (1998), rhyolite-
2621 MELTS v.1.0.2 shows very good convergence at pressures very close to the experimental pressure (Fig. 28e).
2622 However, if rhyolite-MELTS v1.2.0 is used, the clinopyroxene stability curve intersects plagioclase and
2623 orthopyroxene at significantly higher pressures, leading to an estimated pressure of ~ 6 kbar (~ 5 kbar higher
2624 than the experimental pressure, Fig. 28d).



2625

2626 *Figure 28: Assessing the Rhyolite-MELTS Plagioclase 2-pyroxene barometer of Harmon et al. (2018). a-b)*
 2627 *Constructing mineral stability curves for Exp. PEM1 2–19 from Moore and Carmichael (1998) at the experimental*
 2628 *fO_2 ($\Delta NNO=+1.1$) and H_2O contents (3.6 wt%) using two different versions of MELTS. c) Calculating the maximum*
 2629 *T offset at each pressure between the three mineral stability curves. The MELTS barometer takes the minimum*
 2630 *residual as the best-fit T (~ 1 and ~ 6 kbar depending on the MELTS version). d-e) Testing the barometer using*
 2631 *experiments saturated in Plag-2 pyroxene from ArcPL. Calculated pressure using the residual method plotted*
 2632 *against the experimental pressure (calculations performed at experiment fO_2 and H_2O contents). Experiments*
 2633 *with residuals $<20^\circ\text{C}$ are colored white, and larger residuals are colored based on this value. Calculations*
 2634 *performed in pyMELTSCalc (Gleeson et al., 2022) using alphaMELTS for Python (Antoshechkina and Ghiorso,*
 2635 *2018).*

2636 Using rhyolite-MELTS v.1.0.2 for all $N=39$ experiments, $N=10$ do not stabilize all 3 phases at any pressure
 2637 within 200°C of the liquidus (well below the experimental temperature in all cases). Of the remaining $N=29$,
 2638 models converging with a residual $<20^\circ\text{C}$ are shown in white on Fig. 28d-e. These produce a very poor fit to
 2639 experimental pressures. If we take solutions produced at larger temperature residuals (following Harmon et al.
 2640 2018), there is no improvement. Using rhyolite-MELTS v1.2.0, $N=23$ experiments converge, and the fit is similarly

2641 bad, regardless of the temperature residual used. The poor performance of this barometer supports previous
2642 criticism of the ability of MELTS to correctly predict the stability of these phases, pointing to the need for better
2643 solution models (e.g., Klein et al., 2023; Nandedkar et al., 2014; Villiger, 2004).

2644

2645 **9. Other methods**

2646 There are of course, numerous methods to determine magma storage conditions which we do not address in
2647 detail, both in the interest of relative(!) brevity, and because there is insufficient experimental data that wasn't
2648 used during calibration to independently test models.

2649 Additional thermometers have been developed based on:

- 2650 • REE exchange between Opx-Cpx (Liang et al., 2013) and Plag-Cpx (Sun and Liang, 2012)
- 2651 • Mg-Fe exchange between Ol and Cpx (Loucks, 1996)
- 2652 • Ni partitioning between Ol-Liq (resulting in a H₂O-independent thermometer, Pu et al., 2021, 2017)
- 2653 • NaSi-CaAl exchange between Amp-Plag (e.g., Holland and Blundy, 1994; Molina et al., 2021).
- 2654 • Mg exchange between Plag-Cpx (Sun and Lissenberg, 2018).

2655 Hygrometers based on:

- 2656 • Cpx-Liq major element equilibrium (e.g., Armienti et al., 2013; Perinelli et al., 2016)
- 2657 • Ca exchange between Ol-Liq (Gavrilenko et al., 2016),
- 2658 • The highest amphibole Mg# found in a given volcanic system (Krawczynski et al., 2012).
- 2659 • The H₂O contents of nominally-anhydrous minerals (NAMs) combined with models of mineral-melt
2660 partition coefficients (Demoucy et al., 2006; Towbin et al., 2023; Wade et al., 2008).
- 2661 • Projections of the Ol, Cpx and Plag cotectics (Klein et al. 2023).

2662 Barometers based on:

- 2663 • Sr/Y contents of erupted lavas (Profeta et al., 2016).
- 2664 • 'Multi-reaction' thermodynamic models relying on underlying thermodynamic models (e.g., Holland
2665 and Powell, 2011), where predicted and observed mineral compositions and phase fractions are
2666 compared to constrain storage conditions (E.g., Zibera et al. 2017, Nicoli and Matthews, 2019).
- 2667 • Al-Si partitioning between Plag and Amp (Molina et al., 2015).
- 2668 • CaO-Mg# systematics of mid-oceanic ridge magmas (Villiger et al., 2007)

2669 Of course, these lists are by no means exhaustive.

2670 **10. Future developments should be guided by FAIR principles**

2671 It is becoming increasingly recognised that science needs to shift to a framework where research
2672 products are findable, accessible, interoperable, and reusable (FAIR; Wilkinson et al., 2016). In the context of
2673 this review, this applies not only to research data such as analyses of experimental products and natural samples,
2674 but also the tools and workflows used to perform calculations. There have already been a few advances in this
2675 regard, but there is still lots of work to do.

2676 From a data availability perspective, a major advance came in 2008 when Hirschmann et al. (2008)
2677 created a web-hosted database of 6,600 experiments (The Library of Experimental Phase Relationships – LEPR),
2678 which has been widely used to calibrate thermobarometers and chemometers (e.g., Jorgenson et al., 2022;
2679 Petrelli et al., 2020). This compilation represented a massive team effort, requiring most phase compositions
2680 and experimental contents to be hand typed from data tables in journal pdfs. However, the dataset is still
2681 incomplete in many aspects, stemming from missing data in the underlying publications, compounded with
2682 missing information during digitization. For example, in the LEPR download of Cpx-Liq pairs used by Petrelli et
2683 al. (2020) and Putirka (2008), 66% of experiments do not have a glass H₂O content. In some cases, this represents
2684 the fact that the experiment was anhydrous, in others the fact that authors didn't report water, and sometimes
2685 because H₂O is often presented in a different table from other chemical information, so may have been missed
2686 during digitization. Similarly, with few exceptions, the number of analyses used to produce the reported average

2687 for each phase (e.g., N=5 Cpx analyses, N=8 amphibole analyses) is not present in LEPR. This makes filtering out
2688 experiments with compositions defined by small numbers of analyses challenging, despite the importance of
2689 this given the influence of analytical error on minor, pressure-sensitive components (e.g., Cpx, Wieser et al.
2690 2023b).

2691 A bigger challenge is that there is no framework by which LEPR is regularly updated as new experimental
2692 studies are published. This has led to individual authors digitizing data from new experimental papers to use in
2693 their studies (Jorgenson et al., 2022, Wieser et al. 2023a-b). However, individual researchers who compile data
2694 may not have time to format the data for inclusion in the database, and under the current academic publishing
2695 model, would gain no credit for this activity, as citations for use of the database would go to the original author
2696 team from 2008. One option moving forwards may be for LEPR to frequently publish new short articles or a
2697 Zenodo doi with an author team consisting of anyone who has contributed to the curation of the database (as
2698 for open-source tools such as Numpy; e.g., Dubois et al., 1996; Harris et al., 2020). Alternatively, the
2699 responsibility could be placed on people generating experimental data, where journal editors do not allow a
2700 paper to be accepted before the experimental data is included in these databases. However, in many cases,
2701 journals do not mandate authors submitting data to a specific repository. Community guidelines for exactly how
2702 such data should be presented and archived are clearly needed, as well as ways for data curation to be valued
2703 when hiring and promoting researchers (Klöcking et al., 2023).

2704 From a modelling perspective, there has been a rapid increase in the number of open-source, easy to
2705 use tools to perform calculations, making workflows more user-friendly, faster, more reproducible, and less
2706 susceptible to user-error and version control issues. In general, calculation tools have evolved from GUIs, macro-
2707 enabled spreadsheets and web apps where users having to type every single composition by hand, to being able
2708 to automatically run calculations by loading a user-supplied spreadsheet either through a Jupyter Notebook or
2709 a web app built on top of underlying python or R code (e.g., Iacovino and Till, 2019; Weber and Blundy, 2023).
2710 One major contribution towards more automated workflows for thermodynamic calculations has been the
2711 development of the ENKI ThermoEngine (Thermoengine Code Contributors, 2022), allowing the MELTS
2712 thermodynamic models and algorithms to be accessed through Python. This allows creation of modelling
2713 workflows or complete packages based on the underlying MELTS models. For example, the Fe-Ti oxybarometer
2714 and thermometer of Ghiorso and Evans (2008) was originally released as a web-app where users had to hand-
2715 type major element values for each Fe-Ti oxide pair. Ghiorso and Prissel (2020) produced a Jupyter Notebook
2716 using Thermoengine which allows users to upload an excel file of matching Fe-Ti oxide pairs, and all calculations
2717 are performed automatically. The open-source Python3 package VESlcal (Iacovino et al., 2021) relies on
2718 Thermoengine to perform calculations using the solubility model Magmasat (which requires MELTS, Ghiorso and
2719 Gualda, 2015), as well as 6 other popular solubility models. Prior to VESlcal, saturation pressure calculations
2720 were performed using different tools for each solubility model in a myriad of different environments (Excel
2721 macros, web apps, web servers).

2722 The MELTS thermodynamic models can also be accessed using the alphaMELTS for MATLAB/Python
2723 packages (Antoshechkina and Ghiorso, 2018). As the alphaMELTS for MATLAB/Python packages (and
2724 Thermoengine) requires some familiarity with the underlying language, easy-to-use, wrapped functions for
2725 common workflows have been released through the pyMELTSCalc package (used for calculations in Section 8,
2726 Gleeson et al., 2023).

2727 Calculations using the thermodynamic models/databases developed by Holland and Powell (e.g.,
2728 Holland and Powell, 1998; Holland et al. 2018), which represent the main thermodynamic alternative to MELTS
2729 in igneous petrology, have traditionally performed using a variety of different software packages, including
2730 THERMOCALC, Perple_X (Connolly, 2009, 2005) and Theriak-Domino (de Capitani and Petrakakis, 2010). The
2731 learning curve for these tools is typically quite steep, and it remains challenging to integrate the thermodynamic
2732 calculations with common coding languages such as MATLAB, Python3 or Julia. Development of MAGEMin, a C-
2733 based Gibbs Free Energy minimization software with a Julia interface (Reil et al. 2022), improves the ease with
2734 which thermodynamic calculations can be performed using the Holland et al. (2018) thermodynamic database.
2735 This is because the Julia MAGEMin functions can also be used outside of the main GUI and integrated with
2736 Python3 functions. This allows the pyMELTScalc package to perform the same calculations (e.g. LLD, phase

2737 stability, phase diagrams) using MELTS or the Holland et al. (2018) thermodynamic models. Such advances are
2738 vital for model intercomparison (e.g. Fig. 26-27).

2739 For mineral-melt thermobarometry and chemometry, calculations using 100s of different popular
2740 equations can be performed in Thermobar (Wieser et al., 2022b). This tool replaces a very large number of
2741 separate Excel spreadsheets, R and Matlab code released by individual thermobarometry papers, and allows
2742 more complex functions such as assessing all possible pairs for equilibrium, error propagation etc. For
2743 thermobarometers applicable to determining the conditions of mantle melting, Python package meltPT (McNab
2744 and Ball, 2023) can perform calculations using twelve published expressions.

2745 These open-source python tools allow investigation of science questions that were almost impossible to address
2746 using existing tools requiring extensive manual data input. For example, Wieser et al. (2022a) use VESlcal to
2747 perform detailed comparisons of solubility models, including their sensitivities to different parameters. Wieser
2748 et al. (2023a-b) use Thermobar to propagate thermobarometry uncertainties using Monte Carlo methods. Open-
2749 source packages also have the advantage that the source code is version-controlled, and hosted in a public
2750 repository (e.g., on GitHub) for anyone to inspect and adapt. This means even if the authors stop supporting the
2751 packages (perhaps moving from academia into industry), packages could be updated by a third party (although
2752 as a community we need to develop clear guidelines as to how academic credit can be allocated for such an
2753 activity). This is in stark contrast with numerous tools which have simply become unusable with age. For
2754 example, the volatile solubility model of Duan (2014) is no longer available at the website listed in the paper,
2755 requiring authors to rely on archived downloads (e.g., Allison et al., 2022 rely on a version archived in 2017).

2756 **11. Conclusions**

2757 There are a wide diversity of methods which have been used to determine the pressures, temperatures, H₂O
2758 contents and fO_2 conditions at which magmas are stored and staged as they transit from the mantle to the
2759 surface. Many thermometry methods work very well, indicating that silicate melt (\pm mineral) compositions are
2760 very sensitive to temperature. However, it becomes more challenging to determine temperatures in subsolidus
2761 or highly evolved systems. In contrast, many mineral-based and thermodynamical barometers perform
2762 extremely poorly, struggling to reliably distinguish between different storage regions in the crust within ~10–20
2763 km. This partially results from thermodynamic limitations; mineral compositions are not overly sensitive to the
2764 relatively narrow range of crustal pressures in the vast majority of tectonic settings on Earth. This fundamental
2765 limitation is not helped by sources of analytical and experimental uncertainty (e.g., poor analytical precision for
2766 minor components, missing elements such as Cr, Wieser et al. 2023b). Melt inclusion barometers have the
2767 potential to be more precise, because the dissolution of CO₂ and H₂O is highly sensitive to pressure. However,
2768 extensive work is required to resolve discrepancies between solubility models, as well as evaluate the influence
2769 of the vapour bubble CO₂ in many published datasets. Raman-based fluid inclusion has great potential in specific
2770 systems, although further work is needed to investigate the influence of decrepitation, elastic relaxation, and
2771 the influence of other fluid species (e.g. SO₂, H₂O etc). Thermobar-Raman-try also shows great promise, but
2772 further work is required. We propose a number of key frontiers to address in the pursuit of better
2773 thermobarometers, hygrometers and oxybarometers:

2774 1) The development of higher quality experimental and thermodynamic datasets with precisely constrained
2775 mineral compositions, fluid compositions, dissolved volatile contents, and experimental fO_2 for recalibration of
2776 thermodynamic models (e.g., MELTS), mineral-melt thermobarometers, and volatile solubility models. Sufficient
2777 experiments need to be performed to allow full isolation of a test dataset during model calibration. More
2778 experiments using mixed H₂O-CO₂ fluids are clearly needed to understand phase stability in relatively CO₂-rich
2779 arc magmas.

2780 2) Development of more robust infrastructure for compiling experimental and thermodynamic data, alongside
2781 sufficient metadata to assess data quality. This will ensure that application of new and exciting machine learning
2782 techniques will not suffer from the old computer science adage: 'garbage-in, garbage-out'.

2783 3) Further development of open-source methods to perform calculations, allowing easy intercomparison
2784 between models, error propagation, and model updates as new data becomes available.

2785 **12. Author Contributions**
 2786 PW coordinated the review and was responsible for writing and coding for all sections except those listed below.
 2787 MG was responsible for the OPAM, MELTS and MAGEMin sections with edits from PW, and SM for OI-Sp and Fe-
 2788 Ti oxide sections. CD contributed text to the MI and FI section, and provided edits throughout. CD and EG
 2789 contributed to analytical work. All authors reviewed and edited the text.

2790 **13. Acknowledgements**
 2791 PW thanks Iris Buisman for extracting the Cpx counting statistics shown in Fig. 8, and Keith Putirka for many
 2792 useful conversations on thermobarometry and the formulation and calibration of his equations. PW
 2793 acknowledges support from NSF EAR 2217371, the Rose Hills Innovator Program, and start up funds to UC
 2794 Berkeley for computing resources. EG acknowledges support from NSF EAR 2216738.

2795 **13. Useful websites and open-source tools**

Tools for petrologists – Contains Excel workbooks and python scripts for a number of petrographic workflows.	http://www.kaylaiacovino.com/tools-for-petrologists/
VESlcal GitHub, Read The Docs and YouTube pages: Code, documentation and worked examples for calculations using VESlcal	https://github.com/kaylai/VESlcal , https://vesical.readthedocs.io/en/latest/
Thermobar read the docs page: Code, documentation and worked examples for thermobarometry and hygrometry calculations using Thermobar	https://github.com/PennyWieser/Thermobar , https://thermobar.readthedocs.io/en/latest/
Putirka spreadsheet compilation: Contains Excel spreadsheets for different thermobarometry calculations	https://sites.google.com/mail.fresnostate.edu/keithputirka/home
MELTS resources: Links to download different MELTS calculation tools (Matlab, python, GUI, excel).	https://magmasource.caltech.edu/gitlist
MAGEMin: Gibbs free energy minimisation solver package	https://github.com/ComputationalThermodynamics/MAGEMin
PyMageMinCalc: Python package for common petrological workflows using MAGEMin.	https://github.com/gleesonm1/pyMAGEMINcalc
PyMELTScalc: Python package for easier calculations using Melts for Python	https://github.com/gleesonm1/pyMELTScalc
ENKI server: Allows calculations to be performed using ThermoEngine infrastructure without the need for local installation.	http://enki-portal.org/
NIST Web Book: Phase data for CO ₂ and calculations using the CO ₂ equation of state.	https://webbook.nist.gov/cgi/cbook.cgi?ID=C124389&Mask=1
DiadFit: Code, documentation and worked examples using DiadFit for fitting Raman data and performing EOS calculations for CO ₂ .	https://github.com/PennyWieser/DiadFit , https://diadfit.readthedocs.io/en/latest/
CoolProp: A python package for calculating thermodynamic properties of gases using different equation of states.	http://www.coolprop.org/

2796

2797 **14. Data Availability**
 2798 Jupyter Notebooks and Excel workbooks used to make each figure are available on GitHub
 2799 (https://github.com/PennyWieser/Thermobarometry_Review_2023).

2800 **References.**

2801 Acosta, M.D., Watkins, J.M., Reed, M.H., Donovan, J.J., DePaolo, D.J., 2020. Ti-in-quartz: Evaluating the role of
 2802 kinetics in high temperature crystal growth experiments. *Geochimica et Cosmochimica Acta* 281, 149–
 2803 167. <https://doi.org/10.1016/j.gca.2020.04.030>
 2804 Afonso, J.C., Ranalli, G., Fernández, M., 2007. Density structure and buoyancy of the oceanic lithosphere
 2805 revisited. *Geophys. Res. Lett.* 34, L10302. <https://doi.org/10.1029/2007GL029515>

2806 Ague, J.J., 1997. Thermodynamic calculation of emplacement pressures for batholithic rocks, California:
2807 Implications for the aluminum-in-hornblende barometer. *Geol* 25, 563. <https://doi.org/10.1130/0091->
2808 7613(1997)025<0563:TCOEPF>2.3.CO;2

2809 Allison, C.M., Roggensack, K., Clarke, A.B., 2022. MafiCH: a general model for H₂O–CO₂ solubility in mafic
2810 magmas. *Contrib Mineral Petrol* 177, 40. <https://doi.org/10.1007/s00410-022-01903-y>

2811 Allison, C.M., Roggensack, K., Clarke, A.B., 2021. Highly explosive basaltic eruptions driven by CO₂ exsolution.
2812 *Nat Commun* 12, 217. <https://doi.org/10.1038/s41467-020-20354-2>

2813 Almeev, R.R., Bolte, T., Nash, B.P., Holtz, F., Erdmann, M., Cathey, H.E., 2012. High-temperature, low-H₂O
2814 Silicic Magmas of the Yellowstone Hotspot: an Experimental Study of Rhyolite from the Bruneau–
2815 Jarbidge Eruptive Center, Central Snake River Plain, USA. *Journal of Petrology* 53, 1837–1866.
2816 <https://doi.org/10.1093/petrology/egs035>

2817 Alonso-Perez, R., Müntener, O., Ulmer, P., 2009. Igneous garnet and amphibole fractionation in the roots of
2818 island arcs: experimental constraints on andesitic liquids. *Contrib Mineral Petrol* 157, 541–558.
2819 <https://doi.org/10.1007/s00410-008-0351-8>

2820 Andersen, D.J., Lindsley, D.H., 1988. Internally consistent solution models for Fe-Mg-Mn-Ti oxides; Fe-Ti oxides.
2821 *American Mineralogist* 73, 714–726.

2822 Andersen, T., O'Reilly, S.Y., Griffin, W.L., 1984. The trapped fluid phase in upper mantle xenoliths from Victoria,
2823 Australia: implications for mantle metasomatism. *Contr. Mineral. and Petrol.* 88, 72–85.
2824 <https://doi.org/10.1007/BF00371413>

2825 Anderson, A.T., Brown, 1993. CO, contents and formation pressures of some Kilauean melt inclusions.
2826 *American Mineralogist* 78, 794–803.

2827 Anderson, A.T., Davis, A.M., Lu, F., 2000. Evolution of Bishop Tuff rhyolitic magma based on melt and
2828 magnetite inclusions and zoned phenocrysts. *Journal of Petrology* 41, 449–473.

2829 Anderson, J.L., 1996. Status of thermobarometry in granitic batholiths, in: *The Third Hutton Symposium on the*
2830 *Origin of Granites and Related Rocks*. Geological Society of America. <https://doi.org/10.1130/0-8137->
2831 2315-9.125

2832 Anderson, J.L., Barth, A.P., Wooden, J.L., Mazdab, F., 2008. Thermometers and Thermobarometers in Granitic
2833 Systems. *Reviews in Mineralogy and Geochemistry* 69, 121–142.
2834 <https://doi.org/10.2138/rmg.2008.69.4>

2835 Andújar, J., Scaillet, B., Pichavant, M., Druitt, T.H., 2015. Differentiation Conditions of a Basaltic Magma from
2836 Santorini, and its Bearing on the Production of Andesite in Arc Settings. *Journal of Petrology* 56, 765–
2837 794. <https://doi.org/10.1093/petrology/egv016>

2838 Antoshechkina, P., Ghiorso, M.S., 2018. MELTS for MATLAB: A new educational and research tool for
2839 computational thermodynamics. AGU Fall Meeting, abstract #ED44B-23.

2840 Aradi, L., Spránitz, T., Guzmics, T., Szabó, C., Berkesi, M., 2021. 3D Raman imaging of multiphase fluid and melt
2841 inclusions: challenges and perspectives, in: *Goldschmidt2021 Abstracts*. Presented at the
2842 *Goldschmidt2021*, European Association of Geochemistry, Virtual.
2843 <https://doi.org/10.7185/gold2021.8071>

2844 Araya, N., Nakamura, M., Yasuda, A., Okumura, S., Sato, T., Iguchi, M., Miki, D., Geshi, N., 2019. Shallow
2845 magma pre-charge during repeated Plinian eruptions at Sakurajima volcano. *Sci Rep* 9, 1979.
2846 <https://doi.org/10.1038/s41598-019-38494-x>

2847 Ariskin, A.A., Frenkel, M.Ya., Barmina, G.S., Nielsen, R.L., 1993. Comagmat: a Fortran program to model magma
2848 differentiation processes. *Computers & Geosciences* 19, 1155–1170. <https://doi.org/10.1016/0098->
2849 3004(93)90020-6

2850 Armienti, P., Perinelli, C., Putirka, K.D., 2013. A New Model to Estimate Deep-level Magma Ascent Rates, with
2851 Applications to Mt. Etna (Sicily, Italy). *Journal of Petrology* 54, 795–813.
2852 <https://doi.org/10.1093/petrology/egs085>

2853 Aster, E.M., Wallace, P.J., Moore, L.R., Watkins, J., Gazel, E., Bodnar, R.J., 2016. Reconstructing CO₂
2854 concentrations in basaltic melt inclusions using Raman analysis of vapor bubbles. *Journal of*
2855 *Volcanology and Geothermal Research* 323, 148–162.
2856 <https://doi.org/10.1016/j.jvolgeores.2016.04.028>

2857 Azbej, T., Severs, M.J., Rusk, B.G., Bodnar, R.J., 2007. In situ quantitative analysis of individual H₂O–CO₂ fluid
2858 inclusions by laser Raman spectroscopy. *Chemical Geology* 237, 255–263.
2859 <https://doi.org/10.1016/j.chemgeo.2006.06.025>

2860 Bacon, C.R., Newman, S., Stolper, E., 1992. Water, CO₂, Cl, and F in melt inclusions in phenocrysts from three
2861 Holocene explosive eruptions, Crater Lake, Oregon. *American Mineralogist* 77, 1021–1030.

2862 Bakker, R., 2017. Re-Equilibration Processes in Fluid Inclusion Assemblages. *Minerals* 7, 117.
2863 <https://doi.org/10.3390/min7070117>

2864 Bali, E., Hartley, M.E., Halldórsson, S.A., Gudfinnsson, G.H., Jakobsson, S., 2018. Melt inclusion constraints on
2865 volatile systematics and degassing history of the 2014–2015 Holuhraun eruption, Iceland. *Contrib*
2866 *Mineral Petrol* 173, 9. <https://doi.org/10.1007/s00410-017-1434-1>

2867 Barclay, J., 2004. A Hornblende Basalt from Western Mexico: Water-saturated Phase Relations Constrain a
2868 Pressure-Temperature Window of Eruptibility. *Journal of Petrology* 45, 485–506.
2869 <https://doi.org/10.1093/petrology/egg091>

2870 Barker, A.K., Rydeblad, E.M., Silva, S.M., 2021. Magma storage at Ocean Islands: insights from Cape Verde.
2871 *Crustal Magmatic System Evolution: Anatomy, Architecture, and Physico-Chemical Processes* 45–78.
2872 <https://doi.org/10.1002/9781119564485.ch3>

2873 Barth, A., Newcombe, M., Plank, T., Gonnermann, H., Hajimirza, S., Soto, G.J., Saballos, A., Hauri, E., 2019.
2874 Magma decompression rate correlates with explosivity at basaltic volcanoes — Constraints from
2875 water diffusion in olivine. *Journal of Volcanology and Geothermal Research* 387, 106664.
2876 <https://doi.org/10.1016/j.jvolgeores.2019.106664>

2877 Barth, A., Plank, T., 2021. The Ins and Outs of Water in Olivine-Hosted Melt Inclusions: Hygrometer vs.
2878 Speedometer. *Front. Earth Sci.* 9, 614004. <https://doi.org/10.3389/feart.2021.614004>

2879 Baxter, R.J.M., Maclennan, J., Neave, D.A., Thordarson, T., 2023. Depth of Magma Storage Under Iceland
2880 Controlled by Magma Fluxes. *Geochem Geophys Geosyst* 24, e2022GC010811.
2881 <https://doi.org/10.1029/2022GC010811>

2882 Beattie, P., 1993. Olivine-melt and orthopyroxene-melt equilibria. *Contr. Mineral. and Petrol.* 115, 103–111.
2883 <https://doi.org/10.1007/BF00712982>

2884 Befus, K.S., Lin, J.-F., Cisneros, M., Fu, S., 2018. Feldspar Raman shift and application as a magmatic
2885 thermobarometer. *American Mineralogist* 103, 600–609. <https://doi.org/10.2138/am-2018-6157>

2886 Bégué, F., Deering, C.D., Gravley, D.M., Kennedy, B.M., Chambefort, I., Gualda, G.A.R., Bachmann, O., 2014.
2887 Extraction, Storage and Eruption of Multiple Isolated Magma Batches in the Paired Mamaku and
2888 Ohakuri Eruption, Taupo Volcanic Zone, New Zealand. *Journal of Petrology* 55, 1653–1684.
2889 <https://doi.org/10.1093/petrology/egu038>

2890 Bégué, F., Gravley, D.M., Chambefort, I., Deering, C.D., Kennedy, B.M., 2015. Magmatic volatile distribution as
2891 recorded by rhyolitic melt inclusions in the Taupo Volcanic Zone, New Zealand. *Geological Society,*
2892 *London, Special Publications* 410, 71–94. <https://doi.org/10.1144/SP410.4>

2893 Bégué, Florence, Gualda, G.A.R., Ghiorso, M.S., Pamukcu, A.S., Kennedy, B.M., Gravley, D.M., Deering, C.D.,
2894 Chambefort, I., 2014. Phase-equilibrium geobarometers for silicic rocks based on rhyolite-MELTS. Part
2895 2: application to Taupo Volcanic Zone rhyolites. *Contrib Mineral Petrol* 168, 1082.
2896 <https://doi.org/10.1007/s00410-014-1082-7>

2897 Bell, A.F., La Femina, P.C., Ruiz, M., Amelung, F., Bagnardi, M., Bean, C.J., Bernard, B., Ebinger, C., Gleeson, M.,
2898 Grannell, J., Hernandez, S., Higgins, M., Liorzou, C., Lundgren, P., Meier, N.J., Möllhoff, M., Oliva, S.-J.,
2899 Ruiz, A.G., Stock, M.J., 2021. Caldera resurgence during the 2018 eruption of Sierra Negra volcano,
2900 Galápagos Islands. *Nat Commun* 12, 1397. <https://doi.org/10.1038/s41467-021-21596-4>

2901 Bell, I.H., Wronski, J., Quoilin, S., Lemort, V., 2014. Pure and Pseudo-pure Fluid Thermophysical Property
2902 Evaluation and the Open-Source Thermophysical Property Library CoolProp. *Ind. Eng. Chem. Res.* 53,
2903 2498–2508. <https://doi.org/10.1021/ie4033999>

2904 Bennett, E.N., Jenner, F.E., Millet, M.-A., Cashman, K.V., Lissenberg, C.J., 2019. Deep roots for mid-ocean-ridge
2905 volcanoes revealed by plagioclase-hosted melt inclusions. *Nature* 572, 235–239.
2906 <https://doi.org/10.1038/s41586-019-1448-0>

2907 Berman, R.G., 1988. Internally-Consistent Thermodynamic Data for Minerals in the System Na₂O-K₂O-CaO-
2908 MgO-FeO-Fe₂O₃-Al₂O₃-SiO₂-TiO₂-H₂O-CO₂. *Journal of Petrology* 29, 445–522.
2909 <https://doi.org/10.1093/petrology/29.2.445>

2910 Berndt, J., 2004. An Experimental Investigation of the Influence of Water and Oxygen Fugacity on
2911 Differentiation of MORB at 200 MPa. *Journal of Petrology* 46, 135–167.
2912 <https://doi.org/10.1093/petrology/egh066>

2913 Black, B.A., Andrews, B.J., 2020. Petrologic imaging of the architecture of magma reservoirs feeding caldera-
2914 forming eruptions. *Earth and Planetary Science Letters* 552, 116572.
2915 <https://doi.org/10.1016/j.epsl.2020.116572>

2916 Blatter, D.L., Carmichael, I.S.E., 2001. Hydrous phase equilibria of a Mexican high-silica andesite: A candidate
2917 for a mantle origin? *Geochimica et Cosmochimica Acta* 65, 4043–4065.
2918 [https://doi.org/10.1016/S0016-7037\(01\)00708-6](https://doi.org/10.1016/S0016-7037(01)00708-6)

2919 Blatter, D.L., Sisson, T.W., Hanks, W.B., 2013. Crystallization of oxidized, moderately hydrous arc basalt at
2920 mid- to lower-crustal pressures: implications for andesite genesis. *Contrib Mineral Petrol* 166, 861–
2921 886. <https://doi.org/10.1007/s00410-013-0920-3>

2922 Blundy, J., 2022. Chemical Differentiation by Mineralogical Buffering in Crustal Hot Zones. *Journal of Petrology*
2923 63, egac054. <https://doi.org/10.1093/petrology/egac054>

2924 Blundy, J., Cashman, K., 2008. Petrologic Reconstruction of Magmatic System Variables and Processes. *Reviews*
2925 *in Mineralogy and Geochemistry* 69, 179–239. <https://doi.org/10.2138/rmg.2008.69.6>

2926 Blundy, J., Cashman, K.V., Rust, A., Witham, F., 2010. A case for CO₂-rich arc magmas. *Earth and Planetary*
2927 *Science Letters* 290, 289–301. <https://doi.org/10.1016/j.epsl.2009.12.013>

2928 Bodnar, R.J., Binns, P.R., Hall, D.L., 1989. Synthetic fluid inclusions - VI. Quantitative evaluation of the
2929 decrepitation behaviour of fluid inclusions in quartz at one atmosphere confining pressure. *J*
2930 *Metamorph Geol* 7, 229–242. <https://doi.org/10.1111/j.1525-1314.1989.tb00586.x>

2931 Bogaerts, M., Scaillet, B., Auwera, J.V., 2006. Phase Equilibria of the Lyngdal Granodiorite (Norway):
2932 Implications for the Origin of Metaluminous Ferroan Granitoids. *Journal of Petrology* 47, 2405–2431.
2933 <https://doi.org/10.1093/petrology/egl049>

2934 Bohron, W.A., Clague, D.A., 1988. Origin of ultramafic xenoliths containing exsolved pyroxenes from Hualalai
2935 Volcano, Hawaii. *Contrib Mineral Petrol* 100, 139–155. <https://doi.org/10.1007/BF00373581>

2936 Bolte, T., Holtz, F., Almeev, R., Nash, B., 2015. The Blacktail Creek Tuff: an analytical and experimental study of
2937 rhyolites from the Heise volcanic field, Yellowstone hotspot system. *Contrib Mineral Petrol* 169, 15.
2938 <https://doi.org/10.1007/s00410-015-1112-0>

2939 Böttcher, N., Taron, J., Kolditz, O., Liedl, R., Park, C.-H., 2012. Comparison of equations of state for carbon
2940 dioxide for numerical simulations. *Proceedings ModelCARE2011, Leipzig, Germany. IAHS Publ. 355* 9.

2941 Boulanger, M., France, L., Deans, J.R.L., Ferrando, C., Lissenberg, C.J., von der Handt, A., 2020. Magma
2942 Reservoir Formation and Evolution at a Slow-Spreading Center (Atlantis Bank, Southwest Indian
2943 Ridge). *Front. Earth Sci.* 8, 554598. <https://doi.org/10.3389/feart.2020.554598>

2944 Boullier, A.-M., Michot, G., Pecher, A., Barres, O., 1989. Diffusion and/or Plastic Deformation around Fluid
2945 Inclusions in Synthetic Quartz: New Investigations, in: Bridgwater, D. (Ed.), *Fluid Movements —*
2946 *Element Transport and the Composition of the Deep Crust.* Springer Netherlands, Dordrecht, pp. 345–
2947 360. https://doi.org/10.1007/978-94-009-0991-5_28

2948 Brugman, K.K., Till, C.B., 2019. A low-aluminum clinopyroxene-liquid geothermometer for high-silica magmatic
2949 systems. *American Mineralogist* 104, 996–1004. <https://doi.org/10.2138/am-2019-6842>

2950 Bucholz, C.E., Gaetani, G.A., Behn, M.D., Shimizu, N., 2013. Post-entrapment modification of volatiles and
2951 oxygen fugacity in olivine-hosted melt inclusions. *Earth and Planetary Science Letters* 374, 145–155.
2952 <https://doi.org/10.1016/j.epsl.2013.05.033>

2953 Budd, D.A., Troll, V.R., Dahren, B., Burchardt, S., 2016. Persistent multitiered magma plumbing beneath Katla
2954 volcano, Iceland. *Geochem. Geophys. Geosyst.* 17, 966–980. <https://doi.org/10.1002/2015GC006118>

2955 Buddington, A.F., Lindsley, D.H., 1964. Iron-Titanium Oxide Minerals and Synthetic Equivalents. *Journal of*
2956 *Petrology* 5, 310–357. <https://doi.org/10.1093/petrology/5.2.310>

2957 Burke, E.A.J., 2001. Raman microspectrometry of fluid inclusions. *Lithos* 55, 139–158.
2958 [https://doi.org/10.1016/S0024-4937\(00\)00043-8](https://doi.org/10.1016/S0024-4937(00)00043-8)

2959 Buso, R., Laporte, D., Schiavi, F., Cluzel, N., Fonquernie, C., 2022. High-pressure homogenization of olivine-
2960 hosted CO₂-rich melt inclusions in a piston cylinder: insight into the volatile
2961 content of primary mantle melts. *Eur. J. Mineral.* 34, 325–349. <https://doi.org/10.5194/ejm-34-325-2022>

2962

2963 Cadoux, A., Scaillet, B., Druitt, T.H., Deloule, E., 2014. Magma Storage Conditions of Large Plinian Eruptions of
2964 Santorini Volcano (Greece). *Journal of Petrology* 55, 1129–1171.
2965 <https://doi.org/10.1093/petrology/egu021>

2966 Campione, M., Malaspina, N., Frezzotti, M.L., 2015. Threshold size for fluid inclusion decrepitation: Size for
2967 Fluid Inclusion Decrepitation. *Journal of Geophysical Research: Solid Earth* 120, 7396–7402.
2968 <https://doi.org/10.1002/2015JB012086>

2969 Caracciolo, A., Bali, E., Guðfinnsson, G.H., Kahl, M., Halldórsson, S.A., Hartley, M.E., Gunnarsson, H., 2020.
2970 Temporal evolution of magma and crystal mush storage conditions in the Bárðarbunga-Veiðivötn
2971 volcanic system, Iceland. *Lithos* 352–353, 105234. <https://doi.org/10.1016/j.lithos.2019.105234>

2972 Caracciolo, A., Halldórsson, S.A., Bali, E., Marshall, E.W., Jeon, H., Whitehouse, M.J., Barnes, J.D., Guðfinnsson,
2973 G.H., Kahl, M., Hartley, M.E., 2022. Oxygen isotope evidence for progressively assimilating trans-
2974 crustal magma plumbing systems in Iceland. *Geology* 50, 796–800. <https://doi.org/10.1130/G49874.1>

2975 Cashman, K.V., Edmonds, M., 2019. Mafic glass compositions: a record of magma storage conditions, mixing
2976 and ascent. *Phil. Trans. R. Soc. A* 377, 20180004. <https://doi.org/10.1098/rsta.2018.0004>

2977 Chakraborty, S., Dohmen, R., 2022. Diffusion chronometry of volcanic rocks: looking backward and forward.
2978 *Bull Volcanol* 84, 57. <https://doi.org/10.1007/s00445-022-01565-5>

2979 Cheng, L.-L., Yang, Z.-F., Zeng, L., Wang, Y., Luo, Z.-H., 2014. Giant plagioclase growth during storage of basaltic
2980 magma in Emeishan Large Igneous Province, SW China. *Contrib Mineral Petrol* 167, 971.
2981 <https://doi.org/10.1007/s00410-014-0971-0>

2982 Chesner, C.A., Luhr, J.F., 2010. A melt inclusion study of the Toba Tuffs, Sumatra, Indonesia. *Journal of*
2983 *Volcanology and Geothermal Research* 197, 259–278.
2984 <https://doi.org/10.1016/j.jvolgeores.2010.06.001>

2985 Cisneros, M., Befus, K.S., 2020. Applications and Limitations of Elastic Thermobarometry: Insights From Elastic
2986 Modeling of Inclusion-Host Pairs and Example Case Studies. *Geochem. Geophys. Geosyst.* 21.
2987 <https://doi.org/10.1029/2020GC009231>

2988 Connolly, J.A.D., 2009. The geodynamic equation of state: What and how: GEODYNAMIC EQUATION OF STATE-
2989 WHAT AND HOW. *Geochem. Geophys. Geosyst.* 10. <https://doi.org/10.1029/2009GC002540>

2990 Connolly, J.A.D., 2005. Computation of phase equilibria by linear programming: A tool for geodynamic
2991 modeling and its application to subduction zone decarbonation. *Earth and Planetary Science Letters*
2992 236, 524–541. <https://doi.org/10.1016/j.epsl.2005.04.033>

2993 Coogan, L.A., Saunders, A.D., Wilson, R.N., 2014. Aluminum-in-olivine thermometry of primitive basalts:
2994 Evidence of an anomalously hot mantle source for large igneous provinces. *Chemical Geology* 368, 1–
2995 10. <https://doi.org/10.1016/j.chemgeo.2014.01.004>

2996 Costa, F., 2004. Petrological and Experimental Constraints on the Pre-eruption Conditions of Holocene Dacite
2997 from Volcan San Pedro (36 S, Chilean Andes) and the Importance of Sulphur in Silicic Subduction-
2998 related Magmas. *Journal of Petrology* 45, 855–881. <https://doi.org/10.1093/petrology/egg114>

2999 Costa, F., Shea, T., Ubide, T., 2020. Diffusion chronometry and the timescales of magmatic processes. *Nat Rev*
3000 *Earth Environ* 1, 201–214. <https://doi.org/10.1038/s43017-020-0038-x>

3001 Crabtree, S.M., Lange, R.A., 2011. Complex Phenocryst Textures and Zoning Patterns in Andesites and Dacites:
3002 Evidence of Degassing-Induced Rapid Crystallization? *Journal of Petrology* 52, 3–38.
3003 <https://doi.org/10.1093/petrology/egq067>

3004 Dahren, B., Troll, V.R., Andersson, U.B., Chadwick, J.P., Gardner, M.F., Jaxybulatov, K., Koulakov, I., 2012.
3005 Magma plumbing beneath Anak Krakatau volcano, Indonesia: evidence for multiple magma storage
3006 regions. *Contrib Mineral Petrol* 163, 631–651. <https://doi.org/10.1007/s00410-011-0690-8>

3007 Dal-Negro, A., Manoli, S., Secca, L., Piccirillo, E.M., 1989. Megacrystic clinopyroxenes from Victoria (Australia);
3008 crystal chemical comparisons of pyroxenes from high and low pressure regimes. *European Journal of*
3009 *Mineralogy* 1 (1): 105–121.

3010 Danyushevsky, L.V., McNeill, A.W., Sobolev, A.V., 2002. Experimental and petrological studies of melt
3011 inclusions in phenocrysts from mantle-derived magmas: an overview of techniques, advantages and
3012 complications. *Chemical Geology* 183, 5–24. [https://doi.org/10.1016/S0009-2541\(01\)00369-2](https://doi.org/10.1016/S0009-2541(01)00369-2)

3013 Danyushevsky, L.V., Plechov, P., 2011. Petrolog3: Integrated software for modeling crystallization processes.
3014 *Geochemistry, Geophysics, Geosystems* 12, n/a-n/a. <https://doi.org/10.1029/2011GC003516>

3015 Dayton, K., Gazel, E., Wieser, P., Troll, V.R., Carracedo, J.C., La Madrid, H., Roman, D.C., Ward, J., Aulinas, M.,
3016 Geiger, H., Deegan, F.M., Gisbert, G., Perez-Torrado, F.J., 2023. Deep magma storage during the 2021
3017 La Palma eruption. *Sci. Adv.* 9, eade7641. <https://doi.org/10.1126/sciadv.ade7641>

3018 de Capitani, C., Petrakakis, K., 2010. The computation of equilibrium assemblage diagrams with
3019 Theriak/Domino software. *American Mineralogist* 95, 1006–1016.
3020 <https://doi.org/10.2138/am.2010.3354>

3021 Demouchy, S., Jacobsen, S.D., Gaillard, F., Stern, C.R., 2006. Rapid magma ascent recorded by water diffusion
3022 profiles in mantle olivine. *Geol* 34, 429. <https://doi.org/10.1130/G22386.1>

3023 DeVitre, C.L., Allison, C.M., Gazel, E., 2021. A high-precision CO₂ densimeter for Raman spectroscopy using a
3024 Fluid Density Calibration Apparatus. *Chemical Geology* 584, 120522.
3025 <https://doi.org/10.1016/j.chemgeo.2021.120522>

3026 DeVitre, C.L., Dayton, K., Gazel, E., Pamukçu, A., Gaetani, G., Wieser, P.E., 2023b. Laser heating effect on
3027 Raman analysis of CO₂ co-existing as liquid and vapor in olivine-hosted melt inclusion bubbles.
3028 *Volcanica* 6, 201–219. <https://doi.org/10.30909/vol.06.02.201219>

3029

3030 DeVitre, C.L., Gazel, E., Ramalho, R.S., Venugopal, S., Steele-MacInnis, M., Hua, J., Allison, C.M., Moore, L.R.,
3031 Carracedo, J.C., Monteleone, B., 2023a. Oceanic intraplate explosive eruptions fed directly from the
3032 mantle. *Proc. Natl. Acad. Sci. U.S.A.* 120, e2302093120. <https://doi.org/10.1073/pnas.2302093120>
3033 Dixon, J.E., 1997. Degassing of alkalic basalts. *American Mineralogist* 82, 368–378.
3034 <https://doi.org/10.2138/am-1997-3-415>
3035 Dobbin, K.K., Simon, R.M., 2011. Optimally splitting cases for training and testing high dimensional classifiers.
3036 *BMC Med Genomics* 4, 31. <https://doi.org/10.1186/1755-8794-4-31>
3037 Drignon, M.J., Nielsen, R.L., Tepley, F.J., Bodnar, R.J., 2019. Upper mantle origin of plagioclase megacrysts from
3038 plagioclase-ultraphyric mid-oceanic ridge basalt. *Geology* 47, 43–46.
3039 <https://doi.org/10.1130/G45542.1>
3040 Duan, X., 2014. A general model for predicting the solubility behavior of H₂O–CO₂ fluids in silicate melts over a
3041 wide range of pressure, temperature and compositions. *Geochimica et Cosmochimica Acta* 125, 582–
3042 609. <https://doi.org/10.1016/j.gca.2013.10.018>
3043 Dubessy, J., Caumon, M.-C., Rull, F., Sharma, S., 2012. Instrumentation in Raman spectroscopy: elementary
3044 theory and practice, in: Ferraris, G., Dubessy, J., Caumon, M.-C., Rull, F. (Eds.), *Raman Spectroscopy*
3045 *Applied to Earth Sciences and Cultural Heritage*. European Mineralogical Union, pp. 83–172.
3046 <https://doi.org/10.1180/EMU-notes.12.3>
3047 Dubois, P.F., Hinsen, K., Hugunin, J., 1996. Numerical Python. *Comput. Phys.* 10, 262.
3048 <https://doi.org/10.1063/1.4822400>
3049 Erdmann, M., Koepke, J., 2016. Silica-rich lavas in the oceanic crust: experimental evidence for fractional
3050 crystallization under low water activity. *Contrib Mineral Petrol* 171, 83.
3051 <https://doi.org/10.1007/s00410-016-1294-0>
3052 Erdmann, S., Martel, C., Pichavant, M., Bourdier, J.-L., Champallier, R., Komorowski, J.-C., Cholik, N., 2016.
3053 Constraints on Phase Equilibrium Experiments on Pre-eruptive Storage Conditions in Mixed Magma
3054 Systems: a Case Study on Crystal-rich Basaltic Andesites from Mount Merapi, Indonesia. *J. Petrology*
3055 57, 535–560. <https://doi.org/10.1093/petrology/egw019>
3056 Erdmann, S., Martel, C., Pichavant, M., Kushnir, A., 2014. Amphibole as an archivist of magmatic crystallization
3057 conditions: problems, potential, and implications for inferring magma storage prior to the paroxysmal
3058 2010 eruption of Mount Merapi, Indonesia. *Contrib Mineral Petrol* 167, 1016.
3059 <https://doi.org/10.1007/s00410-014-1016-4>
3060 Esposito, R., Klebesz, R., Bartoli, O., Klyukin, Y., Moncada, D., Doherty, A., Bodnar, R., 2012. Application of the
3061 Linkam TS1400XY heating stage to melt inclusion studies. *Open Geosciences* 4.
3062 <https://doi.org/10.2478/s13533-011-0054-y>
3063 Esposito, R., Lamadrid, H.M., Redi, D., Steele-MacInnis, M., Bodnar, R.J., Manning, C.E., De Vivo, B., Cannatelli,
3064 C., Lima, A., 2016. Detection of liquid H₂O in vapor bubbles in reheated melt inclusions: Implications
3065 for magmatic fluid composition and volatile budgets of magmas? *American Mineralogist* 101, 1691–
3066 1695. <https://doi.org/10.2138/am-2016-5689>
3067 Everall, N.J., 2010. Confocal Raman microscopy: common errors and artefacts. *Analyst* 135, 2512.
3068 <https://doi.org/10.1039/c0an00371a>
3069 Fall, A., Tattitch, B., Bodnar, R.J., 2011. Combined microthermometric and Raman spectroscopic technique to
3070 determine the salinity of H₂O–CO₂–NaCl fluid inclusions based on clathrate melting. *Geochimica et*
3071 *Cosmochimica Acta* 75, 951–964. <https://doi.org/10.1016/j.gca.2010.11.021>
3072 First, E.C., Hammer, J.E., Ruprecht, P., Rutherford, M., 2021. Experimental Constraints on Dacite Magma
3073 Storage beneath Volcán Quizapu, Chile. *Journal of Petrology* 62, egab027.
3074 <https://doi.org/10.1093/petrology/egab027>
3075 Fowler, S.J., Spera, F.J., 2010. A Metamodel for Crustal Magmatism: Phase Equilibria of Giant Ignimbrites.
3076 *Journal of Petrology* 51, 1783–1830. <https://doi.org/10.1093/petrology/egq039>
3077 Fowler, S.J., Spera, F.J., Bohron, W.A., Belkin, H.E., De Vivo, B., 2007. Phase Equilibria Constraints on the
3078 Chemical and Physical Evolution of the Campanian Ignimbrite. *Journal of Petrology* 48, 459–493.
3079 <https://doi.org/10.1093/petrology/egl068>
3080 Frezzotti, M.L., Andersen, T., Neumann, E.-R., Simonsen, S.L., 2002. Carbonatite melt–CO₂ fluid inclusions in
3081 mantle xenoliths from Tenerife, Canary Islands: a story of trapping, immiscibility and fluid–rock
3082 interaction in the upper mantle. *Lithos* 64, 77–96. [https://doi.org/10.1016/S0024-4937\(02\)00178-0](https://doi.org/10.1016/S0024-4937(02)00178-0)
3083 Frezzotti, M.L., De Vivo, B., Clochiatti, R., 1991. Melt-mineral-fluid interactions in ultramafic nodules from
3084 alkaline lavas of Mount Etna (Sicily, Italy): Melt and fluid inclusion evidence. *Journal of Volcanology*
3085 *and Geothermal Research* 47, 209–219. [https://doi.org/10.1016/0377-0273\(91\)90001-G](https://doi.org/10.1016/0377-0273(91)90001-G)

3086 Frezzotti, M.L., Peccerillo, A., Bonelli, R., 2003. Magma ascent rates and depths of crustal magma reservoirs
3087 beneath the Aeolian volcanic Arc (Italy): Inferences from fluid and melt inclusions in xenoliths, in:
3088 Developments in Volcanology. Elsevier, pp. 185–205. [https://doi.org/10.1016/S1871-644X\(03\)80030-](https://doi.org/10.1016/S1871-644X(03)80030-)
3089 X

3090 Frezzotti, M.L., Tecce, F., Casagli, A., 2012. Raman spectroscopy for fluid inclusion analysis. *Journal of*
3091 *Geochemical Exploration* 112, 1–20. <https://doi.org/10.1016/j.gexplo.2011.09.009>

3092 Gaetani, G.A., O’Leary, J.A., Shimizu, N., Bucholz, C.E., Newville, M., 2012. Rapid reequilibration of H₂O and
3093 oxygen fugacity in olivine-hosted melt inclusions. *Geology* 40, 915–918.
3094 <https://doi.org/10.1130/G32992.1>

3095 Gaffney, A.M., 2002. Environments of Crystallization and Compositional Diversity of Mauna Loa Xenoliths.
3096 *Journal of Petrology* 43, 963–981. <https://doi.org/10.1093/petrology/43.6.963>

3097 Gao, R., Lassiter, J.C., Clague, D.A., Bohrsen, W.A., 2022. Evolution of Hawaiian Volcano Magmatic Plumbing
3098 System and Implications for Melt/Edifice and Melt/Lithosphere Interaction: Constraints from Hualālai
3099 Xenoliths. *Journal of Petrology* 63, egac091. <https://doi.org/10.1093/petrology/egac091>

3100 Garcia, M.O., 2003. A Petrologic Perspective of Kilauea Volcano’s Summit Magma Reservoir. *Journal of*
3101 *Petrology* 44, 2313–2339. <https://doi.org/10.1093/petrology/egg079>

3102 Gardner, J.E., Befus, K.S., Gualda, G.A.R., Ghiorso, M.S., 2014. Experimental constraints on rhyolite-MELTS and
3103 the Late Bishop Tuff magma body. *Contrib Mineral Petrol* 168, 1051. <https://doi.org/10.1007/s00410->
3104 014-1051-1

3105 Gavrilenko, M., Herzberg, C., Vidito, C., Carr, M.J., Tenner, T., Ozerov, A., 2016. A Calcium-in-Olivine
3106 Geohygrometer and its Application to Subduction Zone Magmatism. *Journal of Petrology* 57, 1811–
3107 1832. <https://doi.org/10.1093/petrology/egw062>

3108 Gavrilenko, M., Krawczynski, M., Ruprecht, P., Li, W., Catalano, J.G., 2019. The quench control of water
3109 estimates in convergent margin magmas. *American Mineralogist* 104, 936–948.
3110 <https://doi.org/10.2138/am-2019-6735>

3111 Geiger, H., Barker, A.K., Troll, V.R., 2016a. Locating the depth of magma supply for volcanic eruptions, insights
3112 from Mt. Cameroon. *Sci Rep* 6, 33629. <https://doi.org/10.1038/srep33629>

3113 Geiger, H., Mattsson, T., Deegan, F.M., Troll, V.R., Burchardt, S., Gudmundsson, Ó., Tryggvason, A., Krumbholz,
3114 M., Harris, C., 2016b. Magma plumbing for the 2014–2015 Holuhraun eruption, Iceland. *Geochem.*
3115 *Geophys. Geosyst.* 17, 2953–2968. <https://doi.org/10.1002/2016GC006317>

3116 Geiger, H., Troll, V.R., Jolis, E.M., Deegan, F.M., Harris, C., Hilton, D.R., Freda, C., 2018. Multi-level magma
3117 plumbing at Agung and Batur volcanoes increases risk of hazardous eruptions. *Sci Rep* 8, 10547.
3118 <https://doi.org/10.1038/s41598-018-28125-2>

3119 Geist, D., Naumann, T., Larson, P., 1998. Evolution of Galapagos Magmas: Mantle and Crustal Fractionation
3120 without Assimilation. *Journal of Petrology* 39, 953–971. <https://doi.org/10.1093/petroj/39.5.953>

3121 Gerlach, T.M., Graeber, E.J., 1985. Volatile budget of Kilauea volcano. *Nature* 313, 273–277.
3122 <https://doi.org/10.1038/313273a0>

3123 Ghiorso, M., Prissel, K., 2020. ENKI Cloud App: Implementation of the Fe-Ti Oxide Geothermoxybarometer of
3124 Ghiorso and Evans, 2008. <https://doi.org/10.5281/ZENODO.3866660>

3125 Ghiorso, M.S., 1990. Thermodynamic properties of hematite - ilmenite - geikielite solid solutions. *Contr.*
3126 *Mineral. and Petrol.* 104, 645–667. <https://doi.org/10.1007/BF01167285>

3127 Ghiorso, M.S., Evans, B.W., 2008. Thermodynamics of Rhombohedral Oxide Solid Solutions and a Revision of
3128 the FE-TI Two-Oxide Geothermometer and Oxygen-Barometer. *American Journal of Science* 308, 957–
3129 1039. <https://doi.org/10.2475/09.2008.01>

3130 Ghiorso, M.S., Gualda, G.A.R., 2015. An H₂O–CO₂ mixed fluid saturation model compatible with rhyolite-
3131 MELTS. *Contrib Mineral Petrol* 169, 53. <https://doi.org/10.1007/s00410-015-1141-8>

3132 Ghiorso, M.S., Gualda, G.A.R., 2013. A method for estimating the activity of titania in magmatic liquids from
3133 the compositions of coexisting rhombohedral and cubic iron–titanium oxides. *Contrib Mineral Petrol*
3134 165, 73–81. <https://doi.org/10.1007/s00410-012-0792-y>

3135 Ghiorso, M.S., Hirschmann, M.M., Reiners, P.W., Kress, V.C., 2002. The pMELTS: A revision of MELTS for
3136 improved calculation of phase relations and major element partitioning related to partial melting of
3137 the mantle to 3 GPa. *Geochem.-Geophys.-Geosyst.* 3, 1–35. <https://doi.org/10.1029/2001GC000217>

3138 Ghiorso, M.S., Sack, O., 1991. Fe-Ti oxide geothermometry: thermodynamic formulation and the estimation of
3139 intensive variables in silicic magmas. *Contr. Mineral. and Petrol.* 108, 485–510.
3140 <https://doi.org/10.1007/BF00303452>

3141 Ghiorso, M.S., Sack, R.O., 1995. Chemical mass transfer in magmatic processes IV. A revised and internally
3142 consistent thermodynamic model for the interpolation and extrapolation of liquid-solid equilibria in

3143 magmatic systems at elevated temperatures and pressures. *Contr. Mineral. and Petrol.* 119, 197–212.
3144 <https://doi.org/10.1007/BF00307281>

3145 Gibson, S.A., Geist, D., 2010. Geochemical and geophysical estimates of lithospheric thickness variation
3146 beneath Galápagos. *Earth and Planetary Science Letters* 300, 275–286.
3147 <https://doi.org/10.1016/j.epsl.2010.10.002>

3148 Gleeson, M.L.M., Gibson, S.A., 2021. Insights Into the Nature of Plume-Ridge Interaction and Outflux of H₂O
3149 From the Galápagos Spreading Center. *Geochem Geophys Geosyst* 22.
3150 <https://doi.org/10.1029/2020GC009560>

3151 Gleeson, M.L.M., Gibson, S.A., Stock, M.J., 2022. Constraints on the behaviour and content of volatiles in
3152 Galápagos magmas from melt inclusions and nominally anhydrous minerals. *Geochimica et*
3153 *Cosmochimica Acta* 319, 168–190. <https://doi.org/10.1016/j.gca.2021.11.005>

3154 Gleeson, M.L.M., Gibson, S.A., Stock, M.J., 2021. Upper Mantle Mush Zones beneath Low Melt Flux Ocean
3155 Island Volcanoes: Insights from Isla Floreana, Galápagos. *Journal of Petrology* 61, ega094.
3156 <https://doi.org/10.1093/petrology/egaa094>

3157 Gleeson, M.L.M., Stock, M.J., Pyle, D.M., Mather, T.A., Hutchison, W., Yirgu, G., Wade, J., 2017. Constraining
3158 magma storage conditions at a restless volcano in the Main Ethiopian Rift using phase equilibria
3159 models. *Journal of Volcanology and Geothermal Research* 337, 44–61.
3160 <https://doi.org/10.1016/j.jvolgeores.2017.02.026>

3161 Goltz, A.E., Krawczynski, M.J., Gavrilenko, M., Gorbach, N.V., Ruprecht, P., 2020. Evidence for superhydrous
3162 primitive arc magmas from mafic enclaves at Shiveluch volcano, Kamchatka. *Contrib Mineral Petrol*
3163 175, 115. <https://doi.org/10.1007/s00410-020-01746-5>

3164 Goranson, R.W., 1931. The solubility of water in granite magmas. *American Journal of Science* s5-22, 481–502.
3165 <https://doi.org/10.2475/ajs.s5-22.132.481>

3166 Grove, T.L., Donnelly-Nolan, J.M., Housh, T., 1997. Magmatic processes that generated the rhyolite of Glass
3167 Mountain, Medicine Lake volcano, N. California. *Contributions to Mineralogy and Petrology* 127, 205–
3168 223. <https://doi.org/10.1007/s004100050276>

3169 Grove, T.L., Kinzler, R.J., Bryan, W.B., 1992. Fractionation of Mid-Ocean Ridge Basalt (MORB), in: *Mantle Flow*
3170 *and Melt Generation at Mid-Ocean Ridges*. American Geophysical Union, pp. 281–311.

3171 Gualda, Guilherme A R, Bégué, F., Pamukcu, A.S., Ghiorso, M.S., 2019. Rhyolite-MELTS vs DERP—Newer Does
3172 not Make it Better: a Comment on ‘The Effect of Anorthite Content and Water on Quartz–Feldspar
3173 Cotectic Compositions in the Rhyolitic System and Implications for Geobarometry’ by Wilke et al.
3174 (2017; *Journal of Petrology*, 58, 789–818). *Journal of Petrology* 60, 855–864.
3175 <https://doi.org/10.1093/petrology/egz003>

3176 Gualda, G.A.R., Ghiorso, M.S., 2014. Phase-equilibrium geobarometers for silicic rocks based on rhyolite-
3177 MELTS. Part 1: Principles, procedures, and evaluation of the method. *Contrib Mineral Petrol* 168,
3178 1033. <https://doi.org/10.1007/s00410-014-1033-3>

3179 Gualda, G.A.R., Ghiorso, M.S., Lemons, R.V., Carley, T.L., 2012. Rhyolite-MELTS: a Modified Calibration of
3180 MELTS Optimized for Silica-rich, Fluid-bearing Magmatic Systems. *Journal of Petrology* 53, 875–890.
3181 <https://doi.org/10.1093/petrology/egr080>

3182 Gualda, Guilherme A.R., Gravley, D.M., Deering, C.D., Ghiorso, M.S., 2019. Magma extraction pressures and
3183 the architecture of volcanic plumbing systems. *Earth and Planetary Science Letters* 522, 118–124.
3184 <https://doi.org/10.1016/j.epsl.2019.06.020>

3185 Guo, K., Zhai, S.-K., Wang, X.-Y., Yu, Z.-H., Lai, Z.-Q., Chen, S., Song, Z.-J., Ma, Y., Chen, Z.-X., Li, X.-H., Zeng, Z.-
3186 G., 2018. The dynamics of the southern Okinawa Trough magmatic system: New insights from the
3187 microanalysis of the An contents, trace element concentrations and Sr isotopic compositions of
3188 plagioclase hosted in basalts and silicic rocks. *Chemical Geology* 497, 146–161.
3189 <https://doi.org/10.1016/j.chemgeo.2018.09.002>

3190 Hagiwara, Y., Kawano, T., Takahata, K., Torimoto, J., Yamamoto, J., 2021. Temperature dependence of a Raman
3191 CO₂ densimeter from 23°C to 200°C and 7.2 to 248.7 MPa: Evaluation of density underestimation by
3192 laser heating. *J Raman Spectrosc* 52, 1744–1757. <https://doi.org/10.1002/jrs.6188>

3193 Halldórsson, S.A., Marshall, E.W., Caracciolo, A., Matthews, S., Bali, E., Rasmussen, M.B., Ranta, E., Robin, J.G.,
3194 Guðfinnsson, G.H., Sigmarsson, O., Maclennan, J., Jackson, M.G., Whitehouse, M.J., Jeon, H., van der
3195 Meer, Q.H.A., Mibei, G.K., Kalliokoski, M.H., Repczynska, M.M., Rúnarsdóttir, R.H., Sigurðsson, G.,
3196 Pfeffer, M.A., Scott, S.W., Kjartansdóttir, R., Kleine, B.I., Oppenheimer, C., Aiuppa, A., Ilyinskaya, E.,
3197 Bitetto, M., Giudice, G., Stefánsson, A., 2022. Rapid shifting of a deep magmatic source at
3198 Fagradalsfjall volcano, Iceland. *Nature* 609, 529–534. <https://doi.org/10.1038/s41586-022-04981-x>

3199 Hammer, J., Jacob, S., Welsch, B., Hellebrand, E., Sinton, J., 2016. Clinopyroxene in postshield Haleakala
3200 ankaramite: 1. Efficacy of thermobarometry. *Contrib Mineral Petrol* 171, 7.
3201 <https://doi.org/10.1007/s00410-015-1212-x>
3202 Hammestrom, J.E., Zen, E.-A., 1986. Aluminum in hornblende: An empirical igneous geobarometer. *American*
3203 *Mineralogist*.
3204 Hansteen, T.H., Klugel, A., 2008. Fluid Inclusion Thermobarometry as a Tracer for Magmatic Processes. *Reviews*
3205 *in Mineralogy and Geochemistry* 69, 143–177. <https://doi.org/10.2138/rmg.2008.69.5>
3206 Hansteen, T.H., Klügel, A., Schmincke, H.-U., 1998. Multi-stage magma ascent beneath the Canary Islands:
3207 evidence from fluid inclusions. *Contributions to Mineralogy and Petrology* 132, 48–64.
3208 <https://doi.org/10.1007/s004100050404>
3209 Hanyu, T., Yamamoto, J., Kimoto, K., Shimizu, K., Ushikubo, T., 2020. Determination of total CO₂ in melt
3210 inclusions with shrinkage bubbles. *Chemical Geology* 557, 119855.
3211 <https://doi.org/10.1016/j.chemgeo.2020.119855>
3212 Harmon, L.J., Cowlyn, J., Gualda, G.A.R., Ghiorsso, M.S., 2018. Phase-equilibrium geobarometers for silicic rocks
3213 based on rhyolite-MELTS. Part 4: Plagioclase, orthopyroxene, clinopyroxene, glass geobarometer, and
3214 application to Mt. Ruapehu, New Zealand. *Contrib Mineral Petrol* 173, 7.
3215 <https://doi.org/10.1007/s00410-017-1428-z>
3216 Harris, C.R., Millman, K.J., van der Walt, S.J., Gommers, R., Virtanen, P., Cournapeau, D., Wieser, E., Taylor, J.,
3217 Berg, S., Smith, N.J., Kern, R., Picus, M., Hoyer, S., van Kerkwijk, M.H., Brett, M., Haldane, A., del Río,
3218 J.F., Wiebe, M., Peterson, P., Gérard-Marchant, P., Sheppard, K., Reddy, T., Weckesser, W., Abbasi, H.,
3219 Gohlke, C., Oliphant, T.E., 2020. Array programming with NumPy. *Nature* 585, 357–362.
3220 <https://doi.org/10.1038/s41586-020-2649-2>
3221 Hartley, M.E., Maclennan, J., Edmonds, M., Thordarson, T., 2014. Reconstructing the deep CO₂ degassing
3222 behaviour of large basaltic fissure eruptions. *Earth and Planetary Science Letters* 393, 120–131.
3223 <https://doi.org/10.1016/j.epsl.2014.02.031>
3224 Hauri, E.H., Maclennan, J., McKenzie, D., Gronvold, K., Oskarsson, N., Shimizu, N., 2018. CO₂ content beneath
3225 northern Iceland and the variability of mantle carbon. *Geology* 46, 55–58.
3226 <https://doi.org/10.1130/G39413.1>
3227 Helz, R.T., Thornber, C.R., 1987. Geothermometry of Kilauea Iki lava lake, Hawaii. *Bulletin of Volcanology* 49,
3228 651–668. <https://doi.org/10.1007/BF01080357>
3229 Hernandez Nava, A., Black, B.A., Gibson, S.A., Bodnar, R.J., Renne, P.R., Vanderkluyzen, L., 2021. Reconciling
3230 early Deccan Traps CO₂ outgassing and pre-KPB global climate. *Proc Natl Acad Sci USA* 118,
3231 e2007797118. <https://doi.org/10.1073/pnas.2007797118>
3232 Hernandez, P.R., Woodcock, A., Estrada, M., Schultz, P.W., 2018. Undergraduate Research Experiences
3233 Broaden Diversity in the Scientific Workforce. *BioScience* 68, 204–211.
3234 <https://doi.org/10.1093/biosci/bix163>
3235 Herzberg, C., 2004. Partial Crystallization of Mid-Ocean Ridge Basalts in the Crust and Mantle. *Journal of*
3236 *Petrology* 45, 2389–2405. <https://doi.org/10.1093/petrology/egh040>
3237 Heywood, L.J., DeBari, S.M., Gill, J.B., Straub, S.M., Schindlbeck-Belo, J.C., Escobar-Burciaga, R.D., Woodhead,
3238 J., 2020. Across-Arc Diversity in Rhyolites From an Intra-oceanic Arc: Evidence From IODP Site U1437,
3239 Izu-Bonin Rear Arc, and Surrounding Area. *Geochem. Geophys. Geosyst.* 21.
3240 <https://doi.org/10.1029/2019GC008353>
3241 Higgins, O., Sheldrake, T., Caricchi, L., 2022. Machine learning thermobarometry and chemometry using
3242 amphibole and clinopyroxene: a window into the roots of an arc volcano (Mount Liamuiga, Saint
3243 Kitts). *Contrib Mineral Petrol* 177, 10. <https://doi.org/10.1007/s00410-021-01874-6>
3244 Hirschmann, M.M., Ghiorsso, M.S., Davis, F.A., Gordon, S.M., Mukherjee, S., Grove, T.L., Krawczynski, M.,
3245 Medard, E., Till, C.B., 2008. Library of Experimental Phase Relations (LEPR): A database and Web
3246 portal for experimental magmatic phase equilibria data: LIBRARY OF EXPERIMENTAL PHASE
3247 RELATIONS. *Geochem. Geophys. Geosyst.* 9, n/a-n/a. <https://doi.org/10.1029/2007GC001894>
3248 Holland, T., Blundy, J., 1994. Non-ideal interactions in calcic amphiboles and their bearing on amphibole-
3249 plagioclase thermometry. *Contr. Mineral. and Petrol.* 116, 433–447.
3250 <https://doi.org/10.1007/BF00310910>
3251 Holland, T.J.B., Green, E.C.R., Powell, R., 2018. Melting of Peridotites through to Granites: A Simple
3252 Thermodynamic Model in the System KNCFMASHTOCr. *Journal of Petrology* 59, 881–900.
3253 <https://doi.org/10.1093/petrology/egy048>
3254 Holland, T.J.B., Powell, R., 2011. An improved and extended internally consistent thermodynamic dataset for
3255 phases of petrological interest, involving a new equation of state for solids: THERMODYNAMIC

3256 DATASET FOR PHASES OF PETROLOGICAL INTEREST. *Journal of Metamorphic Geology* 29, 333–383.
3257 <https://doi.org/10.1111/j.1525-1314.2010.00923.x>

3258 Holland, T.J.B., Powell, R., 2004. An internally consistent thermodynamic data set for phases of petrological
3259 interest. *Journal of Metamorphic Geology* 16, 309–343. <https://doi.org/10.1111/j.1525-1314.1998.00140.x>

3260
3261 Holland, T.J.B., Powell, R., 1998. An internally consistent thermodynamic data set for phases of petrological
3262 interest. *Journal of Metamorphic Geology* 16, 309–343. <https://doi.org/10.1111/j.1525-1314.1998.00140.x>

3263
3264 Holland, T.J.B., Powell, R., 1990. An enlarged and updated internally consistent thermodynamic dataset with
3265 uncertainties and correlations: the system K₂O–Na₂O–CaO–MgO–MnO–FeO–Fe₂O₃–Al₂O₃–TiO₂–
3266 SiO₂–C–H₂–O₂. *J Metamorph Geol* 8, 89–124. <https://doi.org/10.1111/j.1525-1314.1990.tb00458.x>

3267 Hollister, L., Grissom, G., Peters, E.K., Stowell, H.H., Slsson, V., 1987. Confirmation of the empirical correlation
3268 of Al in hornblende with pressure of solidification of calc-alkaline plutons 72 (3–4): 231–239.

3269 Huang, R., Audétat, A., 2012. The titanium-in-quartz (TitaniQ) thermobarometer: A critical examination and re-
3270 calibration. *Geochimica et Cosmochimica Acta* 84, 75–89. <https://doi.org/10.1016/j.gca.2012.01.009>

3271 Humphreys, M.C.S., Cooper, G.F., Zhang, J., Loewen, M., Kent, A.J.R., Macpherson, C.G., Davidson, J.P., 2019.
3272 Unravelling the complexity of magma plumbing at Mount St. Helens: a new trace element partitioning
3273 scheme for amphibole. *Contrib Mineral Petrol* 174, 9. <https://doi.org/10.1007/s00410-018-1543-5>

3274 Hurai, V., 2010. Fluid inclusion geobarometry: Pressure corrections for immiscible H₂O–CH₄ and H₂O–CO₂
3275 fluids. *Chemical Geology* 278, 201–211. <https://doi.org/10.1016/j.chemgeo.2010.09.014>

3276 Hutchison, W., Mather, T.A., Pyle, D.M., Boyce, A.J., Gleeson, M.L.M., Yirgu, G., Blundy, J.D., Ferguson, D.J.,
3277 Vye-Brown, C., Millar, I.L., Sims, K.W.W., Finch, A.A., 2018. The evolution of magma during continental
3278 rifting: New constraints from the isotopic and trace element signatures of silicic magmas from
3279 Ethiopian volcanoes. *Earth and Planetary Science Letters* 489, 203–218.
3280 <https://doi.org/10.1016/j.epsl.2018.02.027>

3281 Iacono-Marziano, G., Morizet, Y., Le Trong, E., Gaillard, F., 2012. New experimental data and semi-empirical
3282 parameterization of H₂O–CO₂ solubility in mafic melts. *Geochimica et Cosmochimica Acta* 97, 1–23.
3283 <https://doi.org/10.1016/j.gca.2012.08.035>

3284 Iacovino, K., Matthews, S., Wieser, P.E., Moore, G., Begue, F., 2021. VESlcal Part I: An open-source
3285 thermodynamic model engine for mixed volatile (H₂O–CO₂) solubility in silicate melt. *Earth and Space*
3286 *Science*. <https://doi.org/10.1029/2020EA001584>

3287 Iacovino, K., Till, C., 2019. DensityX: A program for calculating the densities of hydrous magmatic liquids from
3288 427–1,627 °C and up to 30 kbar. *Volcanica* 2, 1–10. <https://doi.org/10.30909/vol.02.01.0110>

3289 J. Bodnar, R., 2017. Fluid Inclusions, in: Bobrowsky, P., Marker, B. (Eds.), *Encyclopedia of Engineering Geology*,
3290 *Encyclopedia of Earth Sciences Series*. Springer International Publishing, Cham, pp. 1–5.
3291 https://doi.org/10.1007/978-3-319-39193-9_225-1

3292 Jamshidi, K., Ghasemi, H., Troll, V.R., Sadeghian, M., Dahren, B., 2015. Magma storage and plumbing of
3293 adakite-type post-ophiolite intrusions in the Sabzevar ophiolitic zone, northeast Iran. *Solid Earth* 6,
3294 49–72. <https://doi.org/10.5194/se-6-49-2015>

3295 Jeffery, A.J., Gertisser, R., O’Driscoll, B., Pacheco, J.M., Whitley, S., Pimentel, A., Self, S., 2016. Temporal
3296 evolution of a post-caldera, mildly peralkaline magmatic system: Furnas volcano, São Miguel, Azores.
3297 *Contrib Mineral Petrol* 171, 42. <https://doi.org/10.1007/s00410-016-1235-y>

3298 Jeffery, A.J., Gertisser, R., Self, S., Pimentel, A., O’Driscoll, B., Pacheco, J.M., 2017. Petrogenesis of the
3299 Peralkaline Ignimbrites of Terceira, Azores. *Journal of Petrology* 58, 2365–2402.
3300 <https://doi.org/10.1093/petrology/egy012>

3301 Jennings, E.S., Gibson, S.A., MacLennan, J., 2019. Hot primary melts and mantle source for the Paraná-Etendeka
3302 flood basalt province: New constraints from Al-in-olivine thermometry. *Chemical Geology* 529,
3303 119287. <https://doi.org/10.1016/j.chemgeo.2019.119287>

3304 Jennings, E.S., Holland, T.J.B., 2015. A Simple Thermodynamic Model for Melting of Peridotite in the System
3305 NCFMASOCr. *Journal of Petrology* 56, 869–892. <https://doi.org/10.1093/petrology/egv020>

3306 Johnson, E.R., Cashman, K.V., 2020. Understanding the storage conditions and fluctuating eruption style of a
3307 young monogenetic volcano: Blue Lake crater (<3 ka), High Cascades, Oregon. *Journal of Volcanology*
3308 *and Geothermal Research* 408, 107103. <https://doi.org/10.1016/j.jvolgeores.2020.107103>

3309 Johnson, M.C., Rutherford, M.J., 1989. Experimental calibration of the aluminum-in-hornblende geobarometer
3310 with application to Long Valley caldera (California) volcanic rocks. *Geol* 17, 837.
3311 [https://doi.org/10.1130/0091-7613\(1989\)017<0837:ECOTAI>2.3.CO;2](https://doi.org/10.1130/0091-7613(1989)017<0837:ECOTAI>2.3.CO;2)

3312 Jorgenson, C., Caricchi, L., Stueckelberger, M., Fevola, G., Weber, G., 2021. A myriad of melt inclusions: a
3313 synchrotron microtomography study of melt inclusions and vapour bubbles from Colli Albani (Italy)
3314 (other). *pico*. <https://doi.org/10.5194/egusphere-egu21-13287>
3315 Jorgenson, C., Higgins, O., Petrelli, M., Bégué, F., Caricchi, L., 2022. A Machine Learning-Based Approach to
3316 Clinopyroxene Thermobarometry: Model Optimization and Distribution for Use in Earth Sciences. *JGR*
3317 *Solid Earth* 127. <https://doi.org/10.1029/2021JB022904>
3318 Kawakami, Y., Yamamoto, J., Kagi, H., 2003. Micro-Raman Densimeter for CO₂ Inclusions in Mantle-Derived
3319 Minerals. *Appl Spectrosc* 57, 1333–1339. <https://doi.org/10.1366/000370203322554473>
3320 Kawamoto, T., 1996. Experimental constraints on differentiation and H₂O abundance of calc-alkaline magmas.
3321 *Earth and Planetary Science Letters* 144, 577–589. [https://doi.org/10.1016/S0012-821X\(96\)00182-3](https://doi.org/10.1016/S0012-821X(96)00182-3)
3322 Kawasaki, T., Osanai, Y., 2008. Empirical thermometer of TiO₂ in quartz for ultrahigh-temperature granulites of
3323 East Antarctica. *Geological Society, London, Special Publications* 308, 419–430.
3324 <https://doi.org/10.1144/SP308.21>
3325 Keppler, H., 1989. The influence of the fluid phase composition on the solidus temperatures in the
3326 haplogranite system NaAlSi₃O₈-KAlSi₃O₈-SiO₂-H₂O-CO₂. *Contrib Mineral Petrol* 102, 321–327.
3327 <https://doi.org/10.1007/BF00373725>
3328 King, P.L., Holloway, J.R., 2002. CO₂ solubility and speciation in intermediate (andesitic) melts: the role of H₂O
3329 and composition. *Geochimica et Cosmochimica Acta* 66, 1627–1640. [https://doi.org/10.1016/S0016-](https://doi.org/10.1016/S0016-7037(01)00872-9)
3330 [7037\(01\)00872-9](https://doi.org/10.1016/S0016-7037(01)00872-9)
3331 Klein, B.Z., Jagoutz, O., Schmidt, M.W., Kueter, N., 2023. A Global Assessment of the Controls on the
3332 Fractionation of Arc Magmas. *Geochem Geophys Geosyst* 24, e2023GC010888.
3333 <https://doi.org/10.1029/2023GC010888>
3334 Klöcking, M., Wyborn, L., Lehnert, K.A., Ware, B., Prent, A.M., Profeta, L., Kohlmann, F., Noble, W., Bruno, I.,
3335 Lambert, S., Ananuer, H., Barber, N.D., Becker, H., Brodbeck, M., Deng, H., Deng, K., Elger, K., De
3336 Souza Franco, G., Gao, Y., Ghasera, K.M., Hezel, D.C., Huang, J., Kerswell, B., Koch, H., Lanati, A.W., Ter
3337 Maat, G., Martínez-Villegas, N., Nana Yobo, L., Redaa, A., Schäfer, W., Swing, M.R., Taylor, R.J.M.,
3338 Traun, M.K., Whelan, J., Zhou, T., 2023. Community recommendations for geochemical data, services
3339 and analytical capabilities in the 21st century. *Geochimica et Cosmochimica Acta* 351, 192–205.
3340 <https://doi.org/10.1016/j.gca.2023.04.024>
3341 Klügel, A., 1998. Reactions between mantle xenoliths and host magma beneath La Palma (Canary Islands):
3342 constraints on magma ascent rates and crustal reservoirs. *Contributions to Mineralogy and Petrology*
3343 131, 237–257.
3344 Klügel, A., Day, S., Schmid, M., Faria, B., 2020. Magma Plumbing During the 2014–2015 Eruption of Fogo (Cape
3345 Verde Islands). *Front. Earth Sci.* 8, 157. <https://doi.org/10.3389/feart.2020.00157>
3346 Kobayashi, T., Yamamoto, J., Hirajima, T., Ishibashi, H., Hirano, N., Lai, Y., Prikhod'ko, V.S., Arai, S., 2012.
3347 Conformity and precision of CO₂ densimetry in CO₂ inclusions: microthermometry *versus* Raman
3348 microspectroscopic densimetry: Conformity and precision of CO₂ densimetry in CO₂ inclusions. *J.*
3349 *Raman Spectrosc.* 43, 1126–1133. <https://doi.org/10.1002/jrs.3134>
3350 Kohn, M.J., 2014. “Thermoba-Raman-try”: Calibration of spectroscopic barometers and thermometers for
3351 mineral inclusions. *Earth and Planetary Science Letters* 388, 187–196.
3352 <https://doi.org/10.1016/j.epsl.2013.11.054>
3353 Koleszar, A.M., Kent, A.J.R., Wallace, P.J., Scott, W.E., 2012. Controls on long-term low explosivity at andesitic
3354 arc volcanoes: Insights from Mount Hood, Oregon. *Journal of Volcanology and Geothermal Research*
3355 219–220, 1–14. <https://doi.org/10.1016/j.jvolgeores.2012.01.003>
3356 Krawczynski, M.J., Grove, T.L., Behrens, H., 2012. Amphibole stability in primitive arc magmas: effects of
3357 temperature, H₂O content, and oxygen fugacity. *Contrib Mineral Petrol* 164, 317–339.
3358 <https://doi.org/10.1007/s00410-012-0740-x>
3359 Kress, V.C., Ghiorso, M.S., 2004. Thermodynamic modeling of post-entrapment crystallization in igneous
3360 phases. *Journal of Volcanology and Geothermal Research* 137, 247–260.
3361 <https://doi.org/10.1016/j.jvolgeores.2004.05.012>
3362 Lamadrid, H.M., Moore, L.R., Moncada, D., Rimstidt, J.D., Burruss, R.C., Bodnar, R.J., 2017. Reassessment of the
3363 Raman CO₂ densimeter. *Chemical Geology* 450, 210–222.
3364 <https://doi.org/10.1016/j.chemgeo.2016.12.034>
3365 Larocque, J., Canil, D., 2010. The role of amphibole in the evolution of arc magmas and crust: the case from the
3366 Jurassic Bonanza arc section, Vancouver Island, Canada. *Contrib Mineral Petrol* 159, 475–492.
3367 <https://doi.org/10.1007/s00410-009-0436-z>

3368 Le Voyer, M., Kelley, K.A., Cottrell, E., Hauri, E.H., 2017. Heterogeneity in mantle carbon content from CO₂-
3369 undersaturated basalts. *Nat Commun* 8, 14062. <https://doi.org/10.1038/ncomms14062>

3370 Leahy, G.M., Collins, J.A., Wolfe, C.J., Laske, G., Solomon, S.C., 2010. Underplating of the Hawaiian Swell:
3371 evidence from teleseismic receiver functions: Underplating of the Hawaiian Swell. *Geophysical Journal*
3372 *International* 183, 313–329. <https://doi.org/10.1111/j.1365-246X.2010.04720.x>

3373 Lee, C.-T.A., Anderson, D.L., 2015. Continental crust formation at arcs, the arclogite “delamination” cycle, and
3374 one origin for fertile melting anomalies in the mantle. *Science Bulletin* 60, 1141–1156.
3375 <https://doi.org/10.1007/s11434-015-0828-6>

3376 Lerner, Allan H., Sublett, D.M., Cauley, C., Wallace, P., Bodnar, R.J., 2021. Magma storage depths and excess
3377 CO₂ fluids from the explosive Keanakakoi tephra (Kilauea Volcano, Hawaii) based on measurements
3378 of melt and fluid inclusions.

3379 Lerner, A. H., Wallace, P., Shea, T., 2021. The petrologic and degassing behavior of sulfur and other magmatic
3380 volatiles from the 2018 eruption of Kilauea, Hawai'i: melt concentrations, magma storage depths, and
3381 magma recycling. *Bulletin Volcanology* 83:43, 1–32.

3382 Li, X., Kind, R., Yuan, X., Wölbern, I., Hanka, W., 2004. Rejuvenation of the lithosphere by the Hawaiian plume.
3383 *Nature* 427, 827–829. <https://doi.org/10.1038/nature02349>

3384 Liang, Y., Sun, C., Yao, L., 2013. A REE-in-two-pyroxene thermometer for mafic and ultramafic rocks.
3385 *Geochimica et Cosmochimica Acta* 102, 246–260. <https://doi.org/10.1016/j.gca.2012.10.035>

3386 Lissenberg, C.J., MacLeod, C.J., 2016. A Reactive Porous Flow Control on Mid-ocean Ridge Magmatic Evolution.
3387 *Journal of Petrology* 57, 2195–2220. <https://doi.org/10.1093/petrology/egw074>

3388 Liu, Y., Zhang, Y., Behrens, H., 2005. Solubility of H₂O in rhyolitic melts at low pressures and a new empirical
3389 model for mixed H₂O–CO₂ solubility in rhyolitic melts. *Journal of Volcanology and Geothermal*
3390 *Research* 143, 219–235. <https://doi.org/10.1016/j.jvolgeores.2004.09.019>

3391 Lones, M.A., 2021. How to avoid machine learning pitfalls: a guide for academic researchers. arXiv:2108.02497
3392 [cs].

3393 Loucks, R.R., 1996. A precise olivine-augite Mg-Fe-exchange geothermometer. *Contributions to Mineralogy*
3394 *and Petrology* 125, 140–150. <https://doi.org/10.1007/s004100050211>

3395 Lowenstern, J.B., 2003. Melt inclusions come of age: Volatiles, volcanoes, and sorby's legacy, in: *Developments*
3396 *in Volcanology*. Elsevier, pp. 1–21. [https://doi.org/10.1016/S1871-644X\(03\)80021-9](https://doi.org/10.1016/S1871-644X(03)80021-9)

3397 Ludden, J.N., 1978. Magmatic evolution of the basaltic shield volcanoes of Reunion Island. *Journal of*
3398 *Volcanology and Geothermal Research* 4, 171–198. [https://doi.org/10.1016/0377-0273\(78\)90035-5](https://doi.org/10.1016/0377-0273(78)90035-5)

3399 Luo, B., Wang, Z., Song, J., Qian, Y., He, Q., Li, Y., Head, J.W., Moynier, F., Xiao, L., Becker, H., 2023. The
3400 magmatic architecture and evolution of the Chang'e-5 lunar basalts. *Nature Geoscience* 1–8.

3401 Mackwell, S.J., Kohlstedt, D.L., 1990. Diffusion of hydrogen in olivine: Implications for water in the mantle. *J.*
3402 *Geophys. Res.* 95, 5079. <https://doi.org/10.1029/JB095iB04p05079>

3403 Maclennan, J., 2017. Bubble formation and decrepitation control the CO₂ content of olivine-hosted melt
3404 inclusions. *Geochemistry, Geophysics, Geosystems* 18, 597–616.
3405 <https://doi.org/10.1002/2016GC006633>

3406 Maclennan, J., 2008. Concurrent Mixing and Cooling of Melts under Iceland. *Journal of Petrology* 49, 1931–
3407 1953. <https://doi.org/10.1093/petrology/egn052>

3408 Maclennan, J., McKenzie, D., Gronvöld, K., Slater, L., 2001. Crustal accretion under northern Iceland. *Earth and*
3409 *Planetary Science Letters* 191, 295–310. [https://doi.org/10.1016/S0012-821X\(01\)00420-4](https://doi.org/10.1016/S0012-821X(01)00420-4)

3410 Mandler, B.E., Donnelly-Nolan, J.M., Grove, T.L., 2014. Straddling the tholeiitic/calc-alkaline transition: the
3411 effects of modest amounts of water on magmatic differentiation at Newberry Volcano, Oregon.
3412 *Contrib Mineral Petrol* 168, 1066. <https://doi.org/10.1007/s00410-014-1066-7>

3413 Marxer, F., Ulmer, P., Müntener, O., 2022. Polybaric fractional crystallisation of arc magmas: an experimental
3414 study simulating trans-crustal magmatic systems. *Contrib Mineral Petrol* 177, 3.
3415 <https://doi.org/10.1007/s00410-021-01856-8>

3416 Masotta, M., Mollo, S., 2019. A New Plagioclase–Liquid Hygrometer Specific to Trachytic Systems. *Minerals* 9,
3417 375. <https://doi.org/10.3390/min9060375>

3418 Masotta, M., Mollo, S., Freda, C., Gaeta, M., Moore, G., 2013. Clinopyroxene–liquid thermometers and
3419 barometers specific to alkaline differentiated magmas. *Contrib Mineral Petrol* 166, 1545–1561.
3420 <https://doi.org/10.1007/s00410-013-0927-9>

3421 Matthews, S., Shorttle, O., Maclennan, J., 2016. The temperature of the Icelandic mantle from olivine-spinel
3422 aluminum exchange thermometry. *Geochemistry, Geophysics, Geosystems* 17, 4725–4752.
3423 <https://doi.org/10.1002/2016GC006497>

3424 Matthews, S., Wong, K., Shorttle, O., Edmonds, M., Maclennan, J., 2021. Do Olivine Crystallization
3425 Temperatures Faithfully Record Mantle Temperature Variability? *Geochem Geophys Geosyst* 22.
3426 <https://doi.org/10.1029/2020GC009157>

3427 McNab, F., Ball, P., 2023. meltPT: A Python package for basaltic whole-rock thermobarometric analysis with
3428 application to Hawai'i. *Volcanica* 6, 63–76. <https://doi.org/10.30909/vol.06.01.6376>

3429 Médard, E., Le Pennec, J.-L., 2022. Petrologic imaging of the magma reservoirs that feed large silicic eruptions.
3430 *Lithos* 428–429, 106812. <https://doi.org/10.1016/j.lithos.2022.106812>

3431 Mironov, N., Portnyagin, M., Botcharnikov, R., Gurenko, A., Hoernle, K., Holtz, F., 2015. Quantification of the
3432 CO₂ budget and H₂O–CO₂ systematics in subduction-zone magmas through the experimental
3433 hydration of melt inclusions in olivine at high H₂O pressure. *Earth and Planetary Science Letters* 425,
3434 1–11. <https://doi.org/10.1016/j.epsl.2015.05.043>

3435 Molina, José F., Cambeses, A., Moreno, J.A., Morales, I., Lázaro, C., Montero, P., Bea, F., 2021. A Cautionary
3436 Note on Amphibole Geobarometry, in: *The 2nd International Electronic Conference on Mineral
3437 Science*. Presented at the IECMS 2021, MDPI, p. 17. <https://doi.org/10.3390/iecms2021-09346>

3438 Molina, José Francisco, Cambeses, A., Moreno, J.A., Morales, I., Montero, P., Bea, F., 2021. A reassessment of
3439 the amphibole-plagioclase NaSi-CaAl exchange thermometer with applications to igneous and high-
3440 grade metamorphic rocks. *American Mineralogist* 106, 782–800. <https://doi.org/10.2138/am-2021-7400>

3441

3442 Molina, J.F., Moreno, J.A., Castro, A., Rodríguez, C., Fershtater, G.B., 2015. Calcic amphibole thermobarometry
3443 in metamorphic and igneous rocks: New calibrations based on plagioclase/amphibole Al-Si
3444 partitioning and amphibole/liquid Mg partitioning. *Lithos* 232, 286–305.
3445 <https://doi.org/10.1016/j.lithos.2015.06.027>

3446 Mollo, S., Putirka, K., Misiti, V., Soligo, M., Scarlato, P., 2013. A new test for equilibrium based on
3447 clinopyroxene–melt pairs: Clues on the solidification temperatures of Etnean alkaline melts at post-
3448 eruptive conditions. *Chemical Geology* 352, 92–100. <https://doi.org/10.1016/j.chemgeo.2013.05.026>

3449 Moore, G., Carmichael, I.S.E., 1998. The hydrous phase equilibria (to 3 kbar) of an andesite and basaltic
3450 andesite from western Mexico: constraints on water content and conditions of phenocryst growth.
3451 *Contributions to Mineralogy and Petrology* 130, 304–319. <https://doi.org/10.1007/s004100050367>

3452 Moore, L.R., Gazel, E., Bodnar, R.J., 2021. The volatile budget of Hawaiian magmatism: Constraints from melt
3453 inclusions from Haleakala volcano, Hawaii. *Journal of Volcanology and Geothermal Research* 410,
3454 107144. <https://doi.org/10.1016/j.jvolgeores.2020.107144>

3455 Moore, L.R., Gazel, E., Tuohy, R., Lloyd, A.S., Esposito, R., Steele-MacInnis, M., Hauri, E.H., Wallace, P.J., Plank,
3456 T., Bodnar, R.J., 2015. Bubbles matter: An assessment of the contribution of vapor bubbles to melt
3457 inclusion volatile budgets. *American Mineralogist* 100, 806–823. <https://doi.org/10.2138/am-2015-5036>

3458

3459 Moore, L.R., Mironov, N., Portnyagin, M., Gazel, E., Bodnar, R.J., 2018. Volatile contents of primitive bubble-
3460 bearing melt inclusions from Klyuchevskoy volcano, Kamchatka: Comparison of volatile contents
3461 determined by mass-balance versus experimental homogenization. *Journal of Volcanology and
3462 Geothermal Research* 358, 124–131. <https://doi.org/10.1016/j.jvolgeores.2018.03.007>

3463 Müntener, O., Kelemen, P.B., Grove, T.L., 2001. The role of H₂O during crystallization of primitive arc magmas
3464 under uppermost mantle conditions and genesis of igneous pyroxenites: an experimental study.
3465 *Contrib Mineral Petrol* 141, 643–658. <https://doi.org/10.1007/s004100100266>

3466 Mutch, E.J.F., Blundy, J.D., Tattitch, B.C., Cooper, F.J., Brooker, R.A., 2016. An experimental study of amphibole
3467 stability in low-pressure granitic magmas and a revised Al-in-hornblende geobarometer. *Contrib
3468 Mineral Petrol* 171, 85. <https://doi.org/10.1007/s00410-016-1298-9>

3469 Mutch, E.J.F., Maclennan, J., Holland, T.J.B., Buisman, I., 2019a. Millennial storage of near-Moho magma.
3470 *Science* 365, 260–264. <https://doi.org/10.1126/science.aax4092>

3471 Mutch, E.J.F., Maclennan, J., Madden-Nadeau, A.L., 2022. The dichotomous nature of Mg partitioning between
3472 plagioclase and melt: Implications for diffusion chronometry. *Geochimica et Cosmochimica Acta* 339,
3473 173–189. <https://doi.org/10.1016/j.gca.2022.10.035>

3474 Mutch, E.J.F., Maclennan, J., Shorttle, O., Edmonds, M., Rudge, J.F., 2019b. Rapid transcrustal magma
3475 movement under Iceland. *Nat. Geosci.* 12, 569–574. <https://doi.org/10.1038/s41561-019-0376-9>

3476 Nakatani, T., Kudo, T., Suzuki, T., 2022. Experimental Constraints on Magma Storage Conditions of Two
3477 Caldera-Forming Eruptions at Towada Volcano, Japan. *JGR Solid Earth* 127.
3478 <https://doi.org/10.1029/2021JB023665>

3479 Nandedkar, R.H., Ulmer, P., Müntener, O., 2014. Fractional crystallization of primitive, hydrous arc magmas: an
3480 experimental study at 0.7 GPa. *Contrib Mineral Petrol* 167, 1015. <https://doi.org/10.1007/s00410->
3481 014-1015-5

3482 Neave, D.A., Bali, E., Guðfinnsson, G.H., Halldórsson, S.A., Kahl, M., Schmidt, A.-S., Holtz, F., 2019.
3483 Clinopyroxene–Liquid Equilibria and Geothermobarometry in Natural and Experimental Tholeiites: the
3484 2014–2015 Holuhraun Eruption, Iceland. *Journal of Petrology* 60, 1653–1680.
3485 <https://doi.org/10.1093/petrology/egz042>

3486 Neave, D.A., Hartley, M.E., Maclennan, J., Edmonds, M., Thordarson, T., 2017. Volatile and light lithophile
3487 elements in high-anorthite plagioclase-hosted melt inclusions from Iceland. *Geochimica et*
3488 *Cosmochimica Acta* 205, 100–118. <https://doi.org/10.1016/j.gca.2017.02.009>

3489 Neave, D.A., Putirka, K.D., 2017. A new clinopyroxene–liquid barometer, and implications for magma storage
3490 pressures under Icelandic rift zones. *American Mineralogist* 102, 777–794.
3491 <https://doi.org/10.2138/am-2017-5968>

3492 Newcombe, M.E., Fabbrizio, A., Zhang, Y., Ma, C., Le Voyer, M., Guan, Y., Eiler, J.M., Saal, A.E., Stolper, E.M.,
3493 2014. Chemical zonation in olivine-hosted melt inclusions. *Contrib Mineral Petrol* 168, 1030.
3494 <https://doi.org/10.1007/s00410-014-1030-6>

3495 Newville, M., Stensitzki, T., Allen, D.B., Rawlik, M., Ingargiola, A., Nelson, A., 2016. LMFIT: Non-linear least-
3496 square minimization and curve-fitting for Python. *Astrophysics Source Code Library ascl-1606*.

3497 Nimis, P., 1995. A clinopyroxene geobarometer for basaltic systems based on crystal-structure modeling.
3498 *Contrib Mineral Petrol* 121, 115–125. <https://doi.org/10.1007/s004100050093>

3499 Onuma, K., Tohara, T., 1983. Effect of chromium on phase relations in the join forsterite–anorthite–diopside in
3500 air at 1 atm. *Contributions to Mineralogy and Petrology* 84, 174–181.

3501 Pamukcu, A.S., Gualda, G.A.R., Ghiorsio, M.S., Miller, C.F., McCracken, R.G., 2015. Phase-equilibrium
3502 geobarometers for silicic rocks based on rhyolite–MELTS—Part 3: Application to the Peach Spring Tuff
3503 (Arizona–California–Nevada, USA). *Contrib Mineral Petrol* 169, 33. <https://doi.org/10.1007/s00410->
3504 015-1122-y

3505 Pamukçu, A.S., Gualda, G.A.R., Gravley, D.M., 2021. Rhyolite–MELTS and the storage and extraction of large-
3506 volume crystal-poor rhyolitic melts at the Taupō Volcanic Center: a reply to Wilson et al. (2021).
3507 *Contrib Mineral Petrol* 176, 82. <https://doi.org/10.1007/s00410-021-01840-2>

3508 Pamukçu, A.S., Wright, K.A., Gualda, G.A.R., Gravley, D., 2020. Magma residence and eruption at the Taupo
3509 Volcanic Center (Taupo Volcanic Zone, New Zealand): insights from rhyolite–MELTS geobarometry,
3510 diffusion chronometry, and crystal textures. *Contrib Mineral Petrol* 175, 48.
3511 <https://doi.org/10.1007/s00410-020-01684-2>

3512 Papale, P., Moretti, R., Barbato, D., 2006. The compositional dependence of the saturation surface of
3513 H₂O+CO₂ fluids in silicate melts. *Chemical Geology* 229, 78–95.
3514 <https://doi.org/10.1016/j.chemgeo.2006.01.013>

3515 Parat, F., Streck, M., Holtz, F., Almeev, R.R., 2014. Experimental study into the petrogenesis of crystal-rich
3516 basaltic to andesitic magmas at Arenal volcano. *Contributions to Mineralogy and Petrology*.

3517 Paszke, A., Gross, S., Massa, F., Lerer, A., Bradbury, J., Chanan, G., Killeen, T., Lin, Z., Gimelshein, N., Antiga, L.,
3518 2019. Pytorch: An imperative style, high-performance deep learning library. *Advances in neural*
3519 *information processing systems* 32.

3520 Peccerillo, A., 2003. Relationships between Mafic and Peralkaline Silicic Magmatism in Continental Rift
3521 Settings: a Petrological, Geochemical and Isotopic Study of the Gedemsa Volcano, Central Ethiopian
3522 Rift. *Journal of Petrology* 44, 2003–2032. <https://doi.org/10.1093/petrology/egg068>

3523 Pecher, A., 1981. Experimental decrepitation and re-equilibration of fluid inclusions in synthetic quartz.
3524 *Tectonophysics* 78, 567–583. [https://doi.org/10.1016/0040-1951\(81\)90029-9](https://doi.org/10.1016/0040-1951(81)90029-9)

3525 Perinelli, C., Mollo, S., Gaeta, M., De Cristofaro, S.P., Palladino, D.M., Armienti, P., Scarlato, P., Putirka, K.D.,
3526 2016. An improved clinopyroxene-based hygrometer for Etnean magmas and implications for
3527 eruption triggering mechanisms. *American Mineralogist* 101, 2774–2777.
3528 <https://doi.org/10.2138/am-2016-5916>

3529 Petrelli, M., Caricchi, L., Perugini, D., 2020. Machine Learning Thermo-Barometry: Application to
3530 Clinopyroxene-Bearing Magmas. *J. Geophys. Res. Solid Earth* 125.
3531 <https://doi.org/10.1029/2020JB020130>

3532 Pineda, C., Hammer, J., First, E., Morata, D., 2021. Storage conditions of a caldera-forming volcanic eruption:
3533 Insights from the Pudahuel rhyolitic ignimbrite in central Chile (32° 10'S). *Lithos* 400–401, 106382.
3534 <https://doi.org/10.1016/j.lithos.2021.106382>

3535 Plank, T., Kelley, K.A., Zimmer, M.M., Hauri, E.H., Wallace, P.J., 2013. Why do mafic arc magmas contain
3536 ~4wt% water on average? *Earth and Planetary Science Letters* 364, 168–179.
3537 <https://doi.org/10.1016/j.epsl.2012.11.044>

3538 Powell, R., Holland, T., Worley, B., 1998. Calculating phase diagrams involving solid solutions via non-linear
3539 equations, with examples using THERMOCALC. *Journal of metamorphic Geology* 16, 577–588.

3540 Prissel, T.C., Parman, S.W., Head, J.W., 2016. Formation of the lunar highlands Mg-suite as told by spinel.
3541 *American Mineralogist* 101, 1624–1635. <https://doi.org/10.2138/am-2016-5581>

3542 Pritchard, M.E., Mather, T.A., McNutt, S.R., Delgado, F.J., Reath, K., 2019. Thoughts on the criteria to
3543 determine the origin of volcanic unrest as magmatic or non-magmatic. *Phil. Trans. R. Soc. A* 377,
3544 20180008. <https://doi.org/10.1098/rsta.2018.0008>

3545 Profeta, L., Ducea, M.N., Chapman, J.B., Paterson, S.R., Gonzales, S.M.H., Kirsch, M., Petrescu, L., DeCelles,
3546 P.G., 2016. Quantifying crustal thickness over time in magmatic arcs. *Sci Rep* 5, 17786.
3547 <https://doi.org/10.1038/srep17786>

3548 Pu, X., Lange, R.A., Moore, G., 2017. A comparison of olivine-melt thermometers based on D_{Mg} and D_{Ni} : The
3549 effects of melt composition, temperature, and pressure with applications to MORBs and hydrous arc
3550 basalts. *American Mineralogist* 102, 750–765. <https://doi.org/10.2138/am-2017-5879>

3551 Pu, X., Moore, G.M., Lange, R.A., Touran, J.P., Gagnon, J.E., 2021. Experimental evaluation of a new H₂O-
3552 independent thermometer based on olivine-melt Ni partitioning at crustal pressure. *American*
3553 *Mineralogist* 106, 235–250. <https://doi.org/10.2138/am-2020-7014>

3554 Putirka, K., 2017. Geothermometry and geobarometry. *Encyclopedia of Geochemistry: A Comprehensive*
3555 *Reference Source on the Chemistry of the Earth*, edited by: White, WM, Springer International
3556 Publishing, Cham, Switzerland 597–614.

3557 Putirka, K., 2016. Amphibole thermometers and barometers for igneous systems and some implications for
3558 eruption mechanisms of felsic magmas at arc volcanoes. *American Mineralogist* 101, 841–858.
3559 <https://doi.org/10.2138/am-2016-5506>

3560 Putirka, K., 1999. Clinopyroxene + liquid equilibria to 100 kbar and 2450 K. *Contributions to Mineralogy and*
3561 *Petrology* 135, 151–163. <https://doi.org/10.1007/s004100050503>

3562 Putirka, K., Johnson, M., Kinzler, R., Longhi, J., Walker, D., 1996. Thermobarometry of mafic igneous rocks
3563 based on clinopyroxene-liquid equilibria, 0-30 kbar. *Contributions to Mineralogy and Petrology* 123,
3564 92–108. <https://doi.org/10.1007/s004100050145>

3565 Putirka, K.D., 2008. Thermometers and Barometers for Volcanic Systems. *Reviews in Mineralogy and*
3566 *Geochemistry* 69, 61–120. <https://doi.org/10.2138/rmg.2008.69.3>

3567 Putirka, K.D., 2005. Igneous thermometers and barometers based on plagioclase + liquid equilibria: Tests of
3568 some existing models and new calibrations. *American Mineralogist* 90, 336–346.
3569 <https://doi.org/10.2138/am.2005.1449>

3570 Putirka, K.D., Mikaelian, H., Ryerson, F., Shaw, H., 2003. New clinopyroxene-liquid thermobarometers for
3571 mafic, evolved, and volatile-bearing lava compositions, with applications to lavas from Tibet and the
3572 Snake River Plain, Idaho. *American Mineralogist* 88, 1542–1554. <https://doi.org/10.2138/am-2003-1017>

3573

3574 Qin, Z., Lu, F., Anderson, A., 1992. Diffusive reequilibration of melt and fluid inclusions. *American Mineralogist*
3575 77(506), 565–576.

3576 Quinn, E., 2014. Experimental Determination of Pre-Eruptive Storage Conditions And Continuous
3577 Decompression of Rhyodacite Magma Erupted from Chaos Crags, Lassen Volcanic Center, California.
3578 MSci thesis, Humboldt State University.

3579 Rader, E.L., Larsen, J.F., 2013. Experimental phase relations of a low MgO Aleutian basaltic andesite at XH₂O =
3580 0.7–1. *Contrib Mineral Petrol* 166, 1593–1611. <https://doi.org/10.1007/s00410-013-0944-8>

3581 Ranero, C.R., Torne, M., Banda, E., 1995. Gravity and multichannel seismic reflection constraints on the
3582 lithospheric structure of the Canary Swell. *Mar Geophys Res* 17, 519–534.
3583 <https://doi.org/10.1007/BF01204342>

3584 Rasmussen, D.J., Kyle, P.R., Wallace, P.J., Sims, K.W.W., Gaetani, G.A., Phillips, E.H., 2017. Understanding
3585 Degassing and Transport of CO₂-rich Alkalic Magmas at Ross Island, Antarctica using Olivine-Hosted
3586 Melt Inclusions. *Journal of Petrology*. <https://doi.org/10.1093/petrology/egx036>

3587 Rasmussen, D.J., Plank, T.A., Roman, D.C., Zimmer, M.M., 2022. Magmatic water content controls the pre-
3588 eruptive depth of arc magmas. *Science* 375, 1169–1172. <https://doi.org/10.1126/science.abm5174>

3589 Rasmussen, D.J., Plank, T.A., Wallace, P.J., Newcombe, M.E., Lowenstern, J.B., 2020. Vapor-bubble growth in
3590 olivine-hosted melt inclusions. *American Mineralogist* 105, 1898–1919. <https://doi.org/10.2138/am-2020-7377>

3591

3592 Reubi, O., Blundy, J., 2009. A dearth of intermediate melts at subduction zone volcanoes and the petrogenesis
3593 of arc andesites. *Nature* 461, 1269–1273. <https://doi.org/10.1038/nature08510>

3594 Ridolfi, F., 2021. Amp-TB2: An Updated Model for Calcic Amphibole Thermobarometry. *Minerals* 11, 324.
3595 <https://doi.org/10.3390/min11030324>

3596 Ridolfi, F., Renzulli, A., 2012. Calcic amphiboles in calc-alkaline and alkaline magmas: thermobarometric and
3597 chemometric empirical equations valid up to 1,130°C and 2.2 GPa. *Contrib Mineral Petrol* 163, 877–
3598 895. <https://doi.org/10.1007/s00410-011-0704-6>

3599 Ridolfi, F., Renzulli, A., Puerini, M., 2010. Stability and chemical equilibrium of amphibole in calc-alkaline
3600 magmas: an overview, new thermobarometric formulations and application to subduction-related
3601 volcanoes. *Contrib Mineral Petrol* 160, 45–66. <https://doi.org/10.1007/s00410-009-0465-7>

3602 Riel, N., Kaus, B.J.P., Green, E.C.R., Berlie, N., 2022. MAGEMin, an Efficient Gibbs Energy Minimizer: Application
3603 to Igneous Systems. *Geochem Geophys Geosyst* 23. <https://doi.org/10.1029/2022GC010427>

3604 Riker, J.M., 2005. The 1859 eruption of Mauna Loa Volcano, Hawai'i. Controls on the development of long lava
3605 channels. University of Oregon PhD thesis.

3606 Robidou, P., Frezzotti, M.L., Hauri, E.H., Aiuppa, A., 2018. Shrinkage Bubbles: The C–O–H–S Magmatic Fluid
3607 System at San Cristóbal Volcano. *Journal of Petrology* 59, 2093–2122.
3608 <https://doi.org/10.1093/petrology/egy092>

3609 Roedder, E., 1984. Fluid Inclusions, Reviews in Mineralogy. Mineralogical Society of America.

3610 Ronga, F., Lustrino, M., Marzoli, A., Melluso, L., 2010. Petrogenesis of a basalt-comendite-pantellerite rock
3611 suite: the Boseti Volcanic Complex (Main Ethiopian Rift). *Miner Petrol* 98, 227–243.
3612 <https://doi.org/10.1007/s00710-009-0064-3>

3613 Rose-Koga, E.F., Bouvier, A.-S., Gaetani, G.A., Wallace, P.J., Allison, C.M., Andrys, J.A., Angeles de la Torre, C.A.,
3614 Barth, A., Bodnar, R.J., Bracco Gartner, A.J.J., Butters, D., Castillejo, A., Chilson-Parks, B., Choudhary,
3615 B.R., Cluzel, N., Cole, M., Cottrell, E., Daly, A., Danyushevsky, L.V., DeVitre, C.L., Drignon, M.J., France,
3616 L., Gaborieau, M., Garcia, M.O., Gatti, E., Genske, F.S., Hartley, M.E., Hughes, E.C., Iveson, A.A.,
3617 Johnson, E.R., Jones, M., Kagoshima, T., Katzir, Y., Kawaguchi, M., Kawamoto, T., Kelley, K.A.,
3618 Koornneef, J.M., Kurz, M.D., Laubier, M., Layne, G.D., Lerner, A., Lin, K.-Y., Liu, P.-P., Lorenzo-Merino,
3619 A., Luciani, N., Magalhães, N., Marschall, H.R., Michael, P.J., Monteleone, B.D., Moore, L.R.,
3620 Moussallam, Y., Muth, M., Myers, M.L., Narváez, D.F., Navon, O., Newcombe, M.E., Nichols, A.R.L.,
3621 Nielsen, R.L., Pamukcu, A., Plank, T., Rasmussen, D.J., Roberge, J., Schiavi, F., Schwartz, D., Shimizu, K.,
3622 Shimizu, K., Shimizu, N., Thomas, J.B., Thompson, G.T., Tucker, J.M., Ustunisik, G., Waelkens, C.,
3623 Zhang, Y., Zhou, T., 2021. Silicate melt inclusions in the new millennium: A review of recommended
3624 practices for preparation, analysis, and data presentation. *Chemical Geology* 570, 120145.
3625 <https://doi.org/10.1016/j.chemgeo.2021.120145>

3626 Rosso, K.M., Bodnar, R.J., 1995. Microthermometric and Raman spectroscopic detection limits of CO₂ in fluid
3627 inclusions and the Raman spectroscopic characterization of CO₂. *Geochimica et Cosmochimica Acta*
3628 59, 3961–3975. [https://doi.org/10.1016/0016-7037\(95\)94441-H](https://doi.org/10.1016/0016-7037(95)94441-H)

3629 Ruscitto, D.M., Wallace, P.J., Johnson, E.R., Kent, A.J.R., Bindeman, I.N., 2010. Volatile contents of mafic
3630 magmas from cinder cones in the Central Oregon High Cascades: Implications for magma formation
3631 and mantle conditions in a hot arc. *Earth and Planetary Science Letters* 298, 153–161.
3632 <https://doi.org/10.1016/j.epsl.2010.07.037>

3633 Ruscitto, D.M., Wallace, P.J., Kent, A.J.R., 2011. Revisiting the compositions and volatile contents of olivine-
3634 hosted melt inclusions from the Mount Shasta region: implications for the formation of high-Mg
3635 andesites. *Contrib Mineral Petrol* 162, 109–132. <https://doi.org/10.1007/s00410-010-0587-y>

3636 Ruth, D.C.S., Costa, F., 2021. A petrological and conceptual model of Mayon volcano (Philippines) as an
3637 example of an open-vent volcano. *Bull Volcanol* 83, 62. <https://doi.org/10.1007/s00445-021-01486-9>

3638 Rutherford, M.J., 2003. Magmatic Conditions and Magma Ascent as Indicated by Hornblende Phase Equilibria
3639 and Reactions in the 1995–2002 Soufriere Hills Magma. *Journal of Petrology* 44, 1433–1453.
3640 <https://doi.org/10.1093/petrology/44.8.1433>

3641 Rutherford, M.J., Devine, J.D., 1988. The May 18, 1980, eruption of Mount St. Helens: 3. Stability and
3642 chemistry of amphibole in the magma chamber. *J. Geophys. Res.* 93, 11949.
3643 <https://doi.org/10.1029/JB093iB10p11949>

3644 Rutherford, M.J., Sigurdsson, H., Carey, S., Davis, A., 1985. The May 18, 1980, eruption of Mount St. Helens: 1.
3645 Melt composition and experimental phase equilibria. *J. Geophys. Res.* 90, 2929.
3646 <https://doi.org/10.1029/JB090iB04p02929>

3647 Sack, R.O., Ghiorso, M.S., 1994. Thermodynamics of multicomponent pyroxenes: I. Formulation of a general
3648 model. *Contr. Mineral. and Petrol.* 116, 277–286. <https://doi.org/10.1007/BF00306497>

3649 Sack, R.O., Ghiorso, M.S., 1991. An internally consistent model for the thermodynamic properties of Fe²⁺Mg-
3650 titanomagnetite-aluminate spinels. *Contr. Mineral. and Petrol.* 106, 474–505.
3651 <https://doi.org/10.1007/BF00321989>

3652 Sack, R.O., Ghiorso, M.S., 1989. Importance of considerations of mixing properties in establishing an internally
3653 consistent thermodynamic database: thermochemistry of minerals in the system Mg₂SiO₄-Fe₂SiO₄-
3654 SiO₂. *Contr. Mineral. and Petrol.* 102, 41–68. <https://doi.org/10.1007/BF01160190>

3655 Sanfilippo, A., MacLeod, C.J., Tribuzio, R., Lissenberg, C.J., Zanetti, A., 2020. Early-Stage Melt-Rock Reaction in a
3656 Cooling Crystal Mush Beneath a Slow-Spreading Mid-Ocean Ridge (IODP Hole U1473A, Atlantis Bank,
3657 Southwest Indian Ridge). *Front. Earth Sci.* 8, 579138. <https://doi.org/10.3389/feart.2020.579138>

3658 Sas, M., DeBari, S., Clyne, M., Rusk, B., 2017. Using mineral geochemistry to decipher slab, mantle, and crustal
3659 input in the generation of high-Mg andesites and basaltic andesites from the northern Cascade Arc.
3660 *msam.* <https://doi.org/10.2138/am-2017-5756>

3661 Scaillet, B., Macdonald, R., 2001. Phase Relations of Peralkaline Silicic Magmas and Petrogenetic Implications.
3662 *Journal of Petrology* 42, 825–845. <https://doi.org/10.1093/petrology/42.4.825>

3663 Schiavi, F., Bolfan-Casanova, N., Buso, R., Laumonier, M., Laporte, D., Medjoubi, K., Venugopal, S., Gómez-Ulla,
3664 A., Cluzel, N., Hardiagon, M., 2020. Quantifying magmatic volatiles by Raman microtomography of
3665 glass inclusion-hosted bubbles. *Geochem. Persp. Lett.* 16, 17–24.
3666 <https://doi.org/10.7185/geochemlet.2038>

3667 Schmidt, M.W., 1992. Amphibole composition in tonalite as a function of pressure: an experimental calibration
3668 of the Al-in-hornblende barometer. *Contr. Mineral. and Petrol.* 110, 304–310.
3669 <https://doi.org/10.1007/BF00310745>

3670 Scruggs, M.A., Putirka, K.D., 2018. Eruption triggering by partial crystallization of mafic enclaves at Chaos
3671 Crag, Lassen Volcanic Center, California. *American Mineralogist* 103, 1575–1590.
3672 <https://doi.org/10.2138/am-2018-6058>

3673 Shamloo, H.I., Till, C.B., 2019. Decadal transition from quiescence to supereruption: petrologic investigation of
3674 the Lava Creek Tuff, Yellowstone Caldera, WY. *Contrib Mineral Petrol* 174, 32.
3675 <https://doi.org/10.1007/s00410-019-1570-x>

3676 Shedden, K., 2008. Gene expression–based survival prediction in lung adenocarcinoma: a multi-site, blinded
3677 validation study. *Nat Med* 14, 822–827. <https://doi.org/10.1038/nm.1790>

3678 Sheehan, F., Barclay, J., 2016. Staged storage and magma convection at Ambrym volcano, Vanuatu. *Journal of*
3679 *Volcanology and Geothermal Research* 322, 144–157.
3680 <https://doi.org/10.1016/j.jvolgeores.2016.02.024>

3681 Shi, P., 1993. Low-Pressure Phase Relationships in the System Na₂O–CaO–FeO–MgO–Al₂O₃–SiO₂ at 1100 C,
3682 with Implications for the Differentiation of Basaltic Magmas. *Journal of Petrology* 34, 743–762.
3683 <https://doi.org/10.1093/petrology/34.4.743>

3684 Shi, P., 1992. Basalt evolution at low pressure: implications from an experimental study in the system CaO-
3685 FeO-MgO-Al₂O₃-SiO₂. *Contr. Mineral. and Petrol.* 110, 139–153.
3686 <https://doi.org/10.1007/BF00310735>

3687 Shi, S., Barth, A., Plank, T., Towbin, W., Flores, O., Arias, C., 2021. Magma stalling weakens eruption. Presented
3688 at the AGU Fall Meeting Abstracts, pp. V25E-09.

3689 Shinohara, H., 2013. Volatile flux from subduction zone volcanoes: Insights from a detailed evaluation of the
3690 fluxes from volcanoes in Japan. *Journal of Volcanology and Geothermal Research* 268, 46–63.
3691 <https://doi.org/10.1016/j.jvolgeores.2013.10.007>

3692 Shishkina, T.A., Botcharnikov, R.E., Holtz, F., Almeev, R.R., Jazwa, A.M., Jakubiak, A.A., 2014. Compositional and
3693 pressure effects on the solubility of H₂O and CO₂ in mafic melts. *Chemical Geology* 388, 112–129.
3694 <https://doi.org/10.1016/j.chemgeo.2014.09.001>

3695 Sides, Edmonds, M., Maclennan, J., Houghton, B.F., Swanson, D.A., Steele-MacInnis, M.J., 2014a. Magma
3696 mixing and high fountaining during the 1959 Kīlauea Iki eruption, Hawai‘i. *Earth and Planetary Science*
3697 *Letters* 400, 102–112. <https://doi.org/10.1016/j.epsl.2014.05.024>

3698 Sides, Edmonds, M., Maclennan, J., Swanson, D.A., Houghton, B.F., 2014b. Eruption style at Kīlauea Volcano in
3699 Hawai‘i linked to primary melt composition. *Nature Geoscience* 7, 464–469.
3700 <https://doi.org/10.1038/ngeo2140>

3701 Sieburg, M., Klügel, A., Rocholl, A., Bach, W., 2018. Magma plumbing and hybrid magma formation at an
3702 active back-arc basin volcano: North Su, eastern Manus basin. *Journal of Volcanology and Geothermal*
3703 *Research* 362, 1–16. <https://doi.org/10.1016/j.jvolgeores.2018.07.001>

3704 Sisson, T.W., Grove, T.L., 1993. Temperatures and H₂O contents of low-MgO high-alumina basalts. *Contr.*
3705 *Mineral. and Petrol.* 113, 167–184. <https://doi.org/10.1007/BF00283226>

3706 Sisson, T.W., Ratajeski, K., Hankins, W.B., Glazner, A.F., 2005. Voluminous granitic magmas from common
3707 basaltic sources. *Contrib Mineral Petrol* 148, 635–661. <https://doi.org/10.1007/s00410-004-0632-9>
3708 Skirius, C., Peterson, J., Anderson Jr., A.T., 1990. Homogenizing rhyolitic glass inclusions from the Bishop Tuff.
3709 *American Mineralogist* 75, 1381–1398.
3710 Solaro, C., Martel, C., Champallier, R., Boudon, G., Balcone-Boissard, H., Pichavant, M., 2019. Petrological and
3711 experimental constraints on magma storage for large pumiceous eruptions in Dominica island (Lesser
3712 Antilles). *Bull Volcanol* 81, 55. <https://doi.org/10.1007/s00445-019-1313-x>
3713 Sorby, H.C., 1858. On the Microscopical, Structure of Crystals, indicating the Origin of Minerals and Rocks.
3714 *QJGS* 14, 453–500. <https://doi.org/10.1144/GSL.JGS.1858.014.01-02.44>
3715 Span, R., Wagner, W., 1996. A New Equation of State for Carbon Dioxide Covering the Fluid Region from the
3716 Triple-Point Temperature to 1100 K at Pressures up to 800 MPa. *Journal of Physical and Chemical*
3717 *Reference Data* 25, 1509–1596. <https://doi.org/10.1063/1.555991>
3718 Spencer, K.J., Lindsley, D.H., 1981. A solution model for coexisting iron–titanium oxides. *American mineralogist*
3719 66, 1189–1201.
3720 Steele-Macinnis, M., Esposito, R., Bodnar, R.J., 2011. Thermodynamic Model for the Effect of Post-entrapment
3721 Crystallization on the H₂O-CO₂ Systematics of Vapor-saturated, Silicate Melt Inclusions. *Journal of*
3722 *Petrology* 52, 2461–2482. <https://doi.org/10.1093/petrology/egr052>
3723 Sterner, S.M., Pitzer, K.S., 1994. An equation of state for carbon dioxide valid from zero to extreme pressures.
3724 *Contr. Mineral. and Petrol.* 117, 362–374. <https://doi.org/10.1007/BF00307271>
3725 Stock, M.J., Bagnardi, M., Neave, D.A., Maclennan, J., Bernard, B., Buisman, I., Gleeson, M.L.M., Geist, D., 2018.
3726 Integrated Petrological and Geophysical Constraints on Magma System Architecture in the Western
3727 Galápagos Archipelago: Insights From Wolf Volcano. *Geochem. Geophys. Geosyst.* 19, 4722–4743.
3728 <https://doi.org/10.1029/2018GC007936>
3729 Sugawara, T., 2001. Ferric iron partitioning between plagioclase and silicate liquid: thermodynamics and
3730 petrological applications. *Contrib Mineral Petrol* 141, 659–686.
3731 <https://doi.org/10.1007/s004100100267>
3732 Sun, C., Liang, Y., 2012. Distribution of REE between clinopyroxene and basaltic melt along a mantle adiabat:
3733 effects of major element composition, water, and temperature. *Contrib Mineral Petrol* 163, 807–823.
3734 <https://doi.org/10.1007/s00410-011-0700-x>
3735 Sun, C., Lissenberg, C.J., 2018. Formation of fast-spreading lower oceanic crust as revealed by a new Mg–REE
3736 coupled geospeedometer. *Earth and Planetary Science Letters* 487, 165–178.
3737 <https://doi.org/10.1016/j.epsl.2018.01.032>
3738 Tamblyn, R., Hand, M., Morrissey, L., Zack, T., Phillips, G., Och, D., 2020. Resubduction of lawsonite eclogite
3739 within a serpentinite-filled subduction channel. *Contrib Mineral Petrol* 175, 74.
3740 <https://doi.org/10.1007/s00410-020-01712-1>
3741 Taracsák, Z., Hartley, M.E., Burgess, R., Edmonds, M., Iddon, F., Longpré, M.-A., 2019. High fluxes of deep
3742 volatiles from ocean island volcanoes: Insights from El Hierro, Canary Islands. *Geochimica et*
3743 *Cosmochimica Acta* 258, 19–36. <https://doi.org/10.1016/j.gca.2019.05.020>
3744 Taura, H., Yurimoto, H., Kurita, K., Sueno, S., 1998. Pressure dependence on partition coefficients for trace
3745 elements between olivine and the coexisting melts. *Physics and Chemistry of Minerals* 25, 469–484.
3746 <https://doi.org/10.1007/s002690050138>
3747 Teplow, W., Marsh, B., Hulen, 2009. Dacite Melt at the Puna Geothermal Venture Wellfield, Big Island of
3748 Hawaii. *GRC Transactions* 33.
3749 Thermoengine Code Contributors, 2022. ThermoEngine: Software for Model Building and Computational
3750 Thermodynamics Supporting Applications in the Earth Sciences.
3751 <https://doi.org/10.5281/ZENODO.6527840>
3752 Thomas, J.B., Bruce Watson, E., 2012. Application of the Ti-in-quartz thermobarometer to rutile-free systems.
3753 Reply to: a comment on: ‘TitaniQ under pressure: the effect of pressure and temperature on the
3754 solubility of Ti in quartz’ by Thomas et al. *Contrib Mineral Petrol* 164, 369–374.
3755 <https://doi.org/10.1007/s00410-012-0761-5>
3756 Thomas, J.B., Bruce Watson, E., Spear, F.S., Shemella, P.T., Nayak, S.K., Lanzirotti, A., 2010. TitaniQ under
3757 pressure: the effect of pressure and temperature on the solubility of Ti in quartz. *Contrib Mineral*
3758 *Petrol* 160, 743–759. <https://doi.org/10.1007/s00410-010-0505-3>
3759 Thomas, W.M., Ernst, W.G., 1990. The aluminum content of hornblende in calc-alkaline granitic rocks: A
3760 mineralogic barometer calibrated experimentally to 12 kbars 6.

3761 Tommasini, S., Bindi, L., Savia, L., Mangler, M.F., Orlando, A., Petrone, C.M., 2022. Critical assessment of
3762 pressure estimates in volcanic plumbing systems: The case study of Popocatepetl volcano, Mexico.
3763 *Lithos* 408–409, 106540. <https://doi.org/10.1016/j.lithos.2021.106540>
3764 Towbin, W.H., Plank, T., Klein, E., Hauri, E., 2023. Measuring H₂O concentrations in olivine by secondary ion
3765 mass spectrometry: Challenges and paths forward. *American Mineralogist: Journal of Earth and
3766 Planetary Materials* 108, 928–940. <https://doi.org/10.2138/am-2022-8247>
3767 Trela, J., Gazel, E., Sobolev, A.V., Moore, L., Bizimis, M., Jicha, B., Batanova, V.G., 2017. The hottest lavas of the
3768 Phanerozoic and the survival of deep Archaean reservoirs. *Nature Geosci* 10, 451–456.
3769 <https://doi.org/10.1038/ngeo2954>
3770 Tucker, J.M., Hauri, E.H., Pietruszka, A.J., Garcia, M.O., Marske, J.P., Trusdell, F.A., 2019. A high carbon content
3771 of the Hawaiian mantle from olivine-hosted melt inclusions. *Geochimica et Cosmochimica Acta* 254,
3772 156–172. <https://doi.org/10.1016/j.gca.2019.04.001>
3773 Tuohy, R.M., Wallace, P.J., Loewen, M.W., Swanson, D.A., Kent, A.J.R., 2016. Magma transport and olivine
3774 crystallization depths in Kīlauea’s east rift zone inferred from experimentally rehomogenized melt
3775 inclusions. *Geochimica et Cosmochimica Acta* 185, 232–250.
3776 <https://doi.org/10.1016/j.gca.2016.04.020>
3777 Ubide, T., Caulfield, J., Brandt, C., Bussweiler, Y., Mollo, S., Di Stefano, F., Nazzari, M., Scarlato, P., 2019a. Deep
3778 Magma Storage Revealed by Multi-Method Elemental Mapping of Clinopyroxene Megacrysts at
3779 Stromboli Volcano. *Front. Earth Sci.* 7, 239. <https://doi.org/10.3389/feart.2019.00239>
3780 Ubide, T., Larrea, P., Becerril, L., Galé, C., 2022. Volcanic plumbing filters on ocean-island basalt geochemistry.
3781 *Geology* 50, 26–31. <https://doi.org/10.1130/G49224.1>
3782 Ubide, T., Mollo, S., Zhao, J., Nazzari, M., Scarlato, P., 2019b. Sector-zoned clinopyroxene as a recorder of
3783 magma history, eruption triggers, and ascent rates. *Geochimica et Cosmochimica Acta* 251, 265–283.
3784 <https://doi.org/10.1016/j.gca.2019.02.021>
3785 Van Den Kerkhof, A.M., 1990. Isochoric phase diagrams in the systems CO₂–CH₄ and CO₂–N₂: Application to
3786 fluid inclusions. *Geochimica et Cosmochimica Acta* 54, 621–629. [https://doi.org/10.1016/0016-
3787 7037\(90\)90358-R](https://doi.org/10.1016/0016-7037(90)90358-R)
3788 Venezky, D.Y., Rutherford, M.J., 1999. Petrology and Fe–Ti oxide reequilibration of the 1991 Mount Unzen
3789 mixed magma. *Journal of Volcanology and Geothermal Research* 89, 213–230.
3790 [https://doi.org/10.1016/S0377-0273\(98\)00133-4](https://doi.org/10.1016/S0377-0273(98)00133-4)
3791 Venugopal, S., Schiavi, F., Moune, S., Bolfan-Casanova, N., Druitt, T., Williams-Jones, G., 2020. Melt inclusion
3792 vapour bubbles: the hidden reservoir for major and volatile elements. *Sci Rep* 10, 9034.
3793 <https://doi.org/10.1038/s41598-020-65226-3>
3794 Villiger, S., 2004. The Liquid Line of Descent of Anhydrous, Mantle-Derived, Tholeiitic Liquids by Fractional and
3795 Equilibrium Crystallization--an Experimental Study at 1{middle dot}0 GPa. *Journal of Petrology* 45,
3796 2369–2388. <https://doi.org/10.1093/petrology/egh042>
3797 Villiger, S., Müntener, O., Ulmer, P., 2007. Crystallization pressures of mid-ocean ridge basalts derived from
3798 major element variations of glasses from equilibrium and fractional crystallization experiments. *J.
3799 Geophys. Res.* 112, B01202. <https://doi.org/10.1029/2006JB004342>
3800 Vogt, J.H.L., 1931. On the Terms Eutectic, Cotectic, Peritectic, Anchi-Eutectic, Anchi-Cotectic, etc., and their
3801 Importance in Petrogenesis. *The Journal of Geology* 39, 401–431. <https://doi.org/10.1086/623862>
3802 Voigt, A., Cassidy, M., Castro, J.M., Pyle, D.M., Mather, T.A., Helo, C., Abdurrachman, M., Kurniawan, I.A., 2022.
3803 Experimental Investigation of Trachydacite Magma Storage Prior to the 1257 Eruption of Mt Samalas.
3804 *Journal of Petrology* 63, egac066. <https://doi.org/10.1093/petrology/egac066>
3805 Voigt, M., Coogan, L.A., von der Handt, A., 2017. Experimental investigation of the stability of clinopyroxene in
3806 mid-ocean ridge basalts: The role of Cr and Ca/Al. *Lithos* 274–275, 240–253.
3807 <https://doi.org/10.1016/j.lithos.2017.01.003>
3808 Wade, J.A., Plank, T., Hauri, E.H., Kelley, K.A., Roggensack, K., Zimmer, M., 2008. Prediction of magmatic water
3809 contents via measurement of H₂O in clinopyroxene phenocrysts. *Geol* 36, 799.
3810 <https://doi.org/10.1130/G24964A.1>
3811 Walker, B.A., Klemetti, E.W., Grunder, A.L., Dilles, J.H., Tepley, F.J., Giles, D., 2013. Crystal reaming during the
3812 assembly, maturation, and waning of an eleven-million-year crustal magma cycle: thermobarometry
3813 of the Aucanquilcha Volcanic Cluster. *Contrib Mineral Petrol* 165, 663–682.
3814 <https://doi.org/10.1007/s00410-012-0829-2>
3815 Wallace, P.J., 2005. Volatiles in subduction zone magmas: concentrations and fluxes based on melt inclusion
3816 and volcanic gas data. *Journal of Volcanology and Geothermal Research* 140, 217–240.
3817 <https://doi.org/10.1016/j.jvolgeores.2004.07.023>

3818 Wallace, P.J., Anderson, A.T., Davis, A.M., 1999. Gradients in H₂O, CO₂, and exsolved gas in a large-volume
3819 silicic magma system: Interpreting the record preserved in melt inclusions from the Bishop Tuff. *J.*
3820 *Geophys. Res.* 104, 20097–20122. <https://doi.org/10.1029/1999JB900207>
3821 Wallace, P.J., Kamenetsky, V.S., Cervantes, P., 2015. Melt inclusion CO₂ contents, pressures of olivine
3822 crystallization, and the problem of shrinkage bubbles. *American Mineralogist* 100, 787–794.
3823 <https://doi.org/10.2138/am-2015-5029>
3824 Wallace, P.J., Plank, T., Bodnar, R.J., Gaetani, G.A., Shea, T., 2021. Olivine-Hosted Melt Inclusions: A
3825 Microscopic Perspective on a Complex Magmatic World. *Annual Review of Earth and Planetary*
3826 *Sciences*.
3827 Walowski, K.J., Wallace, P.J., Cashman, K.V., Marks, J.K., Clyne, M.A., Ruprecht, P., 2019. Understanding melt
3828 evolution and eruption dynamics of the 1666 C.E. eruption of Cinder Cone, Lassen Volcanic National
3829 Park, California: Insights from olivine-hosted melt inclusions. *Journal of Volcanology and Geothermal*
3830 *Research* 387, 106665. <https://doi.org/10.1016/j.jvolgeoes.2019.106665>
3831 Walowski, K.J., Wallace, P.J., Clyne, M.A., Rasmussen, D.J., Weis, D., 2016. Slab melting and magma formation
3832 beneath the southern Cascade arc. *Earth and Planetary Science Letters* 446, 100–112.
3833 <https://doi.org/10.1016/j.epsl.2016.03.044>
3834 Wan, Z., Coogan, L.A., Canil, D., 2008. Experimental calibration of aluminum partitioning between olivine and
3835 spinel as a geothermometer. *American Mineralogist* 93, 1142–1147.
3836 <https://doi.org/10.2138/am.2008.2758>
3837 Wanamaker, B.J., Evans, B., 1989. Mechanical re-equilibration of fluid inclusions in San Carlos olivine by power-
3838 law creep. *Contr. Mineral. and Petrol.* 102, 102–111. <https://doi.org/10.1007/BF01160194>
3839 Wanamaker, B.J., Wong, T.-F., Evans, B., 1990. Decrepitation and crack healing of fluid inclusions in San Carlos
3840 olivine. *Journal of Geophysical Research* 95, 15623. <https://doi.org/10.1029/JB095iB10p15623>
3841 Wang, W., Caumon, M.-C., Tarantola, A., Pironon, J., Lu, W., Huang, Y., 2019. Raman spectroscopic densimeter
3842 for pure CO₂ and CO₂-H₂O-NaCl fluid systems over a wide P-T range up to 360 °C and 50 MPa.
3843 *Chemical Geology* 528, 119281. <https://doi.org/10.1016/j.chemgeo.2019.119281>
3844 Wang, X., Chou, I.-M., Hu, W., Burruss, R.C., Sun, Q., Song, Y., 2011. Raman spectroscopic measurements of
3845 CO₂ density: Experimental calibration with high-pressure optical cell (HPOC) and fused silica capillary
3846 capsule (FSCC) with application to fluid inclusion observations. *Geochimica et Cosmochimica Acta* 75,
3847 4080–4093. <https://doi.org/10.1016/j.gca.2011.04.028>
3848 Wang, X., Hou, T., Wang, M., Zhang, C., Zhang, Z., Pan, R., Marxer, F., Zhang, H., 2021. A new clinopyroxene
3849 thermobarometer for mafic to intermediate magmatic systems. *Eur. J. Mineral.* 33, 621–637.
3850 <https://doi.org/10.5194/ejm-33-621-2021>
3851 Wark, D.A., Watson, E.B., 2006. Titanite: a titanium-in-quartz geothermometer. *Contrib Mineral Petrol* 152,
3852 743–754. <https://doi.org/10.1007/s00410-006-0132-1>
3853 Waters, L.E., Lange, R.A., 2015. An updated calibration of the plagioclase-liquid hygrometer-thermometer
3854 applicable to basalts through rhyolites. *American Mineralogist* 100, 2172–2184.
3855 <https://doi.org/10.2138/am-2015-5232>
3856 Weber, G., Blundy, J., 2023. A machine learning-based thermometer, barometer and hygrometer for magmatic
3857 liquids (preprint). *Physical Sciences and Mathematics*. <https://doi.org/10.31223/X5NW9P>
3858 Weber, G., Castro, J.M., 2017. Phase petrology reveals shallow magma storage prior to large explosive silicic
3859 eruptions at Hekla volcano, Iceland. *Earth and Planetary Science Letters* 466, 168–180.
3860 <https://doi.org/10.1016/j.epsl.2017.03.015>
3861 White, R.S., McKenzie, D., O’Nions, R.K., 1992. Oceanic crustal thickness from seismic measurements and rare
3862 earth element inversions. *J. Geophys. Res.* 97, 19683. <https://doi.org/10.1029/92JB01749>
3863 Wieser, P., in prep. Thermobar: An open source... in prep.
3864 Wieser, P., DeVitre, C., 2023. DiadFit: An Open-Source Python3 Tool for Peak fitting of Raman Data from silicate
3865 melts and CO₂ fluids (preprint). *Earth Sciences*. <https://doi.org/10.31223/X5CQ1F>
3866 Wieser, P., Kent, A., Till, C., Abers, G., 2023a. Geophysical and Geochemical Constraints on Magma Storage
3867 Depths along the Cascade Arc: Knowns and Unknowns (preprint). *Earth Sciences*.
3868 <https://doi.org/10.31223/X5KX00>
3869 Wieser, P., Till, C., Kent, A., Gleeson, M., 2023b. Comment on ‘The magmatic architecture and evolution of the
3870 Chang’e-5 lunar basalts’ Penny E. Wieser¹, Christy Till², Adam Kent³, Matthew Gleeson¹ (preprint).
3871 *Earth Sciences*. <https://doi.org/10.31223/X5MM3B>
3872 Wieser, P. E., Edmonds, M., Gansecki, C., Maclennan, J., Jenner, F.E., Kunz, B., Antoshechkina, P., Trusdell, F.,
3873 Lee, R.L., Eimf, 2022a. Explosive Activity on Kilauea’s Lower East Rift Zone Fueled by a Volatile-Rich,
3874 Dacitic Melt. *Geochem Geophys Geosyst* 23. <https://doi.org/10.1029/2021GC010046>

3875 Wieser, P.E., Edmonds, M., Maclennan, J., Jenner, F.E., Kunz, B.E., 2019. Crystal scavenging from mush piles
3876 recorded by melt inclusions. *Nat Commun* 10, 5797. <https://doi.org/10.1038/s41467-019-13518-2>
3877 Wieser, P. E., Iacovino, K., Matthews, S., Moore, G., Allison, C.M., 2022b. VESical: 2. A Critical Approach to
3878 Volatile Solubility Modeling Using an Open-Source Python3 Engine. *Earth and Space Science* 9.
3879 <https://doi.org/10.1029/2021EA001932>
3880 Wieser, P.E., Jenner, F., Edmonds, M., Maclennan, J., Kunz, B.E., 2020. Chalcophile elements track the fate of
3881 sulfur at Kīlauea Volcano, Hawai'i. *Geochimica et Cosmochimica Acta* S0016703720303239.
3882 <https://doi.org/10.1016/j.gca.2020.05.018>
3883 Wieser, P.E., Kent, A., Till, C., Donovan, J., Neave, D., Blatter, D., Mike Krawczynski, M., 2023b. Barometers
3884 behaving badly: Assessing the influence of analytical and experimental uncertainty on clinopyroxene
3885 thermobarometry calculations at crustal conditions (preprint). *Earth Sciences*.
3886 <https://doi.org/10.31223/X5JT0N>
3887 Wieser, P.E., Kent, A.J., Till, C., 2023a. Barometers behaving badly II: A critical evaluation of Cpx-only and Cpx-
3888 Liq thermobarometry in variably-hydrous arc magmas. *EarthArxiv*. <https://doi.org/10.31223/X59655>
3889 Wieser, P.E., Lamadrid, H., Maclennan, J., Edmonds, M., Matthews, S., Iacovino, K., Jenner, F.E., Gansecki, C.,
3890 Trudell, F., Lee, R.L., Ilyinskaya, E., 2021. Reconstructing Magma Storage Depths for the 2018
3891 Kīlauean Eruption From Melt Inclusion CO₂ Contents: The Importance of Vapor Bubbles. *Geochem*
3892 *Geophys Geosyst* 22. <https://doi.org/10.1029/2020GC009364>
3893 Wieser, P.E., Petrelli, M., Lubbers, J., Wieser, E., Ozaydin, S., Kent, A., Till, C., 2022b. Thermobar: An open-
3894 source Python3 tool for thermobarometry and hygrometry. *Volcanica* 5, 349–384.
3895 <https://doi.org/10.30909/vol.05.02.349384>
3896 Wilke, S., Holtz, F., Li, X., Neave, D.A., Almeev, R.R., 2019. Rhyolite-MELTS vs DERP – Reply to Comment by
3897 Gualda et al. on ‘The Effect of Anorthite Content and Water on Quartz–Feldspar Cotectic
3898 Compositions in the Rhyolitic System and Implications for Geobarometry’ by Wilke et al. (2017),
3899 *Journal of Petrology*, 58, No. 4, 789–818. *Journal of Petrology* 60, 865–870.
3900 <https://doi.org/10.1093/petrology/egz002>
3901 Wilke, S., Holtz, F., Neave, D.A., Almeev, R., 2017. The Effect of Anorthite Content and Water on Quartz–
3902 Feldspar Cotectic Compositions in the Rhyolitic System and Implications for Geobarometry. *Journal of*
3903 *Petrology* 58, 789–818. <https://doi.org/10.1093/petrology/egx034>
3904 Wilkinson, M.D., Dumontier, M., Aalbersberg, I.J., Appleton, G., Axton, M., Baak, A., Blomberg, N., Boiten, J.-
3905 W., da Silva Santos, L.B., Bourne, P.E., Bouwman, J., Brookes, A.J., Clark, T., Crosas, M., Dillo, I.,
3906 Dumon, O., Edmunds, S., Evelo, C.T., Finkers, R., Gonzalez-Beltran, A., Gray, A.J.G., Groth, P., Goble, C.,
3907 Grethe, J.S., Heringa, J., 't Hoen, P.A.C., Hooft, R., Kuhn, T., Kok, R., Kok, J., Lusher, S.J., Martone, M.E.,
3908 Mons, A., Packer, A.L., Persson, B., Rocca-Serra, P., Roos, M., van Schaik, R., Sansone, S.-A., Schultes,
3909 E., Sengstag, T., Slater, T., Strawn, G., Swertz, M.A., Thompson, M., van der Lei, J., van Mulligen, E.,
3910 Velterop, J., Waagmeester, A., Wittenburg, P., Wolstencroft, K., Zhao, J., Mons, B., 2016. The FAIR
3911 Guiding Principles for scientific data management and stewardship. *Sci Data* 3, 160018.
3912 <https://doi.org/10.1038/sdata.2016.18>
3913 Wilson, C.J.N., Barker, S.J., Charlier, B.L.A., Myers, M.L., Hansen, K.F., 2021. A comment on: magma residence
3914 and eruption at the Taupō Volcanic Center (Taupō Volcanic Zone, New Zealand)—insights from
3915 rhyolite-MELTS geobarometry, diffusion chronometry, and crystal textures, by AS Pamukçu et al.,
3916 *Contrib Mineral Petrol* 175:48 (2020). *Contrib Mineral Petrol* 176, 79.
3917 <https://doi.org/10.1007/s00410-021-01839-9>
3918 Wilson, C.J.N., Seward, T.M., Allan, A.S.R., Charlier, B.L.A., Bello, L., 2012. A comment on: ‘Titanium under
3919 pressure: the effect of pressure and temperature on the solubility of Ti in quartz’, by Jay B. Thomas, E.
3920 Bruce Watson, Frank S. Spear, Philip T. Shemella, Saroj K. Nayak and Antonio Lanzirrotti. *Contrib*
3921 *Mineral Petrol* 164, 359–368. <https://doi.org/10.1007/s00410-012-0757-1>
3922 Winpenny, B., Maclennan, J., 2011. A Partial Record of Mixing of Mantle Melts Preserved in Icelandic
3923 Phenocrysts. *Journal of Petrology* 52, 1791–1812. <https://doi.org/10.1093/petrology/egr031>
3924 Wong, K., Ferguson, D., Matthews, S., Morgan, D., Tadesse, A.Z., Sinetebeb, Y., Yirgu, G., 2022. Exploring rift
3925 geodynamics in Ethiopia through olivine-spinel Al-exchange thermometry and rare-earth element
3926 distributions. *Earth and Planetary Science Letters* 597, 117820.
3927 <https://doi.org/10.1016/j.epsl.2022.117820>
3928 Wong, K., Ferguson, D., Wieser, P., Morgan, D., Edmonds, M., Tadesse, A.Z., Yirgu, G., Harvey, J., Hammond, S.,
3929 2023. Focused Mid-Crustal Magma Intrusion During Continental Break-Up in Ethiopia. *Geophysical*
3930 *Research Letters* 50, e2023GL103257. <https://doi.org/10.1029/2023GL103257>

3931 Wood, B.J., 1974. The solubility of alumina in orthopyroxene coexisting with garnet. *Contr. Mineral. and Petrol.*
3932 46, 1–15. <https://doi.org/10.1007/BF00377989>

3933 Wood, B.J., Blundy, J., 1997. predictive model for rare earth element partitioning between clinopyroxene and
3934 anhydrous silicate melt. *Contributions to Mineralogy and Petrology.*

3935 Wright, H.M., Bacon, C.R., Vazquez, J.A., Sisson, T.W., 2012. Sixty thousand years of magmatic volatile history
3936 before the caldera-forming eruption of Mount Mazama, Crater Lake, Oregon. *Contrib Mineral Petrol*
3937 164, 1027–1052. <https://doi.org/10.1007/s00410-012-0787-8>

3938 Yamamoto, J., Kagi, H., 2006. Extended Micro-Raman Densimeter for CO₂ Applicable to Mantle-originated
3939 Fluid Inclusions. *Chem. Lett.* 35, 610–611. <https://doi.org/10.1246/cl.2006.610>

3940 Yang, H.-J., Kinzler, R.J., Grove, T.L., 1996. Experiments and models of anhydrous, basaltic olivine-plagioclase-
3941 augite saturated melts from 0.001 to 10 kbar. *Contributions to Mineralogy and Petrology* 124, 1–18.
3942 <https://doi.org/10.1007/s004100050169>

3943 Yuan, X., Mayanovic, R.A., 2017. An Empirical Study on Raman Peak Fitting and Its Application to Raman
3944 Quantitative Research. *Appl Spectrosc* 71, 2325–2338. <https://doi.org/10.1177/0003702817721527>

3945 Zanon, V., Frezzotti, M.L., 2013. Magma storage and ascent conditions beneath Pico and Faial islands (Azores
3946 archipelago): A study on fluid inclusions: MAGMA STORAGE BENEATH PICO AND FAIAL. *Geochem.*
3947 *Geophys. Geosyst.* 14, 3494–3514. <https://doi.org/10.1002/ggge.20221>

3948 Zellmer, G.F., Sakamoto, N., Iizuka, Y., Miyoshi, M., Tamura, Y., Hsieh, H.-H., Yurimoto, H., 2014. Crystal uptake
3949 into aphyric arc melts: insights from two-pyroxene pseudo-decompression paths, plagioclase
3950 hygrometry, and measurement of hydrogen in olivines from mafic volcanics of SW Japan. *SP 385,*
3951 161–184. <https://doi.org/10.1144/SP385.3>

3952 Zhang, J., Humphreys, M.C.S., Cooper, G.F., Davidson, J.P., Macpherson, C.G., 2017. Magma mush chemistry at
3953 subduction zones, revealed by new melt major element inversion from calcic amphiboles. *American*
3954 *Mineralogist* 102, 1353–1367. <https://doi.org/10.2138/am-2017-5928>

3955 Zhang, Y., Namur, O., 2022. A re-evaluation of the Al-in-Olivine geothermometer. Presented at the
3956 Goldschmidt 2022 - <https://conf.goldschmidt.info/goldschmidt/2022/meetingapp.cgi/Paper/11383>.

3957 Zhang, Y., Xu, Z., Zhu, M., Wang, H., 2007. Silicate melt properties and volcanic eruptions: SILICATE MELT
3958 PROPERTIES. *Rev. Geophys.* 45. <https://doi.org/10.1029/2006RG000216>

3959 Zhukova, I., O'Neill, H., Campbell, I.H., 2017. A subsidiary fast-diffusing substitution mechanism of Al in
3960 forsterite investigated using diffusion experiments under controlled thermodynamic conditions.
3961 *Contrib Mineral Petrol* 172, 53. <https://doi.org/10.1007/s00410-017-1365-x>

3962 Ziberna, L., Green, E.C.R., Blundy, J.D., 2017. Multiple-reaction geobarometry for olivine-bearing igneous rocks.
3963 *American Mineralogist* 102, 2349–2366. <https://doi.org/10.2138/am-2017-6154>

3964

This is a non peer reviewed preprint submitted to EarthArxiv

It has been accepted pending minor revisions in the Treatise of Geochemistry. Expected publication date 2024. Please feel free to contact us with any suggestions!

Determining the Pressure – Temperature – Composition (P-T-X) conditions of magma storage

Penny E. Wieser¹, Matthew L.M. Gleeson¹, Simon Matthews^{2, 3}, Charlotte DeVitre¹, Esteban Gazel⁴

1. Earth and Planetary Sciences, UC Berkeley. penny_wieser@berkeley.edu, gleesonm@berkeley.edu, cdevitre@berkeley.edu

2. Earth Science Department, University of Cambridge, sm905@cam.ac.uk

3. Institute of Earth Sciences, University of Iceland, Iceland.

4. Department of Earth and Atmospheric Sciences, Cornell University, Ithaca, NY 14850, USA, egazel@cornell.edu

1 **Determining the Pressure – Temperature – Composition (P-T-X) conditions of magma storage**

2 Penny E. Wieser¹, Matthew L.M. Gleeson¹, Simon Matthews^{2,3}, Charlotte DeVitre¹, Esteban Gazel⁴

3 1. Earth and Planetary Sciences, UC Berkeley. penny_wieser@berkeley.edu, gleesonm@berkeley.edu,
4 cdevitre@berkeley.edu

5 2. Earth Science Department, University of Cambridge, sm905@cam.ac.uk

6 3. Institute of Earth Sciences, University of Iceland, Iceland.

7 4. Department of Earth and Atmospheric Sciences, Cornell University, Ithaca, NY 14850, USA,
8 egazel@cornell.edu

9

10 **Key Points**

- 11 • Many mineral-melt barometers have standard errors of $\pm 2\text{--}3$ kbar ($\pm 7\text{--}11$ km), which limits their ability
12 to provide detailed constraints on magma storage in relatively thin-crust settings (MORB and OIB).
- 13 • Different models/equations can yield very different PT conditions; model choice must be considered as
14 one of the largest sources of systematic error in a given study.
- 15 • The paucity of independent test datasets for many methods makes it difficult to truly assess their
16 performance; statistics calculated using the calibration dataset where many variables are known are
17 overly optimistic of performance in natural systems.
- 18 • It has become increasingly clear that melt inclusion studies which did not account for the vapour bubble
19 may have underestimated storage depths by more than a factor of 2, requiring re-evaluation of melt
20 inclusion volatile contents and storage depths globally.

21 **Key words**

- 22 1. Mineral Thermobarometry
- 23 2. Thermodynamics
- 24 3. Melt Inclusions
- 25 4. Fluid inclusions
- 26 5. Raman Spectroscopy
- 27 6. Hygrometry
- 28 7. Chemometry
- 29 8. Experimental Petrology
- 30 9. FAIR Research Framework
- 31 10. MELTS modelling
- 32 11. Pyroxene
- 33 12. Amphibole
- 34 13. Plagioclase

35 **Abstract (100 words)**

36 Determining the pressures and temperatures at which melts are stored in the crust and upper mantle, and the
37 major element composition, redox state and volatile contents of these melts, is vital to constrain the structure
38 and dynamics of magmatic plumbing systems. In turn, constraining these parameters helps understand the
39 geochemical and structural evolution of the Earth's lithosphere, and periods of unrest at active volcanoes. We
40 review common thermobarometers, hygrometers and chemometers based on mineral and/or liquid
41 compositions, before discussing recent advances in melt and fluid inclusion barometry, Raman-based elastic
42 thermobarometry, and thermodynamic modelling methods. Where possible, we investigate the accuracy and
43 precision of each technique, and the implications for the application of each method to different research
44 questions.

45 **1. Introduction.**

46 Determining the pressures, and therefore depths, at which magmas are stored and evolve in the crust
47 and upper mantle is vital to understand the chemical and structural evolution of volcanic plumbing systems,
48 with implications for our understanding of the formation of mineral deposits, and the evolution of the Earth's
49 lithosphere (Lee and Anderson, 2015). Precisely constraining magma storage depths at a specific volcano using

50 past eruptive deposits can also provide vital context to help inform the interpretation of monitoring signals
51 during periods of volcanic unrest (e.g., distinguishing magmatic and hydrothermal signals, Pritchard et al., 2019).

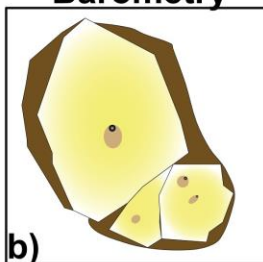
52 Constraining the temperatures of different magmatic processes can reveal the thermal evolution of
53 magmatic systems and are vital inputs for many other common workflows in igneous petrology, such as
54 calculations of timescales from elemental diffusion in erupted crystals (termed “diffusion chronometry” or
55 “geospeedometry”). In fact, because diffusion rates are strongly sensitive to temperature (following an
56 Arrhenius relationship), uncertainty in temperature is one of the largest sources of error when obtaining
57 timescales using these chronometers (Chakraborty and Dohmen, 2022; Costa et al., 2020). For example, Mutch
58 et al. (2019a) show that timescales calculated from Cr diffusion in spinel change from ~4000 years at 1190°C to
59 ~1000 yrs at 1230°C. Thus, uncertainty in temperatures affects interpretations of timescales of crustal residence
60 (Mutch et al., 2019a), re-awakening from quiescence to eruption (Shamloo and Till, 2019), and calculations of
61 magma ascent rates (Mutch et al., 2019b). Of course, accurately constraining magma storage depths is also vital
62 for magma ascent rate calculations, where the speed is calculated by dividing the depth to the inferred magma
63 body by the time calculated from diffusion chronometry (Barth et al., 2019; Klügel, 1998).

64 Here, we describe a multitude of approaches to determine the pressures (P) and temperatures (T) at
65 which magmas were stored in the lithosphere, as well as ways to determine the chemistry of stored melts (Fig.
66 1). We pay particular attention to differences between models (Section 1.1) and the precision and accuracy of
67 calculations (Section 1.2). For barometers, we first evaluate variations in crustal thickness in a wide variety of
68 tectonic settings to compare with estimates of the precision of different barometry methods (Section 1.3). Then,
69 we review the methods used to convert measured mineral compositions (with or without an equilibrium melt)
70 into magma storage pressures and temperatures (mineral barometry and thermometry), and to calculate the
71 chemistry and H₂O contents of the melts from which a specific mineral composition grew (chemometry and
72 hygrometry respectively, Section 2).

Mineral Thermobarometry



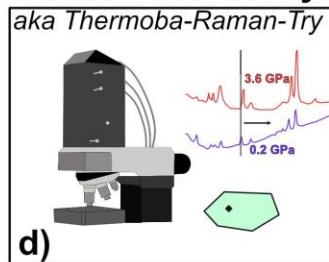
Melt Inclusion Barometry



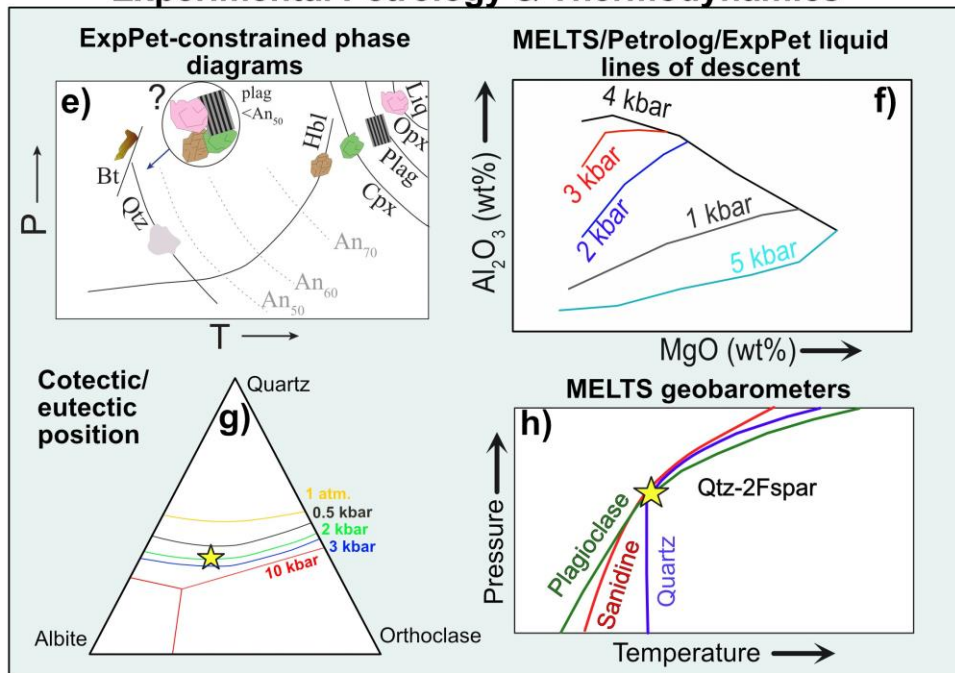
Fluid Inclusion Barometry



Elastic thermobarometry



Experimental Petrology & Thermodynamics



73

74 *Figure 1: Summary of some of the methods used to determine pressures and temperatures of magma storage.*
 75 *Part e) adapted from Rutherford (2003), f) from Cashman and Edmonds (2019), g) and h) adapted from Gualda*
 76 *et al. (2012) and Gualda and Ghiorso (2014), respectively.*

77

78

79 We also evaluate the methods and uncertainties involved in melt inclusion barometry, with a specific
 80 focus on the influence of CO₂ stored within melt inclusion vapour bubbles on calculated pressures (Section 3).

81 The general proliferation of Raman spectroscopy in the Earth Sciences (Dubessy et al., 2012) has not only been
 82 important for performing direct measurements of melt inclusion vapour bubbles; it has also pushed forwards
 83 two other barometric methods. First, Raman spectroscopic measurements of fluid inclusions can provide a
 84 substantially faster method of calculating storage depths than traditional microthermometric techniques
 85 (Section 4). Second, Raman measurements of mineral inclusions in-situ can also be used to calculate pressures
 86 and temperatures (thermobarometry, Section 6). Experimental petrology is not only vital for the formulation
 87 and calibration of mineral-melt thermobarometers and volatile solubility models, it can also be used to provide
 88 direct constraints on magma storage in a specific volcanic system (Section 7). Finally, we discuss approaches
 89 using thermodynamic constraints on phase stability in igneous systems (Section 8), methods not covered in
 90 detail in this review (Section 9) and summarize the general proliferation of community data repositories and
 91 open-source tools to help inform model calibration, and aid calculations of magma storage conditions (Section
 92 10).

93 1.1 Assessing and comparing models

94 When calculating pressure, temperature, and/or melt chemistry from the composition of erupted
 95 melts, crystals and their inclusions, the result can be highly sensitive to the choice of
 96 model/equation/parameterization, relating the measured quantity (e.g., Cpx, Amp, melt inclusion composition)
 97 to the intensive variable (e.g., P, T). Below, we discuss the origin of all these different models, and best practices
 98 for model intercomparison.

99 Mineral thermobarometry (Section 2) utilizes chemical reactions involving the crystallization or re-
 100 equilibration of minerals which are accompanied by a change in volume (sensitive to P) and/or a change in
 101 entropy (sensitive to T, e.g., Putirka, 2008). Chemometry (and hygrometry) relies on the fact that the
 102 composition of crystallizing/re-equilibrating phases is sensitive to the composition of the melt phase. Some
 103 thermobarometry and chemometry expressions are firmly rooted in thermodynamics, with compositional terms
 104 and the functional form of the equation determined from a specific reaction. Typically, these expressions have
 105 coefficients attached to thermodynamic terms which are calibrated empirically using the measured
 106 compositions of minerals in experiments conducted at well-constrained P-T-fO₂-H₂O conditions (e.g., the
 107 Plagioclase-Liquid hygrometer of Waters and Lange, 2015).

108 More commonly, available equations have a general form based on thermodynamics, with the addition
 109 of more empirically derived terms to improve the fit to the calibration dataset (e.g., Neave and Putirka, 2017).
 110 For example, many of the Cpx-Liq barometers of Putirka (2008) have a functional form based on Jadeite
 111 exchange between the liquid and Cpx, which is associated with a change in volume, so is P sensitive (Putirka et
 112 al., 1996):

$$113 \quad P = a + \frac{bT}{10^4} + \frac{cT}{10^4} \ln(\text{Jd}^{\text{Cpx-Liq}}) + \dots [\text{Equation 1}]$$

114 Additional terms help to improve the fit between the calculated parameter and the known experimental
 115 conditions. The inclusion of these terms may be informed at least in part by thermodynamic reasoning (e.g.,
 116 Masotta et al., 2013; Neave and Putirka, 2017; Putirka, 2008). For example, Putirka (1996) EqP1 has a term for
 117 the cation fractions of Na and Al:

$$118 \quad \text{EqP1} = \text{Equation 1 terms} \dots + 367 (X_{\text{Na}}^{\text{Liq}} * X_{\text{Al}}^{\text{Liq}}) [\text{Equation 2}]$$

119 The fact that the best fit involved the multiplication of Na and Al cation fractions implies that these two
 120 components have identical activity coefficients (Putirka et al., 1996). However, the thermodynamic
 121 interpretation is often obscured by decisions to reduce the complexity of equations, such as wanting to avoid
 122 introducing multiple temperature-dependent terms (see Equation 12 of Putirka et al., 1996). In general as
 123 calibration datasets have grown larger, more empirical terms have been added that have a less clear
 124 thermodynamic basis. For example, Putirka (2008, Eq31) has many additional terms relative to EqP1, including
 125 terms for the Ca, Na, K, Si, Mg and Fe_t liquid cation fractions, H₂O in the liquid, and for EnFs, DiHd, and Al cation
 126 fractions in the Cpx:

$$127 \quad \text{Eq31} = \text{Equation 1 terms} \dots + 106 X_{\text{Ca}}^{\text{Liq}} - 166 (X_{\text{Na}}^{\text{Liq}} + X_{\text{K}}^{\text{Liq}})^2 - 50.2 X_{\text{Si}}^{\text{Liq}} * (X_{\text{Mg}}^{\text{Liq}} + X_{\text{Fe}}^{\text{Liq}}) - 3.2 \log(\text{DiHd}) -$$

$$128 \quad 2.2 \log(\text{EnFs}) + 0.86 \log(X_{\text{Al,6 cat}}^{\text{Cpx}}) + 0.4 * \text{H}_2\text{O} [\text{Equation 3}]$$

129 New models not only arise through the addition of new empirical terms, but also through the recalibration of
 130 the coefficients of older equations. For example, Masotta et al. (2013) recalibrate the coefficients of Putirka

131 (2008) for a new dataset of alkaline magmas. Other thermobarometers are purely empirical, including terms and
132 mathematic expressions like logs, exponentials, and different powers which improve the fit to the calibration
133 dataset without a firm tie to the thermodynamics of a specific chemical reaction. For example, the liquid-only
134 thermometer of Helz and Thornber (1987) was calibrated based on the linear relationship between MgO and T
135 in experiments on the Kilauea Iki lava lake. The amphibole-only barometer of Ridolfi and Renzulli (2012) uses
136 multivariate least squares regression to determine the relationship between P and amphibole composition
137 across a number of different P ranges, with highly variable functional forms (Eq1a, Eq1b and Eq1e take the
138 exponential of amphibole cation fractions, Eq1c and Eq1d do not). The results from these equations are selected
139 or combined using an algorithm to give a single P, this algorithm was then tweaked by Ridolfi, (2021), generating
140 yet another model.

141 Most recently, machine learning approaches using regression trees have been used to parameterize the
142 relationship between mineral and melt composition and experimental conditions (e.g., Higgins et al., 2022;
143 Jorgenson et al., 2022; Petrelli et al., 2020). Unlike purely thermodynamic, or mixed thermodynamic-empirical
144 expressions, these approaches do not use any underlying thermodynamic knowledge. They are trained using
145 measured oxide contents, rather than thermodynamically informed mineral components such as Jadeite,
146 Diopside etc. The lack of thermodynamic basis may affect their ability to extrapolate beyond the compositions
147 and P-T conditions for which they are calibrated, but one advantage is that these models can be easily updated
148 as new experimental data becomes available if the code for model training is released.

149 The diversity of empirical, thermodynamic, and machine-learning models for mineral-based
150 thermobarometry/hygrometry/chemometry has resulted in a somewhat overwhelming choice of models to
151 calculate magma storage conditions. Concerningly, these different models can return vastly different results.
152 Wieser et al. (2023a) show that different Cpx-Liq and Cpx-only thermobarometers applied to the same Cpx-Liq
153 pair passing equilibrium tests yield pressures spanning >10 kbar and temperatures spanning >100°C. Clearly,
154 model choice is one of the largest sources of uncertainty when performing such calculations.

155 Melt inclusion barometry uses a volatile solubility model to calculate the pressure at which a specified
156 melt composition (major+volatile elements) is volatile saturated (for a specific temperature). These solubility
157 models range from being purely empirical (Liu et al., 2005; Shishkina et al., 2014) to models formulated in a
158 purely thermodynamic framework (Ghiorso and Gualda, 2015; Papale et al., 2006). Some models lie between
159 these end members, having a general form indicated by thermodynamics and some empirical coefficients
160 accounting for silicate melt composition (semi-empirical, e.g., Dixon, 1997; Iacono-Marziano et al., 2012). Even
161 for fully thermodynamical models, the sign and magnitude of many coefficients attached to thermodynamic
162 terms have been criticized as being physically implausible (see Ghiorso and Gualda, 2015 and Wieser et al. 2022a
163 for discussion of the Papale et al. 2006 model). In addition to their different functional forms, the calibration
164 datasets of solubility models are also highly variable with respect to the range of melt compositions, fluid
165 compositions, and P and T. For example, the model of Shishkina et al. (2014) was calibrated on variably alkaline,
166 relatively mafic melts, and expresses volatile solubility empirically using the cation fractions of Ca, K, Na, Mg, Fe,
167 Si and Al for CO₂, and K and Na for H₂O. In contrast, the solubility model of Dixon (1997) was calibrated on a
168 more restricted range of relatively mafic tholeiitic to alkaline melt compositions. This model has a
169 thermodynamic form, with an empirical correction for the effect of melt composition that is only dependent on
170 the concentration of SiO₂ in the melt. The model MagmaSat (Ghiorso and Gualda, 2015) was calibrated on a very
171 wide range of melt compositions (tholeiite and alkaline, from basalts to rhyolites), and is a fully thermodynamic
172 solubility model sensitive to all the commonly measured major oxide species. Unsurprisingly, given these
173 differences in model formulation and calibration datasets, calculated saturation pressures can vary greatly
174 between models, with systematic offsets of at least a factor of two not being uncommon (Wieser et al., 2022a).

175 In stark contrast to uncertainties associated with model choice when performing mineral
176 thermobarometry or melt inclusion barometry, fluid inclusion barometry (Section 4) relies on the CO₂ equation
177 of state to convert the measured density of a CO₂-rich fluid into a P for a specified entrapment temperature.
178 Other than an ideal gas law (which does a poor job at high P), different published CO₂ equation of states predict
179 very similar P for a given CO₂ density and T (~ 1–5% difference, Böttcher et al., 2012; Lamadrid et al., 2017; Span
180 and Wagner, 1996; Sterner and Pitzer, 1994; Wieser and DeVitre, 2023). For example, at 1150°C for $\rho_{CO_2} = 0.8$
181 g/cm³, the relatively simple empirical expression of Sterner and Pitzer (1994) gives 5.008 kbar, while the more
182 complex thermodynamic model of Span and Wanger (1996) gives 4.956 kbar (~3% difference). However, the
183 conversion between measured CO₂ density to depth is substantially less simple when trapped fluids contain
184 other species, such as H₂O or SO₂ (Hansteen and Klugel, 2008; Hurai, 2010). It is difficult to estimate the initial
185 molar ratios of each species, and EOS for these mixed fluids are poorly constrained (if parameterized at all). Fluid

186 inclusion barometry is also not immune to systematic error; re-equilibrium of the host crystal during magma
187 ascent can increase the inclusion volume, and thus reduce the CO₂ density (and thus the calculated
188 pressure/depth, Hansteen and Klugel, 2008; Wanamaker and Evans, 1989).

189 Thermodynamic approaches to determining the conditions of magma storage and evolution are also
190 sensitive to the choice of model (Section 8). Thermodynamic models are typically constructed from two key
191 components: (i) a dataset of standard state properties (e.g., enthalpy of formation, heat capacity, etc.) for all
192 minerals of interest, and (ii) solution models for phases with variable compositions (describing how composition
193 influences the thermodynamic properties of the phase). Within igneous petrology and volcanology the MELTS
194 ‘family’ of thermodynamic models are the most widely used (Ghiorso et al., 2002; Ghiorso and Sack, 1995;
195 Gualda et al., 2012). The original MELTS model was developed by Ghiorso and Sack (1995), building on the
196 thermodynamic database of Berman (1988) to include thermodynamic models of relevant igneous solid
197 solutions (e.g., Ghiorso, 1990; Ghiorso and Sack, 1991; Sack and Ghiorso, 1994, 1991, 1989). Since the release
198 of this original MELTS model, various updates have been published. pMELTS includes a revised liquid
199 thermodynamic model optimised for mantle-like bulk compositions (Ghiorso et al., 2002). Rhyolite-MELTS
200 v.1.0.2 incorporates changes to the thermodynamic properties of quartz and the orthoclase endmember of the
201 alkali feldspars that enable the eutectic behaviour of high-silica rhyolitic magmas to be recreated (i.e.
202 crystallization over a narrow T range, Gualda et al., 2012). Rhyolite-MELTS v1.2.0 incorporates the mixed H₂O-
203 CO₂ fluid model MagmaSat, and is recommended for use away from the granitic ternary minimum. Rhyolite-
204 MELTSv1.1.0 incorporates the updated CO₂ solubility model, but retains the old H₂O solubility model of rhyolite-
205 MELTSv1.0.2 for calculations at the ternary minimum (Ghiorso and Gualda, 2015).

206 An alternative group of thermodynamic models developed by Tim Holland, Roger Powell and co-
207 workers (Holland and Powell, 2004, 1998, 1990) have traditionally been utilized in metamorphic studies
208 (Tamblyn et al., 2020), but have recently been updated for applications to mantle melting and igneous systems.
209 For example, Jennings and Holland (2015) expand the model system, optimizing its performance for calculations
210 of peridotite melting behaviour and the phase relationships of basaltic liquids at crustal to mantle conditions.
211 Most recently, Holland et al. (2018) presented an updated thermodynamic database that is calibrated on a range
212 of compositions, from peridotites through to granites. The Holland dataset is mostly accessed through a variety
213 of software tools. THERMOCALC calculates the location of known phase boundaries and mineral reactions
214 (Powell et al., 1998). Alternatively, Perple_X (Connolly, 2009, 2005) and Theriak-Domino (de Capitani and
215 Petrakakis, 2010) use a Gibbs Free Energy minimization approach to calculate the phase assemblage and
216 compositions specified P-T conditions.

217 Comparisons between the MELTS and Holland-Powell families of models are relatively uncommon;
218 Jennings and Holland (2015) compare the results of mantle melting calculations, and Hernández-Urbe et al.
219 (2022) compare the equilibrium crystallization behaviour of an N-MORB magma. Importantly, Hernández-Urbe
220 et al. (2022) do not compare fractional crystallization pathways, noting that these would be “relatively laborious”
221 with current software tools. The recent release of MAGEMin, a Gibbs Free Energy minimisation package utilizing
222 the Holland et al. (2018) thermodynamic models written in the programming language C (Riel et al., 2022) allows
223 MELTS-like workflows to be performed including fractional crystallization. MAGEMin has a Julia interface and
224 can be run in Python3 using pyMELTScalc (Gleeson et al. 2023), greatly aiding model intercomparison between
225 the Holland and MELTS databases (see Section 8). There are also several more empirical models which have
226 been used as alternatives to MELTS to model fractional crystallization in magmas, and therefore could place
227 constraints on P and T (see Section 8). These include COMAGMAT (Ariskin et al., 1993) and Petrolog3
228 (Danyushevsky and Plechov, 2011). In Section 8, we show that the choice of thermodynamic model to use (and
229 even the version of MELTS used) has a large influence on calculations of magma storage conditions (see also
230 Hernández-Urbe et al., 2022).

231

232 1.2. Statistics to compare models

233 When trying to decide which model/equation to use to calculate magma storage conditions, and to
234 assess whether the chosen method has sufficient resolution to address the science question of interest, it is
235 important to assess both accuracy and precision. Accuracy describes how close the measurement or model
236 prediction is to the true value, while precision describes how close repeated measurements are to one another.
237 For example, if you measure a small, very homogenous region of a Cpx crystal five times using an electron probe
238 microanalyser (EPMA), and calculate Cpx-only pressures from these measurements, you may obtain 5, 5.5, 6,
239 4.9, and 6.2 kbar. The precision could be quantified using 1 standard deviation of these measurements (e.g.,

240 ±0.47 kbar). However, the Cpx may have formed at 8 kbar, in which case these calculations are relatively precise,
 241 but inaccurate (mean offset of 2.5 kbar). It is also worth distinguishing between random and systematic errors.
 242 Random error describes scatter about the true value (affecting precision, not accuracy), while systematic error
 243 describes a constant offset from the true value (affecting accuracy not precision).

244 Most publications calibrating a new mineral-melt thermobarometer or chemometer describe the fit
 245 between calculated and experimental values for a given parameter using RMSE and R² values (see Table 1,
 246 RMSE=SEE for linear regressions). When equations are applied to natural systems, these RMSE errors are often
 247 quoted as the error on the calculation. This is problematic for several reasons. The RMSE and R² alone do not
 248 properly distinguish between random and systematic error, so fails to capture the complexity of the error on
 249 the calculation. 6 different metrics (Table 1) can be useful to assess model performance. In this review, we put
 250 particular emphasis on the Mean Bias Error (MBE), the gradient and intercept in addition to R² and RMSE help
 251 to identify systematic error.

252

Metric	Good at	Bad at
R ² value: Correlation coefficient of the linear regression between the measured (x) and predicted (y) value.	Assessing precision and random uncertainty. Low precision (lots of random uncertainty) = low R ² value.	Assessing accuracy and systematic uncertainty.
Gradient and Intercept of the linear regression	Assessing systematic uncertainty, which will generate a gradient different from 1, and an intercept different from zero.	Assessing precision/random uncertainty (as averages all measurements).
Root mean square error (RMSE) aka. SEE $RMSE = \sqrt{\frac{1}{N} \sum_{i=1}^N (x_i - y_i)^2}$	Describes how concentrated the data is around the linear regression.	Struggles to distinguish between low precision and accurate vs. high precision with a systematic offset. Sensitive to outliers.
Mean Absolute Error (MAE) $MAE = \frac{1}{N} \sum_{i=1}^N x_i - y_i $	Similar to the RMSE but no squared term. Gives less weight to larger errors than the RMSE	Struggles to distinguish between low precision and accurate vs. high precision with a systematic offset
Mean Bias Error (MBE) $MBE = \frac{1}{N} \sum_{i=1}^N (x_i - y_i)$	Identifies average model bias, as no absolute or squared term.	Doesn't identify random error, as + and - errors cancel out.

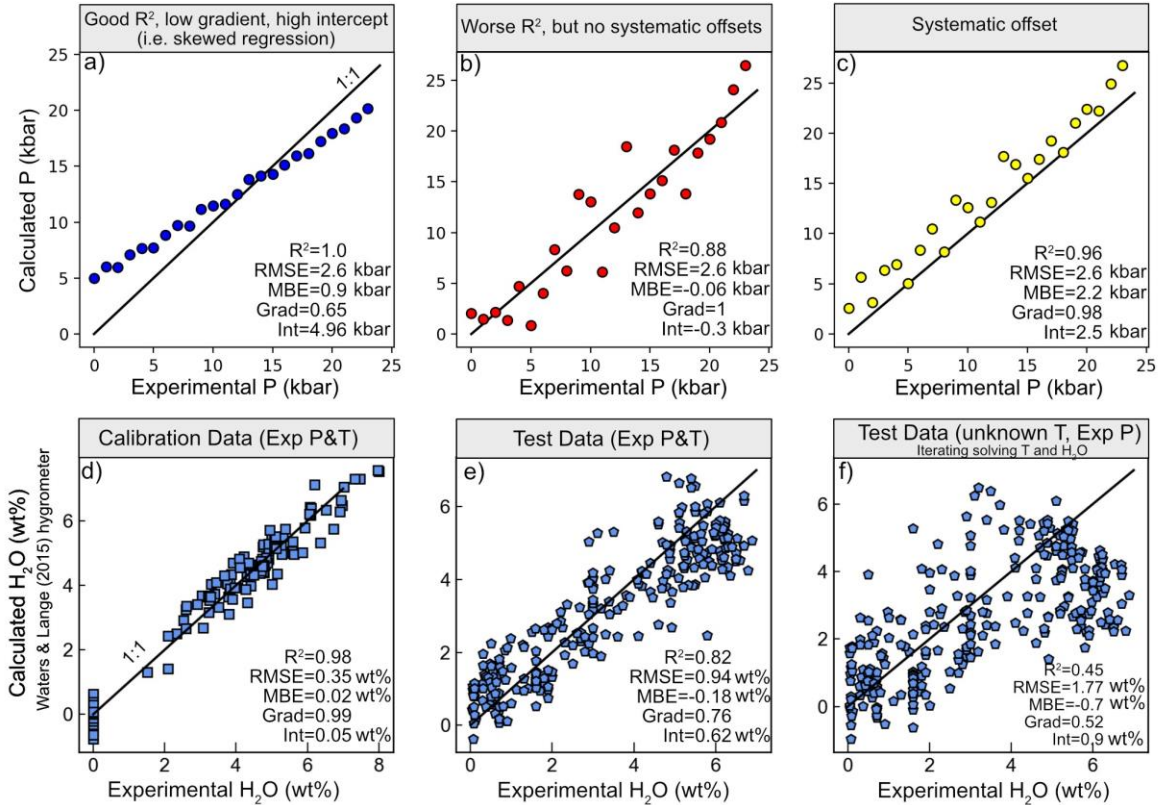
253

254 *Table 1: Metrics used to assess models, where x is the measured parameter (e.g., P, T) and y is the model-*
 255 *predicted parameter. RMSE and SEE are identical for a linear regression, for higher order regressions, they differ*
 256 *as only the SEE accounts for the degrees of freedom.*

257

258 In Fig. 2, we demonstrate the issues associated with using *only* the root mean square error (RMSE)
 259 and R² to assess model performance. Instead, we suggest that the RMSE, R², gradient, intercept and MBE should
 260 all be presented on figures to allow assessment of both random and systematic uncertainty (e.g. Putirka et al.
 261 2003). To demonstrate this, we compare the relative performance of three hypothetical barometers, plotting
 262 the experimental P on the x axis, and the calculated P on the y axis (Fig. 2). All barometers have the same RMSE
 263 error. However, it is visually apparent that their performance varies greatly. While Fig. 2a has a very high R²
 264 value, its low gradient and high intercept reveals that it substantially overpredicts P at P<12 kbar, and
 265 underpredicts P at P>12 kbar. While Fig. 2b has a lower R² value, it has no substantial systematic offsets, meaning
 266 it is a far more accurate barometer across a wide range of pressures than that shown in Fig. 2a (indicated by the
 267 gradient close to one, an intercept close to zero, and the low MBE). The barometer in Fig. 2c also has a gradient

268 close to 1, but the higher intercept and MBE indicate that it systematically overpredicts at all pressures. Clearly,
 269 if you wish to distinguish the absolute depth of magma storage, perhaps to compare to geophysical inversions
 270 of magma storage depths, or signals of unrest, the barometer in Fig. 2b is the best, despite its lower R^2 . However,
 271 if you only wish to distinguish differences in storage pressures between different crystal populations (without
 272 caring about the actual depth), the barometer in Fig. 2a is the best, as it is the most precise. Use of all 5 metrics
 273 in tandem is essential for identifying systematic and random uncertainty.



274
 275 *Figure 2: Schematic figure showing the limitations of using just R^2 and RMSE to assess thermobarometers. a-c)*
 276 *Three hypothetic barometers with the same RMSE, but vastly different performance. d-f) Comparing*
 277 *experimental and calculated H₂O using the Waters and Lange (2015) hygrometer for: d) the calibration dataset*
 278 *using experimental T and P, e) the ArcPL dataset using experimental T and P, and f) the ArcPL dataset iteratively*
 279 *solving H₂O and T (using Eq24a of P2008, see Section 2.8 for more detail).*

280
 281 It is also challenging to directly compare the quoted RMSE and R^2 values from different models,
 282 because these statistics are not equivalent. Many of the statistics reported in the abstracts of papers proposing
 283 new equations describe how well the model fits the calibration dataset (e.g., the commonly quoted ± 1.7 kbar
 284 value for the Cpx-Liq barometer of Putirka et al. 2003; the ± 0.35 wt% H₂O value for the Waters and Lange, 2015,
 285 Plag-Liq hygrometer). In other papers, the number reported in the abstract is the fit to a test dataset (e.g.,
 286 Jorgenson et al., 2022; Petrelli et al., 2020), which inevitably makes the equation look “worse” than one assessed
 287 using calibration data. Indeed, it is apparent in the main text of many thermobarometry papers that the RMSE
 288 is much larger when applied to test data not used in the calibration dataset, or when applied to a global dataset
 289 containing a mix of new and calibration data (e.g., RMSE=4.2 kbar for the Cpx-Liq Putirka et al. 2003 barometer
 290 vs. the commonly quoted RMSE=1.7 kbar, Fig. 3a). The size of the test dataset can also vary greatly, influencing
 291 the statistics. For example, the test dataset of Petrelli et al. (2021) only contains 59 experiments conducted at
 292 <15 kbar, which come from only 4 studies. Some reported statistics are calculated using only experiments for a
 293 select subregion of compositional space (e.g., Neave and Putirka, 2017 for Cpx-Liq equilibria in tholeiites), while
 294 others report the fit for a global dataset with a much larger compositional range, again leading to larger apparent
 295 errors (e.g., Putirka 2008). For many equations, there is so little spare data for each composition, all data was
 296 used for calibration, so the authors do not use a test dataset (e.g., Waters and Lange, 2015 for Plag-Liq
 297 hygrometry, Giorso and Gualda, 2015 for volatile solubility). Additionally, some proportion of the error in any
 298 quoted statistic (e.g. RMSE) will represent uncertainty in the experimental data used for testing (both analytical

299 and experimental sources of scatter), making it difficult to differentiate failures of the calibration equation vs.
300 the data used to assess it. This is a particular problem for models where higher quality data was saved for
301 calibration, with less strict filters applied to test data (Putirka et al. 2003, 2008, K. Putirka, written comms).

302
303 Ideally when calibrating any new equation/model (for thermobarometry, chemometry, volatile solubility
304 modelling etc.), data should be subdivided into a test dataset and a calibration dataset. It is then standard
305 practice for many machine learning workflows to further subdivide the calibration dataset into train and
306 validation datasets (this split may be made repeatedly during model training, e.g., Petrelli et al. 2020). The train-
307 validation split allows investigation of the effect of adding/removing terms, changing the regression algorithm,
308 and tweaking the regression tuning parameters. Only once the model is fully tweaked should it be applied to the
309 test dataset to assess its performance on unseen data. While it is then tempting to continue to change
310 parameters to improve the fit to the test dataset, this strategy is generally criticized in the world of machine
311 learning, as it means the testing dataset has “leaked” into the training of the model, so no longer provides an
312 independent assessment of the model validity. The complete isolation of a testing dataset prior to model tuning
313 and choice of parameters is important for machine learning and other regression workflows, because otherwise
314 it is difficult to assess model performance on samples which are distinct in P-T-X space from those used in model
315 calibration (Lones, 2021). To address this, in some biomedical studies, a test dataset is kept completely separate,
316 and held under “lock and key” by a honest broker to avoid such leakage (Dobbin and Simon, 2011; Shedden,
317 2008). In igneous petrology, the difficult balance to strike is between having a large test dataset to robustly
318 assess model performance, versus having too small a calibration dataset to adequately capture variation in melt
319 or mineral composition.

320
321 It is also worth noting that the RMSE value is an average for the fit across the entire P or T range, while the actual
322 error when applied to natural samples will vary as a function of P and T. RMSE and R^2 values are also not always
323 calculated across the same P and T range (e.g., 0–40 kbar for Putirka, 2008, 0–20 kbar for Petrelli et al. 2020).
324 These pressure ranges are also often far larger than the pressure ranges of interest in volcanic systems, and
325 models tend to perform worse at lower pressures (Putirka, 2008).

326
327 Finally, mineral-melt thermobarometers and chemometers are often assessed using experimental data, where
328 T, P (and often H_2O and fO_2) are constrained. In natural systems, it is common that several intensive parameters
329 are poorly constrained. For example, a T and H_2O -sensitive barometer is normally assessed using the test
330 dataset, inputting the experimental temperature and the measured H_2O content in the experimental charge.
331 Similarly, thermometers with P-sensitive terms are normally assessed using the experimental P, and
332 hygrometers are assessed using experimental T and P. In natural systems, the most common scenario is that
333 *both* P and T are unknown, so must be iteratively solved using a thermometer and a barometer. Thus, to estimate
334 a realistic error when applied to natural systems, statistics should be calculated by iteratively solving the same
335 variables that would be unknown in natural samples. Of course, this adds additional uncertainty; when applying
336 a T-sensitive barometer, any deviation from the true T will affect the calculated P. Additional uncertainties
337 related to parameters which cannot be iteratively solved (e.g., uncertainty in H_2O in Cpx-Liq thermobarometers)
338 should be propagated with Monte-Carlo techniques using a realistic uncertainty for H_2O in a specific system of
339 interest (e.g. Wieser et al. 2022b).

340
341 Using the T-sensitive Plag-Liq hygrometer of Waters and Lange (2015) as an example, we
342 demonstrate how the apparent performance of an equation can vary based on the number of constrained
343 intensive parameters, and the dataset used to test it. First, we show H_2O contents for the model calibration
344 dataset using experimental temperatures (Fig. 2d). This comparison yields the RMSE quoted in the abstract of
345 the Waters and Lange (2015) paper that is commonly quoted in the literature as the error on the method (± 0.35
346 wt%). Next, we evaluate this hygrometer using a newly compiled test dataset of variably hydrous experiments
347 at 0–17 kbar spanning from basalts to dacites (ArcPL, Wieser et al., 2023a-b). We only include experiments where
348 H_2O was measured using quantitative methods (Fourier Transform infrared spectroscopy - FTIR, secondary ion
349 mass spectrometry - SIMS, Raman, calibrated volatiles-by-difference, solubility laws, see Section 2.8), and
350 discard experiments which were present in the Waters and Lange (2015) calibration dataset. Using experimental
351 T to calculate H_2O for this new test dataset yields statistics that are noticeably worse than those calculated from
352 the calibration dataset (e.g., ± 0.94 wt% vs. ± 0.35 wt%, Fig. 2e). In a scenario where T is not known (i.e., when
353 this method is applied to natural systems), the statistics decline further: iterating the hygrometer with the Plag-
354 Liq thermometer of Putirka (2008, Eq24a) results in a RMSE of ± 1.77 wt% (Fig. 2f, see Section 2.8 for detailed

355 discussion). Thus, simply quoting the uncertainty from the original publication may underestimate the error by
356 a factor of ~5 when applied to natural systems. We observe similarly large declines in model performance
357 moving from calibration to test data to iterative solving for many mineral-melt equilibria (see Section 2, and
358 Wieser et al. 2023a).

359

360 Thus, at present, it is not possible to select the best thermobarometer for a given application simply
361 based on quoted statistics alone. Instead, to pick the most suitable model, it is worthwhile to check the natural
362 compositions of interest vs. the calibration range of the model of interest (calibration datasets for many models
363 are available in Thermobar, Wieser et al. 2022b). After identifying models calibrated on suitable compositions,
364 we encourage authors to compile a test dataset of experimental compositions most similar to their system.
365 Ideally these experiments would not have used during calibration of the equation. If the planned workflow in
366 the natural system will involve iterative calculations, these same iterative workflows should be applied to the
367 test dataset. These tests will provide a more realistic estimate of the uncertainty associated with the calculation
368 than simply quoting RMSE values. If there is very little data to help pick, it may be best to perform calculations
369 using several different equations calibrated on relevant compositional and P-T ranges. An average for all these
370 models could be calculated, with the difference between models giving insight into the error in the calculation.
371 At the moment, only a very small proportion of studies compare the results from multiple equations (e.g.,
372 Erdmann et al., 2016; Geiger et al., 2018; Sas et al., 2017; Sheehan and Barclay, 2016 for Cpx-Liq equilibrium,
373 Rasmussen et al., 2022; Wieser et al., 2021 for volatile solubility).

374

375 **1.3. What accuracy and precision are required?**

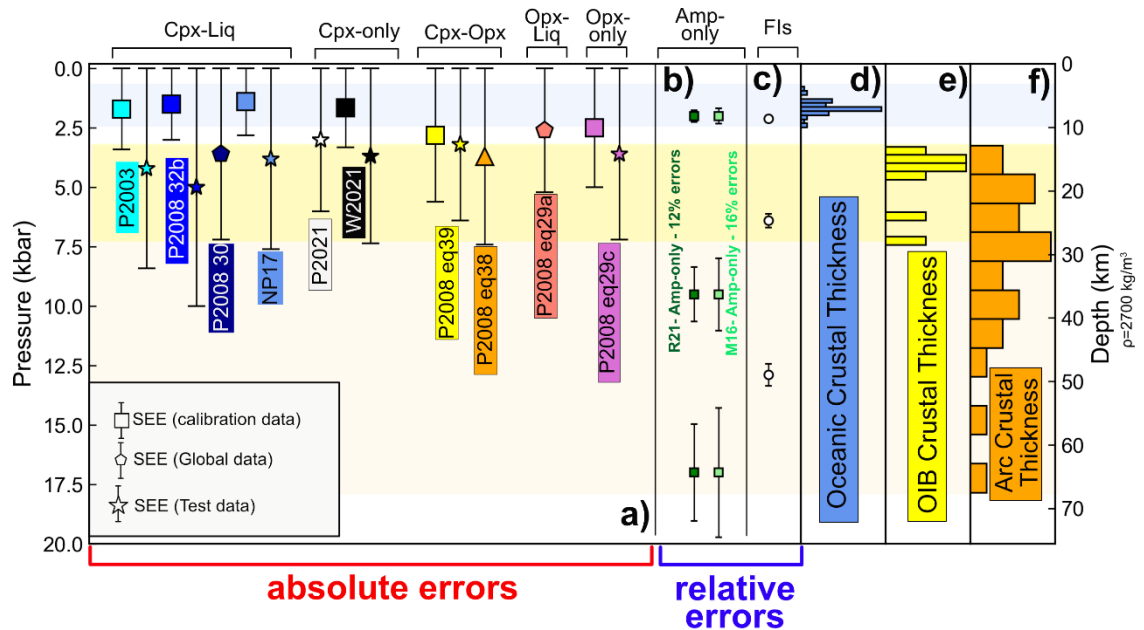
376 In the 2008 RiMG short course, K. Putirka described his Cpx barometer as: '*a chisel, not a pen knife*' (K.
377 Putirka, written comms). Once realistic estimates are made of the precision and accuracy of different
378 thermobarometers using relevant test datasets, it is worth thinking about what scientific questions can be
379 addressed with confidence within the associated uncertainties of each methods. Petrological barometers
380 calculate pressure, which can be converted into depth by making assumptions about crustal and upper mantle
381 densities. Converting pressures to depths allows comparisons to geophysical inversions of magma storage
382 locations within the crust (e.g., Rasmussen et al., 2022), and to field observations in exposed crustal and upper
383 mantle sections. Thus, it is useful to think of errors in the context of crustal and lithospheric thicknesses
384 worldwide.

385 Oceanic crust formed away from the influence of mantle plumes ranges in thickness from ~5–8.5 km,
386 with an average thickness of $\sim 7 \pm 0.8$ km (White et al., 1992). Assuming an average density of 2900–3000 kg/m³
387 (Afonso et al., 2007), this corresponds to an average Moho pressure of ~2 kbar. To be able to conclusively pull
388 apart different crustal storage geometries (e.g., upper vs. lower crust) and distinguish between storage regions
389 at different levels in the crust, a RMSE error of ± 0.25 –0.5 kbar would be needed. No mineral-based barometers
390 applicable to MORB lavas achieve anything like this precision (Fig. 3a vs. d). In fact, even if magma is stored
391 below the Moho (e.g., in slow spreading ridges, Bennett et al., 2019; Drignon et al., 2019), available mineral-
392 melt models can't confidently differentiate upper mantle vs. crustal storage.

393 Crust in OIBs is thicker than in MORB settings because the newer volcanic pile rests on top of older
394 oceanic crust (total crustal thickness of 14–24 km in Hawai'i, Leahy et al., 2010; 14–15 km in La Palma, Ranero
395 et al., 1995), and/or because the plume increases melting extents at the mid-oceanic ridge (e.g., ~11–39 km in
396 Iceland). The elevated crustal thickness in OIBs, corresponding to pressures of 3–4 kbar or greater, means that
397 mineral-based barometers with uncertainties of 2–3 kbar can begin to distinguish storage at the Moho vs. the
398 shallow (e.g., Gleeson et al., 2021). Mineral-based barometers are also aided by the fact that OIB lithosphere
399 can be extremely thick relative to MORB as a result of conductive cooling as the oceanic crust moves away from
400 the ridge (e.g., 45–60 km thick in the Galápagos, Gibson and Geist, 2010; 50–110 km thick in the Hawaiian
401 Islands, Li et al., 2004), and many OIB magmas are stored at sub Moho depths (e.g., Barker et al., 2021; DeVitre
402 et al., 2023; Gleeson et al., 2021). Again, this makes uncertainties of 2-3 kbar less problematic. It is only in
403 volcanic arcs, and particularly continental arcs with thicker crust (Profeta et al., 2016) that mineral-melt
404 barometers can reliably distinguish between storage in the upper, middle and lower crust.

405 While mineral-melt thermobarometers often show a reasonably constant error regardless of the
406 pressure, solubility models show a clear increase in uncertainty at higher volatile contents, so errors are

407 commonly described using percentage errors (e.g., $H_2O = \pm 10\%$ and $CO_2 = \pm 20\%$ for Shishkina et al., 2014,
 408 $H_2O = \pm 10\%$ and $CO_2 = \pm 17\%$ for Iacono-Marziano et al., 2012). Systematic offsets between solubility models also
 409 tend to increase reasonably proportionally with increasing P (Wieser et al., 2022a). Even the large errors
 410 resulting from volume estimates during vapour bubble reconstructions when performing melt inclusion
 411 barometry (more detail in section 3) are percentage, not absolute errors. Many uncertainties associated with
 412 fluid inclusion barometry scale with pressure (Fig. 3, see Section 4). In general, methods with percentage errors
 413 that scale with the value of the quantity, rather than absolute errors, are better suited to distinguishing subtle
 414 variations in magma storage in relatively thin-crustal tectonic settings (Fig 3b-c). Interesting, Ridolfi (2021) and
 415 Mutch et al. (2016) express the errors on their amphibole barometers as percent errors (e.g. 12- 16%, see Fig.
 416 3b), although, these errors only describe the fit to the calibration data, and their magnitude is highly debated
 417 (see Erdman et al. 2016, and section 2.6).



418

419 *Figure 3: Comparison of quoted errors on barometers to estimates of crustal thickness (assuming $\rho=2700 \text{ kg/m}^3$).*
 420 *a) We anchor each method with an absolute uncertainty such that the upper part of the 1σ error bar sits at 0*
 421 *kbar. This visualization shows the range of pressures/depths which cannot be statistically distinguished from*
 422 *storage at the surface. The symbol shape represents whether the quoted SEE/RMSE was for the calibration*
 423 *dataset, a test dataset, or global data. b-c). Relative (%) uncertainties are shown for different pressures. for e),*
 424 *we calculate FI errors assuming an uncertainty in CO_2 density of $\pm 0.01 \text{ g/cm}^3$ and $\pm 50 \text{ K}$ for entrapment T).*
 425 *Oceanic crustal thickness compilation from Chen (1992), OIB thicknesses compiled for this study (see supporting*
 426 *information), Continental arcs from Profeta et al. (2016). Errors for melt inclusions are highly sensitive to bubble*
 427 *volumes, so a generic example cannot be given (see Fig. 24b). Abbreviations: **P2003**: Putirka et al. (2003), **P2008**:*
 428 *Putirka (2008), **NP17**: Neave and Putirka (2017), **W2021**: Wang et al. (2021), **R21**: Ridolfi (2021), **M16**: Mutch et*
 429 *al. (2016).*

430 1.4. Influence of analytical error on precision and accuracy

431 Measurement of any quantity in igneous systems is subject to analytical error. Mineral and melt
 432 compositions are typically measured using an electron microprobe (EPMA), which is associated with random
 433 and systematic uncertainties (see Wieser et al. 2023b for a more detailed discussion). Pressure estimates from
 434 melt inclusions rely on volatile measurements by FTIR or SIMS, EPMA measurements of the host and melt phase,
 435 Raman spectroscopy measurements of the vapour bubble, and estimates of the relative volume of the vapour
 436 bubble (see Section 3 for a detailed discussion). Pressure estimates from fluid inclusions rely on measurements
 437 of the fluid using Raman Spectroscopy/Microthermometry, and an independent estimate of T using mineral or
 438 mineral-melt thermometry (e.g. using EPMA analyses). Thermodynamic methods of inverting liquid

439 compositions or liquid lines of descent rely on EPMA or energy-dispersive spectroscopy (EDS) measurements of
440 glasses, or whole-rock X-ray fluorescence (XRF) measurements.

441 As many of the methods discussed in this review rely on EPMA analysis, we briefly discuss the
442 uncertainties relating to this method. The fundamentally random process of x-ray generation, and subsequent
443 detection by spectrometers is a significant source of uncertainty, termed 'counting statistics'. The magnitude of
444 this uncertainty depends on the concentration in the sample and the beam current and voltage (affecting x-ray
445 production), and the analysis time and spectrometer efficiency (affecting x-ray detection). Most simply, unless
446 long count times and higher beam currents are used, low concentration elements (<1 wt%) tend to be associated
447 with relatively large percentage errors. When analytical errors on all measured oxides are propagated through
448 barometry equations using Monte-Carlo methods, they can generate a large range in calculated P and T.

449 For example, Wieser et al. (2023b) show that measurement of Na₂O in crustal Cpx using popular
450 analytical conditions (e.g. 10 s, 10 nA) is associated with $1\sigma=10-40\%$. Most importantly, the magnitude of this
451 error is often underestimated by factors of 2–4X because secondary standards with higher Na₂O concentrations
452 than the sample are routinely used to assess precision. The large imprecision is problematic because Na₂O in
453 Cpx is often used to calculate the P-sensitive Jadeite component. Propagating typical analytical errors through
454 popular expressions for Cpx-Liq thermobarometry can generate highly correlated PT arrays spanning 3–5 kbar,
455 which could be incorrectly interpreted as transcrustal storage (Wieser et al., 2023b-c). Analytical errors also
456 affect the experimental data used to calibrate thermobarometers. As many experimental studies perform <5
457 measurements on each phase, random analytical error does not get sufficiently averaged out, so the reported
458 phase composition may not be the true phase composition (affecting model calibration, and calculated statistics
459 on test data, see Wieser et al. 2023b, see also Section 2.3).

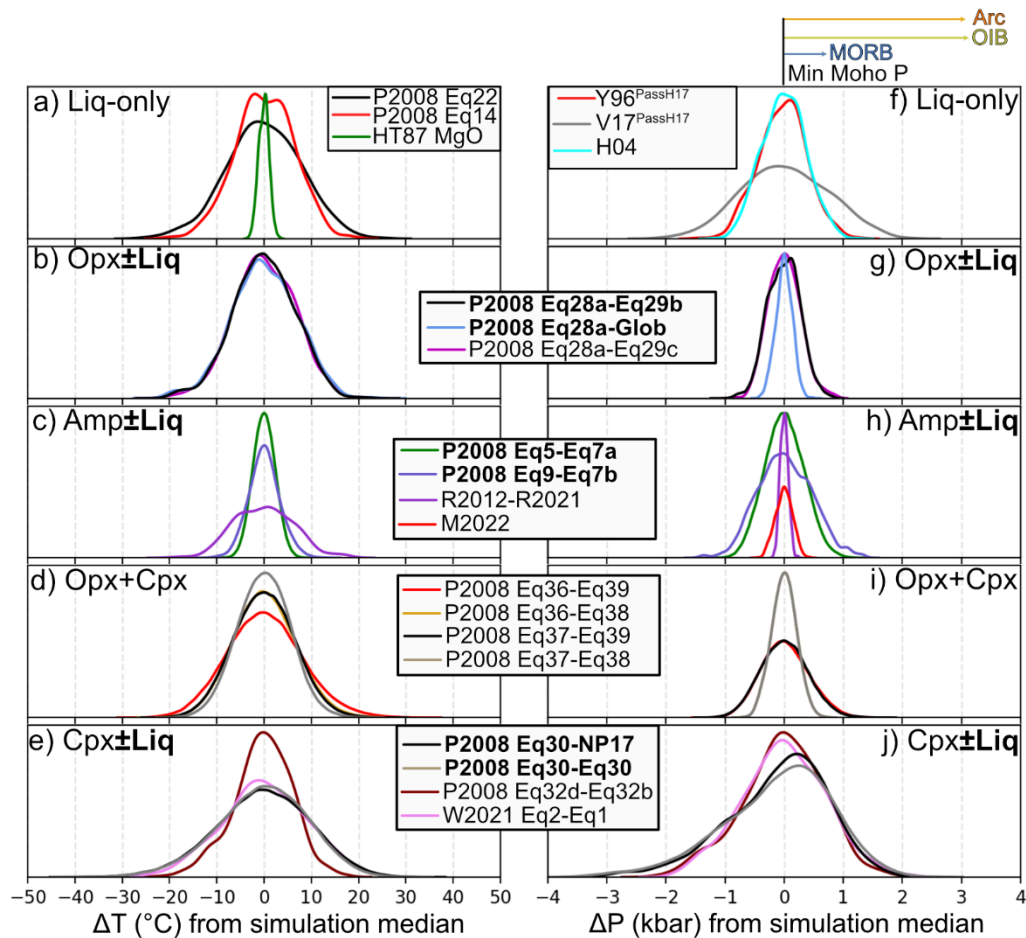
460 To visually demonstrate the effect of analytical error on different mineral-melt thermobarometers, we
461 perform Monte-Carlo simulations using Thermobar (Wieser et al., 2022b, Fig. 4). We use analytical errors
462 estimated by the EPMA based on counting statistics for experimental phase compositions reported by
463 Krawczynski et al. (2012). For each phase, we produce 500 synthetic compositions with each element normally
464 distributed about a measured value in the experiment, with the standard deviation equal to that estimated by
465 the EPMA. We also include $\pm 5\%$ relative error for H₂O in the liquid, which is a very conservative estimate of the
466 error associated with FTIR and SIMS measurements. For two-phase equilibrium (e.g., Cpx-Liq), we consider all
467 possible matches between the 500 synthetic compositions for each phase (250,000 pairs total). We then perform
468 thermobarometry calculations on all synthetic compositions, showing the spread of calculated P and T relative
469 to the median of the distribution (Fig. 4).

470 In general, the influence of analytical error on calculated T is relatively minor ($1\sigma < 20^\circ\text{C}$). The broadest
471 distribution of calculated temperatures comes from equations that are very sensitive to melt H₂O content, such
472 as Liq-only T from P2008 Eq14 and Eq22 (Fig. 4a), Opx-Liq T from P2008 Eq28a (Fig. 4b), and Cpx-Liq T from
473 P2008 Eq30 (Fig. 4e). For calculated P, the spread of simulations is highly variable, with barometry methods
474 sensitive to a component with a relatively low concentration showing a very wide spread of pressure (e.g., Na in
475 Cpx, Fig. 4j). In contrast, barometers sensitive to high concentration elements show very narrow distributions
476 (e.g., Al in Amphibole, Ridolfi, 2021, Medard and Pennec, 2022, Fig. 4h).

477 We also test the OPAM liquid barometer, where pressures are calculated from the composition of melts
478 co-saturated in olivine, plagioclase, and augite (see Section 2.2). As the experiments of Krawczynski et al. (2012)
479 are too H₂O-rich for OPAM, we use estimates of analytical precision for measurements of submarine basaltic
480 glasses from the Galápagos Spreading Centre (Gleeson and Gibson, 2021). Notably, the analytical errors have a
481 very similar magnitude to those from Krawczynski et al. (2012). This method is very sensitive to analytical
482 uncertainty, returning a similar range of calculated pressures to Cpx-based mineral-based barometers. The
483 model of Voigt et al. (2017) is particularly sensitive, because of the inclusion of a term for the Cr content of the
484 liquid, which has a low concentration, so is associated with poor analytical precision.

485 Overall, the effect of propagated analytical error on P and T depends greatly on the selected equation
486 (e.g., Fig. 4f and i), as well as the analytical conditions used. Thus, studies should propagate EPMA-estimates of
487 counting statistic errors from each analysis using their chosen equation. Secondary standards should only be
488 used to assess accuracy, not precision, as precision of an EPMA analysis is very closely related to the concentration

489 of the element of interest, so varies greatly depending on the individual mineral composition. Analytical errors
 490 should be propagated for all thermobarometric techniques, including melt inclusion and fluid inclusion
 491 barometry (see Section 5 for an example). If propagated analytical errors are of similar magnitude to the
 492 resolution required to investigate the geological process of interest, time must be spent optimizing analysis (See
 493 section 2.3). It should of course be noted that analytical variability is only one possible source of error.
 494 Simulations may indicate a precision of 0.1 kbar (random error), but the method may be inaccurate by 3 kbar at
 495 the conditions of interest (systematic error).



496
 497 *Figure 4: Monte Carlo simulations of the influence of analytical precision on thermometry (a-e) and barometry*
 498 *(f-j) calculations. All panels except f show analytical uncertainties from EPMA counting statistics from*
 499 *Krawczynski et al. (2012) with H₂O of ±5%. As OPAM (panel f) is not applied to arc magmas, we propagate EPMA*
 500 *errors from natural Galápagos glasses from Gleeson and Gibson (2021). The bars at the top show approximate*
 501 *minimum and maximum Moho pressures from each tectonic setting (see Fig. 3).*

502
 503 **2. Mineral Thermobarometry and Chemometry**

504 The seminal review of Putirka (2008, hereafter P2008) summarizes several decades of
 505 thermobarometric work, and proposes a large number of new empirical expressions linking the compositions of
 506 Cpx±Liq, Opx±Liq, Cpx+Opx, Plag±Liq, and Plag+Kspar to P and T. These new equations have similar forms to
 507 those published in older papers, but have recalibrated coefficients, and additional terms to improve
 508 performance when applied to the large compilation of experiments published in 2008 (LEPR; Library of
 509 Experimental Phase Relationships, Hirschmann et al., 2008). In the same issue, Anderson et al. (2008)
 510 summarized available P-T constraints on granitic rocks. To avoid repetition, we largely focus on new methods
 511 developed since 2008, as well as assessing the performance of these 2008 models using new experiments
 512 published in the last 15 years. Specifically, we assess models using a new test dataset of experiments conducted
 513 on arc magma compositions (ArcPL – Arc post LEPR, Wieser et al. 2023a-b) at variably hydrous (H₂O= 0–16.6
 514 wt%, median=4.7 wt%) crustal conditions (0–17 kbar). Importantly, the experiments in this new dataset were

515 not used during the calibration of most models, and any overlaps were removed when testing a specific model.
516 Our focus on arcs is partially a result of the experimental data available not used in model calibration, but also
517 reflects the fact there has been very little focus on this tectonic setting, despite the fact it is one of the few places
518 where the crust is thick enough that mineral-based barometers may be able to resolve different crustal storage
519 regions within uncertainty (Fig. 3). Additionally, there has been very little evaluation of these methods in this
520 tectonic setting. For methods not applicable to arc magmas (e.g. OPAM, section 2.2), we compile other available
521 experiments. For other methods, we do not believe sufficient ‘test’ experiments are available for MORB, OIB
522 and alkali lavas to build on the comparisons presented by Masotta et al. (2013), Masotta and Mollo (2019),
523 Neave et al. (2019) and Neave and Putirka (2017).

524

525 **2.1. Liquid-only thermometry**

526 A huge variety of liquid-only thermometers exist, with varying complexity and calibration ranges. For
527 example, the thermometer of Helz and Thornber (1987) uses just the MgO content of the liquid, calibrated on
528 compositions from the Kīlauea Iki lava lake. In contrast, P2008 eq14 has terms for the MgO, FeO_t, Na₂O, K₂O,
529 H₂O and Mg# in the liquid, and was calibrated/tested on 1536 olivine-saturated liquids. There are also a number
530 of olivine-liquid thermometers with a term for the partitioning of Mg between olivine and liquid (D_{Mg}^{Ol-Liq}). In
531 their supporting spreadsheet, Putirka (2008) replace this term with the theoretical value of D_{Mg} predicted by
532 Beattie (1993) to produce a liquid-only thermometer. Here, we discuss the best-performing thermometers for
533 our new test dataset.

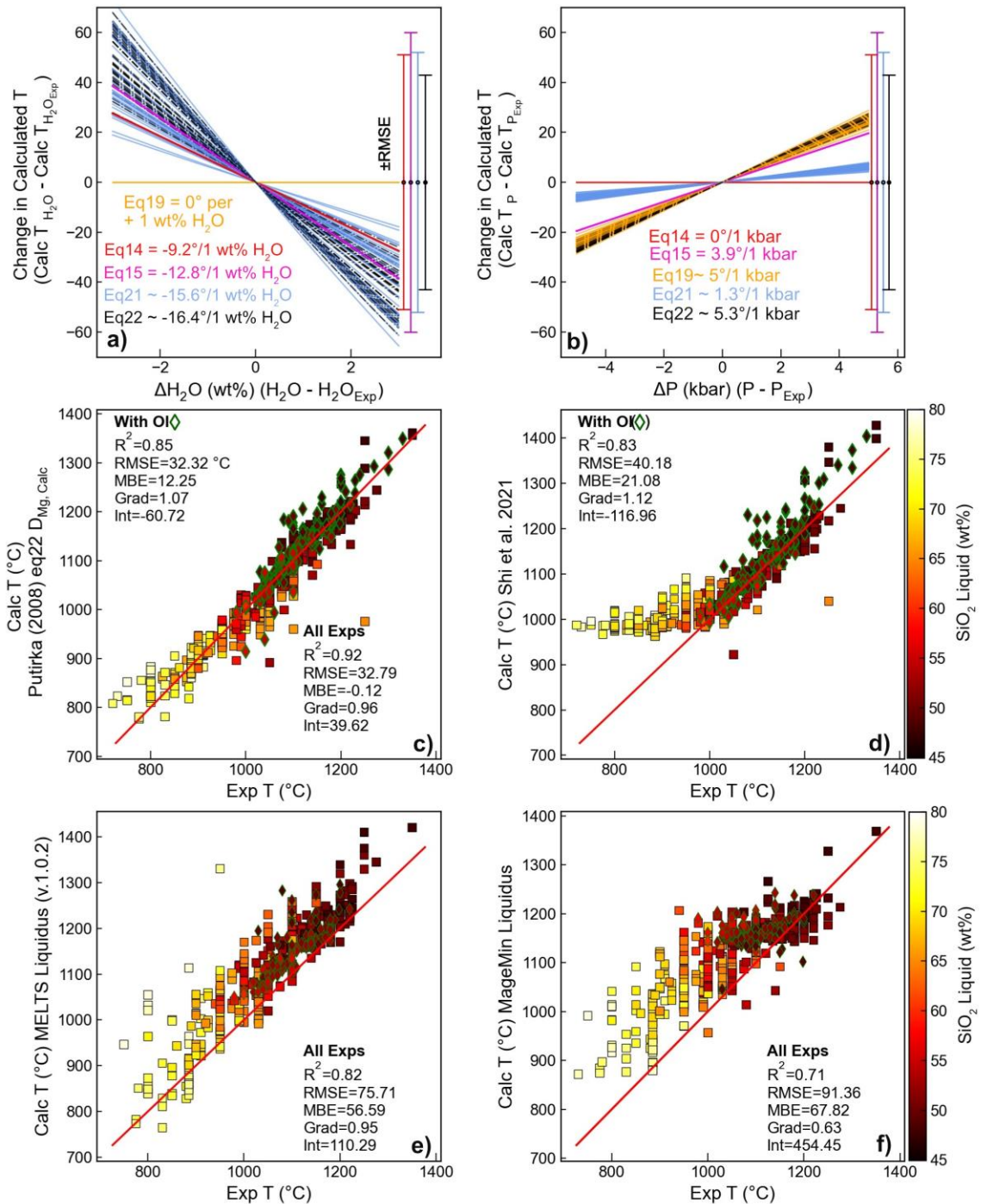
534 As P and H₂O may be poorly constrained in many systems, we first assess the sensitivity of various
535 thermometers to these parameters. We randomly select 40 experiments - for each liquid composition, we make
536 100 duplicates with the experimental H₂O content perturbed by ±3 wt% (Fig. 5a), and separately perturb the
537 experimental P by ±5 kbar (Fig. 5b). We take the calculated T at these perturbed values and subtract the
538 calculated T at the measured P and H₂O (ΔT , ΔP). Thermometers with a H₂O term show variable, but relatively
539 high sensitivity to H₂O, with the average calculated T dropping by ~9 to 16°C per wt% H₂O added (Fig. 5a). For
540 comparison, we show the quoted RMSE of each thermometer. Uncertainty in H₂O of 3 wt% introduces a
541 systematic error comparable in size to the stated RMSE (Fig. 5a). Thermometers are substantially less sensitive
542 to P; uncertainty in P of 5 kbar results in <30°C of variation. Even a full 10 kbar of uncertainty in P doesn’t exceed
543 the quoted RMSE (Fig. 5b).

544 Given the sensitivity of calculated temperatures to H₂O, we only use experiments where H₂O was
545 determined using quantitative methods (calibrated volatile-by-difference, FTIR, SIMS, Raman spectroscopy). We
546 perform calculations using experimental P and measured H₂O, because there are no suitable liquid barometers
547 or hygrometers to iterate for all these unknowns. For the ArcPL dataset, the best liquid-only thermometer is an
548 adapted version of the Ol-Liq thermometer of P2008 Eq22, where the olivine D_{Mg} term is replaced with the
549 calculated D_{Mg} value from Beattie (1993), converting it into a Liq-only thermometer (Fig. 5c). Surprisingly, this
550 adapted Ol-Liq thermometer does a very good job of predicting T in experiments without olivine, including melts
551 with high SiO₂ contents (square symbols). We also use the new liquid-only thermometer calibrated on
552 experiments containing olivine from Shi et al. (2021). This thermometer performs very well for experiments
553 containing olivine, with slightly better statistics than Eq22 D_{Mg} (Fig. 5d). Unsurprisingly, given it was calibrated
554 with Ol-bearing liquids in mind, it drastically overpredicts T at MgO<~ 2–3 wt% for experiments without olivine
555 (Supporting Fig. 1) – although this still presents an interesting contrast with Eq22 D_{Mg} .

556 We also calculate the liquidus T using rhyolite-MELTS v1.2.0, v.1.0.2 and pMELTS (Gualda et al. 2012;
557 Gualda and Ghiorso, 2015, Ghiorso et al., 2002, Fig. 5e, Supporting Fig. 2). All three versions of MELTS give similar
558 statistics; pMELTS has the higher R² and lowest MBE and RMSE (R²=0.89, MBE=44°C, RMSE=58°C), but shows
559 significantly worse performance than v1.0.2 for the lowest T liquids. It is notable that the MBE for all 3 versions
560 is relatively high A (44–56°C vs. -0.12°C for eq22 D_{Mg}), which demonstrates that MELTS consistently
561 overestimates liquidus temperatures (Fig. 5e). The other disadvantage of MELTS calculations vs. empirical
562 approaches is that the calculations are very computationally expensive; 2000 liquidus calculations take 47
563 minutes using pyMELTScalc (through alphaMELTS for Python) compared with 0.015 seconds using eq22 D_{Mg} in
564 Thermobar on a desktop computer with 128 Gb RAM and a 10-core 10th generation Intel i-9 processor. Liquidus

565 temperatures can also be calculated using the Holland et al. (2018) thermodynamic model, implemented
 566 through the Julia-based Gibbs Free Energy minimization software MAGEMin (Reil et al. 2022). The fit between
 567 the experimental and calculated T is considerably worse than that achieved by rhyolite-MELTS v1.2.0, with
 568 temperatures often overestimated by 100–200°C, particularly for experiments performed at <1100°C (Fig. 5f).
 569 These calculations take similar times to MELTS calculations. In summary, if melt H₂O contents are well
 570 constrained, empirical liquid-only thermometers such as eq22DMg of Putirka (2008) perform surprisingly well
 571 across a surprisingly wide range of melt compositions.

572



573

574 *Figure 5: Assessing Liquid-only thermometers. a-b) Sensitivity of calculated T to H₂O (a) and pressure (b). For 40*
 575 *randomly selected experiments (each represented by a line), we perturbate the experimental H₂O content by ±3*

576 wt% (a), and pressure by ± 5 kbar (b). These plots show that increasing H_2O causes a drop in calculated T , and an
577 increase in P causes an increase in T . c-f) Experimental T vs. calculated T for experiments where H_2O was
578 measured by quantitative methods (FTIR, SIMS, Raman, calibrated volatiles by difference). Experiments
579 containing olivine are shown as green-outlined diamonds, and experiments without olivine as black-outlined
580 squares. All symbols are colored by the SiO_2 content of the melt. MELTS (part e) and MAGEMin (part f) liquidus T
581 calculated using $Fe^{3+}/Fe_T=0.15$ (calculated T are not very sensitive to Fe^{3+} but having $Fe^{3+}>0$ is necessary for the
582 algorithm to converge).

583

584 2.2. Liquid-only barometry

585 Barometric methods based on the composition of silicate melts rely on the fact that the thermodynamic
586 variance of the system (i.e., the degrees of freedom) is lower in multi-phase saturated systems, so the melt
587 composition contains information about the conditions of magma storage. This is typically discussed with
588 regards to magma evolution along mineral cotectics, or at invariant points such as eutectics, where the degrees
589 of freedom is close to zero (i.e., high-silica rhyolites, Ludden, 1978; Vogt, 1931). The positions of these cotectics
590 and eutectics are sensitive to pressure because of differences in the volume of common igneous minerals. Thus,
591 if the influence of P and melt composition on the location of cotectics/eutectics can be determined by
592 thermodynamic or empirical parameterisations, measured compositions of lavas saturated in the required
593 phases can be used to calculate P (e.g., Grove et al., 1992; Gualda et al., 2012; Wilke et al., 2017; Yang et al.,
594 1996, Fig. 1g).

595 Thermodynamic approaches to liquid-only barometry have become increasingly common in the last
596 decade, with the rhyolite-MELTS thermodynamic models used to assess the storage pressure of evolved,
597 rhyolitic magmas from several locations worldwide (Gualda and Ghiorso, 2014; Harmon et al., 2018; Pamukcu
598 et al., 2015). The application of thermodynamic methods to liquid-only barometry is addressed in detail in
599 Section 8. Here, we instead focus on empirical methods calibrated using experimental data.

600 2.2.1. OPAM Barometry

601 Experimental work on the location of the olivine-plagioclase-augite-melt (OPAM) cotectic has been
602 ongoing for at least 3 decades. Early work constrained the position of the OPAM cotectic at 0.001 kbar in the
603 simplified $CaO-MgO-Al_2O_3-SiO_2$ (CMAS)+ FeO (Shi, 1992) and $CMAS+FeO+Na_2O$ systems (Shi, 1993). Further
604 experiments on natural MORB compositions demonstrated that minor components in the liquid phase (e.g., Ti,
605 Na, and K) and the expansion of the clinopyroxene stability field at higher pressures strongly influences the
606 cotectic position (Grove et al., 1992; Yang et al., 1996). Using these observations, Grove et al. (1992) provided a
607 set of empirical equations to locate the position of the olivine+plagioclase+melt and OPAM cotectics as a
608 function of melt chemistry and pressure. Yang et al. (1996, hereafter Y96) built on this work with an updated
609 parameterisation for the location of the OPAM cotectic, expressing the Mg, Ca, and Al molar fractions (X_{Mg} , X_{Ca} ,
610 and X_{Al}) of an OPAM-saturated melt as a function of P and the remaining molar fractions (e.g., X_{Si} , X_{Ti}). For
611 example, their expression for the molar fraction of Ca has the following form:

$$612 X_{Ca} = 1.133 - 0.00339 * P(kbar) - 0.569 * X_{Na} - 0.776 * X_K - 0.672 * X_{Ti} - 0.214 * X_{Fe} - 3.355 * X_{Si} +$$
$$613 2.830 * X_{Si}^2 \text{ [Equation 4]}$$

614 In 2017, these equations were updated by Voigt et al. (2017, hereafter V17), who used new experimental data
615 to show that Cr_2O_3 has a strong influence on clinopyroxene phase stability. Their equations have the same
616 functional form, with an addition of a term for the molar fraction of Cr, separate terms for ferrous and ferric Fe
617 molar fractions, and updated coefficients for the other parameters:

$$618 X_{Ca} = 1.07 - 0.02707 * P(GPa) - 0.634 * X_{Na} - 0.618 * X_K - 0.515 * X_{Ti} - 0.188 * X_{Fe^{2+}} - 0.597 *$$
$$619 X_{Fe^{3+}} - 3.044 * X_{Si} + 2.477 * X_{Si}^2 - 9.367 * X_{Cr} \text{ [Equation 5]}$$

620 Herzberg (2004) (hereafter H04), developed an alternative approach, relating P to liquid components projected
621 onto an Anorthite, Diopside, Enstatite ternary diagram from Olivine:

$$622 P(GPa) = -9.1168 + 0.2446 * (0.4645 * En + An)$$

623 $-0.001368 * (0.4645 * En + An)^2$ [Equation 6]

624 Despite the greater simplicity of pressure calculations using the H04 OPAM parameterisation, the Y96
625 and V17 equations for calculated molar fractions have formed the basis of most OPAM barometry over the last
626 decade (V17: Bell et al., 2021; Stock et al., 2018, Y96: (Baxter et al., 2023; Caracciolo et al., 2022, 2020;
627 Halldórsson et al., 2022). The methods used to extract pressure information from these expressions vary. Early
628 studies used the equations of Y96 to calculate the position of the OPAM cotectic at multiple pressures and
629 plotted these positions on an olivine-clinopyroxene-quartz pseudoternary diagram (projected from plagioclase).
630 Visual comparison of the position of the calculated OPAM cotectic to natural melt compositions projected onto
631 the same pseudoternary diagram were used to estimate the pressure of magma storage (Geist et al., 1998;
632 Maclennan et al., 2001). Kelley and Barton (2008) use a complex approach calculating theoretical and measured
633 normative mineral components at different pressures, regressing these components against pressure to
634 determine the best fit for each measured sample. More recent studies have determined the pressure of the
635 minimum misfit between calculated X_{Mg} , X_{Ca} , and X_{Al} using the equations of Y96 or V17, and measured X_{Mg} , X_{Ca} ,
636 and X_{Al} in their samples without requiring the conversion to normative mineral components (Hartley et al. 2018).

637 Regardless of the calculation method used to obtain P, OPAM barometry requires input melt
638 compositions to be saturated in all 3 solid phases (olivine, clinopyroxene, and plagioclase). Solving for pressure
639 using the equations of Y96 or V17 for samples that are not saturated in all 3-phases could lead to erroneous
640 results and may explain the wide range in calculated P estimated for some systems (e.g., 1.4– 7.7 kbar at Laki in
641 Iceland; Kelley and Barton, 2008). Therefore, it is important to determine which samples are co-saturated before
642 interpreting OPAM calculations. One way to ensure 3-phase saturation in the target melts is via textural
643 observations, such as petrographic observations of euhedral crystals with no disequilibrium textures.
644 Alternatively, in systems with abundant whole-rock or matrix glass data spanning a range of MgO contents,
645 comparing liquid lines of descent with mass balance approaches or fractional crystallization models (e.g.,
646 MELTS, Petrolog3, Danyushevsky and Plechov, 2011; Gualda et al., 2012) can be used to confirm 3-phase
647 saturation.

648 An approach that can be applied to individual liquid compositions without textural or LLD context to
649 calculate P and check for cosaturation was developed by Hartley et al. (2018). They determine the probability of
650 three-phase saturation using a Chi-squared distribution to calculate the misfit between the predicted (X_i^{Pred})
651 and measured (X_i^{Meas}) molar fractions for Mg, Ca and Al:

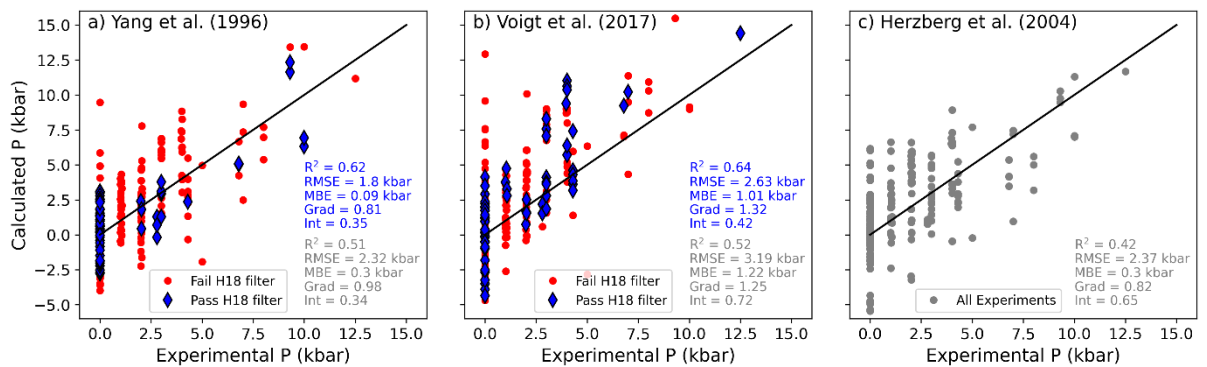
$$652 \chi^2 = \sum_{i=1}^3 \left[\frac{X_i^{Meas} - X_i^{Pred}}{\frac{\sigma_{X_i} X_i^{Meas}}{100}} \right]^2 \text{ [Equation 7]}$$

653 Here, σ_{X_i} is an estimate of the relative analytical uncertainty for each cation under consideration
654 (expressed as a percentage). As X_i^{Pred} is a function of the system pressure, users can determine the best-fit
655 model pressure by locating the position of the minimum possible χ^2 value (χ^2_{Min}). To assess whether the melt
656 is truly three-phase saturated, Hartley et al. (2018) compare χ^2_{Min} to the cumulative distribution function of
657 the Chi-squared distribution with 2 degrees of freedom. A probability is selected as a cut off value (e.g., p=0.05,
658 p=0.2) - Hartley use a probability of fit, P_f , which can be thought of as 1 minus the p value. If χ^2_{Min} is less than
659 the critical value of the chi squared cumulative distribution function for this chosen cut off (i.e., chosen p-value
660 and n=2 degrees of freedom), the liquid is assumed to be three-phase saturated. By considering the results of
661 OPAM calculations on experimental melt compositions (including the Yang et al. 1996 calibration data), Hartley
662 et al. (2018) determine that a 'probability of fit' filter of p~0.2 ($P_f=0.8$) results in a good fit between the
663 experimental and calculated pressures, while minimising the number of 'false negatives' (i.e., melt compositions
664 which are OPAM saturated, but would fail this test). The minimisation method and co-saturation check of Hartley
665 et al. (2018) (hereafter H18) has been utilised by several studies investigating the storage conditions of MORBs
666 and OIBs (Bell et al., 2021; Stock et al., 2018, Baxter et al., 2023; Caracciolo et al., 2022, 2020; Halldórsson et al.,
667 2022).

668 Baxter et al. (2023) evaluated the performance of the Y96 equations using 315 OPAM saturated
669 experimental melt compositions, ranging from 1 atm to 12.5 kbar pressure. They filter these experiments using

670 the H18 filter and exclude those with MgO<4 wt%, leaving 95 experiments. Comparing calculated and
 671 experimental pressures for these filtered experiments yields a RMSE of ± 1.51 kbar, which is similar to the
 672 'random error' of ± 1.32 kbar estimated by Hartley et al. (2018, definition uncertain). However, both studies
 673 evaluated the performance of the Y96 equations using a dataset including some experiments used in the Y96
 674 calibration. For example, 57% of the 95 experiments assessed by Baxter et al. (2023) are part of the Y96
 675 calibration dataset. If we rerun the comparison using only experimental data that was not used in the Y96
 676 calibration the RMSE increases from ± 1.51 kbar to ± 1.89 kbar. A particular issue is that only 7/41 of the remaining
 677 experiments were conducted at >0.001 kbar, making it very hard to assess the performance of the Y96
 678 barometer without new test data at higher pressures.

679 To test the performance of all three OPAM barometers listed here (Y96, V17, and H04), and the success
 680 of the H18 filter, we compile an experimental dataset of OPAM saturated experiments not used to calibrate
 681 either Y96 or V17. N=188 overlap with the dataset of Baxter et al. (2023), with N=38 experiments not in that
 682 compilation. Fig. 6 demonstrates that there are strong correlations between the calculated and experimental
 683 pressures for all OPAM methods when the H18 saturation check is not applied (R^2 of 0.51, 0.52, and 0.42 for
 684 Y96, V17, and H04 respectively, all symbols, grey statistics on Fig. 6). Despite having the highest R^2 value of the
 685 three methods tested here, calculated pressures determined using the V17 expressions display the largest
 686 uncertainties (RMSE=3.19 kbar) and a systematic offset to high pressures (MBE = 1.22 kbar, Fig. 6b). The Y96
 687 expression has a smaller systematic offset (gradient=0.98, MBE=0.3 kbar), as well as a lower RMSE (2.32 kbar,
 688 Fig. 6a). The parameterisation of H04 also returns a relatively low RMSE (2.37 kbar) and similar MBE to the Y96
 689 method (0.3 kbar), but has a lower gradient of the correlation (0.82; Fig. 6c).



690

691 *Figure 6: Experimental vs. calculated P using the OPAM expressions of Yang et al. (1996), Voigt et al. (2017) and*
 692 *Herzberg (2004) for OPAM-saturated experiments on MORB-like compositions. The calculated pressure was*
 693 *determined using the Chi-squared method of Hartley et al. (2018, H18) for the Yang et al. (1996) and Voigt et al.*
 694 *(2017) equations (a,b). Samples passing the co-saturation filter of Hartley et al. (2018) are shown as blue*
 695 *diamonds, while those that fail are shown as red circles. The filter is not applicable to the method of Herzberg et*
 696 *al. (2004, part c).*

697 The larger uncertainty and systematic offset in pressures estimated using V17 likely originates from the
 698 sensitivity of these expressions to the Cr_2O_3 content of the melt phase. Only 53 of the 225 experiments used in
 699 this analysis (~24%) report melt Cr_2O_3 contents, despite most experiments using natural basalt compositions
 700 that likely contain at least trace amounts of Cr_2O_3 . Adding Cr_2O_3 into the melt phase changes the stability of
 701 pyroxene (see Fig. 3, Onuma and Tohara, 1983), and thus the pressure estimated by OPAM barometry (Voigt et
 702 al., 2017). Consequently, the systematic offset to higher pressures obtained by applying the V17 expressions to
 703 our compiled experimental database might result from the absence of reported Cr_2O_3 in most experiments, and
 704 uncertainty as to whether Cr was even present in starting materials (Wieser et al. 2023b). Additionally, it is
 705 unclear how precise the analyses of Cr_2O_3 in these experiments are; typical analytical conditions can result in
 706 large errors for this low concentration oxide (propagating into a much wider spread of pressures than using Y96
 707 or H04, Fig. 4f). Despite its poor performance on our test dataset, we cannot rule out the possibility that V17
 708 may be the best parameterization in natural Cr containing systems, even if it behaves poorly on Cr-free
 709 experiments. Further experimental work on Cr-bearing experiments where the Cr content of the melt was

710 characterized with high precision at a range of pressures are required to assess the performance of the V17
711 expressions as an OPAM barometer in natural systems.

712 Interestingly, although all N=225 experiments were OPAM saturated, only 27% (N=61) pass the H18
713 cosaturation filter when the equations of Y96 are used (blue diamonds, Fig. 6a). While the statistics for calculated
714 vs. experimental pressures are greatly improved using only experiments which pass the filter, it is concerning
715 how many false negatives this filter produces, particularly as only 18 of the experiments which passed the filter
716 were performed at pressures above 0.001 kbar. To further assess the performance of the H18 saturation filter,
717 we isolated experiments on MORB-like compositions that are saturated in only one or two (N = 172) of the three
718 key mineral phases in OPAM barometry. Using the Y96 expression, 19% of these non-OPAM saturated
719 experiments pass the H18 co-saturation filter (false positives). These results demonstrate that the H18 co-
720 saturation filter should not be used in isolation to identify which samples are suitable for OPAM barometry.
721 Therefore, petrological observations of three-phase saturation remain critical for determining pressures via
722 OPAM barometry.

723 To date, OPAM barometry has mostly been used to evaluate the storage pressure of MORBs, or
724 tholeiitic to transitional OIBs (as these compositions broadly overlap with the calibration dataset of Yang et al.
725 1996). Unfortunately, the uncertainty associated with OPAM barometry assessed using our independent test
726 dataset (RMSE = 1.8 – 2.32 kbar, Fig. 6) indicates that this method does not have the resolution to distinguish
727 between upper vs lower crustal storage at most mid-ocean ridges. However, at hotspot influenced ridges (e.g.,
728 Iceland) and regions of plume derived volcanism (e.g., ocean islands), the thickened crust (Fig. 3e) means that
729 OPAM can provide insights into the characteristics of magma storage in these locations if independent checks
730 for 3-phase saturation are performed prior to pressure calculation (via petrographic observations or liquid line
731 of descent analysis). For example, melt inclusion and matrix glass data from Barðarbunga, Iceland, indicates that
732 there is a slight difference in the entrapment pressure of melt inclusions and the final equilibration pressure of
733 the matrix glasses (Hartley et al. 2018; Caraccioli et al. 2022).

734 **2.2.2. Other liquid-based barometers**

735 The effect of H₂O on phase boundaries in the OPAM system has not been investigated in detail, meaning
736 this method cannot be applied to arc magmas with confidence. To provide a liquid-based thermobarometer with
737 application to more hydrous systems like volcanic arcs, Blundy (2022) create parametrizations for the stability
738 of clinopyroxene-hornblende-orthopyroxene-plagioclase-ilmenite (CHOMPI) as a function of P, T, and the ratio
739 of H₂O and CO₂ in the fluid, including a cosaturation check to establish whether CHOMPI phases were present
740 based on just a liquid composition. However, Wieser et al. (2023d) show this cosaturation test classifies ~44%
741 of ArcPL experiments lacking the CHOMPI assemblage as CHOMPI-saturated (false positives), and unsurprisingly
742 these experiments show a poor correspondence between calculated and experimental pressure (as the system
743 is not low variance). The logic behind the CHOMPI approach has been generalized to liquids saturated in a wider
744 variety of phases by Weber and Blundy (2023), who apply a regression tree machine learning algorithm to a
745 training dataset of liquids ranging from basalt to rhyolite. As this model is still being tweaked and is currently a
746 preprint (Weber, written comms), we do not comment on it further.

747 **2.3. Clinopyroxene±Liquid**

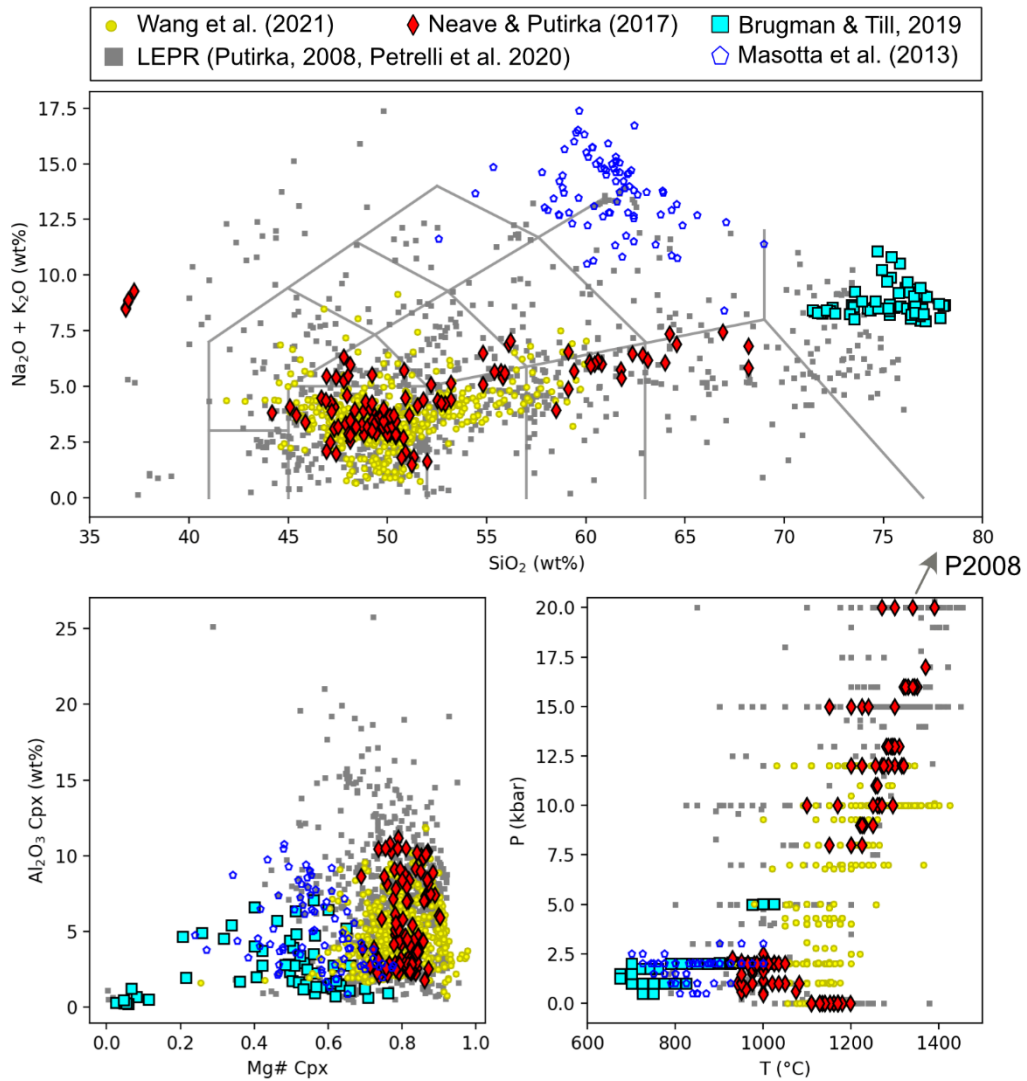
748 The majority of Cpx-Liq thermobarometers rely on the exchange of diopside hedenbergite (DiHd,
749 CaFeSi₂O₆) and Jadeite (Jd, NaAlSi₂O₆) between Cpx and liquid. Here, we briefly summarize the most recent
750 parameterizations of Cpx equilibrium, and workflows that have been developed for calculating P and T in natural
751 systems. A detailed discussion of pre-2008 models can be found in Putirka (2008, and refs within), and a
752 description of the best Cpx-Liq models for our test dataset and sensitivity to P and T as well as the best
753 equilibrium tests to use can be found in Wieser et al. (2023a-b).

754 Putirka (2008) propose a number of equations based on Cpx-Liq equilibria (Eq30, Eq31, Eq32c for P,
755 Eq33 for T), expanding and recalibrating the models of Nimis (1995) and Putirka et al. (1996, 2003) to account
756 for an increase in experimental data (particularly hydrous experiments). More recently, several new equations
757 have been calibrated which focus on a more limited subset of compositional space than these global regressions
758 (Fig. 7). Neave and Putirka (2017) calibrate a Cpx-Liq barometer for application to tholeiitic basalts from ocean
759 island settings (specifically Iceland) using 6 experimental studies (N=113 experiments) from LEPR with mafic-
760 intermediate compositions, and pressures ranging from atmospheric to 20 kbar (Neave and Putirka, 2017, Fig.

761 7, red diamonds). Masotta et al. (2013) conduct experiments and compile available literature data on melts with
762 trachytic to phonolitic compositions (Fig. 7, blue pentagons), calibrating a Cpx-Liq barometer applicable to more
763 alkaline compositions (which are poorly represented in the calibration dataset of P2008). Their expressions have
764 a very similar/identical form to those of Putirka (2008), with recalibrated coefficients. Brugman and Till (2019)
765 note that in high-silica melts, there is very little Al_2O_3 in Cpx (<2 wt%), and the calculated Jd component is very
766 low or even zero. Along with the fact that high Si compositions are very poorly represented in P2008, they
767 showed that existing Cpx-Liq thermometers overestimated temperatures in evolved melts by up to 170°C. Thus,
768 Brugman and Till (2019) compiled recent studies from the literature on rhyolitic compositions (e.g., Almeev et
769 al., 2012; Bolte et al., 2015; Gardner et al., 2014) supplemented with their own experiments on the Scaup Lake
770 Rhyolite (Fig. 7, cyan squares), to calibrate a new thermometer for highly evolved melts which is independent
771 of Jadeite, P, and H_2O content.

772 Another key shift in the use of Cpx-based barometry since 2008 has accompanied the rapid rise in
773 programming literacy amongst petrologists, allowing the development of new workflows based on existing
774 thermobarometry equations. For example, while experimental studies have clearly paired Cpx and liquid
775 compositions, it is significantly more challenging in natural systems to identify such pairs. Typically, a given
776 volcanic eruption will erupt a narrow range of liquid compositions along with a much more chemically diverse
777 crystal cargo, incorporating Cpx crystals grown from a wide variety of melt compositions. Additionally, many
778 whole rock compositions are a mix of crystals and melts, and not representative of true liquids (Reubi and
779 Blundy, 2009; Ubide et al., 2022). A variety of algorithms have been developed to try to identify matched pairs,
780 by combining erupted Cpx compositions with liquids erupted over a longer time period at a given edifice, or even
781 compilations of whole-rock data from an entire volcanic region.

782 For example, Maclennan et al. (2001) assessed magma storage pressures of basalts from the Icelandic
783 Northern Volcanic Zone by filtering possible Cpx-Liq matches using the K_D equilibrium test of Putirka (1999).
784 Winpenny and Maclennan (2011) devised a more complex test for Cpx-Liq equilibrium, using equation 35 of
785 Wood and Blundy (1997) for K_D , and trace element equilibrium tests. Specifically, they use trace elements
786 measured in Cpx, and then use the partition coefficients from Wood and Blundy (1997) to calculate the expected
787 trace element contents of equilibrium liquid compositions. By comparing these predicted liquid compositions to
788 available trace element data for compiled liquids (for Ce or La, Nd or Sm, and Yb, Dy and Y depending on data
789 availability), they assess all possible matches between Cpx erupted at Borgarhraun, and ~1000 whole-rock and
790 glass analyses from Icelandic Basalts for equilibrium. However, this method requires trace element data in both
791 Cpx and liquids/whole-rock, which isn't widely available in the literature for different volcanic systems (and is
792 rarely collected as part of thermobarometric studies). Furthermore, the trace element partition coefficients used
793 in these calculations are highly sensitive to the temperature of the system, complicating calculations (Sun and
794 Liang, 2012; Wood and Blundy, 1997).



795

796 *Figure 7: Calibration range of Cpx-Liq and Cpx-only thermobarometers. Since the compilation of the LEPR*
 797 *database in 2008 (Hirschmann et al., 2008) used to calibrate Putirka (2008) and Petrelli et al. (2020, grey*
 798 *squares), many new thermobarometers have focused on specific regions of compositional space: Brugman and*
 799 *Till (2019, cyan squares), Masotta et al. (2013, blue pentagons), Neave and Putirka (2017, red diamonds). TAS*
 800 *lines drawn using Stevenson (2015).*

801

802 Neave and Putirka (2017) and Neave et al. (2019) develop an R code (also used by Gleeson et al., 2021
 803 and Stock et al., 2018) to assess equilibrium in Cpx-Liq pairs using components which can be calculated from
 804 elements measured routinely by electron microprobe (Diopside-Hedenbergite, DiHd; Enstatite-Ferrosilite, EnFs;
 805 Calcium Tschermak, CaTs). Specifically, they assess the difference in the measured components in the Cpx and
 806 the equilibrium components calculated from the liquid composition using Eq35 of P2008 for K_D , from Mollo et
 807 al. (2013) for DiHd and EnFs, and Putirka (1999) for CaTs. As the selected K_D equilibrium equation is sensitive to
 808 T, and DiHd, EnFs and CaTs to P and T, equilibrium tests must be calculated alongside P and T estimates. A
 809 computationally optimized algorithm loosely based on the Neave R algorithm (which was never publicly
 810 released) was published as part of the Open-Source Python3 tool Thermobar (Wieser et al. in 2022b). This tool
 811 allows comparison of 100s of Cpx and Liq within seconds, with highly customizable equilibrium filters. Even with
 812 fast matching codes, identifying Cpx-Liq pairs is associated with substantial uncertainty regarding choice of
 813 equilibrium tests, and the chosen cut-off parameter (see Wieser et al. 2023a for arc magmas). In many systems,
 814 very few to no matches are found with erupted liquids, requiring generation of synthetic liquids to match to
 815 measured Cpx (e.g., Scruggs and Putirka, 2018). Another approach is to pair Cpx rims with matrix glass or
 816 groundmass separates (Klügel et al., 2020), although because this method focuses on rims, it may only reveal

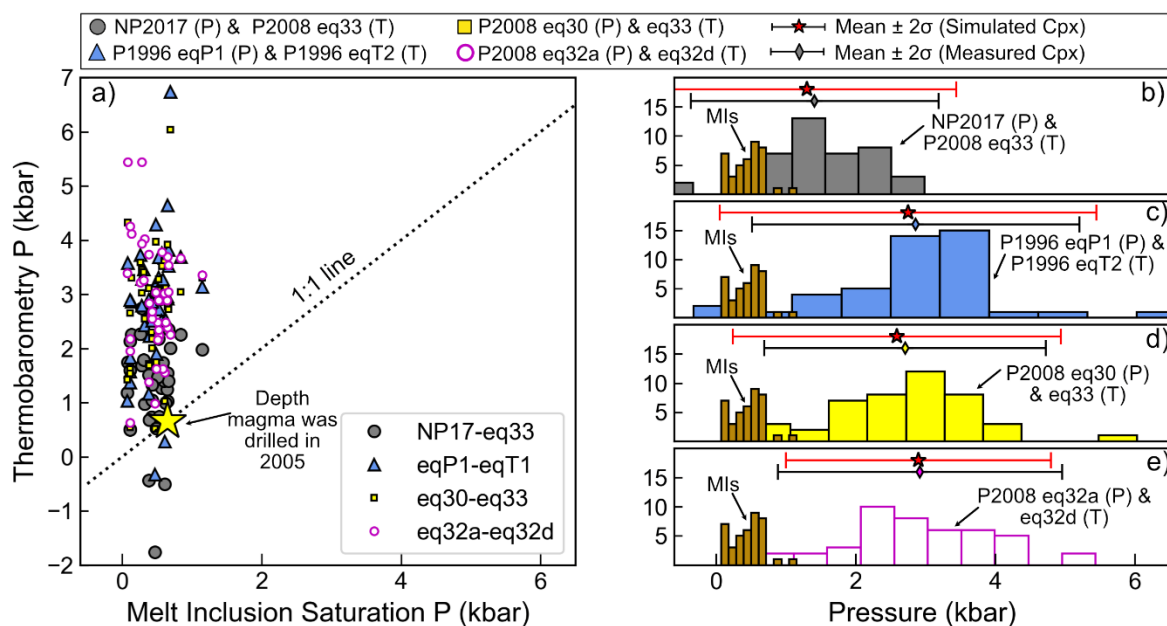
817 the depth of the uppermost storage chambers (neglecting deeper pressure information preserved in core
818 compositions).

819 Issues associated with identifying equilibrium liquids can be circumvented using Cpx-only barometers.
820 Putirka (2008) present two Cpx-only barometers (eq32a-b) and a Cpx-only thermometer (eq32d). Wang et al.
821 (2021) show that these (and other existing) Cpx-only thermobarometers perform poorly in mafic and
822 intermediate melt compositions. To address this, Wang et al. (2021) select 559 experiments conducted at 0–12
823 kbar with liquid SiO₂ contents between 42–60 wt% to calibrate a new barometer which is independent of T and
824 H₂O (Fig. 7, yellow circles). They use the PyTorch python library (Paszke et al., 2019) to implement a gradient
825 descent algorithm to select Cpx cation components to include in a non-linear term for a Cpx-only barometer,
826 rather than selecting components based on thermodynamic reasoning. They also present a thermometer, which
827 is independent of P but requires knowledge of the H₂O content of the liquid.

828 Most recently, supervised machine learning methods have been applied to Cpx-based equilibrium to
829 develop thermobarometry expressions (e.g., random forests, Higgins et al., 2022, extra trees, Jorgenson et al.,
830 2022; Petrelli et al., 2020). Unlike more traditional empirical thermobarometers which are underlain by
831 thermodynamic principles, measured oxide data are fed into these algorithm, rather than calculated
832 components such as Jadeite. Wieser et al. (2023a) show that the Cpx-only barometers of Wang et al. (2021) and
833 Jorgenson et al. (2022) show similar performance to popular Cpx-Liq barometers for the ArcPL dataset, justifying
834 the use of Cpx-only barometers as an alternative to trying to identify equilibrium liquids. That said, just because
835 Cpx-Liq and Cpx-only barometry show similar performance, it is worth nothing that neither approach performs
836 particularly well, with neither method yielding R²>0.74, or RMSE <2.1 kbar. Additionally, all expressions have
837 low gradients, overpredicting at lower pressures, and underpredicting at higher pressures.

838 The relatively poor performance of Cpx-based barometry on independent test datasets (e.g., high
839 RMSE, low gradients, inability to distinguish magma storage within ~10–15 km) is at least partially the result of
840 low analytical precision when measuring Na₂O in experiments used to calibrate and test barometers (see Wieser
841 et al. 2023b, and Section 1.4). Analytical precision also affects measurements of natural samples and can result
842 in an anomalously large spread of calculated P and T, which can be incorrectly attributed to transcrustal storage
843 because of spurious trends in P-T space. For example, Wieser et al. (2023c) show that a the entire P-T range of
844 the lunar Cpx analysed by Luo et al. (2023) can be explained by the propagation of analytical uncertainty. To
845 further demonstrate the importance of such error propagation, we calculate pressures using Cpx and melt
846 inclusion compositions from the first two weeks of the 2018 eruption of Kīlauea Volcano (Wieser et al., 2022c).
847 Cpx-hosted melt inclusions yield relatively shallow saturation pressures, which overlap very well with the
848 pressure at which a highly evolved magma was drilled in this region in 2005 (Teplow et al., 2009, yellow star, Fig.
849 8a). We use the PEC-corrected melt inclusion compositions and analyses of the Cpx composition close to the
850 melt inclusion to calculate Cpx-Liq and Cpx-only pressures. These barometers return a much greater spread of
851 pressures than melt inclusion saturation pressures, with a notable offset to significantly higher values (Fig. 8). In
852 fact, these calculated depths are similar to the 3–4 kbar estimated by Putirka (2008) for Cpx erupted during the
853 Pu’u O’o eruption of Kīlauea. However, there are no other geological or geophysical indications that Cpx-
854 saturated magmas are stored this deep.

855 To interpret the large spread of calculated pressures, we simulate 5000 Cpx compositions, with the
856 variability of each oxide following a normal distribution centred on the mean measured Cpx composition, with
857 a standard deviation equal to the average counting statistic precision estimated from the EPMA output. We
858 calculate pressures using these 5000 synthetic Cpx paired with the average liquid composition, and show ±2σ of
859 these simulations as a red error bar (Fig 8b-e). The simulated spread in calculated pressures resulting from
860 analysis of an entirely homogenous Cpx using typical EPMA operating conditions almost exactly matches the
861 observed spread in calculated pressures (2σ error bars for each overlain on each histogram). This illustrates how,
862 without sufficient averaging of individual analyses, it would be easy to incorrectly invoke storage at a range of
863 pressures spread throughout the crust. While iteration of Putirka (2008, eq30) for T and Neave and Putirka
864 (2017) for P produces calculated pressures that align within error of the melt inclusion saturation pressures, the
865 other Cpx-based barometers estimate far too high pressures compared to melt inclusions and drilling depths.
866 This demonstrates both the lack of precision and accuracy of Cpx-based methods. Even without analytical
867 uncertainty, the RMSE on these barometers mean there is no way to reliably distinguish storage at ~0.5 kbar
868 from storage at 4 kbar; limiting the applicability of these methods in systems where magma is stored in the
869 upper part of a relatively thin crust.



870
 871 *Figure 8: Comparison of melt inclusion saturation pressures (Wieser et al. 2022c), and Cpx-Liq and Cpx-only*
 872 *barometry for samples erupted during the first two weeks of the 2018 Kīlauea eruption. a) Melt inclusion*
 873 *saturation pressures calculated in MagmaSat (Ghiorso and Gualda, 2015) using VESICAL (Iacovino et al., 2021)*
 874 *cluster tightly at shallow pressures. These pressures are very similar to the pressure at which an evolved magma*
 875 *body was drilled in 2005 in the same area (yellow star, Teplow et al. 2009). Cpx-Liq and Cpx-only pressures*
 876 *calculating using PEC-corrected melt inclusion-host pairs show substantial scatter, extending to substantially*
 877 *deeper pressures. B-e) Histograms showing calculated pressures for each iterative mineral barometry calculation.*
 878 *Error bars with black lines show $\pm 2\sigma$ for these calculations. Red error bars show $\pm 2\sigma$ for Monte-Carlo simulations*
 879 *for the mean composition of each Cpx and Liq, with 5000 Cpx compositions simulated using estimates of*
 880 *analytical precision for these Cpx measurements.*

881
 882 The relatively poor performance of many Cpx-based barometers can also be attributed to the fact that
 883 many expressions are parameterized in terms of Cpx components (e.g. Jd, DiHd) calculated from EPMA oxide
 884 data (e.g., Neave and Putirka, 2017, Putirka, 2008). An alternative technique calculates site occupancy and cell
 885 volumes using a combination of single-crystal X-ray diffraction and measured oxide data (Dal-Negro et al., 1989).
 886 This technique was used extensively in the 80s-90s, and was recently applied by Tommasini et al. (2022) to
 887 natural Cpx crystals from Popocatepetl Volcano. They show that XRD-informed site assignments and the
 888 resulting calculated mineral components differ greatly from the routines used by Neave and Putirka (2017) and
 889 Putirka (2008) using EPMA data alone. This discrepancy between components calculated using EPMA data and
 890 the true crystal structure may reflect an additional source of uncertainty plaguing Cpx-based barometers. Single
 891 crystal XRD may also be vital to help us determine where Na is going (pairing with Al, Fe³⁺ or Cr³⁺), which will
 892 further enhance our understanding of how Cpx composition relates to pressure. However, while single-crystal
 893 X-ray diffraction has been applied to natural crystals, the small size of experimental Cpx means that it is very
 894 difficult to obtain these parameters for experiments in order to calibrate expressions using these parameters
 895 (Dal-Negro et al., 1989, Tommasini et al. 2022). Additionally, a workflow involving XRD would be far more time
 896 consuming from a sample preparation perspective than existing EPMA-based techniques, which may severely
 897 restrict its uptake by the community, even if it results in improved barometer performance.

898 A number of papers have also shown the importance of considering the petrogenetic history of a Cpx
 899 population when interpreting thermobarometry calculations. For example, Hammer et al. (2016) assessed the
 900 influence of disequilibrium crystal growth on Cpx barometry using X-ray mapping and quantitative spot analyses
 901 of clinopyroxene crystals from a post-shield ankaramite erupted from Haleakalā volcano, Hawai'i. Their work
 902 demonstrates the complexity of interpreting Cpx compositions in regions where disequilibrium growth
 903 processes occur. Specifically, texturally and compositionally distinct domains within individual crystals thought
 904 to have formed by high degrees of undercooling during crystallisation have distinct distributions of Cpx Jd
 905 contents, so return very different P estimates. They find offsets within individual crystals up to ~3.5 kbar. In

906 contrast, Ubide et al. (2019a, 2019b) calculate P-T-H₂O for different domains in sector zoned Cpx from Stromboli,
907 and show remarkably constant results regardless of the textural context (although without individual calculated
908 PTs, it is not possible to directly compare the statistical differences between these different studies). Clearly,
909 further work is required to understand how the formation of different chemical domains in magmatic systems
910 affect the distribution of P- and T-sensitive Cpx components, and thus the results from thermobarometric
911 calculations.

912 The relatively recent appreciation that most magmas are stored in predominantly crystal-rich “mushy”
913 environments also adds additional complexity to the interpretation of clinopyroxene-based barometric
914 estimates, because clinopyroxene chemistry can be influenced by chemical processing in these crystal-rich
915 regions. For example, residual melt compositions can be modified by reactive porous flow, driven by
916 disequilibrium between a percolating melt phase and the surrounding crystal framework (Boulanger et al., 2020;
917 Gleeson et al., 2021; Lissenberg and MacLeod, 2016; Sanfilippo et al., 2020). Critically, the melts formed from
918 this process are rarely observed at the surface, which makes it difficult to quantify their chemistry to pair with
919 erupted Cpx compositions. Cpx-Liq and Cpx-only barometry is also affected by the fact that reactive porous flow
920 might drive interstitial melt compositions (and thus the Cpx compositions) outside the compositional range used
921 to calibrate existing expressions (Fig. 7). Gleeson et al. (2021) demonstrate the importance of accounting for
922 mush processes in their study of Cpx from wehrlite xenoliths found on Isla Floreana in the southern Galápagos.
923 These crystals have Na₂O contents up to ~1.3 wt% and returned apparent crystallisation pressures up to ~18
924 kbar using the clinopyroxene-only thermobarometers of Putirka (2008; eq. 32b-32d). In contrast, Cpx-Opx
925 barometry (using the same crystals), melt inclusion and clinopyroxene-liquid thermobarometry from
926 neighbouring scoria cones on the same island indicate that magma storage was dominantly located at around
927 ~7 kbar (Gleeson et al., 2022, 2021). Based on rare earth element signatures in these pyroxenes (elevated LREE
928 contents relative to MREE and HREE contents) the authors concluded that the anomalously high pressure
929 estimates of the wehrlitic clinopyroxene crystals result from chemical modification of Na₂O (and REE) by reactive
930 porous flow in olivine ±clinopyroxene mush zones. Comparison with other thermobarometric techniques (E.g.,
931 Opx-Cpx, melt inclusions, Gao et al., 2022, Gleeson et al. 2021), as well as identifying trace element patterns
932 indicative of reactive flow, provide one method to interpret the spuriously high pressure estimates returned
933 from these cumulate Cpx.

934 In summary, to push Cpx-based thermobarometry forward, we need to improve the experimental
935 datasets available to calibrate and test barometers (see Wieser et al. 2023a-b), develop new methods to relate
936 chemical components to parameters we can easily measure in natural samples and experimental charges (e.g.,
937 Tommasini et al. 2022), and increase our understanding of natural processes causing variation in Cpx
938 compositions (e.g., Gleeson et al., 2021; Hammer et al. 2017, Neave et al., 2019; Ubide et al., 2019b, 2019a),

939 **2.4. Orthopyroxene±Liq**

940 Beattie (1993) presented the first Opx-Liq thermometer based on the use of non-regular solution
941 models to calculate saturation temperatures. Putirka (2008) then calibrated two different equations (Eq28a,
942 28b) using the LEPR dataset, both of which are sensitive to P and H₂O. Eq28a uses the composition of the Opx
943 and Liq, while Eq28b only uses the composition of the liquid to calculate the temperature of Opx saturation.
944 Wood (1974) published the first Opx barometer, which used the Al content of Opx in equilibrium with Garnet.
945 Putirka (2008) calibrated a more widely applicable Opx-only barometer (Eq29c) and two Opx-Liq barometers
946 (Eq29a, Eq29b) using the LEPR database. The main pressure-sensitive component in Eq29a is a Jadeite-like
947 component in the Opx, while Eq29b uses the (Fe, Mg)₂Al₂SiO₆ Opx component. Both equations also contain terms
948 for other liquid cation fractions, and opx cation fractions on the basis of 6 oxygens. Eq29c (Opx-only) uses the
949 cation fractions of Al, Ca, Cr and Al in the Opx, as well as terms for T. It is worth noting that several of the Putirka
950 (2008) Opx thermobarometers are prone to numerical issues resulting from the presence of logarithmic terms.
951 For example, Eq29c (Opx-only) has a term for the logarithm of the cation fraction of Cr in Opx. If Cr was not
952 measured or reported in Opx, this term cannot be evaluated (the case for 63% of the experiments in our test
953 dataset). Similarly, Eq28b has a term calculated from the log of the (Fe, Mg)₂Al₂SiO₆ component in the Opx
954 divided by terms involving the cation fractions of Si, Al, Fe, Mn, and Mg in the liquid. In ~9% of experiments
955 (mostly at <3 kbar, but a few at 5 and 8 kbar), the (Fe, Mg)₂Al₂SiO₆ component in the Opx is 0, the log of which
956 yields infinity. A value of zero for the (Fe, Mg)₂Al₂SiO₆ component can also occur in Opx where the calculated
957 Al_{Vl} component is zero, which is particularly common in low pressure Opx (Al_{Vl}=0 in 7% of the Opx considered
958 here, all at <2.5 kbar). To address the numerical issue associated with the (Fe, Mg)₂Al₂SiO₆ component, in later
959 versions of the spreadsheets from Putirka (2008), two additional Opx-Liq barometers were included (“Global”

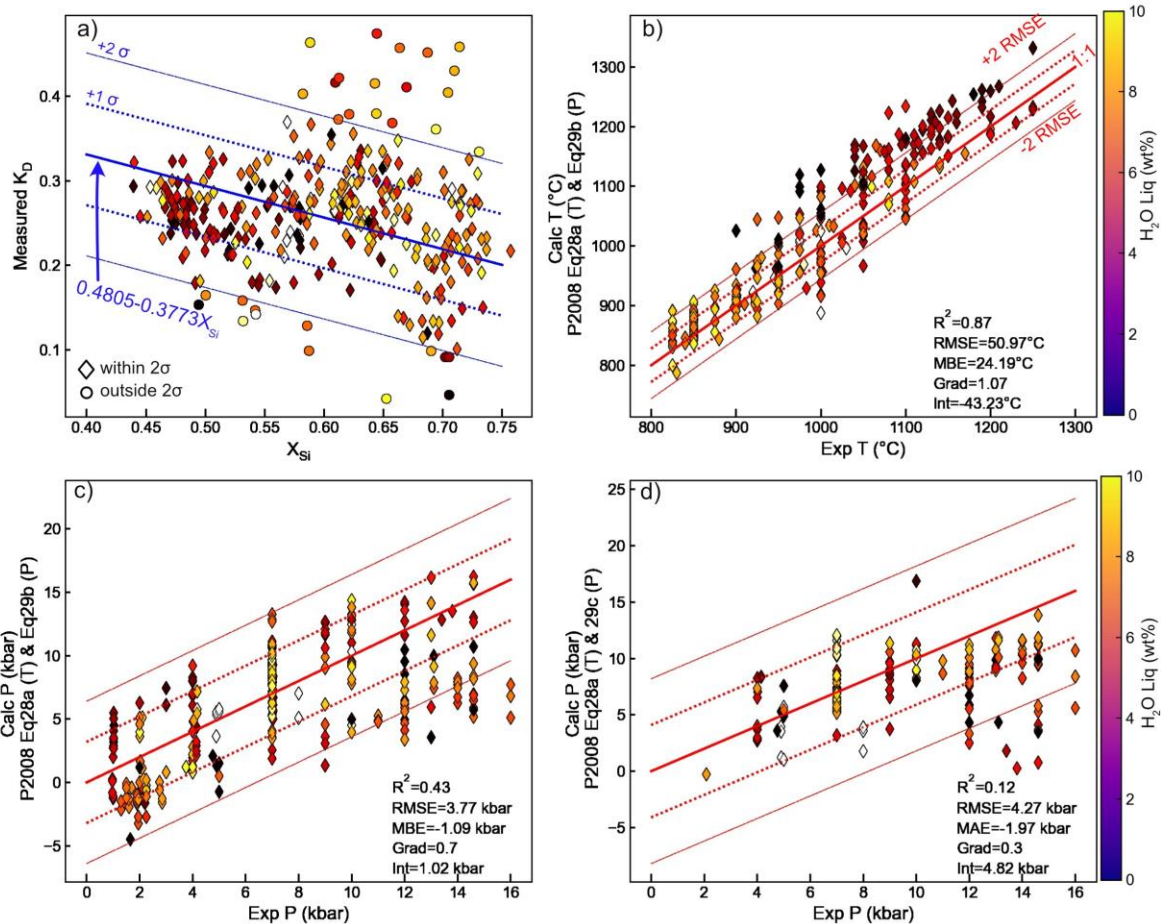
960 and “Felsic”). These equations simply use the ratio of the measured Al_2O_3 content in Opx and Liq. The global
961 model was calibrated on 795 Opx-Liq pairs, and the felsic model on 40 pairs.

962 In natural systems, it is even more difficult to assess the equilibrium relationships between erupted Opx
963 and Liquid compositions than for Cpx-Liq, because only $K_{D,Fe-Mg}^{Opx-Liq}$ has been widely explored as an equilibrium
964 test. Putirka (2008) find that K_D in experimental charges roughly correlates with the cation fraction of Si in the
965 liquid (X_{Si}) ($1\sigma=0.06$). In the ArcPL dataset, there is no significant correlation between K_D and X_{Si} ($R^2=0.01$, Fig.
966 9a), although ~67% lie within the given error bound of the predicted value. In natural systems is it very plausible
967 that liquids and orthopyroxenes that are not chemically related could yield K_D values passing these relatively
968 broad equilibrium tests (particularly if 2σ is used as the cut off). One way to avoid this problem is to use an Opx-
969 only barometer (e.g., Eq29c of P2008), However, this equation contains a temperature-sensitive term, and given
970 no Opx-only thermometer exists to our knowledge, a liquid composition may still need to be used to estimate
971 (or iteratively calculate) the temperature.

972 Using experimental P and H_2O (that was measured by quantitative methods), Eq28a (Opx and Liq
973 comps) and Eq28b (only Liq comps) are remarkably good thermometers. Eq28a has a slightly higher R^2 (0.90 vs
974 0.85), and lower RMSE (39 vs. 48°C, Supporting Fig. 3). Using experimental T and H_2O measured by quantitative
975 methods, Eq29b is the best Opx-Liq barometer ($R^2=0.58$, RMSE=3.01 kbar, Supporting Fig. 4), and has a decent
976 gradient and intercept relative to other mineral-melt barometers we evaluate in this review (grad=0.67, int=1.2).
977 Eq29a performs slightly worse in terms of R^2 and RMSE but has a slightly better gradient and intercept ($R^2=0.50$,
978 RMSE=3.65 Gradient=0.74, Int=0.3 kbar). The global barometer is noticeably worse ($R^2=0.47$, RMSE=3.47 kbar,
979 grad=0.59, int=1.4). The Opx-only barometer (Eq29c) is difficult to compare because of the presence of many
980 experiments without reported Cr measurements in Opx that return numerical errors; for available data, $R^2=0.04$,
981 RMSE=4.63 (Supporting Fig. 4d).

982 As discussed, it is probable in natural systems that neither T nor P is known, and melt H_2O is relatively
983 uncertain. We investigate the sensitivity of calculated P to T, and calculated T to P (Fig. 10) by perturbing the
984 experimental T by $\pm 100^\circ\text{C}$ and P by ± 5 kbar. The Putirka (2008) Global and Felsic barometers have no T term, so
985 show no changes in P with T. Eq29a (dark blue lines, Fig. 10a) shows a relatively small increase in calculated P
986 with increasing T, while Eq29b shows a larger increase (light blue lines, Fig. 10a). Eq29c, the Opx-only barometer,
987 shows variable sensitivity to T, with P increasing in some samples, and decreasing in others as T is increased
988 (grey lines, Fig. 10a). The strong change in calculated P as a function of T for Eq29c, a drop of up to 10 kbar for
989 $+100^\circ\text{C}$ for some samples, is problematic, as there is no way to determine temperature simply from Opx
990 compositions at present. The three Opx-Liq thermometers also show variable changes with P (some increasing,
991 some decreasing, Fig. 10b). However, the uncertainty in calculated T for changes in P of 10 kbar (equivalent to
992 the crustal thickness in most arcs) is comparable to the stated RMSE on these thermometers.

993 Overall, the relatively large change in calculated P (and to a lesser extent T) with relatively small changes in the
994 other parameter means that we can expect Opx-based thermobarometers to show far worse statistics when
995 solved iteratively than when tested with only a single unknown.



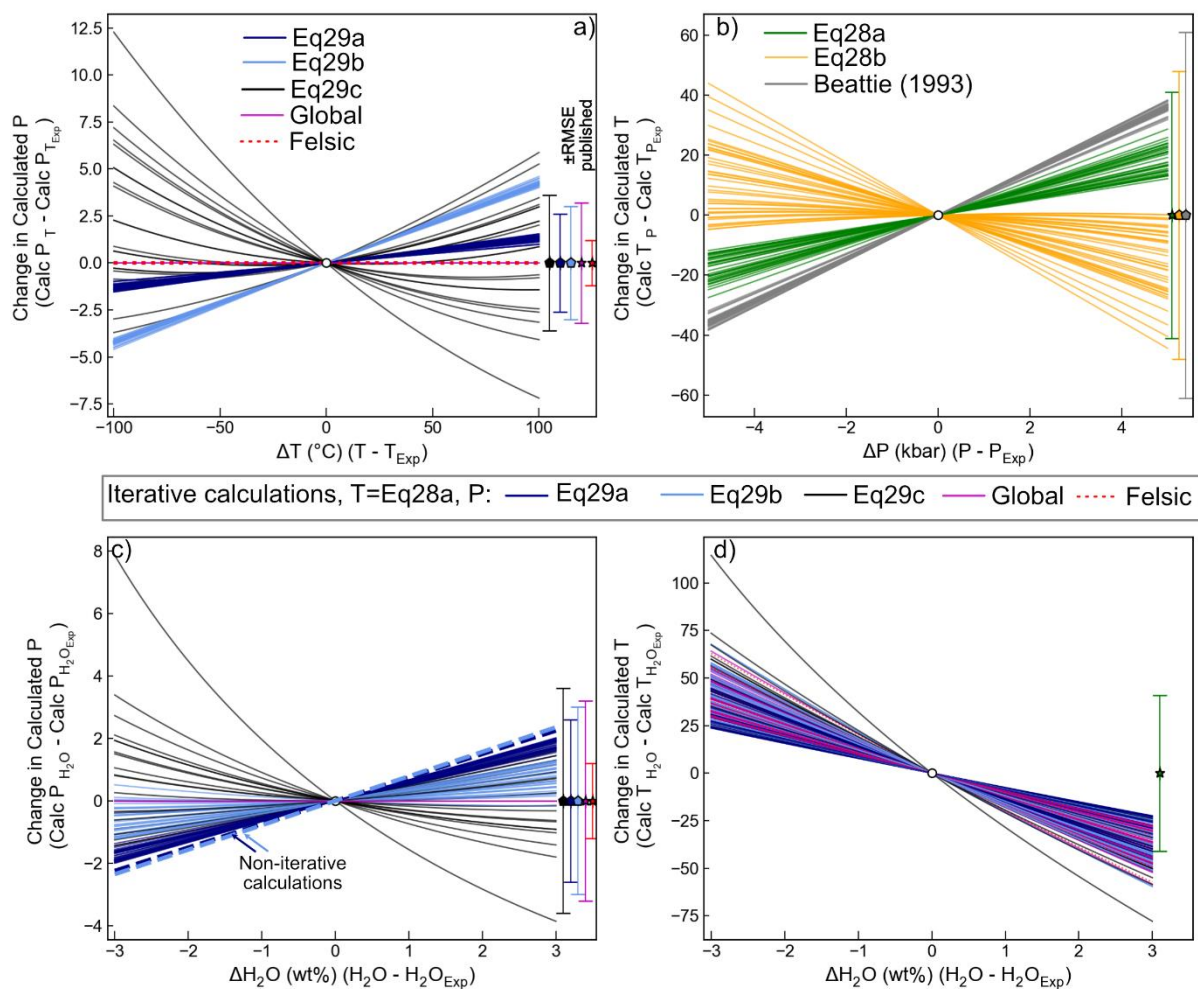
996

997 *Figure 9: Opx-Liq and Opx-only Thermobarometry. a) Comparison of measured K_D with that predicted from the*
 998 *X_{Si} content of the liquid using Putirka (2008). b-c) Comparison of calculated and experimental T and P by iterating*
 999 *Eq28a(T) and Eq29b(P). d) Iteration of Eq28a (for T, Opx-Liq) with Eq29c (Opx-only, P) of Putirka (2008). Dotted*
 1000 *lines around the 1:1 line show \pm the quoted σ , with dashed lines showing $\pm 2 \sigma$. All symbols colored by H_2O content,*
 1001 *with $H_2O > 10$ wt% white, to emphasize the scale at lower H_2O contents.*

1002 We also investigate the change in P when using iterative calculations when we perturb the experimental
 1003 H_2O content by ± 3 wt%. When T from Eq28a is iterated with all barometers, calculated T decreases with
 1004 increasing H_2O (Fig. 10d). Iteration of Eq28a (T)-Eq29a (P) (dark blue line) and Eq28a (T)-Eq29b (P) (light blue
 1005 line) show a small increase in calculated P with increasing H_2O content (Fig 10c). Both these barometers have
 1006 terms multiplying H_2O by a constant, resulting in a consistent change in P for varying H_2O contents in non-
 1007 iterative calculations ($+0.748$ kbar/1 wt% H_2O for Eq29a, and $+0.784$ for Eq29b, dashed blue lines, Fig. 10c).
 1008 However, because increased H_2O contents cause T to drop using Eq28a (Fig. 10b), which causes a decrease in
 1009 the calculated P (Fig. 10a), the influence of H_2O on calculated P in iterative calculations is slightly less than that
 1010 obtained in calculations using the experimental T. This complex feedback between equations during iterative
 1011 calculations results in a greater variability in the influence of H_2O on calculated P for different samples. Eq29c
 1012 has no H_2O term but shows the strongest sensitivity to T (Fig. 10a), resulting in a large drop in P with increasing
 1013 H_2O when iterated with Eq28a (Fig. 10c). The high sensitivity of Eq29c to H_2O is concerning because an Opx-only
 1014 barometer is most likely to be applied in systems where liquid compositions (and thus, H_2O contents) are poorly
 1015 constrained. As the Global and Felsic barometers have no T or H_2O term, they show no sensitivity to H_2O .

1016

1017



1018

1019 *Figure 10: Assessing the sensitivity of Opx thermobarometry to variation in P, T and H₂O for N=40 randomly*
 1020 *selected experiments. a) Change in calculated P for perturbing the experimental T by ± 100 °C. b) Change in*
 1021 *calculated T by perturbing P by ± 5 kbar. c-d) Change in calculated P and T for iterative calculations perturbing*
 1022 *experimental H₂O content by ± 3 wt%. For all plots, the calculated P or T at experimental conditions is subtracted*
 1023 *from the calculation at experimental conditions (plotting at 0, 0). Calculations performed in Thermobar (Wieser*
 1024 *et al., 2022b).*

1025 Ideally, given the effects of H₂O on calculated P and T (Fig. 10c-d), we would only assess experiments
 1026 where H₂O is known by quantitative methods (as for Liq-only). However, only 147/324 experiments from 10/23
 1027 studies have reported Opx-Liq compositions where H₂O was measured quantitatively. Thus, all experiments are
 1028 shown in Fig. 9, with the same calculations using only experiments with quantitative H₂O measurements shown
 1029 in Supporting Fig. 5 (which shows worse statistics).

1030 Iterating the best thermometer (Eq28a) and barometer (Eq29b) yields a very good match to
 1031 experimental T in ArcPL using experimental H₂O contents (Fig. 9b). The thermometer performs worse for
 1032 experiments with low H₂O contents (darker symbols, < 2–3 wt%). Based on a similar observation for the LEPR
 1033 dataset, Putirka (2008) suggest that Opx may re-equilibrate faster in more hydrous liquids. Calculated P from
 1034 iteration of Eq28a-Eq29b is reasonably accurate (Fig. 9c, grad=0.7, MBE=-1.09 kbar, int=-1 kbar), but very
 1035 imprecise (RMSE=3.77 kbar), so this barometer will be of limited utility in relatively thin-crustal settings such as
 1036 OIBs and MORBs (Fig. 3). Unlike for thermometers, there is no clear relationship between barometer
 1037 performance and H₂O content. Although we cannot perform very many calculations for Eq29c because of the
 1038 absence of Cr data, calculated Opx-only pressures (Eq29c) iterated with Eq28a shows a reasonable
 1039 correspondence to the 1:1 line (Fig. 9d) at <12 kbar, although substantially more experiments with reported Cr
 1040 contents are required to robustly assess this barometer.

1041 Overall, Opx-Liq thermobarometry has been relatively neglected given its performance; no new
 1042 calibrations have been proposed since 2008. In particular, the relative absence of systematic uncertainty when
 1043 Opx-based barometers are tested on ArcPL contrast strongly with other mineral barometers discussed here. We
 1044 suggest that future experimental and theoretical work to further develop Opx-based thermobarometry is
 1045 warranted, with a particular focus on the development of more robust equilibrium tests. Ensuring starting
 1046 materials contain Cr contents comparable to natural systems, and ensuring all elements are measured at high
 1047 precision within experimental Opx (particularly Cr) may lead to improved thermobarometry calibrations. This
 1048 may provide a particularly promising barometer in arc magmas, where Opx is relatively common, and magmas
 1049 are relatively H₂O-rich.

1050 2.5. Two Pyroxene (Cpx-Opx) Thermobarometry

1051 Two pyroxene (Cpx-Opx) thermobarometry is widely used in the literature, likely reflecting the fact that
 1052 these phases crystallize together across a wide range of P, T, and H₂O contents in a variety of tectonic settings.
 1053 For example, Cpx-Opx thermobarometry has been applied to OIB basalts from the Galápagos by Gleeson et al.
 1054 (2021), to mafic arc basalts from SW Japan by Zellmer et al. (2014), and to arc dacites from the Aucanquilcha
 1055 Volcanic Cluster by Walker et al. (2013). Additionally, it is common that Cpx and Opx form crystal clusters, and
 1056 calculations from these touching pairs are easier to justify than trying to select equilibrium liquids for each crystal
 1057 (c.f. Opx-Liq and Cpx-Liq thermobarometry). Opx-Cpx thermobarometry can also be applied in systems where it
 1058 is difficult to analyse the composition of the liquid (e.g., highly crystalline lavas or xenoliths, Gao et al., 2022;
 1059 Gleeson et al., 2021).

1060 As discussed above for Opx-Liq equilibrium, one of the main limitations of Cpx-Opx thermobarometry
 1061 is the paucity of equilibrium tests to help filter out pairs which are not in equilibrium (in experiments and natural
 1062 samples). The only established equilibrium test compares the exchange of Fe-Mg in Cpx and Opx ($K_{D,Fe-Mg}^{Cpx-Opx}$).
 1063 Putirka (2008) suggest that $K_D=1.09\pm 0.14$ in high temperature systems, while $K_D=0.7\pm 0.2$ in subsolidus systems.
 1064 However, it is difficult to know where to draw the line between these different filters; what value would be
 1065 correct to use in a supra-solidus dacitic-rhyolitic melt that is a similar temperature to a subsolidus mafic
 1066 cumulate? K_D values for our compiled experiments lie mostly within the high T bracket ($\pm 1\sigma$ shown in pink),
 1067 although a number extend to higher values (Fig. 11a). There is no strong relationship between T and measured
 1068 K_D . Another way to assess the equilibrium value would assume that the Cpx and Opx are each in equilibrium
 1069 with the liquid, so the Opx-Cpx K_D value can be obtained from the Cpx-Liq and Opx-Liq K_D values from Putirka
 1070 (2008):

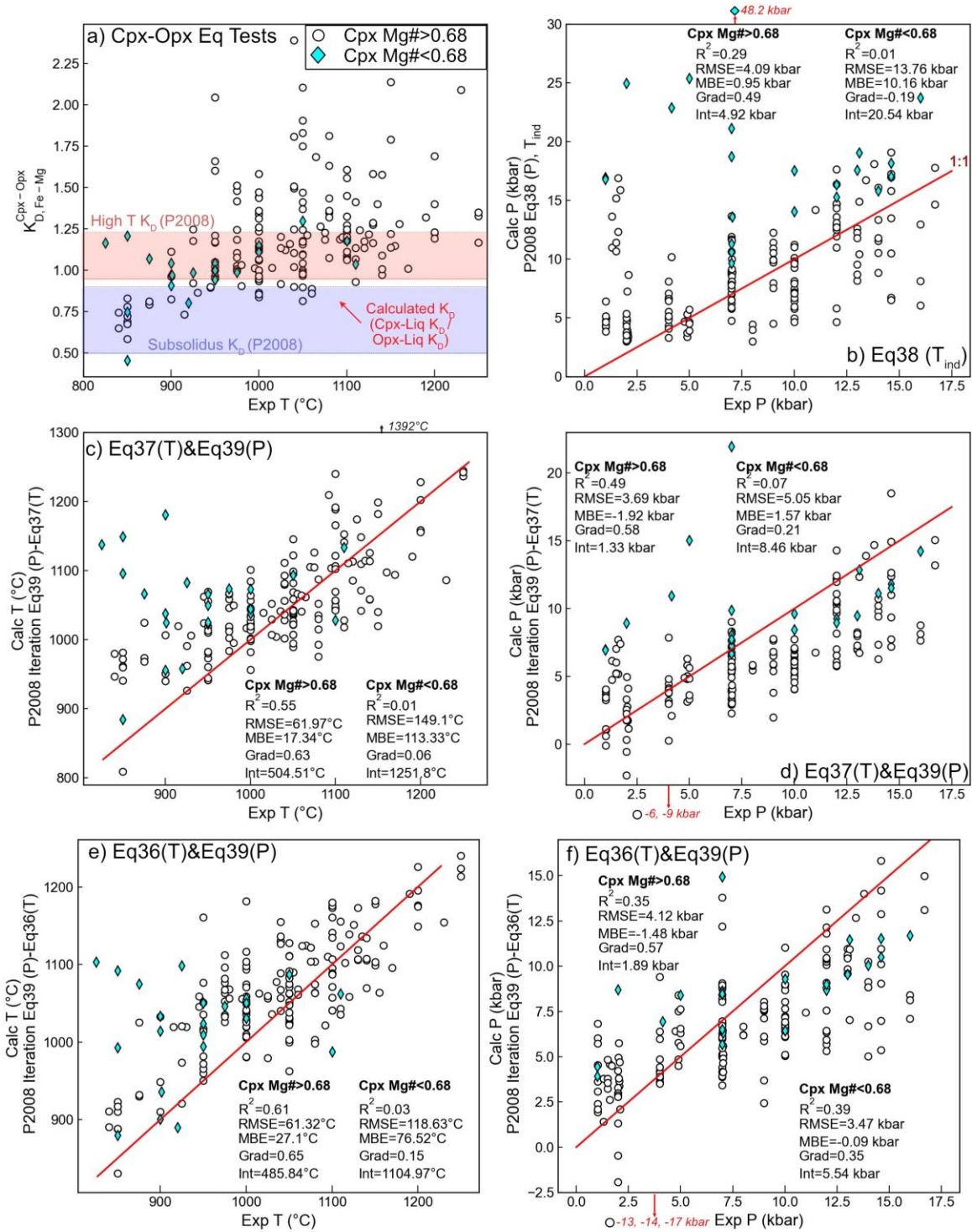
$$1071 K_{D,Fe-Mg}^{Cpx-Opx} = \frac{K_{D,Fe-Mg}^{Cpx-Liq}}{K_{D,Fe-Mg}^{Opx-Liq}} = \frac{e^{-0.107 - \frac{1719}{T(K)}}}{0.4805 - 0.3733 * X_{Si,Liq}} \text{ [Equation 8]}$$

1072 This approach could be advantageous, because there are far more Cpx-Liq and Opx-Liq experiments
 1073 than Cpx-Opx experiments, so the individual Px-Liq equilibrium values are better constrained. Values calculated
 1074 using this expression lay between the subsolidus and high T value (red dots, Fig. 11a), with very little variation
 1075 with temperature. This is because higher T drives up the Cpx-Liq K_D , but higher T liquids tend to have lower Si
 1076 contents, which drives up Opx-Liq K_D . Unfortunately, Equation 8 appears to underestimate the K_D value for many
 1077 of the experimental samples given here, which is perhaps unsurprising as we find the Cpx-Liq K_D expression
 1078 underestimates many of the Cpx-Liq K_D values (by up to ~0.5), while the Opx-Liq expression tends to
 1079 overestimate many of the Opx-Liq K_D values. Dividing these two relatively uncertain quantities compounds
 1080 errors. The fact so many of our experimental Cpx-Opx pairs sit outside any estimate of equilibrium could suggest
 1081 that several are not in equilibrium, so should not be used to assess thermobarometers. However, we find no
 1082 discrepancy between K_D and the offset between calculated and predicted P and T. This suggests instead, that
 1083 more experimental and theoretical work is needed to robustly assess K_D . Thus, we proceed to assess
 1084 thermobarometers using all Cpx and Opx pairs in the ArcPL compilation.

1085 The T-independent barometer of P2008 (Eq38) performs very poorly for high Mg# Cpx ($R^2=0.29$,
 1086 RMSE=4.09) and even worse for low Mg# Cpx (<0.68, cyan diamonds, Fig. 11b, $R^2=0.01$, RMSE=13.72). Iteration
 1087 of P2008 Eq37–39 and Eq36–Eq39 show very similar statistics to one another for calculated P and T, with Eq36–
 1088 Eq39 showing slightly better behaviour. Neither thermometer is very promising (Fig. 11c, e) producing more of

1089 a data cloud than a meaningful correlation. Iterated barometers are similarly disappointing; even for Cpx with
 1090 Mg#>0.68, the RMSE is 3.69 kbar (Eq3 7–Eq39, Fig. 11d) and 4.12 kbar (Eq3 6–Eq39, Fig. 11c).

1091 Overall, we suggest that substantially more experiments where Opx and Cpx are stabilized at a variety
 1092 of pressures and melt compositions are required to improve Cpx-Opx barometers, particularly in more evolved
 1093 systems with lower Cpx Mg#. Additional experiments would also help to better constrain controls over the
 1094 equilibrium value at a variety of temperatures and melt compositions.



1095

1096 *Figure 11: Assessing two-pyroxene thermobarometers. a) Measured $K_{D,Fe-Mg}^{Cpx-Opx}$*
 1097 *against experimental T. The range of equilibrium values from Putirka (2008) for “HighT” and “Subsolidus”*

1098 systems are shown as colored bars. K_D values calculated from the Cpx-Liq (T-dependent) and Opx-Liq (Si-
1099 dependent) K_D values (Equation 12) are shown as small red dots. b-f) Comparison of predicted and experimental
1100 P and T for different combinations of equations from P2008. 1:1 line shown in red. In all plots, Cpx-Opx pairs with
1101 Cpx Mg#<0.68 are colored cyan, and Mg#>0.68 colored white. To maintain scale, a few experiments returning
1102 extreme values are excluded from plots. Their y coordinate is labelled with a red arrow.

1103 2.6. Amphibole thermobarometry and Chemometry

1104 Amphibole (Amp)-only and Amp-Liq thermobarometry have been used extensively to calculate P and T
1105 in volcanic and plutonic igneous systems (e.g., Higgins et al., 2022; Scruggs and Putirka, 2018). Amphibole
1106 chemometers are also becoming widely used to probe the compositions of melts present at depth within
1107 plumbing systems which are not always well represented at the surface (e.g., Humphreys et al., 2019; Zhang et
1108 al., 2017).

1109 2.6.1 Amphibole thermobarometry

1110 Amphibole barometry stems from the seminal work of Hammestrom and Zen (1986), who showed that
1111 the Al^{VI} and Al^{Tot} contents of hornblendes from calc-alkaline plutons emplaced at different depths correlate with
1112 estimates of pressure, and that the same compositional-pressure relationships were seen in experimental
1113 products. Hollister et al. (1987) analysed rim compositions from plutons where the pressure of emplacement
1114 could be estimated from phase assemblages in the surrounding country rock. They confirmed the Al-pressure
1115 relationship of Hammestrom and Zen (1986) and proposed an updated calibration. Additional calibrations have
1116 also been developed for Amp-Plag, Amp-Garnet, and Amp-Plag-Qtz (see Molina et al., 2021 and refs. within).

1117 More recently, Mutch et al. (2016) present an Amp-only barometer parameterized in terms of Al^{Tot}
1118 calibrated using a dataset comprising: i) their new experiments on 3 different bulk compositions, ii) the
1119 experiments of Johnson and Rutherford (1989), Schmidt (1992), Thomas and Ernst', 1990), iii) published analyses
1120 from plutons with independent depth constraints (Ague, 1997; Hammestrom and Zen, 1986), and iv) their new
1121 analyses on amphiboles from the Yerrington Batholith in Nevada. Mutch et al. (2016) exclude experiments where
1122 garnet or phengite was stabilized, as this alters the Al^T -pressure relationship. Importantly, their compiled dataset
1123 shows a curvature in Al^T vs. pressure space relationship at 0.5–3 kbar not seen by previous workers. They
1124 parameterize this empirically relating pressure to a second order polynomial of Al^T .

1125 While Al^T in amphibole is controlled by both T and P, so can only be used as a barometer on an isotherm
1126 or near a solidus (Médard and Le Pennec, 2022), correlations between P and Al^{VI} have been noted by Krawczynski
1127 et al. (2012), Helz (1982), Larocque and Canil (2010) and Schmidt (1992) in a wide variety of systems. Médard
1128 and Le Pennec (2022) present a T-independent barometer using a simple linear regression of P and Al^{VI} ,
1129 calibrated on 47 published experimental compositions with Si-rich silicate melts in equilibrium with Biotite,
1130 Plagioclase, and Magnetite. They state that this barometer has a RMSE of 0.86 kbar (or 0.72 kbar for <4 kbar).
1131 They also test their expression on 22 biotite-bearing experiments not used in calibration, which lie within the
1132 stated RMSE window. However, all their tests are at <4 kbar, which makes it difficult to evaluate the precision
1133 of the barometer at higher pressures.

1134 Importantly, all the Al-based amphibole-only barometers discussed so far are only applicable in the
1135 presence of certain phases. For example, Hammestrom and Zen (1986) warned about the applicability of their
1136 regressions in rocks without quartz, where Al^T can be significantly higher at a given P. Mutch et al. (2016)
1137 emphasize that their barometer should only be applied to amphibole rims in equilibrium with melts saturated
1138 in plagioclase (An_{15-80}), biotite, quartz, alkali feldspar, Fe-Ti oxides, and apatite (e.g., near solidus, low variance
1139 volcanic systems). In higher T melts with fewer co-crystallizing phases and higher thermodynamic variance, the
1140 equilibria controlling amphibole composition are still poorly understood (Putirka, 2016). Médard and Le Pennec
1141 (2022) test their barometer using 7 Bt-free experiments, resulting in a RMSE of 1.4 kbar, which is a large % error
1142 given these experiments were conducted at ~ 1–2 kbar. Thus, they suggest that this barometer should not be
1143 used in biotite-free rocks. While limited in their applicability to silicic systems saturated in a large number of
1144 phases, the amphibole-only barometers discussed thus far are extremely useful for determining pluton
1145 emplacement depths and crustal exhumation rates in orogenic belts, or when investigating the formation and
1146 evolution of Porphyry copper deposits (Anderson, 1996; Hollister et al., 1987; Mutch et al., 2016).
1147

1148 In contrast to these studies focused on low variance silicic systems, Ridolfi et al. (2010) compile calcic
1149 amphibole analyses from experiments conducted on a wide range of melt compositions and phase assemblages

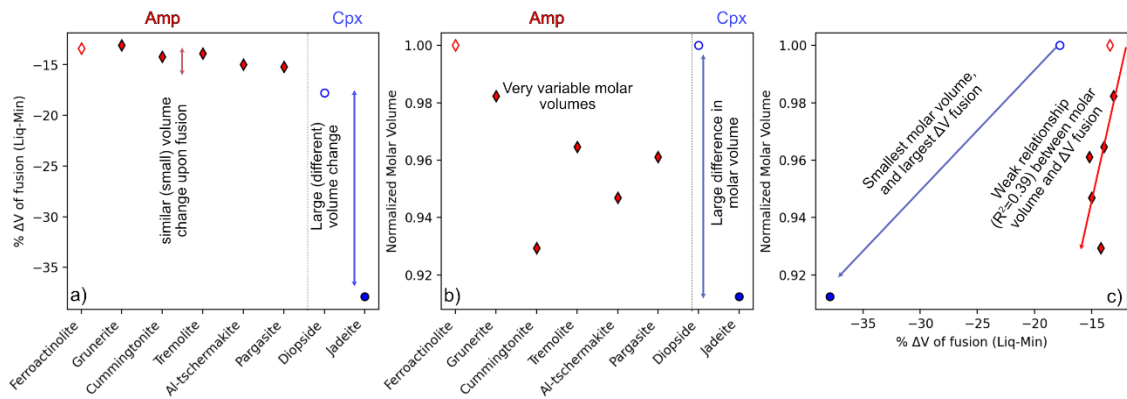
1150 to generate an empirical amphibole-only thermometer (Eq1), oxybarometer (Eq2) and hygrometer (Eq3). Ridolfi
1151 et al. (2010) justify the application of Amp-based methods in less evolved systems with fewer phases (and
1152 therefore higher variance) by pointing out that most volcanic amphiboles exist close to their stability limits
1153 (shown by abundant breakdown textures). They suggest that close to the amphibole stability curve, the variance
1154 of the system is lower so amphibole composition is more closely related to P, T and fO_2 . Ridolfi et al. (2010) also
1155 present an Al^T barometer calibrated on 9 amphiboles (Eq4) but find that attempts to perform a similar calibration
1156 on their larger experimental dataset performs poorly, particularly for magnesiohastingsite amphiboles which
1157 are common in nature, but sparse in available experiments.

1158 Ridolfi and Renzulli (2012) compile additional experiments and apply more stringent filters to produce
1159 an amphibole-only barometer (e.g., removing amphiboles with 1σ for $SiO_2 > 0.9$ wt%, Piston cylinder experiments
1160 conducted at < 6 kbar etc.). Of the 61 experimental amphiboles remaining, 19 (31%) are magnesiohastingsite,
1161 which is close to the proportion of magnesiohastingsites (42%) in their natural compilation. This is in stark
1162 contrast to the dataset of Ridolfi et al. (2010), which contained no magnesiohastingsites (or pargasites or
1163 kaersutites). Ridolfi and Renzulli (2012) create several different regressions to calculate P using amphibole cation
1164 fractions calculated on the basis of 13 oxygens. For example, Eq. 1a was calibrated on $N=61$ experiments, and
1165 expresses P in terms of the exponential of compositional terms (Si, Ti, Al, Fe, Mg, Ca, Na, K). However, using
1166 comparisons to seismic depths from Ridolfi et al. (2010) for a variety of natural systems, they show that this
1167 equation overestimates at low P, and underestimates at high P. They calibrate 4 additional expressions using a
1168 smaller subset of analyses ($N=20-41$) in different pressure ranges (Eq1b and 1e use exponentials, 1c and 1d use
1169 multilinear regressions). They present an algorithm where the user calculates P for each equation, and these
1170 different values are averaged/combined in a variety of different ways to construct a final P.

1171 To test the expressions of Ridolfi and Renzulli (2012), Erdmann et al. (2014) compile a series of
1172 experiments not used in their calibration dataset. While T, melt SiO_2 content and fO_2 are reasonably well
1173 predicted in their new dataset, they demonstrate a very poor correspondence between calculated and
1174 experimental P, and calculated and experimental H_2O contents. Erdmann et al. (2014) suggest the P discrepancy
1175 results from the fact that the Si-Al content of an amphibole is more strongly related to the liquid composition
1176 and T than P. In particular, they note that the calibration dataset of Ridolfi and Renzulli (2012) is skewed, with
1177 amphiboles from felsic and intermediate melts clustered at lower P, and mafic to intermediate melts at higher
1178 Molina et al. (2021a) also publish a short note stating that they test Ridolfi and Renzulli (2012) using a dataset
1179 of experiments compiled by Molina et al. (2021b), and obtain “*unsustainable pressure estimates*”.

1180 Putirka (2016) further examine Amp-only and Amp-Liq equilibrium, presenting two P-independent
1181 Amp-only thermometers (Eq5 and SiHbl), two P-dependent Amp-only thermometers (Eq6 and Eq8), two P-
1182 independent Amp-Liq thermometer (Eq4b and Eq9), and a P-independent Liq-only amphibole saturation
1183 thermometer (Eq4a). He also presents three T-independent Amp-Liq barometers (Eq7a, b, c). Using an extensive
1184 test dataset, Putirka (2016) show that Amp-only and Amp-Liq equilibrium do a reasonably good job of predicting
1185 pressure when averaged, but conclude that P estimates from individual amphibole grains are ‘*nearly useless for*
1186 *understanding crustal processes*’. They hypothesize that the main limitation of Amp-based barometry is the fact
1187 that none of the common amphibole components have particularly large changes in volume when they
1188 precipitate from the liquid (ΔV fusion), or large molar volume contrasts between different components in the
1189 amphibole itself. For example, even though Jadeite in pyroxene is not a particularly sensitive barometer at
1190 crustal conditions, relative to Diopside it has a significantly more negative ΔV fusion (Fig. 12a), and a smaller
1191 molar volume (8% smaller, Fig. 12b, Putirka, 2016). As Jadeite has both a smaller molar volume and a more
1192 negative ΔV fusion (Fig. 12c), the amount of Jadeite vs. Diopside in Cpx are sensitive to P. In contrast, there is a
1193 pretty weak relationship between the ΔV fusion and the molar volume for different amphibole components (Fig.
1194 12b-c, Putirka, 2016). While the exchange of different amphibole components is not particularly P-sensitive,
1195 Putirka (2016) do show that the partition coefficient of Al between amphibole and liquid is correlated to P,
1196 explaining why amphibole barometers are normally parameterized in terms of Al and other oxides, rather than
1197 explicitly calculated mineral components (e.g. Jadeite in Cpx).

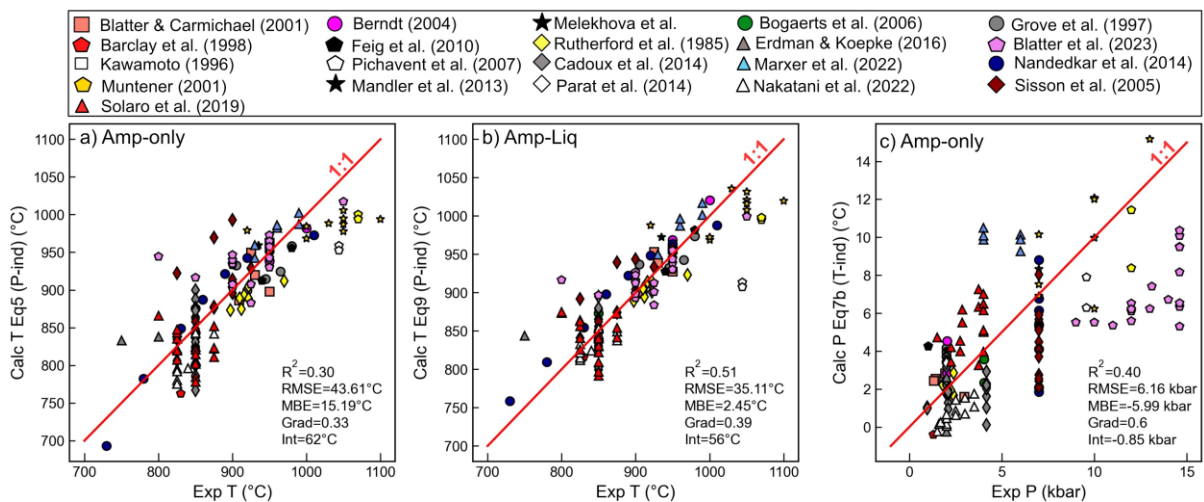
1198



1199

1200 *Figure 12. Comparison of molar volumes and volumes of fusion for Amp vs. Cpx components. a) Changes in*
 1201 *volume following precipitation of different mineral components from the liquid (ΔV fusion). Amphibole*
 1202 *components show significantly smaller changes than jadeite, and the different Amp components show very*
 1203 *similar ΔV fusion. b) Molar volume normalized to the component of each phase with the highest molar volume*
 1204 *(ferroactinolite for Amp, Diopside for Cpx). c) Correlation between normalized molar volume and ΔV fusion.*
 1205 *Thermodynamic data from table 1 of Putirka (2016).*

1206 We use data not included in the calibration of the Putirka (2016) equations to test their performance (see
 1207 Supporting Figs. 6–8), and sensitivity to other terms present in the regression. The best performing Amp-only
 1208 thermometer for this dataset is Eq5 ($R^2=0.7$, $RMSE=41.5^\circ C$, Fig. 13a, Supporting Fig. 6), which has the advantage
 1209 of being independent of P and H_2O in the liquid. The best Amp-Liq thermometer is Eq9 ($R^2=0.76$, $RMSE=34^\circ C$,
 1210 Fig. 13b, Supporting Fig. 8), which is P independent and not very sensitive to H_2O in the liquid (Supporting Fig. 7,
 1211 $\sim 1^\circ C$ change in T per 1 wt% H_2O). Like Putirka (2016), we find that all three Amp-Liq barometers show
 1212 disappointing statistics ($RMSE= 3\text{--}4$ kbar, $Grad=0. 3\text{--}0.5$, Supporting Fig. 8, e.g., Fig. 13c). In particular, the
 1213 pressures for the higher P experiments of Blatter et al. (2023), and Muntener et al. (2001) are greatly
 1214 underestimated, although the barometer does a reasonable job of the lower P data, which clusters around the
 1215 1:1 line at $\sim 2\text{--}5$ kbar. The skew at high P means that even after the averaging suggested by Putirka (2016), Amp-
 1216 Liq barometry can give misleading results.



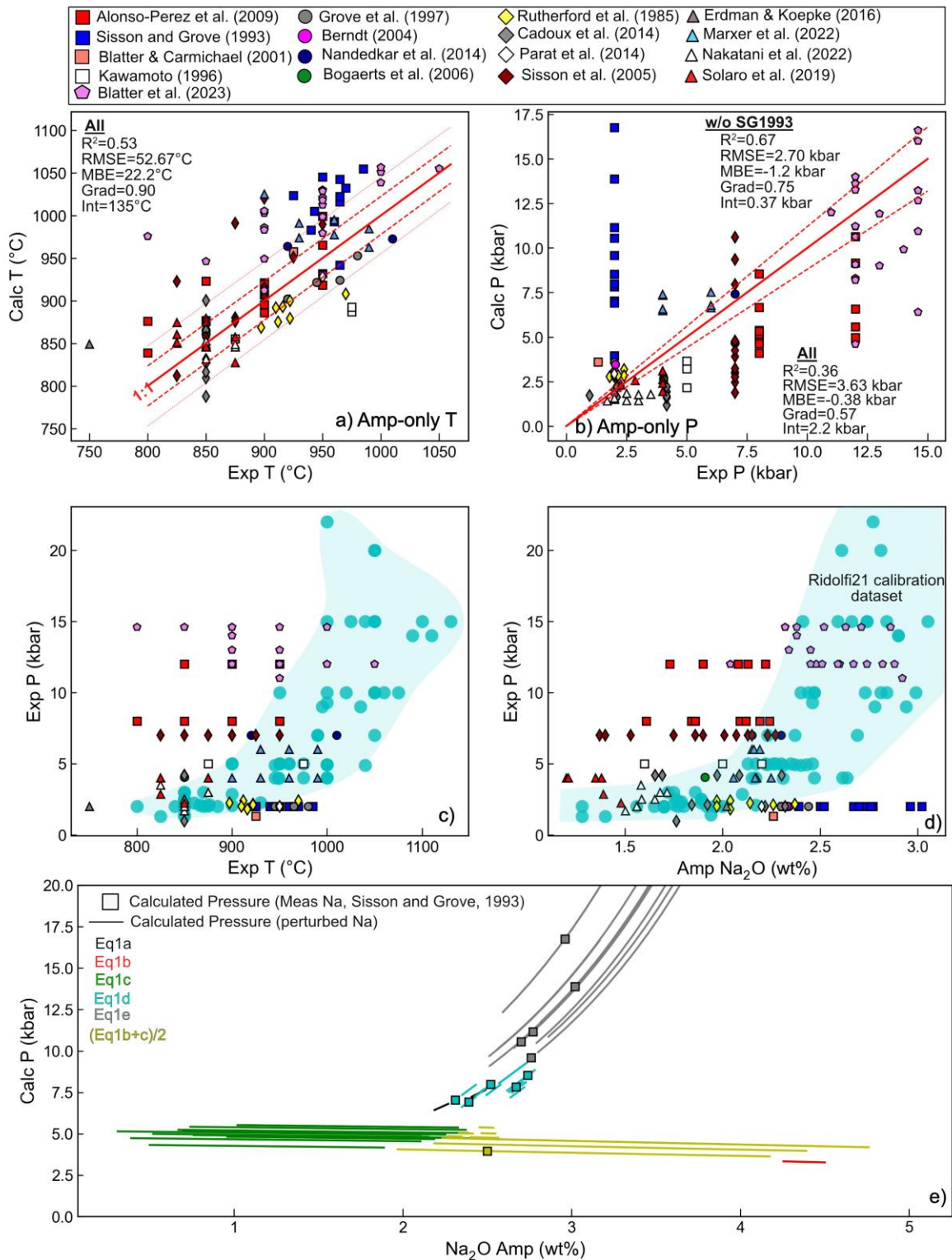
1217

1218 *Figure 13 – Assessing Amp-Liq and Amp-only thermobarometers from Putirka (2016) using experiments not used*
 1219 *during model calibration. Only experiments passing the K_D filter of Putirka (2016) are shown.*

1220 Ridolfi (2021) recently updated the Ridolfi and Renzulli (2012) amphibole-only barometer, perhaps
 1221 partially in response to the criticism of Erdmann et al. (2014), Molina et al. (2021) and Putirka (2016), and
 1222 partially because of an increase in the number of amphibole-bearing experiments. Using an expanded
 1223 experimental dataset, they tweak the algorithms used to select between different P equations and add more

1224 stringent filters to give users warning of when the equations are being applied to amphiboles failing quality tests
1225 or outside the model calibration range (based on totals, unbalanced charge, low B cations, etc, low and high Ca
1226 cations, low Mg cations). We tested this new algorithm and filter criteria on a dataset of experiments not used
1227 during calibration (Alonso-Perez et al., 2009; Berndt, 2004; Blatter and Carmichael, 2001; Bogaerts et al., 2006;
1228 Cadoux et al., 2014; Erdmann and Koepke, 2016; Grove et al., 1997; Kawamoto, 1996; Marxer et al., 2022;
1229 Nakatani et al., 2022; Parat et al., 2014; Rutherford et al., 1985; Sisson et al., 2005; Sisson and Grove, 1993;
1230 Solaro et al., 2019, Blatter et al. 2023). Of our compiled experiments (N=193), 112 pass the quality check filters
1231 of Ridolfi (2021, Fig. 14a). Calculated P show a moderate correspondence to experimental P, although
1232 calculations clearly lie well outside the stated $\pm 12\%$ error in the abstract of Ridolfi (2021, red dashed lines, Fig.
1233 14b). The overall fit to all experiments yields $R^2=0.36$ and $RMSE=3.6$ kbar. The experiments conducted at 2 kbar
1234 by Sisson and Grove (1993) show particularly poor results, returning pressures which are up to 15 kbar too high.
1235 Excluding these experiments yields $R^2=0.67$ and $RMSE=2.7$ kbar. Compared to the Putirka (2016) Amp-Liq
1236 barometers, this Amp-only barometer does a much better job of recreating the high pressures of Blatter et al.
1237 (2023), although it does still underestimate to a degree. Despite the criticism of this method in the literature, it
1238 is noteworthy that Amp-only barometry doesn't perform any worse than Opx-Liq and Opx-Cpx based on our
1239 dataset - none of these methods are precise enough to be useful to many volcanological questions. It just seems
1240 that Amp-based methods have received the bulk of the critique until recently. As amphibole-only T from Ridolfi
1241 and Renzulli (2012) require a P to be entered, we also test how effective this thermometer is using pressures
1242 obtained from the 2021 barometer. For these 112, the correlation between calculated and experimental T is
1243 reasonably good (Fig. 14a, $R^2=0.53$, $RMSE=53^\circ\text{C}$), although the RMSE is twice that stated in the abstract of Ridolfi
1244 (2021, 22°C , shown with dashed red lines, Fig. 14a).

1245 We examined the Sisson and Grove (1993) experiments in the context of the calibration dataset of
1246 Ridolfi (2021) to try to understand the poor performance of the barometer. These experiments plot to
1247 substantially higher amphibole Na_2O contents at lower pressures than any of the calibration experiments (Fig.
1248 14d). To investigate whether this offset to lower Na_2O contents could explain the anomalously high calculated
1249 P, for each Sisson and Grove (1993) amphibole, we perturb the Na_2O content by ± 2 wt%. Pressures for measured
1250 amphibole compositions are shown as squares (Fig. 14e), with a line stretching from each square showing the
1251 change in pressure as Na_2O is changed. The colors indicate the root equation from Ridolfi (2021) algorithm used
1252 to determine P, with the rapid jumps in pressure reflect a flip to a different equation selected by the algorithm.
1253 For the samples with high calculated P (>7.5 kbar), it is very clear that Eq1e (and to a lesser extent 1d and 1a) is
1254 highly sensitive to the Na_2O content, rapidly shooting up to extremely high pressures for very small changes in
1255 Na contents. It may well be that these natural samples lie outside the Na_2O range used to calibrate Eq1e (the
1256 calibration data for each specific equation is not available). The Alonso-Perez et al. (2009) experiments (red
1257 squares) where pressure is underestimated are also clearly offset from the calibration dataset in T – Na_2O space
1258 (Fig. 14c). This comparison emphasises the importance of ensuring that sample compositions are well
1259 represented in the calibration dataset of the chosen model, not just in terms of P-T space, but also compositional
1260 space. It also shows that having the correct functional form for a barometer rooted in thermodynamics is
1261 essential to minimize extrapolation issues commonly seen with empirical fits.



1262

1263 *Figure 14: Assessing Amp-only thermometers and barometers. a) Comparing experimental and calculated T using*
 1264 *the thermometer of Ridolfi and Renzulli (2012) iterated with Ridolfi (2021). b) Comparing experimental and*
 1265 *calculated P using the new barometer of Ridolfi (2021, T-independent). c-d) Visualizing experimental*
 1266 *compositions relative to the calibration dataset (cyan dots and field) of Ridolfi (2021). Many of the experiments*
 1267 *showing the largest discrepancies in calculated pressure (e.g., red and blue squares, magenta diamonds) lie*
 1268 *outside the calibration range of Ridolfi (2021) in Pressure-Na₂O space. e) To visualize the effect of Na₂O on*
 1269 *calculated pressure, we perturb the Na₂O content of the experiments of Sisson and Grove (1993) by ±2 wt%. The*
 1270 *lines are not continuous, with jumps to a different pressure as the algorithm flips between different 'root'*

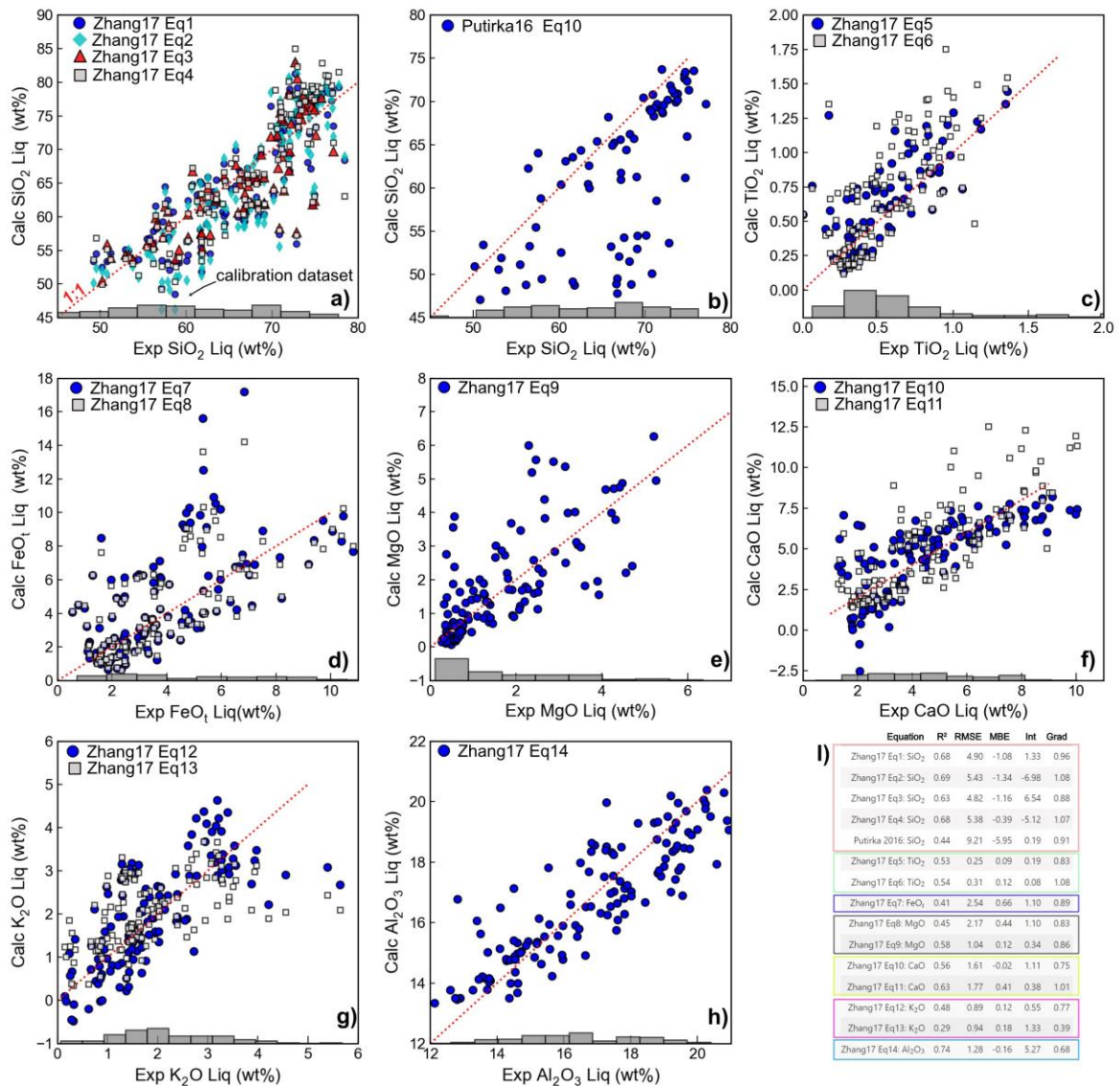
1271 equations (indicated by the color of the line). Experimental Na_2O (and calculated pressures) are indicated with
1272 squares, with the calculations following the perturbation shown as lines.

1273

1274 2.6.2 Amphibole Chemometry

1275 Ridolfi and Renzulli (2012) also present equations to calculate the contents of SiO_2 , TiO_2 , Al_2O_3 , FeO_t ,
1276 MgO , CaO , and K_2O in the melt from which amphiboles crystallized. These equations are parameterized in terms
1277 of amphibole composition and pressure. However, given the uncertainties discussed above calculating pressures
1278 from amphibole compositions, these P-sensitive parameterizations can be problematic to implement in natural
1279 systems. Erdmann et al. (2014) show that the predicted SiO_2 content is a reasonable match above 65 wt% SiO_2 ,
1280 but tends to overpredict SiO_2 for more mafic melts. Putirka (2016) use their newly compiled dataset to produce
1281 an updated expression (Eq10) for melt SiO_2 from the amphibole using the temperature of the melt and the cation
1282 fraction of Al in the amphibole.

1283 Zhang et al. (2017) compile a reasonably similar calibration dataset to Putirka (2016), and produce
1284 multiple regressions to calculate melt oxide components from a variety of amphibole site positions (e.g., Si-Ti-
1285 Mg-Fe-Ca in amphibole for predicting SiO_2 in the melt). These expressions are P-independent, and only Eq3 (for
1286 SiO_2) and Eq5 (for TiO_2) are T-sensitive. Zhang et al. (2017) calibrate multiple equations for some melt oxide
1287 contents (e.g., 4 equations for SiO_2 , 2 equations for FeO_t). We test the 133 ArcLEPR amphiboles which pass the
1288 Zhang et al. (2017) equilibrium filter ($K_{\text{D, Fe-Mg}}=0.28\pm 0.11$, and do not appear in their calibration dataset. The
1289 calculated statistics are similar if a K_{D} filter isn't used. Overall, unlike many of the barometers discussed in this
1290 review, these chemometers perform very well for experiments they were not calibrated on (Fig. 15). Eq2 of
1291 Zhang et al. (2017) does a good job of predicting melt SiO_2 content across a wide range, showing much better
1292 performance than Eq10 of Putirka, 2016 (Fig. 15a vs. b). The statistics of the fit are similarly good for melt Al_2O_3
1293 (Eq14). There is more scatter for other oxides, and reasonably large differences between the different provided
1294 equations, but it is not always clear which equation is better (e.g., Fig. 15c). It is notable that the worst
1295 performance is seen for experiments with oxide contents towards the tail end of the calibration dataset (grey
1296 histograms, Fig. 15). For example, Eq12 and Eq13 do a good job of predicting K_2O until ~3.5 wt% K_2O ; very few
1297 experiments in the calibration dataset had such high K_2O contents (Fig. 15g). Similarly, the fit is better at lower
1298 MgO contents, where the calibration dataset is concentrated (Fig. 15e). In general, our tests demonstrate that
1299 amphibole compositions can be used to estimate the melt compositions from which they grew, as long as the
1300 results are carefully evaluated relative to the calibration range of the model.



1301

1302 *Figure 15 – Assessment of amphibole chemometers of Zhang et al. (2017, panel a, c-h) and Putirka (2016, panel*
 1303 *b). For equation 3 and 5 of Zhang et al. (2017) and Putirka (2016) eq10, we use temperatures calculated from co-*
 1304 *solving T from Ridolfi and Renzulli (2012) and P from Ridolfi (2021). Putirka (2016) eq10 also requires P from*
 1305 *Ridolfi (2021) to be input. These equations have fewer datapoints on the plot, as we exclude P and Ts where*
 1306 *Ridolfi (2021) returns an input warning. i) shows the statistics for each equation. The filtered test dataset*
 1307 *comprises 133 experimental charges not used by Zhang et al. (2017) during calibration, and 10 experimental*
 1308 *charges from Barclay (2004), Blatter and Carmichael (2001), and Grove et al. (1997), which were used by Zhang*
 1309 *et al. (2017) in their test, but not calibration dataset.*

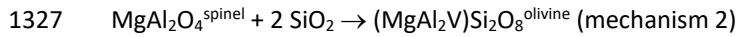
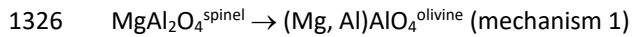
1310 We do not test predictions of H₂O and fO₂ using amphibole-only chemometers, as there are limited
 1311 reliable experimental data with well constrained values for these parameters that were not used during model
 1312 calibration.

1313 2.7. Olivine-Spinel Aluminium-exchange thermometry

1314 The aluminium content of olivine has been used as a thermometer in the mantle (De Hoog et al., 2010),
 1315 and Al partitioning between olivine and spinel has been used in igneous rocks (Wan et al., 2008; Coogan et al.,
 1316 2014). Here we focus on the olivine-spinel Al-exchange thermometer, which offers an advantage over Mg-Fe
 1317 olivine-liquid thermometry because Al in spinel and olivine and Cr in spinel are more resistant to diffusional
 1318 modification during crystal storage and transport than Fe-Mg in olivine (Spandler & O'Neill, 2009). Additionally,
 1319 while olivine crystals are frequently out of equilibrium with erupted liquids (Sides et al., 2014b; Wieser et al.,

1320 2019), the fact spinels are trapped inside olivine crystals makes it more straightforward to identify mineral-
1321 mineral pairs that grew together.

1322 The mechanism by which aluminium substitutes into olivine remains somewhat uncertain, despite the
1323 fact that constraining this reaction is vital to identify which chemical parameters should appear in a
1324 thermodynamically-constrained thermometry model. Of the possible substitutions, two mechanisms have been
1325 the focus of the most attention:



1328 In the first mechanism there is a coupled substitution of Al into both the octahedral and tetrahedral
1329 sites in olivine, while the second has substitution only onto the octahedral site, with charge balance maintained
1330 by vacancies (V). It is also possible coupled substitutions could take place with Cr and Na in the octahedral site
1331 (and Al in the tetrahedral site), or Al in the octahedral site with Fe^{+3} in the tetrahedral site (Taura et al., 1998).
1332 Critically, if the mechanism 1 is dominant, the thermometer should depend only on the Al contents of the co-
1333 existing olivine and spinel (in addition to any chemical parameters controlling the activity coefficient for Al in
1334 either phase), but if mechanism 2 dominates, the thermometer will depend also on the activity of SiO_2 (a_{SiO_2}).

1335 A thermometer based on Al-exchange was first calibrated by Wan et al. (2008) using a series of
1336 experiments at 1 bar with the bulk composition varied such that olivine and spinel co-crystallised at a range of
1337 temperatures and Cr contents. They found that the experimental data could be adequately modelled with a
1338 formula depending on the ratio of Al in olivine to Al in spinel, as well as the spinel Cr# ($\text{Cr}/[\text{Cr} + \text{Al}]$, molar). The
1339 dependency on Cr# comes from its effect on the activity coefficient of Al in spinel. Wan et al. (2008) justified the
1340 extrapolation of the thermometer to higher P and T than the calibration dataset by comparing temperatures
1341 derived from the Al-exchange thermometer with temperatures calculated from the two-pyroxene thermometer
1342 for a suite of olivine and spinel bearing mantle xenoliths. Although there was considerable scatter around the
1343 1:1 line ($1\sigma = 64^\circ\text{C}$) they found no systematic offset between the two thermometers. The behaviour of the
1344 thermometer at 1 bar was tested with an additional set of experiments, for which experimental temperatures
1345 were reproduced with $1\sigma=22^\circ\text{C}$.

1346 The thermometer was further tested and recalibrated with new experimental data by Coogan et al.
1347 (2014), extending the calibration range to higher $f\text{O}_2$ values ($\Delta\text{QFM}=-0.5$ to $\Delta\text{QFM} = +1.3$). They also tested the
1348 thermometer's dependence on a_{SiO_2} . They found $f\text{O}_2$ had no systematic effect on the performance of the
1349 thermometer and the effect of a_{SiO_2} was within the uncertainty of the thermometer, indicating that Al
1350 incorporation into olivine by vacancy formation (mechanism 2) is unlikely to be important in most systems. This
1351 was corroborated by an experimental diffusion study by Zhukova et al. (2017) which found that Al incorporation
1352 by vacancy formation was favoured only at higher a_{SiO_2} values than is found in most igneous systems where the
1353 thermometer is applied. Further improvements have been made to both the calibration and the mathematical
1354 formulation of the thermometer by Zhang and Namur (2022).

1355 Despite the increased calibration range of the Coogan et al. (2014) model, many natural samples
1356 possess olivine and spinel pairs with compositions which still lie outside the calibration range. This includes the
1357 study reporting the highest equilibration temperatures from this method ($\sim 1570^\circ\text{C}$, Trela et al., 2017), which
1358 have spinels with Cr_2O_3 contents higher than any of the spinel crystals used to calibrate the thermometer. Trela
1359 et al. justified such an extrapolation based on the global correlation between the Al_2O_3 K_D and spinel Cr#, and
1360 the fact that these melts also recorded extreme mantle potential temperatures and olivine liquidus T_s . However,
1361 it has also been suggested in other locations that application of this method to spinel crystals with much higher
1362 TiO_2 contents than the calibration dataset may be invalid, because these higher TiO_2 may affect the activity
1363 coefficient of Al in spinel (e.g., Jennings et al., 2019; Wong et al., 2022). Jennings et al. (2019) suggest that in the
1364 absence of a wider calibration range, it is best to apply the thermometer only to spinel crystals that are close to
1365 the calibration range.

1366 To robustly assess how effectively the olivine-spinel method can be extrapolated, we need a suite of
1367 experiments with compositions lying outside the current calibration range. However, because application of the

1368 thermometer relies on precise measurements of the low concentrations of Al₂O₃ in olivine, generally only
1369 experiments performed for the purpose of calibrating this thermometer can be used, and all such experiments
1370 have been used during model regression (by Wan et al. 2009, or Coogan et al. 2014). Experiments conducted for
1371 other purposes cannot be used to formulate a test dataset, because Al₂O₃ concentrations in olivine were
1372 generally not measured at all, or were measured with low precision.

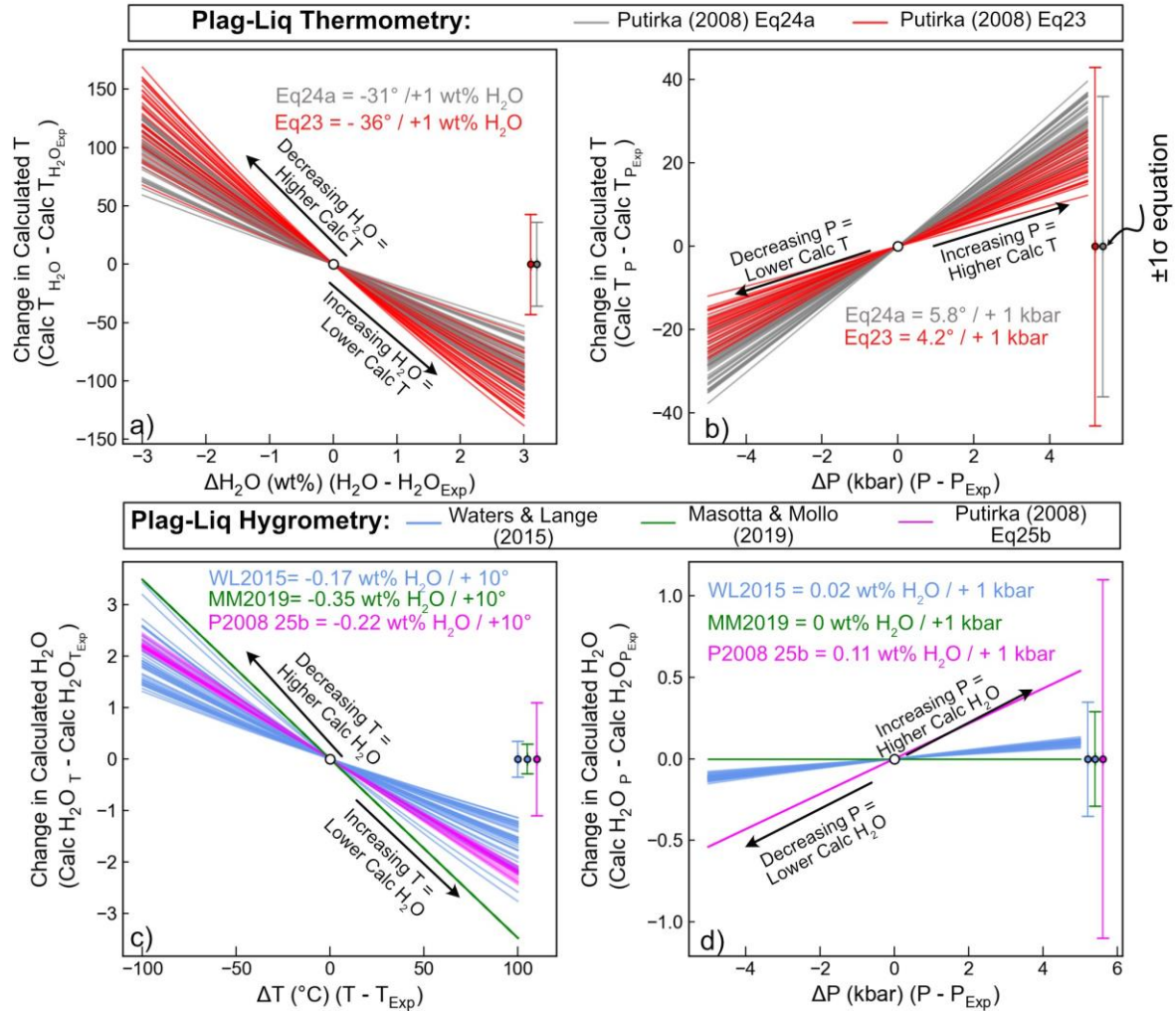
1373 The lack of an independent test dataset also makes it difficult to robustly constrain the uncertainty of
1374 this method even when applied within the calibration range. Most studies cite the quoted standard error on the
1375 fit for the calibration data as being a minimum estimate of the uncertainty (Matthews et al., 2021, 2016; Wong
1376 et al., 2022), but as discussed above, statistics calculated on calibration datasets tend not to reflect the true
1377 error when applied to data not used for calibration. A final problem with this method is that there is no
1378 independent equilibrium test to assess whether the spinel and olivine are in equilibrium. The ubiquity of Mg-Fe
1379 diffusive resetting means these elements are an unreliable test of equilibrium (c.f. Prissel et al., 2016). The slow
1380 diffusion of Al in olivine (Spandler & O'Neill, 2009) means that parts of a host olivine crystal could be out of
1381 equilibrium with their spinel inclusions if olivine crystallisation occurred over a protracted time with changing
1382 temperature (or melt composition). Maps of the aluminium content of olivine crystals have revealed near-
1383 ubiquitous zoning in crystals from Iceland (Matthews et al., 2021), adding complexity to identifying equilibrium
1384 pairs. Matthews et al. (2021) and Trela et al. (2017) therefore recommended the aluminium content of olivine
1385 crystals should be mapped with a high current electron beam before identifying locations for quantitative
1386 analysis.

1387 **2.8. Plagioclase-Liquid thermometry and hygrometry**

1388 Plagioclase (Plag) is a very common mineral in a wide variety of tectonic settings (e.g., MORBs, OIBs,
1389 Arcs), motivating the development of a number of thermometers, barometers and hygrometers parameterizing
1390 the exchange of components between plagioclase and liquid (Putirka, 2008, 2005; Sugawara, 2001; Waters and
1391 Lange, 2015). However, the exchange of the anorthite (An)-albite (Ab) component between liquid and Plag is
1392 sensitive to T, P, and H₂O. If none of these variables are constrained by independent methods, there is a
1393 substantial solution space to explore. There also isn't much consensus as to what equilibrium tests should be
1394 used to filter Plag-Liq pairs. Putirka (2008) note that Ab-An exchange values for experiments (K_D^{An-Ab}) are
1395 normally distributed, with experiments with T<1050°C having values of 0.1±0.05, and experiments with
1396 T>1050°C having values of 0.27±0.1. However, plotting our experimental data (along with the calibration dataset
1397 of Waters and Lange, 2015) shows a more continuous variation of K_D with temperature (Supporting Fig. 9)
1398 although there is a relatively abrupt step up to higher values between 1000–1100°C. We tentatively suggest this
1399 step up may result from the C1–I1 structural phase transition which occurs near this temperature, which has
1400 been shown to affect plagioclase Mg partitioning behaviour (Mutch et al., 2022). Using the criteria of Putirka
1401 (2008) would exclude a number of experiments close to the cut off (Supporting Fig. 9)– We instead apply an
1402 exponential fit through the experimental data (excluding experiments outside ±0.11, Supporting Fig. 9a-b). Not
1403 applying this filter affects calculated statistics very little for the following discussion.

1404 First, we assess sensitivity of thermometers to H₂O (Fig. 16a), thermometers to P (Fig. 16b),
1405 hygrometers to T (Fig. 16c), and hygrometers to P (Fig. 16d), by independently perturbing experimental P, T and
1406 H₂O. It is apparent from Fig. 16a that Plag-Liq temperatures are strongly sensitive to H₂O; an increase of just 1
1407 wt% H₂O causes an average drop in T of ~31°C for eq24a and 36°C for eq23. This change in calculated T is
1408 comparable to the RMSE of these thermometers. Thermometers are less sensitive to P; with the calculated
1409 change in T only reaching the same magnitude as the RMSE for a change of ~10 kbar (Fig. 16b). Notably, the
1410 Plag-Liq hygrometers of Masotta and Mollo (2019), Putirka (2008) and Waters and Lange (2015) are extremely
1411 sensitive to T; calculated H₂O contents drop by the standard error estimate of the hygrometer for a change in T
1412 of just 10–20°C (Fig. 16c). These hygrometers are less sensitive to P, with P changes of 10 kbar causing variations
1413 well within the quoted RMSE (Fig. 16d).

1414



1415

1416 *Figure 16: Testing the sensitivity of Plag-Liq thermometers to H_2O (a) and pressure (b), and Plag-Liq hygrometers*
 1417 *to T (c) and P (d). 40 experiments from our new compilation were randomly selected (each represented by a*
 1418 *colored line). We perform calculations at the experimental P, T and H_2O content (0,0) on all plots, and then vary*
 1419 *H_2O by ± 3 wt% (a), P by ± 5 kbar (b, d), and T by ± 100 $^\circ C$ (c). We subtract the quantity calculated at experimental*
 1420 *conditions from the quantity at these new conditions. Error bars show the quoted RMSE on each expression. We*
 1421 *label the average perturbation for these 40 samples on the figure.*

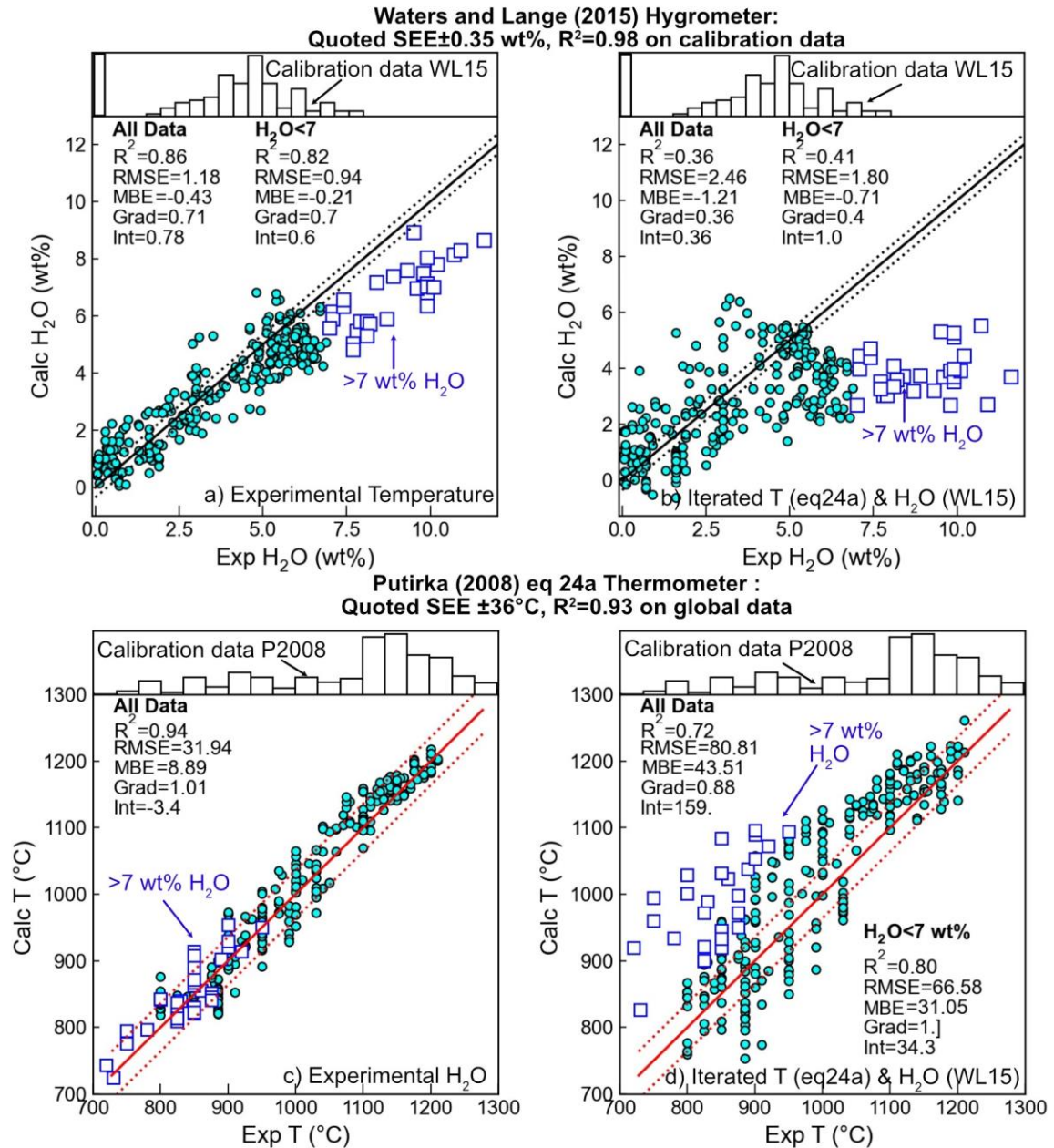
1422

1423 Before assessing hygrometers using our new dataset, it is worth considering how well we really know the “true”
 1424 value of H_2O in each experiment. In the compiled Plag-Liq dataset, only 33% measure water by FTIR, 5% by SIMS
 1425 and 4.8% by Raman spectroscopy. A further 16% report water using the electron microprobe water-by-
 1426 difference method, with some mention of a calibration method. 17% have calculated H_2O using a solubility
 1427 model, assuming pure H_2O saturation, or using a measured X_{H_2O} value in the fluid (Andújar et al., 2015; Costa,
 1428 2004; Mandler et al., 2014), or enough information for us to perform these calculations using MagmaSat in
 1429 VESlcal (Ghiorso and Gualda, 2015; Iacovino et al. 2019). Interestingly, Waters and Lange (2015) calibrate their
 1430 hygrometer by calculating H_2O in each experiment in their calibration dataset using the solubility model of Zhang
 1431 et al. (2007), rather than using measured H_2O contents. If they had they used MagmaSat instead, calculated H_2O
 1432 contents for these experiments would differ by an average of 0.3 wt% (the max discrepancy is 0.78 wt%), which
 1433 would likely result in slightly different model parameters. Additionally, if the starting materials contained even
 1434 small amounts of CO_2 (e.g., from contamination, Blatter et al., 2013), the amount of H_2O in the melt would not
 1435 equal that calculated using a pure H_2O solubility model.

1436 Ideally, we would restrict our comparison to experiments which performed FTIR, SIMS or Raman
1437 measurements of H₂O. However, this results in a much smaller dataset, with N=163 vs. N=358 if calibrated VBD
1438 and solubility water contents are included. This smaller dataset also has a very restricted T range (Supporting
1439 Fig. 10). It also seems unjustified to exclude experiments using solubility models, given that is how the H₂O
1440 contents were determined to calibrate the Waters and Lange (2015) model. Thus, we choose to proceed with
1441 the larger experimental dataset.

1442 Using experimental T and P, the Waters and Lange hygrometer performs reasonably well on the ArcPL
1443 dataset, with a RMSE of ± 1.21 wt% (Fig. 16a). There is a marked deviation to anomalously low calculated H₂O
1444 contents for experiments with H₂O > 7 wt% (cyan squares); if these are excluded, the RMSE is 0.94 wt%, although
1445 this is still far higher than the quoted RMSE of 0.35 wt%. The poor performance at high H₂O may reflect the fact
1446 that these super-hydrous compositions are poorly represented in the calibration dataset of this hygrometer
1447 (white histogram, Fig. 16a-b). When using experimental H₂O contents and pressures, the statistics reported for
1448 the thermometer of P2008 Eq24a on a global dataset are very similar to those estimated from our new dataset
1449 (we calculate RMSE=33°C vs. the stated RMSE=36°C shown as red dotted lines, Fig. 16c).

1450 As discussed in section 1.2, the extreme sensitivity of Plag-Liq thermometers to H₂O content, and
1451 hygrometers to T, means that the comparisons shown in Fig. 16a and c do not accurately represent the true
1452 error when these equations are applied to natural systems, where in the vast majority of instances, neither H₂O
1453 nor T is known. To address this issue with many under constrained intensive variables, we investigate whether
1454 H₂O and T can be solved iteratively using a plagioclase hygrometer and thermometer, as an adaptation of the
1455 popular workflow of iterating barometers and thermometers. Arguably, as we perform these calculations using
1456 experimental P, we are still overestimating their performance on natural systems where H₂O, T and P are all
1457 unknown. The absence of a reliable plagioclase-liquid barometer (see Section 2.9) means that three-way
1458 iteration will not work. However, given these equations are far less sensitive to pressure (Fig. 16), uncertainty in
1459 pressure shouldn't hinder the model performance substantially.



1460

1461 *Figure 16. Evaluating Plag-Liquid hygrometers (a-b) and thermometers (c-d). Only experiments with H₂O*
 1462 *measured by quantitative methods are shown. a) Calculations of H₂O using Waters and Lange (2015) with*
 1463 *calculations performed using experimental T. The hygrometers performance drops substantially for H₂O>7; the*
 1464 *white histogram on top indicates that relatively few experiments used to calibrate this model had such high H₂O*
 1465 *contents. b) Iterative calculations using Waters and Lange (2015) and Putirka (2008) eq24a. c) Calculations using*
 1466 *Putirka (2008) eq24a and experimental H₂O contents, and d) Iterative calculations using Putirka (2008) eq24a*
 1467 *and Waters and Lange (2015). 1:1 line shown with ±stated RMSE for each expression*

1468 Unsurprisingly, iteration of Plag-Liq hygrometers and thermometers yields worse statistics than
 1469 hygrometry calculations performed using experimental T. For example, excluding experiments with H₂O>7 wt%,
 1470 the iterated RMSE is 1.77 wt% (vs. 0.94 wt% using experimental; Fig 16a vs. b). Calculated T using the iterative
 1471 method are also substantially worse than those obtained using known H₂O contents (RMSE=66 vs. 33°C for all
 1472 data, RMSE=58°C for H₂O<7 wt%, Fig. 17c-d). The statistics for these iterative calculations are more indicative of
 1473 the sort of precision these methods can achieve in natural system. We also suggest that such an iterative
 1474 approach may be more accurate than calculating H₂O using temperatures derived from other phases which may

1475 not have formed at the same temperature as Plag (e.g., Fe-Ti thermometry, Black and Andrews, 2020; Crabtree
1476 and Lange, 2011; Pineda et al., 2021).

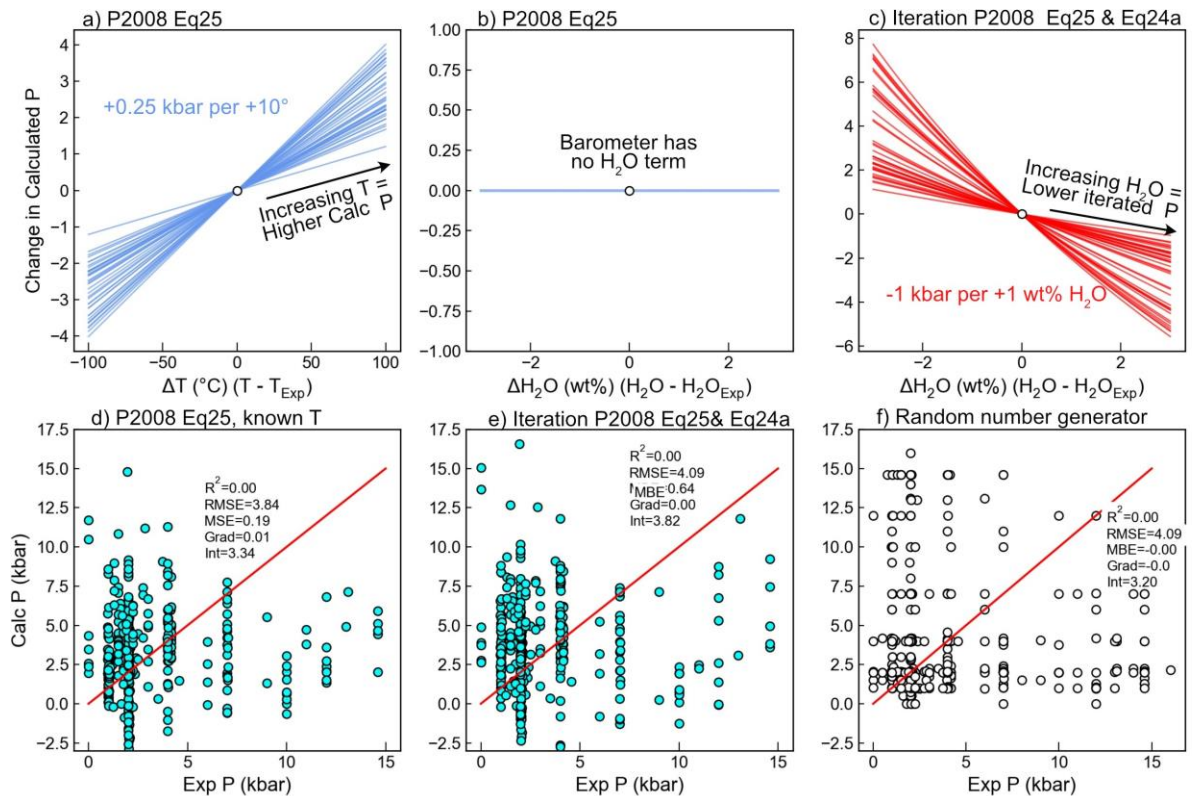
1477 The iterated thermometer has reasonable performance compared to other mineral-melt
1478 thermometers discussed, and the hygrometer has sufficient precision to distinguish dry (0–2 wt%), moderately
1479 wet (2–4 wt%) and wet (>4 wt%) lavas. However, when applied outside of the experimental products used for
1480 calibration, Plag-Liq hygrometry cannot achieve anything like the <<0.5 wt% error often quoted for this method.
1481 Future improvements would be possible with a larger dataset of experiments where H₂O contents are known,
1482 as combining different methods for estimating H₂O contents in experiments undoubtedly adds uncertainty,
1483 particularly when using volatile contents calculated using volatile solubility models (see Wieser et al., 2022a).
1484 Additionally, given the relative success of iterating two different expressions with different underlying datasets,
1485 we suggest that recalibrating Plag-Liq hygrometers without a T term, but with compositional terms like those in
1486 Plag-Liq thermometers to incorporate the effect of temperature, may be more successful than having to iterate
1487 two independently calibrated expressions.

1488 **2.9. Plagioclase-Liquid barometry**

1489 Putirka (2005) proposed a Plag-Liq barometer calibrated on 187 Plag-Liq pairs, which yields a RMSE of
1490 ± 1.8 kbar for the calibration dataset and $\text{RMSE}=\pm 2.2$ kbar on $N=292$ test data. However, Putirka (2008) re-
1491 evaluated this barometer using new experimental data, and found that it performed very badly, with a
1492 $\text{RMSE}=\pm 3.8$ kbar excluding 1 atm data, and even worse statistics when this 1atm data was included. They tried
1493 to find a global model to adequately predict pressures in their new dataset and found that while some regression
1494 worked on some subsets of the database, no regression could fit all data. They suggested that new experiments
1495 with the specific purpose of developing a Plag-Liq barometer are required to move forward. Despite their
1496 warning that “*the status of plagioclase-liquid as a barometer is firmly in doubt*”, a concerning number of
1497 studies have performed Plag-Liq barometry after 2008 (e.g., Budd et al., 2016; Cheng et al., 2014; Dahren et al.,
1498 2012; Geiger et al., 2018, 2016a, 2016b; Guo et al., 2018; Jamshidi et al., 2015; Siegburg et al., 2018). The
1499 majority of these studies quote a ± 2.47 kbar RMSE to justify this approach. However, this value from Putirka
1500 (2008) was only the fit to under half the data; the full dataset gave $\text{RMSE}=\pm 3.6\text{--}3.8$ kbar.

1501 As Plag-Liq barometers are still being widely used in the community, we briefly assess their sensitivity
1502 to T and H₂O, and then evaluate their performance on our new dataset. The T term in P2008 Eq25b means that
1503 the barometer is reasonably sensitive to T, with an average increase in +0.25 kbar per +10°C increase in T (Fig.
1504 18a). The barometer alone isn’t sensitive to H₂O. However, this barometer is normally used in natural systems
1505 through iteration with the Eq24a thermometer, which is H₂O-sensitive (Fig. 18b). When iterated, the barometer
1506 is very H₂O-sensitive; an increase in H₂O by 1 wt% causes the P to drop by an average of ~1 kbar (Fig. 18c).

1507 We assess barometry performance on our test dataset, filtering out pairs which fail the anorthite-albite
1508 (An-Ab) equilibrium test provided in the supporting spreadsheet of Putirka (2008). Using experimental T, the
1509 barometer performs extremely poorly ($\text{RMSE}=3.8$ kbar, R^2 of 0, Fig. 18d). When P and T are iterated, the
1510 performance is even worse ($\text{RMSE}=4.0$ kbar, Fig. 18e). It is notable that in Fig. 18d-e that experiments performed
1511 at 2 kbar yield $P>10$ kbar, while experiments performed at 10 kbar yield $P<0$ kbar. To put the performance of
1512 these barometers into perspective, we compare each experimental P to a random experimental pressure drawn
1513 without replacement from the experimental dataset (Fig. 18f). The RMSE for this randomly selected number is
1514 almost identical to that of the iterated barometer. Thus, until new experiments are done to specifically
1515 investigate the Plag-Liq barometer, this method is only as reliable as researchers using a random number
1516 generator spanning the crustal thickness in their location of interest than Plag-Liq barometry to estimate magma
1517 storage pressures!

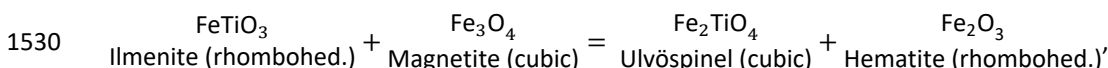


1518

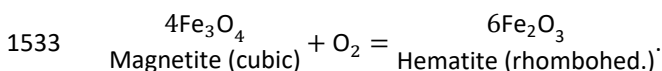
1519 *Figure 18. Assessment of the Plag-Liq barometer of Putirka (2008) Eq25. a-b) Assessing sensitivity of the*
 1520 *barometer to T and H₂O for a subset of experiments. c) Testing the sensitivity of the iterative combination of Eq25*
 1521 *(P) and Eq24a (T) to melt H₂O content. d) Testing the barometer using experimental T and H₂O contents, after*
 1522 *applying the An-Ab equilibrium test of Putirka (2008). e) As for panel d, but solving P and T iteratively (still using*
 1523 *experimental H₂O). f) Assessing the performance of a randomly selecting a P value from the experimental*
 1524 *dataset.*

1525 2.10. Fe-Ti oxides

1526 The partitioning of Fe and Ti between cubic and rhombohedral oxides has been employed in estimating
 1527 magmatic T and fO_2 . The Fe-Ti geothermobarometer is advantageous owing to the rapid cation exchange
 1528 between the oxides, allowing equilibrium to be restored quickly following a change in magmatic conditions (days
 1529 to weeks; Venezky and Rutherford, 1999). The exchange is described by the following reaction:



1531 where there is solid solution between ilmenite and hematite (the rhombohedral oxides), and magnetite and
 1532 ulvöspinel (spinel series, or cubic oxides). The dependence on oxygen fugacity is described by the redox reaction:



1534 The main challenge in calibrating a Fe-Ti geothermobarometer comes from the extremely complex solid
 1535 solution of the rhombohedral oxides. Naturally occurring rhombohedral oxides incorporate significant quantities
 1536 of MgO, MnO, and Al₂O₃ in addition to FeO, Fe₂O₃, and TiO₂, and have complex cation ordering transitions at
 1537 lower temperatures, in addition to magnetic ordering. This means that complex expressions are required to
 1538 accurately represent endmember activities, and multiple miscibility gaps exist. This complexity prevents simple
 1539 empirical calibration of a geothermobarometer expression, and instead requires numerical solutions of
 1540 expressions derived from a complex thermodynamic formulation.

1541 The first implementation of the Fe-Ti geothermobarometer was made by Buddington and Lindsley
 1542 (1964), and improved by a number of subsequent studies as further experimental data became available (e.g.,
 1543 Andersen and Lindsley, 1988; Spencer and Lindsley, 1981). The most recent update of the geothermobarometer

1544 was provided by Ghiorso and Evans (2008), building on the older thermodynamic model of Ghiorso and Sack
1545 (1991) using a calibration dataset with 5X more experiments (N=267 vs. N=57) and much better experimental
1546 constraints on cation ordering. In particular, the calibration range was extended to significantly higher T and fO_2 ,
1547 where previous versions of the model extrapolated poorly. Each update to the thermometer represents
1548 increasing sophistication of the underlying thermodynamic model, and therefore more complex numerical
1549 techniques to apply them as a geothermobarometer. An open-source implementation of the
1550 geothermobarometer was provided by Ghiorso and Prissel (2020) through the ENKI portal.

1551 Blundy and Cashman (2008) use an independent set of experiments to estimate the uncertainty on
1552 several versions of the Fe-Ti geothermobarometer, finding one sigma uncertainties of 44°C and 0.2–0.34 log
1553 units fO_2 for the Ghiorso and Evans (2008) model, but no systematic deviation at high or low temperatures.
1554 However, it is likely that the uncertainty will vary across composition space, as the sensitivity of the thermometer
1555 depends on the composition of the Fe-Ti oxides, with the best sensitivity below the NNO buffer and away from
1556 the miscibility gap (Ghiorso and Evans, 2008).

1557 **2.11. Ti in Quartz (TitaniQ) thermometer**

1558 In silicic rocks where quartz is a dominant phenocryst (e.g., granites and rhyolites), there are far fewer
1559 available thermometers relative to more mafic systems. To address this, Wark and Watson (2006) perform
1560 experiments containing quartz and rutile at 600–1000°C at 10 kbar to produce an empirical relationship relating
1561 the Ti content of quartz to the temperature. They state that this thermometer has an uncertainty of $\pm 2^\circ\text{C}$ at
1562 $>500^\circ\text{C}$ using SIMS measurements of Ti, and that this thermometer can also be applied to systems without rutile
1563 if an independent estimate of Ti activity is obtained (e.g., from Fe-Ti equilibrium). This thermometer was
1564 recalibrated by Kawasaki and Osanai (2008) using natural metamorphic rocks in ultrahigh temperature granulites
1565 and Thomas et al. (2010), who perform additional experiments between 5–20 kbar, generating an expression
1566 incorporating a term for pressure.

1567 Importantly, Thomas et al. (2010) implied that if temperature was known independently, the equation
1568 could be inverted to solve for pressure. Wilson et al. (2012) test this inversion method on samples from the
1569 Oruanui eruption, which has been well studied, so has independent estimates of pressure from melt inclusions,
1570 and temperature and Ti activity from Fe-Ti oxides. They show that using Fe-Ti oxides to constrain temperature
1571 and Ti activity, calculated pressures from Ti in quartz are 3–10X higher than those inferred from melt inclusion
1572 saturation pressures. Similarly, if melt inclusion and Fe-Ti oxide temperatures and pressures are used, inferred
1573 Ti activity is far too low. If pressures are used from melt inclusions and Ti activity from Fe-Ti oxide, temperatures
1574 are well below the H_2O -saturated solidus for granite. Similar discrepancies with previously published pressures,
1575 temperatures and Ti activities are present for calculations on the Bishop tuff. Wilson et al. (2012) suggest that
1576 Ti activities may be highly variable in igneous systems, so activities from Fe-Ti oxides cannot be reliably used
1577 with TitaniQ. Additionally, they suggest Ti in Qtz records complex histories that cannot be simply related to
1578 changes in pressure and temperature over other variables, such as quartz growth conditions or melt
1579 composition. For example, Huang and Audétat (2012) show that Ti concentrations in Qtz depend on the crystal
1580 growth rate, so this thermobarometer should not be applied to hydrothermal fluids where growth rates are fast
1581 and highly variable.

1582 Thomas and Watson (2012) partially rebut Wilson et al. (2012), in particular critiquing the validity of
1583 their calculations of Ti activity (e.g., Ghiorso and Gualda, 2013) and temperature estimates from Fe-Ti oxides
1584 (Ghiorso and Evans, 2008) in the Oruanui rhyolites that underly a lot of the arguments of Wilson et al. (2012).
1585 Instead, Thomas and Watson (2012) use MELTS to estimate temperature and Ti activity based on the affinity for
1586 rutile saturation from inputted melt compositions, yielding pressures similar to melt inclusions. They admit that
1587 the approach of Wark and Watson (2006) was oversimplified in its suggestion of using a fixed value of Ti activity.
1588 An excellent discussion of this Bishop Tuff controversy can be found in Putirka (2017), along with adjustment of
1589 published coefficients for different equations.

1590 Acosta et al. (2020) identified that Ti in Qtz temperatures are offset ~ 100 – 150°C to lower temperatures
1591 than other thermometers in silicic systems, particularly at <4 kbar. To address the source of these offsets, they
1592 perform hydrothermal quartz growth experiments at 800°C and 1 kbar with different fluid compositions. They

1593 find that Ti in Qtz is sensitive to the Ti/Si ratio of the fluid, rather than the concentration or activity of Ti. Clearly,
1594 significantly more experimental work is needed to determine magma storage conditions precisely and accurately
1595 in silicic systems from Ti in Qtz.

1596 **3. Melt inclusion barometry**

1597 Melt inclusions (MIs) are small pockets of melt trapped during crystal growth, which become isolated
1598 from the external melt as the surrounding crystalline host fully encloses them. MI which were trapped from a
1599 volatile-saturated magma can be used to deduce magma storage depths because the solubility of CO₂ and H₂O
1600 in silicate melts is a strong function of pressure (Dixon, 1997; Goranson, 1931). If MI were trapped from a
1601 volatile-undersaturated magma, calculated pressures are minimum estimates (Hauri et al., 2018; Matthews et
1602 al., 2016).

1603 Numerous recent reviews have detailed the theory, methods and advances relating to melt inclusion
1604 analysis and interpretation, as well as several specific problems associated with determination of magma storage
1605 depths from these archives. For example, Wallace et al. (2021) present a comprehensive review of olivine-hosted
1606 melt inclusions, describing melt inclusion formation, post-entrapment crystallization, and the wealth of
1607 information recorded by melt inclusions (e.g., trace element contents for tracking magma batches, processes
1608 controlling magmatic H₂O contents, calculating ascent rates, and storage pressures). Rose-Koga et al. (2021)
1609 provide a number of guidelines involving sample preparation, analysis and data reporting associated with melt
1610 inclusion analysis and interpretation. Barth and Plank (2021) discuss the processes which can alter H₂O contents
1611 in melt inclusions after their entrapment, producing regime diagrams describing how melt inclusions can act as
1612 hygrometers and barometers (revealing pre-eruptive H₂O contents), or speedometers (revealing ascent rates
1613 using H⁺ diffusion). Wieser et al. (2022a) provide a detailed history of different solubility models used to calculate
1614 melt inclusion saturation pressures and highlight the large discrepancies between different models. In particular,
1615 they emphasize the importance of carefully examining the calibration range of each solubility model compared
1616 to the P-T-X range of melt inclusions from a given volcano. To avoid repetition, we refer readers to these papers,
1617 and focus our discussion on issues involving magma storage depth determinations from melt inclusions which
1618 have not yet been reviewed in detail. We specifically focus on the growing realization that the CO₂ contents of
1619 melt inclusions have been significantly underestimated, because of the presence of a substantial CO₂ within
1620 vapour bubbles that were not measured in most published studies.

1621 **3.1 Vapour bubble growth systematics**

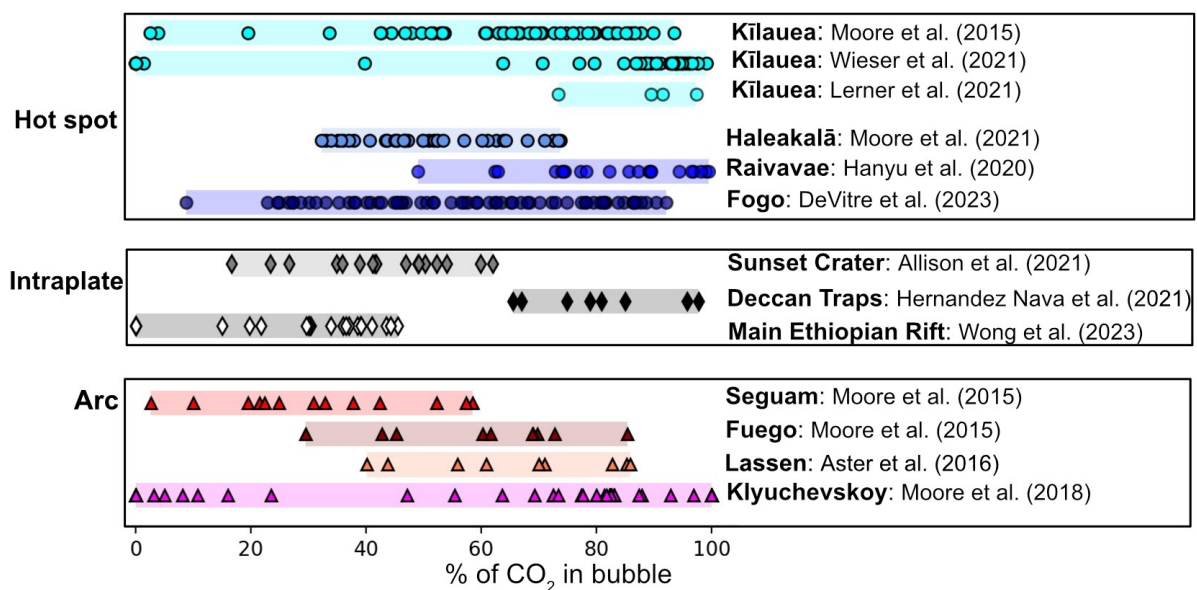
1622 The vast majority of studies have used olivine-hosted melt inclusions to determine magma storage
1623 depths (e.g., Aster et al., 2016; Moore et al., 2015; Ruscitto et al., 2010; Sides et al., 2014; Wallace et al., 2021).
1624 This focus on olivine may reflect the fact that it is one of the first crystallizing phases (important for studies
1625 focusing on the most primitive melt compositions), it is relatively abundant, and tends to have melt inclusions
1626 which are larger than those in other phases from the same sample suite (Bennett et al., 2019, Wieser et al.
1627 2022c). It has also been suggested that the absence of cleavage in olivine makes leakage less likely than in say
1628 pyroxene, which has a strong cleavage (Kress and Ghiorso, 2004). Finally, the simple chemistry of olivine, well-
1629 constrained $K_{D,Fe-Mg}$, and low partition coefficients for REE and other trace elements of geological interest means
1630 that correcting melt inclusions for post-entrapment crystallization (PEC) is more straightforward than in
1631 plagioclase and pyroxene (Danyushevsky and Plechov, 2011; Kress and Ghiorso, 2004; Neave et al., 2017; Wieser
1632 et al., 2022c).

1633 However, as a consequence of the fact that olivine is often the first phase to crystallize in a magma,
1634 there is significant potential for melt inclusions to experience substantial amounts of cooling prior to eruption
1635 (e.g., ~150–170°C in high forsterite olivines from the 2018 eruption of Kīlauea, Lerner et al., 2021; Wieser et al.,
1636 2021). This results in a large amount of PEC. Crystallization of denser olivine from less dense silicate melt,
1637 combined with differential contraction of the melt and host during cooling, causes the pressure in the inclusion
1638 to drop, driving the growth of a vapour bubble (often termed a shrinkage bubble, Kress and Ghiorso, 2004;
1639 Steele-Macinnis et al., 2011; Wallace et al., 2015). Because the solubility of CO₂ is strongly dependent on
1640 pressure, if there is sufficient time between bubble growth and syn-eruptive quenching, a significant proportion
1641 of the total CO₂ content of the melt inclusion will diffuse into the vapour bubble (Fig. 19, MacLennan, 2017,
1642 Wieser et al. 2021). Rapid diffusive re-equilibration of H₂O between the melt inclusion and a more H₂O-poor

1643 carrier melt as a result of fast H⁺ diffusion rates in olivine can also drive the growth of a vapour bubble (Aster et
 1644 al., 2016; Gaetani et al., 2012).

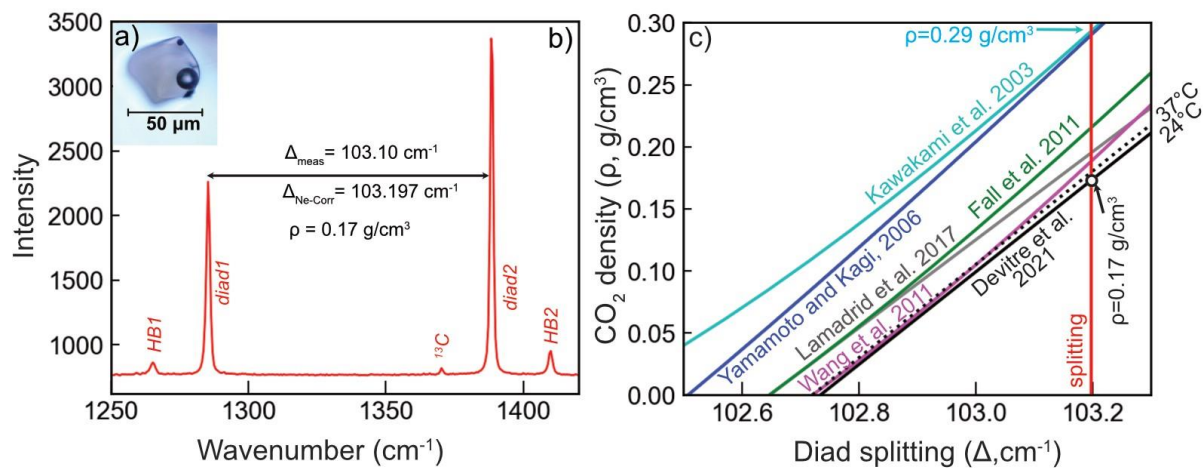
1645 3.2 Raman measurements of vapour bubbles

1646 In situ Raman spectroscopic measurements of vapour bubbles over the last decade have demonstrated
 1647 that a large and often dominant proportion of the total CO₂ content of melt inclusions is held within the bubble
 1648 (Fig. 19, Allison et al., 2021; Aster et al., 2016; DeVitre et al., 2023a; Hanyu et al., 2020; Hernandez et al., 2018;
 1649 Lerner et al., 2021; Moore et al., 2015, 2018, 2021; Wieser et al., 2021). To our knowledge, the first Raman
 1650 analyses of a melt inclusion vapour bubble were made by Steele-Macinnis et al. (2011) in samples from Solchiaro
 1651 Volcano, Italy. They found a distinctive signal consisting of two strong peaks which is indicative of the presence
 1652 of a CO₂ fluid (Fig. 20b). This contradicted the dominant hypothesis at the time that these bubbles were vacuums
 1653 or voids. In two almost concurrent papers, Hartley et al. (2014) and Moore et al. (2015) present Raman
 1654 measurements in melt inclusion vapour bubbles from Laki, Kīlauea, Fuego and Seguam, demonstrating that 40
 1655 to >90% of the total CO₂ is held within the bubble. More recent work has found similar proportions in a wide
 1656 range of volcanoes spanning a range of tectonic settings (Fig. 19).



1657
 1658 *Figure 19 – Percent of the total melt inclusion CO₂ content held in the vapour bubbles from studies which have*
 1659 *used an instrument-specific Raman calibration. Refs: Allison et al., 2021; Aster et al., 2016; DeVitre et al., 2023a;*
 1660 *Hanyu et al., 2020; Hernandez Nava et al., 2021; A. H. Lerner et al., 2021; Moore et al., 2021, 2018, 2015; Wong*
 1661 *et al., 2023.*

1662 Raman spectroscopic analyses of CO₂ in vapour bubbles rely on the strong correlation between the
 1663 density of CO₂ and the distance between the two strong CO₂ spectral peaks collectively termed the Fermi diad.
 1664 This distance is commonly called the splitting, diad splitting, or diad separation (Δ , Fig. 20b). However, the
 1665 relationship between density and diad splitting has been shown to vary as a function of instrument hardware
 1666 and acquisition parameters (Lamadrid et al., 2017, Fig. 20c). This means that the relationship between the diad
 1667 splitting and CO₂ density must be determined for the acquisition parameters and specific data processing
 1668 strategy used by each Raman laboratory. The absolute differences in CO₂ densities for a measured diad splitting
 1669 on different Raman instruments are very large (Fig. 20c). For example, the vapour bubble shown in Fig. 20a yields
 1670 a splitting of 103.10 cm⁻¹ on the Cornell WITEC Alpha300R (Fig. 20b). Following the protocol of Lamadrid et al.
 1671 (2017), this splitting is corrected based on the measured distance between two peaks from the atomic spectra
 1672 of Ne to give a splitting of 103.197 cm⁻¹. Using the densimeter calibrated for this exact instrument, acquisition
 1673 parameters and Ne correction regime (DeVitre et al. 2021), the density of this bubble is $\rho=0.17$ g/cm³ (Fig. 20c).
 1674 However, if the densimeter of Kawakami et al. (2003) was instead used, the calculated density would be nearly
 1675 twice as high ($\rho=0.29$ g/cm³, Fig. 20c).



1676
 1677 *Figure 20 – Determining CO₂ density using Raman Spectroscopy. a) Image of an olivine-hosted melt inclusion*
 1678 *from the Twin Lakes Crater, OR. b) Raman spectra showing the strong Fermi diad (peaks at ~1285 and 1388 cm⁻¹)*
 1679 *with hot bands on either side. The distance between the peaks is the diad splitting ($\Delta=103.10$ cm⁻¹). After*
 1680 *correction for the measured splitting of the Ne emission spectra (Lamadrid et al. 2017), this corresponds to a CO₂*
 1681 *density of 0.17 g/cm³ using the splitting-density relationship developed on this specific instrument (DeVitre et al.*
 1682 *2021). c) The relationship between density and splitting is different on each Raman instrument (e.g., DeVitre et*
 1683 *al., 2021; Fall et al., 2011; Kawakami et al., 2003; Lamadrid et al., 2017; Rosso and Bodnar, 1995; Wang et al.,*
 1684 *2019; Yamamoto and Kagi, 2006). If the Kawakami et al. (2003) densimeter was used for this vapour bubble, it*
 1685 *would give a density of 0.29 g/cm³.*

1686
 1687 The most robust way to calibrate a specific Raman spectrometer for a given analytical protocol is to measure
 1688 the diad splitting for ultra-pure CO₂ gas held at a variety of pressures (and thus densities). This is often achieved
 1689 using a high-pressure optical cell (HPOC) or a fluid density calibration apparatus (FDCA). These apparatus feed
 1690 pure CO₂ gas into a chamber where the pressure is tightly controlled (and ideally the temperature too). The
 1691 measured P and T in the cell can be converted into a CO₂ density using the CO₂ equation of state (EOS, e.g., Span
 1692 and Wagner, 1996). Raman measurements are made on this trapped fluid with known density, and the splitting
 1693 is determined for each Raman acquisition. The relationship between the measured diad splitting and CO₂ density
 1694 is often parameterized over a number of discrete density windows, as the shape of the curves vary (DeVitre et
 1695 al., 2021).

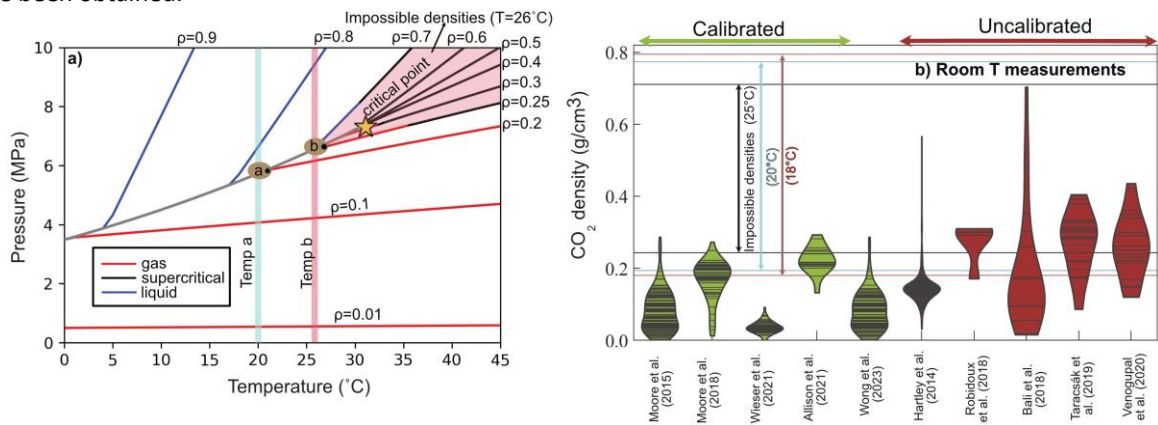
1696 Despite the importance of measuring CO₂ in melt inclusion vapour bubbles being recognised in ~2014–2015
 1697 (Hartley et al., 2014; Moore et al., 2015) and the calibration issue being highlighted in 2017 (Lamadrid et al.,
 1698 2017), only published melt inclusion vapour bubble measurements made at Virginia Tech and Cornell have
 1699 calibrated their Raman using a gas cell apparatus.

1700 Only the Cornell calibration closely controls and measures the T of the CO₂ gas, which is required to convert
 1701 pressure into density with high accuracy and precision (DeVitre et al., 2021). A few more laboratories have used
 1702 lower cost methods, where samples with known CO₂ densities are measured in a manner analogous to primary
 1703 standards for EPMA calibration. For example, Allison et al. (2021) developed a calibration line by measuring the
 1704 splitting-density relationships for fused silica capillary capsules (FSCC). The CO₂ density in these capsules was
 1705 calculated from the mass of loaded CO₂ and the volume of the capillary, which allowed the calibration line to be
 1706 determined at low densities (FSCCs ranged from 0.008–0.133 g/cm³). Wieser et al. (2021) calibrated their Raman
 1707 at low densities using 19 synthetic fluid inclusions (SFI) in quartz standards (0.04–0.14 g/cm³) which were
 1708 measured on the calibrated Virginia Tech Raman, with the same calibration being used by Wong et al. (2023).
 1709 Mironov et al. (2020) use a similar approach, developing a calibration line using 8 melt inclusion vapour bubbles
 1710 measured at Virginia Tech with densities between 0.013–0.22 g/cm³.

1711 Other studies measuring vapour bubbles have converted measured diad splitting into densities using a
 1712 published calibration line developed in a different laboratory (e.g., Bali et al., 2018; Hartley et al., 2014; Taracsák
 1713 et al., 2019; Venugopal et al., 2020). The choice of densimeter in these studies varies widely, and the choice of
 1714 one densimeter instead of another is not justified. For example, Hartley et al. (2014) using Kawakami et al. (2003,

1715 cyan line on Fig. 19c), Taracsák et al. (2019) and Venugopal et al. (2020) using Wang et al. (2011, salmon line),
 1716 and Bali et al. (2018) and Robidoux et al. (2018) using Fall et al. (2011, green line). The offset of their densities
 1717 from the true value is not known, although a correction could be applied retrospectively if samples with known
 1718 CO₂ densities were analysed on the same instrument with the same analytical conditions.

1719 Thermodynamic limits on the density of CO₂ at ambient conditions reveal the issue with the selection
 1720 of a densimeter from the literature developed for a different instrument. The CO₂ phase diagram shows that at
 1721 room T (20–26°C), the maximum possible density of CO₂ gas is ~0.2–0.26 g/cm³ (Fig. 21a). A vapour bubble with
 1722 a higher bulk density will consist of an inner sphere of CO₂ gas of $\rho=0.2\text{--}0.26\text{ g/cm}^3$, and a coexisting outer shell
 1723 of CO₂ liquid with $\rho>0.7\text{ g/cm}^3$ (see inclusion at Temp b on Fig. 21a). It is not thermodynamically possible for
 1724 densities between these values to be measured by Raman spectroscopy unless the sample is heated above the
 1725 critical point of CO₂ at 31°C (supercritical CO₂ can have any density, Span and Wagner et al. 1996). While a small
 1726 amount of laser heating may occur during Raman analysis, which can account for the small number of
 1727 measurements above 0.26 g/cm³ on calibrated instruments (Fig. 21b, DeVitre et al., 2023b; Dubessy et al., 2012;
 1728 Hagiwara et al., 2021), the presence of a significantly larger number of measurements with $\rho>0.26\text{ g/cm}^3$ in
 1729 studies which did not perform an instrument specific calibration indicates that these densities have been
 1730 overestimated through selection of an inappropriate literature calibration. For example, had the Kawakami et
 1731 al. (2003) densimeter been used for the melt Inclusion in Fig. 20a, an impossible density of 0.29 g/cm³ would
 1732 have been obtained.



1733 **Figure 21 – a) Phase diagram of CO₂, drawn using the NIST webbook with the Span and Wagner (1996) EOS. At**
 1734 **Temp a (20°C), a CO₂ fluid with $\rho>0.2\text{ g/cm}^3$ will comprise of a vapour with $\rho=0.194\text{ g/cm}^3$, and a liquid with**
 1735 **$\rho=0.773\text{ g/cm}^3$. At Temp B (26°C), the liquid will have a density of $\sim\rho=0.7\text{ g/cm}^3$ and the vapour will have a density**
 1736 **of $\sim\rho=0.25\text{ g/cm}^3$. Impossible densities at 26°C are shown in pink. b) Compilation of the densities of room T melt**
 1737 **inclusion vapour bubble measurements by Raman spectroscopy, shown as a Violin plot where each horizontal**
 1738 **line represents 1 measurement. Studies which used an instrument-specific calibration are colored green, those**
 1739 **which did not are colored dark red. The maximum density of a vapour and minimum density of a liquid phase at**
 1740 **three temperatures are shown with horizontal lines. Even with a room T of 25°C, many of the densities reported**
 1741 **by uncalibrated studies are thermodynamically impossible. Refs: (Allison et al., 2021; Bali et al., 2018; Hartley et**
 1742 **al., 2014; Moore et al., 2018, 2015; Robidoux et al., 2018; Taracsák et al., 2019; Venugopal et al., 2020; Wieser**
 1743 **et al., 2021; Wong et al., 2023)**

1745 Once the relationship between measured splitting and CO₂ density for a specific Raman instrument and data
 1746 reduction strategy is determined, the amount of the CO₂ held in the vapour bubble (in ppm equivalent in the
 1747 glass) is calculated using mass balance:

$$1749 \quad CO_2(\text{ppm equivalent}) = 10^4 \frac{Vol\%_{VB} \times \rho_{CO_2}}{\rho_{melt}} \text{ [Equation 8]}$$

1750
 1751 Where $Vol\%_{VB}$ is the vol% of the vapour bubble, ρ_{CO_2} is the density of the CO₂ fluid (determined by
 1752 Raman spectroscopy), and ρ_{melt} is the density of the silicate melt (e.g., using DensityX, Iacovino and Till, 2019).
 1753 Equation 8 can be used to demonstrate the large effect of the choice of densimeter on calculated CO₂ contents.
 1754 For example, using a typical melt density (e.g., 2.7 g/cm³) and a bubble volume percent of ~3.9% (as in the melt

1755 inclusion shown in Fig. 20a), the true vapour bubble CO₂ density of 0.17 g/cm³ means the bubble contributes
1756 2455 ppm CO₂ to the melt inclusion. However, if a literature densimeter was randomly chosen from those in Fig.
1757 20b, the amount of CO₂ contributed by the bubble could be as high as 4188 ppm. These discrepancies in Raman
1758 calibration propagate to large uncertainties in magma storage depths. Wieser et al. (2021) show that for a typical
1759 Kīlauea melt inclusion with a vapour bubble occupying 5% of the inclusion volume, different densimeters could
1760 yield storage depths ranging from 4 to 18 km. Thus, constraining the splitting to CO₂ density relationship for
1761 each individual instrument is vital to avoid the introduction of very large systematic errors on calculated storage
1762 pressures (and therefore depths). Arbitrary choice of a Raman calibration is likely the largest source of
1763 systematic error in many published melt inclusion studies, only overshadowed by studies which didn't measure
1764 the bubble at all. Raman analyses without an instrument-specific calibration must be considered as qualitative.
1765 They are useful to determine whether CO₂ is present in vapour bubbles in any given system, but systematic
1766 errors spanning a factor of 3 are unacceptable when it comes to determining magma storage depths.

1767

1768 **3.3 Other uncertainties reconstructing vapour bubbles**

1769 Once a Raman instrument is calibrated, there are four additional major sources of uncertainty affecting
1770 estimates of the amount of CO₂ held in vapour bubbles, discussed below.

1771 **3.3.1. Volume proportions of vapour bubbles**

1772 The first source of uncertainty is associated with determining the relative volume of the vapour bubble
1773 and melt inclusion (i.e. the $Vol\%_{VB}$ term in Equation 8). The vast majority of melt inclusion studies estimate
1774 volumes using transmitted light images, where a best fit ellipse is fitted to the 2D outline of the melt inclusion
1775 and vapour bubble, and the third (z) dimension is estimated either as an average of the two visible axes, or the
1776 minimum of the two measured axes. Tucker et al. (2019) simulate the uncertainty associated with 2D sectioning
1777 of 3D ellipsoids, concluding that the best estimate is obtained when the third (z) dimension is calculated from
1778 the average of the 2 visible dimensions. They quantify the 1 σ uncertainty of this method (-48% to +37%), which
1779 translates into a significant error in calculated storage depths where vapour bubbles contain a large proportion
1780 of the total inclusion CO₂.

1781 However, in many cases, melt inclusions have faceted faces (e.g., Fig. 20a) or more complex shapes that
1782 can deviate significantly from a perfect ellipsoid. For example, a best fit ellipse fitted to a more cubic shape may
1783 result in the melt volume being overestimated, and by extension, the bubble volume and CO₂ content
1784 underestimated (Hanyu et al., 2020). Mironov et al. (2020) compared methods of calculating the z dimension
1785 using the measured x-y dimensions to direct measurements of the 3rd dimension using a vertically calibrated
1786 microscope, or by polishing two orthogonal faces so the x-y and z direction can be measured. They find that
1787 volume measurements using z from a vertically calibrated microscope or by polishing an orthogonal plane were
1788 in good agreement ($\pm 10\%$) with each other, but differed from the z-axis assumption methods by up to 45%.
1789 Thus, they suggest that researchers should measure the 3rd axis using these relatively low-cost methods, rather
1790 than inferring it from 2D measurements.

1791 The most accurate and precise approach is to determine the volume of each phase using x-ray
1792 tomography (i.e. nanoCT, μ CT; Richard et al., 2019; Hanyu et al., 2020; Jorgenson et al., 2021). Hanyu et al.
1793 (2020) showed that optical methods fitting ellipses tend to overestimate MI volumes by $\sim 20\%$, even in fairly
1794 ellipsoidal shaped MI (they did not assess the effect of strong asymmetry or faceting). Attempts have been made
1795 to constrain volumes using 3D confocal Raman imaging (Aradi et al., 2021; Schiavi et al., 2020). There are
1796 additional complications associated with the fact that the different refractive indices of the host crystal, melt and
1797 vapour can cause vertical distortion (Everall, 2010). This can make vapour bubbles appear oblate (Schiavi et al.,
1798 2020). Raman mapping is also significantly slower than μ CT, and data segmentation is even more time
1799 consuming.

1800 Most recently, DeVitre et al. (2023a) perform nano-CT scans for MI of various shapes and sizes,
1801 including those with extreme asymmetry or faceting. They compare these CT volumes to those calculated using
1802 2D methods (measuring x-y, calculating z), and 3D methods where z is measured using a vertically calibrated
1803 microscope, or by polishing an orthogonal surface. For relatively ellipsoidal shapes, the median offset between
1804 2D and CT methods is $\sim \pm 15\text{--}20\%$ (similar to Hanyu et al. 2020), although for certain melt inclusion morphologies,
1805 the offsets can be $\sim \pm 50\%$, similar to the uncertainty estimated from slicing simulations of Tucker et al. (2019) of

1806 1σ =-48% to +37%. For the most faceted or complex shaped MI, the systematic mis-prediction of volume inflicted
1807 using averaging or minimum axis 2D methods results in an uncertainty of up to ~3 kbar in the saturation
1808 pressures (i.e. meaning MI could have been trapped at crustal levels at 7–8 km, or in the mantle, 17–18km). For
1809 regular, relatively ellipsoidal-shaped melt inclusions, DeVitre et al. (2023a) find that measuring the 3rd dimension
1810 (via microscope, motorized-z stage Raman, or on an orthogonal plane) returns values within $\pm 10\%$ of CT
1811 measurements, although the offsets are larger for more irregularly shaped inclusions. Overall, DeVitre et al.
1812 (2023a) suggest that the orthogonal plane method is the most time-and cost-effective way to reduce uncertainty
1813 associated with bubble volumes. While CT is clearly superior, these measurements cost ~100\$/hr, with high
1814 quality scans needing several hours. Data reduction is also time consuming and computationally expensive. At
1815 the moment, the CT method has not been scaled up to datasets typical of melt inclusion studies (e.g., $N > 100$) in
1816 a time or cost-effective manner. We suggest that it makes more sense to constrain the volumes of all melt
1817 inclusion to within $\pm 20\%$ of the true value for all melt inclusions (and published studies), compared with a smaller
1818 number of super precise CT scans, and a larger number of imprecise 2D optical methods. Developing fast,
1819 inexpensive, and precise ways to estimate vapour bubble volumes is an important frontier to address to optimize
1820 melt inclusion barometry.

1821

1822 **3.3.2. Secondary phases in vapour bubbles**

1823 Another major source of uncertainty when reconstructing bubble CO_2 comes from the presence of
1824 carbon-bearing phases on the wall of the bubble, which may sequester 100s-1000s of ppm of CO_2 (Aster et al.,
1825 2016; Moore et al., 2015; Schiavi et al., 2020; Tucker et al., 2019; Venugopal et al., 2020). These phases can be
1826 identified optically in larger bubbles (Tucker et al., 2019), and produce distinctive peaks in Raman spectra,
1827 particularly if the laser is focused near the bubble wall or line scans and 3D maps are used (Fig. 22d, Moore et
1828 al., 2015; Robidoux et al., 2018; Schiavi et al., 2020). Secondary phases can also be identified using BSE, SE and/or
1829 EDS imaging on an SEM of an exposed bubble walls (Robidoux et al., 2018; Schiavi et al., 2020; Tucker et al.,
1830 2019; Wieser et al., 2020).

1831 The occurrence of secondary phases on bubble walls is highly variable, and their genesis is poorly
1832 understood. It appears that carbonate species (e.g., Mg, Fe, Na, and Ca carbonates) are more common in more
1833 H_2O -rich melt inclusions (e.g., arcs and wet OIBS vs. dry OIBs such as Kīlauea). Even at a given volcano, some
1834 eruptions may have a reasonable proportion of melt inclusions containing carbonate (e.g., 1960 Kīlauea, Moore
1835 et al., 2015; Tucker et al., 2019), while other eruptions have no carbonate (e.g., 2018 Kīlauea, Lerner et al., 2021;
1836 Wieser et al., 2021). Most intriguingly, even within a single crystal, some melt inclusions contain carbonate while
1837 others do not, and within a single melt inclusion with multiple bubbles, some have all their CO_2 as carbonate,
1838 some have a mix of carbonate and CO_2 fluid, and some consist only of CO_2 fluid (Fig. 23). It has been suggested
1839 that solid phases form on bubble walls as a paragenetic sequence during cooling of the vapour bubble, with
1840 sulfide precipitation at 500–700°C, magnesite (MgCO_3) precipitation at < 350 °C, and carbonate and sulfide
1841 precipitation from liquid H_2O at < 150 °C (Robidoux et al., 2018).

1842

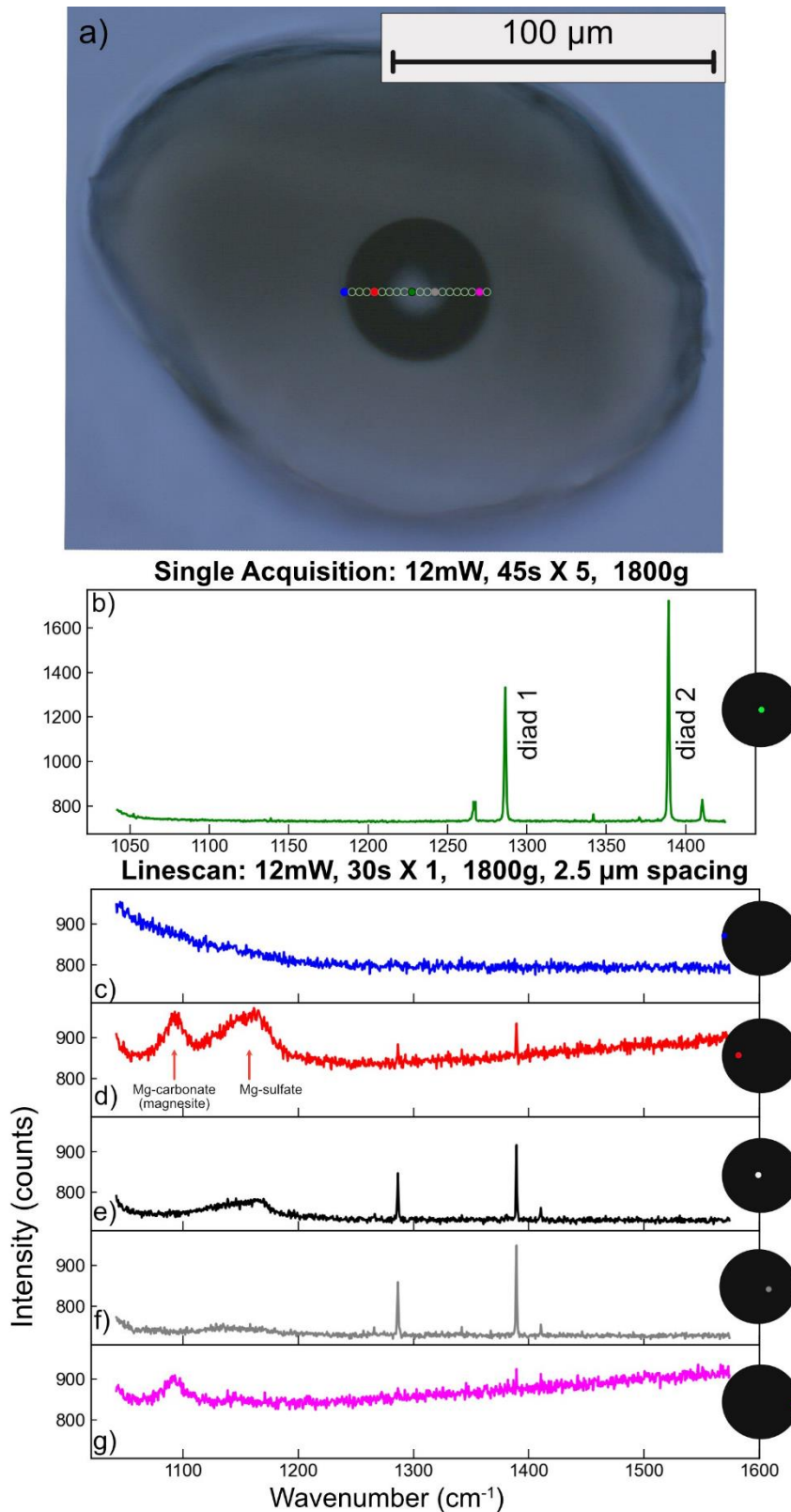


Figure 22 – Comparing a Raman acquisition in the centre of a melt inclusion vapour bubble (scan b) with individual acquisitions taken as part of a line scan across the bubble (c-g). A carbonate and sulfate peak is only apparent at specific locations near the bubble edge, and does not appear in the central acquisition.

Clearly, the carbonate forming reactions are subject to very local variations in condition (on the scale of the diameter of a single melt inclusion), and significant further work is required to understand them further. Quantifying the amount of CO_2 present within carbonate is non-trivial. Tucker et al. (2019) do preliminary mass balance calculations based on optical observations, considering different thicknesses of carbon on the wall of bubbles. Schiavi et al. (2020) determine the volume of carbonate and S-bearing species using 3D Raman mapping, showing that solid phases can account for 21–50% and 16–60% of the C and S budget respectively. Several experimental approaches have been developed for bubble-bearing melt inclusions as an alternative to mass balance reconstructions using Raman Spectroscopy (see below), some of which can help to resolve the carbonate problem.

3.3.2.1 Experimental homogenization approaches

1889 Two broad homogenization strategies have been used to account for Carbonate in vapour bubbles. The ‘in situ’
 1890 strategy involves reheating of individual crystals in a Linkam or Vernadsky heating stage in an $f\text{O}_2$ controlled Ar
 1891 or He atmosphere, making observations of the melt inclusion of interest under an optical microscope. The crystal
 1892 is heated until the vapour bubble and other secondary phases redissolve, and then the sample is rapidly
 1893 quenched to obtain a single-phase melt inclusion. This method allows the operator to view the melt inclusion
 1894 and quench the crystal just after the inclusion homogenizes, meaning a different reheating path can be used for

1895 each crystal. The 'bulk' strategy heats crystals in batches in various experimental apparatus. This had the
1896 advantage of being far less time consuming and allowing reheating at different pressures (see below), but has
1897 the disadvantage of meaning crystals trapped at a range of temperatures may be overheated or underheated
1898 (e.g., Esposito et al., 2012).

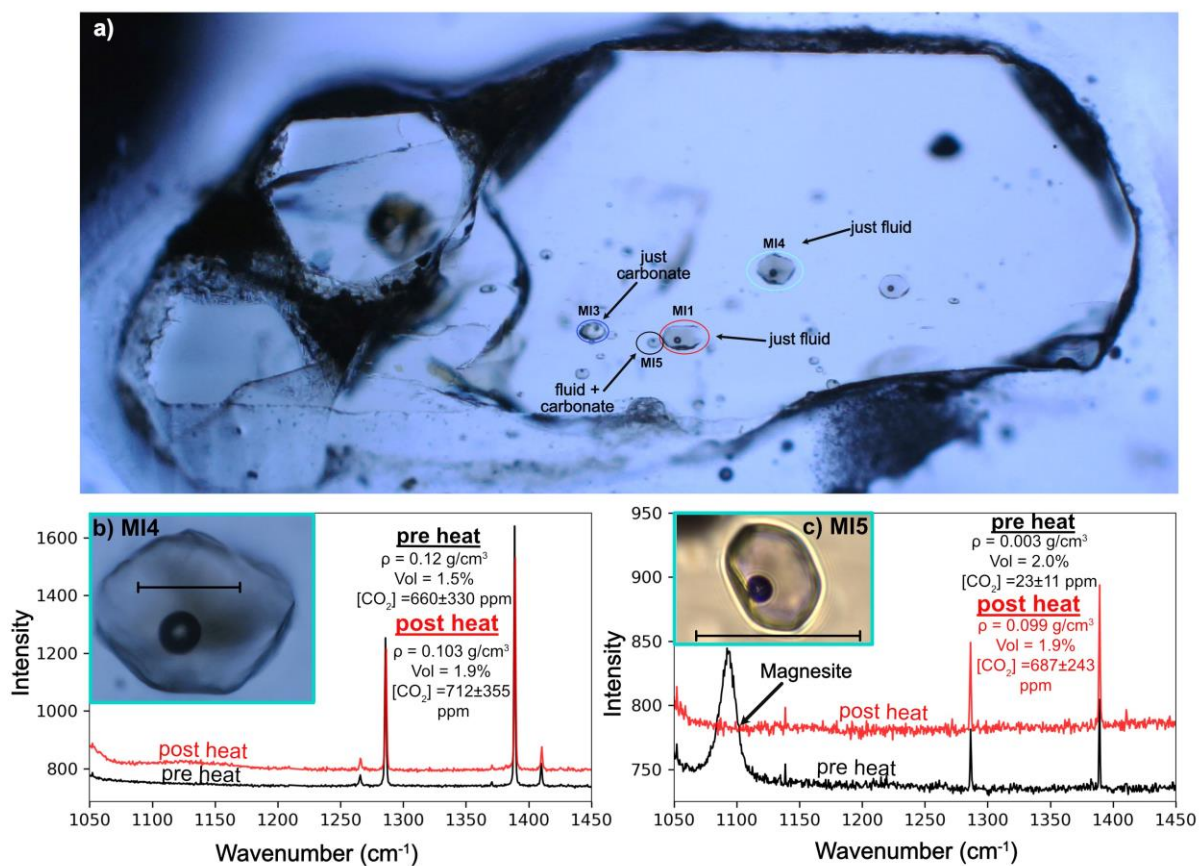
1899 Regardless of whether a single crystal or a batch of crystals is heated, performing reheating experiments
1900 at atmospheric pressure often results in vapour bubbles not fully redissolving, or dissolving at spuriously high
1901 temperatures. For example, Le Voyer et al. (2017) individually heat melt inclusions from Mt. Shasta in the
1902 Cascade Arc using a Vernadsky-type heating stage, noting that many inclusions retain their vapour bubble, even
1903 if they are heated up to 1500°C. The failure to homogenize the bubble has been attributed to the fact that at
1904 atmospheric pressure, the host exerts less pressure on the melt inclusion than was present during natural
1905 cooling at depth in the magmatic system (Danyushevsky et al., 2002; Esposito et al., 2012). Additionally, if
1906 sufficient time passes between post-entrapment crystallization and syn-eruptive quenching, chemical changes
1907 such as FeO or H⁺-loss through the host crystal may occur, which cannot be reversed by reheating (Aster et al.,
1908 2016; Bucholz et al., 2013). To account for the excess bubble growth resulting from these irreversible changes,
1909 the inclusion must be overheated, often by many hundreds of degrees to get the bubble to disappear. This is
1910 concerning because overheating results in extensive re-equilibration between the melt inclusion and host,
1911 erasing important chemical information (e.g., major element zoning preserving quench rate, Newcombe et al.,
1912 2014; information on the amount of PEC; Wieser et al., 2021). An additional problem with heating at 1
1913 atmosphere is that melt inclusions may rupture/decrepitate (Tuohy et al., 2016). This is a particular problem for
1914 melt inclusions closer to the polished surface or the crystal, inclusions trapped at high pressures in the plumbing
1915 system, and more H₂O-rich inclusions.

1916 Crystals can also be heated at elevated pressures (e.g., Piston cylinder apparatus, Rasmussen et al.,
1917 2020, internally heated gas pressure vessel, Skirius, 1990). The confining pressure exerted around the crystal
1918 can help prevent decrepitation, and aid bubble dissolution. To get around the issue that reheating can cause H⁺
1919 loss, and to try to resorb bubbles which have experienced extensive H⁺ loss, Mironov et al. (2015) homogenize
1920 melt inclusions in an internally heated pressure vessel (IHPV) under high H₂O pressure achieved through a
1921 hydrated silicate melt matrix. Specifically, they heat melt inclusions from lavas which are thought to have
1922 diffusively lost 3 wt% H₂O (such extensive H₂O-loss favours near-ubiquitous bubble growth). They find that
1923 bubbles remain after heating under dry and damp conditions, but a large proportion disappear at higher H₂O
1924 pressures where the melt inclusion is rehydrated. This indicates that, at least in wet arc magmas, diffusive H₂O
1925 loss can account for the observation that bubbles often persists after heating (rather than resulting from a lack
1926 of confining pressure during heating in 1 atm apparatus). This reheating method was adapted by Rasmussen et
1927 al. (2020), who use a piston cylinder apparatus with KBr and Mg(OH)₂ as the hydrated matrix to achieve a higher
1928 experimental success rate.

1929 One limitation of these hydrated experimental reheating methods is that the initial H₂O content of the
1930 system must be estimated when preparing the hydrated matrix, and melt inclusion water contents will be reset
1931 to this value (Buso et al., 2022). While Rasmussen et al. (2020) use unheated melt inclusion volatile contents as
1932 a guide, there is still the risk of adding too much or too little H₂O to any specific inclusion. Additionally, while an
1933 approximate estimate of initial H₂O contents can be placed based on the point of homogenization, there is a
1934 non-unique play off between the confining P, T and H₂O content required to obtain complete homogenization
1935 of the bubble (e.g. Mironov et al., 2015 show that instead of increasing H₂O by 1 wt%, P could be increased by
1936 6.5 kbar, or T increased by 100°C). Thus, as with the techniques mentioned above, a limitation of these bulk
1937 homogenization experiments is that the same experimental conditions must be applied to all melt inclusions in
1938 a given capsule, even if they formed on different P-T-H₂O paths in nature (Rasmussen et al., 2020).

1939 All the methods discussed so far attempt to redissolve the bubble entirely, so measurements only need
1940 to be performed on a single homogenous glass phase. In contrast, DeVitre et al. (2023a) developed a reheating
1941 method where the aim is to redissolve the carbonate phase back into the vapour bubble where it can be
1942 measured using Raman spectroscopy, rather than redissolve the bubble into the melt. They heat individual
1943 crystals using a Linkam TS1400XY stage which can heat from room T to 1400°C at up to 200 °C/min, and can
1944 quench using Ar or He flow combined with a water-cooled plate at 240 °C/min. Heating is conducted in an fO₂
1945 controlled Ar atmosphere to prevent oxidation of the melt and olivine. As the melt inclusion is progressively
1946 heated under a microscope, it passes through the glass transition temperature, and goes dark. The liquidus

1947 temperature is estimated from the major element composition of the system and a reasonable range of volatile
 1948 contents (using MELTS, or a liq thermometer). As the liquidus temperature is reached, the melt inclusion clears
 1949 to a brown glass, and the inclusion is held at this temperature for ~8–10 minutes to redissolve any carbonate on
 1950 the walls of the bubble back into the fluid phase, before being rapidly quenched on a water-cooled plate. The
 1951 advantage of this method is that it only heats the inclusion to the liquidus, rather than to higher temperatures
 1952 needed to resorb the bubble. Heating to the lowest possible T is advantageous, because it limits olivine
 1953 dissolution, and preserves the major element information held in the melt and olivine. Raman acquisitions
 1954 collected before and after heating indicate that the carbonate is effectively redissolved back into the bubble
 1955 (Fig. 23e), and that inclusions experience minimal H₂O-loss. After heating, bubbles without carbonate return CO₂
 1956 contents within uncertainty of pre-heating estimates (CO₂ contents change by ~±10% accounting for slight
 1957 changes in bubble volume, or errors associated with measuring the same bubble proportion using 2D images).
 1958 The main disadvantage of this method over complete homogenization methods is the fact that Raman is used
 1959 to measure the bubble after heating, which requires accurate estimates of the relative volume of the vapour
 1960 and melt phase.



1961
 1962 *Figure 23: Olivine crystal with numerous melt inclusions with variable carbon partitioning between fluid and solid*
 1963 *phases. A) Two melt inclusions (MI1, MI4) have a strong fermi diad but no carbonate phases (see spectra b),*
 1964 *while MI5 has a fermi diad and a carbonate peak (see spectra c), and MI3 has just a carbonate peak b) pre and*
 1965 *post-heating, MI4 has very similar densities and volumes, with CO₂ contents within error. c) pre-heating, MI5 has*
 1966 *a prominent magnesite peak, and weak Fermi diads. After reheating using the method of DeVitre et al., 2023a,*
 1967 *the amount of CO₂ increases substantially, and the magnesite peak completely disappears. Scalebar on b-c shows*
 1968 *50 μm*

1969
 1970 **3.3.3. Theoretical vapour bubble reconstruction methods**

1971 A variety of methods have also been developed to reconstruct the CO₂ content of a vapour bubble
 1972 theoretically, although there have been relatively few comparisons with Raman approaches on a single inclusion
 1973 basis (e.g. Aster et al., 2016, Wieser et al. 2021). Anderson and Brown (1993) investigated bubble CO₂ in a suite

1974 of melt inclusions from Kīlauea Iki, calculating an internal pressure for each melt inclusion using the measured
1975 CO₂ content in the melt phase of the inclusion. This internal pressure was then used to calculate the density of
1976 CO₂ in the coexisting vapour phase using an equation of state. To convert these densities into CO₂ amounts, they
1977 assumed all bubbles occupied 0.5 vol% prior to syn-eruptive quenching, which is the point at which CO₂ diffusion
1978 and bubble growth become decoupled. Riker (2005) adapt this method for Mauna Loa, calculating the pre-
1979 quench bubble volume as a factor of the T drop experienced by each melt inclusion, accounting for the fact
1980 different melt inclusions experience different amounts of cooling, and therefore PEC. Aster et al. (2016) further
1981 adapt this method for melt inclusions from Lassen Volcanic Centre, Cascades, tracking the volume of a growing
1982 vapour bubble using phase volume and density information from Rhyolite-MELTS, and vapour compositions to
1983 partition elements into the bubble using the volatile solubility model of Iacono-Marziano et al. (2012). This
1984 method was also used in the Cascades by Johnson and Cashman (2020) and Walowski et al. (2016).

1985 In contrast to these methods reconstructing the vapour bubble volume *prior* to bubble expansion
1986 accompanying syn-eruptive quenching, Tucker et al. (2019) use the equation of state method outlined by
1987 Anderson and Brown (1993) to calculate CO₂ density in the bubble, and then calculate the amount of CO₂ in the
1988 bubble using the measured bubble volume. This measured-volume method generates extremely high CO₂
1989 estimates (and therefore storage pressures) for Hawaiian melt inclusions (4000–10,000 ppm). Using the
1990 measured bubble volume assumes that the vapour bubble and melt continue to exchange CO₂ until the glass
1991 transition T (~725°C), such that the bubble is always in equilibrium with the measured melt composition.
1992 However, vapour bubbles experience two distinct phases of growth. The first phase of bubble growth at high T
1993 accompanies PEC or diffusive H₂O loss. High temperatures mean that CO₂ can easily diffuse from the melt into
1994 the growing vapour bubble. The second phase of bubble growth occurs during syn-eruptive quenching, where
1995 CO₂ becomes diffusion-limited as the temperature drops, but the bubble volume continues to grow until the
1996 temperature cools below the glass transition temperature (Maclennan, 2017). Wieser et al. (2021) compare the
1997 Tucker EOS method to direct Raman measurements at Kīlauea and show that the Tucker method overestimates
1998 the amount of CO₂ in the bubble by a factor of 10–20X compared to the Raman method for melt inclusions which
1999 grew most their bubble during syn-eruptive quenching (where CO₂ migration was diffusion limited). The
2000 measured-volume EOS method results in calculated magma storage depth of 5–20 km for melt inclusions where
2001 the Raman method (and geophysics) indicate were actually trapped at 1–5 km. For melt inclusions contained in
2002 high-Fo olivines, where most of the bubble grew during PEC at high temperatures, EOS methods are still 1.5–2X
2003 too high, as the method still neglects a non-negligible increase in bubble volume upon quench which is not
2004 accompanied by CO₂ diffusion.

2005 To unravel the relative importance of these two stages of vapour bubble growth, good estimates are
2006 required of the amount of PEC, the amount of H₂O-loss, the quench rate, and the glass transition T (Maclennan,
2007 2017; Rasmussen et al., 2020). Rasmussen et al. (2020) produce a Python3 tool, MIMiC (Melt Inclusion
2008 Modification Corrections), which calculates bubble CO₂ using empirical parametrizations of volume and density
2009 changes, with uncertainties quantified by Monte-Carlo techniques. However, while constraining the amount of
2010 PEC is relatively straightforward in systems with a well-defined liquid line of descent where the initial FeO
2011 content can be easily estimated (e.g., Kīlauea Volcano, Wieser et al., 2021), it can be very challenging in systems
2012 with a large amount of scatter in FeO at a given MgO number (e.g., Rasmussen et al., 2017; Walowski et al.,
2013 2019), perhaps because of variability in primary FeO contents and/or mixing of diverse melt compositions (e.g.,
2014 Maclennan, 2008). Reconstructing initial H₂O contents can also be very challenging, and the arc magmas from
2015 which melt inclusions were trapped may be substantially more hydrous than the amount of H₂O left in the melt
2016 inclusion (Gavrilenko et al., 2019; Goltz et al., 2020).

2017

2018 **3.3.4. Co-entrapped vapour bubbles**

2019 All the methods discussed thus far rely on the assumption that vapour bubbles formed after melt
2020 inclusion entrapment, through some combination of PEC, cooling, and H⁺ loss. However, it has been long
2021 recognised that bubbles may also become trapped at the point of melt inclusion formation. These are termed
2022 co-entrapped bubbles. In fact, determining magma storage depths from melt inclusion saturation pressures
2023 *requires* that the melt was volatile saturated at the point of melt inclusion formation. This assumption

2024 necessitates that there is an excess volatile phase available to co-entrap. If co-entrapped bubbles are added
2025 back in by mass balance techniques, the amount of CO₂ could be drastically overestimated.

2026 Many studies simply select a threshold volume above which bubbles are assumed to be co-entrapped
2027 (e.g., 5%, Lowenstern, 2003; Robidoux et al., 2018, or 10%, Buso et al., 2022; Moore et al., 2015). However, the
2028 maximum vapour bubble volume that can form without requiring co-entrapment is a function of the amount of
2029 cooling, and the amount of diffusion H⁺ loss, and varies greatly between different eruptions (Tucker et al., 2019).
2030 Tucker et al. (2019) examine distributions of bubble volumes from Hawai'i, discarding outliers which clearly lie
2031 outside the main distribution of bubble volumes (8 vol%+). In suites where there are abundant fluid inclusions
2032 in crystals addition to bubble-bearing melt inclusions, co-entrapped bubbles can often be identified based on
2033 the fact that they have larger relative volumes than other vapour bubbles, and CO₂ densities more similar to
2034 fluid inclusions (Lerner et al., 2021, Hanyu et al., 2020).

2035 Alternatively, co-entrapped bubbles can be identified by comparing bubble volumes to variables such
2036 as H₂O content, CO₂ density, and PEC amount. For example, Wieser et al. (2021) show that there is a correlation
2037 between the amount of PEC (0–33%) and the volume of the vapour bubble (1–6 vol%) at Kīlauea. The 5% cut off
2038 from Lowenstern (2003) would clearly be inappropriate in this instance. Instead, samples lying significantly off
2039 the observed PEC-volume trend were classified as co-entrapped. While bubble growth in H₂O-poor, CO₂-rich
2040 systems can be relatively well predicted based on the amount of PEC and the cooling path alone (Maclennan,
2041 2017; Riker, 2005; Wieser et al., 2021), it is more complicated in H₂O-rich magmas which have the potential to
2042 experience large amounts of bubble growth following H₂O loss. In these situations it is more robust to use bubble
2043 growth models, and any bubbles which exceed even the most extreme model scenarios were likely co-entrapped
2044 (e.g., Allison et al. 2021, DeVitre et al. 2023a). For example, Ruscitto et al. (2011) report the presence of bubbles
2045 with volumes spanning 6–16 vol % in high Mg olivines from Mt. Shasta, and conclude that these bubble volumes
2046 can grow through a combination of PEC and H₂O loss, so were not necessarily co-entrapped. In contrast, Allison
2047 et al. (2021) found that melt inclusions at Sunset Crater, Arizona, with bubbles >3.5 vol% were likely to be co-
2048 entrapped. These two contrasting scenarios highlight the issue with selecting a single universal volume % as a
2049 cut off.

2050 Even using bubble growth models, the details of specific inclusion must be considered, else co-
2051 entrapped bubbles with volumes within the range predicted by the growth model could be overlooked, even if
2052 they were co-entrapped. Allison et al. (2021) subdivide bubble-bearing melt inclusions from Sunset Crater, AZ,
2053 into 2 groups based on bubble volumes, densities, offset trends in Olivine forsterite-total CO₂ space, and bubble
2054 growth models. They conclude that group 2 inclusions (>3.5 vol%) co-entrapped a bubble. To more robustly
2055 identify co-entrapped vapour bubbles, we are in desperate need of a forward-model of bubble growth,
2056 accounting for both H₂O and CO₂. The model of Maclennan (2017) only considered CO₂ (not H₂O) and is not
2057 publicly available. While the Monte-Carlo methods incorporated in the model of Rasmussen et al. (2020) have
2058 huge potential for this problem, currently this code only works to correct melt inclusions, and cannot be run
2059 forward for a hypothetical P-T-X path post-entrapment. In summary, it is becoming very clear that the CO₂
2060 contents of bubbles must be accounted for to obtain reliable storage depths, and that as a community,
2061 substantially more work is required to a) develop reliable bubble growth models to ensure co-entrapped bubbles
2062 don't result in spurious CO₂ contents b) calibrate individual Raman instruments and perform measurements at
2063 >33°C and appropriate laser powers c) improve methods to determine relative volumes d) further investigate
2064 experimental homogenization methods.

2065 **3.4. Decrepitation**

2066 Another issue affecting melt inclusion saturation pressures is the process of decrepitation, where the
2067 internal pressure of the inclusion exceeds the strength of the host mineral, and cracks open. Decrepitation
2068 commonly occurs during magma ascent, as the confining pressure exerted by the surrounding liquid drops.
2069 Maclennan (2017) compile a global dataset of melt inclusions from MORBs, OIBS, and continental settings,
2070 noting that 95% yield saturation pressures <2 kbar, which is close to the experimental decrepitation threshold
2071 of Wanamaker et al. (1990). Using their model of P-T-V-X evolution of melt inclusions, they conclude that
2072 pressure difference between olivine and melt causes decrepitation in most tectonic settings, so preserved CO₂
2073 contents are minimum estimates. They note that decrepitation can be partially mitigated if the melt inclusion is

2074 trapped from a significantly undersaturated melt, so the melt inclusion experiences significant cooling and PEC
2075 at depth before it ascends, because this reduces the internal pressure of their inclusion. Similarly, sequestration
2076 of CO₂ in a vapour bubble can also help to reduce the pressure of the liquid below the decrepitation threshold.
2077 The modelling of Maclennan (2017) suggested that entrapment pressures up to twice the decrepitation
2078 threshold (i.e., ~4 kbar) could be preserved if ascent conditions allow for bubble formation while remaining
2079 below the decrepitation threshold.

2080 However, a number of studies have been published since 2017 yielding significantly higher saturation
2081 pressures than the compilation of Maclennan (2017). In the glass phase alone, DeVitre et al. (2023a) measure
2082 CO₂ contents of up to 1.3 wt% resulting in glass-only saturation pressures of ~1-7 kbar. Once CO₂ in the vapour
2083 bubble is included, pressures rise to ~2-11 kbar. Similarly high glass CO₂ contents (1.2 wt%) are reported by Buso
2084 et al. (2022) in melt inclusions from the French Massive Central, corresponding to entrapment depths of >10
2085 kbar. Once bubbles are dissolved using homogenization methods, saturation pressures extend to 15–25 kbar.
2086 Glass-only measurements from Haleakala, HI, cluster at 1–3 kbar, and extend to 2–6 kbar after accounting for
2087 the bubble (Moore et al., 2021). Melt inclusions from Isla Floreana in the Galápagos record glass-only saturation
2088 pressures of 1.1–7.2 kbar (median=5 kbar, bubbles not measured). Critically, one bubble-free inclusion records
2089 a glass-only saturation pressure of ~7 kbar. This high pressure overlaps with the pressure calculated from Cpx-
2090 based barometry, indicating it is not an outlier (Gleeson et al., 2022, 2021), and the lack of decrepitation cannot
2091 be attributed to the presence of a bubble keeping the inclusion below the decrepitation threshold. There are
2092 numerous other examples of saturation pressures calculated from the glass phase only yield saturation
2093 pressures >2 kbar from many alkali ocean island settings (e.g., French Polynesia, Hanyu et al., 2020; El Hierro,
2094 Taracsák et al., 2019), and studies accounting for the glass and bubble exceeding 2-4 kbar (e.g., Sunset Crater,
2095 AZ, at 3-5 kbar, Allison et al., 2021, Deccan Traps between ~ 2–7 kbar, Hernandez Nava et al., 2021).

2096 The existence of melt inclusions with glass-only saturation pressures of >>2-4 kbar and glass + bubble
2097 saturation pressures of >4 kbar suggests decrepitation may not be as important a process as Maclennan (2017)
2098 suggests. While Maclennan (2017) conclude that “*decrepitation of melt inclusions, where the inclusion ruptures
2099 and loses CO₂ to the external melt, is the dominant process that controls the observed distribution of CO₂ in the
2100 compiled data set*”. We suggest that the paucity of alkaline, CO₂-rich settings in the compilation of Maclennan
2101 (2017), combined with the fact most studies did not measure the vapour bubble, led to a dataset that was
2102 skewed to anomalously low pressures.

2103 **3.5. Melt inclusions hosted in other mineral species**

2104 While storage depths calculated from olivine-hosted melt inclusions have dominated the literature in
2105 the past few decades, there are a growing number of studies measuring melt inclusions in plagioclase (Bennett
2106 et al., 2019; Blundy et al., 2010; Drignon et al., 2019; Koleszar et al., 2012; Neave et al., 2017; Wieser et al.,
2107 2022c), ortho- and clinopyroxene (Araya et al., 2019; Koleszar et al., 2012; Wieser et al., 2022c), and amphibole
2108 (Koleszar et al., 2012). In more silicic systems, quartz-hosted inclusions are also commonly examined (Bégué et
2109 al., 2015; Quinn, 2014; Wallace et al., 1999), along with plagioclase (Bacon et al., 1992, Wright et al., 2012) and
2110 ortho- and clinopyroxene (Wright et al., 2012).

2111 Saturation pressures from inclusions in other phases often overlap with those determined from olivine
2112 (Wieser et al., 2022c), and may even yield deeper saturation pressures (Bennett et al. 2019) indicating that the
2113 “rupture resistance” of these other mineral phases may have been underestimated. Also, to gain an unbiased
2114 understanding of storage condition in a wide range of melt compositions, it is certainly advantageous to consider
2115 more than one mineral phase, particularly as in many systems olivine is restricted to a relatively narrow range
2116 of melt compositions (if present at all). However, significantly more work is needed to understand bubble growth
2117 and post-entrapment processes in these other phases, as well as rates of diffusive H₂O-loss.

2118

2119 **4. Fluid inclusion Barometry**

2120 Crystals growing in a fluid-saturated magma trap pockets of melt and exsolved fluid in varying
2121 proportions, varying from pure melt (melt inclusions), melt and varying proportions of fluids (melt inclusions
2122 with co-entrapped vapour bubbles), and pockets of pure fluid with little or no attached melts (fluid inclusions –
2123 FI, Steele-Macinnis et al., 2011). In CO₂-rich, H₂O-poor volcanic systems such as mid-oceanic ridge basalts and
2124 ocean island basalts (OIBs), the exsolved vapour phase (and thus the fluid being trapped) is almost pure CO₂ at

2125 pressures >200 bars (Gerlach and Graeber, 1985). In these relatively anhydrous systems, the density of FI can
2126 act as an excellent barometer, because the density of a CO₂-rich fluid, along with an estimate of its entrapment
2127 temperature, can be converted into a pressure using the pure CO₂ equation of state (e.g., Span and Wagner,
2128 1996).

2129 Despite clear potential, a Web of Science search demonstrates that FI barometry has been
2130 underutilized by igneous petrologists in the last 10 years relative to other petrological barometers (Fig. 24c-d).
2131 Conventionally, the densities of FIs have been determined by observing phase changes during heating and
2132 cooling in a temperature-controlled microscope stage (microthermometry, Sorby, 1858). The relatively small
2133 number of existing studies in volcanic settings that use microthermometric techniques to obtain FI densities
2134 show the enormous potential of this method (Fig. 24c, see Hansteen and Klügel, 2008 and refs within). For
2135 example, FI in quartz-rich xenoliths from volcanoes in the Aeolian arc yield densities corresponding to both deep
2136 (~16–20 km) and shallow (4–6 km) pressures within the crust (Frezza et al., 2003). The deeper regions likely
2137 represent the primary magma storage zones, with shallower depths recording re-equilibration of FI during
2138 temporary residence at shallower levels during ascent towards the surface. The ability of FI to identify multi-
2139 stage ascent has also been demonstrated at Mt Etna (Frezza et al., 1991) at Mt. Etna, Cabo Verde (Klügel et
2140 al., 2020), Azores (Zanon and Frezza, 2013) and the Canary Islands (Hansteen et al., 1998).

2141 It has long been established that Raman spectroscopy can be used as an alternative to
2142 Microthermometry to determine the density of CO₂-rich fluid inclusions (e.g., Rosso and Bodnar, 1995). More
2143 recently, improvements in the spatial and spectral resolution of confocal Raman spectroscopy, along with the
2144 development of precise ways to calibrate the relationship between peak parameters and CO₂ density for
2145 different Raman instruments (e.g., DeVitre et al., 2021; Kawakami et al., 2003; Lamadrid et al., 2017, see section
2146 3.2) has made it possible to determine fluid inclusion densities using Raman spectroscopy (Dayton et al., 2023;
2147 Kobayashi et al., 2012; Rosso and Bodnar, 1995). Raman analyses have many advantages over
2148 Microthermometry:

2149 1. Confocal Raman spectrometers are becoming increasingly common in universities, where they are
2150 widely used in other subdisciplines within the Earth Sciences (e.g., paleontology, mineral physics). In contrast,
2151 the use of heating-cooling stages and the associated expertise to conduct microthermometry is more restricted.

2152 2. Raman analyses are faster (2–4 mins) compared with the 10s of minutes required to conduct a single
2153 heating and cooling experiment. This is particularly true if there is only one fluid inclusion within the field of view
2154 at high magnification. Microthermometry can be faster on fluid inclusion trails as phase changes in multiple
2155 inclusions can be observed in one experiment.

2156 3. Raman analyses only require only one surface to be ground down to within ~50–100 µm of the fluid
2157 inclusion, with a good enough polish to be able to visualize the FI on the Raman microscope. Normally, all that
2158 is required to achieve this is relatively fine wet-and-dry paper (2000–7000 grade) and a quick 30 s polish on 1
2159 µm Aluminium polishing paper, while microthermometry requires a crystal to be prepared into a double polished
2160 wafer, with a good enough polish to see phase changes in detail.

2161 4. Raman spectroscopy can be used on CO₂ fluid inclusions with a very wide range of densities (e.g.
2162 0.01–1.24 g/cm³) densities. In contrast, it is very hard to observe the homogenization temperature of a fluid
2163 inclusion with a density less than the critical density of CO₂ (<~0.47 g/cm³) or a density higher than the triple
2164 point (>1.18 g/cm³) using microthermometry (Kobayashi et al., 2012).

2165 5. Raman spectroscopy can be applied on FIs with diameters down to ~1 µm (Frezza et al., 2012,
2166 Dayton et al., 2023), while it is very difficult to observe phase changes during microthermometry for inclusions
2167 < 3–10 µm (Kobayashi et al., 2012). This is of particular importance in volcanic systems, where many fluid
2168 inclusions are very small (and smaller inclusions are more resistant to decrepitation during ascent, Bodnar et al.,
2169 1989; Campione et al., 2015; Wanamaker et al., 1990).

2170 Relative to melt inclusion analyses and mineral barometry, estimates of magma storage depths from
2171 FIs are significantly more precise than both melt inclusions and mineral barometry, and have fewer sources of
2172 systematic uncertainty relating to the conversion of the measured quantity (density) to pressure. Unlike the
2173 complex relationships relating pressure to mineral components (e.g., Jd in Cpx) or dissolved H₂O and CO₂
2174 concentrations in silicate melts, the CO₂ equation of state is extremely well constrained, with very little offset
2175 between different parameterizations (~3% at 7 kbar, Span and Wagner, 1996; Sterner and Pitzer, 1994; Wieser
2176 and DeVitre, 2023). Additionally, unlike many mineral-melt barometers which are very temperature sensitive,
2177 the P calculated from the EOS is not all that sensitive to T (Fig. 24a). To demonstrate the high precision of this
2178 method, we propagate a ±30 K uncertainty in trapping temperature and a Raman analytical error of ±0.02 g/cm³
2179 using Monte-Carlo methods (Wieser and DeVitre, 2023), which yields a 12% 1σ error at 0.6 kbar, a 7% error at
2180 2.2 kbar, and a 5% error at 5.2 kbar. These errors are significantly smaller than other petrological barometers
2181 (Fig. 24b). A final advantage over melt inclusion barometry is that far fewer analytical steps are required to

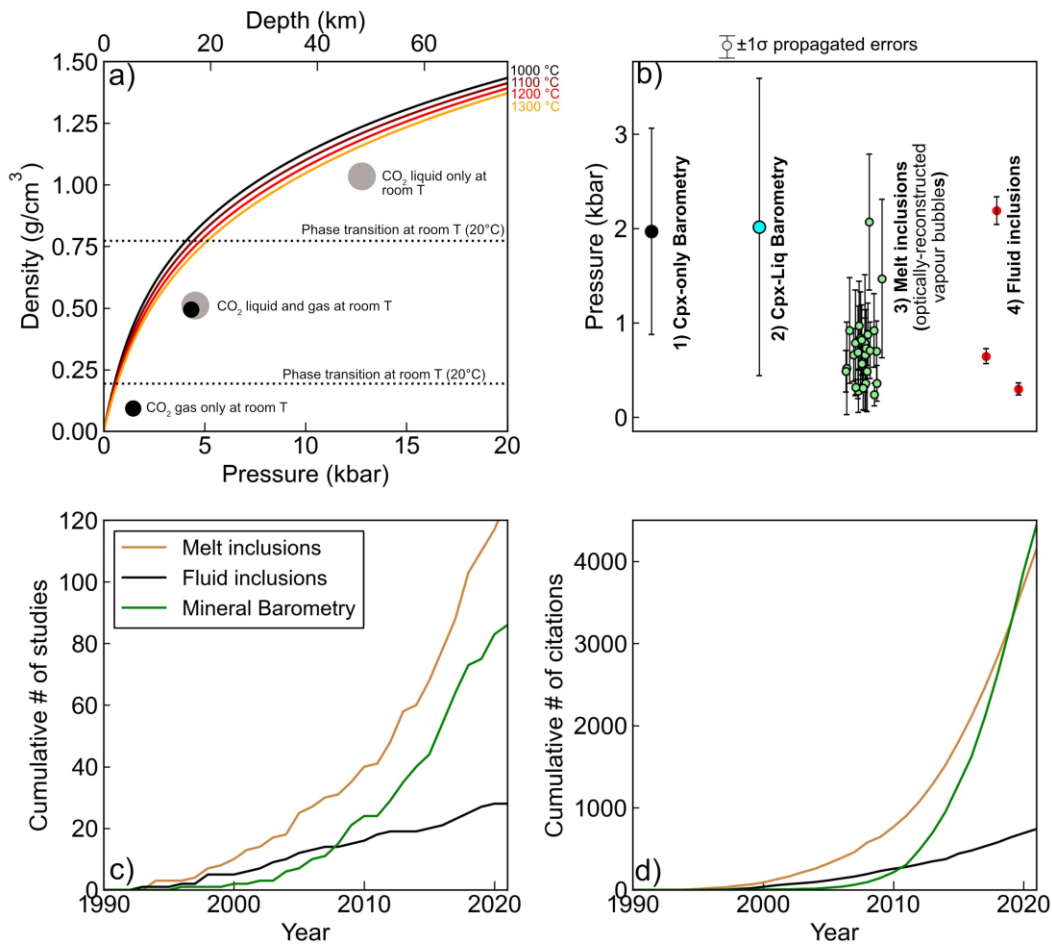
2182 obtain FI pressures (no μ CT, FTIR/SIMS, EPMA measurements of glass), increasing the speed at which depths can
2183 be determined, at a far lower cost (Dayton et al., 2023). This speed is aided by open-source Python3 packages
2184 which help to automate data processing and CO₂ equation of state calculations, which were previously some of
2185 the slower parts of the Raman fluid inclusion method (Wieser and DeVitre, 2023).

2186 Several sources of systematic error must still be considered when interpreting fluid inclusion pressures.
2187 First, like melt inclusions, fluid inclusions may experience decrepitation and rehealing upon ascent. These fluid
2188 inclusions can yield anomalously shallow densities. Second, the pressure the inclusion exerts on the host can
2189 also cause plastic deformation of the host, increasing the inclusion volume. These two processes are captured
2190 by two of the three 'Roedders' rules of fluid inclusions: '2) *the inclusion represents a constant volume*, 3) *nothing*
2191 *has been added or lost from the inclusion*' (Bodnar, 2017; Roedder, 1984). Namely, fluid inclusion barometry
2192 assumes that a fixed mass of CO₂ was trapped in the crystal, with a fixed volume, meaning the inclusion has a
2193 fixed density, so the density measured in the laboratory is the same as the density at which the inclusion was
2194 trapped. Decrepitation violates rule 3 (and possibly 2 as well), while re-equilibration violates rule 2. While
2195 numerous work has been conducted to determine re-equilibration processes for quartz-hosted fluid inclusions
2196 (Bakker, 2017; Boullier et al., 1989; Pecher, 1981; Qin et al., 1992), to our knowledge, the only experimental
2197 constraint on olivine re-equilibration was performed by Wanamaker and Evans (1989). They re-equilibrate fluid
2198 inclusions within San Carlos olivine by holding crystals at 1400°C and atmospheric pressure for several days. We
2199 suggest that further experimental work is required to confidently predict how fluid inclusions in common mafic
2200 phases (olivine, pyroxenes etc) re-equilibrate when subject to a specific P-T-t path, with the aim of having models
2201 which can be run for a given set of samples similar to those used to model H⁺ loss from melt inclusions (E.g.,
2202 Barth and Plank, 2021). However, it is clear from analyses of fluid inclusions in mantle xenoliths that return
2203 crustal pressures that re-equilibration should be taken as the norm rather than the exception, and fluid
2204 inclusions will normally be reset to the pressures corresponding to the final region of prolonged magma stalling
2205 prior to eruption (Hansteen and Klugel, 2008).

2206 The presence of fluid species other than CO₂ can also influence the accuracy of calculated pressures by
2207 both Raman spectroscopy and microthermometry. In igneous systems, the most common species present in the
2208 exsolved fluid phase are H₂O, SO₂, Cl, F, H₂S, N₂, CH₄, CO, and He. While some species are strongly Raman active
2209 with peaks that are close enough to the CO₂ diad to be visible in most high resolution acquisitions (e.g. SO₂
2210 produces a sharp peak at 1151 cm⁻¹, Frezzotti et al., 2012), others will require a separate acquisition centered at
2211 higher wavenumbers (e.g. the N₂ peak is at 2331 cm⁻¹, CH₄ at 2917, Frezzotti et al., 2012), and monoatomic
2212 gases (e.g. He) are Raman inactive, meaning they don't produce any peaks. Molar proportions can be estimated
2213 from peak area ratios and knowledge of scattering cross sections for different Raman-active gases (Burke, 2001).
2214 Some fluid species can also be identified (and sometimes quantified) from changes in the freezing and melting
2215 temperatures by microthermometry (Hansteen and Klugel, 2008; Van Den Kerkhof, 1990), although in many
2216 cases, the relevant phase diagram has not been constrained (e.g. C-He).

2217 Mixed H₂O-CO₂ fluids present a particularly challenging problem to fluid inclusion barometry, because
2218 H₂O is so ubiquitous in the exsolved vapour phase in igneous systems. In arc magmas H₂O will be present in non
2219 negligible molar proportions at all crustal levels (>>10 mol%, Wieser et al. 2023d). Even in CO₂ dominated
2220 systems (e.g. Hawai'i), exsolved fluids will have substantial proportions of H₂O in the vapour phase as magmas
2221 ascend towards the surface. H₂O can be identified by microthermometry through the appearance of clathrate
2222 phases, and by Raman spectroscopy through identification of the O-H stretching band at ~3600 cm⁻¹ (Azbej et
2223 al., 2007). However, at room temperatures, H₂O will be present as a thin film of liquid along the edge of the
2224 inclusion. This can make it very hard to identify by Raman spectroscopy, unless the inclusion is heated to the
2225 point at which H₂O dissolves into CO₂ (e.g., to ~150°C, Esposito et al., 2016). It has also been demonstrated that
2226 this H₂O film can react with the host crystal or a thin film of melt around the fluid inclusion (Andersen et al.,
2227 1984; Esposito et al., 2016; Frezzotti et al., 2002), and/or be lost through diffusive re-equilibration with a
2228 degassed carrier melt (Mackwell and Kohlstedt, 1990). This means it can be hard to identify which FIs had non
2229 negligible quantities of H₂O at the time of entrapment.

2230 The presence of other fluid species complicates calculations of pressure in two ways. First, CO₂ densities
2231 obtained by Raman spectroscopy or microthermometry are normally converted into an entrapment pressure
2232 using a pure CO₂ EOS, which will deviate from the true relationship defined by a mix of the species of interest.
2233 Secondly, the reaction of secondary phases to form precipitates on walls, solid crystals, or liquid films means
2234 that the measured density represents only that of the residual CO₂ fluid phase, not the initial trapped fluid.
2235 Hansteen and Klugel (2008) discuss possible corrections for mixed fluids in their review (e.g. estimating H₂O/CO₂
2236 ratios, then using a mixed H₂O-CO₂ EOS). Looking forward, we suggest that further work into mixed fluid
2237 equation of states and phase diagrams, as well as experiments of fluid inclusion re-equilibration, is required to



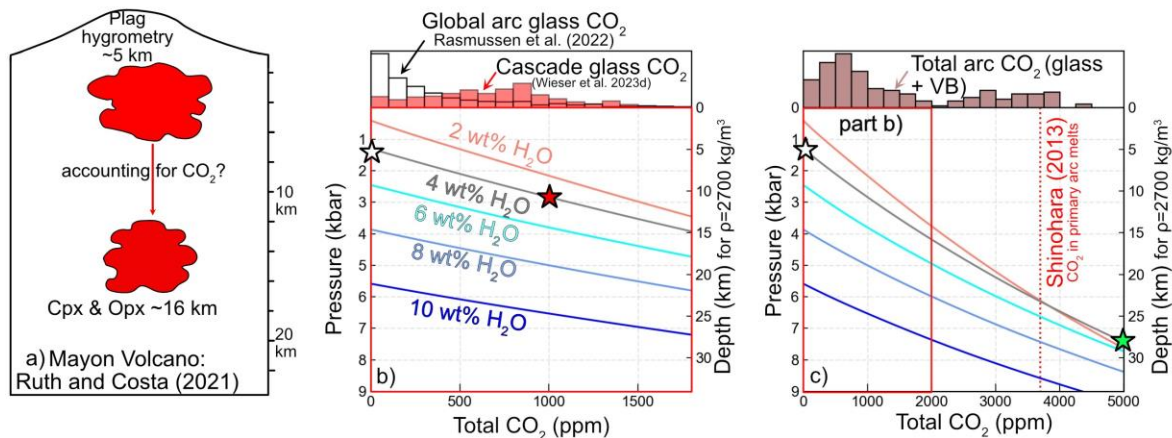
2239 *Figure 24: a) Relationship between pressure and the density of a pure CO₂ fluid (calculated using the Span and*
 2240 *Wagner, 1996 EOS implemented in CoolProp, Bell et al., 2014). Storage depths shown for crustal densities of*
 2241 *$\rho=2700 \text{ kg/m}^3$. b) Monte Carlo simulations of 1σ errors for different barometry methods resulting from analytical*
 2242 *uncertainty. Uncertainties calculated using Putirka (2008) eq32d-32b for Cpx-only and eq3 3–30 for Cpx-Liq*
 2243 *arising from the EPMA analytical uncertainties of Neave et al. (2019, see Wieser et al. 2023b). Melt inclusion*
 2244 *uncertainties show propagated errors in melt inclusions with vapour bubbles from the 2018 eruption of Kilauea*
 2245 *(Wieser et al. 2021). The large relative errors ($\pm 50\%$, $\sim 1\text{--}1.5 \text{ kbar}$) arise from reconstructions of the volume of*
 2246 *the vapour bubble using optical microscopy (with $z=(x+y)/2$, after Tucker et al. 2019). 1σ errors on calculated*
 2247 *pressures for 3 FIs trapped at different crustal pressures, assuming an analytical error of 0.02 g/cm^3 from Raman*
 2248 *spectroscopy, and uncertainty in T of $1\sigma=30 \text{ K}$. c) Web of Science search for number of articles using each method*
 2249 *for barometry (full search criteria given in supporting information), and d) number of citations to these articles.*

2251 **5. Can hygrometers be used as barometers?**

2252 At the opposite end of the spectra to determining pressures from fluid inclusions in CO₂-rich systems
 2253 assuming the exsolved fluid is pure CO₂, many studies have used H₂O contents to estimate pressures using a
 2254 pure H₂O solubility model, either through direct measurements in melt inclusions (e.g., Blundy and Cashman,
 2255 2005, Rutherford et al., 1985) or calculated H₂O contents from mineral and mineral-melt hygrometers (e.g.,
 2256 Amphibole Mg#s – Goltz et al., 2020, Krawczynski et al., 2012, Plag-Liq hygrometry – Ruth and Costa, 2021). For
 2257 example, Ruth and Costa (2021) conduct thermobarometry on a variety of phases from Mayon Volcano (Fig.
 2258 25a). Cpx-Liq, Opx-Liq and Cpx-Opx pressures show a prominent peak at $\sim 4 \text{ kbar}$ (16 km). In contrast, they invoke
 2259 a shallower magma reservoir at $\sim 5 \text{ km}$ based on H₂O-only saturation pressures calculated from plagioclase-
 2260 liquid hygrometry (and H⁺ in pyroxene). However, it is well established that primary arc magmas have non-
 2261 negligible quantities of CO₂ (Shinohara, 2013; Wallace, 2005). While such H₂O-only calculations are often quoted

2262 as minimum estimates, it is worth questioning whether such minimum estimates are even useful, given that
 2263 uncertainty in the amount of CO₂ can change the calculated pressure by up to an order of magnitude (Black and
 2264 Andrews, 2020; Wieser et al., 2022a).

2265 Using a global compilation of CO₂ in the glass phase of melt inclusions (Rasmussen et al., 2020, white
 2266 histogram, Fig. 25b) and a compilation from the Cascade arc (red histogram, Fig. 25b, Wieser et al., 2023d), it is
 2267 apparent that arc magmas have, at the very minimum, several hundred to a thousand ppm of CO₂. These
 2268 quantities of CO₂ have a very significant effect on the calculated saturation pressures. For example, the H₂O-only
 2269 saturation pressure of a typical arc basalt with 4 wt% H₂O (Plank et al., 2013) is ~ 1.3 kbar (white star on grey line)
 2270 (line), while the saturation pressure accounting for 1000 ppm CO₂ is 2.8 kbar (red star on grey line, Fig. 25b). In
 2271 reality, it is becoming apparent that glass-only melt inclusion measurements have substantially underestimated
 2272 the CO₂ content of arc magmas. A compilation of CO₂ contents in arc magmas for studies accounting the vapour
 2273 bubble extends up to ~5000 ppm (Fig. 25c). For a magma with 4 wt% H₂O, a H₂O-only saturation pressure
 2274 underestimates the true storage depth of a magma with 5000 ppm CO₂ by a factor of 5.7X (Fig. 25c, white star
 2275 vs. green star). While H₂O depths are indeed minimum estimates, this example shows just how misleading they
 2276 can be. Even for a magma with 10 wt% H₂O, H₂O-only pressures underestimate by ~1.8X if there is 5000 ppm
 2277 CO₂. Thus, we speculate in many cases that accounting for CO₂ will push hygrometry estimated magma storage
 2278 pressure substantially deeper, perhaps more in line with other barometry estimates (Fig. 25a).



2279
 2280 *Figure 25: Sensitivity of saturation pressures to CO₂ contents. a) Schematic model of plumbing system at Mahon*
 2281 *Volcano, adapted from Ruth and Costa (2021), where the depth of the shallower reservoir was calculated using*
 2282 *a H₂O-only solubility model. b-c) Increase in saturation pressure with CO₂ for 5 different H₂O contents (for a*
 2283 *typical mafic Cascade melt composition, SiO₂=54.3 wt%), calculated using the solubility MagmaSat (Ghiorso and*
 2284 *Gualda, 2015) in VESlcal (Iacovino et al., 2021). The histograms in b) show a global compilation of arc CO₂*
 2285 *contents just measuring the glass phase (Rasmussen et al., 2022), and a compilation from the Cascade Arc. c)*
 2286 *Expanded x scale (region shown in b) indicated in the red box) up to 5000 ppm CO₂. Histogram shows a compilation*
 2287 *of total arc CO₂ accounting for the vapour bubble through Raman spectroscopy or homogenization (from Mironov*
 2288 *et al., 2015; Moore et al., 2018, Rasmussen et al., 2020). We overlay the estimate of primitive arc magma CO₂*
 2289 *contents from Shinohara (2013)*

2290
 2291 Therefore, we suggest that H₂O-only saturation pressures should only be used in systems where it has been
 2292 demonstrated that very little CO₂ is present, in the same way that fluid inclusion barometry using the pure CO₂
 2293 EOS can only be used in systems where there is very little H₂O in the fluid phase. In more CO₂-rich systems,
 2294 calculations should be performed for a wide range of possible CO₂ contents to determine the uncertainty
 2295 associated with H₂O-only saturation pressures.

2296 6. Elastic Thermobarometry/Thermoba-Raman-try

2297 Elastic thermobarometry exploits information held within the crystal structure of mineral inclusions
 2298 and hosts to determine formation and re-equilibration conditions (Cisneros and Befus, 2020). As these
 2299 measurements are typically made by Raman spectroscopy because the band/peak positions of many minerals

2300 are P-sensitive, this technique was termed *Thermoba-Raman-try* by Kohn (2014). One form of elastic
2301 thermobarometry uses host-inclusion pairs. At the time of mineral growth and entrapment, the host and
2302 inclusion have the same pressure. However, after entrapment, the different thermal expansivity (change in
2303 volume with T) and compressibility (change in volume with P) of the two mineral species means that a residual
2304 pressure develops as the pair cool and/or ascend to the surface. The magnitude of the residual pressure depends
2305 on the P-T path taken (see Fig. 1 from Kohn, 2014). The final stress measured in the inclusion is a function of the
2306 initial P-T conditions of trapping, and the influence of differential contraction of the host-mineral pair (which
2307 can be modelled using knowledge of expansivity and incompressibility of different mineral species; Kohn, 2014).
2308 The most effective barometers are those where there is a large difference between the isothermal
2309 compressibility of the inclusion and host (i.e., changes in volume during pressure changes), while the most
2310 effective thermometers are those with the largest variations in isobaric expansivity (i.e., changes in volume
2311 during temperature changes).

2312 Traditionally, elastic thermobarometry techniques have been applied to inclusion-host pairs in
2313 metamorphic systems or xenoliths. Diamond, garnet and zircon are commonly examined hosts, and host-
2314 inclusion pairs include olivine-in-diamond, coesite-in-diamond, and coesite-in-zircon (Kohn, 2014, Cisneros and
2315 Befus, 2020). *Thermoba-Raman-try* techniques can be remarkably precise; the estimated error in calculated
2316 pressure for Qtz-in-Gt inclusions is 0.3–0.5 kbar, resulting from uncertainty in the Raman band position of 0.5
2317 cm^{-1} (Kohn, 2014).

2318 Befus et al. (2018) provide the first assessment of elastic thermobarometry in igneous systems by
2319 pressurizing feldspar in a diamond anvil cell and measuring the Raman bands in situ. They find a clear shift of
2320 peak positions to higher pressure from 0 to ~30 kbar, with Raman shifts of the band at $\sim 485 \text{ cm}^{-1}$ of $\sim 0.42 \text{ cm}^{-1}$
2321 per kbar for Albite, 0.45 cm^{-1} per kbar for andesine, and 0.31 cm^{-1} per kbar for anorthite. Their calibrations
2322 relating peak position with pressure could be applied to natural feldspars inclusions with known compositions,
2323 using models of host-inclusion relaxation along a PT path. They suggest that the main limitation of applying this
2324 technique to shallower crustal storage where peak shifts are rather small results from the limited spectral
2325 resolution of many Raman spectrometers ($\sim 1 \text{ cm}^{-1}$). However, the most recent generation of Raman
2326 spectrometers have improved spectral resolution ($0.1\text{--}0.4 \text{ cm}^{-1}$). Additionally, Befus et al. (2018) fit a cubic spline
2327 to the Raman data. If the peak shape can be determined (i.e. a Lorentzian or Gaussian), peak fitting can achieve
2328 significantly higher precision than the spectra resolution (Yuan and Mayanovic, 2017). This increase in spectral
2329 resolution accompanying peak fitting is vital for precise quantification of CO_2 densities using Raman
2330 spectroscopy. For example, a WITEC alpha300R Raman has a spectra resolution of 0.57 cm^{-1} using the 1800
2331 grating. However, the peak fitting error on the CO_2 peaks using a pseudovoigt ranges from 0.002–0.05 cm^{-1}
2332 (error quantified in *lmfit* implemented in *DiadFit*, Newville et al., 2016; Wieser and DeVitre, 2023).

2333 Befus et al. (2018) also note that feldspar inclusions within olivine and clinopyroxene could act as an
2334 effective thermometer (with a predicted resolution of $\sim 100^\circ\text{C}$). This seminal paper was followed by an
2335 assessment of a wider set of inclusion-host pairs by Cisneros and Befus (2020). They identify the need for
2336 significant further work for elastic thermobarometry to become useful in igneous systems (e.g., understanding
2337 anisotropy on residual P, viscoelastic effects, nonideal geometries). Despite the potential of this method, in the
2338 5 years that have passed since Befus et al. (2018) and 3 years since Cisneros and Befus (2020), none of the citing
2339 studies have applied *Thermoba-Raman-try* methods to volcanic rocks. Significantly more work is needed, along
2340 with comparison to other methods, to gain community acceptance of these techniques. However, the recent
2341 proliferation of interest and expertise in Raman spectroscopy by igneous petrologists measuring vapour bubbles
2342 should aid such efforts.

2343

2344 **7. Experimental Petrology**

2345 Experimental petrology fundamentally underpins the melt inclusion, mineral-melt thermobarometry,
2346 and *Thermoba-Raman-try* methods discussed so far, because the composition of experimental products are used
2347 to calibrate models. However, experimental petrology can also be used directly to investigate magma storage
2348 conditions in a specific system. Generally, such experiments use a starting composition characteristic of a specific
2349 volcanic system or eruption, and perform experiments at a range of P, T, H_2O and $f\text{O}_2$ conditions. Then,
2350 experimental phase compositions are compared to natural samples to determine the most probable storage
2351 conditions (e.g., comparing glass compositions, mineral core and rim conditions, occurrence of breakdown
2352 reactions; First et al., 2021; Rutherford et al., 1985; Weber and Castro, 2017).

2353 For example, Voigt et al. (2022) perform experiments at 0.25–5 kbar and 850–1100°C on natural starting
2354 materials from the 1257 Samalas eruption. They observe plagioclase and amphibole in their samples, so the PT

2355 space between amphibole breakdown and plagioclase instability places constraints on pre-eruptive PT
2356 conditions. Generally, once a stability region is identified, additional constraints are required to narrow down
2357 the magma storage conditions (Bohrson and Clague, 1988). For example, Cadoux et al. (2014) overlay Fe-Ti oxide
2358 temperatures on their phase diagrams, concluding that the observed phase assemblage at Santorini is recreated
2359 experimentally at 2 and 4 kbar.

2360 When performing experiments to deduce magma storage conditions at a given volcano, there can be a
2361 very large solution space to explore, in terms of pressure, temperature, and f_{O_2} . If a natural Cpx has
2362 compositional similarities to one grown experimentally at a specific set of conditions, it is difficult to quantify
2363 the true uncertainty on storage conditions without exploring a very large number of experimental conditions to
2364 determine whether a very similar composition may appear at a different set of P-T- f_{O_2} conditions, particularly
2365 from a slightly different bulk composition). It is also vital to consider the composition of the fluid phase, which
2366 is often described in terms of the partial pressure of H₂O, P_{H_2O} , or the mole fraction of H₂O in the starting
2367 composition or fluid phase, X_{H_2O} . In order to reduce the size of one variable of the solution space, many
2368 experiments are performed at water-saturated conditions (i.e., $X_{H_2O} = 1$, Blatter and Carmichael, 2001; First et
2369 al., 2021; Grove et al., 1997; Nakatani et al., 2022; Sisson and Grove, 1993; Voigt et al., 2022). However, many
2370 natural systems may not contain enough H₂O to be volatile saturated at high pressures, or may contain relatively
2371 large amounts of CO₂, meaning the system is volatile saturated in a fluid with $X_{H_2O} < 1$. Experiments with H₂O
2372 below the quantity required for H₂O saturation have been performed (e.g., Kawamoto, 1996), as have
2373 experiments in equilibrium with mixed CO₂-H₂O fluids (e.g., Alonso-Perez et al., 2009; Cadoux et al., 2014),
2374 although these are far less common than pure H₂O-saturated experiments.

2375 Interestingly, there are many reports in the literature of phase stability being affected by X_{H_2O} . For
2376 example, Keppler (1989) investigate solidus temperatures in the haplogranite system, and find that the solidus
2377 position varies as a function of the fluid phase composition for a mix of H₂O and CO₂. However, if X_{H_2O} is reduced
2378 by the addition of N₂ instead, this relationship is not seen. These experiments indicate that at X_{H_2O} close to 1,
2379 CO₂ is not just acting as an inert component to reduce the activity of H₂O, but is modifying the structure of the
2380 melt. Rutherford et al. (1985) also note that experiments where X_{H_2O} is reduced by the presence of H₂ are not
2381 directly comparable to those where it is reduced by CO₂ (e.g., the addition of CO₂ is not simple Henry's law
2382 behaviour).

2383 It has been shown numerous times that CO₂ affects the stability of amphibole. Given the increasing
2384 amounts of CO₂ being measured in melt inclusions in mafic arc magmas (Fig. 19), it is highly likely that the
2385 majority of high Mg# amphiboles examined at the surface formed in a system with $X_{H_2O} \ll 1$. For example, Ridolfi
2386 et al. (2010) suggested that large amounts of CO₂ in a relatively high T igneous system with relatively low
2387 amounts of H₂O stabilizes OH⁻ bearing phases such as amphibole. They suggest this may occur because of
2388 increasing solubility of OH⁻ in the melt with increasing CO₂ dissolution. For example, King and Holloway (2002)
2389 suggest a reaction where molecular CO₂ and H₂O react to form carbonate and OH⁻. Ridolfi et al. (2010) note that
2390 the paucity of magnesiohastingsite amphiboles in predominantly H₂O-saturated experiments may indicate that
2391 these compositions only form at high T and high CO₂ contents. Krawczynski et al. (2012) also find amphibole is
2392 stabilized at a higher temperature, with a lower Mg#. in experiments with more CO₂.

2393 In their experiments on the Mt. St. Helens dacite, Rutherford et al. (1985) find radical changes in the
2394 crystallization temperature of different phases as CO₂ is added, reducing P_{H_2O} at a constant P_{total} ; Plag, Px and
2395 Fe-Ti oxides crystallization temperatures increase, while the amphibole liquidus temperatures decrease.
2396 Additional experiments by Rutherford and Devine (1988) confirm that the observed phase stability is produced
2397 experimentally at 920°C, P=220Mpa, and $X_{H_2O}=0.67$. Rader and Larsen (2013) perform experiments on low MgO
2398 basaltic-andesites to constrain the impact of small amounts of CO₂, running experiments at a range of T (90–
2399 1200°C) and P (0.001–1.8 kbar) at both $X_{H_2O}=1$ and $X_{H_2O} \sim 0.7$. They found that the plagioclase stability curve was
2400 the most sensitive to X_{H_2O} , shifting 25°C for $X_{H_2O} \sim 0.7$. They also observe shifts in amphibole stability. Finally,
2401 Cadoux et al. (2014) found that at 850°C and 4 kbar, there was more amphibole present when X_{H_2O} was 0.9 than
2402 1. They also find changes in the stability of both pyroxenes, ilmenite and plagioclase, as well as the liquidus phase
2403 with changes in X_{H_2O} . In particular, they find that orthopyroxene is generally not stable where $X_{H_2O}=1$ at 2–4 kbar.

2404 In summary, these experiments show that $X_{\text{H}_2\text{O}}$ is clearly a very important variable to investigate in
2405 further experiments, and comparison of natural samples to experimental products should factor in possible
2406 differences in $X_{\text{H}_2\text{O}}$. We believe this avenue of investigation is particularly important given the last decade of
2407 Raman work has clearly demonstrated that mafic arc magmas have substantially more CO_2 (and thus a lower
2408 $X_{\text{H}_2\text{O}}$ ratio) than previously thought.

2409

2410 **8. Thermobarometers based on thermodynamic modelling**

2411 Thermodynamic modelling is a powerful tool in igneous systems for exploring various hypotheses, such as
2412 whether the chemical variations in a suite of lavas can be produced by equilibrium or fractional crystallization
2413 alone, or whether processes such as crustal melting/assimilation are required (Heywood et al., 2020). However,
2414 in addition to general hypothesis testing, thermodynamical models have also been used to place quantitative
2415 constraints on magma storage conditions. Two main methods are discussed below, matching liquid lines of
2416 descent to erupted lava compositions, and multiphase saturation methods.

2417 **8.1 Liquid lines of descent**

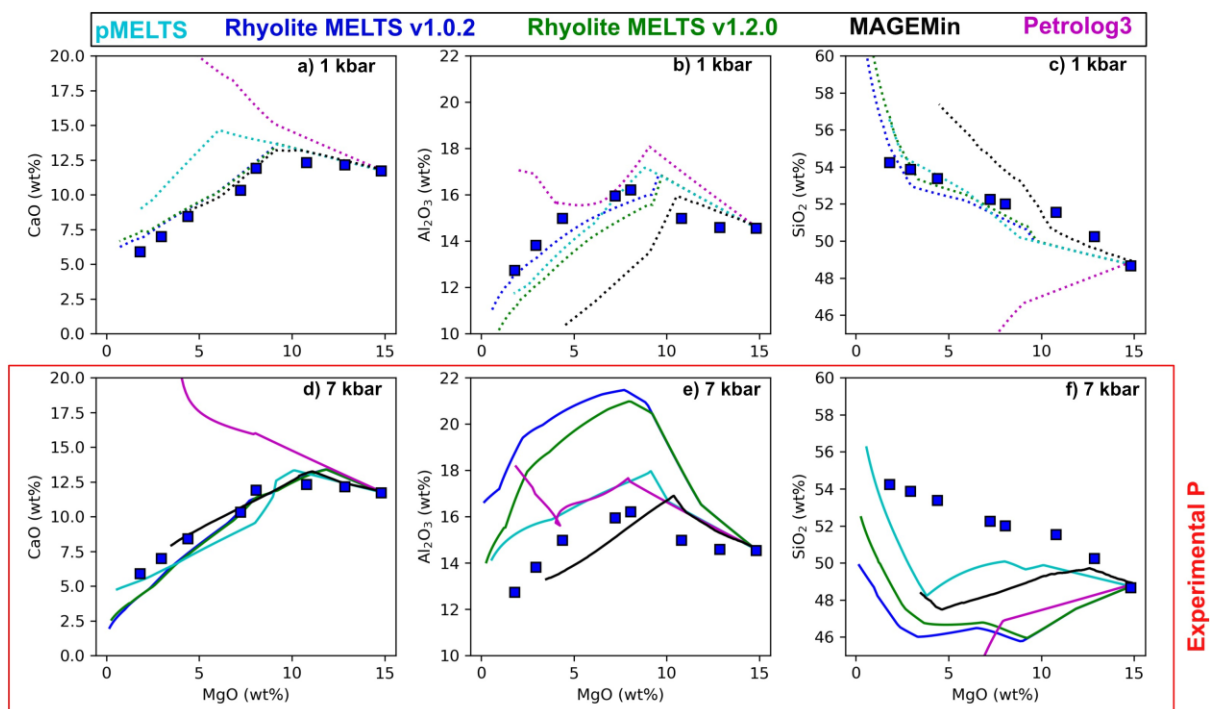
2418 One method to determine magma storage conditions compares fractional crystallization models
2419 conducted at different conditions (e.g., P , $f\text{O}_2$, melt H_2O content) to observed liquid lines of descent (LLD, e.g.,
2420 whole-rock XRF, glass EPMA data). The conditions producing the best fit model are taken as indicative of the
2421 magma storage conditions in the system of interest. Comparison of observed and modelled LLDs have been used
2422 to deduce storage conditions in explosive silicic eruptions (e.g., the Campanian Ignimbrite, Campi Flegrei, Fowler
2423 et al., 2007, and the Bishop Tuff, Long Valley, Fowler and Spera, 2010), in trachytes and pantellerites of the East
2424 African Rift (Gleeson et al., 2017; Hutchison et al., 2018; Peccerillo, 2003; Ronga et al., 2010), in peralkaline
2425 rhyolites from Atlantic Ocean hotspots (Jeffery et al., 2017, 2016), and in basalts from Mauna Loa (Gaffney,
2426 2002).

2427 LLD methods are typically performed in MELTS, but other tools for modelling fractional crystallization
2428 such as COMAGMAT or Petrolog3 could also be used (Ariskin et al., 1993; Danyushevsky and Plechov, 2011). In
2429 general, studies perform calculations to identify whether the observed variations in measured oxide
2430 concentrations can be produced by protracted fractional crystallisation within the crust. If so, the best fit model
2431 is often determined by visual comparison between model outputs and natural samples (e.g., Fowler et al. 2007)
2432 or statistical methods. For example, Gleeson et al. (2017) develop an algorithm to calculate the smallest misfit
2433 between each datapoint and the modelled LLD path for each MELTS model. They combine the residuals of all
2434 individual samples into a weighted RMSE offset for each model.

2435 In certain situations, storage conditions determined by LLD methods are supported by independent
2436 lines of evidence. For example, there is a close agreement between the depths of magma storage estimated by
2437 MELTS modelling and geophysical estimates of magma storage depths in the East African Rift (Hutchison et al.
2438 2016; Gleeson et al. 2017), and between MELTS-estimated $f\text{O}_2$ and experiment constraints (Scaillet and
2439 Macdonald, 2001). However, as pointed out by Gleeson et al. (2017), even the best-fit models display systematic
2440 offsets between the MELTS predictions and the natural data for certain oxides (e.g., CaO , P_2O_5). These offsets
2441 indicate that there are several inaccuracies or omissions in the MELTS thermodynamic models (e.g. absence of
2442 amphibole or biotite in calc-alkaline magmas) that present severe limitations for the use of MELTS-based
2443 crystallisation models as a thermobarometric technique.

2444 In most cases, MELTS correctly identifies the directionality caused by changing P , H_2O , or $f\text{O}_2$ on the LLD
2445 (e.g. enhancing or suppressing the stability of a given mineral). However, it is unclear whether the predicted
2446 mineral stability for a given value of P , H_2O , or $f\text{O}_2$ is correct, or whether it is just relative differences that are
2447 trustworthy. While MELTS modelling may be able to distinguish a dry vs. wet LLD, it may not be able to determine
2448 whether a magma has 0.1 or 0.6 wt% H_2O . It has been shown that MELTS models at Kīlauea Volcano must be
2449 run with melt H_2O contents far below those measured in melt inclusions to recreate the MgO content at which
2450 plagioclase and Fe-Ti oxide crystallize (Garcia, 2003; Wieser et al., 2022c). If H_2O contents were not
2451 independently constrained, such models could lead to incorrect inferences about the hydration state of magmas
2452 at this volcano.

2453 To assess LLD methods further, we compare the measured composition of experimental liquids
 2454 produced during fractional crystallisation experiments on a H₂O-poor tholeiitic basalts to MELTS crystallisation
 2455 models (Villiger et al., 2007). We run a fractional crystallization model at the specified experimental pressure (7
 2456 kbar), *f*O₂ and H₂O content. We also run models at pressures of 1, 4 and 10 kbar (Fig. 26a, Supporting Figs. 11–
 2457 13). We use three different MELTS versions (pMELTS, rhyolite-MELTS v1.0.2 and v1.2.0), Petrolog3
 2458 (Danyushevsky and Plechov, 2011), and MAGEMin (Riel et al., 2022) using the Holland et al. (2018)
 2459 thermodynamic database. Both versions of rhyolite-MELTS show a very poor fit at the experimental pressure,
 2460 predicting extensive Al₂O₃ enrichment and SiO₂ depletion relative to the experimental products (dark blue and
 2461 green lines, Fig. 26e-f). The fit is far better at 1 kbar, which could lead to anomalous inferences of magma storage
 2462 depth if only LLD methods were used. pMELTS doesn't show such extreme Al₂O₃ enrichment at the experimental
 2463 pressure, but the fit for Al₂O₃ is still better at 4 kbar than 7 kbar, and the fit for SiO₂ is best at 1–4 kbar (cyan
 2464 lines). It is worth noting that pMELTS has a different liquid model than rhyolite-MELTS. Petrolog3 shows
 2465 anomalous SiO₂ depletion at all pressures (magenta lines, Fig. 26), and none of the 4 pressures used here provide
 2466 a satisfactory fit to most elements (Supporting Fig. 11). The Holland et al. (2018) database, implemented through
 2467 MAGEMin, certainly does the best job of recreating Al₂O₃ systematics, although the fit to SiO₂ is far better at 4
 2468 kbar than 7 kbar (black lines, Fig. 26, Supporting Fig. 11).

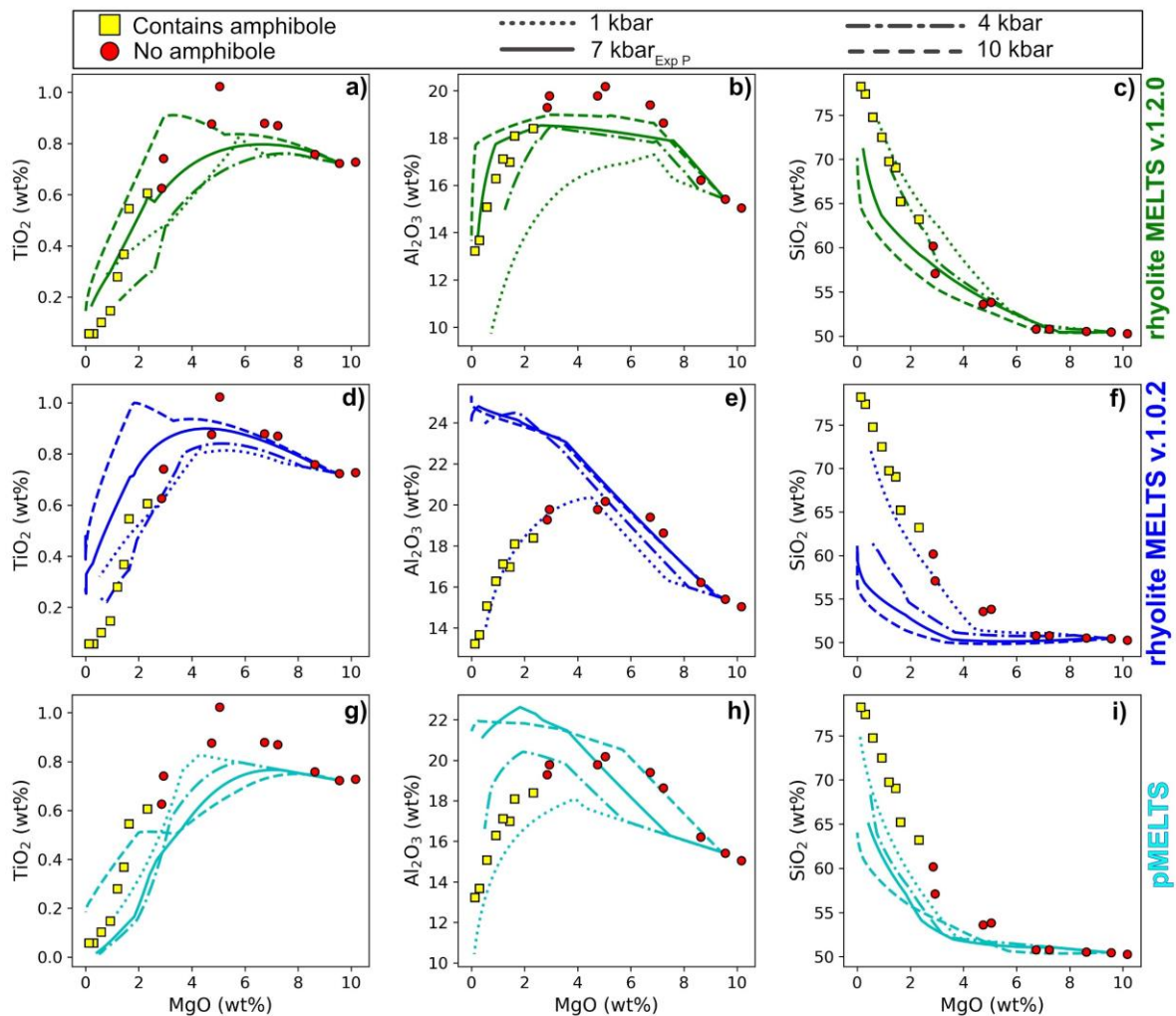


2469
 2470 *Figure 26 – Comparison of fractional crystallisation models run in rhyolite-MELTS, pMELTS, Petrolog3 and*
 2471 *MageMin (using the Holland et al. 2018 database) to fractional crystallization experiments from a nominally*
 2472 *anhydrous, tholeiitic basalt from Villiger et al. (2007). MELTS calculations are performed at the experiment *f*O₂*
 2473 *(NNO), with H₂O=0.2 wt% (i.e. nominally anhydrous). While experiments were conducted at 7 kbar (solid lines),*
 2474 *models run at 1–4 kbar provide a much better fit (particularly regarding the onset of plagioclase). Other pressures*
 2475 *shown in Supporting Fig. 11.*

2476 To further assess LLD methods, we use all three MELTS versions to model the fractional crystallization
 2477 experiments of Nandedkar et al. (2014) conducted on a hydrous arc basalt (Fig. 27). The hydrous nature of these
 2478 experiments means that the differences between rhyolite-MELTS v1.2.0 and v1.0.2 are far more noticeable
 2479 compared to the H₂O-poor experiments of Villiger et al. (2007). Using v1.2.0, models run at 4 to 10 kbar provide
 2480 a reasonable match to observed oxide contents. In contrast, using v1.0.2, models run at 1 kbar provide the best
 2481 fit to both SiO₂ and Al₂O₃. It is concerning that these models give such different results, given they are used
 2482 somewhat interchangeably in the literature, and obviously, any studies conducted prior to the release of v1.2.0

2483 in 2015 must have used v1.0.2. pMELTS shows behaviour between the two rhyolite-MELTS models, with trends
 2484 best recreated at 1–4 kbar.

2485 These comparisons to two experimental studies demonstrate that the pressure you would deduce from LLD
 2486 methods is very sensitive to both the choice of model and the oxides used for assessment of the ‘best model’.
 2487 In neither comparison does the experimental pressure stand out as the best model fit. It is also worth noting
 2488 that for both these examples, we are using known fO_2 and H_2O contents. In reality, it is likely that P , fO_2 , and
 2489 H_2O are all uncertain, which leaves a very large solution space to explore (and can result in even greater
 2490 ambiguity regarding the best fit model). Overall, we conclude that in their current state, LLD methods are not a
 2491 reliable way to deduce storage pressure, particularly given the result can differ so much simply based on the
 2492 choice of fractional crystallization model. It may be that an update of the MELTS liquid model, and/or tweaks to
 2493 the thermodynamic data controlling the mineral stability fields (as performed for the qtz-2 fspar ternary) can
 2494 revive this method. These comparisons also demonstrate that it is absolutely vital for papers to state the version
 2495 of MELTS that they used.



2496

2497 *Figure 27 – Comparison of fractional crystallization experiments from Nandedkar et al. (2014) at 7 kbar to MELTS*
 2498 *fractional crystallization models run using three different versions. Experiments containing amphibole are shown*
 2499 *in yellow, those without amphibole in red. Models were run at the experimental fO_2 and H_2O contents, at 1, 4, 7*
 2500 *(Exp P) and 10 kbar. MELTS models run in pyMELTScalc using alphaMELTS for Python (Gleeson et al., 2023,*
 2501 *Antoshechkina and Ghiorso, 2018).*

2502 8.2 Multi-phase saturation

2503 As discussed in Section 2.2, pressure influences the location of mineral cotectics and eutectics. Under
 2504 the assumption that the measured composition of a multi-phase saturated melt might contain information

2505 about the pressure of the system, rhyolite-MELTS has been used to address the crystallisation pressure of silicic
2506 and intermediate magmas that are co-saturated in quartz+feldspar (Bégué et al., 2014; Gualda et al., 2019;
2507 Gualda and Ghiorso, 2014; Pamukcu et al., 2015), feldspar+orthopyroxene±quartz (Pamukçu et al., 2021) or
2508 plagioclase+clinopyroxene+orthopyroxene (Harmon et al., 2018).

2509 Specifically, these methods work by performing crystallisation calculations at several discrete pressures
2510 (and a specified H_2O and fO_2 value). T is progressively dropped from the liquidus, and the appearance of different
2511 phases is tracked. Mineral saturation curves (see Fig. 28a-b) are determined from these individual isobaric
2512 crystallization calculations. A residual is calculated as the maximum temperature difference between the
2513 saturation curves of the phases of interest (ΔT , Fig. 28c). In many cases, the mineral saturation curves never
2514 intersect exactly at a single point, so the best fit pressure is calculated from the minimum point on the residual
2515 curve. A solution is only considered valid if the residual T gets within a pre-specified threshold value of a perfect
2516 intersection (e.g., 5°C for quartz – plagioclase – alkali-feldspar equilibrium; Gualda and Ghiorso, 2014). This
2517 threshold varies - in their application of this method to Plag-Opx-Cpx equilibrium, Harmon et al. (2018) compare
2518 experimental pressures to calculated pressures with minimum residuals from 16–121°C.

2519 One complication of these methods is that the position of saturation curves is not just influenced by
2520 pressure, but also fO_2 and melt H_2O content. This means for natural samples; calculations must be repeated at
2521 different melt fO_2 and H_2O contents to identify the location of the minimum T offset in multivariate P - fO_2 - H_2O
2522 space. In an ideal world, this would mean that MELTS could be used simultaneously as a barometer,
2523 oxybarometer, and hygrometer. However, in reality, this very large solution space can result in substantial errors
2524 which do not reproduce the true conditions for P , fO_2 , or H_2O .

2525 **8.2.1 Quartz – 2 Feldspar MELTS barometry**

2526 Interest in using the co-saturation of quartz, plagioclase and alkali feldspar to help constrain pressure
2527 (Gualda and Ghiorso, 2014) led to a substantial update to the MELTS algorithm in 2012. To recreate the near
2528 invariant behaviour of pumice and melt inclusion compositions from the early erupted Bishop Tuff which have
2529 major and trace element systematics indicating a low degree of freedom, Gualda et al. (2012) tweaked the
2530 enthalpy of formation of quartz and the potassic endmember in the alkali-feldspar solid-solution (Gualda et al.
2531 2012, rhyolite-MELTS v1.0.2). Using this new model, and the residual T method described above, Gualda and
2532 Ghiorso (2014) estimated storage pressures for a variety of quartz-saturated rhyolites. They compared these
2533 MELTS pressures to H_2O - CO_2 saturation pressures from the Bishop Tuff (Anderson et al., 2000), the Younger
2534 Toba Tuff (Chesner and Luhr, 2010) and the Mamaku Ignimbrite (Bégué et al., 2014), and found a close
2535 agreement. Based on the results in Fig. 10 of Gualda and Ghiorso (2014), we calculate an R^2 of 0.75 and RMSE
2536 of 0.38 kbar for $N=30$ melt inclusions when performing a linear regression between the two pressure methods.
2537 However, it is worth noting $N=17$ of these inclusions are from the Bishop Tuff, which was used as a reference
2538 point for the tweaking of the rhyolite-MELTS model calibration (Gualda et al. 2012).

2539 The rhyolite-MELTS quartz-feldspar barometers have since been applied to several other systems
2540 worldwide. This includes the application of quartz-plagioclase barometry to rhyolitic eruptions of the Taupo
2541 Volcano Zone, New Zealand (Bégué et al., 2014), and quartz – 2-feldspar barometry on the matrix glass of the
2542 Peach Spring Tuff, USA (Pamukcu et al., 2015). Results indicate spatial and/or temporal variations in the magma
2543 storage conditions beneath the Taupo Volcanic Zone, as well as correlations between rhyolite SiO_2 contents and
2544 pressure (Bégué et al., 2014; Pamukçu et al., 2020). However, these papers have been the subject to a number
2545 of comment-reply articles (e.g., Wilson et al., 2021, Pamukçu et al., 2021). Most notably, Wilke et al. (2017)
2546 question the accuracy of the rhyolite-MELTS barometer following comparison of the results of the rhyolite-
2547 MELTS geobarometer with their new empirical expression for the pressure of quartz+feldspar saturated liquids.
2548 The Wilke et al. (2017) method, termed DERP (Determining Rhyolitic Pressures), is based on experiments on
2549 haplogranitic compositions which examine the influence of melt H_2O content (or activity) and the normative
2550 melt An content (largely determined by the CaO content of the liquid) on the quartz+feldspar saturation surface.
2551 Comparison of rhyolite-MELTS and DERP barometric results for melt-inclusions and matrix glasses from the
2552 Taupo Volcanic Zone and Peach Spring Tuff revealed a large offset between the two methods, with DERP typically
2553 returning pressures around twice as large as those from rhyolite-MELTS. The pressure discrepancy between the
2554 two methods correlates with the normative melt An content (a key part of the new DERP parameterisation).

2555 Thus, Wilke et al. (2017) suggest that rhyolite-MELTS may underestimate magma storage pressures in Ca-bearing
2556 rhyolites.

2557 The relative performance of DERP and rhyolite-MELTS was revisited by Gualda et al. (2019b), who
2558 argued that the use of multi-linear fits in DERP to determine the influence of P, An content and H₂O on the quartz
2559 – 2 feldspar thermal minimum results in a functional form that is thermodynamically impossible. As a result,
2560 extrapolation of the DERP barometer outside the range of the calibration data could lead to systematic errors.
2561 Gualda et al. (2019b) also question the use of TitaniQ as an independent barometer to compare to the results
2562 from DERP in Wilke et al. (2017), as the Ti content in quartz is influenced by a wide number of parameters,
2563 including the mineral growth rate and melt Ti activity, which may limit its use as a geobarometer (see section
2564 2.11). To assess the performance of the 2 barometers in natural systems, Gualda et al. (2019b) compare the
2565 results derived from the DERP and rhyolite-MELTS barometers to independent pressure estimates from H₂O-
2566 CO₂ saturation in melt inclusions and amphibole thermobarometry. In general, the barometric estimates
2567 provided by rhyolite-MELTS are in good agreement with the independent pressure estimates. DERP-derived
2568 pressures are typically more scattered and often higher than those derived from melt inclusion or amphibole
2569 thermobarometry. However, given the issues with amphibole barometry discussed in section 2.6, such
2570 comparisons should perhaps be interpreted with caution.

2571 Wilke et al. (2019) responded by stating that the large range of pressures estimated by the DERP
2572 barometer in Gualda et al. (2019b) result from its sensitivity to glass Na₂O and K₂O contents, which are used to
2573 calculate the normative Qz, Or, and Ab values. Wilke et al. (2019) suggest that in hydrous rhyolitic glasses where
2574 alkali migration during analysis is a serious issue, DERP should only be used to estimate storage pressures when
2575 data quality is assured. Furthermore, Wilke et al. (2019) note that the experimental compositions used to
2576 calibrate the DERP barometer all contain normative corundum, meaning that all CaO in the glass is used to
2577 calculate the normative An content. In many natural samples, such as the Peach Spring Tuff used by Pamukcu
2578 et al. (2015), lower Al₂O₃ contents lead to the presence of Wollastonite in the normative mineral assemblage,
2579 complicating the determination of the normative melt An content. As normative Wollastonite is not accounted
2580 for in the DERP calibration, this could explain the offset between the two barometers and indicates that DERP
2581 should only be used in systems where Corundum appears in the normative mineral assemblage.

2582 Therefore, for most natural samples where Wollastonite is present in the normative mineral
2583 assemblage, the rhyolite-MELTS geobarometer might be more reliable than empirically calibrated alternatives
2584 like DERP. Nevertheless, questions regarding the application of the rhyolite-MELTS barometer to natural systems
2585 still remain, especially as the test datasets used to evaluate this barometer have largely relied on data from the
2586 Bishop Tuff (part of the 2012 recalibration). In addition, inclusion of the updated H₂O-CO₂ model of Ghiorso and
2587 Gualda (2015) in the rhyolite-MELTS calculations (i.e., rhyolite-MELTS v1.2.0) shifts the quartz and sanidine
2588 stability field to such an extent that 3–phase saturation cannot be simulated at any pressure for the compositions
2589 of Gualda and Ghiorso (2014) and Pamukcu et al. (2015). This indicates a further update to the quartz + sanidine
2590 ± plagioclase thermodynamic properties is necessary to align with the most recent volatile solubility model, so
2591 that users do not need to perform calculations for magmas that are typically saturated in a mixed H₂O-CO₂ fluid
2592 phase using an outdated H₂O solubility model (Ghiorso et al. 1995). We are not aware of any new experiments
2593 that can be used as an independent test dataset for resolving the rhyolite-MELTS vs. DERP debate, and to gain a
2594 better understanding of the errors involved. Further experiments in this compositional range will be vital to
2595 move this approach forward in a rigorous manner.

2596 **8.2.2 Plagioclase – 2 pyroxene MELTS barometry**

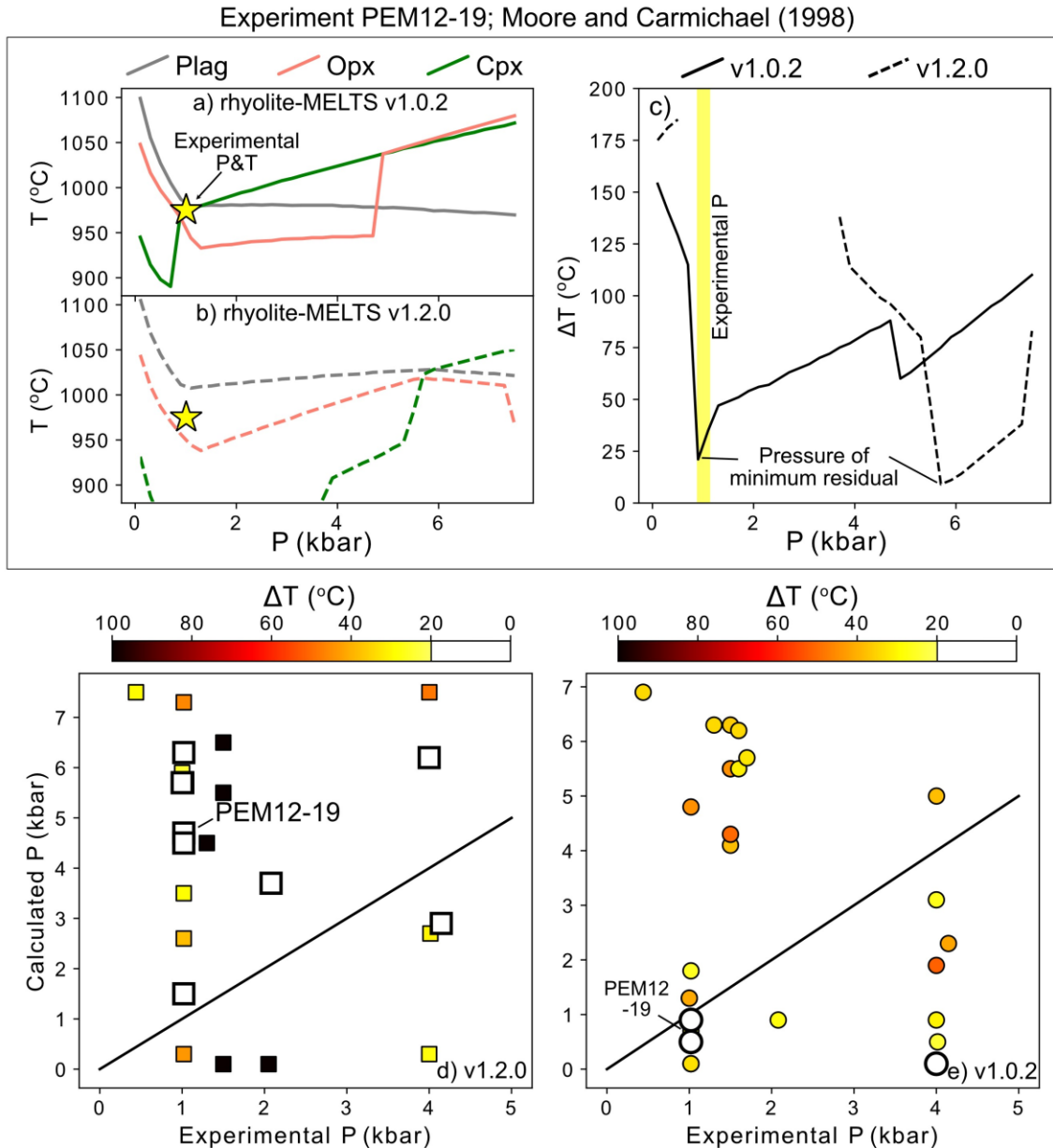
2597 Since the inception of the rhyolite-MELTS geobarometer in 2014, the general method developed by
2598 Gualda and Ghiorso (2014) has been expanded to examine the cosaturation of other phases. Harmon et al.
2599 (2018) suggest that the rhyolite-MELTS thermodynamic models could be used to provide pressure estimates for
2600 intermediate magmas saturated in plagioclase, clinopyroxene and orthopyroxene.

2601 To test the plagioclase – 2–pyroxene geobarometer, Harmon et al. (2018) apply their method to N = 8
2602 experiments from the LEPR database that are saturated in 2 or more of the phases of interest. As the plagioclase
2603 – 2 pyroxene geobarometer is significantly more sensitive to fO_2 and H₂O content than the quartz 2–feldspar

2604 barometer, they use experimental fO_2 and melt H_2O contents for these comparisons to eliminate the multi-
2605 dimensional aspects of mineral stability, allowing the best fit pressure to be found. Of the 8 experiments they
2606 use, only one returned a ΔT between the 3 mineral saturation curves of $<20^\circ C$, with the minimum T offset for
2607 other experiments stretching up to $121^\circ C$ (i.e., the saturation curves never intercept close to one another).

2608 The single experiment with a minimum T offset $<20^\circ C$ (1140mf #27 from Grove et al. 1997) returns a
2609 predicted P only 0.2 kbar offset from the true experimental P. If the threshold for the minimum T offset is
2610 relaxed, experiments with minimum T offsets between 20 and $40^\circ C$ also return P estimates within ~ 0.25 kbar of
2611 their experimental P. However, convergence of only 4 experiments conducted at 0.00 1–1 kbar where fO_2 and
2612 melt H_2O contents are known makes it difficult to robustly assess the accuracy of the geobarometer in natural
2613 systems when applied up to the 5 kbar limit suggested by Harmon et al. (2018).

2614 We investigate this method further using experiments from variably hydrous magmas cosaturated in
2615 plagioclase, orthopyroxene and clinopyroxene present in the ArcPL dataset conducted within the pressure range
2616 suggested by Harmon et al. (2018, 0–5 kbar, N=39). As for LLD methods, we find that the version of MELTS used
2617 for these calculations drastically affects calculations of storage conditions. Based on the flowchart provided on
2618 the MELTS-OFM website (<https://melts.ofm-research.org/MELTS-decision-tree.html>), rhyolite-MELTS v1.2.0
2619 should be used for these calculations, as these experiments contain dissolved H_2O ($\pm CO_2$). However, Harmon et
2620 al. (2018) use rhyolite-MELTS v.1.0.2. For experiment PEM12–19 from Moore and Carmichael (1998), rhyolite-
2621 MELTS v.1.0.2 shows very good convergence at pressures very close to the experimental pressure (Fig. 28e).
2622 However, if rhyolite-MELTS v1.2.0 is used, the clinopyroxene stability curve intersects plagioclase and
2623 orthopyroxene at significantly higher pressures, leading to an estimated pressure of ~ 6 kbar (~ 5 kbar higher
2624 than the experimental pressure, Fig. 28d).



2625

2626 *Figure 28: Assessing the Rhyolite-MELTS Plagioclase 2-pyroxene barometer of Harmon et al. (2018). a-b)*
 2627 *Constructing mineral stability curves for Exp. PEM1 2–19 from Moore and Carmichael (1998) at the experimental*
 2628 *fO_2 ($\Delta NNO=+1.1$) and H_2O contents (3.6 wt%) using two different versions of MELTS. c) Calculating the maximum*
 2629 *T offset at each pressure between the three mineral stability curves. The MELTS barometer takes the minimum*
 2630 *residual as the best-fit T (~ 1 and ~ 6 kbar depending on the MELTS version). d-e) Testing the barometer using*
 2631 *experiments saturated in Plag-2 pyroxene from ArcPL. Calculated pressure using the residual method plotted*
 2632 *against the experimental pressure (calculations performed at experiment fO_2 and H_2O contents). Experiments*
 2633 *with residuals $<20^\circ\text{C}$ are colored white, and larger residuals are colored based on this value. Calculations*
 2634 *performed in pyMELTSCalc (Gleeson et al., 2022) using alphaMELTS for Python (Antoshechkina and Ghiorso,*
 2635 *2018).*

2636 Using rhyolite-MELTS v.1.0.2 for all $N=39$ experiments, $N=10$ do not stabilize all 3 phases at any pressure
 2637 within 200°C of the liquidus (well below the experimental temperature in all cases). Of the remaining $N=29$,
 2638 models converging with a residual $<20^\circ\text{C}$ are shown in white on Fig. 28d-e. These produce a very poor fit to
 2639 experimental pressures. If we take solutions produced at larger temperature residuals (following Harmon et al.
 2640 2018), there is no improvement. Using rhyolite-MELTS v1.2.0, $N=23$ experiments converge, and the fit is similarly

2641 bad, regardless of the temperature residual used. The poor performance of this barometer supports previous
2642 criticism of the ability of MELTS to correctly predict the stability of these phases, pointing to the need for better
2643 solution models (e.g., Klein et al., 2023; Nandedkar et al., 2014; Villiger, 2004).

2644

2645 **9. Other methods**

2646 There are of course, numerous methods to determine magma storage conditions which we do not address in
2647 detail, both in the interest of relative(!) brevity, and because there is insufficient experimental data that wasn't
2648 used during calibration to independently test models.

2649 Additional thermometers have been developed based on:

- 2650 • REE exchange between Opx-Cpx (Liang et al., 2013) and Plag-Cpx (Sun and Liang, 2012)
- 2651 • Mg-Fe exchange between Ol and Cpx (Loucks, 1996)
- 2652 • Ni partitioning between Ol-Liq (resulting in a H₂O-independent thermometer, Pu et al., 2021, 2017)
- 2653 • NaSi-CaAl exchange between Amp-Plag (e.g., Holland and Blundy, 1994; Molina et al., 2021).
- 2654 • Mg exchange between Plag-Cpx (Sun and Lissenberg, 2018).

2655 Hygrometers based on:

- 2656 • Cpx-Liq major element equilibrium (e.g., Armienti et al., 2013; Perinelli et al., 2016)
- 2657 • Ca exchange between Ol-Liq (Gavrilenko et al., 2016),
- 2658 • The highest amphibole Mg# found in a given volcanic system (Krawczynski et al., 2012).
- 2659 • The H₂O contents of nominally-anhydrous minerals (NAMs) combined with models of mineral-melt
2660 partition coefficients (Demoucy et al., 2006; Towbin et al., 2023; Wade et al., 2008).
- 2661 • Projections of the Ol, Cpx and Plag cotectics (Klein et al. 2023).

2662 Barometers based on:

- 2663 • Sr/Y contents of erupted lavas (Profeta et al., 2016).
- 2664 • 'Multi-reaction' thermodynamic models relying on underlying thermodynamic models (e.g., Holland
2665 and Powell, 2011), where predicted and observed mineral compositions and phase fractions are
2666 compared to constrain storage conditions (E.g., Ziberna et al. 2017, Nicoli and Matthews, 2019).
- 2667 • Al-Si partitioning between Plag and Amp (Molina et al., 2015).
- 2668 • CaO-Mg# systematics of mid-oceanic ridge magmas (Villiger et al., 2007)

2669 Of course, these lists are by no means exhaustive.

2670 **10. Future developments should be guided by FAIR principles**

2671 It is becoming increasingly recognised that science needs to shift to a framework where research
2672 products are findable, accessible, interoperable, and reusable (FAIR; Wilkinson et al., 2016). In the context of
2673 this review, this applies not only to research data such as analyses of experimental products and natural samples,
2674 but also the tools and workflows used to perform calculations. There have already been a few advances in this
2675 regard, but there is still lots of work to do.

2676 From a data availability perspective, a major advance came in 2008 when Hirschmann et al. (2008)
2677 created a web-hosted database of 6,600 experiments (The Library of Experimental Phase Relationships – LEPR),
2678 which has been widely used to calibrate thermobarometers and chemometers (e.g., Jorgenson et al., 2022;
2679 Petrelli et al., 2020). This compilation represented a massive team effort, requiring most phase compositions
2680 and experimental contents to be hand typed from data tables in journal pdfs. However, the dataset is still
2681 incomplete in many aspects, stemming from missing data in the underlying publications, compounded with
2682 missing information during digitization. For example, in the LEPR download of Cpx-Liq pairs used by Petrelli et
2683 al. (2020) and Putirka (2008), 66% of experiments do not have a glass H₂O content. In some cases, this represents
2684 the fact that the experiment was anhydrous, in others the fact that authors didn't report water, and sometimes
2685 because H₂O is often presented in a different table from other chemical information, so may have been missed
2686 during digitization. Similarly, with few exceptions, the number of analyses used to produce the reported average

2687 for each phase (e.g., N=5 Cpx analyses, N=8 amphibole analyses) is not present in LEPR. This makes filtering out
2688 experiments with compositions defined by small numbers of analyses challenging, despite the importance of
2689 this given the influence of analytical error on minor, pressure-sensitive components (e.g., Cpx, Wieser et al.
2690 2023b).

2691 A bigger challenge is that there is no framework by which LEPR is regularly updated as new experimental
2692 studies are published. This has led to individual authors digitizing data from new experimental papers to use in
2693 their studies (Jorgenson et al., 2022, Wieser et al. 2023a-b). However, individual researchers who compile data
2694 may not have time to format the data for inclusion in the database, and under the current academic publishing
2695 model, would gain no credit for this activity, as citations for use of the database would go to the original author
2696 team from 2008. One option moving forwards may be for LEPR to frequently publish new short articles or a
2697 Zenodo doi with an author team consisting of anyone who has contributed to the curation of the database (as
2698 for open-source tools such as Numpy; e.g., Dubois et al., 1996; Harris et al., 2020). Alternatively, the
2699 responsibility could be placed on people generating experimental data, where journal editors do not allow a
2700 paper to be accepted before the experimental data is included in these databases. However, in many cases,
2701 journals do not mandate authors submitting data to a specific repository. Community guidelines for exactly how
2702 such data should be presented and archived are clearly needed, as well as ways for data curation to be valued
2703 when hiring and promoting researchers (Klöcking et al., 2023).

2704 From a modelling perspective, there has been a rapid increase in the number of open-source, easy to
2705 use tools to perform calculations, making workflows more user-friendly, faster, more reproducible, and less
2706 susceptible to user-error and version control issues. In general, calculation tools have evolved from GUIs, macro-
2707 enabled spreadsheets and web apps where users having to type every single composition by hand, to being able
2708 to automatically run calculations by loading a user-supplied spreadsheet either through a Jupyter Notebook or
2709 a web app built on top of underlying python or R code (e.g., Iacovino and Till, 2019; Weber and Blundy, 2023).
2710 One major contribution towards more automated workflows for thermodynamic calculations has been the
2711 development of the ENKI ThermoEngine (Thermoengine Code Contributors, 2022), allowing the MELTS
2712 thermodynamic models and algorithms to be accessed through Python. This allows creation of modelling
2713 workflows or complete packages based on the underlying MELTS models. For example, the Fe-Ti oxybarometer
2714 and thermometer of Ghiorso and Evans (2008) was originally released as a web-app where users had to hand-
2715 type major element values for each Fe-Ti oxide pair. Ghiorso and Prissel (2020) produced a Jupyter Notebook
2716 using Thermoengine which allows users to upload an excel file of matching Fe-Ti oxide pairs, and all calculations
2717 are performed automatically. The open-source Python3 package VESlcal (Iacovino et al., 2021) relies on
2718 Thermoengine to perform calculations using the solubility model Magmasat (which requires MELTS, Ghiorso and
2719 Gualda, 2015), as well as 6 other popular solubility models. Prior to VESlcal, saturation pressure calculations
2720 were performed using different tools for each solubility model in a myriad of different environments (Excel
2721 macros, web apps, web servers).

2722 The MELTS thermodynamic models can also be accessed using the alphaMELTS for MATLAB/Python
2723 packages (Antoshechkina and Ghiorso, 2018). As the alphaMELTS for MATLAB/Python packages (and
2724 Thermoengine) requires some familiarity with the underlying language, easy-to-use, wrapped functions for
2725 common workflows have been released through the pyMELTSCalc package (used for calculations in Section 8,
2726 Gleeson et al., 2023).

2727 Calculations using the thermodynamic models/databases developed by Holland and Powell (e.g.,
2728 Holland and Powell, 1998; Holland et al. 2018), which represent the main thermodynamic alternative to MELTS
2729 in igneous petrology, have traditionally performed using a variety of different software packages, including
2730 THERMOCALC, Perple_X (Connolly, 2009, 2005) and Theriak-Domino (de Capitani and Petrakakis, 2010). The
2731 learning curve for these tools is typically quite steep, and it remains challenging to integrate the thermodynamic
2732 calculations with common coding languages such as MATLAB, Python3 or Julia. Development of MAGEMin, a C-
2733 based Gibbs Free Energy minimization software with a Julia interface (Reil et al. 2022), improves the ease with
2734 which thermodynamic calculations can be performed using the Holland et al. (2018) thermodynamic database.
2735 This is because the Julia MAGEMin functions can also be used outside of the main GUI and integrated with
2736 Python3 functions. This allows the pyMELTScalc package to perform the same calculations (e.g. LLD, phase

2737 stability, phase diagrams) using MELTS or the Holland et al. (2018) thermodynamic models. Such advances are
2738 vital for model intercomparison (e.g. Fig. 26-27).

2739 For mineral-melt thermobarometry and chemometry, calculations using 100s of different popular
2740 equations can be performed in Thermobar (Wieser et al., 2022b). This tool replaces a very large number of
2741 separate Excel spreadsheets, R and Matlab code released by individual thermobarometry papers, and allows
2742 more complex functions such as assessing all possible pairs for equilibrium, error propagation etc. For
2743 thermobarometers applicable to determining the conditions of mantle melting, Python package meltPT (McNab
2744 and Ball, 2023) can perform calculations using twelve published expressions.

2745 These open-source python tools allow investigation of science questions that were almost impossible to address
2746 using existing tools requiring extensive manual data input. For example, Wieser et al. (2022a) use VESlcal to
2747 perform detailed comparisons of solubility models, including their sensitivities to different parameters. Wieser
2748 et al. (2023a-b) use Thermobar to propagate thermobarometry uncertainties using Monte Carlo methods. Open-
2749 source packages also have the advantage that the source code is version-controlled, and hosted in a public
2750 repository (e.g., on GitHub) for anyone to inspect and adapt. This means even if the authors stop supporting the
2751 packages (perhaps moving from academia into industry), packages could be updated by a third party (although
2752 as a community we need to develop clear guidelines as to how academic credit can be allocated for such an
2753 activity). This is in stark contrast with numerous tools which have simply become unusable with age. For
2754 example, the volatile solubility model of Duan (2014) is no longer available at the website listed in the paper,
2755 requiring authors to rely on archived downloads (e.g., Allison et al., 2022 rely on a version archived in 2017).

2756 **11. Conclusions**

2757 There are a wide diversity of methods which have been used to determine the pressures, temperatures, H₂O
2758 contents and fO_2 conditions at which magmas are stored and staged as they transit from the mantle to the
2759 surface. Many thermometry methods work very well, indicating that silicate melt (\pm mineral) compositions are
2760 very sensitive to temperature. However, it becomes more challenging to determine temperatures in subsolidus
2761 or highly evolved systems. In contrast, many mineral-based and thermodynamical barometers perform
2762 extremely poorly, struggling to reliably distinguish between different storage regions in the crust within ~10–20
2763 km. This partially results from thermodynamic limitations; mineral compositions are not overly sensitive to the
2764 relatively narrow range of crustal pressures in the vast majority of tectonic settings on Earth. This fundamental
2765 limitation is not helped by sources of analytical and experimental uncertainty (e.g., poor analytical precision for
2766 minor components, missing elements such as Cr, Wieser et al. 2023b). Melt inclusion barometers have the
2767 potential to be more precise, because the dissolution of CO₂ and H₂O is highly sensitive to pressure. However,
2768 extensive work is required to resolve discrepancies between solubility models, as well as evaluate the influence
2769 of the vapour bubble CO₂ in many published datasets. Raman-based fluid inclusion has great potential in specific
2770 systems, although further work is needed to investigate the influence of decrepitation, elastic relaxation, and
2771 the influence of other fluid species (e.g. SO₂, H₂O etc). Thermobar-Raman-try also shows great promise, but
2772 further work is required. We propose a number of key frontiers to address in the pursuit of better
2773 thermobarometers, hygrometers and oxybarometers:

2774 1) The development of higher quality experimental and thermodynamic datasets with precisely constrained
2775 mineral compositions, fluid compositions, dissolved volatile contents, and experimental fO_2 for recalibration of
2776 thermodynamic models (e.g., MELTS), mineral-melt thermobarometers, and volatile solubility models. Sufficient
2777 experiments need to be performed to allow full isolation of a test dataset during model calibration. More
2778 experiments using mixed H₂O-CO₂ fluids are clearly needed to understand phase stability in relatively CO₂-rich
2779 arc magmas.

2780 2) Development of more robust infrastructure for compiling experimental and thermodynamic data, alongside
2781 sufficient metadata to assess data quality. This will ensure that application of new and exciting machine learning
2782 techniques will not suffer from the old computer science adage: 'garbage-in, garbage-out'.

2783 3) Further development of open-source methods to perform calculations, allowing easy intercomparison
2784 between models, error propagation, and model updates as new data becomes available.

2785 **12. Author Contributions**
 2786 PW coordinated the review and was responsible for writing and coding for all sections except those listed below.
 2787 MG was responsible for the OPAM, MELTS and MAGEMin sections with edits from PW, and SM for OI-Sp and Fe-
 2788 Ti oxide sections. CD contributed text to the MI and FI section, and provided edits throughout. CD and EG
 2789 contributed to analytical work. All authors reviewed and edited the text.

2790 **13. Acknowledgements**
 2791 PW thanks Iris Buisman for extracting the Cpx counting statistics shown in Fig. 8, and Keith Putirka for many
 2792 useful conversations on thermobarometry and the formulation and calibration of his equations. PW
 2793 acknowledges support from NSF EAR 2217371, the Rose Hills Innovator Program, and start up funds to UC
 2794 Berkeley for computing resources. EG acknowledges support from NSF EAR 2216738.

2795 **13. Useful websites and open-source tools**

Tools for petrologists – Contains Excel workbooks and python scripts for a number of petrographic workflows.	http://www.kaylaiacovino.com/tools-for-petrologists/
VESlcal GitHub, Read The Docs and YouTube pages: Code, documentation and worked examples for calculations using VESlcal	https://github.com/kaylai/VESlcal , https://vesical.readthedocs.io/en/latest/
Thermobar read the docs page: Code, documentation and worked examples for thermobarometry and hygrometry calculations using Thermobar	https://github.com/PennyWieser/Thermobar , https://thermobar.readthedocs.io/en/latest/
Putirka spreadsheet compilation: Contains Excel spreadsheets for different thermobarometry calculations	https://sites.google.com/mail.fresnostate.edu/keithputirka/home
MELTS resources: Links to download different MELTS calculation tools (Matlab, python, GUI, excel).	https://magmasource.caltech.edu/gitlist
MAGEMin: Gibbs free energy minimisation solver package	https://github.com/ComputationalThermodynamics/MAGEMin
PyMageMinCalc: Python package for common petrological workflows using MAGEMin.	https://github.com/gleesonm1/pyMAGEMinCalc
PyMELTScalc: Python package for easier calculations using Melts for Python	https://github.com/gleesonm1/pyMELTScalc
ENKI server: Allows calculations to be performed using ThermoEngine infrastructure without the need for local installation.	http://enki-portal.org/
NIST Web Book: Phase data for CO ₂ and calculations using the CO ₂ equation of state.	https://webbook.nist.gov/cgi/cbook.cgi?ID=C124389&Mask=1
DiadFit: Code, documentation and worked examples using DiadFit for fitting Raman data and performing EOS calculations for CO ₂ .	https://github.com/PennyWieser/DiadFit , https://diadfit.readthedocs.io/en/latest/
CoolProp: A python package for calculating thermodynamic properties of gases using different equation of states.	http://www.coolprop.org/

2796

2797 **14. Data Availability**
 2798 Jupyter Notebooks and Excel workbooks used to make each figure are available on GitHub
 2799 (https://github.com/PennyWieser/Thermobarometry_Review_2023).

2800 **References.**

2801 Acosta, M.D., Watkins, J.M., Reed, M.H., Donovan, J.J., DePaolo, D.J., 2020. Ti-in-quartz: Evaluating the role of
 2802 kinetics in high temperature crystal growth experiments. *Geochimica et Cosmochimica Acta* 281, 149–
 2803 167. <https://doi.org/10.1016/j.gca.2020.04.030>
 2804 Afonso, J.C., Ranalli, G., Fernández, M., 2007. Density structure and buoyancy of the oceanic lithosphere
 2805 revisited. *Geophys. Res. Lett.* 34, L10302. <https://doi.org/10.1029/2007GL029515>

2806 Ague, J.J., 1997. Thermodynamic calculation of emplacement pressures for batholithic rocks, California:
2807 Implications for the aluminum-in-hornblende barometer. *Geol* 25, 563. <https://doi.org/10.1130/0091->
2808 7613(1997)025<0563:TCOEPF>2.3.CO;2

2809 Allison, C.M., Roggensack, K., Clarke, A.B., 2022. MafiCH: a general model for H₂O–CO₂ solubility in mafic
2810 magmas. *Contrib Mineral Petrol* 177, 40. <https://doi.org/10.1007/s00410-022-01903-y>

2811 Allison, C.M., Roggensack, K., Clarke, A.B., 2021. Highly explosive basaltic eruptions driven by CO₂ exsolution.
2812 *Nat Commun* 12, 217. <https://doi.org/10.1038/s41467-020-20354-2>

2813 Almeev, R.R., Bolte, T., Nash, B.P., Holtz, F., Erdmann, M., Cathey, H.E., 2012. High-temperature, low-H₂O
2814 Silicic Magmas of the Yellowstone Hotspot: an Experimental Study of Rhyolite from the Bruneau–
2815 Jarbidge Eruptive Center, Central Snake River Plain, USA. *Journal of Petrology* 53, 1837–1866.
2816 <https://doi.org/10.1093/petrology/egs035>

2817 Alonso-Perez, R., Müntener, O., Ulmer, P., 2009. Igneous garnet and amphibole fractionation in the roots of
2818 island arcs: experimental constraints on andesitic liquids. *Contrib Mineral Petrol* 157, 541–558.
2819 <https://doi.org/10.1007/s00410-008-0351-8>

2820 Andersen, D.J., Lindsley, D.H., 1988. Internally consistent solution models for Fe-Mg-Mn-Ti oxides; Fe-Ti oxides.
2821 *American Mineralogist* 73, 714–726.

2822 Andersen, T., O'Reilly, S.Y., Griffin, W.L., 1984. The trapped fluid phase in upper mantle xenoliths from Victoria,
2823 Australia: implications for mantle metasomatism. *Contr. Mineral. and Petrol.* 88, 72–85.
2824 <https://doi.org/10.1007/BF00371413>

2825 Anderson, A.T., Brown, 1993. CO, contents and formation pressures of some Kilauean melt inclusions.
2826 *American Mineralogist* 78, 794–803.

2827 Anderson, A.T., Davis, A.M., Lu, F., 2000. Evolution of Bishop Tuff rhyolitic magma based on melt and
2828 magnetite inclusions and zoned phenocrysts. *Journal of Petrology* 41, 449–473.

2829 Anderson, J.L., 1996. Status of thermobarometry in granitic batholiths, in: *The Third Hutton Symposium on the*
2830 *Origin of Granites and Related Rocks*. Geological Society of America. <https://doi.org/10.1130/0-8137->
2831 2315-9.125

2832 Anderson, J.L., Barth, A.P., Wooden, J.L., Mazdab, F., 2008. Thermometers and Thermobarometers in Granitic
2833 Systems. *Reviews in Mineralogy and Geochemistry* 69, 121–142.
2834 <https://doi.org/10.2138/rmg.2008.69.4>

2835 Andújar, J., Scaillet, B., Pichavant, M., Druitt, T.H., 2015. Differentiation Conditions of a Basaltic Magma from
2836 Santorini, and its Bearing on the Production of Andesite in Arc Settings. *Journal of Petrology* 56, 765–
2837 794. <https://doi.org/10.1093/petrology/egv016>

2838 Antoshechkina, P., Ghiorso, M.S., 2018. MELTS for MATLAB: A new educational and research tool for
2839 computational thermodynamics. AGU Fall Meeting, abstract #ED44B-23.

2840 Aradi, L., Spránitz, T., Guzmics, T., Szabó, C., Berkesi, M., 2021. 3D Raman imaging of multiphase fluid and melt
2841 inclusions: challenges and perspectives, in: *Goldschmidt2021 Abstracts*. Presented at the
2842 *Goldschmidt2021*, European Association of Geochemistry, Virtual.
2843 <https://doi.org/10.7185/gold2021.8071>

2844 Araya, N., Nakamura, M., Yasuda, A., Okumura, S., Sato, T., Iguchi, M., Miki, D., Geshi, N., 2019. Shallow
2845 magma pre-charge during repeated Plinian eruptions at Sakurajima volcano. *Sci Rep* 9, 1979.
2846 <https://doi.org/10.1038/s41598-019-38494-x>

2847 Ariskin, A.A., Frenkel, M.Ya., Barmina, G.S., Nielsen, R.L., 1993. Comagmat: a Fortran program to model magma
2848 differentiation processes. *Computers & Geosciences* 19, 1155–1170. <https://doi.org/10.1016/0098->
2849 3004(93)90020-6

2850 Armienti, P., Perinelli, C., Putirka, K.D., 2013. A New Model to Estimate Deep-level Magma Ascent Rates, with
2851 Applications to Mt. Etna (Sicily, Italy). *Journal of Petrology* 54, 795–813.
2852 <https://doi.org/10.1093/petrology/egs085>

2853 Aster, E.M., Wallace, P.J., Moore, L.R., Watkins, J., Gazel, E., Bodnar, R.J., 2016. Reconstructing CO₂
2854 concentrations in basaltic melt inclusions using Raman analysis of vapor bubbles. *Journal of*
2855 *Volcanology and Geothermal Research* 323, 148–162.
2856 <https://doi.org/10.1016/j.jvolgeores.2016.04.028>

2857 Azbej, T., Severs, M.J., Rusk, B.G., Bodnar, R.J., 2007. In situ quantitative analysis of individual H₂O–CO₂ fluid
2858 inclusions by laser Raman spectroscopy. *Chemical Geology* 237, 255–263.
2859 <https://doi.org/10.1016/j.chemgeo.2006.06.025>

2860 Bacon, C.R., Newman, S., Stolper, E., 1992. Water, CO₂, Cl, and F in melt inclusions in phenocrysts from three
2861 Holocene explosive eruptions, Crater Lake, Oregon. *American Mineralogist* 77, 1021–1030.

2862 Bakker, R., 2017. Re-Equilibration Processes in Fluid Inclusion Assemblages. *Minerals* 7, 117.
2863 <https://doi.org/10.3390/min7070117>

2864 Bali, E., Hartley, M.E., Halldórsson, S.A., Gudfinnsson, G.H., Jakobsson, S., 2018. Melt inclusion constraints on
2865 volatile systematics and degassing history of the 2014–2015 Holuhraun eruption, Iceland. *Contrib*
2866 *Mineral Petrol* 173, 9. <https://doi.org/10.1007/s00410-017-1434-1>

2867 Barclay, J., 2004. A Hornblende Basalt from Western Mexico: Water-saturated Phase Relations Constrain a
2868 Pressure-Temperature Window of Eruptibility. *Journal of Petrology* 45, 485–506.
2869 <https://doi.org/10.1093/petrology/egg091>

2870 Barker, A.K., Rydeblad, E.M., Silva, S.M., 2021. Magma storage at Ocean Islands: insights from Cape Verde.
2871 *Crustal Magmatic System Evolution: Anatomy, Architecture, and Physico-Chemical Processes* 45–78.
2872 <https://doi.org/10.1002/9781119564485.ch3>

2873 Barth, A., Newcombe, M., Plank, T., Gonnermann, H., Hajimirza, S., Soto, G.J., Saballos, A., Hauri, E., 2019.
2874 Magma decompression rate correlates with explosivity at basaltic volcanoes — Constraints from
2875 water diffusion in olivine. *Journal of Volcanology and Geothermal Research* 387, 106664.
2876 <https://doi.org/10.1016/j.jvolgeores.2019.106664>

2877 Barth, A., Plank, T., 2021. The Ins and Outs of Water in Olivine-Hosted Melt Inclusions: Hygrometer vs.
2878 Speedometer. *Front. Earth Sci.* 9, 614004. <https://doi.org/10.3389/feart.2021.614004>

2879 Baxter, R.J.M., Maclennan, J., Neave, D.A., Thordarson, T., 2023. Depth of Magma Storage Under Iceland
2880 Controlled by Magma Fluxes. *Geochem Geophys Geosyst* 24, e2022GC010811.
2881 <https://doi.org/10.1029/2022GC010811>

2882 Beattie, P., 1993. Olivine-melt and orthopyroxene-melt equilibria. *Contr. Mineral. and Petrol.* 115, 103–111.
2883 <https://doi.org/10.1007/BF00712982>

2884 Befus, K.S., Lin, J.-F., Cisneros, M., Fu, S., 2018. Feldspar Raman shift and application as a magmatic
2885 thermobarometer. *American Mineralogist* 103, 600–609. <https://doi.org/10.2138/am-2018-6157>

2886 Bégué, F., Deering, C.D., Gravley, D.M., Kennedy, B.M., Chambefort, I., Gualda, G.A.R., Bachmann, O., 2014.
2887 Extraction, Storage and Eruption of Multiple Isolated Magma Batches in the Paired Mamaku and
2888 Ohakuri Eruption, Taupo Volcanic Zone, New Zealand. *Journal of Petrology* 55, 1653–1684.
2889 <https://doi.org/10.1093/petrology/egu038>

2890 Bégué, F., Gravley, D.M., Chambefort, I., Deering, C.D., Kennedy, B.M., 2015. Magmatic volatile distribution as
2891 recorded by rhyolitic melt inclusions in the Taupo Volcanic Zone, New Zealand. *Geological Society,*
2892 *London, Special Publications* 410, 71–94. <https://doi.org/10.1144/SP410.4>

2893 Bégué, Florence, Gualda, G.A.R., Ghiorso, M.S., Pamukcu, A.S., Kennedy, B.M., Gravley, D.M., Deering, C.D.,
2894 Chambefort, I., 2014. Phase-equilibrium geobarometers for silicic rocks based on rhyolite-MELTS. Part
2895 2: application to Taupo Volcanic Zone rhyolites. *Contrib Mineral Petrol* 168, 1082.
2896 <https://doi.org/10.1007/s00410-014-1082-7>

2897 Bell, A.F., La Femina, P.C., Ruiz, M., Amelung, F., Bagnardi, M., Bean, C.J., Bernard, B., Ebinger, C., Gleeson, M.,
2898 Grannell, J., Hernandez, S., Higgins, M., Liorzou, C., Lundgren, P., Meier, N.J., Möllhoff, M., Oliva, S.-J.,
2899 Ruiz, A.G., Stock, M.J., 2021. Caldera resurgence during the 2018 eruption of Sierra Negra volcano,
2900 Galápagos Islands. *Nat Commun* 12, 1397. <https://doi.org/10.1038/s41467-021-21596-4>

2901 Bell, I.H., Wronski, J., Quoilin, S., Lemort, V., 2014. Pure and Pseudo-pure Fluid Thermophysical Property
2902 Evaluation and the Open-Source Thermophysical Property Library CoolProp. *Ind. Eng. Chem. Res.* 53,
2903 2498–2508. <https://doi.org/10.1021/ie4033999>

2904 Bennett, E.N., Jenner, F.E., Millet, M.-A., Cashman, K.V., Lissenberg, C.J., 2019. Deep roots for mid-ocean-ridge
2905 volcanoes revealed by plagioclase-hosted melt inclusions. *Nature* 572, 235–239.
2906 <https://doi.org/10.1038/s41586-019-1448-0>

2907 Berman, R.G., 1988. Internally-Consistent Thermodynamic Data for Minerals in the System Na₂O-K₂O-CaO-
2908 MgO-FeO-Fe₂O₃-Al₂O₃-SiO₂-TiO₂-H₂O-CO₂. *Journal of Petrology* 29, 445–522.
2909 <https://doi.org/10.1093/petrology/29.2.445>

2910 Berndt, J., 2004. An Experimental Investigation of the Influence of Water and Oxygen Fugacity on
2911 Differentiation of MORB at 200 MPa. *Journal of Petrology* 46, 135–167.
2912 <https://doi.org/10.1093/petrology/egh066>

2913 Black, B.A., Andrews, B.J., 2020. Petrologic imaging of the architecture of magma reservoirs feeding caldera-
2914 forming eruptions. *Earth and Planetary Science Letters* 552, 116572.
2915 <https://doi.org/10.1016/j.epsl.2020.116572>

2916 Blatter, D.L., Carmichael, I.S.E., 2001. Hydrous phase equilibria of a Mexican high-silica andesite: A candidate
2917 for a mantle origin? *Geochimica et Cosmochimica Acta* 65, 4043–4065.
2918 [https://doi.org/10.1016/S0016-7037\(01\)00708-6](https://doi.org/10.1016/S0016-7037(01)00708-6)

2919 Blatter, D.L., Sisson, T.W., Hanks, W.B., 2013. Crystallization of oxidized, moderately hydrous arc basalt at
2920 mid- to lower-crustal pressures: implications for andesite genesis. *Contrib Mineral Petrol* 166, 861–
2921 886. <https://doi.org/10.1007/s00410-013-0920-3>

2922 Blundy, J., 2022. Chemical Differentiation by Mineralogical Buffering in Crustal Hot Zones. *Journal of Petrology*
2923 63, egac054. <https://doi.org/10.1093/petrology/egac054>

2924 Blundy, J., Cashman, K., 2008. Petrologic Reconstruction of Magmatic System Variables and Processes. *Reviews*
2925 *in Mineralogy and Geochemistry* 69, 179–239. <https://doi.org/10.2138/rmg.2008.69.6>

2926 Blundy, J., Cashman, K.V., Rust, A., Witham, F., 2010. A case for CO₂-rich arc magmas. *Earth and Planetary*
2927 *Science Letters* 290, 289–301. <https://doi.org/10.1016/j.epsl.2009.12.013>

2928 Bodnar, R.J., Binns, P.R., Hall, D.L., 1989. Synthetic fluid inclusions - VI. Quantitative evaluation of the
2929 decrepitation behaviour of fluid inclusions in quartz at one atmosphere confining pressure. *J*
2930 *Metamorph Geol* 7, 229–242. <https://doi.org/10.1111/j.1525-1314.1989.tb00586.x>

2931 Bogaerts, M., Scaillet, B., Auwera, J.V., 2006. Phase Equilibria of the Lyngdal Granodiorite (Norway):
2932 Implications for the Origin of Metaluminous Ferroan Granitoids. *Journal of Petrology* 47, 2405–2431.
2933 <https://doi.org/10.1093/petrology/egl049>

2934 Bohron, W.A., Clague, D.A., 1988. Origin of ultramafic xenoliths containing exsolved pyroxenes from Hualalai
2935 Volcano, Hawaii. *Contrib Mineral Petrol* 100, 139–155. <https://doi.org/10.1007/BF00373581>

2936 Bolte, T., Holtz, F., Almeev, R., Nash, B., 2015. The Blacktail Creek Tuff: an analytical and experimental study of
2937 rhyolites from the Heise volcanic field, Yellowstone hotspot system. *Contrib Mineral Petrol* 169, 15.
2938 <https://doi.org/10.1007/s00410-015-1112-0>

2939 Böttcher, N., Taron, J., Kolditz, O., Liedl, R., Park, C.-H., 2012. Comparison of equations of state for carbon
2940 dioxide for numerical simulations. *Proceedings ModelCARE2011, Leipzig, Germany. IAHS Publ. 355* 9.

2941 Boulanger, M., France, L., Deans, J.R.L., Ferrando, C., Lissenberg, C.J., von der Handt, A., 2020. Magma
2942 Reservoir Formation and Evolution at a Slow-Spreading Center (Atlantis Bank, Southwest Indian
2943 Ridge). *Front. Earth Sci.* 8, 554598. <https://doi.org/10.3389/feart.2020.554598>

2944 Boullier, A.-M., Michot, G., Pecher, A., Barres, O., 1989. Diffusion and/or Plastic Deformation around Fluid
2945 Inclusions in Synthetic Quartz: New Investigations, in: Bridgwater, D. (Ed.), *Fluid Movements —*
2946 *Element Transport and the Composition of the Deep Crust.* Springer Netherlands, Dordrecht, pp. 345–
2947 360. https://doi.org/10.1007/978-94-009-0991-5_28

2948 Brugman, K.K., Till, C.B., 2019. A low-aluminum clinopyroxene-liquid geothermometer for high-silica magmatic
2949 systems. *American Mineralogist* 104, 996–1004. <https://doi.org/10.2138/am-2019-6842>

2950 Bucholz, C.E., Gaetani, G.A., Behn, M.D., Shimizu, N., 2013. Post-entrapment modification of volatiles and
2951 oxygen fugacity in olivine-hosted melt inclusions. *Earth and Planetary Science Letters* 374, 145–155.
2952 <https://doi.org/10.1016/j.epsl.2013.05.033>

2953 Budd, D.A., Troll, V.R., Dahren, B., Burchardt, S., 2016. Persistent multitiered magma plumbing beneath Katla
2954 volcano, Iceland. *Geochem. Geophys. Geosyst.* 17, 966–980. <https://doi.org/10.1002/2015GC006118>

2955 Buddington, A.F., Lindsley, D.H., 1964. Iron-Titanium Oxide Minerals and Synthetic Equivalents. *Journal of*
2956 *Petrology* 5, 310–357. <https://doi.org/10.1093/petrology/5.2.310>

2957 Burke, E.A.J., 2001. Raman microspectrometry of fluid inclusions. *Lithos* 55, 139–158.
2958 [https://doi.org/10.1016/S0024-4937\(00\)00043-8](https://doi.org/10.1016/S0024-4937(00)00043-8)

2959 Buso, R., Laporte, D., Schiavi, F., Cluzel, N., Fonquernie, C., 2022. High-pressure homogenization of olivine-
2960 hosted CO₂-rich melt inclusions in a piston cylinder: insight into the volatile
2961 content of primary mantle melts. *Eur. J. Mineral.* 34, 325–349. [https://doi.org/10.5194/ejm-34-325-
2962 2022](https://doi.org/10.5194/ejm-34-325-2022)

2963 Cadoux, A., Scaillet, B., Druitt, T.H., Deloule, E., 2014. Magma Storage Conditions of Large Plinian Eruptions of
2964 Santorini Volcano (Greece). *Journal of Petrology* 55, 1129–1171.
2965 <https://doi.org/10.1093/petrology/egu021>

2966 Campione, M., Malaspina, N., Frezzotti, M.L., 2015. Threshold size for fluid inclusion decrepitation: Size for
2967 Fluid Inclusion Decrepitation. *Journal of Geophysical Research: Solid Earth* 120, 7396–7402.
2968 <https://doi.org/10.1002/2015JB012086>

2969 Caracciolo, A., Bali, E., Guðfinnsson, G.H., Kahl, M., Halldórsson, S.A., Hartley, M.E., Gunnarsson, H., 2020.
2970 Temporal evolution of magma and crystal mush storage conditions in the Bárðarbunga-Veiðivötn
2971 volcanic system, Iceland. *Lithos* 352–353, 105234. <https://doi.org/10.1016/j.lithos.2019.105234>

2972 Caracciolo, A., Halldórsson, S.A., Bali, E., Marshall, E.W., Jeon, H., Whitehouse, M.J., Barnes, J.D., Guðfinnsson,
2973 G.H., Kahl, M., Hartley, M.E., 2022. Oxygen isotope evidence for progressively assimilating trans-
2974 crustal magma plumbing systems in Iceland. *Geology* 50, 796–800. <https://doi.org/10.1130/G49874.1>

2975 Cashman, K.V., Edmonds, M., 2019. Mafic glass compositions: a record of magma storage conditions, mixing
2976 and ascent. *Phil. Trans. R. Soc. A.* 377, 20180004. <https://doi.org/10.1098/rsta.2018.0004>

2977 Chakraborty, S., Dohmen, R., 2022. Diffusion chronometry of volcanic rocks: looking backward and forward.
2978 *Bull Volcanol* 84, 57. <https://doi.org/10.1007/s00445-022-01565-5>

2979 Cheng, L.-L., Yang, Z.-F., Zeng, L., Wang, Y., Luo, Z.-H., 2014. Giant plagioclase growth during storage of basaltic
2980 magma in Emeishan Large Igneous Province, SW China. *Contrib Mineral Petrol* 167, 971.
2981 <https://doi.org/10.1007/s00410-014-0971-0>

2982 Chesner, C.A., Luhr, J.F., 2010. A melt inclusion study of the Toba Tuffs, Sumatra, Indonesia. *Journal of*
2983 *Volcanology and Geothermal Research* 197, 259–278.
2984 <https://doi.org/10.1016/j.jvolgeores.2010.06.001>

2985 Cisneros, M., Befus, K.S., 2020. Applications and Limitations of Elastic Thermobarometry: Insights From Elastic
2986 Modeling of Inclusion-Host Pairs and Example Case Studies. *Geochem. Geophys. Geosyst.* 21.
2987 <https://doi.org/10.1029/2020GC009231>

2988 Connolly, J.A.D., 2009. The geodynamic equation of state: What and how: GEODYNAMIC EQUATION OF STATE-
2989 WHAT AND HOW. *Geochem. Geophys. Geosyst.* 10. <https://doi.org/10.1029/2009GC002540>

2990 Connolly, J.A.D., 2005. Computation of phase equilibria by linear programming: A tool for geodynamic
2991 modeling and its application to subduction zone decarbonation. *Earth and Planetary Science Letters*
2992 236, 524–541. <https://doi.org/10.1016/j.epsl.2005.04.033>

2993 Coogan, L.A., Saunders, A.D., Wilson, R.N., 2014. Aluminum-in-olivine thermometry of primitive basalts:
2994 Evidence of an anomalously hot mantle source for large igneous provinces. *Chemical Geology* 368, 1–
2995 10. <https://doi.org/10.1016/j.chemgeo.2014.01.004>

2996 Costa, F., 2004. Petrological and Experimental Constraints on the Pre-eruption Conditions of Holocene Dacite
2997 from Volcan San Pedro (36 S, Chilean Andes) and the Importance of Sulphur in Silicic Subduction-
2998 related Magmas. *Journal of Petrology* 45, 855–881. <https://doi.org/10.1093/petrology/egg114>

2999 Costa, F., Shea, T., Ubide, T., 2020. Diffusion chronometry and the timescales of magmatic processes. *Nat Rev*
3000 *Earth Environ* 1, 201–214. <https://doi.org/10.1038/s43017-020-0038-x>

3001 Crabtree, S.M., Lange, R.A., 2011. Complex Phenocryst Textures and Zoning Patterns in Andesites and Dacites:
3002 Evidence of Degassing-Induced Rapid Crystallization? *Journal of Petrology* 52, 3–38.
3003 <https://doi.org/10.1093/petrology/egq067>

3004 Dahren, B., Troll, V.R., Andersson, U.B., Chadwick, J.P., Gardner, M.F., Jaxybulatov, K., Koulakov, I., 2012.
3005 Magma plumbing beneath Anak Krakatau volcano, Indonesia: evidence for multiple magma storage
3006 regions. *Contrib Mineral Petrol* 163, 631–651. <https://doi.org/10.1007/s00410-011-0690-8>

3007 Dal-Negro, A., Manoli, S., Secca, L., Piccirillo, E.M., 1989. Megacrystic clinopyroxenes from Victoria (Australia);
3008 crystal chemical comparisons of pyroxenes from high and low pressure regimes. *European Journal of*
3009 *Mineralogy* 1 (1): 105–121.

3010 Danyushevsky, L.V., McNeill, A.W., Sobolev, A.V., 2002. Experimental and petrological studies of melt
3011 inclusions in phenocrysts from mantle-derived magmas: an overview of techniques, advantages and
3012 complications. *Chemical Geology* 183, 5–24. [https://doi.org/10.1016/S0009-2541\(01\)00369-2](https://doi.org/10.1016/S0009-2541(01)00369-2)

3013 Danyushevsky, L.V., Plechov, P., 2011. Petrolog3: Integrated software for modeling crystallization processes.
3014 *Geochemistry, Geophysics, Geosystems* 12, n/a-n/a. <https://doi.org/10.1029/2011GC003516>

3015 Dayton, K., Gazel, E., Wieser, P., Troll, V.R., Carracedo, J.C., La Madrid, H., Roman, D.C., Ward, J., Aulinas, M.,
3016 Geiger, H., Deegan, F.M., Gisbert, G., Perez-Torrado, F.J., 2023. Deep magma storage during the 2021
3017 La Palma eruption. *Sci. Adv.* 9, eade7641. <https://doi.org/10.1126/sciadv.ade7641>

3018 de Capitani, C., Petrakakis, K., 2010. The computation of equilibrium assemblage diagrams with
3019 Theriak/Domino software. *American Mineralogist* 95, 1006–1016.
3020 <https://doi.org/10.2138/am.2010.3354>

3021 Demouchy, S., Jacobsen, S.D., Gaillard, F., Stern, C.R., 2006. Rapid magma ascent recorded by water diffusion
3022 profiles in mantle olivine. *Geol* 34, 429. <https://doi.org/10.1130/G22386.1>

3023 DeVitre, C.L., Allison, C.M., Gazel, E., 2021. A high-precision CO₂ densimeter for Raman spectroscopy using a
3024 Fluid Density Calibration Apparatus. *Chemical Geology* 584, 120522.
3025 <https://doi.org/10.1016/j.chemgeo.2021.120522>

3026 DeVitre, C.L., Dayton, K., Gazel, E., Pamukçu, A., Gaetani, G., Wieser, P.E., 2023a. Laser heating effect on
3027 Raman analysis of CO₂ co-existing as liquid and vapor in olivine-hosted melt inclusion bubbles.
3028 *Volcanica* 6, 201–219. <https://doi.org/10.30909/vol.06.02.201219>

3029 DeVitre, C.L., Gazel, E., Ramalho, R., in review. Volatile-rich intraplate explosive eruptions sustained from the
3030 mantle. *Science*.

3031 DeVitre, C.L., Gazel, E., Ramalho, R.S., Venugopal, S., Steele-MacInnis, M., Hua, J., Allison, C.M., Moore, L.R.,
3032 Carracedo, J.C., Monteleone, B., 2023b. Oceanic intraplate explosive eruptions fed directly from the
3033 mantle. *Proc. Natl. Acad. Sci. U.S.A.* 120, e2302093120. <https://doi.org/10.1073/pnas.2302093120>
3034 Dixon, J.E., 1997. Degassing of alkalic basalts. *American Mineralogist* 82, 368–378.
3035 <https://doi.org/10.2138/am-1997-3-415>
3036 Dobbin, K.K., Simon, R.M., 2011. Optimally splitting cases for training and testing high dimensional classifiers.
3037 *BMC Med Genomics* 4, 31. <https://doi.org/10.1186/1755-8794-4-31>
3038 Drignon, M.J., Nielsen, R.L., Tepley, F.J., Bodnar, R.J., 2019. Upper mantle origin of plagioclase megacrysts from
3039 plagioclase-ultraphyric mid-oceanic ridge basalt. *Geology* 47, 43–46.
3040 <https://doi.org/10.1130/G45542.1>
3041 Duan, X., 2014. A general model for predicting the solubility behavior of H₂O–CO₂ fluids in silicate melts over a
3042 wide range of pressure, temperature and compositions. *Geochimica et Cosmochimica Acta* 125, 582–
3043 609. <https://doi.org/10.1016/j.gca.2013.10.018>
3044 Dubessy, J., Caumon, M.-C., Rull, F., Sharma, S., 2012. Instrumentation in Raman spectroscopy: elementary
3045 theory and practice, in: Ferraris, G., Dubessy, J., Caumon, M.-C., Rull, F. (Eds.), *Raman Spectroscopy*
3046 *Applied to Earth Sciences and Cultural Heritage*. European Mineralogical Union, pp. 83–172.
3047 <https://doi.org/10.1180/EMU-notes.12.3>
3048 Dubois, P.F., Hinsen, K., Hugunin, J., 1996. Numerical Python. *Comput. Phys.* 10, 262.
3049 <https://doi.org/10.1063/1.4822400>
3050 Erdmann, M., Koepke, J., 2016. Silica-rich lavas in the oceanic crust: experimental evidence for fractional
3051 crystallization under low water activity. *Contrib Mineral Petrol* 171, 83.
3052 <https://doi.org/10.1007/s00410-016-1294-0>
3053 Erdmann, S., Martel, C., Pichavant, M., Bourdier, J.-L., Champallier, R., Komorowski, J.-C., Cholik, N., 2016.
3054 Constraints from Phase Equilibrium Experiments on Pre-eruptive Storage Conditions in Mixed Magma
3055 Systems: a Case Study on Crystal-rich Basaltic Andesites from Mount Merapi, Indonesia. *J. Petrology*
3056 57, 535–560. <https://doi.org/10.1093/petrology/egw019>
3057 Erdmann, S., Martel, C., Pichavant, M., Kushnir, A., 2014. Amphibole as an archivist of magmatic crystallization
3058 conditions: problems, potential, and implications for inferring magma storage prior to the paroxysmal
3059 2010 eruption of Mount Merapi, Indonesia. *Contrib Mineral Petrol* 167, 1016.
3060 <https://doi.org/10.1007/s00410-014-1016-4>
3061 Esposito, R., Klebesz, R., Bartoli, O., Klyukin, Y., Moncada, D., Doherty, A., Bodnar, R., 2012. Application of the
3062 Linkam TS1400XY heating stage to melt inclusion studies. *Open Geosciences* 4.
3063 <https://doi.org/10.2478/s13533-011-0054-y>
3064 Esposito, R., Lamadrid, H.M., Redi, D., Steele-MacInnis, M., Bodnar, R.J., Manning, C.E., De Vivo, B., Cannatelli,
3065 C., Lima, A., 2016. Detection of liquid H₂O in vapor bubbles in reheated melt inclusions: Implications
3066 for magmatic fluid composition and volatile budgets of magmas? *American Mineralogist* 101, 1691–
3067 1695. <https://doi.org/10.2138/am-2016-5689>
3068 Everall, N.J., 2010. Confocal Raman microscopy: common errors and artefacts. *Analyst* 135, 2512.
3069 <https://doi.org/10.1039/c0an00371a>
3070 Fall, A., Tattitch, B., Bodnar, R.J., 2011. Combined microthermometric and Raman spectroscopic technique to
3071 determine the salinity of H₂O–CO₂–NaCl fluid inclusions based on clathrate melting. *Geochimica et*
3072 *Cosmochimica Acta* 75, 951–964. <https://doi.org/10.1016/j.gca.2010.11.021>
3073 First, E.C., Hammer, J.E., Ruprecht, P., Rutherford, M., 2021. Experimental Constraints on Dacite Magma
3074 Storage beneath Volcán Quizapu, Chile. *Journal of Petrology* 62, egab027.
3075 <https://doi.org/10.1093/petrology/egab027>
3076 Fowler, S.J., Spera, F.J., 2010. A Metamodel for Crustal Magmatism: Phase Equilibria of Giant Ignimbrites.
3077 *Journal of Petrology* 51, 1783–1830. <https://doi.org/10.1093/petrology/egq039>
3078 Fowler, S.J., Spera, F.J., Bohron, W.A., Belkin, H.E., De Vivo, B., 2007. Phase Equilibria Constraints on the
3079 Chemical and Physical Evolution of the Campanian Ignimbrite. *Journal of Petrology* 48, 459–493.
3080 <https://doi.org/10.1093/petrology/egl068>
3081 Frezzotti, M.L., Andersen, T., Neumann, E.-R., Simonsen, S.L., 2002. Carbonatite melt–CO₂ fluid inclusions in
3082 mantle xenoliths from Tenerife, Canary Islands: a story of trapping, immiscibility and fluid–rock
3083 interaction in the upper mantle. *Lithos* 64, 77–96. [https://doi.org/10.1016/S0024-4937\(02\)00178-0](https://doi.org/10.1016/S0024-4937(02)00178-0)
3084 Frezzotti, M.L., De Vivo, B., Clochiatti, R., 1991. Melt-mineral-fluid interactions in ultramafic nodules from
3085 alkaline lavas of Mount Etna (Sicily, Italy): Melt and fluid inclusion evidence. *Journal of Volcanology*
3086 *and Geothermal Research* 47, 209–219. [https://doi.org/10.1016/0377-0273\(91\)90001-G](https://doi.org/10.1016/0377-0273(91)90001-G)

3087 Frezzotti, M.L., Peccerillo, A., Bonelli, R., 2003. Magma ascent rates and depths of crustal magma reservoirs
3088 beneath the Aeolian volcanic Arc (Italy): Inferences from fluid and melt inclusions in xenoliths, in:
3089 Developments in Volcanology. Elsevier, pp. 185–205. [https://doi.org/10.1016/S1871-644X\(03\)80030-](https://doi.org/10.1016/S1871-644X(03)80030-)
3090 X

3091 Frezzotti, M.L., Tecce, F., Casagli, A., 2012. Raman spectroscopy for fluid inclusion analysis. *Journal of*
3092 *Geochemical Exploration* 112, 1–20. <https://doi.org/10.1016/j.gexplo.2011.09.009>

3093 Gaetani, G.A., O’Leary, J.A., Shimizu, N., Bucholz, C.E., Newville, M., 2012. Rapid reequilibration of H₂O and
3094 oxygen fugacity in olivine-hosted melt inclusions. *Geology* 40, 915–918.
3095 <https://doi.org/10.1130/G32992.1>

3096 Gaffney, A.M., 2002. Environments of Crystallization and Compositional Diversity of Mauna Loa Xenoliths.
3097 *Journal of Petrology* 43, 963–981. <https://doi.org/10.1093/petrology/43.6.963>

3098 Gao, R., Lassiter, J.C., Clague, D.A., Bohrsen, W.A., 2022. Evolution of Hawaiian Volcano Magmatic Plumbing
3099 System and Implications for Melt/Edifice and Melt/Lithosphere Interaction: Constraints from Hualālai
3100 Xenoliths. *Journal of Petrology* 63, egac091. <https://doi.org/10.1093/petrology/egac091>

3101 Garcia, M.O., 2003. A Petrologic Perspective of Kilauea Volcano’s Summit Magma Reservoir. *Journal of*
3102 *Petrology* 44, 2313–2339. <https://doi.org/10.1093/petrology/egg079>

3103 Gardner, J.E., Befus, K.S., Gualda, G.A.R., Ghiorso, M.S., 2014. Experimental constraints on rhyolite-MELTS and
3104 the Late Bishop Tuff magma body. *Contrib Mineral Petrol* 168, 1051. <https://doi.org/10.1007/s00410->
3105 014-1051-1

3106 Gavrilenko, M., Herzberg, C., Vidito, C., Carr, M.J., Tenner, T., Ozerov, A., 2016. A Calcium-in-Olivine
3107 Geohygrometer and its Application to Subduction Zone Magmatism. *Journal of Petrology* 57, 1811–
3108 1832. <https://doi.org/10.1093/petrology/egw062>

3109 Gavrilenko, M., Krawczynski, M., Ruprecht, P., Li, W., Catalano, J.G., 2019. The quench control of water
3110 estimates in convergent margin magmas. *American Mineralogist* 104, 936–948.
3111 <https://doi.org/10.2138/am-2019-6735>

3112 Geiger, H., Barker, A.K., Troll, V.R., 2016a. Locating the depth of magma supply for volcanic eruptions, insights
3113 from Mt. Cameroon. *Sci Rep* 6, 33629. <https://doi.org/10.1038/srep33629>

3114 Geiger, H., Mattsson, T., Deegan, F.M., Troll, V.R., Burchardt, S., Gudmundsson, Ó., Tryggvason, A., Krumbholz,
3115 M., Harris, C., 2016b. Magma plumbing for the 2014–2015 Holuhraun eruption, Iceland. *Geochem.*
3116 *Geophys. Geosyst.* 17, 2953–2968. <https://doi.org/10.1002/2016GC006317>

3117 Geiger, H., Troll, V.R., Jolis, E.M., Deegan, F.M., Harris, C., Hilton, D.R., Freda, C., 2018. Multi-level magma
3118 plumbing at Agung and Batur volcanoes increases risk of hazardous eruptions. *Sci Rep* 8, 10547.
3119 <https://doi.org/10.1038/s41598-018-28125-2>

3120 Geist, D., Naumann, T., Larson, P., 1998. Evolution of Galapagos Magmas: Mantle and Crustal Fractionation
3121 without Assimilation. *Journal of Petrology* 39, 953–971. <https://doi.org/10.1093/petroj/39.5.953>

3122 Gerlach, T.M., Graeber, E.J., 1985. Volatile budget of Kilauea volcano. *Nature* 313, 273–277.
3123 <https://doi.org/10.1038/313273a0>

3124 Ghiorso, M., Prissel, K., 2020. ENKI Cloud App: Implementation of the Fe-Ti Oxide Geothermoxybarometer of
3125 Ghiorso and Evans, 2008. <https://doi.org/10.5281/ZENODO.3866660>

3126 Ghiorso, M.S., 1990. Thermodynamic properties of hematite - ilmenite - geikielite solid solutions. *Contr.*
3127 *Mineral. and Petrol.* 104, 645–667. <https://doi.org/10.1007/BF01167285>

3128 Ghiorso, M.S., Evans, B.W., 2008. Thermodynamics of Rhombohedral Oxide Solid Solutions and a Revision of
3129 the FE-TI Two-Oxide Geothermometer and Oxygen-Barometer. *American Journal of Science* 308, 957–
3130 1039. <https://doi.org/10.2475/09.2008.01>

3131 Ghiorso, M.S., Gualda, G.A.R., 2015. An H₂O–CO₂ mixed fluid saturation model compatible with rhyolite-
3132 MELTS. *Contrib Mineral Petrol* 169, 53. <https://doi.org/10.1007/s00410-015-1141-8>

3133 Ghiorso, M.S., Gualda, G.A.R., 2013. A method for estimating the activity of titania in magmatic liquids from
3134 the compositions of coexisting rhombohedral and cubic iron–titanium oxides. *Contrib Mineral Petrol*
3135 165, 73–81. <https://doi.org/10.1007/s00410-012-0792-y>

3136 Ghiorso, M.S., Hirschmann, M.M., Reiners, P.W., Kress, V.C., 2002. The pMELTS: A revision of MELTS for
3137 improved calculation of phase relations and major element partitioning related to partial melting of
3138 the mantle to 3 GPa. *Geochem.-Geophys.-Geosyst.* 3, 1–35. <https://doi.org/10.1029/2001GC000217>

3139 Ghiorso, M.S., Sack, O., 1991. Fe-Ti oxide geothermometry: thermodynamic formulation and the estimation of
3140 intensive variables in silicic magmas. *Contr. Mineral. and Petrol.* 108, 485–510.
3141 <https://doi.org/10.1007/BF00303452>

3142 Ghiorso, M.S., Sack, R.O., 1995. Chemical mass transfer in magmatic processes IV. A revised and internally
3143 consistent thermodynamic model for the interpolation and extrapolation of liquid-solid equilibria in

3144 magmatic systems at elevated temperatures and pressures. *Contr. Mineral. and Petrol.* 119, 197–212.
3145 <https://doi.org/10.1007/BF00307281>

3146 Gibson, S.A., Geist, D., 2010. Geochemical and geophysical estimates of lithospheric thickness variation
3147 beneath Galápagos. *Earth and Planetary Science Letters* 300, 275–286.
3148 <https://doi.org/10.1016/j.epsl.2010.10.002>

3149 Gleeson, M.L.M., Gibson, S.A., 2021. Insights Into the Nature of Plume-Ridge Interaction and Outflux of H₂O
3150 From the Galápagos Spreading Center. *Geochem Geophys Geosyst* 22.
3151 <https://doi.org/10.1029/2020GC009560>

3152 Gleeson, M.L.M., Gibson, S.A., Stock, M.J., 2022. Constraints on the behaviour and content of volatiles in
3153 Galápagos magmas from melt inclusions and nominally anhydrous minerals. *Geochimica et*
3154 *Cosmochimica Acta* 319, 168–190. <https://doi.org/10.1016/j.gca.2021.11.005>

3155 Gleeson, M.L.M., Gibson, S.A., Stock, M.J., 2021. Upper Mantle Mush Zones beneath Low Melt Flux Ocean
3156 Island Volcanoes: Insights from Isla Floreana, Galápagos. *Journal of Petrology* 61, ega094.
3157 <https://doi.org/10.1093/petrology/egaa094>

3158 Gleeson, M.L.M., Stock, M.J., Pyle, D.M., Mather, T.A., Hutchison, W., Yirgu, G., Wade, J., 2017. Constraining
3159 magma storage conditions at a restless volcano in the Main Ethiopian Rift using phase equilibria
3160 models. *Journal of Volcanology and Geothermal Research* 337, 44–61.
3161 <https://doi.org/10.1016/j.jvolgeores.2017.02.026>

3162 Goltz, A.E., Krawczynski, M.J., Gavrilenko, M., Gorbach, N.V., Ruprecht, P., 2020. Evidence for superhydrous
3163 primitive arc magmas from mafic enclaves at Shiveluch volcano, Kamchatka. *Contrib Mineral Petrol*
3164 175, 115. <https://doi.org/10.1007/s00410-020-01746-5>

3165 Goranson, R.W., 1931. The solubility of water in granite magmas. *American Journal of Science* s5-22, 481–502.
3166 <https://doi.org/10.2475/ajs.s5-22.132.481>

3167 Grove, T.L., Donnelly-Nolan, J.M., Housh, T., 1997. Magmatic processes that generated the rhyolite of Glass
3168 Mountain, Medicine Lake volcano, N. California. *Contributions to Mineralogy and Petrology* 127, 205–
3169 223. <https://doi.org/10.1007/s004100050276>

3170 Grove, T.L., Kinzler, R.J., Bryan, W.B., 1992. Fractionation of Mid-Ocean Ridge Basalt (MORB), in: *Mantle Flow*
3171 *and Melt Generation at Mid-Ocean Ridges*. American Geophysical Union, pp. 281–311.

3172 Gualda, Guilherme A R, Bégué, F., Pamukcu, A.S., Ghiorso, M.S., 2019. Rhyolite-MELTS vs DERP—Newer Does
3173 not Make it Better: a Comment on ‘The Effect of Anorthite Content and Water on Quartz–Feldspar
3174 Cotectic Compositions in the Rhyolitic System and Implications for Geobarometry’ by Wilke et al.
3175 (2017; *Journal of Petrology*, 58, 789–818). *Journal of Petrology* 60, 855–864.
3176 <https://doi.org/10.1093/petrology/egz003>

3177 Gualda, G.A.R., Ghiorso, M.S., 2014. Phase-equilibrium geobarometers for silicic rocks based on rhyolite-
3178 MELTS. Part 1: Principles, procedures, and evaluation of the method. *Contrib Mineral Petrol* 168,
3179 1033. <https://doi.org/10.1007/s00410-014-1033-3>

3180 Gualda, G.A.R., Ghiorso, M.S., Lemons, R.V., Carley, T.L., 2012. Rhyolite-MELTS: a Modified Calibration of
3181 MELTS Optimized for Silica-rich, Fluid-bearing Magmatic Systems. *Journal of Petrology* 53, 875–890.
3182 <https://doi.org/10.1093/petrology/egr080>

3183 Gualda, Guilherme A.R., Gravley, D.M., Deering, C.D., Ghiorso, M.S., 2019. Magma extraction pressures and
3184 the architecture of volcanic plumbing systems. *Earth and Planetary Science Letters* 522, 118–124.
3185 <https://doi.org/10.1016/j.epsl.2019.06.020>

3186 Guo, K., Zhai, S.-K., Wang, X.-Y., Yu, Z.-H., Lai, Z.-Q., Chen, S., Song, Z.-J., Ma, Y., Chen, Z.-X., Li, X.-H., Zeng, Z.-
3187 G., 2018. The dynamics of the southern Okinawa Trough magmatic system: New insights from the
3188 microanalysis of the An contents, trace element concentrations and Sr isotopic compositions of
3189 plagioclase hosted in basalts and silicic rocks. *Chemical Geology* 497, 146–161.
3190 <https://doi.org/10.1016/j.chemgeo.2018.09.002>

3191 Hagiwara, Y., Kawano, T., Takahata, K., Torimoto, J., Yamamoto, J., 2021. Temperature dependence of a Raman
3192 CO₂ densimeter from 23°C to 200°C and 7.2 to 248.7 MPa: Evaluation of density underestimation by
3193 laser heating. *J Raman Spectrosc* 52, 1744–1757. <https://doi.org/10.1002/jrs.6188>

3194 Halldórsson, S.A., Marshall, E.W., Caracciolo, A., Matthews, S., Bali, E., Rasmussen, M.B., Ranta, E., Robin, J.G.,
3195 Guðfinnsson, G.H., Sigmarsson, O., Maclennan, J., Jackson, M.G., Whitehouse, M.J., Jeon, H., van der
3196 Meer, Q.H.A., Mibei, G.K., Kalliokoski, M.H., Repczynska, M.M., Rúnarsdóttir, R.H., Sigurðsson, G.,
3197 Pfeffer, M.A., Scott, S.W., Kjartansdóttir, R., Kleine, B.I., Oppenheimer, C., Aiuppa, A., Ilyinskaya, E.,
3198 Bitetto, M., Giudice, G., Stefánsson, A., 2022. Rapid shifting of a deep magmatic source at
3199 Fagradalsfjall volcano, Iceland. *Nature* 609, 529–534. <https://doi.org/10.1038/s41586-022-04981-x>

3200 Hammer, J., Jacob, S., Welsch, B., Hellebrand, E., Sinton, J., 2016. Clinopyroxene in postshield Haleakala
3201 ankaramite: 1. Efficacy of thermobarometry. *Contrib Mineral Petrol* 171, 7.
3202 <https://doi.org/10.1007/s00410-015-1212-x>
3203 Hammestrom, J.E., Zen, E.-A., 1986. Aluminum in hornblende: An empirical igneous geobarometer. *American*
3204 *Mineralogist*.
3205 Hansteen, T.H., Klugel, A., 2008. Fluid Inclusion Thermobarometry as a Tracer for Magmatic Processes. *Reviews*
3206 *in Mineralogy and Geochemistry* 69, 143–177. <https://doi.org/10.2138/rmg.2008.69.5>
3207 Hansteen, T.H., Klügel, A., Schmincke, H.-U., 1998. Multi-stage magma ascent beneath the Canary Islands:
3208 evidence from fluid inclusions. *Contributions to Mineralogy and Petrology* 132, 48–64.
3209 <https://doi.org/10.1007/s004100050404>
3210 Hanyu, T., Yamamoto, J., Kimoto, K., Shimizu, K., Ushikubo, T., 2020. Determination of total CO₂ in melt
3211 inclusions with shrinkage bubbles. *Chemical Geology* 557, 119855.
3212 <https://doi.org/10.1016/j.chemgeo.2020.119855>
3213 Harmon, L.J., Cowlyn, J., Gualda, G.A.R., Ghiorsso, M.S., 2018. Phase-equilibrium geobarometers for silicic rocks
3214 based on rhyolite-MELTS. Part 4: Plagioclase, orthopyroxene, clinopyroxene, glass geobarometer, and
3215 application to Mt. Ruapehu, New Zealand. *Contrib Mineral Petrol* 173, 7.
3216 <https://doi.org/10.1007/s00410-017-1428-z>
3217 Harris, C.R., Millman, K.J., van der Walt, S.J., Gommers, R., Virtanen, P., Cournapeau, D., Wieser, E., Taylor, J.,
3218 Berg, S., Smith, N.J., Kern, R., Picus, M., Hoyer, S., van Kerkwijk, M.H., Brett, M., Haldane, A., del Río,
3219 J.F., Wiebe, M., Peterson, P., Gérard-Marchant, P., Sheppard, K., Reddy, T., Weckesser, W., Abbasi, H.,
3220 Gohlke, C., Oliphant, T.E., 2020. Array programming with NumPy. *Nature* 585, 357–362.
3221 <https://doi.org/10.1038/s41586-020-2649-2>
3222 Hartley, M.E., Maclennan, J., Edmonds, M., Thordarson, T., 2014. Reconstructing the deep CO₂ degassing
3223 behaviour of large basaltic fissure eruptions. *Earth and Planetary Science Letters* 393, 120–131.
3224 <https://doi.org/10.1016/j.epsl.2014.02.031>
3225 Hauri, E.H., Maclennan, J., McKenzie, D., Gronvold, K., Oskarsson, N., Shimizu, N., 2018. CO₂ content beneath
3226 northern Iceland and the variability of mantle carbon. *Geology* 46, 55–58.
3227 <https://doi.org/10.1130/G39413.1>
3228 Helz, R.T., Thornber, C.R., 1987. Geothermometry of Kilauea Iki lava lake, Hawaii. *Bulletin of Volcanology* 49,
3229 651–668. <https://doi.org/10.1007/BF01080357>
3230 Hernandez Nava, A., Black, B.A., Gibson, S.A., Bodnar, R.J., Renne, P.R., Vanderkluysen, L., 2021. Reconciling
3231 early Deccan Traps CO₂ outgassing and pre-KPB global climate. *Proc Natl Acad Sci USA* 118,
3232 e2007797118. <https://doi.org/10.1073/pnas.2007797118>
3233 Hernandez, P.R., Woodcock, A., Estrada, M., Schultz, P.W., 2018. Undergraduate Research Experiences
3234 Broaden Diversity in the Scientific Workforce. *BioScience* 68, 204–211.
3235 <https://doi.org/10.1093/biosci/bix163>
3236 Herzberg, C., 2004. Partial Crystallization of Mid-Ocean Ridge Basalts in the Crust and Mantle. *Journal of*
3237 *Petrology* 45, 2389–2405. <https://doi.org/10.1093/petrology/egh040>
3238 Heywood, L.J., DeBari, S.M., Gill, J.B., Straub, S.M., Schindlbeck-Belo, J.C., Escobar-Burciaga, R.D., Woodhead,
3239 J., 2020. Across-Arc Diversity in Rhyolites From an Intra-oceanic Arc: Evidence From IODP Site U1437,
3240 Izu-Bonin Rear Arc, and Surrounding Area. *Geochem. Geophys. Geosyst.* 21.
3241 <https://doi.org/10.1029/2019GC008353>
3242 Higgins, O., Sheldrake, T., Caricchi, L., 2022. Machine learning thermobarometry and chemometry using
3243 amphibole and clinopyroxene: a window into the roots of an arc volcano (Mount Liamuiga, Saint
3244 Kitts). *Contrib Mineral Petrol* 177, 10. <https://doi.org/10.1007/s00410-021-01874-6>
3245 Hirschmann, M.M., Ghiorsso, M.S., Davis, F.A., Gordon, S.M., Mukherjee, S., Grove, T.L., Krawczynski, M.,
3246 Medard, E., Till, C.B., 2008. Library of Experimental Phase Relations (LEPR): A database and Web
3247 portal for experimental magmatic phase equilibria data: LIBRARY OF EXPERIMENTAL PHASE
3248 RELATIONS. *Geochem. Geophys. Geosyst.* 9, n/a-n/a. <https://doi.org/10.1029/2007GC001894>
3249 Holland, T., Blundy, J., 1994. Non-ideal interactions in calcic amphiboles and their bearing on amphibole-
3250 plagioclase thermometry. *Contr. Mineral. and Petrol.* 116, 433–447.
3251 <https://doi.org/10.1007/BF00310910>
3252 Holland, T.J.B., Green, E.C.R., Powell, R., 2018. Melting of Peridotites through to Granites: A Simple
3253 Thermodynamic Model in the System KNCFMASHTOCr. *Journal of Petrology* 59, 881–900.
3254 <https://doi.org/10.1093/petrology/egy048>
3255 Holland, T.J.B., Powell, R., 2011. An improved and extended internally consistent thermodynamic dataset for
3256 phases of petrological interest, involving a new equation of state for solids: THERMODYNAMIC

3257 DATASET FOR PHASES OF PETROLOGICAL INTEREST. *Journal of Metamorphic Geology* 29, 333–383.
3258 <https://doi.org/10.1111/j.1525-1314.2010.00923.x>

3259 Holland, T.J.B., Powell, R., 2004. An internally consistent thermodynamic data set for phases of petrological
3260 interest. *Journal of Metamorphic Geology* 16, 309–343. [https://doi.org/10.1111/j.1525-](https://doi.org/10.1111/j.1525-1314.1998.00140.x)
3261 [1314.1998.00140.x](https://doi.org/10.1111/j.1525-1314.1998.00140.x)

3262 Holland, T.J.B., Powell, R., 1998. An internally consistent thermodynamic data set for phases of petrological
3263 interest. *Journal of Metamorphic Geology* 16, 309–343. [https://doi.org/10.1111/j.1525-](https://doi.org/10.1111/j.1525-1314.1998.00140.x)
3264 [1314.1998.00140.x](https://doi.org/10.1111/j.1525-1314.1998.00140.x)

3265 Holland, T.J.B., Powell, R., 1990. An enlarged and updated internally consistent thermodynamic dataset with
3266 uncertainties and correlations: the system K₂O–Na₂O–CaO–MgO–MnO–FeO–Fe₂O₃–Al₂O₃–TiO₂–
3267 SiO₂–C–H₂–O₂. *J Metamorph Geol* 8, 89–124. <https://doi.org/10.1111/j.1525-1314.1990.tb00458.x>

3268 Hollister, L., Grissom, G., Peters, E.K., Stowell, H.H., Slsson, V., 1987. Confirmation of the empirical correlation
3269 of Al in hornblende with pressure of solidification of calc-alkaline plutons 72 (3–4): 231–239.

3270 Huang, R., Audétat, A., 2012. The titanium-in-quartz (TitaniQ) thermobarometer: A critical examination and re-
3271 calibration. *Geochimica et Cosmochimica Acta* 84, 75–89. <https://doi.org/10.1016/j.gca.2012.01.009>

3272 Humphreys, M.C.S., Cooper, G.F., Zhang, J., Loewen, M., Kent, A.J.R., Macpherson, C.G., Davidson, J.P., 2019.
3273 Unravelling the complexity of magma plumbing at Mount St. Helens: a new trace element partitioning
3274 scheme for amphibole. *Contrib Mineral Petrol* 174, 9. <https://doi.org/10.1007/s00410-018-1543-5>

3275 Hurai, V., 2010. Fluid inclusion geobarometry: Pressure corrections for immiscible H₂O–CH₄ and H₂O–CO₂
3276 fluids. *Chemical Geology* 278, 201–211. <https://doi.org/10.1016/j.chemgeo.2010.09.014>

3277 Hutchison, W., Mather, T.A., Pyle, D.M., Boyce, A.J., Gleeson, M.L.M., Yirgu, G., Blundy, J.D., Ferguson, D.J.,
3278 Vye-Brown, C., Millar, I.L., Sims, K.W.W., Finch, A.A., 2018. The evolution of magma during continental
3279 rifting: New constraints from the isotopic and trace element signatures of silicic magmas from
3280 Ethiopian volcanoes. *Earth and Planetary Science Letters* 489, 203–218.
3281 <https://doi.org/10.1016/j.epsl.2018.02.027>

3282 Iacono-Marziano, G., Morizet, Y., Le Trong, E., Gaillard, F., 2012. New experimental data and semi-empirical
3283 parameterization of H₂O–CO₂ solubility in mafic melts. *Geochimica et Cosmochimica Acta* 97, 1–23.
3284 <https://doi.org/10.1016/j.gca.2012.08.035>

3285 Iacovino, K., Matthews, S., Wieser, P.E., Moore, G., Begue, F., 2021. VESlcal Part I: An open-source
3286 thermodynamic model engine for mixed volatile (H₂O–CO₂) solubility in silicate melt. *Earth and Space*
3287 *Science*. <https://doi.org/10.1029/2020EA001584>

3288 Iacovino, K., Till, C., 2019. DensityX: A program for calculating the densities of hydrous magmatic liquids from
3289 427–1,627 °C and up to 30 kbar. *Volcanica* 2, 1–10. <https://doi.org/10.30909/vol.02.01.0110>

3290 J. Bodnar, R., 2017. Fluid Inclusions, in: Bobrowsky, P., Marker, B. (Eds.), *Encyclopedia of Engineering Geology*,
3291 *Encyclopedia of Earth Sciences Series*. Springer International Publishing, Cham, pp. 1–5.
3292 https://doi.org/10.1007/978-3-319-39193-9_225-1

3293 Jamshidi, K., Ghasemi, H., Troll, V.R., Sadeghian, M., Dahren, B., 2015. Magma storage and plumbing of
3294 adakite-type post-ophiolite intrusions in the Sabzevar ophiolitic zone, northeast Iran. *Solid Earth* 6,
3295 49–72. <https://doi.org/10.5194/se-6-49-2015>

3296 Jeffery, A.J., Gertisser, R., O’Driscoll, B., Pacheco, J.M., Whitley, S., Pimentel, A., Self, S., 2016. Temporal
3297 evolution of a post-caldera, mildly peralkaline magmatic system: Furnas volcano, São Miguel, Azores.
3298 *Contrib Mineral Petrol* 171, 42. <https://doi.org/10.1007/s00410-016-1235-y>

3299 Jeffery, A.J., Gertisser, R., Self, S., Pimentel, A., O’Driscoll, B., Pacheco, J.M., 2017. Petrogenesis of the
3300 Peralkaline Ignimbrites of Terceira, Azores. *Journal of Petrology* 58, 2365–2402.
3301 <https://doi.org/10.1093/petrology/egy012>

3302 Jennings, E.S., Gibson, S.A., MacLennan, J., 2019. Hot primary melts and mantle source for the Paraná-Etendeka
3303 flood basalt province: New constraints from Al-in-olivine thermometry. *Chemical Geology* 529,
3304 119287. <https://doi.org/10.1016/j.chemgeo.2019.119287>

3305 Jennings, E.S., Holland, T.J.B., 2015. A Simple Thermodynamic Model for Melting of Peridotite in the System
3306 NCFMASOcr. *Journal of Petrology* 56, 869–892. <https://doi.org/10.1093/petrology/egv020>

3307 Johnson, E.R., Cashman, K.V., 2020. Understanding the storage conditions and fluctuating eruption style of a
3308 young monogenetic volcano: Blue Lake crater (<3 ka), High Cascades, Oregon. *Journal of Volcanology*
3309 *and Geothermal Research* 408, 107103. <https://doi.org/10.1016/j.jvolgeores.2020.107103>

3310 Johnson, M.C., Rutherford, M.J., 1989. Experimental calibration of the aluminum-in-hornblende geobarometer
3311 with application to Long Valley caldera (California) volcanic rocks. *Geol* 17, 837.
3312 [https://doi.org/10.1130/0091-7613\(1989\)017<0837:ECOTAI>2.3.CO;2](https://doi.org/10.1130/0091-7613(1989)017<0837:ECOTAI>2.3.CO;2)

- 3313 Jorgenson, C., Caricchi, L., Stueckelberger, M., Fevola, G., Weber, G., 2021. A myriad of melt inclusions: a
3314 synchrotron microtomography study of melt inclusions and vapour bubbles from Colli Albani (Italy)
3315 (other). *pico*. <https://doi.org/10.5194/egusphere-egu21-13287>
- 3316 Jorgenson, C., Higgins, O., Petrelli, M., Bégué, F., Caricchi, L., 2022. A Machine Learning-Based Approach to
3317 Clinopyroxene Thermobarometry: Model Optimization and Distribution for Use in Earth Sciences. *JGR*
3318 *Solid Earth* 127. <https://doi.org/10.1029/2021JB022904>
- 3319 Kawakami, Y., Yamamoto, J., Kagi, H., 2003. Micro-Raman Densimeter for CO₂ Inclusions in Mantle-Derived
3320 Minerals. *Appl Spectrosc* 57, 1333–1339. <https://doi.org/10.1366/000370203322554473>
- 3321 Kawamoto, T., 1996. Experimental constraints on differentiation and H₂O abundance of calc-alkaline magmas.
3322 *Earth and Planetary Science Letters* 144, 577–589. [https://doi.org/10.1016/S0012-821X\(96\)00182-3](https://doi.org/10.1016/S0012-821X(96)00182-3)
- 3323 Kawasaki, T., Osanai, Y., 2008. Empirical thermometer of TiO₂ in quartz for ultrahigh-temperature granulites of
3324 East Antarctica. *Geological Society, London, Special Publications* 308, 419–430.
3325 <https://doi.org/10.1144/SP308.21>
- 3326 Keppler, H., 1989. The influence of the fluid phase composition on the solidus temperatures in the
3327 haplogranite system NaAlSi₃O₈-KAlSi₃O₈-SiO₂-H₂O-CO₂. *Contrib Mineral Petrol* 102, 321–327.
3328 <https://doi.org/10.1007/BF00373725>
- 3329 King, P.L., Holloway, J.R., 2002. CO₂ solubility and speciation in intermediate (andesitic) melts: the role of H₂O
3330 and composition. *Geochimica et Cosmochimica Acta* 66, 1627–1640. [https://doi.org/10.1016/S0016-7037\(01\)00872-9](https://doi.org/10.1016/S0016-7037(01)00872-9)
- 3331 Klein, B.Z., Jagoutz, O., Schmidt, M.W., Kueter, N., 2023. A Global Assessment of the Controls on the
3332 Fractionation of Arc Magmas. *Geochem Geophys Geosyst* 24, e2023GC010888.
3333 <https://doi.org/10.1029/2023GC010888>
- 3334 Klöcking, M., Wyborn, L., Lehnert, K.A., Ware, B., Prent, A.M., Profeta, L., Kohlmann, F., Noble, W., Bruno, I.,
3335 Lambert, S., Ananuer, H., Barber, N.D., Becker, H., Brodbeck, M., Deng, H., Deng, K., Elger, K., De
3336 Souza Franco, G., Gao, Y., Ghasera, K.M., Hezel, D.C., Huang, J., Kerswell, B., Koch, H., Lanati, A.W., Ter
3337 Maat, G., Martínez-Villegas, N., Nana Yobo, L., Redaa, A., Schäfer, W., Swing, M.R., Taylor, R.J.M.,
3338 Traun, M.K., Whelan, J., Zhou, T., 2023. Community recommendations for geochemical data, services
3339 and analytical capabilities in the 21st century. *Geochimica et Cosmochimica Acta* 351, 192–205.
3340 <https://doi.org/10.1016/j.gca.2023.04.024>
- 3341 Klügel, A., 1998. Reactions between mantle xenoliths and host magma beneath La Palma (Canary Islands):
3342 constraints on magma ascent rates and crustal reservoirs. *Contributions to Mineralogy and Petrology*
3343 131, 237–257.
- 3344 Klügel, A., Day, S., Schmid, M., Faria, B., 2020. Magma Plumbing During the 2014–2015 Eruption of Fogo (Cape
3345 Verde Islands). *Front. Earth Sci.* 8, 157. <https://doi.org/10.3389/feart.2020.00157>
- 3346 Kobayashi, T., Yamamoto, J., Hirajima, T., Ishibashi, H., Hirano, N., Lai, Y., Prikhod'ko, V.S., Arai, S., 2012.
3347 Conformity and precision of CO₂ densimetry in CO₂ inclusions: microthermometry *versus* Raman
3348 microspectroscopic densimetry: Conformity and precision of CO₂ densimetry in CO₂ inclusions. *J.*
3349 *Raman Spectrosc.* 43, 1126–1133. <https://doi.org/10.1002/jrs.3134>
- 3350 Kohn, M.J., 2014. “Thermoba-Raman-try”: Calibration of spectroscopic barometers and thermometers for
3351 mineral inclusions. *Earth and Planetary Science Letters* 388, 187–196.
3352 <https://doi.org/10.1016/j.epsl.2013.11.054>
- 3353 Koleszar, A.M., Kent, A.J.R., Wallace, P.J., Scott, W.E., 2012. Controls on long-term low explosivity at andesitic
3354 arc volcanoes: Insights from Mount Hood, Oregon. *Journal of Volcanology and Geothermal Research*
3355 219–220, 1–14. <https://doi.org/10.1016/j.jvolgeores.2012.01.003>
- 3356 Krawczynski, M.J., Grove, T.L., Behrens, H., 2012. Amphibole stability in primitive arc magmas: effects of
3357 temperature, H₂O content, and oxygen fugacity. *Contrib Mineral Petrol* 164, 317–339.
3358 <https://doi.org/10.1007/s00410-012-0740-x>
- 3359 Kress, V.C., Ghiorso, M.S., 2004. Thermodynamic modeling of post-entrapment crystallization in igneous
3360 phases. *Journal of Volcanology and Geothermal Research* 137, 247–260.
3361 <https://doi.org/10.1016/j.jvolgeores.2004.05.012>
- 3362 Lamadrid, H.M., Moore, L.R., Moncada, D., Rimstidt, J.D., Burruss, R.C., Bodnar, R.J., 2017. Reassessment of the
3363 Raman CO₂ densimeter. *Chemical Geology* 450, 210–222.
3364 <https://doi.org/10.1016/j.chemgeo.2016.12.034>
- 3365 Larocque, J., Canil, D., 2010. The role of amphibole in the evolution of arc magmas and crust: the case from the
3366 Jurassic Bonanza arc section, Vancouver Island, Canada. *Contrib Mineral Petrol* 159, 475–492.
3367 <https://doi.org/10.1007/s00410-009-0436-z>
- 3368

3369 Le Voyer, M., Kelley, K.A., Cottrell, E., Hauri, E.H., 2017. Heterogeneity in mantle carbon content from CO₂-
3370 undersaturated basalts. *Nat Commun* 8, 14062. <https://doi.org/10.1038/ncomms14062>

3371 Leahy, G.M., Collins, J.A., Wolfe, C.J., Laske, G., Solomon, S.C., 2010. Underplating of the Hawaiian Swell:
3372 evidence from teleseismic receiver functions: Underplating of the Hawaiian Swell. *Geophysical Journal*
3373 *International* 183, 313–329. <https://doi.org/10.1111/j.1365-246X.2010.04720.x>

3374 Lee, C.-T.A., Anderson, D.L., 2015. Continental crust formation at arcs, the arclogite “delamination” cycle, and
3375 one origin for fertile melting anomalies in the mantle. *Science Bulletin* 60, 1141–1156.
3376 <https://doi.org/10.1007/s11434-015-0828-6>

3377 Lerner, Allan H., Sublett, D.M., Cauley, C., Wallace, P., Bodnar, R.J., 2021. Magma storage depths and excess
3378 CO₂ fluids from the explosive Keanakakoi tephra (Kilauea Volcano, Hawaii) based on measurements
3379 of melt and fluid inclusions.

3380 Lerner, A. H., Wallace, P., Shea, T., 2021. The petrologic and degassing behavior of sulfur and other magmatic
3381 volatiles from the 2018 eruption of Kilauea, Hawai'i: melt concentrations, magma storage depths, and
3382 magma recycling. *Bulletin Volcanology* 83:43, 1–32.

3383 Li, X., Kind, R., Yuan, X., Wölbern, I., Hanka, W., 2004. Rejuvenation of the lithosphere by the Hawaiian plume.
3384 *Nature* 427, 827–829. <https://doi.org/10.1038/nature02349>

3385 Liang, Y., Sun, C., Yao, L., 2013. A REE-in-two-pyroxene thermometer for mafic and ultramafic rocks.
3386 *Geochimica et Cosmochimica Acta* 102, 246–260. <https://doi.org/10.1016/j.gca.2012.10.035>

3387 Lissenberg, C.J., MacLeod, C.J., 2016. A Reactive Porous Flow Control on Mid-ocean Ridge Magmatic Evolution.
3388 *Journal of Petrology* 57, 2195–2220. <https://doi.org/10.1093/petrology/egw074>

3389 Liu, Y., Zhang, Y., Behrens, H., 2005. Solubility of H₂O in rhyolitic melts at low pressures and a new empirical
3390 model for mixed H₂O–CO₂ solubility in rhyolitic melts. *Journal of Volcanology and Geothermal*
3391 *Research* 143, 219–235. <https://doi.org/10.1016/j.jvolgeores.2004.09.019>

3392 Lones, M.A., 2021. How to avoid machine learning pitfalls: a guide for academic researchers. arXiv:2108.02497
3393 [cs].

3394 Loucks, R.R., 1996. A precise olivine-augite Mg-Fe-exchange geothermometer. *Contributions to Mineralogy*
3395 *and Petrology* 125, 140–150. <https://doi.org/10.1007/s004100050211>

3396 Lowenstern, J.B., 2003. Melt inclusions come of age: Volatiles, volcanoes, and sorby's legacy, in: *Developments*
3397 *in Volcanology*. Elsevier, pp. 1–21. [https://doi.org/10.1016/S1871-644X\(03\)80021-9](https://doi.org/10.1016/S1871-644X(03)80021-9)

3398 Ludden, J.N., 1978. Magmatic evolution of the basaltic shield volcanoes of Reunion Island. *Journal of*
3399 *Volcanology and Geothermal Research* 4, 171–198. [https://doi.org/10.1016/0377-0273\(78\)90035-5](https://doi.org/10.1016/0377-0273(78)90035-5)

3400 Luo, B., Wang, Z., Song, J., Qian, Y., He, Q., Li, Y., Head, J.W., Moynier, F., Xiao, L., Becker, H., 2023. The
3401 magmatic architecture and evolution of the Chang'e-5 lunar basalts. *Nature Geoscience* 1–8.

3402 Mackwell, S.J., Kohlstedt, D.L., 1990. Diffusion of hydrogen in olivine: Implications for water in the mantle. *J.*
3403 *Geophys. Res.* 95, 5079. <https://doi.org/10.1029/JB095iB04p05079>

3404 Maclennan, J., 2017. Bubble formation and decrepitation control the CO₂ content of olivine-hosted melt
3405 inclusions. *Geochemistry, Geophysics, Geosystems* 18, 597–616.
3406 <https://doi.org/10.1002/2016GC006633>

3407 Maclennan, J., 2008. Concurrent Mixing and Cooling of Melts under Iceland. *Journal of Petrology* 49, 1931–
3408 1953. <https://doi.org/10.1093/petrology/egn052>

3409 Maclennan, J., McKenzie, D., Gronvöld, K., Slater, L., 2001. Crustal accretion under northern Iceland. *Earth and*
3410 *Planetary Science Letters* 191, 295–310. [https://doi.org/10.1016/S0012-821X\(01\)00420-4](https://doi.org/10.1016/S0012-821X(01)00420-4)

3411 Mandler, B.E., Donnelly-Nolan, J.M., Grove, T.L., 2014. Straddling the tholeiitic/calc-alkaline transition: the
3412 effects of modest amounts of water on magmatic differentiation at Newberry Volcano, Oregon.
3413 *Contrib Mineral Petrol* 168, 1066. <https://doi.org/10.1007/s00410-014-1066-7>

3414 Marxer, F., Ulmer, P., Müntener, O., 2022. Polybaric fractional crystallisation of arc magmas: an experimental
3415 study simulating trans-crustal magmatic systems. *Contrib Mineral Petrol* 177, 3.
3416 <https://doi.org/10.1007/s00410-021-01856-8>

3417 Masotta, M., Mollo, S., 2019. A New Plagioclase–Liquid Hygrometer Specific to Trachytic Systems. *Minerals* 9,
3418 375. <https://doi.org/10.3390/min9060375>

3419 Masotta, M., Mollo, S., Freda, C., Gaeta, M., Moore, G., 2013. Clinopyroxene–liquid thermometers and
3420 barometers specific to alkaline differentiated magmas. *Contrib Mineral Petrol* 166, 1545–1561.
3421 <https://doi.org/10.1007/s00410-013-0927-9>

3422 Matthews, S., Shorttle, O., Maclennan, J., 2016. The temperature of the Icelandic mantle from olivine-spinel
3423 aluminum exchange thermometry. *Geochemistry, Geophysics, Geosystems* 17, 4725–4752.
3424 <https://doi.org/10.1002/2016GC006497>

3425 Matthews, S., Wong, K., Shorttle, O., Edmonds, M., Maclennan, J., 2021. Do Olivine Crystallization
3426 Temperatures Faithfully Record Mantle Temperature Variability? *Geochem Geophys Geosyst* 22.
3427 <https://doi.org/10.1029/2020GC009157>

3428 McNab, F., Ball, P., 2023. meltPT: A Python package for basaltic whole-rock thermobarometric analysis with
3429 application to Hawai'i. *Volcanica* 6, 63–76. <https://doi.org/10.30909/vol.06.01.6376>

3430 Médard, E., Le Pennec, J.-L., 2022. Petrologic imaging of the magma reservoirs that feed large silicic eruptions.
3431 *Lithos* 428–429, 106812. <https://doi.org/10.1016/j.lithos.2022.106812>

3432 Mironov, N., Portnyagin, M., Botcharnikov, R., Gurenko, A., Hoernle, K., Holtz, F., 2015. Quantification of the
3433 CO₂ budget and H₂O–CO₂ systematics in subduction-zone magmas through the experimental
3434 hydration of melt inclusions in olivine at high H₂O pressure. *Earth and Planetary Science Letters* 425,
3435 1–11. <https://doi.org/10.1016/j.epsl.2015.05.043>

3436 Molina, José F., Cambeses, A., Moreno, J.A., Morales, I., Lázaro, C., Montero, P., Bea, F., 2021. A Cautionary
3437 Note on Amphibole Geobarometry, in: *The 2nd International Electronic Conference on Mineral
3438 Science*. Presented at the IECMS 2021, MDPI, p. 17. <https://doi.org/10.3390/iecms2021-09346>

3439 Molina, José Francisco, Cambeses, A., Moreno, J.A., Morales, I., Montero, P., Bea, F., 2021. A reassessment of
3440 the amphibole-plagioclase NaSi-CaAl exchange thermometer with applications to igneous and high-
3441 grade metamorphic rocks. *American Mineralogist* 106, 782–800. <https://doi.org/10.2138/am-2021-7400>

3442

3443 Molina, J.F., Moreno, J.A., Castro, A., Rodríguez, C., Fershtater, G.B., 2015. Calcic amphibole thermobarometry
3444 in metamorphic and igneous rocks: New calibrations based on plagioclase/amphibole Al-Si
3445 partitioning and amphibole/liquid Mg partitioning. *Lithos* 232, 286–305.
3446 <https://doi.org/10.1016/j.lithos.2015.06.027>

3447 Mollo, S., Putirka, K., Misiti, V., Soligo, M., Scarlato, P., 2013. A new test for equilibrium based on
3448 clinopyroxene–melt pairs: Clues on the solidification temperatures of Etnean alkaline melts at post-
3449 eruptive conditions. *Chemical Geology* 352, 92–100. <https://doi.org/10.1016/j.chemgeo.2013.05.026>

3450 Moore, G., Carmichael, I.S.E., 1998. The hydrous phase equilibria (to 3 kbar) of an andesite and basaltic
3451 andesite from western Mexico: constraints on water content and conditions of phenocryst growth.
3452 *Contributions to Mineralogy and Petrology* 130, 304–319. <https://doi.org/10.1007/s004100050367>

3453 Moore, L.R., Gazel, E., Bodnar, R.J., 2021. The volatile budget of Hawaiian magmatism: Constraints from melt
3454 inclusions from Haleakala volcano, Hawaii. *Journal of Volcanology and Geothermal Research* 410,
3455 107144. <https://doi.org/10.1016/j.jvolgeores.2020.107144>

3456 Moore, L.R., Gazel, E., Tuohy, R., Lloyd, A.S., Esposito, R., Steele-MacInnis, M., Hauri, E.H., Wallace, P.J., Plank,
3457 T., Bodnar, R.J., 2015. Bubbles matter: An assessment of the contribution of vapor bubbles to melt
3458 inclusion volatile budgets. *American Mineralogist* 100, 806–823. <https://doi.org/10.2138/am-2015-5036>

3459

3460 Moore, L.R., Mironov, N., Portnyagin, M., Gazel, E., Bodnar, R.J., 2018. Volatile contents of primitive bubble-
3461 bearing melt inclusions from Klyuchevskoy volcano, Kamchatka: Comparison of volatile contents
3462 determined by mass-balance versus experimental homogenization. *Journal of Volcanology and
3463 Geothermal Research* 358, 124–131. <https://doi.org/10.1016/j.jvolgeores.2018.03.007>

3464 Müntener, O., Kelemen, P.B., Grove, T.L., 2001. The role of H₂O during crystallization of primitive arc magmas
3465 under uppermost mantle conditions and genesis of igneous pyroxenites: an experimental study.
3466 *Contrib Mineral Petrol* 141, 643–658. <https://doi.org/10.1007/s004100100266>

3467 Mutch, E.J.F., Blundy, J.D., Tattitch, B.C., Cooper, F.J., Brooker, R.A., 2016. An experimental study of amphibole
3468 stability in low-pressure granitic magmas and a revised Al-in-hornblende geobarometer. *Contrib
3469 Mineral Petrol* 171, 85. <https://doi.org/10.1007/s00410-016-1298-9>

3470 Mutch, E.J.F., Maclennan, J., Holland, T.J.B., Buisman, I., 2019a. Millennial storage of near-Moho magma.
3471 *Science* 365, 260–264. <https://doi.org/10.1126/science.aax4092>

3472 Mutch, E.J.F., Maclennan, J., Madden-Nadeau, A.L., 2022. The dichotomous nature of Mg partitioning between
3473 plagioclase and melt: Implications for diffusion chronometry. *Geochimica et Cosmochimica Acta* 339,
3474 173–189. <https://doi.org/10.1016/j.gca.2022.10.035>

3475 Mutch, E.J.F., Maclennan, J., Shorttle, O., Edmonds, M., Rudge, J.F., 2019b. Rapid transcrustal magma
3476 movement under Iceland. *Nat. Geosci.* 12, 569–574. <https://doi.org/10.1038/s41561-019-0376-9>

3477 Nakatani, T., Kudo, T., Suzuki, T., 2022. Experimental Constraints on Magma Storage Conditions of Two
3478 Caldera-Forming Eruptions at Towada Volcano, Japan. *JGR Solid Earth* 127.
3479 <https://doi.org/10.1029/2021JB023665>

3480 Nandedkar, R.H., Ulmer, P., Müntener, O., 2014. Fractional crystallization of primitive, hydrous arc magmas: an
3481 experimental study at 0.7 GPa. *Contrib Mineral Petrol* 167, 1015. <https://doi.org/10.1007/s00410->
3482 014-1015-5

3483 Neave, D.A., Bali, E., Guðfinnsson, G.H., Halldórsson, S.A., Kahl, M., Schmidt, A.-S., Holtz, F., 2019.
3484 Clinopyroxene–Liquid Equilibria and Geothermobarometry in Natural and Experimental Tholeiites: the
3485 2014–2015 Holuhraun Eruption, Iceland. *Journal of Petrology* 60, 1653–1680.
3486 <https://doi.org/10.1093/petrology/egz042>

3487 Neave, D.A., Hartley, M.E., Maclennan, J., Edmonds, M., Thordarson, T., 2017. Volatile and light lithophile
3488 elements in high-anorthite plagioclase-hosted melt inclusions from Iceland. *Geochimica et*
3489 *Cosmochimica Acta* 205, 100–118. <https://doi.org/10.1016/j.gca.2017.02.009>

3490 Neave, D.A., Putirka, K.D., 2017. A new clinopyroxene–liquid barometer, and implications for magma storage
3491 pressures under Icelandic rift zones. *American Mineralogist* 102, 777–794.
3492 <https://doi.org/10.2138/am-2017-5968>

3493 Newcombe, M.E., Fabbrizio, A., Zhang, Y., Ma, C., Le Voyer, M., Guan, Y., Eiler, J.M., Saal, A.E., Stolper, E.M.,
3494 2014. Chemical zonation in olivine-hosted melt inclusions. *Contrib Mineral Petrol* 168, 1030.
3495 <https://doi.org/10.1007/s00410-014-1030-6>

3496 Newville, M., Stensitzki, T., Allen, D.B., Rawlik, M., Ingargiola, A., Nelson, A., 2016. LMFIT: Non-linear least-
3497 square minimization and curve-fitting for Python. *Astrophysics Source Code Library* ascl-1606.

3498 Nimis, P., 1995. A clinopyroxene geobarometer for basaltic systems based on crystal-structure modeling.
3499 *Contrib Mineral Petrol* 121, 115–125. <https://doi.org/10.1007/s004100050093>

3500 Onuma, K., Tohara, T., 1983. Effect of chromium on phase relations in the join forsterite–anorthite–diopside in
3501 air at 1 atm. *Contributions to Mineralogy and Petrology* 84, 174–181.

3502 Pamukcu, A.S., Gualda, G.A.R., Ghiroso, M.S., Miller, C.F., McCracken, R.G., 2015. Phase-equilibrium
3503 geobarometers for silicic rocks based on rhyolite–MELTS—Part 3: Application to the Peach Spring Tuff
3504 (Arizona–California–Nevada, USA). *Contrib Mineral Petrol* 169, 33. <https://doi.org/10.1007/s00410->
3505 015-1122-y

3506 Pamukçu, A.S., Gualda, G.A.R., Gravley, D.M., 2021. Rhyolite–MELTS and the storage and extraction of large-
3507 volume crystal-poor rhyolitic melts at the Taupō Volcanic Center: a reply to Wilson et al. (2021).
3508 *Contrib Mineral Petrol* 176, 82. <https://doi.org/10.1007/s00410-021-01840-2>

3509 Pamukçu, A.S., Wright, K.A., Gualda, G.A.R., Gravley, D., 2020. Magma residence and eruption at the Taupo
3510 Volcanic Center (Taupo Volcanic Zone, New Zealand): insights from rhyolite–MELTS geobarometry,
3511 diffusion chronometry, and crystal textures. *Contrib Mineral Petrol* 175, 48.
3512 <https://doi.org/10.1007/s00410-020-01684-2>

3513 Papale, P., Moretti, R., Barbato, D., 2006. The compositional dependence of the saturation surface of
3514 H₂O+CO₂ fluids in silicate melts. *Chemical Geology* 229, 78–95.
3515 <https://doi.org/10.1016/j.chemgeo.2006.01.013>

3516 Parat, F., Streck, M., Holtz, F., Almeev, R.R., 2014. Experimental study into the petrogenesis of crystal-rich
3517 basaltic to andesitic magmas at Arenal volcano. *Contributions to Mineralogy and Petrology*.

3518 Paszke, A., Gross, S., Massa, F., Lerer, A., Bradbury, J., Chanan, G., Killeen, T., Lin, Z., Gimelshein, N., Antiga, L.,
3519 2019. Pytorch: An imperative style, high-performance deep learning library. *Advances in neural*
3520 *information processing systems* 32.

3521 Peccerillo, A., 2003. Relationships between Mafic and Peralkaline Silicic Magmatism in Continental Rift
3522 Settings: a Petrological, Geochemical and Isotopic Study of the Gedemsa Volcano, Central Ethiopian
3523 Rift. *Journal of Petrology* 44, 2003–2032. <https://doi.org/10.1093/petrology/egg068>

3524 Pecher, A., 1981. Experimental decrepitation and re-equilibration of fluid inclusions in synthetic quartz.
3525 *Tectonophysics* 78, 567–583. [https://doi.org/10.1016/0040-1951\(81\)90029-9](https://doi.org/10.1016/0040-1951(81)90029-9)

3526 Perinelli, C., Mollo, S., Gaeta, M., De Cristofaro, S.P., Palladino, D.M., Armienti, P., Scarlato, P., Putirka, K.D.,
3527 2016. An improved clinopyroxene-based hygrometer for Etnean magmas and implications for
3528 eruption triggering mechanisms. *American Mineralogist* 101, 2774–2777.
3529 <https://doi.org/10.2138/am-2016-5916>

3530 Petrelli, M., Caricchi, L., Perugini, D., 2020. Machine Learning Thermo-Barometry: Application to
3531 Clinopyroxene-Bearing Magmas. *J. Geophys. Res. Solid Earth* 125.
3532 <https://doi.org/10.1029/2020JB020130>

3533 Pineda, C., Hammer, J., First, E., Morata, D., 2021. Storage conditions of a caldera-forming volcanic eruption:
3534 Insights from the Pudahuel rhyolitic ignimbrite in central Chile (32° 10'S). *Lithos* 400–401, 106382.
3535 <https://doi.org/10.1016/j.lithos.2021.106382>

3536 Plank, T., Kelley, K.A., Zimmer, M.M., Hauri, E.H., Wallace, P.J., 2013. Why do mafic arc magmas contain
3537 ~4wt% water on average? *Earth and Planetary Science Letters* 364, 168–179.
3538 <https://doi.org/10.1016/j.epsl.2012.11.044>

3539 Powell, R., Holland, T., Worley, B., 1998. Calculating phase diagrams involving solid solutions via non-linear
3540 equations, with examples using THERMOCALC. *Journal of metamorphic Geology* 16, 577–588.

3541 Prissel, T.C., Parman, S.W., Head, J.W., 2016. Formation of the lunar highlands Mg-suite as told by spinel.
3542 *American Mineralogist* 101, 1624–1635. <https://doi.org/10.2138/am-2016-5581>

3543 Pritchard, M.E., Mather, T.A., McNutt, S.R., Delgado, F.J., Reath, K., 2019. Thoughts on the criteria to
3544 determine the origin of volcanic unrest as magmatic or non-magmatic. *Phil. Trans. R. Soc. A* 377,
3545 20180008. <https://doi.org/10.1098/rsta.2018.0008>

3546 Profeta, L., Ducea, M.N., Chapman, J.B., Paterson, S.R., Gonzales, S.M.H., Kirsch, M., Petrescu, L., DeCelles,
3547 P.G., 2016. Quantifying crustal thickness over time in magmatic arcs. *Sci Rep* 5, 17786.
3548 <https://doi.org/10.1038/srep17786>

3549 Pu, X., Lange, R.A., Moore, G., 2017. A comparison of olivine-melt thermometers based on D_{Mg} and D_{Ni} : The
3550 effects of melt composition, temperature, and pressure with applications to MORBs and hydrous arc
3551 basalts. *American Mineralogist* 102, 750–765. <https://doi.org/10.2138/am-2017-5879>

3552 Pu, X., Moore, G.M., Lange, R.A., Touran, J.P., Gagnon, J.E., 2021. Experimental evaluation of a new H₂O-
3553 independent thermometer based on olivine-melt Ni partitioning at crustal pressure. *American*
3554 *Mineralogist* 106, 235–250. <https://doi.org/10.2138/am-2020-7014>

3555 Putirka, K., 2017. Geothermometry and geobarometry. *Encyclopedia of Geochemistry: A Comprehensive*
3556 *Reference Source on the Chemistry of the Earth*, edited by: White, WM, Springer International
3557 Publishing, Cham, Switzerland 597–614.

3558 Putirka, K., 2016. Amphibole thermometers and barometers for igneous systems and some implications for
3559 eruption mechanisms of felsic magmas at arc volcanoes. *American Mineralogist* 101, 841–858.
3560 <https://doi.org/10.2138/am-2016-5506>

3561 Putirka, K., 1999. Clinopyroxene + liquid equilibria to 100 kbar and 2450 K. *Contributions to Mineralogy and*
3562 *Petrology* 135, 151–163. <https://doi.org/10.1007/s004100050503>

3563 Putirka, K., Johnson, M., Kinzler, R., Longhi, J., Walker, D., 1996. Thermobarometry of mafic igneous rocks
3564 based on clinopyroxene-liquid equilibria, 0-30 kbar. *Contributions to Mineralogy and Petrology* 123,
3565 92–108. <https://doi.org/10.1007/s004100050145>

3566 Putirka, K.D., 2008. Thermometers and Barometers for Volcanic Systems. *Reviews in Mineralogy and*
3567 *Geochemistry* 69, 61–120. <https://doi.org/10.2138/rmg.2008.69.3>

3568 Putirka, K.D., 2005. Igneous thermometers and barometers based on plagioclase + liquid equilibria: Tests of
3569 some existing models and new calibrations. *American Mineralogist* 90, 336–346.
3570 <https://doi.org/10.2138/am.2005.1449>

3571 Putirka, K.D., Mikaelian, H., Ryerson, F., Shaw, H., 2003. New clinopyroxene-liquid thermobarometers for
3572 mafic, evolved, and volatile-bearing lava compositions, with applications to lavas from Tibet and the
3573 Snake River Plain, Idaho. *American Mineralogist* 88, 1542–1554. <https://doi.org/10.2138/am-2003-1017>

3574

3575 Qin, Z., Lu, F., Anderson, A., 1992. Diffusive reequilibration of melt and fluid inclusions. *American Mineralogist*
3576 77(506), 565–576.

3577 Quinn, E., 2014. Experimental Determination of Pre-Eruptive Storage Conditions And Continuous
3578 Decompression of Rhyodacite Magma Erupted from Chaos Crags, Lassen Volcanic Center, California.
3579 MSci thesis, Humboldt State University.

3580 Rader, E.L., Larsen, J.F., 2013. Experimental phase relations of a low MgO Aleutian basaltic andesite at XH₂O =
3581 0.7–1. *Contrib Mineral Petrol* 166, 1593–1611. <https://doi.org/10.1007/s00410-013-0944-8>

3582 Ranero, C.R., Torne, M., Banda, E., 1995. Gravity and multichannel seismic reflection constraints on the
3583 lithospheric structure of the Canary Swell. *Mar Geophys Res* 17, 519–534.
3584 <https://doi.org/10.1007/BF01204342>

3585 Rasmussen, D.J., Kyle, P.R., Wallace, P.J., Sims, K.W.W., Gaetani, G.A., Phillips, E.H., 2017. Understanding
3586 Degassing and Transport of CO₂-rich Alkalic Magmas at Ross Island, Antarctica using Olivine-Hosted
3587 Melt Inclusions. *Journal of Petrology*. <https://doi.org/10.1093/petrology/egx036>

3588 Rasmussen, D.J., Plank, T.A., Roman, D.C., Zimmer, M.M., 2022. Magmatic water content controls the pre-
3589 eruptive depth of arc magmas. *Science* 375, 1169–1172. <https://doi.org/10.1126/science.abm5174>

3590 Rasmussen, D.J., Plank, T.A., Wallace, P.J., Newcombe, M.E., Lowenstern, J.B., 2020. Vapor-bubble growth in
3591 olivine-hosted melt inclusions. *American Mineralogist* 105, 1898–1919. <https://doi.org/10.2138/am-2020-7377>

3592

3593 Reubi, O., Blundy, J., 2009. A dearth of intermediate melts at subduction zone volcanoes and the petrogenesis
3594 of arc andesites. *Nature* 461, 1269–1273. <https://doi.org/10.1038/nature08510>

3595 Ridolfi, F., 2021. Amp-TB2: An Updated Model for Calcic Amphibole Thermobarometry. *Minerals* 11, 324.
3596 <https://doi.org/10.3390/min11030324>

3597 Ridolfi, F., Renzulli, A., 2012. Calcic amphiboles in calc-alkaline and alkaline magmas: thermobarometric and
3598 chemometric empirical equations valid up to 1,130°C and 2.2 GPa. *Contrib Mineral Petrol* 163, 877–
3599 895. <https://doi.org/10.1007/s00410-011-0704-6>

3600 Ridolfi, F., Renzulli, A., Puerini, M., 2010. Stability and chemical equilibrium of amphibole in calc-alkaline
3601 magmas: an overview, new thermobarometric formulations and application to subduction-related
3602 volcanoes. *Contrib Mineral Petrol* 160, 45–66. <https://doi.org/10.1007/s00410-009-0465-7>

3603 Riel, N., Kaus, B.J.P., Green, E.C.R., Berlie, N., 2022. MAGEMin, an Efficient Gibbs Energy Minimizer: Application
3604 to Igneous Systems. *Geochem Geophys Geosyst* 23. <https://doi.org/10.1029/2022GC010427>

3605 Riker, J.M., 2005. The 1859 eruption of Mauna Loa Volcano, Hawai'i. Controls on the development of long lava
3606 channels. University of Oregon PhD thesis.

3607 Robidou, P., Frezzotti, M.L., Hauri, E.H., Aiuppa, A., 2018. Shrinkage Bubbles: The C–O–H–S Magmatic Fluid
3608 System at San Cristóbal Volcano. *Journal of Petrology* 59, 2093–2122.
3609 <https://doi.org/10.1093/petrology/egy092>

3610 Roedder, E., 1984. Fluid Inclusions, Reviews in Mineralogy. Mineralogical Society of America.

3611 Ronga, F., Lustrino, M., Marzoli, A., Melluso, L., 2010. Petrogenesis of a basalt-comendite-pantellerite rock
3612 suite: the Boseti Volcanic Complex (Main Ethiopian Rift). *Miner Petrol* 98, 227–243.
3613 <https://doi.org/10.1007/s00710-009-0064-3>

3614 Rose-Koga, E.F., Bouvier, A.-S., Gaetani, G.A., Wallace, P.J., Allison, C.M., Andrys, J.A., Angeles de la Torre, C.A.,
3615 Barth, A., Bodnar, R.J., Bracco Gartner, A.J.J., Butters, D., Castillejo, A., Chilson-Parks, B., Choudhary,
3616 B.R., Cluzel, N., Cole, M., Cottrell, E., Daly, A., Danyushevsky, L.V., DeVitre, C.L., Drignon, M.J., France,
3617 L., Gaborieau, M., Garcia, M.O., Gatti, E., Genske, F.S., Hartley, M.E., Hughes, E.C., Iveson, A.A.,
3618 Johnson, E.R., Jones, M., Kagoshima, T., Katzir, Y., Kawaguchi, M., Kawamoto, T., Kelley, K.A.,
3619 Koornneef, J.M., Kurz, M.D., Laubier, M., Layne, G.D., Lerner, A., Lin, K.-Y., Liu, P.-P., Lorenzo-Merino,
3620 A., Luciani, N., Magalhães, N., Marschall, H.R., Michael, P.J., Monteleone, B.D., Moore, L.R.,
3621 Moussallam, Y., Muth, M., Myers, M.L., Narváez, D.F., Navon, O., Newcombe, M.E., Nichols, A.R.L.,
3622 Nielsen, R.L., Pamukcu, A., Plank, T., Rasmussen, D.J., Roberge, J., Schiavi, F., Schwartz, D., Shimizu, K.,
3623 Shimizu, K., Shimizu, N., Thomas, J.B., Thompson, G.T., Tucker, J.M., Ustunisik, G., Waelkens, C.,
3624 Zhang, Y., Zhou, T., 2021. Silicate melt inclusions in the new millennium: A review of recommended
3625 practices for preparation, analysis, and data presentation. *Chemical Geology* 570, 120145.
3626 <https://doi.org/10.1016/j.chemgeo.2021.120145>

3627 Rosso, K.M., Bodnar, R.J., 1995. Microthermometric and Raman spectroscopic detection limits of CO₂ in fluid
3628 inclusions and the Raman spectroscopic characterization of CO₂. *Geochimica et Cosmochimica Acta*
3629 59, 3961–3975. [https://doi.org/10.1016/0016-7037\(95\)94441-H](https://doi.org/10.1016/0016-7037(95)94441-H)

3630 Ruscitto, D.M., Wallace, P.J., Johnson, E.R., Kent, A.J.R., Bindeman, I.N., 2010. Volatile contents of mafic
3631 magmas from cinder cones in the Central Oregon High Cascades: Implications for magma formation
3632 and mantle conditions in a hot arc. *Earth and Planetary Science Letters* 298, 153–161.
3633 <https://doi.org/10.1016/j.epsl.2010.07.037>

3634 Ruscitto, D.M., Wallace, P.J., Kent, A.J.R., 2011. Revisiting the compositions and volatile contents of olivine-
3635 hosted melt inclusions from the Mount Shasta region: implications for the formation of high-Mg
3636 andesites. *Contrib Mineral Petrol* 162, 109–132. <https://doi.org/10.1007/s00410-010-0587-y>

3637 Ruth, D.C.S., Costa, F., 2021. A petrological and conceptual model of Mayon volcano (Philippines) as an
3638 example of an open-vent volcano. *Bull Volcanol* 83, 62. <https://doi.org/10.1007/s00445-021-01486-9>

3639 Rutherford, M.J., 2003. Magmatic Conditions and Magma Ascent as Indicated by Hornblende Phase Equilibria
3640 and Reactions in the 1995–2002 Soufriere Hills Magma. *Journal of Petrology* 44, 1433–1453.
3641 <https://doi.org/10.1093/petrology/44.8.1433>

3642 Rutherford, M.J., Devine, J.D., 1988. The May 18, 1980, eruption of Mount St. Helens: 3. Stability and
3643 chemistry of amphibole in the magma chamber. *J. Geophys. Res.* 93, 11949.
3644 <https://doi.org/10.1029/JB093iB10p11949>

3645 Rutherford, M.J., Sigurdsson, H., Carey, S., Davis, A., 1985. The May 18, 1980, eruption of Mount St. Helens: 1.
3646 Melt composition and experimental phase equilibria. *J. Geophys. Res.* 90, 2929.
3647 <https://doi.org/10.1029/JB090iB04p02929>

3648 Sack, R.O., Ghiorso, M.S., 1994. Thermodynamics of multicomponent pyroxenes: I. Formulation of a general
3649 model. *Contr. Mineral. and Petrol.* 116, 277–286. <https://doi.org/10.1007/BF00306497>

3650 Sack, R.O., Ghiorso, M.S., 1991. An internally consistent model for the thermodynamic properties of Fe²⁺Mg-
3651 titanomagnetite-aluminate spinels. *Contr. Mineral. and Petrol.* 106, 474–505.
3652 <https://doi.org/10.1007/BF00321989>

3653 Sack, R.O., Ghiorso, M.S., 1989. Importance of considerations of mixing properties in establishing an internally
3654 consistent thermodynamic database: thermochemistry of minerals in the system Mg₂SiO₄-Fe₂SiO₄-
3655 SiO₂. *Contr. Mineral. and Petrol.* 102, 41–68. <https://doi.org/10.1007/BF01160190>

3656 Sanfilippo, A., MacLeod, C.J., Tribuzio, R., Lissenberg, C.J., Zanetti, A., 2020. Early-Stage Melt-Rock Reaction in a
3657 Cooling Crystal Mush Beneath a Slow-Spreading Mid-Ocean Ridge (IODP Hole U1473A, Atlantis Bank,
3658 Southwest Indian Ridge). *Front. Earth Sci.* 8, 579138. <https://doi.org/10.3389/feart.2020.579138>

3659 Sas, M., DeBari, S., Clynne, M., Rusk, B., 2017. Using mineral geochemistry to decipher slab, mantle, and crustal
3660 input in the generation of high-Mg andesites and basaltic andesites from the northern Cascade Arc.
3661 *msam.* <https://doi.org/10.2138/am-2017-5756>

3662 Scaillet, B., Macdonald, R., 2001. Phase Relations of Peralkaline Silicic Magmas and Petrogenetic Implications.
3663 *Journal of Petrology* 42, 825–845. <https://doi.org/10.1093/petrology/42.4.825>

3664 Schiavi, F., Bolfan-Casanova, N., Buso, R., Laumonier, M., Laporte, D., Medjoubi, K., Venugopal, S., Gómez-Ulla,
3665 A., Cluzel, N., Hardiagon, M., 2020. Quantifying magmatic volatiles by Raman microtomography of
3666 glass inclusion-hosted bubbles. *Geochem. Persp. Lett.* 16, 17–24.
3667 <https://doi.org/10.7185/geochemlet.2038>

3668 Schmidt, M.W., 1992. Amphibole composition in tonalite as a function of pressure: an experimental calibration
3669 of the Al-in-hornblende barometer. *Contr. Mineral. and Petrol.* 110, 304–310.
3670 <https://doi.org/10.1007/BF00310745>

3671 Scruggs, M.A., Putirka, K.D., 2018. Eruption triggering by partial crystallization of mafic enclaves at Chaos
3672 Crag, Lassen Volcanic Center, California. *American Mineralogist* 103, 1575–1590.
3673 <https://doi.org/10.2138/am-2018-6058>

3674 Shamloo, H.I., Till, C.B., 2019. Decadal transition from quiescence to supereruption: petrologic investigation of
3675 the Lava Creek Tuff, Yellowstone Caldera, WY. *Contrib Mineral Petrol* 174, 32.
3676 <https://doi.org/10.1007/s00410-019-1570-x>

3677 Shedden, K., 2008. Gene expression–based survival prediction in lung adenocarcinoma: a multi-site, blinded
3678 validation study. *Nat Med* 14, 822–827. <https://doi.org/10.1038/nm.1790>

3679 Sheehan, F., Barclay, J., 2016. Staged storage and magma convection at Ambrym volcano, Vanuatu. *Journal of*
3680 *Volcanology and Geothermal Research* 322, 144–157.
3681 <https://doi.org/10.1016/j.jvolgeores.2016.02.024>

3682 Shi, P., 1993. Low-Pressure Phase Relationships in the System Na₂O–CaO–FeO–MgO–Al₂O₃–SiO₂ at 1100 C,
3683 with Implications for the Differentiation of Basaltic Magmas. *Journal of Petrology* 34, 743–762.
3684 <https://doi.org/10.1093/petrology/34.4.743>

3685 Shi, P., 1992. Basalt evolution at low pressure: implications from an experimental study in the system CaO-
3686 FeO-MgO-Al₂O₃-SiO₂. *Contr. Mineral. and Petrol.* 110, 139–153.
3687 <https://doi.org/10.1007/BF00310735>

3688 Shi, S., Barth, A., Plank, T., Towbin, W., Flores, O., Arias, C., 2021. Magma stalling weakens eruption. Presented
3689 at the AGU Fall Meeting Abstracts, pp. V25E-09.

3690 Shinohara, H., 2013. Volatile flux from subduction zone volcanoes: Insights from a detailed evaluation of the
3691 fluxes from volcanoes in Japan. *Journal of Volcanology and Geothermal Research* 268, 46–63.
3692 <https://doi.org/10.1016/j.jvolgeores.2013.10.007>

3693 Shishkina, T.A., Botcharnikov, R.E., Holtz, F., Almeev, R.R., Jazwa, A.M., Jakubiak, A.A., 2014. Compositional and
3694 pressure effects on the solubility of H₂O and CO₂ in mafic melts. *Chemical Geology* 388, 112–129.
3695 <https://doi.org/10.1016/j.chemgeo.2014.09.001>

3696 Sides, Edmonds, M., Maclennan, J., Houghton, B.F., Swanson, D.A., Steele-MacInnis, M.J., 2014a. Magma
3697 mixing and high fountaining during the 1959 Kīlauea Iki eruption, Hawai‘i. *Earth and Planetary Science*
3698 *Letters* 400, 102–112. <https://doi.org/10.1016/j.epsl.2014.05.024>

3699 Sides, Edmonds, M., Maclennan, J., Swanson, D.A., Houghton, B.F., 2014b. Eruption style at Kīlauea Volcano in
3700 Hawai‘i linked to primary melt composition. *Nature Geoscience* 7, 464–469.
3701 <https://doi.org/10.1038/ngeo2140>

3702 Sieburg, M., Klügel, A., Rocholl, A., Bach, W., 2018. Magma plumbing and hybrid magma formation at an
3703 active back-arc basin volcano: North Su, eastern Manus basin. *Journal of Volcanology and Geothermal*
3704 *Research* 362, 1–16. <https://doi.org/10.1016/j.jvolgeores.2018.07.001>

3705 Sisson, T.W., Grove, T.L., 1993. Temperatures and H₂O contents of low-MgO high-alumina basalts. *Contr.*
3706 *Mineral. and Petrol.* 113, 167–184. <https://doi.org/10.1007/BF00283226>

3707 Sisson, T.W., Ratajeski, K., Hankins, W.B., Glazner, A.F., 2005. Voluminous granitic magmas from common
3708 basaltic sources. *Contrib Mineral Petrol* 148, 635–661. <https://doi.org/10.1007/s00410-004-0632-9>
3709 Skirius, C., Peterson, J., Anderson Jr., A.T., 1990. Homogenizing rhyolitic glass inclusions from the Bishop Tuff.
3710 *American Mineralogist* 75, 1381–1398.
3711 Solaro, C., Martel, C., Champallier, R., Boudon, G., Balcone-Boissard, H., Pichavant, M., 2019. Petrological and
3712 experimental constraints on magma storage for large pumiceous eruptions in Dominica island (Lesser
3713 Antilles). *Bull Volcanol* 81, 55. <https://doi.org/10.1007/s00445-019-1313-x>
3714 Sorby, H.C., 1858. On the Microscopical, Structure of Crystals, indicating the Origin of Minerals and Rocks.
3715 *QJGS* 14, 453–500. <https://doi.org/10.1144/GSL.JGS.1858.014.01-02.44>
3716 Span, R., Wagner, W., 1996. A New Equation of State for Carbon Dioxide Covering the Fluid Region from the
3717 Triple-Point Temperature to 1100 K at Pressures up to 800 MPa. *Journal of Physical and Chemical*
3718 *Reference Data* 25, 1509–1596. <https://doi.org/10.1063/1.555991>
3719 Spencer, K.J., Lindsley, D.H., 1981. A solution model for coexisting iron–titanium oxides. *American mineralogist*
3720 66, 1189–1201.
3721 Steele-Macinnis, M., Esposito, R., Bodnar, R.J., 2011. Thermodynamic Model for the Effect of Post-entrapment
3722 Crystallization on the H₂O-CO₂ Systematics of Vapor-saturated, Silicate Melt Inclusions. *Journal of*
3723 *Petrology* 52, 2461–2482. <https://doi.org/10.1093/petrology/egr052>
3724 Sterner, S.M., Pitzer, K.S., 1994. An equation of state for carbon dioxide valid from zero to extreme pressures.
3725 *Contr. Mineral. and Petrol.* 117, 362–374. <https://doi.org/10.1007/BF00307271>
3726 Stock, M.J., Bagnardi, M., Neave, D.A., Maclennan, J., Bernard, B., Buisman, I., Gleeson, M.L.M., Geist, D., 2018.
3727 Integrated Petrological and Geophysical Constraints on Magma System Architecture in the Western
3728 Galápagos Archipelago: Insights From Wolf Volcano. *Geochem. Geophys. Geosyst.* 19, 4722–4743.
3729 <https://doi.org/10.1029/2018GC007936>
3730 Sugawara, T., 2001. Ferric iron partitioning between plagioclase and silicate liquid: thermodynamics and
3731 petrological applications. *Contrib Mineral Petrol* 141, 659–686.
3732 <https://doi.org/10.1007/s004100100267>
3733 Sun, C., Liang, Y., 2012. Distribution of REE between clinopyroxene and basaltic melt along a mantle adiabat:
3734 effects of major element composition, water, and temperature. *Contrib Mineral Petrol* 163, 807–823.
3735 <https://doi.org/10.1007/s00410-011-0700-x>
3736 Sun, C., Lissenberg, C.J., 2018. Formation of fast-spreading lower oceanic crust as revealed by a new Mg–REE
3737 coupled geospeedometer. *Earth and Planetary Science Letters* 487, 165–178.
3738 <https://doi.org/10.1016/j.epsl.2018.01.032>
3739 Tamblyn, R., Hand, M., Morrissey, L., Zack, T., Phillips, G., Och, D., 2020. Resubduction of lawsonite eclogite
3740 within a serpentinite-filled subduction channel. *Contrib Mineral Petrol* 175, 74.
3741 <https://doi.org/10.1007/s00410-020-01712-1>
3742 Taracsák, Z., Hartley, M.E., Burgess, R., Edmonds, M., Iddon, F., Longpré, M.-A., 2019. High fluxes of deep
3743 volatiles from ocean island volcanoes: Insights from El Hierro, Canary Islands. *Geochimica et*
3744 *Cosmochimica Acta* 258, 19–36. <https://doi.org/10.1016/j.gca.2019.05.020>
3745 Taura, H., Yurimoto, H., Kurita, K., Sueno, S., 1998. Pressure dependence on partition coefficients for trace
3746 elements between olivine and the coexisting melts. *Physics and Chemistry of Minerals* 25, 469–484.
3747 <https://doi.org/10.1007/s002690050138>
3748 Teplow, W., Marsh, B., Hulen, 2009. Dacite Melt at the Puna Geothermal Venture Wellfield, Big Island of
3749 Hawaii. *GRC Transactions* 33.
3750 Thermoengine Code Contributors, 2022. ThermoEngine: Software for Model Building and Computational
3751 Thermodynamics Supporting Applications in the Earth Sciences.
3752 <https://doi.org/10.5281/ZENODO.6527840>
3753 Thomas, J.B., Bruce Watson, E., 2012. Application of the Ti-in-quartz thermobarometer to rutile-free systems.
3754 Reply to: a comment on: ‘TitaniQ under pressure: the effect of pressure and temperature on the
3755 solubility of Ti in quartz’ by Thomas et al. *Contrib Mineral Petrol* 164, 369–374.
3756 <https://doi.org/10.1007/s00410-012-0761-5>
3757 Thomas, J.B., Bruce Watson, E., Spear, F.S., Shemella, P.T., Nayak, S.K., Lanzirotti, A., 2010. TitaniQ under
3758 pressure: the effect of pressure and temperature on the solubility of Ti in quartz. *Contrib Mineral*
3759 *Petrol* 160, 743–759. <https://doi.org/10.1007/s00410-010-0505-3>
3760 Thomas, W.M., Ernst, W.G., 1990. The aluminum content of hornblende in calc-alkaline granitic rocks: A
3761 mineralogic barometer calibrated experimentally to 12 kbars 6.

3762 Tommasini, S., Bindi, L., Savia, L., Mangler, M.F., Orlando, A., Petrone, C.M., 2022. Critical assessment of
3763 pressure estimates in volcanic plumbing systems: The case study of Popocatepetl volcano, Mexico.
3764 *Lithos* 408–409, 106540. <https://doi.org/10.1016/j.lithos.2021.106540>
3765 Towbin, W.H., Plank, T., Klein, E., Hauri, E., 2023. Measuring H₂O concentrations in olivine by secondary ion
3766 mass spectrometry: Challenges and paths forward. *American Mineralogist: Journal of Earth and
3767 Planetary Materials* 108, 928–940. <https://doi.org/10.2138/am-2022-8247>
3768 Trela, J., Gazel, E., Sobolev, A.V., Moore, L., Bizimis, M., Jicha, B., Batanova, V.G., 2017. The hottest lavas of the
3769 Phanerozoic and the survival of deep Archaean reservoirs. *Nature Geosci* 10, 451–456.
3770 <https://doi.org/10.1038/ngeo2954>
3771 Tucker, J.M., Hauri, E.H., Pietruszka, A.J., Garcia, M.O., Marske, J.P., Trusdell, F.A., 2019. A high carbon content
3772 of the Hawaiian mantle from olivine-hosted melt inclusions. *Geochimica et Cosmochimica Acta* 254,
3773 156–172. <https://doi.org/10.1016/j.gca.2019.04.001>
3774 Tuohy, R.M., Wallace, P.J., Loewen, M.W., Swanson, D.A., Kent, A.J.R., 2016. Magma transport and olivine
3775 crystallization depths in Kīlauea’s east rift zone inferred from experimentally rehomogenized melt
3776 inclusions. *Geochimica et Cosmochimica Acta* 185, 232–250.
3777 <https://doi.org/10.1016/j.gca.2016.04.020>
3778 Ubide, T., Caulfield, J., Brandt, C., Bussweiler, Y., Mollo, S., Di Stefano, F., Nazzari, M., Scarlato, P., 2019a. Deep
3779 Magma Storage Revealed by Multi-Method Elemental Mapping of Clinopyroxene Megacrysts at
3780 Stromboli Volcano. *Front. Earth Sci.* 7, 239. <https://doi.org/10.3389/feart.2019.00239>
3781 Ubide, T., Larrea, P., Becerril, L., Galé, C., 2022. Volcanic plumbing filters on ocean-island basalt geochemistry.
3782 *Geology* 50, 26–31. <https://doi.org/10.1130/G49224.1>
3783 Ubide, T., Mollo, S., Zhao, J., Nazzari, M., Scarlato, P., 2019b. Sector-zoned clinopyroxene as a recorder of
3784 magma history, eruption triggers, and ascent rates. *Geochimica et Cosmochimica Acta* 251, 265–283.
3785 <https://doi.org/10.1016/j.gca.2019.02.021>
3786 Van Den Kerkhof, A.M., 1990. Isochoric phase diagrams in the systems CO₂–CH₄ and CO₂–N₂: Application to
3787 fluid inclusions. *Geochimica et Cosmochimica Acta* 54, 621–629. [https://doi.org/10.1016/0016-7037\(90\)90358-R](https://doi.org/10.1016/0016-7037(90)90358-R)
3788
3789 Venezky, D.Y., Rutherford, M.J., 1999. Petrology and Fe–Ti oxide reequilibration of the 1991 Mount Unzen
3790 mixed magma. *Journal of Volcanology and Geothermal Research* 89, 213–230.
3791 [https://doi.org/10.1016/S0377-0273\(98\)00133-4](https://doi.org/10.1016/S0377-0273(98)00133-4)
3792 Venugopal, S., Schiavi, F., Moune, S., Bolfan-Casanova, N., Druitt, T., Williams-Jones, G., 2020. Melt inclusion
3793 vapour bubbles: the hidden reservoir for major and volatile elements. *Sci Rep* 10, 9034.
3794 <https://doi.org/10.1038/s41598-020-65226-3>
3795 Villiger, S., 2004. The Liquid Line of Descent of Anhydrous, Mantle-Derived, Tholeiitic Liquids by Fractional and
3796 Equilibrium Crystallization--an Experimental Study at 1{middle dot}0 GPa. *Journal of Petrology* 45,
3797 2369–2388. <https://doi.org/10.1093/petrology/egh042>
3798 Villiger, S., Müntener, O., Ulmer, P., 2007. Crystallization pressures of mid-ocean ridge basalts derived from
3799 major element variations of glasses from equilibrium and fractional crystallization experiments. *J.
3800 Geophys. Res.* 112, B01202. <https://doi.org/10.1029/2006JB004342>
3801 Vogt, J.H.L., 1931. On the Terms Eutectic, Cotectic, Peritectic, Anchi-Eutectic, Anchi-Cotectic, etc., and their
3802 Importance in Petrogenesis. *The Journal of Geology* 39, 401–431. <https://doi.org/10.1086/623862>
3803 Voigt, A., Cassidy, M., Castro, J.M., Pyle, D.M., Mather, T.A., Helo, C., Abdurrachman, M., Kurniawan, I.A., 2022.
3804 Experimental Investigation of Trachydacite Magma Storage Prior to the 1257 Eruption of Mt Samalas.
3805 *Journal of Petrology* 63, egac066. <https://doi.org/10.1093/petrology/egac066>
3806 Voigt, M., Coogan, L.A., von der Handt, A., 2017. Experimental investigation of the stability of clinopyroxene in
3807 mid-ocean ridge basalts: The role of Cr and Ca/Al. *Lithos* 274–275, 240–253.
3808 <https://doi.org/10.1016/j.lithos.2017.01.003>
3809 Wade, J.A., Plank, T., Hauri, E.H., Kelley, K.A., Roggensack, K., Zimmer, M., 2008. Prediction of magmatic water
3810 contents via measurement of H₂O in clinopyroxene phenocrysts. *Geol* 36, 799.
3811 <https://doi.org/10.1130/G24964A.1>
3812 Walker, B.A., Klemetti, E.W., Grunder, A.L., Dilles, J.H., Tepley, F.J., Giles, D., 2013. Crystal reaming during the
3813 assembly, maturation, and waning of an eleven-million-year crustal magma cycle: thermobarometry
3814 of the Aucanquilcha Volcanic Cluster. *Contrib Mineral Petrol* 165, 663–682.
3815 <https://doi.org/10.1007/s00410-012-0829-2>
3816 Wallace, P.J., 2005. Volatiles in subduction zone magmas: concentrations and fluxes based on melt inclusion
3817 and volcanic gas data. *Journal of Volcanology and Geothermal Research* 140, 217–240.
3818 <https://doi.org/10.1016/j.jvolgeores.2004.07.023>

3819 Wallace, P.J., Anderson, A.T., Davis, A.M., 1999. Gradients in H₂O, CO₂, and exsolved gas in a large-volume
3820 silicic magma system: Interpreting the record preserved in melt inclusions from the Bishop Tuff. *J.*
3821 *Geophys. Res.* 104, 20097–20122. <https://doi.org/10.1029/1999JB900207>
3822 Wallace, P.J., Kamenetsky, V.S., Cervantes, P., 2015. Melt inclusion CO₂ contents, pressures of olivine
3823 crystallization, and the problem of shrinkage bubbles. *American Mineralogist* 100, 787–794.
3824 <https://doi.org/10.2138/am-2015-5029>
3825 Wallace, P.J., Plank, T., Bodnar, R.J., Gaetani, G.A., Shea, T., 2021. Olivine-Hosted Melt Inclusions: A
3826 Microscopic Perspective on a Complex Magmatic World. *Annual Review of Earth and Planetary*
3827 *Sciences*.
3828 Walowski, K.J., Wallace, P.J., Cashman, K.V., Marks, J.K., Clyne, M.A., Ruprecht, P., 2019. Understanding melt
3829 evolution and eruption dynamics of the 1666 C.E. eruption of Cinder Cone, Lassen Volcanic National
3830 Park, California: Insights from olivine-hosted melt inclusions. *Journal of Volcanology and Geothermal*
3831 *Research* 387, 106665. <https://doi.org/10.1016/j.jvolgeores.2019.106665>
3832 Walowski, K.J., Wallace, P.J., Clyne, M.A., Rasmussen, D.J., Weis, D., 2016. Slab melting and magma formation
3833 beneath the southern Cascade arc. *Earth and Planetary Science Letters* 446, 100–112.
3834 <https://doi.org/10.1016/j.epsl.2016.03.044>
3835 Wan, Z., Coogan, L.A., Canil, D., 2008. Experimental calibration of aluminum partitioning between olivine and
3836 spinel as a geothermometer. *American Mineralogist* 93, 1142–1147.
3837 <https://doi.org/10.2138/am.2008.2758>
3838 Wanamaker, B.J., Evans, B., 1989. Mechanical re-equilibration of fluid inclusions in San Carlos olivine by power-
3839 law creep. *Contr. Mineral. and Petrol.* 102, 102–111. <https://doi.org/10.1007/BF01160194>
3840 Wanamaker, B.J., Wong, T.-F., Evans, B., 1990. Decrepitation and crack healing of fluid inclusions in San Carlos
3841 olivine. *Journal of Geophysical Research* 95, 15623. <https://doi.org/10.1029/JB095iB10p15623>
3842 Wang, W., Caumon, M.-C., Tarantola, A., Pironon, J., Lu, W., Huang, Y., 2019. Raman spectroscopic densimeter
3843 for pure CO₂ and CO₂-H₂O-NaCl fluid systems over a wide P-T range up to 360 °C and 50 MPa.
3844 *Chemical Geology* 528, 119281. <https://doi.org/10.1016/j.chemgeo.2019.119281>
3845 Wang, X., Chou, I.-M., Hu, W., Burruss, R.C., Sun, Q., Song, Y., 2011. Raman spectroscopic measurements of
3846 CO₂ density: Experimental calibration with high-pressure optical cell (HPOC) and fused silica capillary
3847 capsule (FSCC) with application to fluid inclusion observations. *Geochimica et Cosmochimica Acta* 75,
3848 4080–4093. <https://doi.org/10.1016/j.gca.2011.04.028>
3849 Wang, X., Hou, T., Wang, M., Zhang, C., Zhang, Z., Pan, R., Marxer, F., Zhang, H., 2021. A new clinopyroxene
3850 thermobarometer for mafic to intermediate magmatic systems. *Eur. J. Mineral.* 33, 621–637.
3851 <https://doi.org/10.5194/ejm-33-621-2021>
3852 Wark, D.A., Watson, E.B., 2006. Titanite: a titanium-in-quartz geothermometer. *Contrib Mineral Petrol* 152,
3853 743–754. <https://doi.org/10.1007/s00410-006-0132-1>
3854 Waters, L.E., Lange, R.A., 2015. An updated calibration of the plagioclase-liquid hygrometer-thermometer
3855 applicable to basalts through rhyolites. *American Mineralogist* 100, 2172–2184.
3856 <https://doi.org/10.2138/am-2015-5232>
3857 Weber, G., Blundy, J., 2023. A machine learning-based thermometer, barometer and hygrometer for magmatic
3858 liquids (preprint). *Physical Sciences and Mathematics*. <https://doi.org/10.31223/X5NW9P>
3859 Weber, G., Castro, J.M., 2017. Phase petrology reveals shallow magma storage prior to large explosive silicic
3860 eruptions at Hekla volcano, Iceland. *Earth and Planetary Science Letters* 466, 168–180.
3861 <https://doi.org/10.1016/j.epsl.2017.03.015>
3862 White, R.S., McKenzie, D., O’Nions, R.K., 1992. Oceanic crustal thickness from seismic measurements and rare
3863 earth element inversions. *J. Geophys. Res.* 97, 19683. <https://doi.org/10.1029/92JB01749>
3864 Wieser, P., in prep. Thermobar: An open source... in prep.
3865 Wieser, P., DeVitre, C., 2023. DiadFit: An Open-Source Python3 Tool for Peak fitting of Raman Data from silicate
3866 melts and CO₂ fluids (preprint). *Earth Sciences*. <https://doi.org/10.31223/X5CQ1F>
3867 Wieser, P., Kent, A., Till, C., Abers, G., 2023a. Geophysical and Geochemical Constraints on Magma Storage
3868 Depths along the Cascade Arc: Knowns and Unknowns (preprint). *Earth Sciences*.
3869 <https://doi.org/10.31223/X5KX00>
3870 Wieser, P., Till, C., Kent, A., Gleeson, M., 2023b. Comment on ‘The magmatic architecture and evolution of the
3871 Chang’e-5 lunar basalts’ Penny E. Wieser¹, Christy Till², Adam Kent³, Matthew Gleeson¹ (preprint).
3872 *Earth Sciences*. <https://doi.org/10.31223/X5MM3B>
3873 Wieser, P. E., Edmonds, M., Gansecki, C., Maclennan, J., Jenner, F.E., Kunz, B., Antoshechkina, P., Trusdell, F.,
3874 Lee, R.L., Eimf, 2022a. Explosive Activity on Kilauea’s Lower East Rift Zone Fueled by a Volatile-Rich,
3875 Dacitic Melt. *Geochem Geophys Geosyst* 23. <https://doi.org/10.1029/2021GC010046>

3876 Wieser, P.E., Edmonds, M., Maclennan, J., Jenner, F.E., Kunz, B.E., 2019. Crystal scavenging from mush piles
3877 recorded by melt inclusions. *Nat Commun* 10, 5797. <https://doi.org/10.1038/s41467-019-13518-2>
3878 Wieser, P. E., Iacovino, K., Matthews, S., Moore, G., Allison, C.M., 2022b. VESical: 2. A Critical Approach to
3879 Volatile Solubility Modeling Using an Open-Source Python3 Engine. *Earth and Space Science* 9.
3880 <https://doi.org/10.1029/2021EA001932>
3881 Wieser, P.E., Jenner, F., Edmonds, M., Maclennan, J., Kunz, B.E., 2020. Chalcophile elements track the fate of
3882 sulfur at Kīlauea Volcano, Hawai'i. *Geochimica et Cosmochimica Acta* S0016703720303239.
3883 <https://doi.org/10.1016/j.gca.2020.05.018>
3884 Wieser, P.E., Kent, A., Till, C., Donovan, J., Neave, D., Blatter, D., Mike Krawczynski, M., 2023a. Barometers
3885 behaving badly: Assessing the influence of analytical and experimental uncertainty on clinopyroxene
3886 thermobarometry calculations at crustal conditions (preprint). *Earth Sciences*.
3887 <https://doi.org/10.31223/X5JT0N>
3888 Wieser, P.E., Kent, A.J., Till, C., 2023b. Barometers behaving badly II: A critical evaluation of Cpx-only and Cpx-
3889 Liq thermobarometry in variably-hydrous arc magmas. *EarthArxiv*. <https://doi.org/10.31223/X59655>
3890 Wieser, P.E., Lamadrid, H., Maclennan, J., Edmonds, M., Matthews, S., Iacovino, K., Jenner, F.E., Gansecki, C.,
3891 Trusdell, F., Lee, R.L., Ilyinskaya, E., 2021. Reconstructing Magma Storage Depths for the 2018
3892 Kīlauean Eruption From Melt Inclusion CO₂ Contents: The Importance of Vapor Bubbles. *Geochem*
3893 *Geophys Geosyst* 22. <https://doi.org/10.1029/2020GC009364>
3894 Wieser, P.E., Petrelli, M., Lubbers, J., Wieser, E., Ozaydin, S., Kent, A., Till, C., 2022. Thermobar: An open-source
3895 Python3 tool for thermobarometry and hygrometry. *Volcanica* 5, 349–384.
3896 <https://doi.org/10.30909/vol.05.02.349384>
3897 Wilke, S., Holtz, F., Li, X., Neave, D.A., Almeev, R.R., 2019. Rhyolite-MELTS vs DERP – Reply to Comment by
3898 Gualda et al. on ‘The Effect of Anorthite Content and Water on Quartz–Feldspar Cotectic
3899 Compositions in the Rhyolitic System and Implications for Geobarometry’ by Wilke et al. (2017),
3900 *Journal of Petrology*, 58, No. 4, 789–818. *Journal of Petrology* 60, 865–870.
3901 <https://doi.org/10.1093/petrology/egz002>
3902 Wilke, S., Holtz, F., Neave, D.A., Almeev, R., 2017. The Effect of Anorthite Content and Water on Quartz–
3903 Feldspar Cotectic Compositions in the Rhyolitic System and Implications for Geobarometry. *Journal of*
3904 *Petrology* 58, 789–818. <https://doi.org/10.1093/petrology/egx034>
3905 Wilkinson, M.D., Dumontier, M., Aalbersberg, I.J., Appleton, G., Axton, M., Baak, A., Blomberg, N., Boiten, J.-
3906 W., da Silva Santos, L.B., Bourne, P.E., Bouwman, J., Brookes, A.J., Clark, T., Crosas, M., Dillo, I.,
3907 Dumon, O., Edmunds, S., Evelo, C.T., Finkers, R., Gonzalez-Beltran, A., Gray, A.J.G., Groth, P., Goble, C.,
3908 Grethe, J.S., Heringa, J., 't Hoen, P.A.C., Hooft, R., Kuhn, T., Kok, R., Kok, J., Lusher, S.J., Martone, M.E.,
3909 Mons, A., Packer, A.L., Persson, B., Rocca-Serra, P., Roos, M., van Schaik, R., Sansone, S.-A., Schultes,
3910 E., Sengstag, T., Slater, T., Strawn, G., Swertz, M.A., Thompson, M., van der Lei, J., van Mulligen, E.,
3911 Velterop, J., Waagmeester, A., Wittenburg, P., Wolstencroft, K., Zhao, J., Mons, B., 2016. The FAIR
3912 Guiding Principles for scientific data management and stewardship. *Sci Data* 3, 160018.
3913 <https://doi.org/10.1038/sdata.2016.18>
3914 Wilson, C.J.N., Barker, S.J., Charlier, B.L.A., Myers, M.L., Hansen, K.F., 2021. A comment on: magma residence
3915 and eruption at the Taupō Volcanic Center (Taupō Volcanic Zone, New Zealand)—insights from
3916 rhyolite-MELTS geobarometry, diffusion chronometry, and crystal textures, by AS Pamukçu et al.,
3917 *Contrib Mineral Petrol* 175:48 (2020). *Contrib Mineral Petrol* 176, 79.
3918 <https://doi.org/10.1007/s00410-021-01839-9>
3919 Wilson, C.J.N., Seward, T.M., Allan, A.S.R., Charlier, B.L.A., Bello, L., 2012. A comment on: ‘Titanium under
3920 pressure: the effect of pressure and temperature on the solubility of Ti in quartz’, by Jay B. Thomas, E.
3921 Bruce Watson, Frank S. Spear, Philip T. Shemella, Saroj K. Nayak and Antonio Lanzirrotti. *Contrib*
3922 *Mineral Petrol* 164, 359–368. <https://doi.org/10.1007/s00410-012-0757-1>
3923 Winpenny, B., Maclennan, J., 2011. A Partial Record of Mixing of Mantle Melts Preserved in Icelandic
3924 Phenocrysts. *Journal of Petrology* 52, 1791–1812. <https://doi.org/10.1093/petrology/egr031>
3925 Wong, K., Ferguson, D., Matthews, S., Morgan, D., Tadesse, A.Z., Sinetebeb, Y., Yirgu, G., 2022. Exploring rift
3926 geodynamics in Ethiopia through olivine-spinel Al-exchange thermometry and rare-earth element
3927 distributions. *Earth and Planetary Science Letters* 597, 117820.
3928 <https://doi.org/10.1016/j.epsl.2022.117820>
3929 Wong, K., Ferguson, D., Wieser, P., Morgan, D., Edmonds, M., Tadesse, A.Z., Yirgu, G., Harvey, J., Hammond, S.,
3930 2023. Focused Mid-Crustal Magma Intrusion During Continental Break-Up in Ethiopia. *Geophysical*
3931 *Research Letters* 50, e2023GL103257. <https://doi.org/10.1029/2023GL103257>

3932 Wood, B.J., 1974. The solubility of alumina in orthopyroxene coexisting with garnet. *Contr. Mineral. and Petrol.*
3933 46, 1–15. <https://doi.org/10.1007/BF00377989>

3934 Wood, B.J., Blundy, J., 1997. predictive model for rare earth element partitioning between clinopyroxene and
3935 anhydrous silicate melt. *Contributions to Mineralogy and Petrology.*

3936 Wright, H.M., Bacon, C.R., Vazquez, J.A., Sisson, T.W., 2012. Sixty thousand years of magmatic volatile history
3937 before the caldera-forming eruption of Mount Mazama, Crater Lake, Oregon. *Contrib Mineral Petrol*
3938 164, 1027–1052. <https://doi.org/10.1007/s00410-012-0787-8>

3939 Yamamoto, J., Kagi, H., 2006. Extended Micro-Raman Densimeter for CO₂ Applicable to Mantle-originated
3940 Fluid Inclusions. *Chem. Lett.* 35, 610–611. <https://doi.org/10.1246/cl.2006.610>

3941 Yang, H.-J., Kinzler, R.J., Grove, T.L., 1996. Experiments and models of anhydrous, basaltic olivine-plagioclase-
3942 augite saturated melts from 0.001 to 10 kbar. *Contributions to Mineralogy and Petrology* 124, 1–18.
3943 <https://doi.org/10.1007/s004100050169>

3944 Yuan, X., Mayanovic, R.A., 2017. An Empirical Study on Raman Peak Fitting and Its Application to Raman
3945 Quantitative Research. *Appl Spectrosc* 71, 2325–2338. <https://doi.org/10.1177/0003702817721527>

3946 Zanon, V., Frezzotti, M.L., 2013. Magma storage and ascent conditions beneath Pico and Faial islands (Azores
3947 archipelago): A study on fluid inclusions: MAGMA STORAGE BENEATH PICO AND FAIAL. *Geochem.*
3948 *Geophys. Geosyst.* 14, 3494–3514. <https://doi.org/10.1002/ggge.20221>

3949 Zellmer, G.F., Sakamoto, N., Iizuka, Y., Miyoshi, M., Tamura, Y., Hsieh, H.-H., Yurimoto, H., 2014. Crystal uptake
3950 into aphyric arc melts: insights from two-pyroxene pseudo-decompression paths, plagioclase
3951 hygrometry, and measurement of hydrogen in olivines from mafic volcanics of SW Japan. *SP 385*,
3952 161–184. <https://doi.org/10.1144/SP385.3>

3953 Zhang, J., Humphreys, M.C.S., Cooper, G.F., Davidson, J.P., Macpherson, C.G., 2017. Magma mush chemistry at
3954 subduction zones, revealed by new melt major element inversion from calcic amphiboles. *American*
3955 *Mineralogist* 102, 1353–1367. <https://doi.org/10.2138/am-2017-5928>

3956 Zhang, Y., Namur, O., 2022. A re-evaluation of the Al-in-Olivine geothermometer. Presented at the
3957 Goldschmidt 2022 - <https://conf.goldschmidt.info/goldschmidt/2022/meetingapp.cgi/Paper/11383>.

3958 Zhang, Y., Xu, Z., Zhu, M., Wang, H., 2007. Silicate melt properties and volcanic eruptions: SILICATE MELT
3959 PROPERTIES. *Rev. Geophys.* 45. <https://doi.org/10.1029/2006RG000216>

3960 Zhukova, I., O'Neill, H., Campbell, I.H., 2017. A subsidiary fast-diffusing substitution mechanism of Al in
3961 forsterite investigated using diffusion experiments under controlled thermodynamic conditions.
3962 *Contrib Mineral Petrol* 172, 53. <https://doi.org/10.1007/s00410-017-1365-x>

3963 Ziberna, L., Green, E.C.R., Blundy, J.D., 2017. Multiple-reaction geobarometry for olivine-bearing igneous rocks.
3964 *American Mineralogist* 102, 2349–2366. <https://doi.org/10.2138/am-2017-6154>

3965

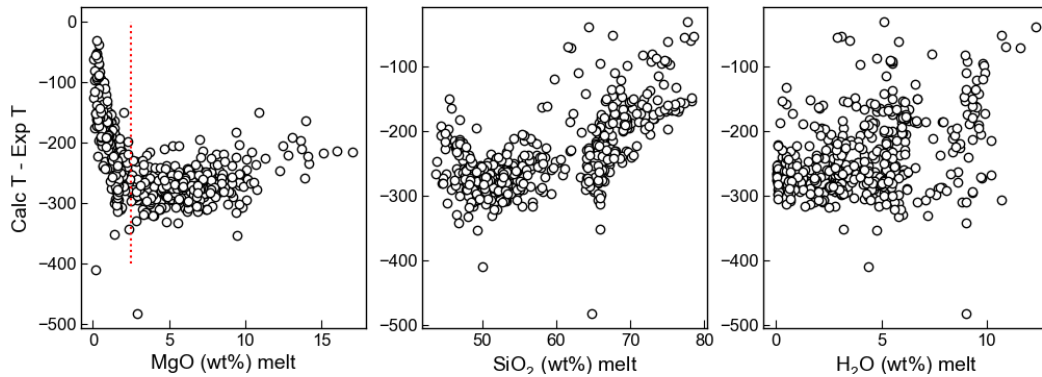
Supporting Information: P-T-X conditions of magmas

Penny E. Wieser¹, Matthew L.M. Gleeson¹, Simon Matthews², Charlotte DeVitre¹, Esteban Gazel³

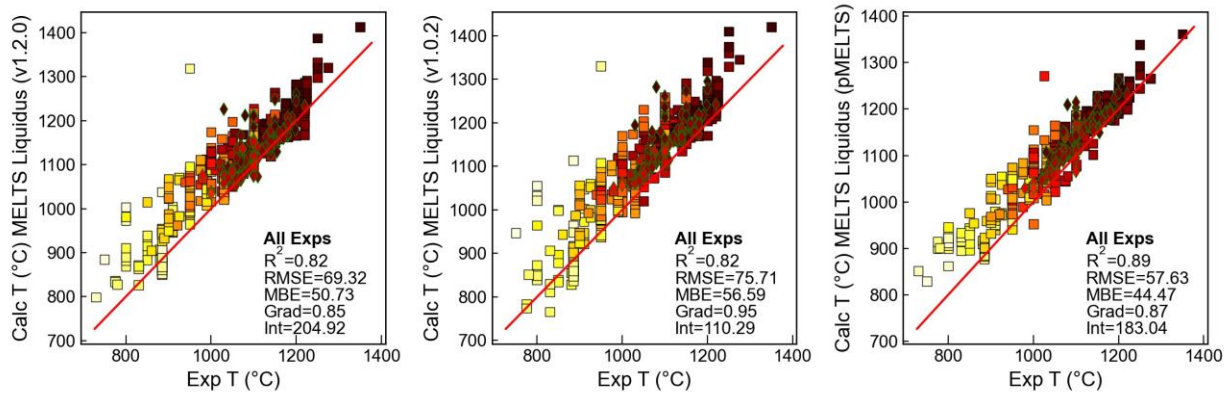
1. Earth and Planetary Sciences, UC Berkeley

2. Earth Science Department, University of Cambridge

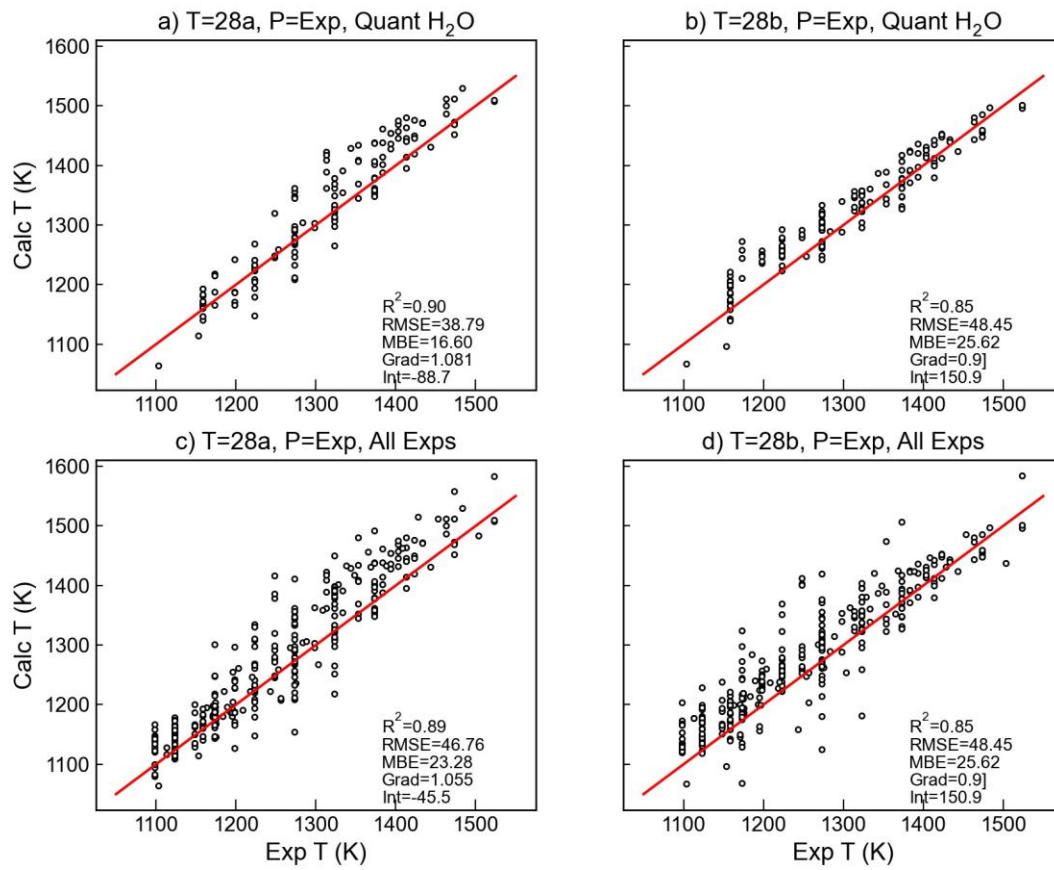
3. Department of Earth and Atmospheric Sciences, Cornell University, Ithaca, NY 14850, USA



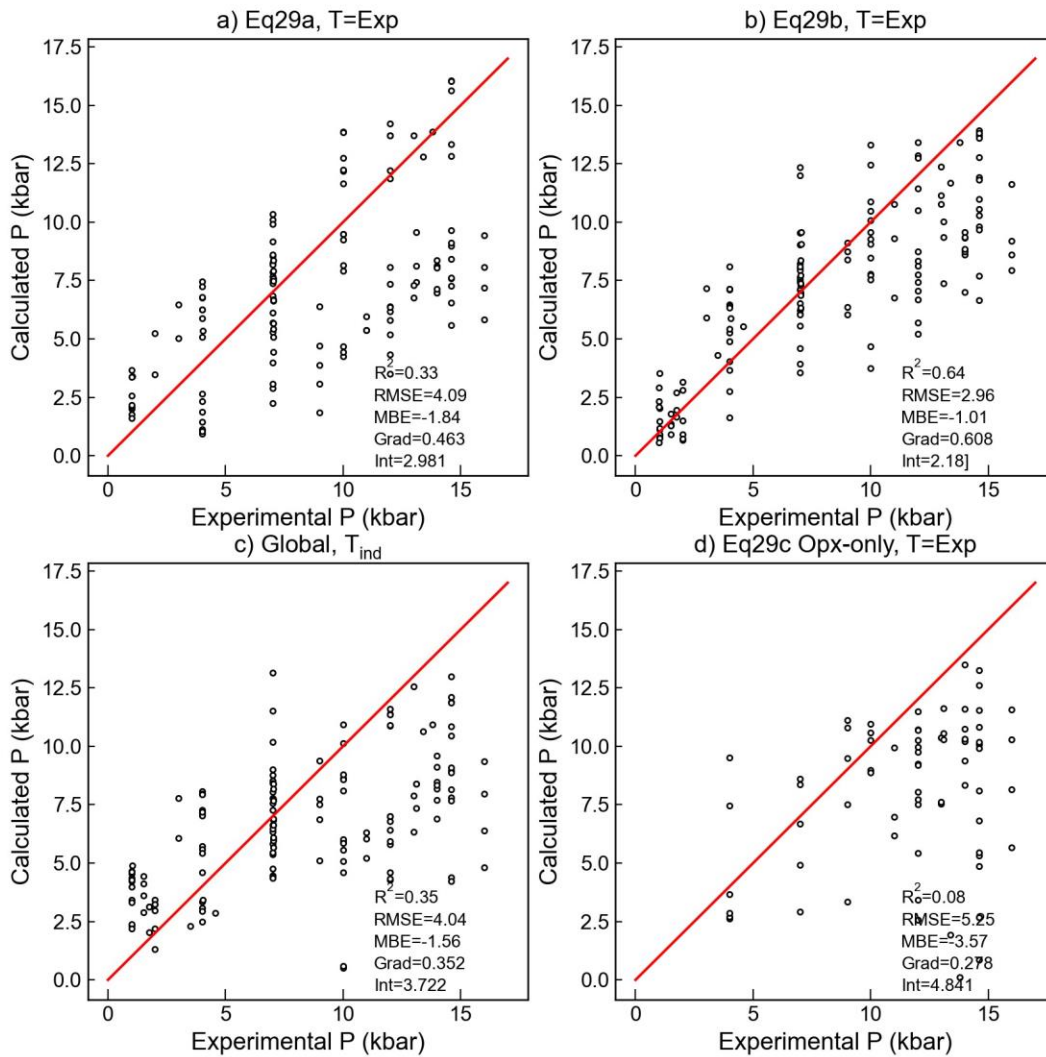
Supporting Fig. 1 – Offset between calculated temperature using Shi et al. (2021) and experimental temperature shows a strong relationship with MgO content.



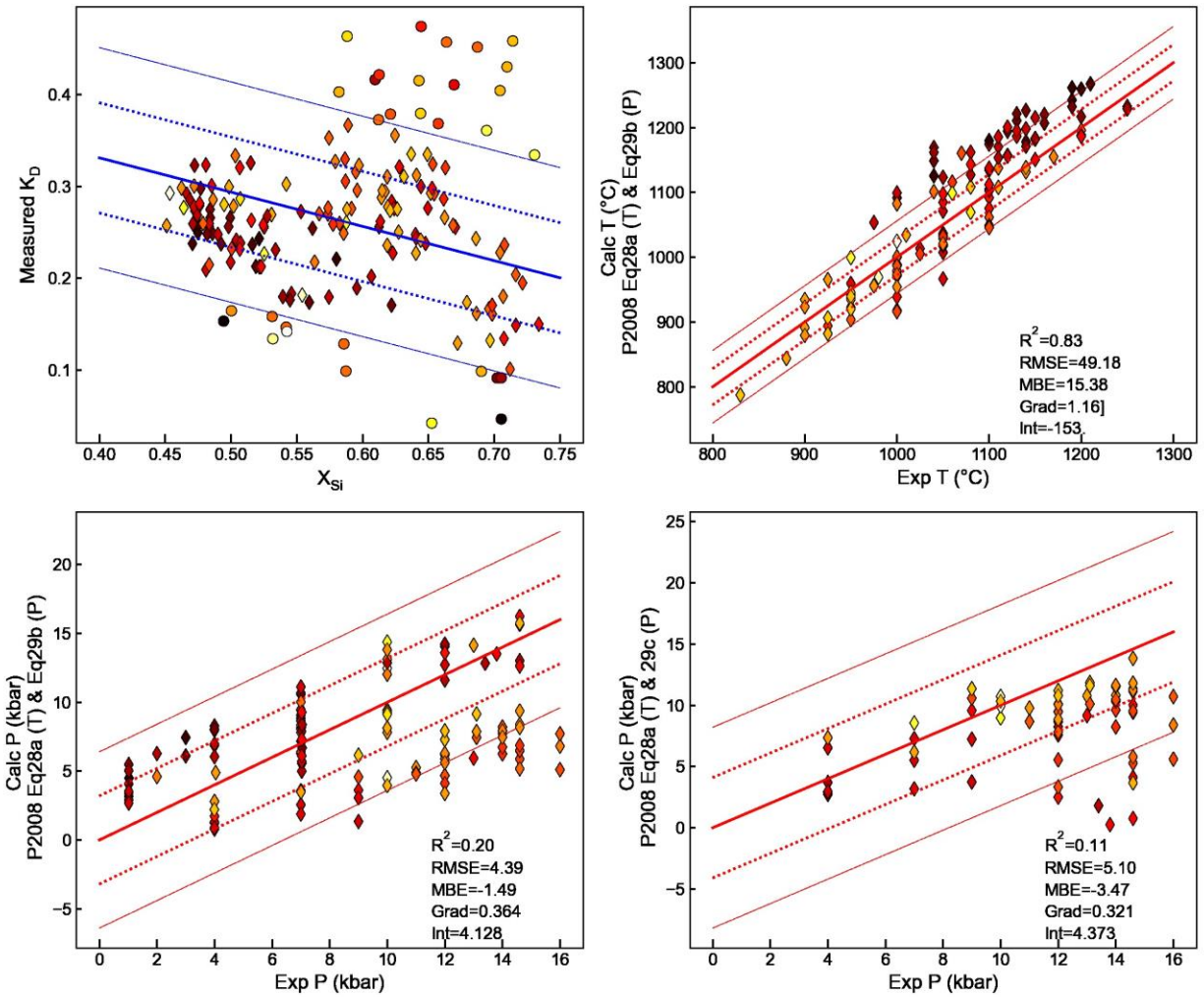
Supporting Fig. 2 – Liquidus calculations performed with different versions of MELTS for comparison with the main text.



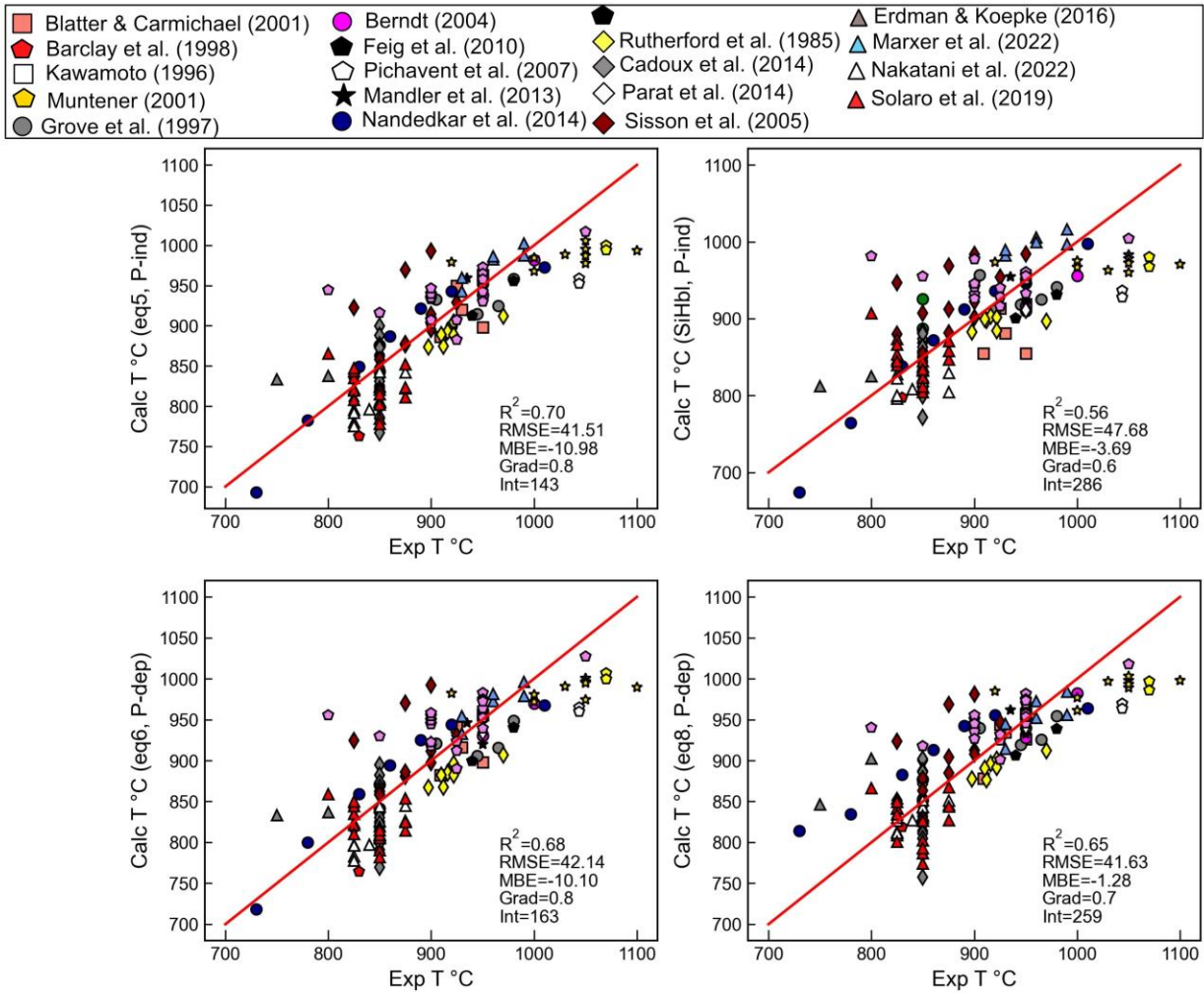
Supporting Fig. 3– Comparison of different Opx-Liq thermometers. a-b) uses only experiments where H₂O was measured using a quantitative method, while c-d shows all experiments.



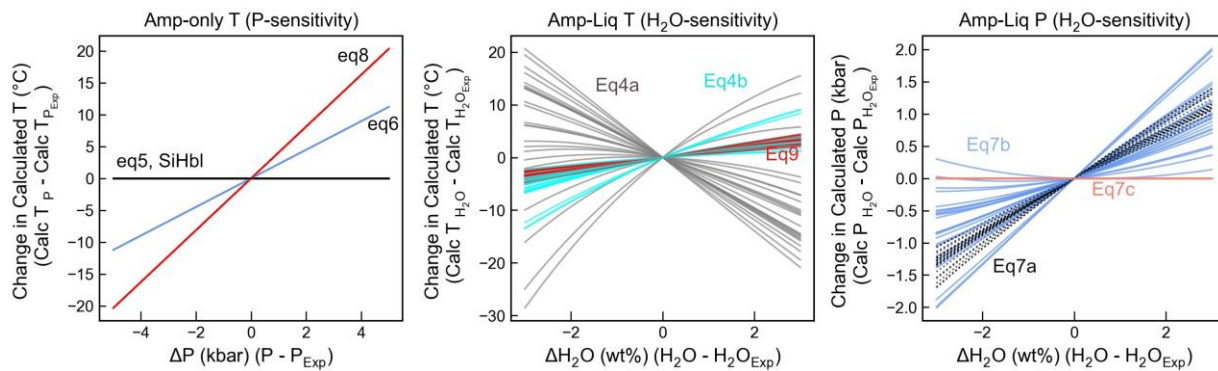
Supporting Fig. 4: Comparison of 4 different Opx-Liq and Opx-only barometers using experimental temperatures and H₂O contents. Eq29b provides the best match.



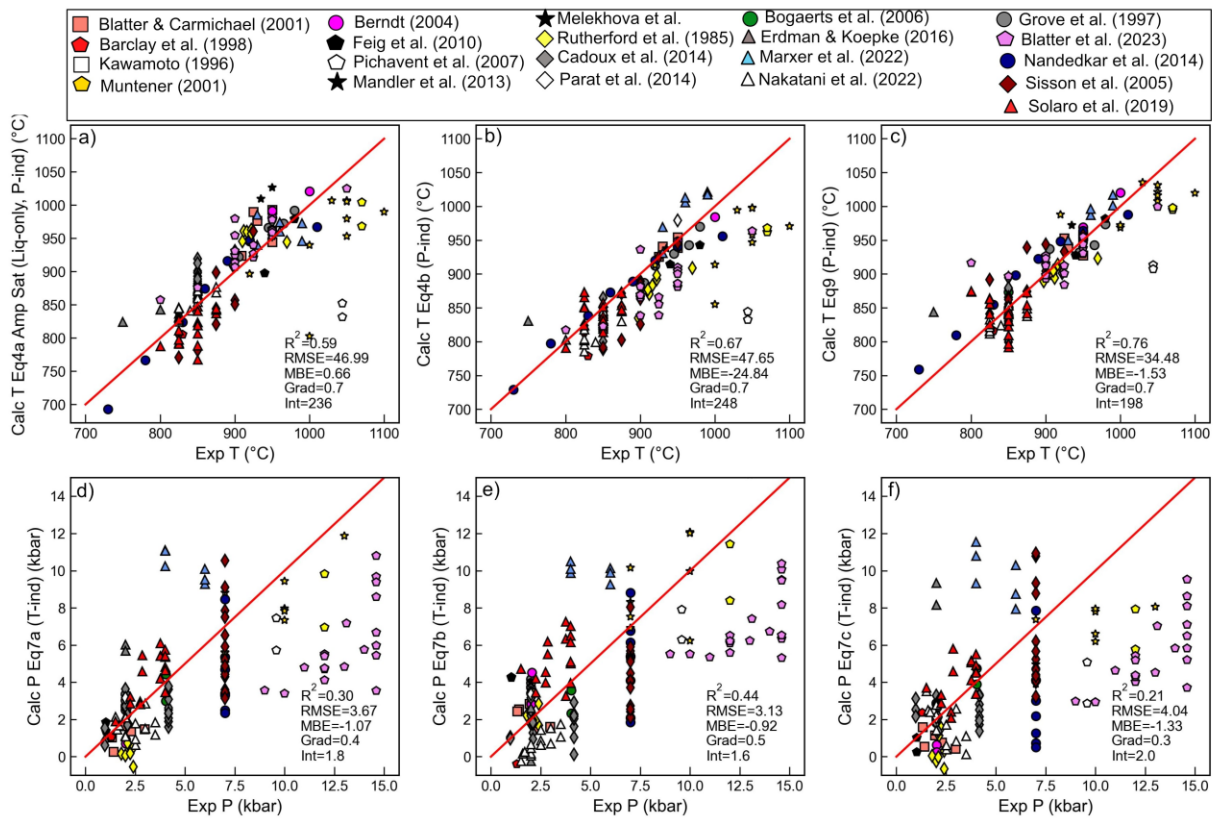
Supporting Fig. 5 – As for Fig. 9 in the main text, but only using experiments where H_2O was reported using a quantitative method.



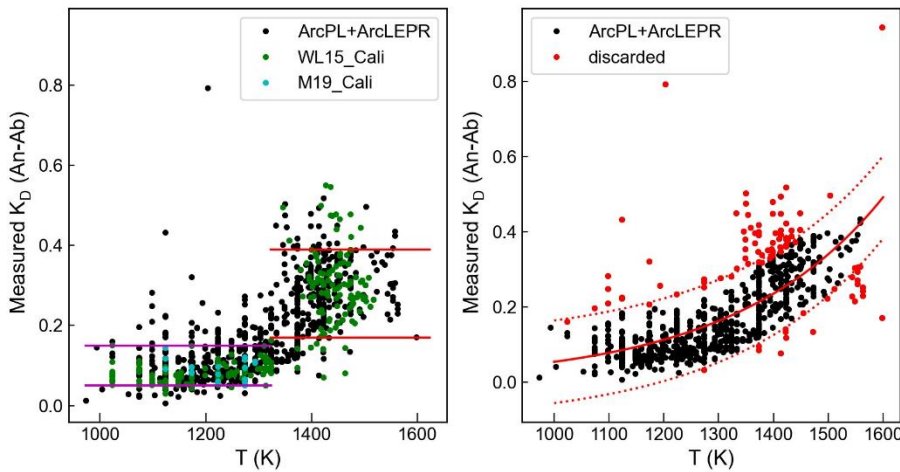
Supporting Fig. 6 – Assessment of Amp-only thermometers from Putirka (2016) on data not used during equation calibration.



Supporting Fig. 7 – Sensitivity testing of Putirka (2016) Amp expressions to unknowns in each equation.

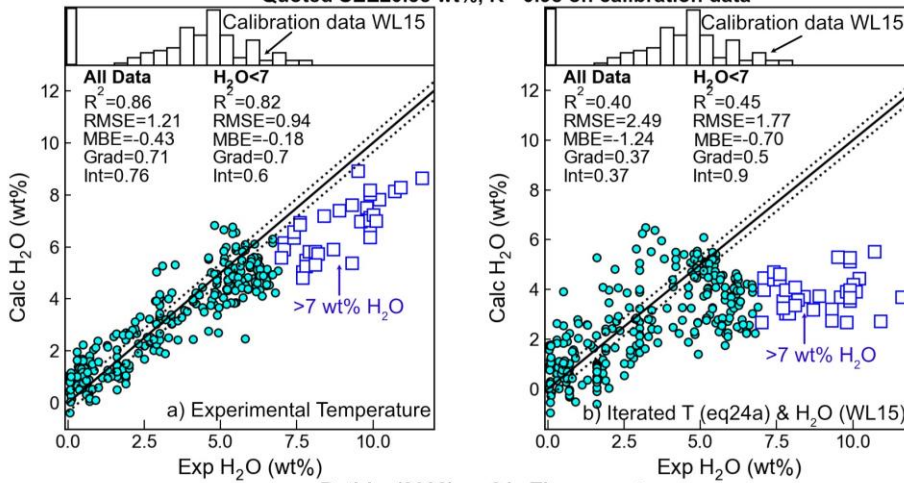


Supporting Fig. 8 – Assessment of Amp-Liq thermometers and barometers from Putirka (2016) on data not used during equation calibration.

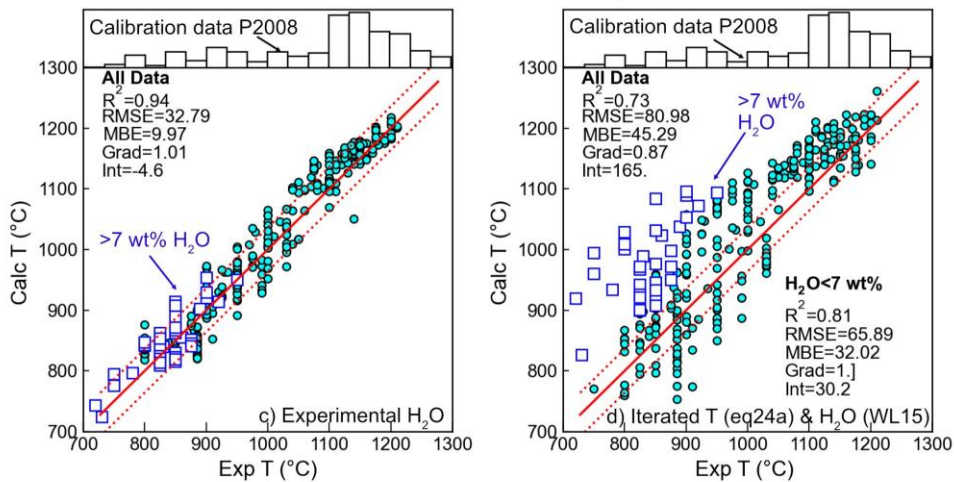


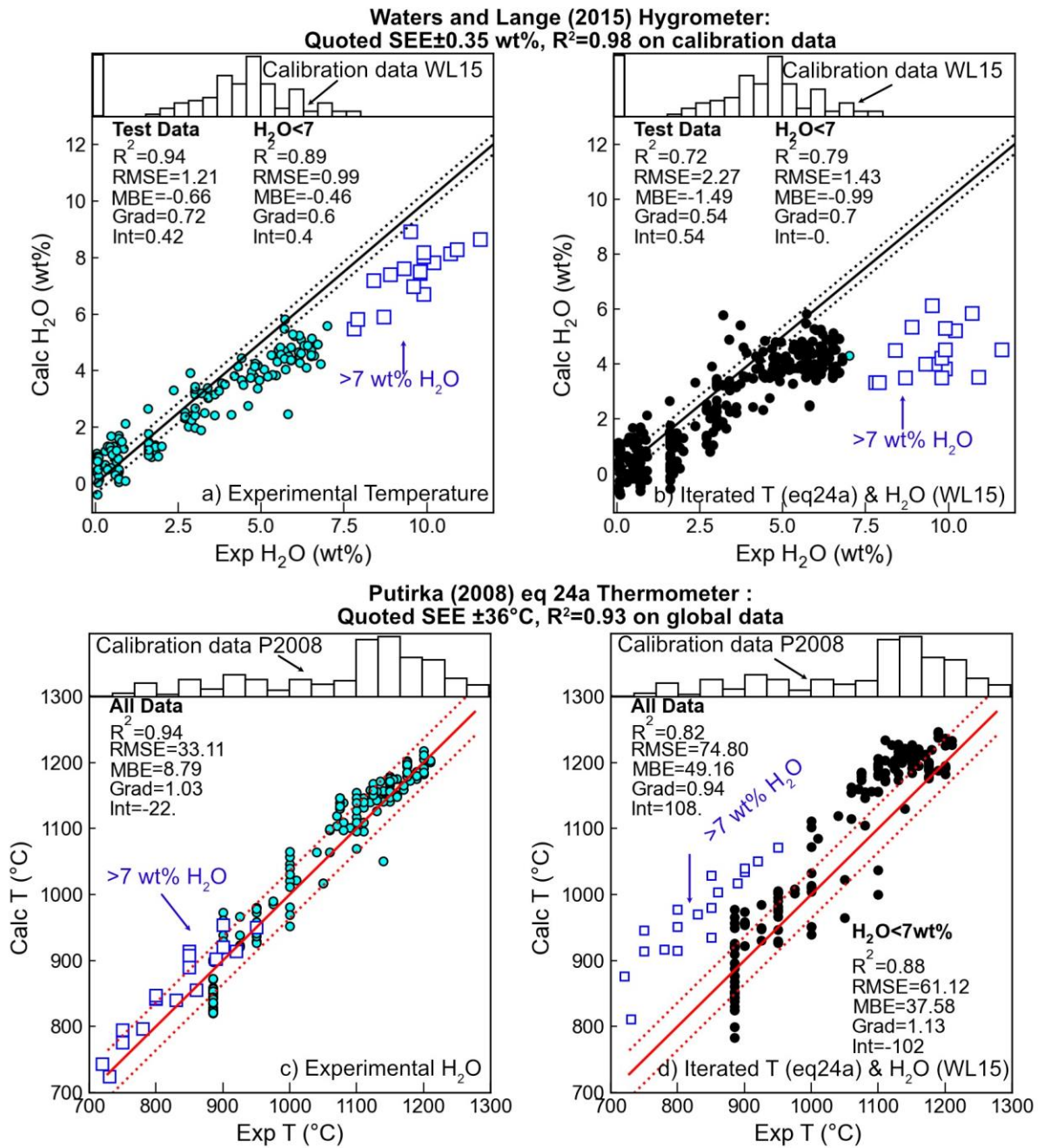
Supporting Fig. 9 –
Assessing Plag-Liquid equilibrium tests using our new dataset. WL15 – Waters and Lange (2015) calibration dataset. M19- Masotta et al. (2019) calibration dataset. Lower plots are the same as Fig 16 in the main text, but without application of any equilibrium filters.

Waters and Lange (2015) Hygrometer:
Quoted SEE ± 0.35 wt%, $R^2=0.98$ on calibration data

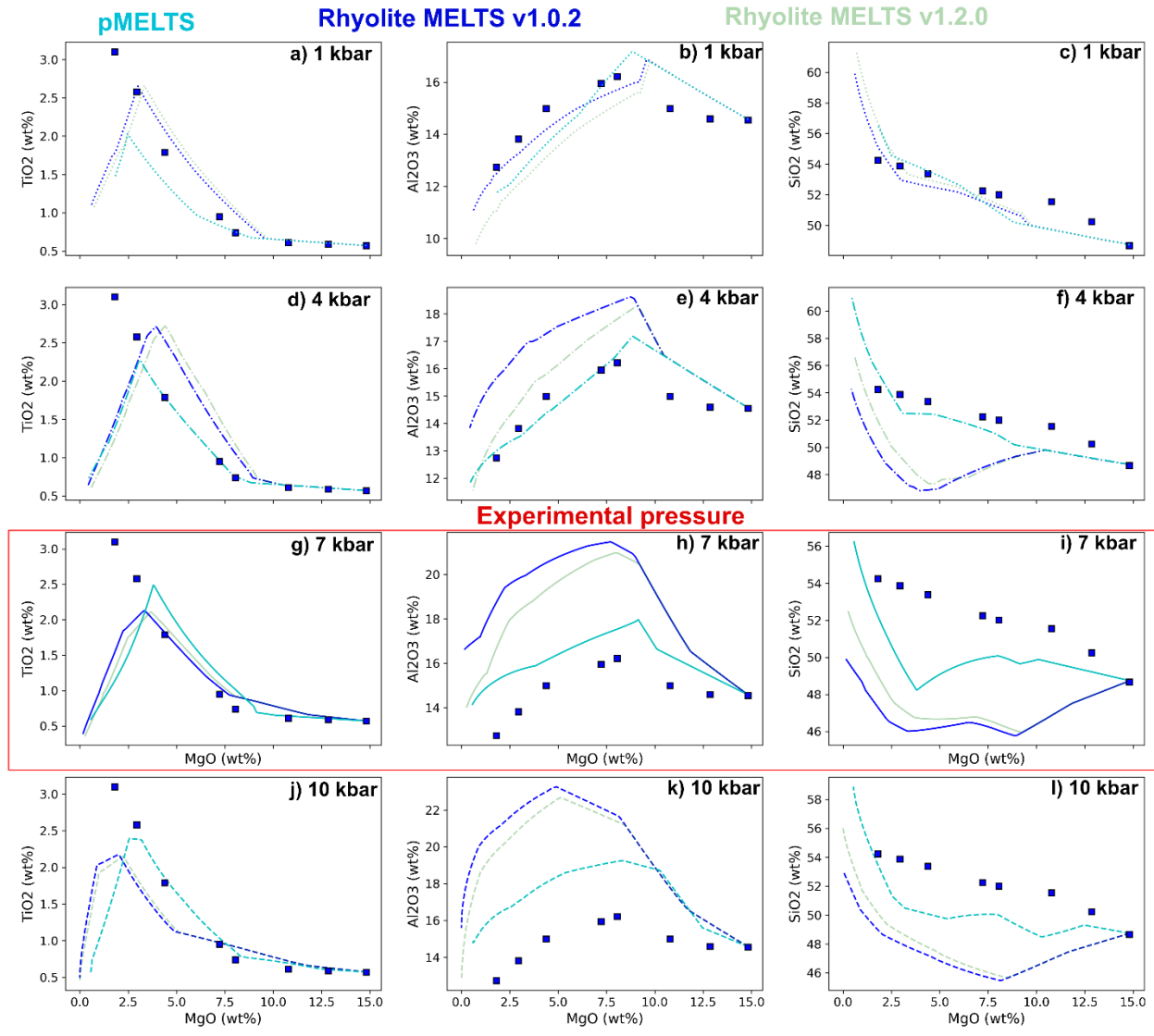


Putirka (2008) eq 24a Thermometer :
Quoted SEE $\pm 36^\circ\text{C}$, $R^2=0.93$ on global data

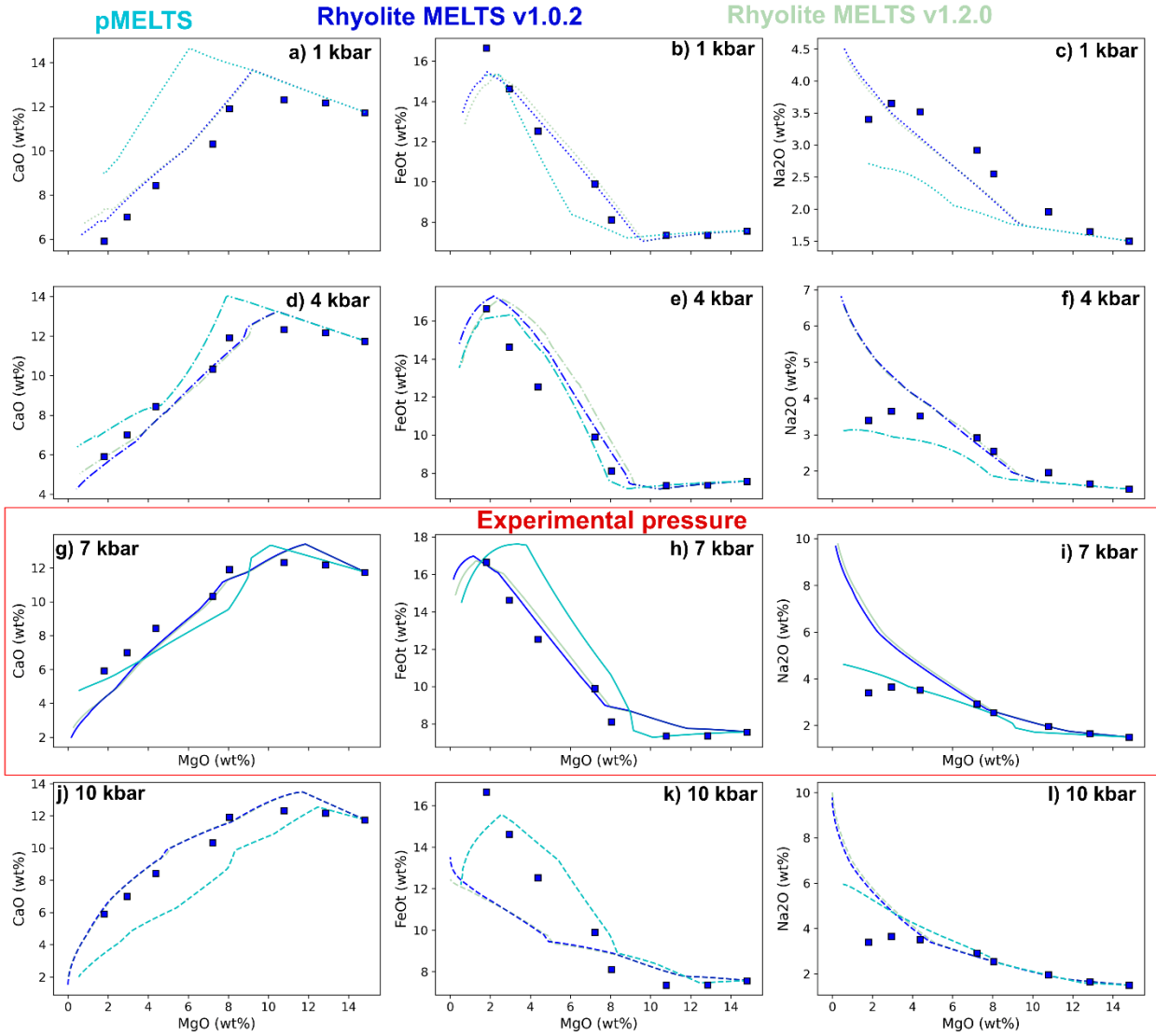




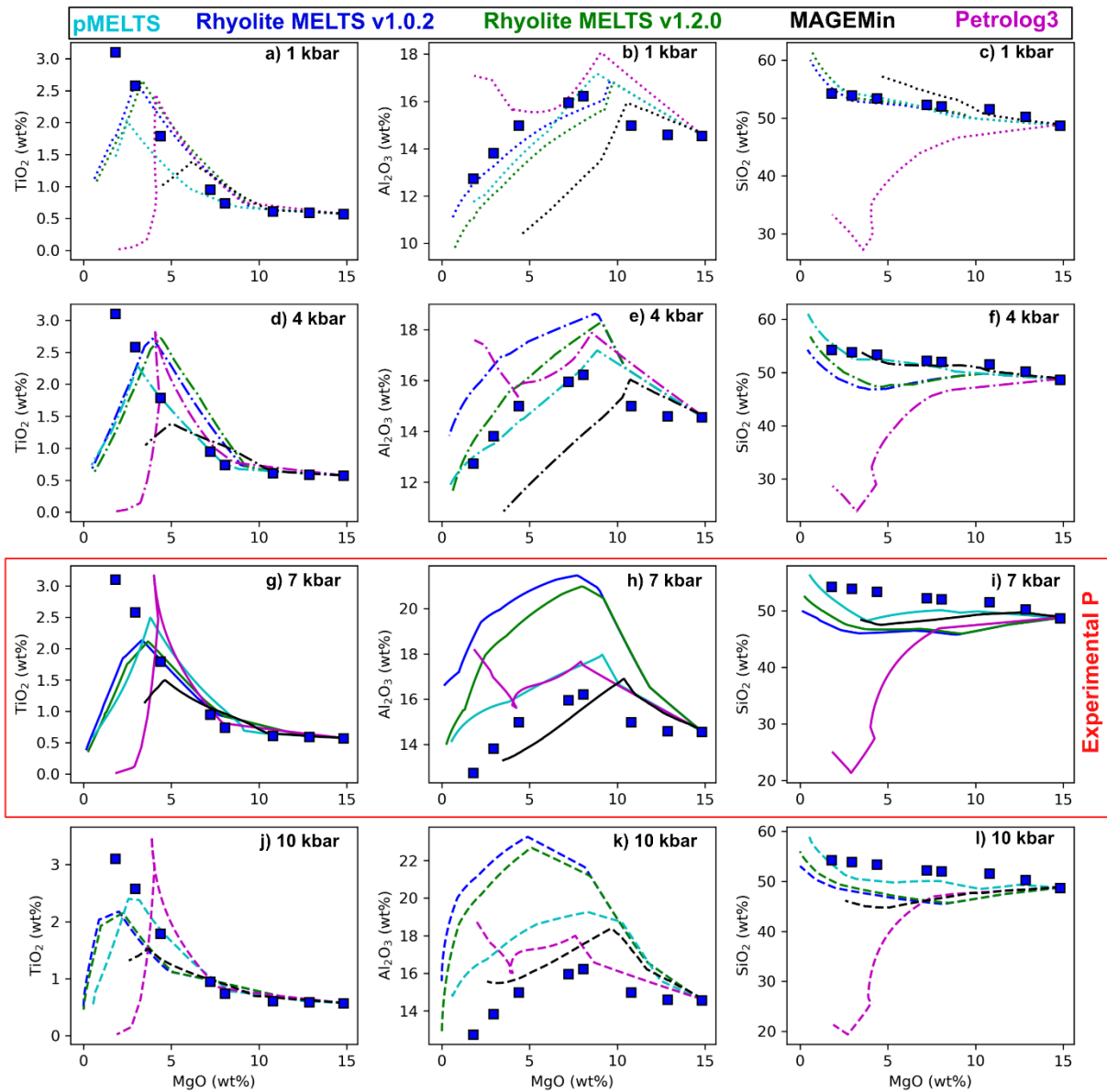
Supporting Fig. 10 – As for Fig. 16 in the text, but only using experiments where H₂O was measured using Raman, FTIR or SIMS.



Supporting Fig 11 – As for main text, but showing different MELTS models against the experimental data of Villiger et al. (2007).



Supporting Fig 12 – As for Fig. 11, but for different major elements



Supporting Fig. 13 – Models at 4 pressures for the Villiger et al. (2007) experiments, showing MageMin and Petrolog3